A MODEL STUDY OF THE BEHAVIOUR OF STEEP EXCAVATED ROCK SLOPES

A Thesis
Submitted To The
University Of London
(Imperial College Of Science And Technology)
For The Degree Of Doctor Of Philosophy
In The Faculty Of Engineering.

by Nicholas Ryland Barton B.Sc. (Eng.)

January 1971

ABSTRACT

Part I of the thesis describes the physical properties of an extremely weak and deformable model material, which is found to be ideally suited to the modelling of large gravitationally loaded rock masses. The strength-deformation characteristics are found to be very similar to those of rock at a reduced scale of 500 to 1. A method is described for generating parallel sets of tension fractures through the material. Tests on these interlocking model joints are compared with large scale shear tests on rock joints. The shear and normal stiffness of the model joints are found to dominate the deformation behaviour of the jointed material.

Part 2 of the thesis describes a detailed study of the behaviour of model tension joints in shear. Strength-size and displacement-size effects are evaluated, and a simple peak strength criterion for rock joints is derived. A closer estimate of the peak shear strength of surfaces of different roughness is obtained from a statistical analysis of the roughness profiles. The peak strength criterion is used to obtain approximate strength envelopes, by extrapolation of the results from back analyses of slope failures in southern Spain. The effect of peak and residual shear strength is demonstrated in a limit equilibrium approach to progressive failure of rock slopes.

Part 3 of the thesis describes the results of experiments on two-dimensional jointed model slopes. Preliminary tests were made on slopes which were rotated to induce failure. Large models were finally constructed, having three joint sets and approximately 40,000 discrete blocks. These were loaded horizontally to simulate different tectonic stress levels, and vertically by gravity. Open-cuts were excavated and the pre-failure displacements recorded photogrammetrically. The failures induced by excavation to increased slope angles were recorded on cine film. Some unexpected results of pre-consolidation were discovered.

ACKNOWLEDGMENTS

The author has been generously supported both academically, financially and technically during the course of a long research project. Without this support much of the work to be described would have been impossible. Sincere thanks are therefore expressed to the following:

Professor E. Hoek, supervisor of the author's research; Dr. J. Bray; Professor N. Morgenstern; Professor R. Goodman; for their many invaluable suggestions during the early stages of the project; Peter Cundall and Jim Markland for their kind help and computing expertise; Chris St. John, David Pentz, Dr. Herbert Kutter and Mike Freitas for their material contributions; the stimulating environment of Professor Hoek's Rock Mechanics Group at Imperial College. The author is also indebted to the Photogrammetry Department of University College, London for all the work they performed. In particular mention should be made of Mr. Ernie Wickens and Mr. Don Proctor.

The momentum generated by the above would have been dissipated without the generous financial support of Rio Tinto Zinc Corporation Ltd., on behalf of Rio Tinto Espanola, S.A.; Anglo American International (U.K.), Ltd.; Bongainville Copper Pty. Ltd.; Consolidated Goldfields, Ltd.; English China Clays, Ltd.; Iranian Selection Trust, Ltd.; National Coal Board Opencast Executive; Pallabora Mining Co. Ltd.; Roan Selection Trust, Ltd.; and seven member companies of the Australian Mineral Industries Research Association Ltd.

The experimental nature of most of the work called for a high degree of collaboration between designer and technical staff. The author is extremely grateful to Mr. John Sullivan, Mr. Frank Coombes, Mr. Laurie Wilson and Mr. Roger Sidey for their invaluable assistance, and for all the lessons learned at the expense of their time. Visual aid and photographic services were kindly supplied by Messrs. B. Harman, D. Murgatroyd and J. Gee, and sincere thanks are due to Miss Judith Richardson for all the typing, and to Mr. Barry Holt for the production of numerous copies of a rather heavy thesis.

This list of acknowledgments would be incomplete without mentioning the infectious enthusiasm of the late Professor A. Black, without whom the Slope Stability Project might not have been conceived.

CONTENTS

PART 1

CONTENTS

PART 2

CONTENTS

PART 3

CONTENTS

APPENDICES

INTRODUCTION

The complex nature of discontinuous rock slope behaviour was a subject imperfectly understood when this project was begun late in 1966. Despite advances in various parts of the world during this time, the subject is still in its infancy. Powerful numerical methods of analysis have been developed, but their use has helped to define the problem as much as solve it.

A detailed model study was undertaken in the belief that, at the time, no better method was available for evaluating the behaviour of discontinuous rock masses. Great care was taken to develop realistic model materials, and in particular model joints. Nearly two years were spent on these basic problems alone. As a result of these studies and the application of the methods to jointed slope problems, it must be admitted that a similar approach would be adopted if a new start were to be made at this time. The extremely sophisticated numerical methods which have been developed, while representing significant advances are, in real terms, extremely crude simulations of real processes.

It is believed that physical models, although extremely inflexible analogs, should always be used as a preliminary to numerical methods. Many of the latter would have developed differently if joint behaviour had been more clearly understood.

PART 1

1.1 PHYSICAL PARAMETERS OF ROCK MASSES AT REDUCED SCALE

SUMMARY

The differences between modelling underground rock excavations and rock slopes are discussed. These can be summarized as follows. Gravity induced stresses and joint properties must be carefully modelled in slope stability studies. Generally a slope model will be simulating a much larger dimension of jointed rock. This means that if simple gravity loading is to be used to load the model then the geometric scale factor will need to be unusually large.

A basic set of dimensionless products is presented which governs the model-prototype mechanical scaling. The most important one is found to be that which relates density, Young's modulus (or stress) and the geometry of model and prototype. This governs the scaling of all the stress-deformation properties.

The mechanical properties of intact rock are presented in diagrammatic form and the correctly scaled model performance is discussed. It is concluded that brittleness and brittle-ductile transition, tensile strength and compressive strength are properties which have an important bearing on the shear strengths of joints.

The mechanical properties of discontinuous rock are presented diagrammatically in the form of direct shear characteristics. The scaling of shear stiffness - the displacement at which the peak shear strength is mobilized, and the scaling of normal stiffness - relating joint closure and normal stress, are considered to be important properties of rock mass behaviour. It is concluded that model joints should ideally have a roughness geometrically similar to that of the particular large scale joints in the field. Then, given identical intact properties, the dilation across any shear surface will be correctly scaled. It is thought that the dilation occurring before peak strength is mobilized largely controls the peak shear strength envelope, and the post-peak dilation controls the eventual position of the failure surface since in certain cases continued dilation will arrest failure due to increases in normal stress and a consequent shear strength increase.

1.1 PHYSICAL PARAMETERS OF ROCK MASSES AT REDUCED SCALE

INTRODUCTION.

The laws of similitude relating the behaviour of a geomechanical model and prototype are extensively covered in rock mechanics literature. Buckingham's important second theorem, on which the entire theory of dimensional analysis is based, has been rigorously proved by Langhaar[1]. Hoek[2], Fumagalli[3] and Hobbs[4] to name only three, give fairly detailed discussions of the more significant factors affecting their particular modelling problems. In view of the fact that most of the available literature on geomechanical models concerns dams and foundations and underground excavations, it is perhaps advisable to pay some attention to the dimensional problems that are peculiar to the modelling of excavated rock slopes.

The fundamental differences between modelling underground rock excavations and surface or near surface rock structures can be divided broadly into two parts. Firstly, the dimensions of most underground excavations which are modelled are probably between one and two orders of magnitude smaller than the mean depth of the excavation below the surface. It has therefore been considered perfectly acceptable to ignore any gradient of stress due to the different depth below surface of the top and bottom of the excavations. By comparison, the mean depth of rock slope or open pit below surface is one half of the height of the slope. This reversal means that gravity induced stress gradients have to be modelled in the case of rock slopes, while they can justifiably be ignored in underground mine models.

Secondly, by the very nature of the different magnitude of the applied stresses, discontinuities dividing the rock matrix are fundamentally important to rock slope studies. Until recently discontinuities have been considered as relatively unimportant for the stability of underground excavations. Ergun[5] has found that in certain cases the presence of discontinuities can actually improve the stability of an underground excavation, due to the possibility of redistribution of stress in highly stressed zones. It seems therefore that more emphasis should be paid to the modelling of rock masses (implying the presence of discontinuities) in all forms of geomechanical modelling. It is in this respect that the highly complex problem of modelling the interaction of dams and their foundations is most unreliable. The lack of suitable model materials has also induced somewhat artificial methods of self-weight loading to be used in a problem which is, afterall, governed by gravity induced stress gradients to the same extent as rock stability.

There is a third though less important difference between near surface and underground model studies - the question of scale. It is considered important that a model of an open pit excavation should include the modelling of a large dimension of jointed rock beyond the pit limits. In this way the effect of the excavation on the applied stress distribution out at the boundaries of the model will be reduced. Excavated slopes in excess of one thousand feet depth are not uncommon, which means that acceptable models of open pit operations should have prototype dimensions of several thousand feet as a minimum. This is in marked contrast to models of underground excavations where in general, prototype dimensions are at least an order of magnitude less than this. Reconcilliation is therefore needed between available laboratory space and the smallest model-prototype scale factor that can be achieved.

1.1.1. DIMENSIONLESS PRODUCTS.

It is a simple matter to obtain the set of dimensionless products relevant to the problem in hand. The first step is to choose some basic parameters which are considered to be fundamental to rock mass behaviour. It is not necessary to make a comprehensive list since once the basic form of the dimensionless products has been ascertained, complications can be formulated at will.

The following parameters will be considered initially:

		Dimensions
σ_t	Tensile strength	$ML^{-1}T^{-2}$
σ_c	Compressive strength	$ML^{-1}T^{-2}$
σ	Local normal and)	$ML^{-1}T^{-2}$
τ	shear stress)	$ML^{-1}T^{-2}$
E	Young's modulus	$ML^{-1}T^{-2}$
ρ	Density	ML^{-3}
g	Acceleration due to gravity	LT^{-2}
L	Any linear dimension	L
ϕ	Angle of friction	-
c	Cohesion	$ML^{-1}T^{-2}$
K	Stiffness	$ML^{-2}T^{-2}$
ν	Poisson's ratio	-

The set of dimensionless products that can be obtained from these is as follows:

$$\sigma_c/\sigma_t\ ,\ \sigma_c/E\ ,\ \sigma/E\ ,\ \tau/\sigma\ ,\ c/\sigma_c\ ,\ \rho g L/E\ ,\ KL/\sigma\ ,\ \phi\ ,\ \nu.$$

For similitude to be achieved between model (m) and prototype (p), it is necessary that these dimensionless products be equal in model and prototype. For instance:

$$\left(\sigma_c/\sigma_t\right)_m = \left(\sigma_c/\sigma_t\right)_p$$

$$\left(\rho g L/E\right)_m = \left(\rho g L/E\right)_p$$

$$\left(\phi\right)_m = \left(\phi\right)_p$$

The most important equality to be satisfied is the second one relating density, Young's modulus and the geometry of model and prototype. It is this relationship which poses the problem of gravity loading. If a weak and deformable model material cannot be obtained then some means of increasing the self weight stresses must be found, such as loading the model in a centrifuge. At no stage was this method of loading considered feasable for a structure as complex as an open pit model, in which the whole mass is divided by systems of discontinuities.

Since it is therefore decided that simple gravity loading is to be applied in the model as in the prototype, the second equality reduces to:

$$\rho_m/\rho_p \cdot E_p/E_m = L_p/L_m$$

$$\text{or} \quad \psi \cdot \rho_m/\rho_p = \lambda$$

Where ψ = the stress scale factor
λ = the geometric scale factor.

This is an extremely important relationship which governs all the stress-displacement properties of the model. Once the geometric scale factor is chosen, all physical parameters with the dimensions of stress in the prototype will need to be reduced in a ratio:

$$1 : \rho_p/\rho_m \cdot \lambda$$

in the model. The density of the model material finally used in this study was approximately four fifths that of rock (see Section 1.2) Therefore a geometric scale factor (λ) of 1:500 results in a stress scale factor (ψ) of 1:666.

The time and velocity scale factors between a model and prototype depend on the ratio of the acceleration due to gravity between the two. Since this ratio has been made equal to one in this study, the time scale can be shown to be $(\lambda)^{\frac{1}{2}}$. Therefore the velocity scale is also $(\lambda)^{\frac{1}{2}}$ since the dimension of velocity is (L/T).

It will be obvious that the scale factor (λ) controls the scaling of joint spacing, displacements, depths of excavation and all things connected with the geometry. Having presented these fundamental similitude requirements it is necessary to look in more detail at some of the physical characteristics of rock masses underload. In doing so the dimensionless products will be extended to cover a more comprehensive range of physical behaviour particularly with regard to shearing of rock masses.

1.1.2 SCALING THE MECHANICAL PROPERTIES OF INTACT ROCK

Suppose that a cylinder of rock 1 inch in diameter and 2 inches long is tested in unconfined compression, giving a peak strength of σ_c. It is usually most convenient to test the same size of model specimen. Suppose that this gives a peak strength of (σ_c/ψ). It would appear that the strength scale factor is adequately defined by the ratio of these two strengths. However, interpreting the model test correctly it will be realized that the model represents a cylinder of rock (λ) inches in diameter and (2λ) inches in length. Inserting the geometric scale (1:500) this represents approximately 42 feet in diameter and 84 feet in length.

There are two impractical solutions to this problem. The model cylinder could be correctly scaled geometrically, giving dimensions of 0.002 inches in diameter and 0.004 inches in length. Alternatively an in-situ test of a cylinder of rock 42 feet by 84 feet could be carried out in the field. Unfortunately even a compromise between the two extreme sets of dimensions would not be entirely satisfactory due to the presence of discontinuities in the rock: For instance, in-situ compression tests on 4 feet by 8 feet of rock, and laboratory compression tests on model cylinders 0.1 inch by 0.2 inch would be practical possibilities, and would still satisfy the theoretical geometric scale factor. However, even for the most massively jointed rock the presence of micro fissures and small joints causes a reduction in compressive strength (σ_c) the larger the specimen of supposedly intact rock that is tested. The author is unaware of any large scale experimental evidence of this effect for hard rocks, except indirectly from plate-bearing tests. However several authors report of a significant strength-size relationship for coal. Evans and Pomeroy[6] have found marked strength variation for such small size ranges as $\frac{1}{8}$ inch to 2 inch cubes. Bieniawski[7]

reported reduction of strength up to cube dimensions of 60 inches, though there seems no reason why he should consider this a limiting size.

It would be unreasonable to suggest that hard rock might behave in as marked manner as coal because obviously the mode of origin and physical structure of coal sets it apart from the large majority of rock types. In addition, when testing very large cubes the end effects and machine stiffness become significant variables of the test. The problem will remain unresolved therefore until more data from large in-situ tests becomes available in time. These arguments demonstrate perhaps as well as any the need for large scale tests, and the need is particularly acute where realistic physical modelling is to be achieved. It might therefore be better to interpret the model with this strength-size effect in mind at least in a qualitative sense. Thus a model material of strength ($\sigma c/\psi$) is in reality scaling a prototype rock such that the strength simulated is actually somewhat greater than σc.

Figure 1.1.1 shows diagrammatically the model-prototype scaling relations that should ideally to satisfied if a model material is to be taken as a realistic physical model of unjointed (intact) rock. It is probably true to say that the properties of joints developed in the model material will be more closely representative of unweathered rock joints if these strength-deformation conditions are satisfied, since shear failure of interlocking rock surfaces incorporates several phenomena of intact rock.

The dimensionless axial strain at failure (ε) and the brittle-ductile transition phenomena encountered in triaxial tests shown in diagrams (a) and (b) are two important properties in this respect. The true contact stresses across mating rock joints are in reality very large compared to the apparent contact stresses and this probably means that joint behaviour will not be governed entirely by brittle fracture phenomena. Likewise, the tensile strength (σ_t) and the compressive strength (σc) , may both be important properties, the first concerning pre-failure tensile fracture in the base of joint asperities, and the second the residual shear strength which results from the crushing of debris on the shear surface.

Diagram (c) shows in a qualitative manner that the triaxial strength envelopes of model and prototype should be geometrically similar. A more useful quantitative comparison is shown by diagram (d), where the triaxial peak strength data (in the compressive range) is divided by the uniaxial compressive strength thereby reducing it to dimensionless form. In this case model and prototype curves should be identical. In the same way the modulus ratio ($E/\sigma c$) proposed by Deere[8] as a simple rock classification system is a useful dimensionless number for comparing the model and prototype performance directly, rather than qualitatively. In Section 1.2 the

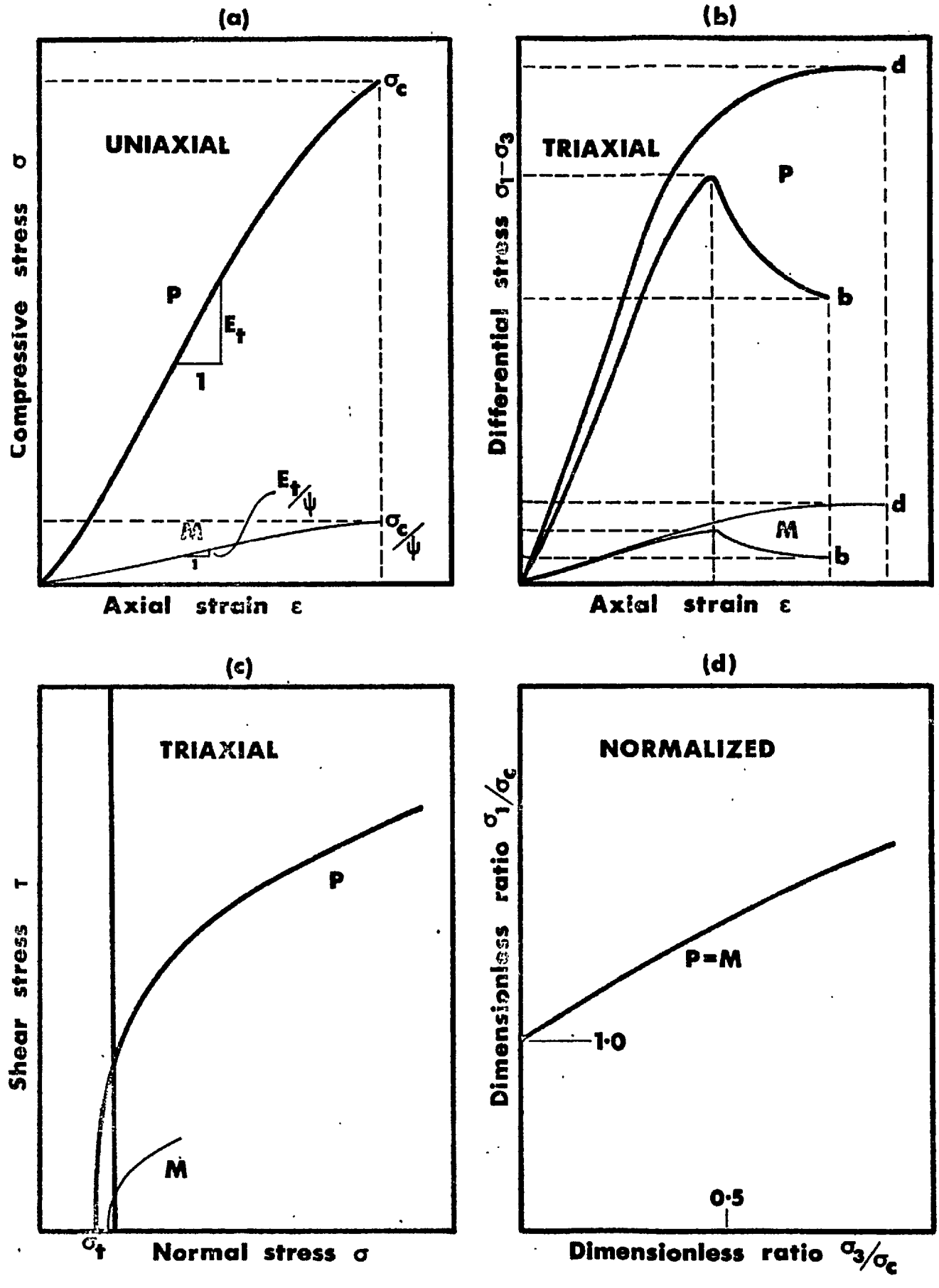

Figure 1.1.1 Model-prototype scaling of the properties of intact rock

comparison of model and prototype performance is extended qualitively using normalized strength data appearing in the literature.

1.1.3 SCALING THE MECHANICAL PROPERTIES OF DISCONTINUOUS ROCK

The scaling of shear strength properties of rock joints differs in one important aspect from the preceeding arguments. Since a joint is a discontinuity of the intact properties it is no longer realistic to describe stress-displacement characteristics in terms of stress-strain data. There is undoubtedly a stiffness-size effect with respect to direct shear properties of rock joints, but this will depend on the effect of joint roughness. It is therefore customary to describe direct shear tests of joints in terms of shear stress-displacement data, while the peak and residual strengths are plotted conventionally as shear stress-normal stress values.

Figure 1.1.2 shows four diagrammatic representations of joint behaviour in direct shear. Suppose that for one of the prototype curves in diagram (a), the peak shear strength (Tp) is mobilized after a displacement of (dp) horizontally - representing a shear stiffness (Ks) of (Tp/dp). When modelling this stiffness the dimensionless product given in part 1.1.1 has to be satisfied. Thus the model shear stress - displacement data should be scaled as follows:

$$T_p/\psi \quad \text{versus} \quad d_p/\lambda$$

and for the residual strength:

$$T_r/\psi \quad \text{versus} \quad d_r/\lambda$$

Since the stress scale factor (ψ) is usually larger than the geometric scale factor (λ), the stiffness of the model joint as defined above should be lower than that of the prototype - one and a quarter to one in this case.

The same arguments apply to the normal stiffness (Kn) of joints. The closure (dn) of a joint under a given normal stress (σ_n) causes an important reduction of the deformation modulus of a rock mass compared to the Young's modulus of the unjointed matrix. It is therefore an important property to be modelled.

The dimensionless ratios (Tp/Tr) and (Tp/ σn) which are sometimes presented in the literature (Krsmanovic[9] and Krsmanovic, Tufo and Langof[10]) need to be identical for the model and prototype.

Diagram (c) shows the form of a dilation diagram, which is the graph of vertical and horizontal displacements across a joint during direct shear. The angle of dilation (incremental dv/dh) has considerable influence on the gradient of the peak strength

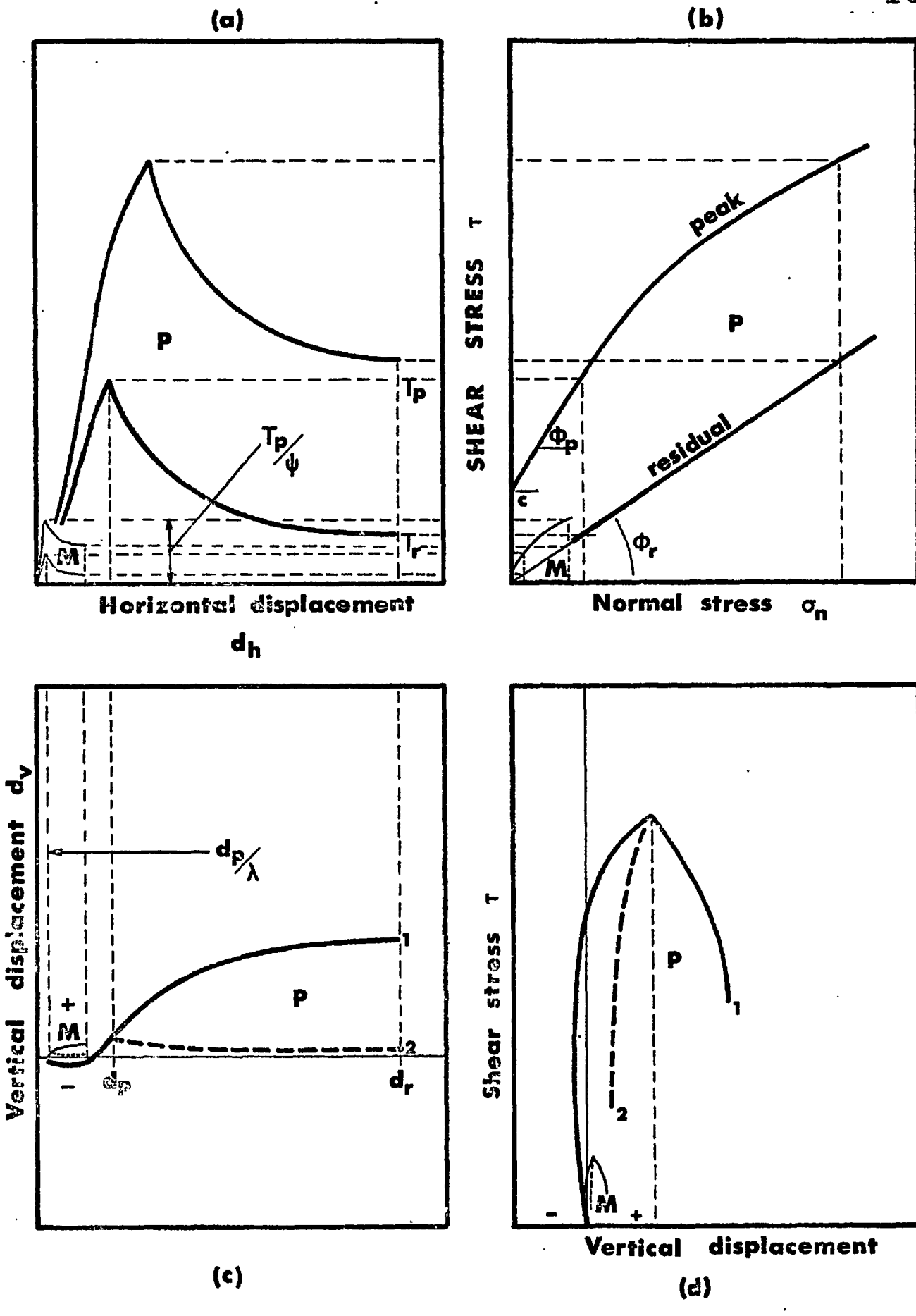

Figure 1.1.2 Model-prototype scaling of the direct shear performance of joints in rock

envelope (diagram(b)). In addition, the degree of roughness of a joint surface more or less dictates this peak angle of dilation at the stress levels under consideration. Therefore it will probably not be possible to satisfy the relation:

$$(\tau / \sigma_n)_p = (\tau / \sigma_n)_m$$

unless the joint roughness in the model is geometrically similar to that of the prototype large scale rock joint. Very rough model joints tested under low normal stress levels will automatically produce a very steep peak shear strength envelope. This means that the relevant angle of friction (ϕ) and probably the cohesion intercept (c) will be too high compared to the prototype. The cohesion intercept (c) for the prototype joint should of course be reduced to (c/ψ) in the model.

In general the true residual strength envelope will pass through the origin, since after large displacements the strength potential is purely frictional. Thus the residual strength envelope for the model joint should follow the same line as that of the prototype, implying also that the residual angle of friction (ϕ_r) should be identical for model and prototype.

Diagram (d) shows two possible shear stress - dilation relationships. No.1 represents a shear test at a normal stress level that is low enough for the rock joint to continue to dilate (at a reduced rate) after the peak strength is passed. No. 2 represents a test at a much higher normal stress such that the post-peak dilation is prevented. (The peak angle of dilation will in reality be less for the latter than for the former.) Along a potential shear surface in-situ, any fundamental differences between the dilation characteristics of the model and prototype will cause important local differences in the mobilized shear strength due to different normal stress changes occurring during continued shear. Alternatively, the actual position of the failure surface may be governed by dilation properties to such an extent that irreversible failure will occur only on a shear surface which does not develop significant normal stress increases during shear. Having satisfied this condition failure will then be governed by the conventional stress-strength laws.

It can thus be appreciated that the post-peak dilation characteristics can in certain cases assume more importance than the small pre-peak dilation; which largely controls the conventional shear strength. This can readily be appreciated for the case of stability of underground excavations.

It has already been suggested that the shear characteristics of clean interlocking rock surfaces are dependent to a large extent on several phenomena of intact rock failure. It would seem therefore that a realistic model material must first scale the properties of intact rock. If geometrically scaled joint surfaces can then be

produced in the model material, there is a good chance of correct scaling of the discontinuous properties which, taken separately, are far more important to slope stability than the intact properties, but in reality are inseparably linked to them.

1.2 PHYSICAL CHARACTERISTICS OF THE UNJOINTED MODEL MATERIALS

SUMMARY

An unusually low strength brittle model material was developed from a cured combination of red lead-sand/ballotini-plaster-water.

The mechanical properties are reported under three test catagories: uniaxial compression, tensile (Brazilian) and triaxial compression. Model materials with unconfined comression strengths as low as 5 lbf/in^2 could readily be produced and the values of Young's moduli for a range of strengths gave acceptable modulus ratios of between 350 and 560. In addition to a range of strengths, it was possible to obtain a range of deformation properties for a given strength of material. The Brazilian disc tensile test indicated a ratio of tensile to compressive strength of up to 1 to 10.

The series of triaxial tests at low confining pressures (0 to 3½ lbf/in^2) are reported in detail and indicated a further useful property: the intrinsic shear characteristics could be altered for a given strength of material by variations in the sand/ballotini proportions in the mix.

The model material behaviour in unconfined and triaxial compression is critically examined in relation to two rock classification systems. From the comparisons drawn, the unjointed material appears to be particularly well suited to many aspects of rock mechanics modelling, where self weight loading and large geometric scale factors are required.

Appendix 1. contains details of the preparation of the unjointed model materials.
Appendix 2. contains details of the compression test equipment (uniaxial and triaxial) and some comments on the stiffness of these machines.

1.2 PHYSICAL CHARACTERISTICS OF THE UNJOINED MODEL MATERIALS

In order that a model study should provide quantitative information on rock slope failure it is important that relevant strength-deformation parameters which govern the behaviour of the rock slope should be correctly scaled. The parameters and scaling factors relevant to intact rock behaviour have been discussed in detail in Section 1.1. It will be sufficient to summarize here that for the relationship between the strength scaling, the geometric scaling and the density to be satisfied, a model material having both high density and low strength will need to be employed. This problem is peculiar to rock slope modelling, and to similar studies where gravity induced stress gradients are of importance. In addition the prototype scale of a slope stability study is so large that unless capital and laboratory space are unlimited then very large geometric scale factors have to be employed.

The combined effect is that a model material has to be found which is considerably weaker and denser than those commonly in use in engineering rock mechanics modelling. Of the large number of materials in use none appeared suitable for the present problem. An extremely comprehensive survey of existing materials is given by Stimpson.[11]

After careful consideration of the problem of modelling an open pit mine in a gravitationally loaded model, a geometric scale factor of 1:500 was adopted. If an average rock density ρ_p of 160 lbf/ft^3 is assumed, then with ρ_m equal to, say 120 lbf/ft^3 the stress scale ($\frac{1}{\mu}$) would be fixed at 1:666. Thus, if similitude was to be attained, all mechanical properties in the model material with the dimensions of stress would need to be $\frac{1}{666}$ times those of the prototype rock. Model densities less than 120 lbf/ft^3 would mean that even lower strength materials had to be found.

Strength and deformation range

The design of the model material was not directed towards the modelling of any specific rock type or lithological group. The aim throughout was to produce a material which exhibited (at reduced scale) the broadly characteristic properties of rocks as a group of materials, both in terms of strength and deformation properties. The range of strength in engineering practice clearly demanded a range of model strengths, if the same scale factors were to be employed throughout. This basic requirement was readily satisfied. However, the variations in deformation properties for a given strength of material were not so easy to simulate. This, and the mode of failure under given stress systems were two features demanding special attention. As a general rule, it may be true to say that rock characteristics

will be more closely approached in a model material if the constituent elements of this material are derived from rock.

For the present it will be helpful to state the approximate range of basic strength and deformation properties which were dictated by engineering rock mechanics experience in open pit mines. Unconfined compressive strengths of between 5000 and 25000 lbf/in^2 were generally to be expected of unweathered rock. Selecting a medium value for the modulus ratio (E/ϵ) of rock types of 400 (See Deere[8]), the zone of interest with respect to values of Young's modulus was approximately 2×10^6 to 10×10^6 lbf/in^2. With the possible stress scale (ψ) of 1:666 for a material density of 120 lbf/ft^3, it was necessary to consider the following ranges of unconfined compressive strengths and Young's moduli in the potential model material:

σ_c 7.5 - 37.5 lbf/in^2

E_t 0.3×10^4 - 1.5×10^4 lbf/in^2

The tensile strengths which were to be achieved are difficult to state categorically, since there will be some variety depending on the testing technique employed (Hobbs [12]). Broadly speaking a ratio of compressive to tensile strength (σ_c/σ_t) of between 10 and 20 was considered to be acceptable, though clearly there are rock types having values on either side of this range. The maximum range of tensile strengths dictated by these figures was approximately 0.4 to 3.8 lbf/in^2 for the model.

The axial strain at failure associated with unconfined and triaxial compression tests is dimensionless and needs to be the same for the model and prototype. A range of between 0.15 and 0.4% for unconfined failure strains was considered broadly representative of the required brittle behaviour. The failure strains under triaxial compression vary widely, depending on the strength of the specimens and the confining pressure employed, and no attempt was made to state any range of acceptable behaviour.

Having stated the approximate range of basic properties that were required from a potential model material, it may be of interest to summarise the properties of some of the many test mixes which were tried before the successful combination of red lead - sand/ballotini-plaster-water was arrived at.

1.2.1 PRELIMINARY TRIAL MIXES

The search for suitable materials began with exploratory tests on plaster-sand mixtures, which have been used by several research workers, including Hobbs[4]. His technique for reducing the strength of the material by curing at about 90°C was adopted from the start and was used throughout for plaster cemented

materials (See Appendix 1.) Two drawbacks to this material relating to the present study, were the relatively high axial strain (ε) at failure (0.7 to 0.9%) in unconfined compression) and low density (between 80 and 90 lbf/ft^3). However, the unconfined compressive strength could be reduced to about 15 lbf/in^2 without difficulty, by suitable reduction of the plaster-sand ratio. The ratio of $\sigma c/\sigma t$ measured by Hobbs varied between approximately 1.5 and 3 which was disappointingly low for this study.

The need for a high density filler was clearly indicated. A large number of trial mixes were tested so that the most suitable high density powder could be found. Plaster and water with barite ($BaSO_4$), litharge (PbO), iron powder (H_2 reduced) and red lead (Pb_3O_4) were tried separately and some in combination. Densities as high as 170 lbf/ft^3 were obtained with barite-iron powder-plaster-water mixes, but for all the mixes tested the strength was never below about 60 lbf/in^2, and the strains at failure ranged above 0.7%. The plaster-filler ratio was reduced almost to the point where no set could occur. It appeared that some of these high density powders acted as retarders in much the same way as celite retards the setting of plaster-water systems (Raphael[13]).

The following table summarises some of the mixes tested. These were generally pourable, and set without too much 'bleeding' and settlement in the moulds. They were rejected from mechanical considerations. All results are the mean from unconfined compression tests on about five specimens of each mix.

SECTION 1.2

Table I : The Properties of some trial model materials

Mix components	Weight proportions	Properties of the minimum strength mix				
		σ_c	$E \times 10^4$	E/σ_c	ε %	ρ
S-P-W	600-150-250	19.4	0.32	165	0.79	89
Fe-P-W	1500-200-360	183.4	1.54	84	-	177
Fe-Ba-P-W	1050-220-220-300	67.8	1.96 / 0.81	290 / 120	0.75	172
Pb-P-W	950-160-350	111.6	3.13	280	0.68	139
Pb-Fe-S-P-W	250-150-500-25-200	6.2	0.23	372	0.40	139

Where the symbols are as follows:-

S = sand W = water
P = plaster Fe = iron powder
Ba = barium sulphate
Pb = lead sesquioxide (red lead)

The units of (σ_c) and (E) are lbf/in^2, and of the density (ρ), lbf/ft^3. It will be noticed that two values are given for the Young's modulus of the third material. The stress-strain curve was distinctly bi-linear, with the transition at a stress level of about one half of the compressive strength. All the materials containing iron powder rusted during curing, and perhaps for this reason were rather unreliable from the point of view of reproducibility, and reasonably linear stress strain curves.

The finally adopted combination of red lead-sand/ballotini-plaster-water was unique in that the fine red lead powder acted both as a lubricant to the sand during mixing, and increased the density to an acceptable level without retarding the setting of the plaster. A large number of trial mixes were performed before a ratio of red lead-sand/ballotini of 1 : 2 by weight was chosen as the optimum. Full details of the preparation of this material are given in Appendix 1., together with a design chart for the three series of mixes, A,B and C which contained different ratios of sand/ballotini thereby altering their shear characteristics.

SECTION 1.2

The results of the strength and deformation testing are reported under three separate categories:-

1. Unconfined compression test
2. Tensile test
3. Triaxial test

1.2.2. UNCONFINED COMPRESSION TEST

Prismatic specimens with the dimensions 1" x 1" x 2" were chosen as the standard for unconfined compression testing. The ease of fabrication of multispecimen moulds, and the speed of removal of set specimens were obvious reasons for the choice. The specimens were tested not only for ultimate compressive strength results for the various mixes, but also for the value of Young's modulus (E_t) at 50% of the ultimate compressive stress, the percent strain at failure, and the bulk density from weight measurements.

In Table 2, details of the nine mixes are given, together with the weight proportions of the constituent materials, which were read off the mix design chart (see Appendix 1.) Mix numbers 1 and 5 for each of the types A, B and C were not tested in this series, since they were a little to each side of the zone of interest when scaled up to prototype stresses. In the right hand column values of the dimensionless modulus ratio (E_t/σ_c) are given.

Table 2 : Unconfined Compression Test Details

Type/ mix	Pb_3O_4-sand/ballotini-plaster-H_2O	σ_c (lbf/in^2)	$E_t \times 10^4$ (lbf/in^2)	ε_f (%)	ρ (lbf/ft^3)	E_t/σ_c
A2	600-1200/0- 75-435	10.3	0.36	0.37	123.1	350
A3	600-1200/0-100-442.5	17.8	0.73	0.37	122.2	410
A4	600-1200/0-125-450	31.9	1.44	0.40	123.7	450
B2	600-0/1200- 75-397.5	15.6	0.79	0.29	122.8	510
B3	600-0/1200-100-405	28.7	1.60	0.29	122.7	560
B4	600-0/1200-125-412.5	49.7	2.56	0.33	121.6	520
C2	600-600/600- 75-416	8.6	0.40	0.29	122.1	470
C3	600-600/600-100-423.5	20.14	1.07	0.31	121.2	530
C4	600-600/600-125-431	29.85	1.45	0.34	120.8	480

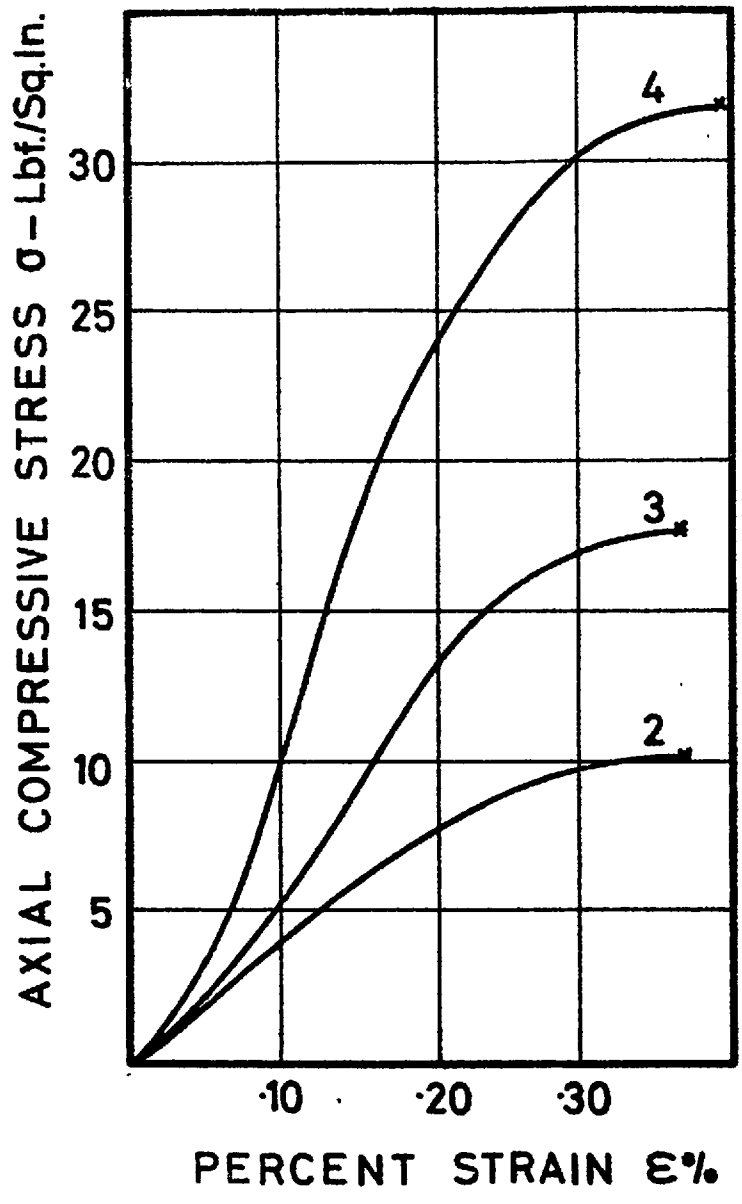

Figure 1.2.1 Stress-strain curves for type A, mixes 2,3 and 4 in uncenfined compression

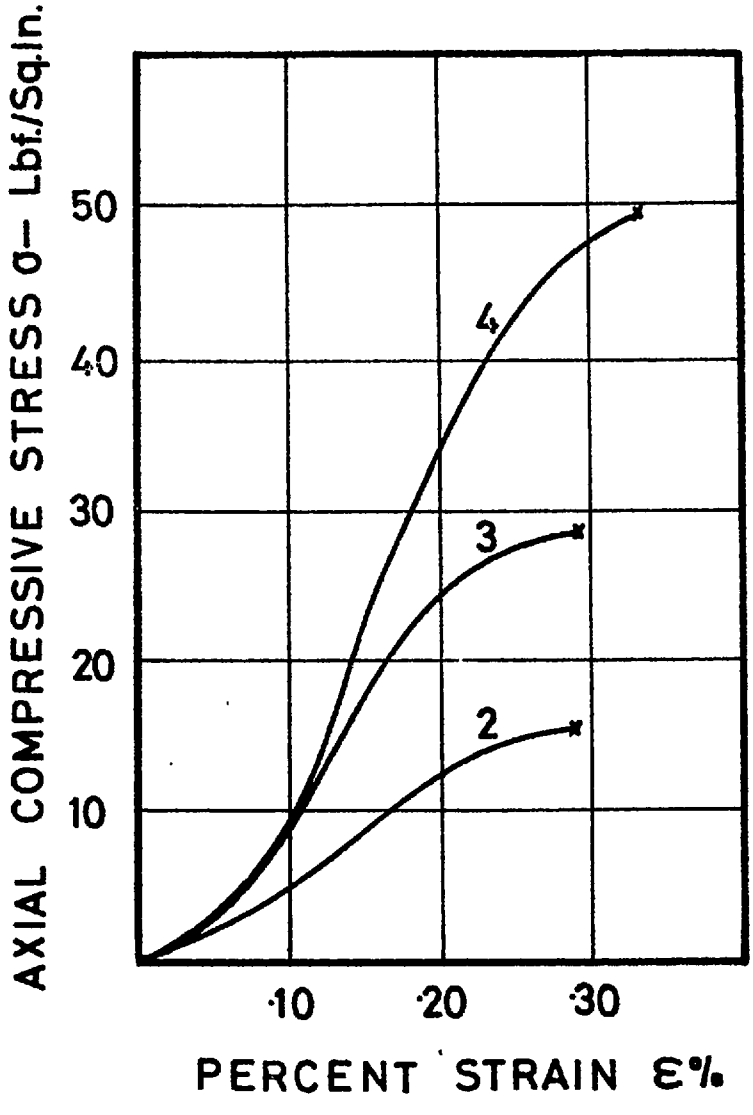

Figure 1.2.2 Stress-strain curves for type B, mixes 2,3 and 4 in unconfined compression

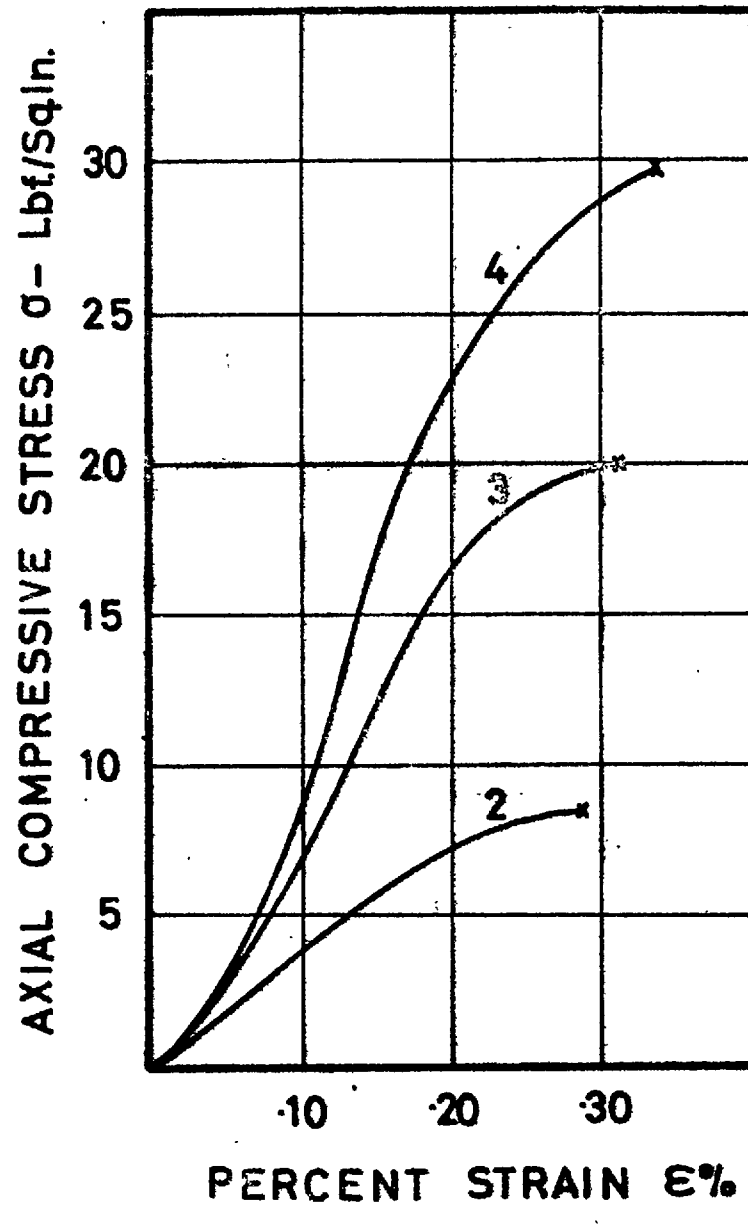

Figure 1.2.3 Stress strain curves for type C, mixes 2, 3 and 4 in unconfined compression.

SECTION 1.2

(a) Deformation behaviour

The stress-strain curves of type A, B and C mixes for mix designs 2, 3 and 4 are given in Figures 1.2.1., 1.2.2, and 1.2.3 respectively. Each curve represents the average stress-strain readings for the twelve prisms cast from each mix. The scatter of results of ultimate compressive strength was as high as 15% in one or two cases, but the large majority of results were within 10% of the mean for that batch. Type A mixes produced the greatest scatter and type C mixes the least. The problem of variability of batches of sand is discussed in Appendix I. Obviously a large volume of mix will tend to reduce the scatter.

The apparently high rates of initial strain of the specimens are clearly visible in all the stress-strain curves and may be due to 'bedding-in' of the end faces. With a material so weak and abrasive it was not possible to prepare end faces on a lathe, and the smoothness was entirely dependent on the care with which the specimens were slid out from the lightly greased moulds. There may have been certain minor irregularities which caused an uneven stress distribution in the early stages of testing. It is reasonable to conclude that the axial failure strains measured were probably higher than they would otherwise have been, if perfect end faces could have been prepared. The behaviour was, however, sufficiently brittle for this aspect of performance to be acceptable. It was concluded in Section 1.1 that the model specimens should be interpreted as representing 42ft by 84ft. of prototype rock. The strength-size effect of rock ensures therefore that the model behaviour was in fact adequately brittle.

(b) Modes of Failure

The mode of failure of the specimens is clearly seen in Figure 1.2.4, which shows a selection of typical failed specimens. A particularly noticeable effect was the difference in behaviour between ballotini and sand specimens after the peak strength was passed. A much more rapid fall-off in strength occurred for the lower friction ballotini specimens. In some cases the shear resistance of the fracture was insufficient to support the weight of the upper part and this slid down the surface of rupture.

(c) Strength Behaviour

The high strength of the B mixes clearly demonstrates the effect of porosity on the set strength. The water demand of the 100% ballotini mixes was some 8% less than that of the 100% sand mixes. The reason for this is thought to be chiefly due to the much reduced friction and ease of pour with ballotini mixes, but it will also be partly due to the greater specific surface area of the sand. The net result was a lower porosity and higher strength

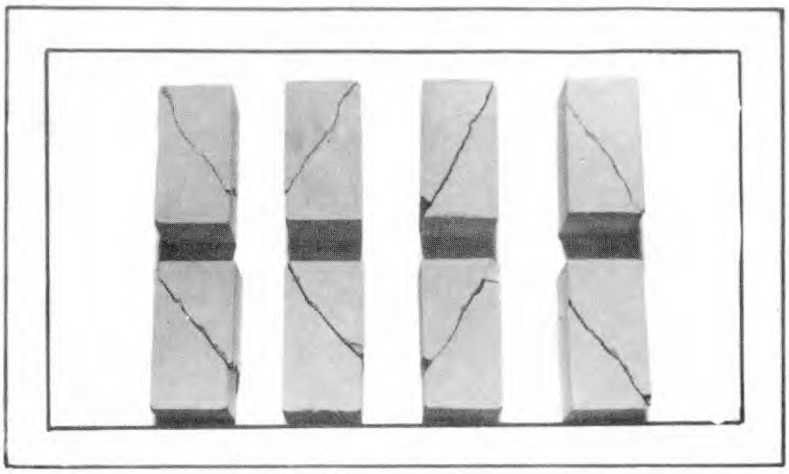

Figure 1.2.4 Failure of model material in unconfined compression

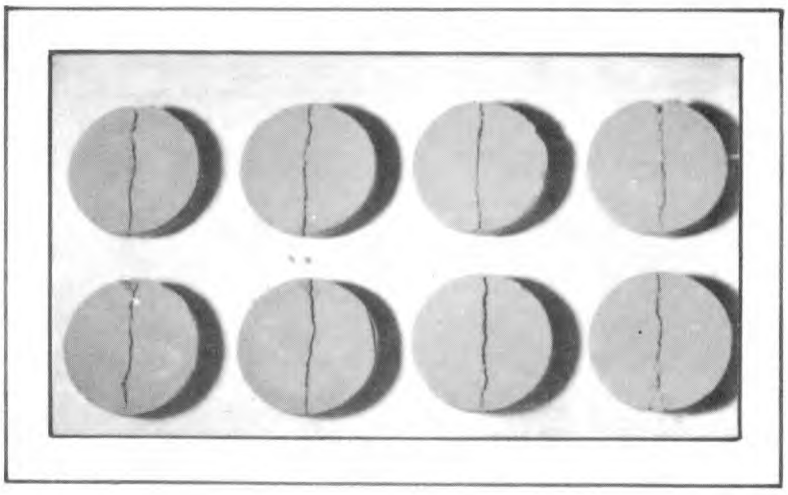

Figure 1.2.5 Failure of model material in tension (Brazilian disc test)

for cured ballotini mixes. The effect of this appeared to override the lower internal friction of the latter, which is clearly seen in the triaxial results which appear later.

It will be clear from the results of the unconfined compressive strength (σ_c) for the range of mix types, that the material broadly satisfied the basic strength requirements which were outlined earlier. With the possible exception of the B mixes, any strength of material in the given range could be produced by suitable adjustment of the quantity of plaster used.

(d) Effects of Vibration on the Mechanical Properties

The results of an investigation into the effects of vibrating partially set mixes are reported here. The technique would appear to have very promising application to the more sophisticated of model studies. The tests were performed on only one material, a mix similar to A1 but containing one of the two sands that were finally rejected in favour of Kingslynn (SS), (See Appendix I). The study was in three parts, and each set of unconfined compression tests were made on six 1" x 1" x 2" prisms of the material. Firstly, the mix was poured into the mould and allowed to set without any vibration, the set occurring three to four minutes after pouring. Secondly, the mix was poured and allowed to stand undisturbed for 1 minute, following which it was vibrated for 15 seconds, and then allowed to set. Thirdly, the mix was vibrated for 30 seconds, again 1 minute after pouring into the moulds. The comparative effects on the stress-strain curves are given in Figure 1.2.6 where each curve is the average for 6 specimens. Three fundamental changes are seen:-

(i) A reduction in the strain at failure (0.42% to 0.28%)
(ii) A reduction in the ultimate compressive strength (6.60 to 4.95 lbf/in^2)
(iii) An increase in Young's modulus (0.19 x 10^4 to 0.29 x 10^4 lbf/in^2)

No. (i) may be attributed to an increase in density with vibration, with a little of the excess water reaching the surface before the set occurs, thus reducing the porosity of the set material. This may also explain No. (iii). However, it is felt that a different explanation is needed to clarify No. (ii). No vibration was applied until one minute after pouring, and it seems probable that during this time a skeleton network of gypsum crystals was establishing itself. Two explanations for the reduction in strength appear credible:

a) Vibration causing partial destruction of the network of crystals, with consequent malformed crystals limiting growth in the final period before setting, and constituting flaws in the material.

b) An anisotropic reorientation of crystal growth due to the consolidating effect of vibration. The consolidation

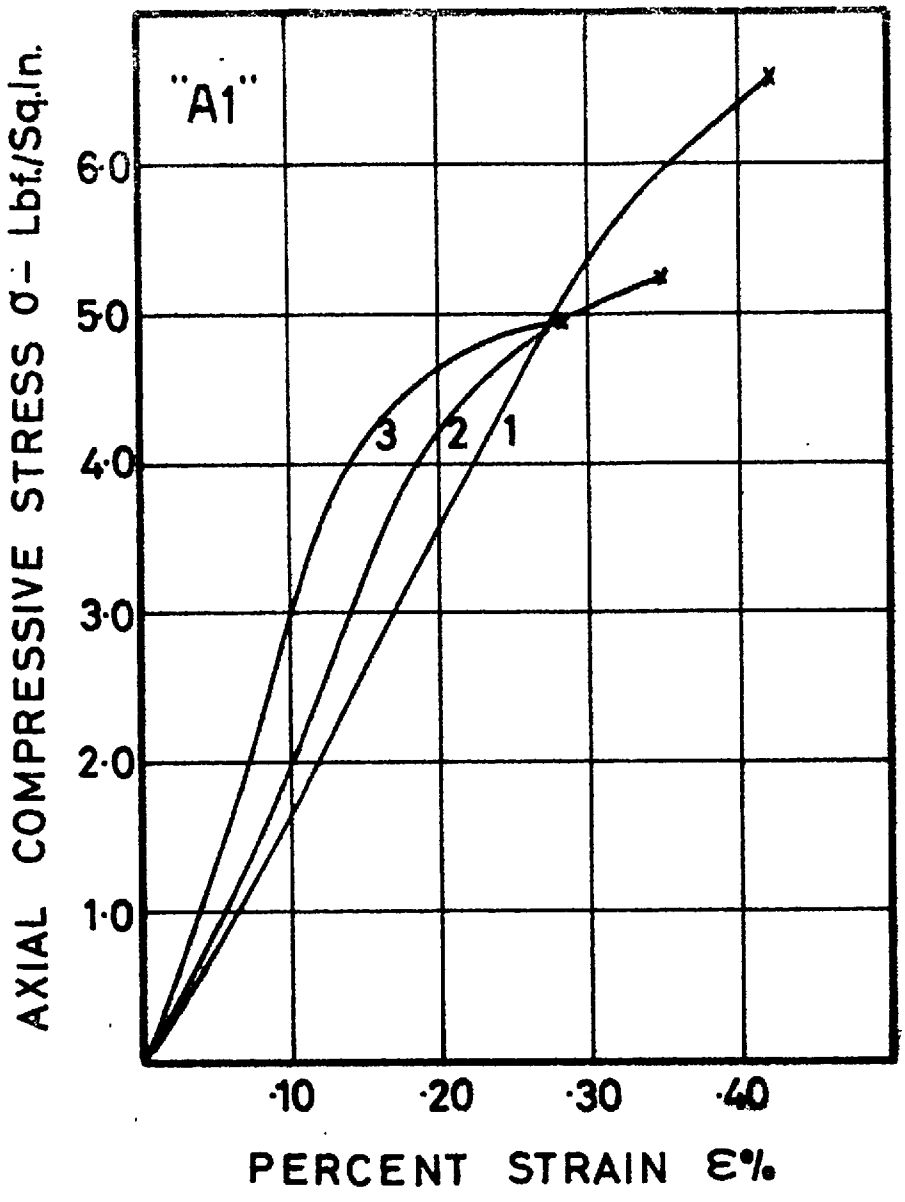

Figure 1.2.6 Stress-strain curves of vibrated mix

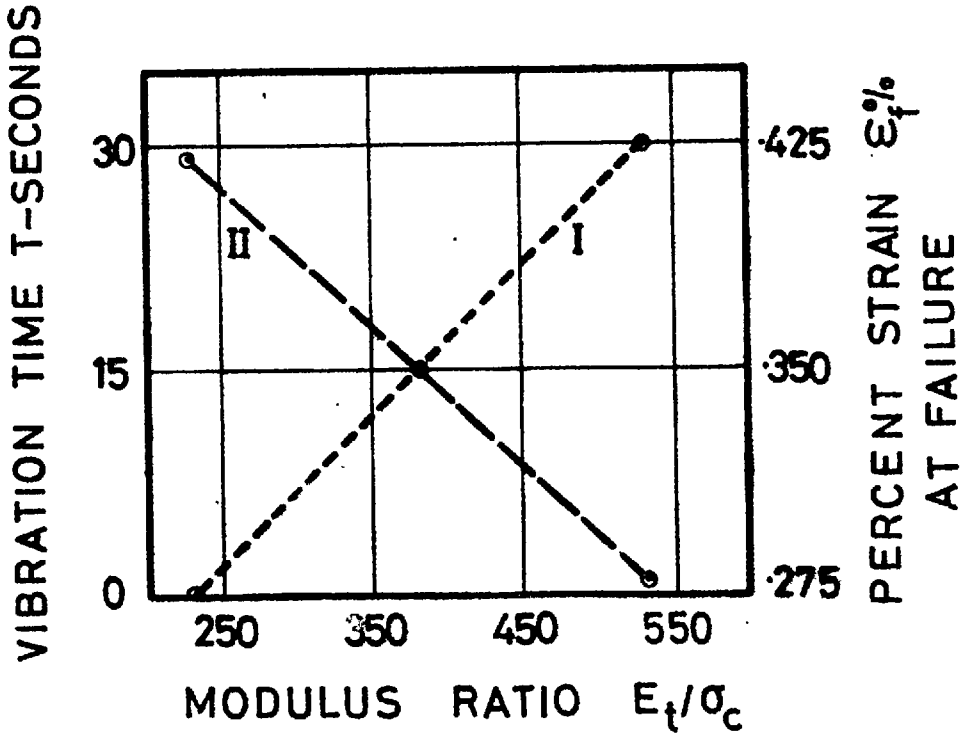

Figure 1.2.7 I Vibration time vs. modulus ratio.
II Percent strain at failure vs. modulus ratio

was in a direction perpendicular to the long axis of the prisms as tested.

The net effect as stated was a material which failed at a lower unconfined compressive stress the more vibration it was subjected to during the partially set phase. Two surprising results emerge from these tests. Figure 1.2.7 shows the following plotted results:

(i) Periods of vibration (0,15 and 30 seconds) vs. modulus ratios are in apparent linear relationship

(ii) Strains at failure vs. modulus ratios are also in apparent linear relationship.

Obviously, a more comprehensive testing programme is needed to confirm the linearity, but nevertheless, the trends indicated were of considerable interest. These results are discussed later in relation to the engineering classifications for intact rocks given by Deere[8].

1.2.3 TENSILE TEST

A test in wide use for determining the tensile strength of rocks was selected, so that the model results could be more easily related to the bulk of data available. The Brazilian disc test consists of loading a disc across a diameter, which causes a partly uniform tensile stress to be set up in a direction at right angles to the loaded diameter. The magnitude of the stress (σ_t) at failure is related to the applied load (P), the disc thickness (L) and the diameter (D) in the following manner:-

$$\sigma_t = \frac{2P}{\pi DL}$$

The disc diameter used was 1.50 inches and the thickness 0.25 inches. These dimensions, when inserted in the above equation, give:

$$\sigma_t = 1.70\ P \text{ lbf/in}^2 \quad \text{for P measured in lbf.}$$

Four mix types were tested, namely A2, B2, C2 and C3. Two separate batches of each mix were cast, each producing four solid discs and two cylindrical specimens. The average results are given in Table 3.

Table 3 : Brazilian Test Results

Mix Type	No. of Specimens	Average σ_t (lbf/in^2)	Average $\frac{\sigma_c}{\sigma_t}$
A2	8	0.84	8.10
B2	5	1.44	8.45
C2	7	0.87	10.27
C3	7	2.44	7.62

A total of five disc specimens were rejected, one through careless handling and the other four for suspect failure mechanisms. Hobbs [12] has drawn attention to the types of failure which may be observed in such tests. Four of the eight typical failed specimens shown in Figure 1.2.5 appear to have wedge-shaped fractures adjacent to one or other of the loading plattens. The problems of handling failed discs were in great part responsible for these. At the point of failure no wedges were visible, but the slightest jar after removal from the plattens frequently caused some of this previously highly stressed zone to crumble and drop out. In every case a small 'flat' was observed on the curved edge of the disc adjacent to the plattens, by the time the failure load was reached.

The average values of the ratio of compressive to tensile strength (σ_c/σ_t) lie between 7.6 and 10.3, which is an encouraging indication of the rock-like characteristics of the material. The ratios of σ_c/σ_t in excess of 10 found in many rock materials are believed to be due to the existence of Griffith type flaws in the grain boundaries of these materials (see review by Jaeger [14]). In the case of the model material the shape of the pores is difficult to imagine, but it seems possible that the major pore spaces will not only occur in the interstices between the grains of sand, but also partly around the grains, thereby making a semi-continuous network. This argument is based on the assumption that the layers of water which surround the saturated grains become pore spaces after curing. The process of dissociation may be responsible for the production of extremely fine flaws in the cementing crystals, but the material will probably not contain the potential Griffith type flaws mentioned above.

1.2.4 TRIAXIAL COMPRESSION TEST

For a representative picture to be gained from this series of low pressure triaxial tests, it is necessary to relate the confining pressures used to the prototype scale. Since the modelling of open pits was the major problem under consideration in this study

the triaxial test programme was chosen to cover the behaviour of rock at a depth equal to the pit slope height, and also to a depth more than twice this dimension, for a representative structural response to be observed. This involved simulating up to two thousand feet of overburden for, say an eight hundred foot deep pit.

If the condition of confining pressure equal to the overburden pressure is considered, then for a rock of density 160 lbf/ft^3 the confining pressure equivalent to 2000 feet of rock overburden is 2220 lbf/in^2. With a stress scaling (ψ) of 1:666 this reduces to approximately 3.3. lbf/in^2. The range of confining pressures chosen for the tests was in fact, 0 to 3.4 lbf/in^2. This low pressure range made it necessary to employ a mercury U tube manometer for sensitive measurement of the confining pressure. A diagram of the apparatus is given in Appendix 2 (Figure 4.2.1), together with details of the adjustments which have to be made when calculating the exact pressures acting on the specimens.

The 3" x 1½" diameter specimens were tested dry, under 'full drainage' conditions. There was no possibility of testing the material in a saturated state (under either effective stress conditions or drained) since, on contact with water, it rapidly lost the little strength it had and became non-brittle. A thin rubber membrane was used to isolate the specimens from the confining water, and was sealed to the capping plattens with O ring rubber seals. The latter were made as loose as possible (consistent with no leakage) to reduce the possible damage to the specimens during assembly.

For a given mix type, two specimens were tested at each of the six confining pressures. Two batches of each mix were mixed and cast separately and all the results reported here are the average of two tests each from separate batches.

The results of tests on four of the mix types; namely A2, B2, C2, and C3 are given in Table 4. Axial strain measurements were obtained for the whole range of each test by direct computation from the loading ring dial gauge readings and from the known rate of jack advance, which was carefully measured under test conditions beforehand. The time taken to reach the failure stress ranged between about three minutes for the specimens under low confining pressure up to about twenty minutes for the weakest specimens tested at the highest confining pressure of 3.42 lbf/in^2.

Table 4 : Results of the Triaxial Tests

σ_3 (lbf/in^2)	σ_1 at failure (lbf/in^2)/% axial strain at failure							
	A2		B2		C2		C3	
	σ_1	ε	σ_1	ε	σ_1	ε	σ_1	ε
0	8.29	0.40	14.89	0.24	7.40	0.34	15.21	0.28
0.25	10.44	0.57	15.41	0.27	8.90	0.46	17.59	0.32
0.85	11.73	0.63	17.36	0.29	8.73	0.45	19.71	0.45
1.71	13.97	0.77	17.59	0.39	10.70	0.97	22.20	0.53
2.56	17.17	1.63	19.60	0.46	13.73	2.58	23.72	0.87
3.42	20.82	4.51	21.88	0.62	16.39	5.30	25.79	1.15

(a) Deformation behaviour

Materials A2 and C2 deformed axially far more than B2 or C3, and there appeared to be a rapid increase in the percent failure strain for the two highest confining pressures. This characteristic is clearly shown by Figure 1.2.8, which gives the failure strain vs. confining pressure behaviour of the four mixes. Large increases in strain can be seen for the two weak materials when tested under confining pressures above one quarter of their unconfined compressive strength. The same may be the case for B2 and C3 but the confining pressure range only extended to about 20 or 25% of their unconfined strength, so the effect could not be verified.

The behaviour of C3 with increasing confining pressure can be seen in Figure 1.2.9, which is a plot of the axial load vs. the axial strain for the six pressures applied. There was a slight increase in Young's modulus with increasing confining pressure and the behaviour close to failure became increasingly non-linear with increasing confining pressure, indicating a brittle-ductile transition.

(b) Poisson's ratio

An inportant characteristic which was not investigated was the Poisson's ratio for the material. It is clear that some method which is less constraining than strain gauging must be employed, since the material was weak enough to be drastically effected by any high modulus skin of cementing agent. The nature of the material and its general similarity to rock would indicate that the values of Poisson's ratio were likely to be less than 0.2 and the hypothesis of a reducing porosity with increasing applied stress suggests that values may have been actually below those common to rocks.

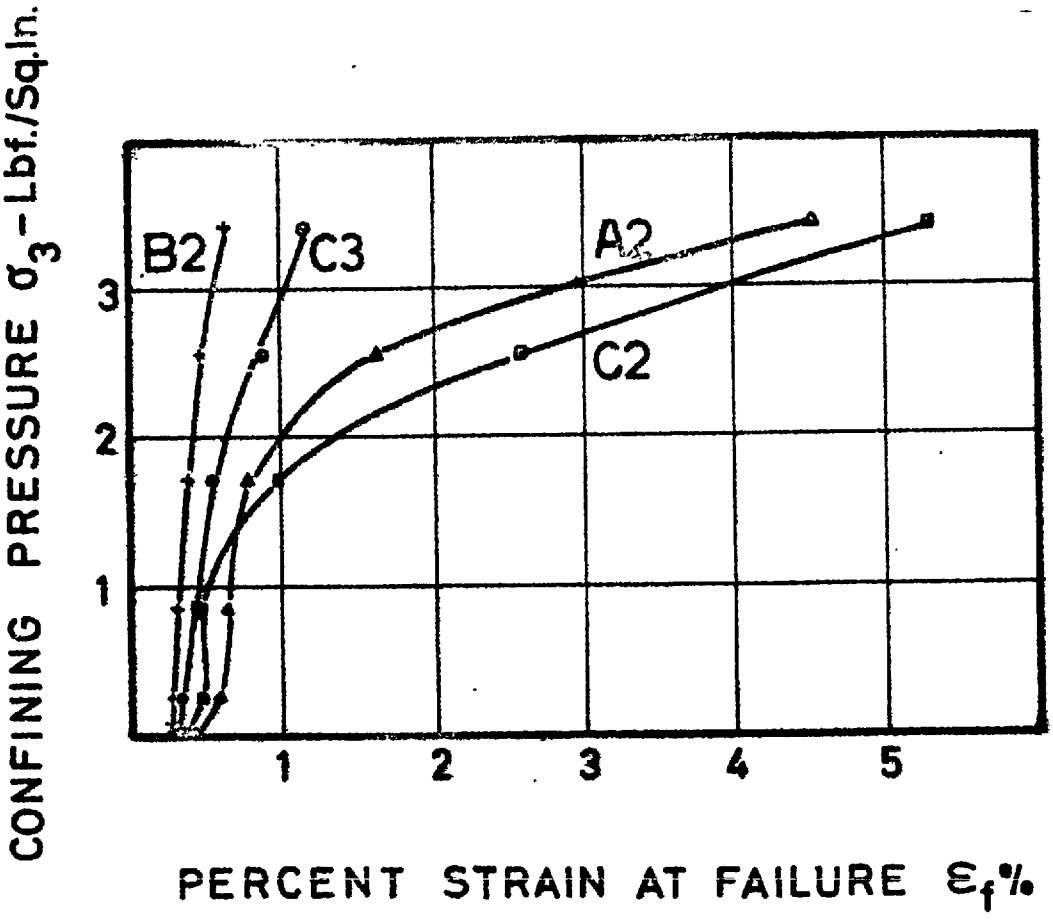

Figure 1.2.8 Relationship between confining pressure and percent axial failure strain for mixes A2, B2, C2 and C3

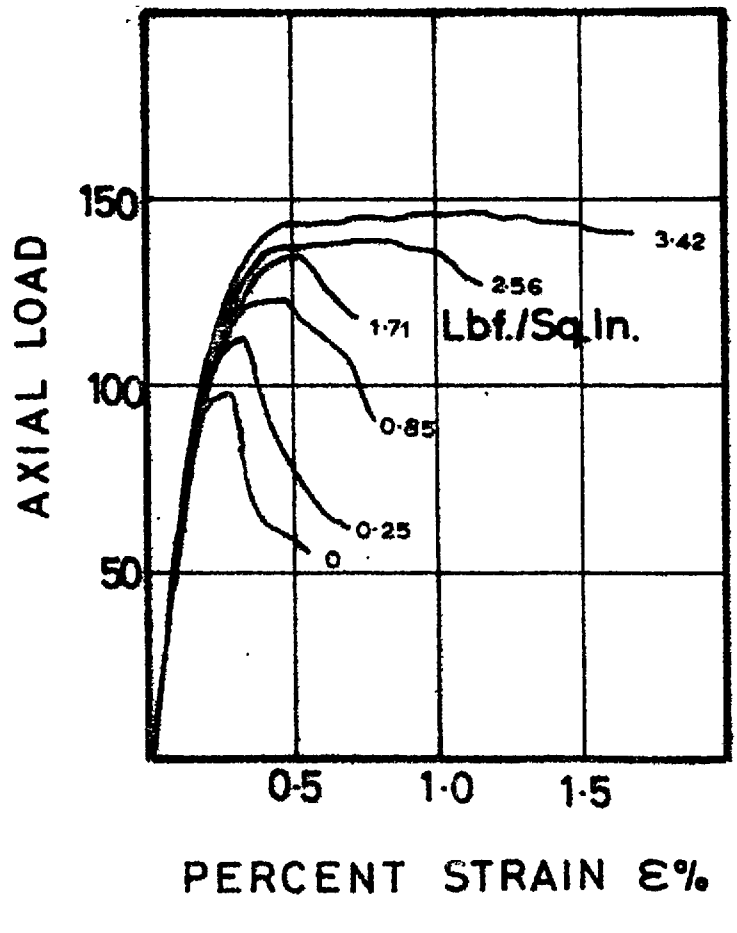

Figure 1.2.9 Axial load - axial strain curves for mix C3 at six confining pressures

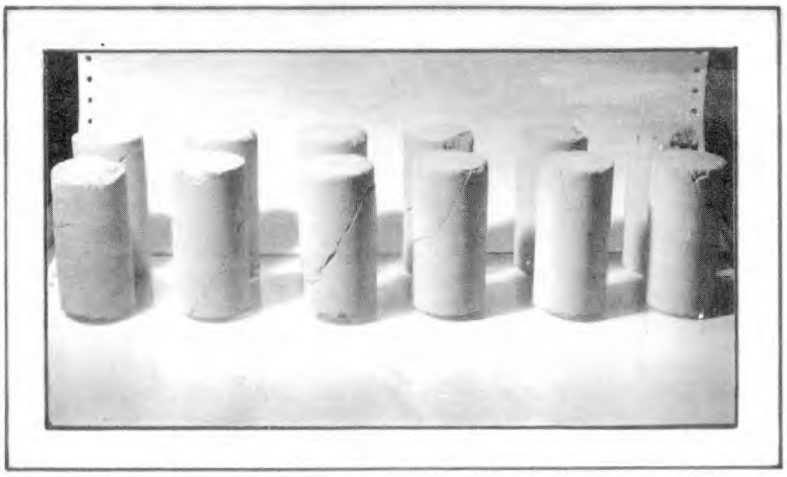

Figure 1.2.10 Failure of model material in triaxial compression

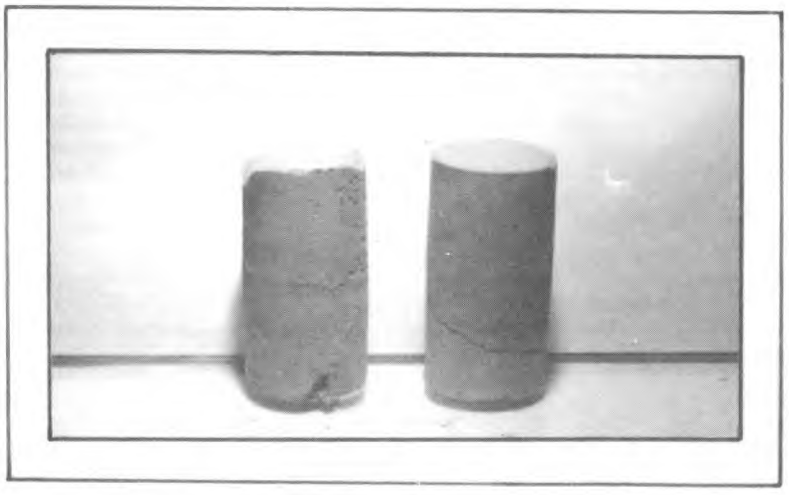

Figure 1.2.11 Barrelling of the low strength specimens when tested under the highest confining pressure

(c) Modes of failure

The modes of failure of the specimens can be seen in Figure 1.2.10. Each pair are representative of the failed specimens of each confining pressure. At the lowest σ_3 values (right hand side), the failure surface appeared partly conical. In addition, several near-vertical fractures were developed in the thin-walled 'shell' surrounding the cone. At higher confining pressures most failure surfaces appeared to be single and steeply inclined, with a slight curvature across their faces. Two specimens are highlighted in Figure 1.2.11. They were typical of the weakest mixes (A2 and C2) tested at the highest confining pressure. Large axial strains occured in these two materials (4.51% and 5.30% respectively) before the maximum stress was reached, and slight barrelling can be seen, particularly in the left hand specimen. In this state the specimens had to be handled with extreme care, as the whole of the central zone was badly fractured and in an extremely friable state.

(d) Strength behaviour

The Mohr rupture envelopes for the four materials A2, B2, C2 and C3 are given in Figure 1.2.12. Two conclusions can be drawn from a qualitative examination of the results: (a) the two lowest strength mix types A2 and C2 demonstrate a greater increase in strength with confining pressure than was the case for B2 or C3; (b) the slopes of the rupture envelopes for type C mixes lay between the upper limit of A (100% sand) and the lower limit of B (100% ballotini). This was of particular significance since it indicated that the intrinsic shear characteristics of the material could be manipulated at will between the two limits, by altering the constitution of the coarse filler.

A simple and much better method for comparing the rates of strength increase with confining pressure is obtained by plotting the results of the axial stress at failure (σ_1) directly with the values of confining pressure (σ_3). It is of great advantage if this function can be in dimensionless form, so that the model results can be compared directly with those of rock materials. A simple technique used by Hoek[15] and Franklin[16] consists of dividing the data by the respective unconfined compressive strengtths, thus converting the data to normalised form, i.e. σ_1/σ_c, σ_3/σ_c. Figure 1.2.13 shows a normalised plot of the results for the four materials A2, B2, C2 and C3. The large strength increase for A2 and C2 is shown particularly clearly with this typw of plot.

The two failure criteria discussed above allow a visual comparison to be made between the triaxial performance of the model material and the performance of the rock material that is being simulated. Correct strength scaling requires geometrically similar Mohr rupture envelopes and geometrically identical normalised plots. In the final part of this Section, some of the mechanical properties of the model material will be briefly discussed in relation to two broad systems of rock classification developed from unconfined and triaxial compression results.

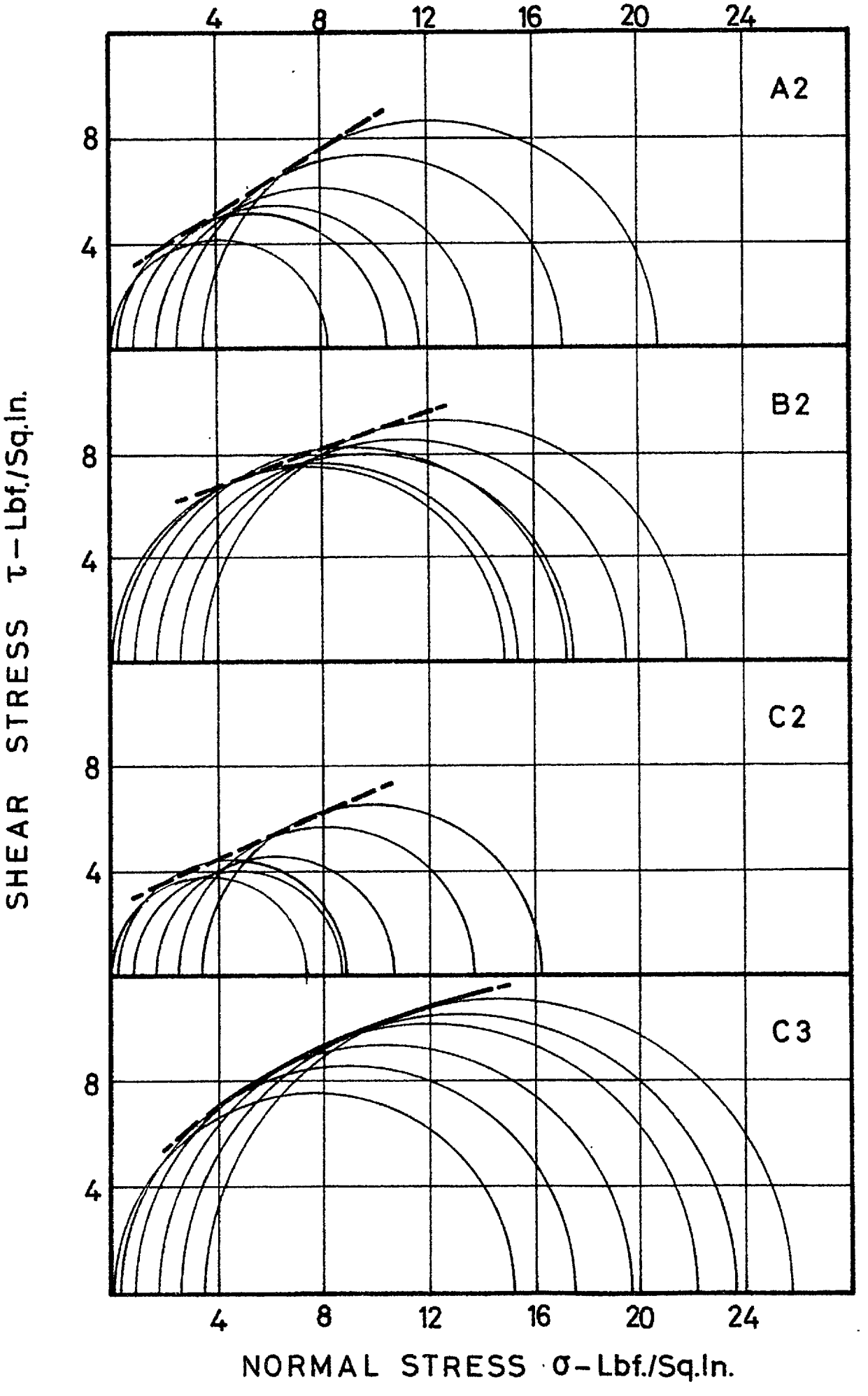

Figure 1.2.12 Mohr rupture envelopes for mixes A2,B2,C2 and C3

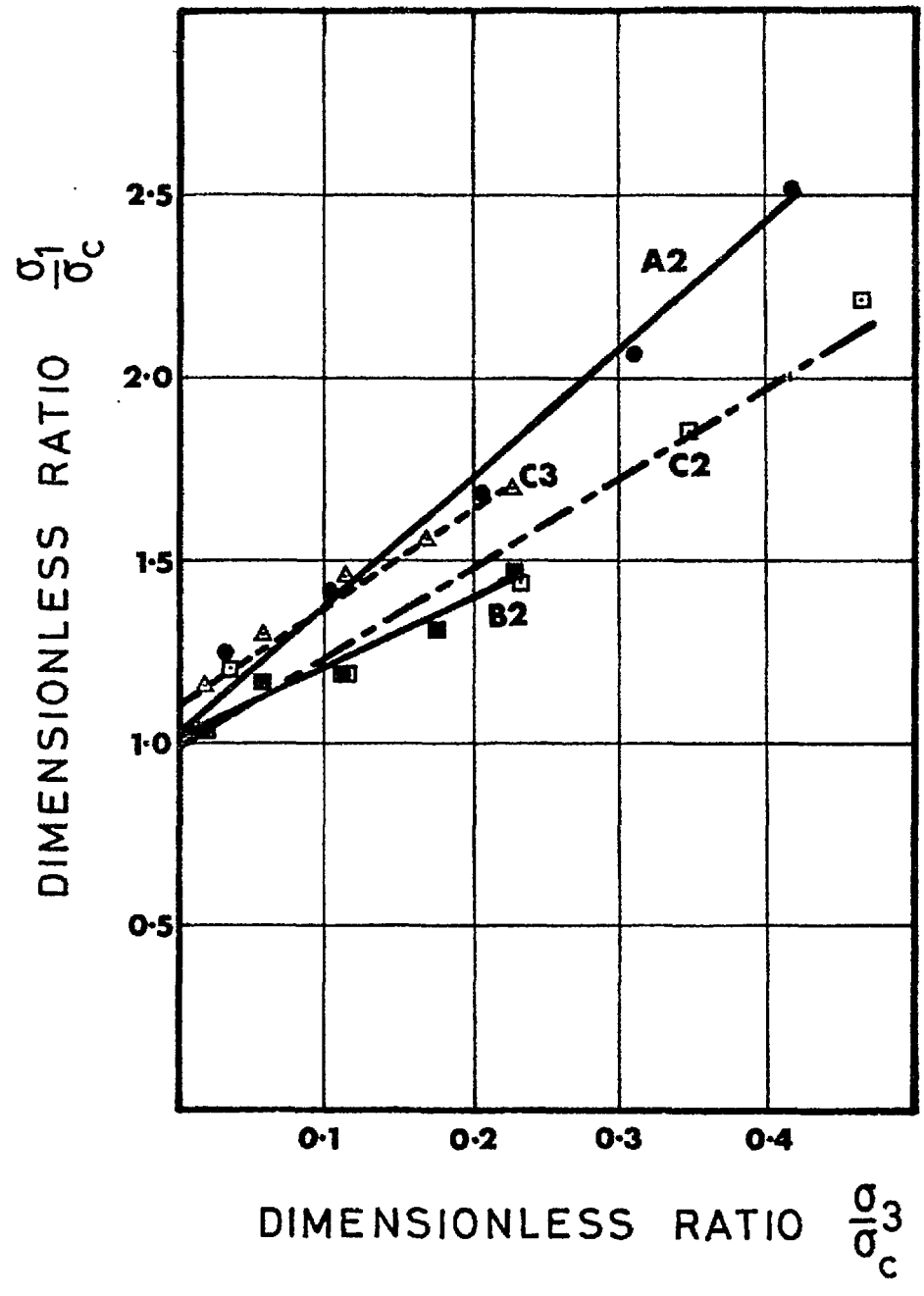

Figure 1.2.13 Relationship between the normalised values of σ_1 and σ_3 at failure for mixes A2, B2, C2 and C3

DISCUSSION

1.2.5 UNCONFINED COMPRESSION BEHAVIOUR

The non-linear stress-strain behaviour for all the mix types reported was noted in Figures 1.2.1, 1.2.2 and 1.2.3. The high rate of strain was thought to be largely due to 'bedding-in' of the end faces. However, it may also have been a function of the closure of the pores. Sandstones exhibit this non-linear behaviour, due to partial closure of micro-cracks, when initially stressed (Morgenstern and Phukan[17]). This behaviour was found to be greatly influenced by the porosity of the particular sandstone under test, an observation which is of particular relevance to the present work with a material of high porosity (40-47%) (See Appendix I).

The essentially linear central portions of the curves enabled values of E_t (tangent modulus at 50% of ultimate strength) to be determined quite closely, though small errors here may have been the cause of an appreciable scatter on the modulus ratios (E_t/σ_c) for the same mix type. The second non-linear portion of the curve can be seen to extend over the last 10 to 20% of the stress range. However, unlike the case of triaxial compression when the highly stressed material was 'supported' by a confining pressure, the non-linear strains that occurred before failure in this case were of a lower order - between 0.10 and 0.15% axial strain in general.

It will be convenient for comparison if the strength results are related to the full scale behaviour which is being simulated. In Section 1.1 on the dimensional requirements, a stress scale (ψ) of 1:666 was obtained by adopting a geometric scale (λ) of 1:500, and by assuming a full scale rock density of 160 lbf/ft^3 compared to the model density of approximately 120 lbf/ft^3. Table 5 below shows the values of the unconfined compressive strength (σ_c) and Young's modulus (E_t) obtained by converting the model results to the full scale values. The modulus ratio (E_t/σ_c) remains constant.

Table 5 : Full Scale Unconfined Compression Test Results

lbf/in^2	A2	A3	A4	B2	B3	B4
σ_c	6,860	11,860	21,260	10,390	19,120	33,140
E_t (x10^6)	2.40	4.87	9.60	5.26	10,66	17.07

	C2	C3	C4
	5,730	13,420	19,890
	2.66	7.13	9.66

SECTION 1.2

A useful and simple method of rock classification was reported by Deere[8] after the report by Deere and Miller (1966). It is based on only two variables; the unconfined compressive strength (σ_c) and the tangent modulus (E_t) of intact rock specimens. The values of the compressive strength and the modulus are plotted to a logarithmic scale. The modulus ratio (E_t/σ_c) is obtained from the plotted position with respect to the diagonal lines. The essential features of the system can be seen in Figure 1.2.14. The values of σ_c and E_t that were obtained by scaling up the model results are shown plotted in their prototype scale positions (See Table 5). The envelope shown dashed encloses results of 75% of the specimens of limestone and dolomite collected by Deere and Miller. Two-thirds of the model specimens are also contained in this envelope. The comparison can be extended to several other rock types reported by Deere and Miller; basalt and other flow rocks, granites, many of the sandstones, gneisses and so on. However, the closest similarity is with the limestone and dolomite group.

The flexibility of the model material properties is well demonstrated by the relative positions of the three varieties taken from the vibration study (See Fig. 1.2.6). The material (nominally close to A1) has been scaled up to the prototype stresses and the three positions are shown in Figure 1.2.14.(A1 (1), (2) and (3). If this technique could be extended also to the higher strength mixes then a considerable range of rock performance could be simulated by varied amounts of vibration. At this point attention should be drawn to Figure 1.2.7 (II) which is a plot of the strain at failure vs. the modulus ratio for the vibration tests. The tendency for higher failure strains with materials of lower modulus ratios is well demonstrated by the envelope Miller and Deere give for 75% of their results for shales. At least 75% of this area covers modulus ratios of less than 200:1,and a high failure strain is certainly to be expected from such materials.

1.2.6 TRIAXIAL COMPRESSION BEHAVIOUR

As an aid to comparison, the hypothetical full scale confining pressures and failure stresses are tabulated. They were obtained by multiplying the model stresses by 666 which is the previously selected stress scale.

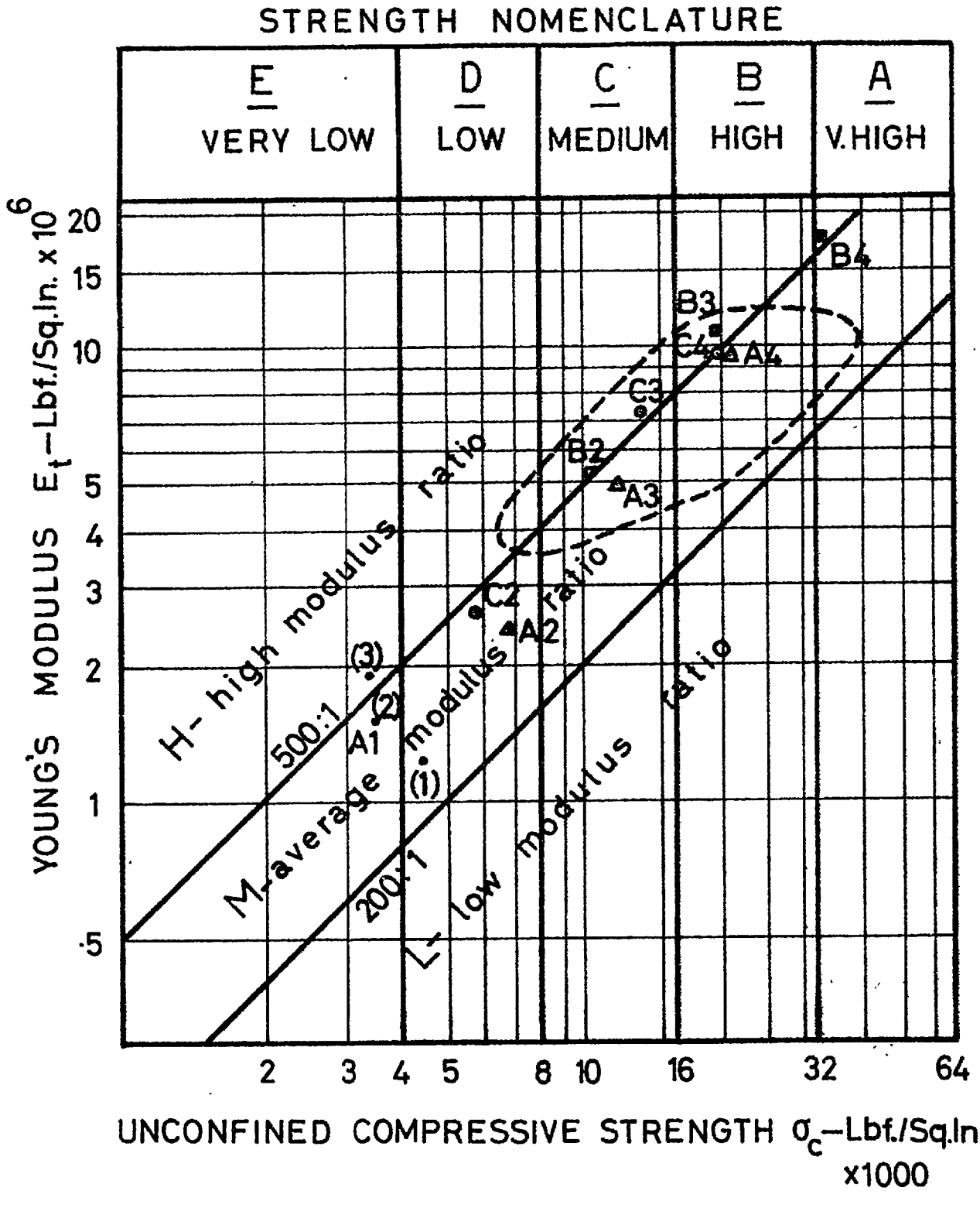

Figure 1.2.14 Engineering classification for intact rocks (after Deere[8]) showing relative position of the model materials

Table 6 : Full Scale Triaxial Test Results

σ_3 (lbf/in^2)	σ_1 at failure (lbf/in^2)			
	A2	B2	C2	C3
0	5,530	9,920	4,930	10,130
170	6,960	10,270	5,930	11,720
570	7,820	11,560	5,820	13,130
1140	9,310	11,720	7,130	14,790
1710	11,440	13,060	9,150	15,800
2280	13,870	14,590	10,920	17,180

In a previous part of this section, the Mohr rupture envelopes for four of the mix types were given, together with a normalised plot of the axial stress at failure vs. the confining pressure. It was possible to compare their triaxial characteristics with those of rocks, but only on a qualitative basis. This final comparative discussion is based on the strength criterion for rock given by Franklin[16]. His strength criterion incorporates both unconfined compression data and triaxial data, and is based on the trends exhibited by the maximum shear stress loci of 1100 triaxial compressive strength results collected from the literature.

The maximum shear stress locus was suggested in previous studies by Hoek[15] as a useful form of failure criterion. The locus is defined by the points of maximum shear stress (τ_m) acting on the specimen at failure, and the normal stress (σ_m) acting on the plane of maximum shear stress. (These points are simply the tops of the Mohr circles).

$$\tau_m = \frac{\sigma_1 - \sigma_3}{2} \quad , \quad \sigma_m = \frac{\sigma_1 + \sigma_3}{2}$$

Normalising the results in the standard way:

$$\tau_m' = \frac{\sigma_1 - \sigma_3}{2\sigma_c} \quad , \quad \sigma_m' = \frac{\sigma_1 + \sigma_3}{2\sigma_c}$$

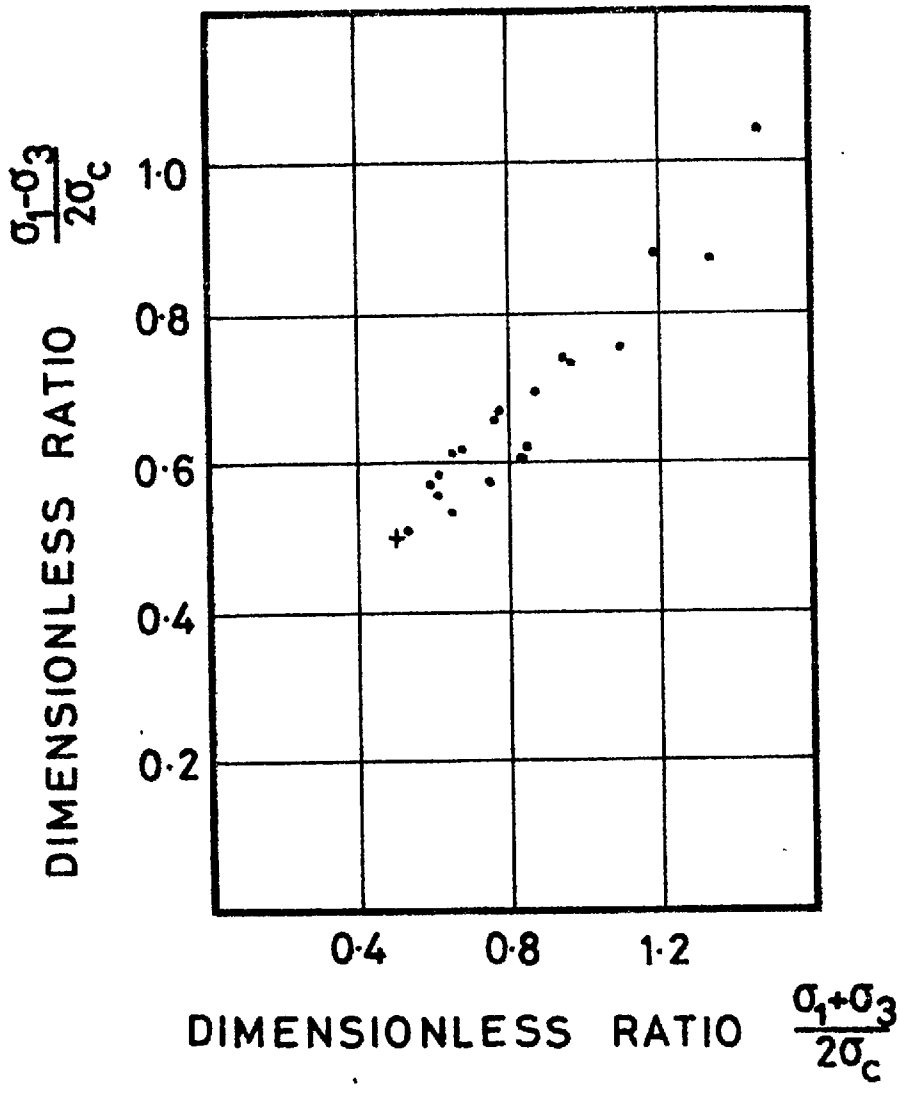

Figure 1.2.15 Normalised values of the maximum shear stress loci for mixes A2, B2, C2 and C3

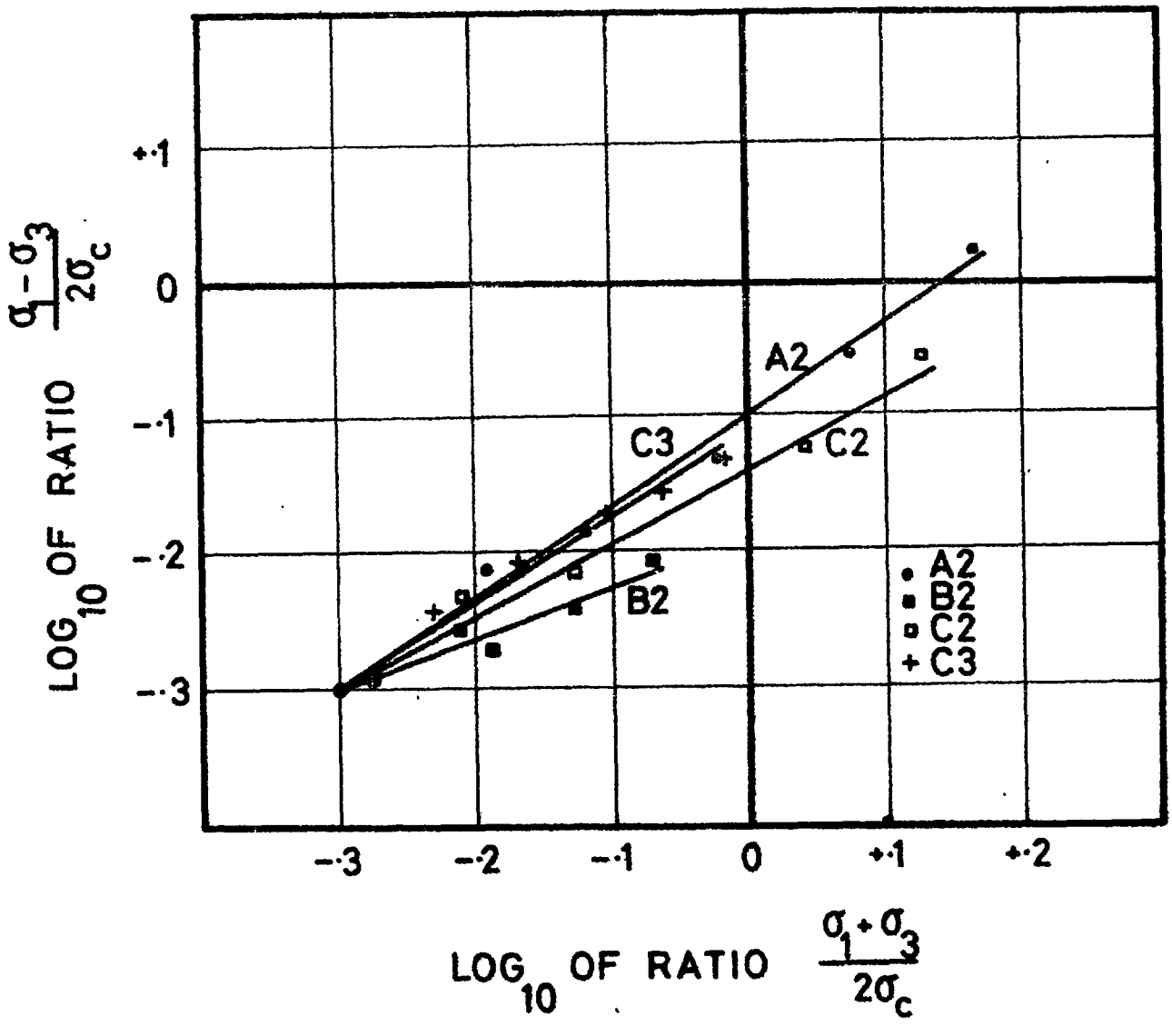

Figure 1.2.16 Straight line relationships of log normalised values of the maximum shear stress loci for mixes A2,B2.C2 and C3.

Franklin[16] gives scatter diagrams of this data for twelve lithological groups; sandstones, limestones, quartzites and so on, each showing a surprisingly similar trend in view of the variety of different materials. The scatter diagram for the four model materials tested is shown in Figure 1.2.15. It is possible to compare it directly with Franklin's diagrams, since the plotted data is dimensionless. Bearing in mind the relatively low simulated confining pressure range (0 to 2280 lbf/in^2), the results appear to bear most resemblance to the limestone group.

A certain separation in behaviour becomes apparent if the data is replotted on logarithmic axes. Franklin found a near linear relationship to exist between $\log \tau'_m$ and $\log \sigma'_m$ for the various lethological groups. He obtained the following empirical failure criterion for brittle compressive failure:-

$$\tau'_m = \tfrac{1}{2}(2.\sigma'_m)^B$$

where B is the gradient of the $\log \tau'_m$ vs. $\log \sigma'_m$ diagram. This function (to the base of ten) is shown in Figure 1.2.16 for the four model mixes A2, B2, C2 and C3. The approximate gradients (B values) are as follows:

A2	B2	C2	C3
0.67	0.38	0.53	0.64

Mix types A2 and C3 thus lie within the typical range of B values given as 0.6 to 0.8. Franklin observed that little could be seen in the way of systematic variation between rock types. It is therefore important that all potential model materials should also have a close range of B values, corresponding to the approximate limits just given. In addition, it has been shown that the strength envelopes in the brittle compressive range are geometrically similar between model and prototype, if the respective B values are identical.

The above argument suggests that B type mixes should be viewed with suspicion, since the B value of 0.38 is well outside the common range for most rock types. However, support is lent to the belief that A and C type materials are well suited to the task of modelling both a range of rock types and the consequent range of properties. The resemblance to limestones is strengthened by the fact that the average B value for this group has been given as 0.65 by Franklin. This may be indicative of a relation between the B value and the plotted position of a group of rocks on the Deere and Miller diagram.

CONCLUDING REMARKS

The influence of discontinuities on the stability of open-pit slopes and rock slopes in general has been emphasised in Section 1.1. It is most important that the frictional characteristics of discontinuities built into the model closely reproduce the estimated shearing characteristics of rock discontinuities. Such features

should include peak and residual strength and dilation, where the magnitudes of these will be based on results extrapolated from insitu and large shear-box direct shear tests. It is clear that the frictional properties of rock discontinuities will depend not only on the inherent shear characteristics of the intact material, but also on the roughness of the interlocking surfaces of rock.

A material has been produced in which, for a given compressive strength, the inherent shear characteristics of the solid can be varied by the use of sand or ballotini coarse filler.

A method has been developed for producing systems of intersecting discontinuities in the same material. The great advantage of this low strength brittle material is that it can be readily split into uniformly orientated fractures. It is this type of interlocking surface that has the closest resemblance to those intersecting a rock mass. Full details of the direct shear characteristics of these interlocking surfaces are given in the next Section.

1.3 PHYSICAL CHARACTERISTICS OF MODEL JOINTS FROM DIRECT SHEAR TESTS

SUMMARY

Existing techniques of joint modelling are reviewed. It is concluded that no methods in present use are acceptable as either realistic simulations of joints or as mass production methods. Some preliminary tests are described on flat, roughened surfaces of the red lead-sand-plaster-water material. Unfortunately the most realistic surfaces were the most difficult to produce systematically.

A method is described for producing interlocking tension fractures in the model material using guillotine devices. A comparison of fractures through three different model materials shows that the direct shear characteristics of material C3 have optimum features. A realistic drop from peak to residual strength, and an approximately bi-linear envelope of peak shear strength (with curved transition) is obtained. An initial angle of friction of 56° and a cohesion intercept of 0.08 lbf/in^2 are indicated. Considerable importance is attached to the variation of shear strength with horizontal (and vertical) displacement. Both pre-peak and post-peak strength characteristics are thought to have a fundamental effect on slope behaviour.

The concept of primary and secondary jointing is discussed. Model joints can be produced in the guillotines which are continuous, cross jointed or offset (stepped) depending upon the chronological order of fracturing. The direct shear properties of these three types are compared and evaluated.

The model joints, which simulate prototype dimensions of 96 feet by 42 feet, are compared where possible with the results of large scale in-situ tests reported in the literature. It is concluded that the model shear strength envelopes display similarity, their being only a small strength-size effect for joint surfaces. However the comparison of displacements at which peak strength is mobilized, suggest that a marked displacement-size effect exists, which is probably controlled by the joint roughness wave form.

1.3 PHYSICAL CHARACTERISTICS OF MODEL JOINTS FROM DIRECT SHEAR TESTS

Introduction

Model materials with realistic intact properties have been described in Section 1.2. The remaining problem was to produce artificial joints with realistic shear properties. Two features of particular importance have to be considered.

Firstly, direct shear characteristics for the joints showing an 'unstable mode' of failure rather than a 'stable mode' have to be created by some means. That is to say a graph of shear strength and shear displacement was required showing a marked drop from a peak strength at small displacements to a residual strength at large displacements. This would be in direct contrast to one showing stable characteristics; in which a maximum strength is reached followed by unchanging shear resistance with increasing shear displacement. The contrasted effects of these two modes on the progressive failure of rock slopes do not require emphasis here.

Secondly, when an 'unstable mode' of failure has been successfully simulated the technique involved must be critically examined for its practical possibilities. The final large model to be constructed (described in Part 3 of this thesis) took two weeks to construct and test. Four days were spent in simulating joint sets in the intact model material. At least forty thousand discrete blocks were produced in this short period and this of course implies that some mass production technique was employed.

A comprehensive review of joint modelling was given by Stimpson[11]. It is apparent that this aspect of modelling has received a minimum of attention in the past. Of the limited number of techniques in use many are suspect from several points of view. The simplest technique which is widely used is to cast discrete blocks of model material in smooth sided moulds. When these are cured the model structure is assembled by packing the blocks into the model frame. A regular packing is usually employed such that two orthogonal 'joint sets' are produced.

The next logical step that is taken is to find some means of varying the frictional properties of the mating block faces. Several authors have reported the variable angle of friction that can be achieved by inserting various materials between the flat faces of cast bricks or layers of the model material. Fumagalli[3] has achieved friction angles as high as 40°-46° by inserting sand of various grain sizes. However it would appear that this might tend to produce a markedly stable joint behaviour rather similar to the residual strength of rock joints. This residual is largely controlled by sliding and rolling in the intermittent bed of debris which builds up between shear blocks after large displacements.

Ladanyi and Archambault[18], and Krsmanovic, Tufo and Langof[19] tackled the problem of joint roughness rather more directly.

Imbricated (stepped) surfaces were produced by interlocking model bricks which could be set at various angles and with various heights of step. Total 'friction angles' (joint inclinations included) of between 40° and 65° were obtained by the second authors. These angles were dependent on both the height of the step and the normal stresses. It seems likely that this form of joint would tend to produce some cohesion intercept when the direction of sliding was against steep teeth. However no details were given of this directional dependence.

Patton[20] produced interlocking teeth joints by casting directly against moulds with teeth. These teeth, ranging from 15° to 45° inclination and with 90° ends, produced his well known bilinear approximation to shear strength envelopes, and obvious drops from peak to residual strength.

None of the above methods seemed to be practical possibilities where large, highly jointed models were required. A programme of direct shear testing was therefore initiated, firstly to find the basic friction angle for sliding on flat surfaces of the red lead-sand/ballotini-plaster-water material, and secondly to see if any simple methods could be found for producing unstable characteristics.

SECTION 1.3

1.3.1 SOME PRELIMINARY TESTS ON MODEL JOINTS

Flat joints were investigated first, where the surfaces in contact were produced by direct moulding against perspex mould faces. Two roughened variations were also tested. The three joint types can be summarised as follows.

1. Smooth, as cast flat surfaces
2. Flat surfaces roughened before setting.
3. Flat surfaces roughened after setting.

Joint surfaces Nos. 2 and 3 were produced as follows. Bricks were cast in moulds which had one open face (uppermost). Before final setting of the model material a steel straight edge was drawn across the open face to produce a flat but 'granular' surface. Alternatively the bricks were removed from the moulds after setting but before curing, and were scraped once with the same straight edge. This again produced a flat 'granular' surface but in this case the surface was slightly loose due to loss of cohesive bonds.

The shear blocks had an apparent contact area of 5.3 in^2. These just fitted into a standard soil mechanics type direct shear box (6 cm. by 6 cm.). One important modification was made. The upper and lower split halves of the box, which conventionally slide in contact during a test, were separated by 1/16 inch P.T.F.E. (Teflon) strips. In this way the discontinuity under test could be located midway in the small gap between the upper and lower halves of the box. This prevented end interference occurring after small amounts of shear displacement. Without this device one edge of each block is sheared into by the adjacent edge of shear box, thereby rendering the results meaningless.

The shearforce-displacement and dilation characteristics of the three flat joint types are shown in Figure 1.3.1. The intact material used in all three was an experimental one similar to A.1 but using one of the sands which was finally rejected in favour of Kingslynn sand (See Appendix 1.) The intact properties were as follows:

"A.1"	Unconfined compression strength	4.2	lbf/in^2.
	Young's modulus	0.2×10^4	
	Strain at failure	0.41%	
	Density	130.6 $lbf/ft.^3$	

It can be seen from the results of No. 1 joint type that the smooth surfaces became increasingly damaged both with large displacements and higher normal stresses. (Range 0.25 to 0.93 lbf/in^2). A small drop in shear strength was followed by a significant increase in strength after displacements of about 0.06 inch. No.2 joint type was slightly unstable as desired.

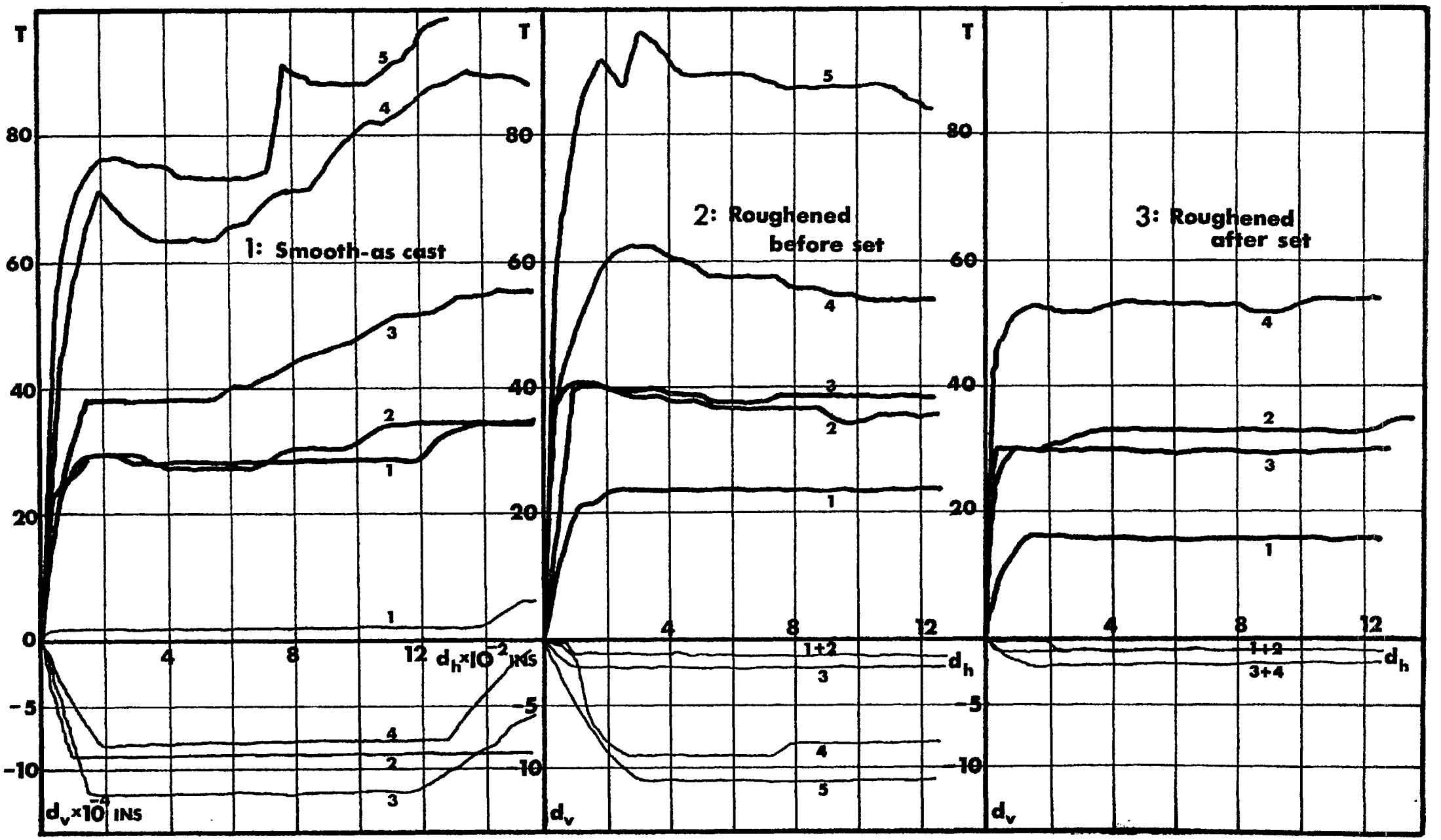

Figure 1.3.1 Shear force-displacement and dilation characteristics of three model joints types.

However, as for the cases reported in the literature it was also the most impractical surface to produce, since only one face out of six could be treated in the desired manner. No. 3 joint type, which was relatively simple to produce on all sides of a cast block, gave completely stable results corresponding to the residual case discussed previously.

Linear shear strength envelopes were found to fit the rather scattered data best. The following results were obtained.

Joint type	Angle of friction	Shear Displacement (inch)
1	34° 31° 38°	0.02 0.04 0.14
2	36° 31°	0.01-0.03 0.12
3	32° (approx).	0.0-0.12

Note: A cohesion intercept of zero was assumed for all envelopes.

Later tests on flat surfaces of materials A3 and C3 (see Section 1.2 for strength data) gave residual angles of friction of $31\frac{1}{2}^{\circ}$ and $28\frac{1}{2}^{\circ}$ respectively. This was for displacements of 0.12 inch. This illustrated the potential of ballotini for reducing the angle of 'basic friction' as compared to materials containing only sandfiller. The term 'basic friction', which will be used throughout this thesis, is used to describe the shear strength when sliding occurs between flat surfaces after displacements corresponding to residual conditions. When rough surfaces are sheared and the residual condition is not reached by the end of a shear test, the friction angle will be referred to as the 'ultimate' friction angle. This is the term used by Krsmanovic, Tufo and Langof[19].

At the same time that the above three joint types were tested, a single series of direct shear tests were performed on intact blocks of material "A.1." A normal stress range of 0.29 to 1.78 lbf/in^2 was applied. The peak shear strength envelope that was obtained was remarkably linear over the full range. It represented a peak angle of friction of 42° and a cohesion intercept of 1.50 lbf/in^2.

Peak strength was developed after an average of 0.055 inch shear displacement which was unexpectedly large. After 0.12 inch displacement the strength envelope had reduced to an inclination of 31°, but it still showed an apparent cohesion intercept of 0.80 lbf/in^2 if assumed linear. A significant feature of the test which was consistent with later results was that the maximum angle of dilation occurred at the same horizontal displacement as that at which peak strength was developed. It appeared that the development of initial shear surfaces at presumably very small displacements did not represent the peak strength. This was a suprising result, but in fact it supported some in-situ results discussed later.

1.3.2 A METHOD FOR PRODUCING ROUGH JOINTS

Soon after performing the series of shear tests on flat joints a discovery was made which was to affect all the following work. When a sharp edge such as a chisel was gently tapped against a block of the weak model material a fracture was readily propagated which passed right through the block. Such discontinuities which were in reality tension (or extension) fractures had the torn appearance of tension joints found in the field. They were however excessively rough and non planar when produced in this way.

A small guillotine was designed (See Figure 1.3.2) in which a block of model material could be place so that its bottom face was supported on a blade projecting from a base plate. A weighted upper blade could be dropped from various heights (0 to $2\frac{1}{2}$ inches) to strike the upper face of the block. The blade angles were 50° (upper) and 30° (lower). Limit screws could be adjusted to prevent too deep a penetration of the upper blade. The lower blade was also adjustable in this manner.

The lower blade penetrated the base of the block due to the momentum imparted to the block by the falling blade. Obviously there was some time delay between the two penetrations, each of which was about 0.03 inch deep. However the mechanism produced somewhat more planar fractures than with a single penetration. It is believed that the mechanism was one of 'static' wedging causing extension fractures since the blade velocity at contact was hardly sufficient to produce any dynamic effects from wave reflections at the blade faces.

A series of test fractures were made in different thicknesses of model blocks using the experimental material "A.1." Thickness of $2\frac{1}{2}$ inches and $1\frac{1}{2}$ inches were rejected in favour of 1 inch, through which the most planar fractures could be produced.

Figure 1.3.3 shows various components of the shear box arrangement used for testing the new 'tension joints'. The upper

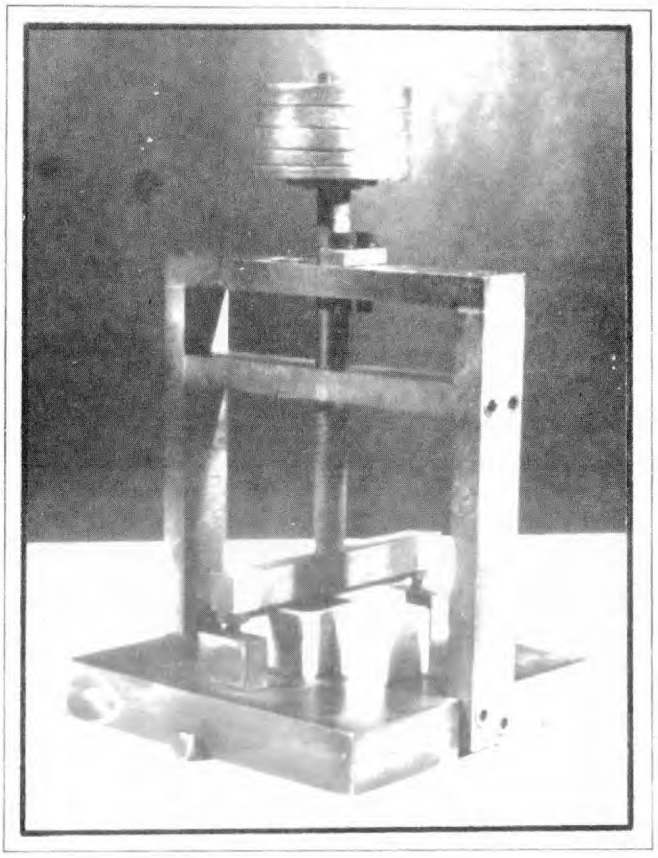

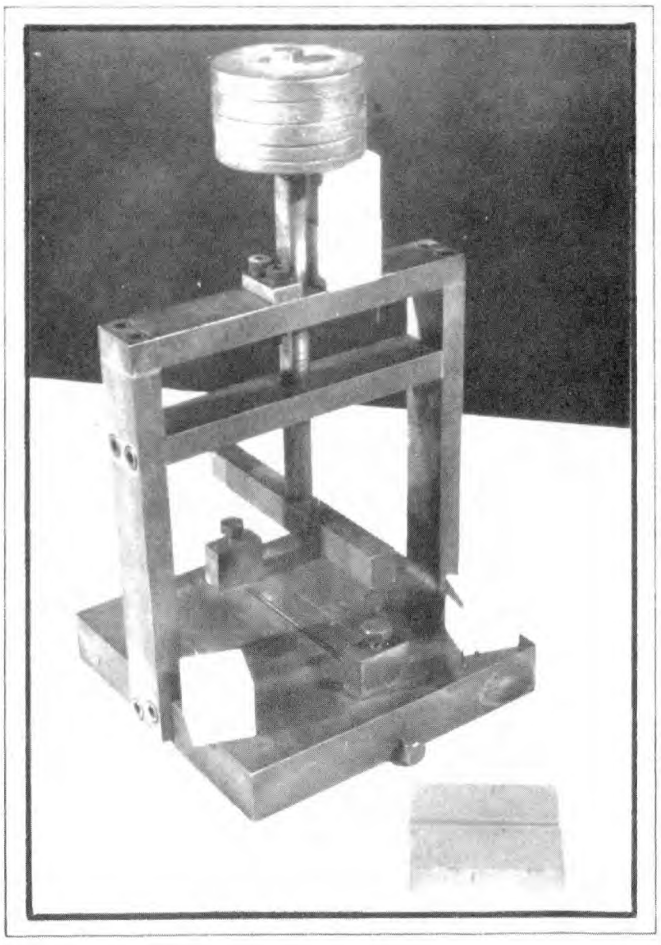

Figure 1.3.2 A small guillotine for generating tension fractures in the model material.

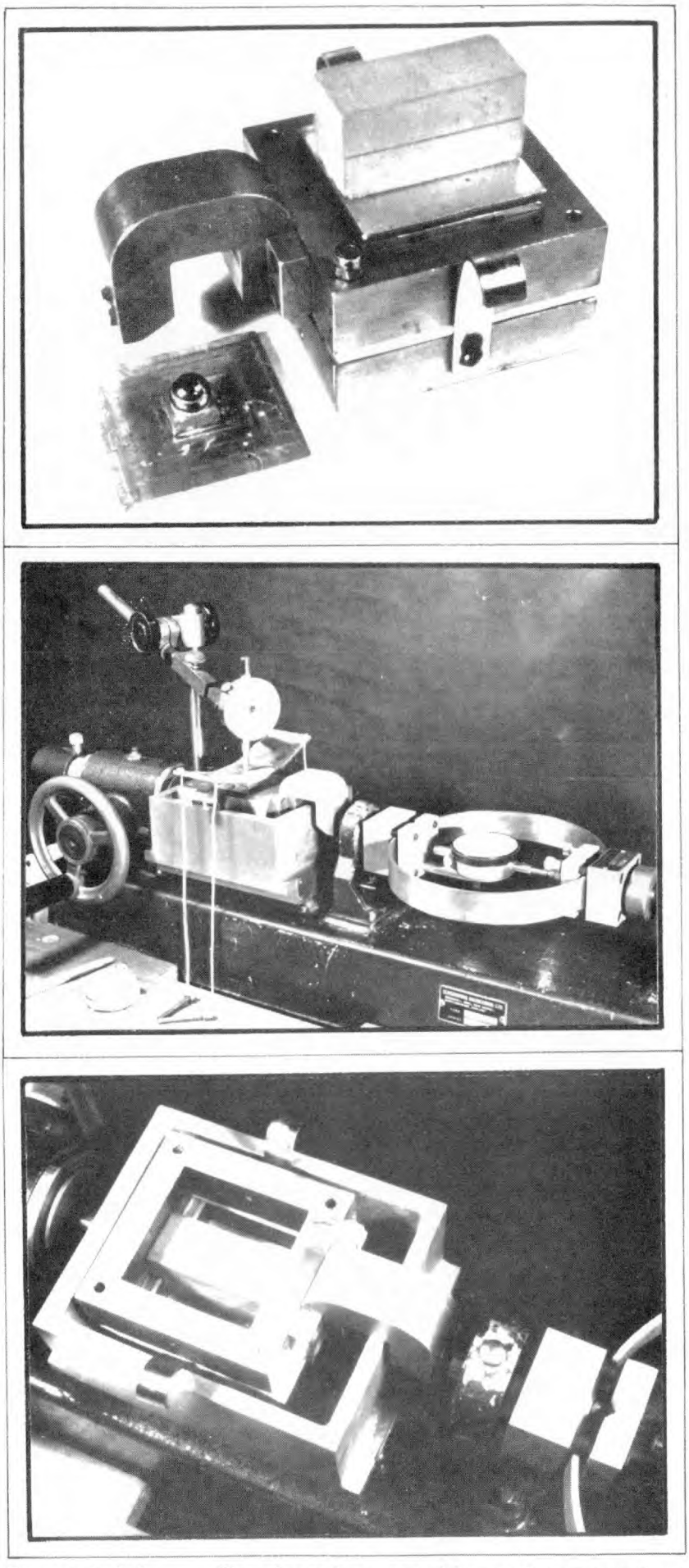

Figure 1.3.3 The shear box assembly used for testing tension joints in direct shear.

and lower figures show the P.T.F.E. shear box separator, which was increased in thickness to $\frac{1}{8}$ inch to encompass the maximum expected roughness of these joints ($\pm \frac{1}{16}$ inch).* Note also the light aluminum loading platten and loading yoke to which weights were attached by four light wires. By this means extremely low normal stresses could be applied.

A preliminary series of shear tests was performed using experimental materials "A.I" and "A.4." The tension joint surfaces were 1 inch wide and 2.3 inches long, and were aligned with their long axes parallel to the direction of shearing. Eight different normal stresses were applied. The smallest of these was simply generated by the weight of the upper block of $\frac{5}{8}$ inch depth. With model-prototype scales of 1 : 500 (geometric) and 1 : 666 (stress) this simulated an overburden of approximately twenty five feet of rock. It was hoped that at such low stresses the presence or absence of a cohesion intercept might be indicated.

Figures 1.3.4 and 1.3.5 show the shear force-displacement, dilation and strength envelope characteristics for a series of tests on material "A.1." The strength envelopes were obtained from the mean of two tests at each normal stress, and are the best-fit curves to somewhat scattered data. The normal stress levels, which are denoted by numbers 1 to 8 were as follows.

1.	0.047	5.	0.480	
2.	0.174	6.	0.667	
3.	0.292	7.	0.856	(lbf/in^2)
4.	0.386	8.	1.232	

Characteristics such as those shown were extremely encouraging. However the results for the stronger material "A.4", which had an unconfined compression strength of 24 lbf/in^2, showed that the roughness of fracture was probably still too great. Initial angles of friction (at low normal stress) of about 70°, and ultimate angles of friction (after 0.18 inch displacement) of about 48° appeared to be unacceptably high.

The solution to the problem of excessive roughness of fracture was tackled in two stages. Firstly it was anticipated that the inherent frictional strength of the model material could be lowered by using finer grades of sand and combinations of this sand with ballotini. The concurrent work on the intact properties reported in Section 1.2 showed that this was true. Materials

* This means that the shear force was applied $\frac{1}{16}$ inch below below the mean joint plane. It is possible that this small moment improved upon the conventional distribution of stress. It is widely assumed that a tensile region exists at the rear of a shear block, when loaded conventionally.

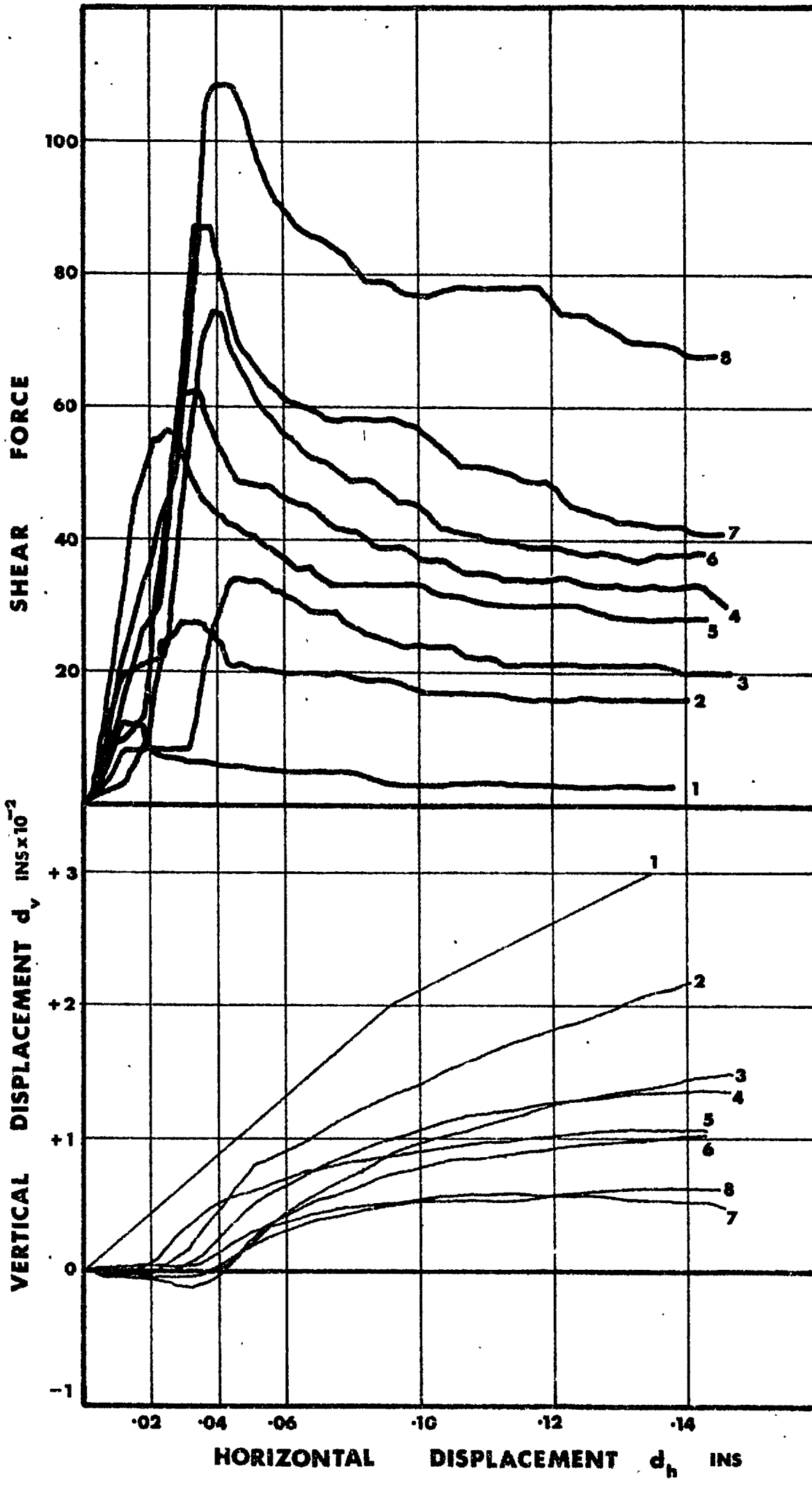

Figure 1.3.4 Shear force-displacement and dilation characteristics of tension joints in model material "A.1."

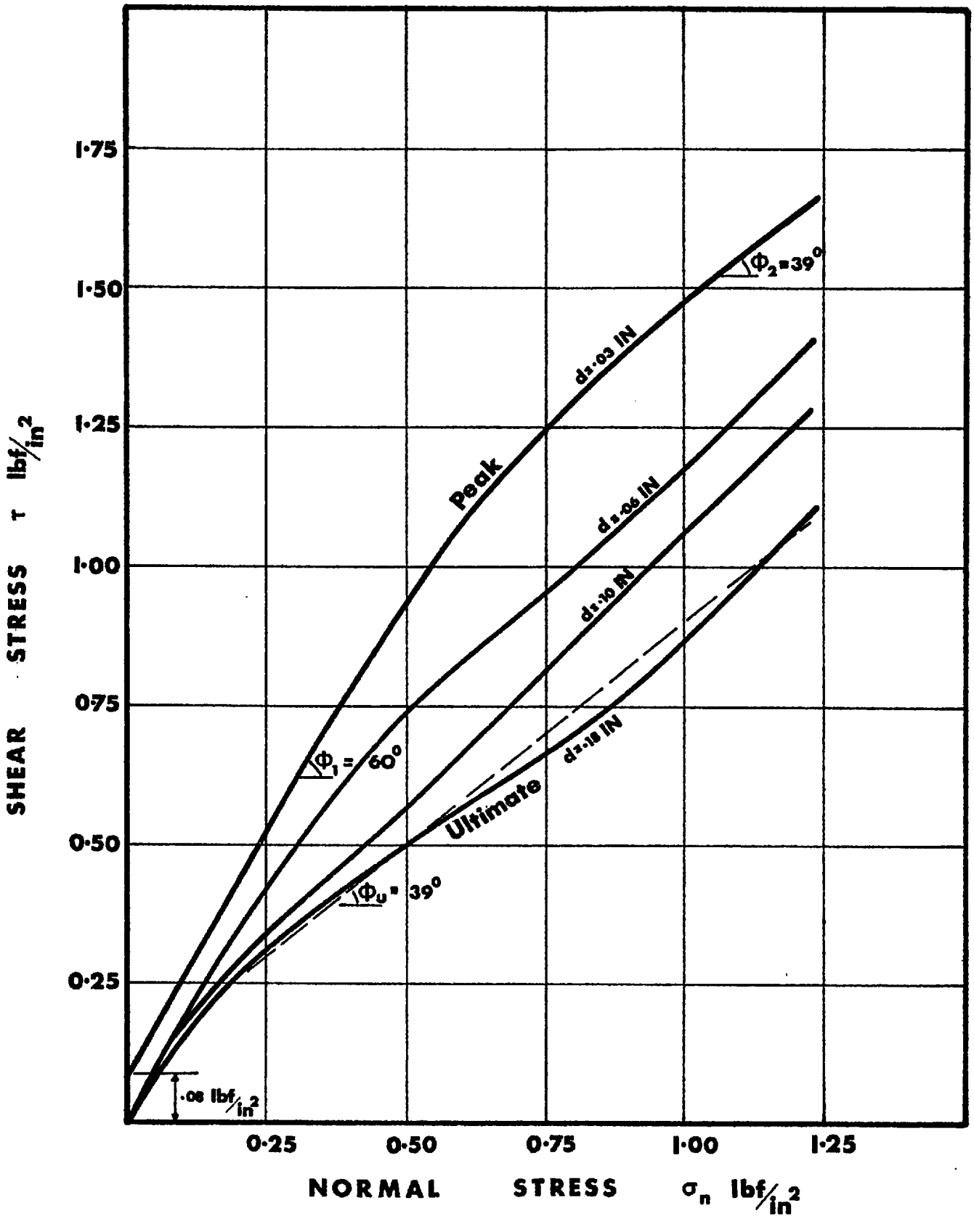

Figure 1.3.5 The shear strength envelopes of tension joints in model material "A.1."

containing the largest proportion of ballotini to sand demonstrated the lowest inclination of shear strength envelope.

Secondly it was decided to devote some time to the design of a larger guillotine. The special feature required was for both the upper and lower blades to strike the bricks simultaneously such that an extension fracture would be propagated from both sides at once. The mass production of jointed slabs of the model material was also envisaged, and necessary features were incorporated in the design.

Figure 1.3.6 shows the eventual form of this large guillotine. A lot of time was involved in having it constructed, and several months were spent on trials and modifications after its eventual delivery. However the end result was entirely satisfactory. Certain features of the design of the guillotine, and the methods used for mass production of jointed slabs are given in Appendix 3. All the joints that were generated for direct shear testing that are reported in the remaining sections of this thesis were produced on this large guillotine. With both upper and lower blades striking the model blocks simultaneously above and below, the roughness of fracture was reduced to acceptable levels.

Selection of the optimum model material

Figure 1.3.7 shows the direct shear envelopes of tension joints generated in model materials A3, C2 and C3 which were three of the materials described in detail in Section 1.2. It will be remembered that the C series contained coarse filler which was a 50/50 mixture of sand and ballotini. The inherent frictional characteristics of type C materials obtained from triaxial tests appeared to lie approximately midway between those of materials containing 100% sand filler (type A) and those containing 100% ballotini (type B). Figure 1.3.7 shows that the difference in shear strength obtained from triaxial tests on the three intact materials, was also prevalent in direct shear tests of joints in these same materials.

Since joints with the lowest shear strength were required, C2 and C3 were preferred to A3. However the final choice of a single model material, for use in all the models, depended on one further factor. The materials were so weak that damage of specimens when handling them presented considerable problems. This factor, and the low range of stresses anticipated in the final slope failure models pointed to the adoption of material C3. It can be seen from Figure 1.3.7 that despite a compressive strength almost twice that of C2, and representing 13,800 lbf/in^2 at full scale, the direct shear envelope for joints in C3 is almost inseparable from that of joints in C2 at the four lowest normal stresses. For this reason material C3 was selected as the optimum model. All the test results presented in the remaining half of this Section are for material C3, and all the slope models described in Part 3 were constructed from the same material.

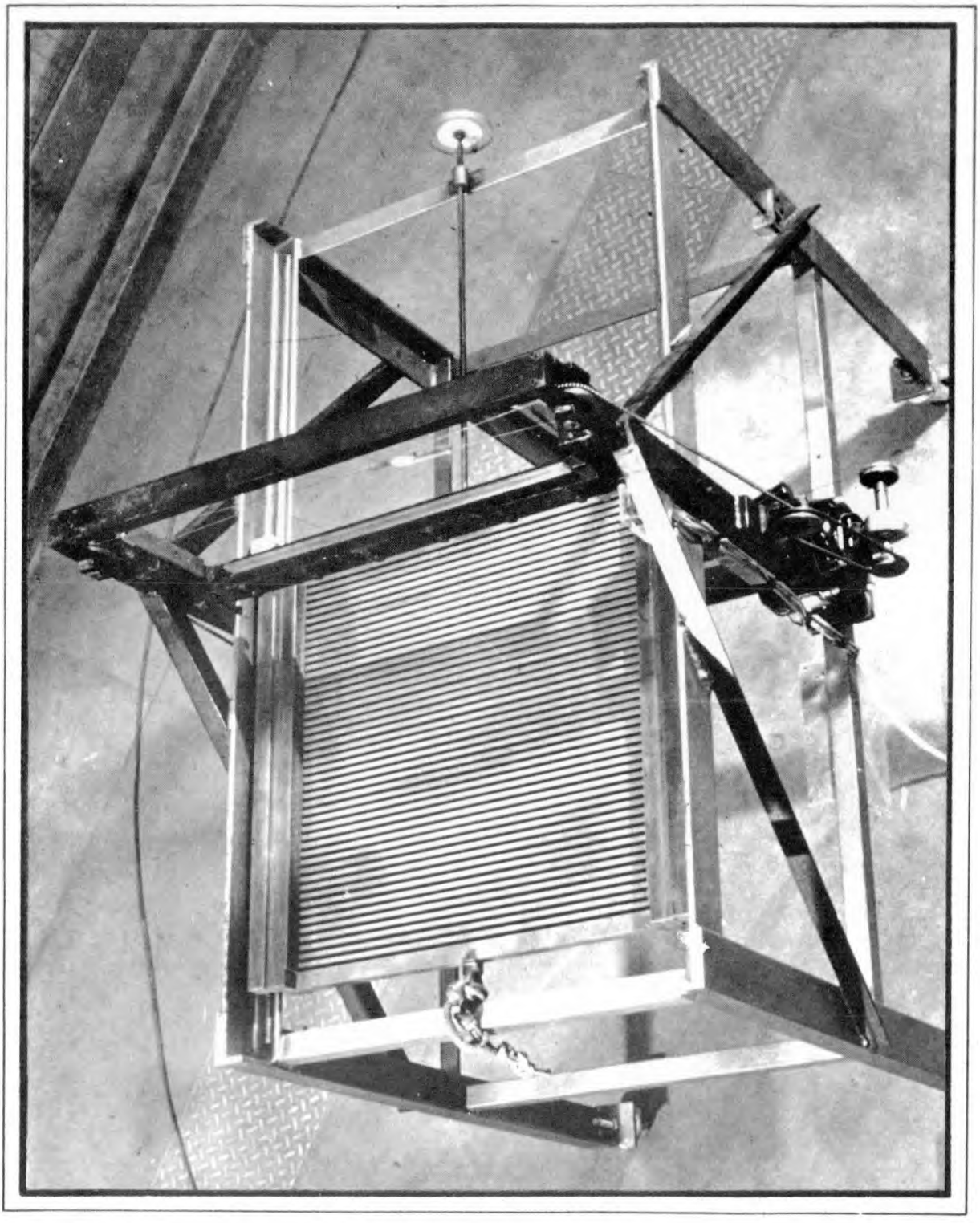

Figure 1.3.6 The large guillotine used for generating joints sets through slabs of the model material.

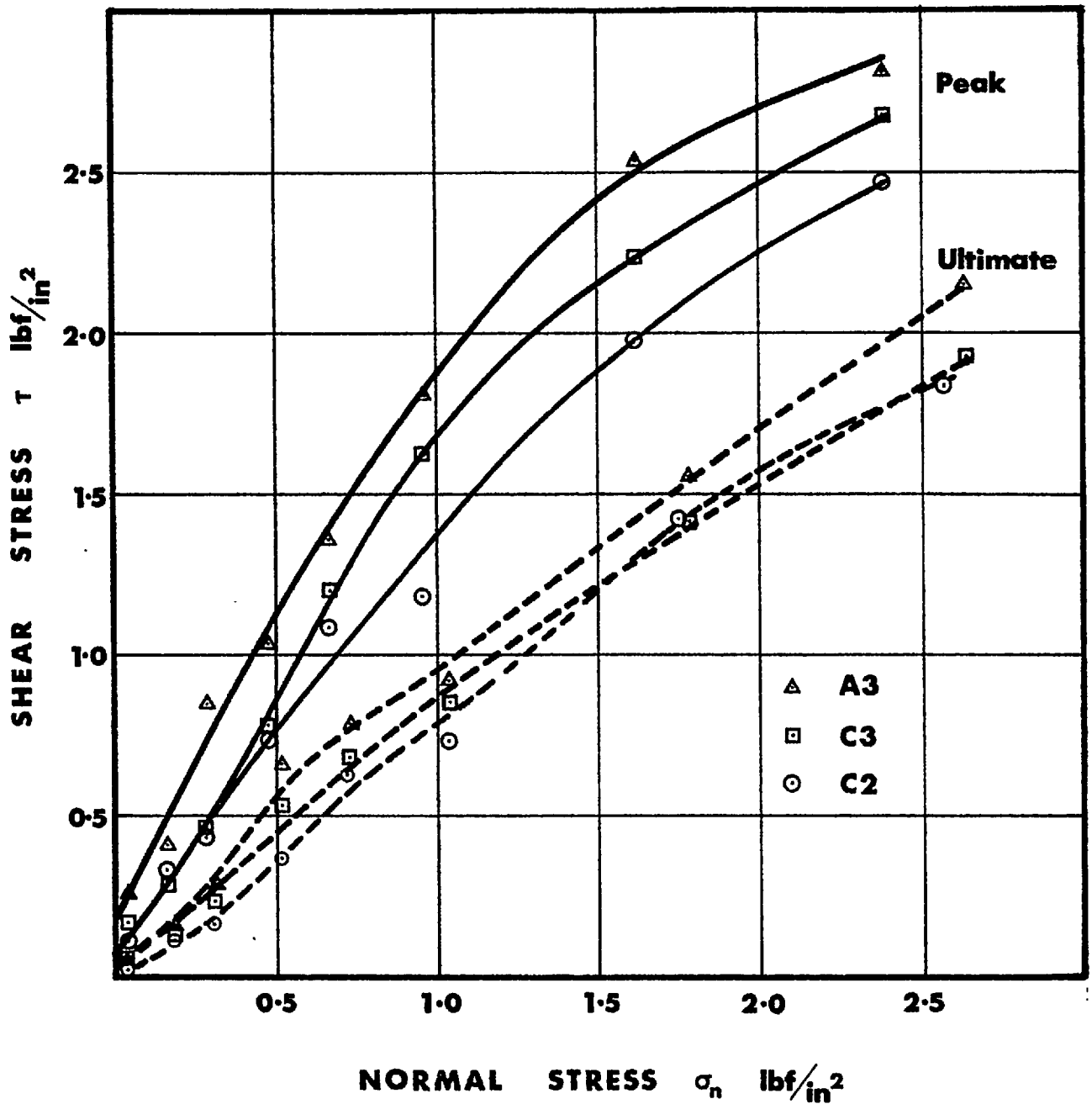

Figure 1.3.7 The shear strength envelopes of tension joints in model materials A3, C2 and C3

Selection of the optimum strength test

Triaxial tests on intact rock, and direct shear tests on rock joints are standard proceedures in rock mechanics practice. However there are certain schools of thought which favour triaxial tests for obtaining the shear strength of joints in rock. Jaeger[21] and Rosengren[22] have used this technique extensively.

It is obvious that for the determination of the peak strength of joints a triaxial system of stress application is most relevant to field conditions. However displacements are severely restricted both perpendicular and parallel to the failure plane. This means that the residual strength of joints and general post-peak behaviour cannot be determined with any degree of confidence, despite the elaborate corrections for displacements devised by Rosengren.

The direct shear apparatus is the obvious alternative strength test machine since there need be no limit on displacements and these can be monitored continuously during each test. It must be admitted that neglect of the intermediate principle stress is of some importance. However this is not important when testing joints that are only to be used in so called 'two dimensional' models. Two drawbacks to the direct shear apparatus are the non uniformity of shear and normal stress distributions, and the consequent tendency for progressive failure to be induced by application of the shear force at one end of the joint. However, it would seem that large joint surfaces in-situ can only be tested by direct shear techniques. Since the bulk of available data has been obtained from such tests it seemed advisable to test all model joints in this way also. From a practical point of view it is much the simpler method.

1.3.3 DIRECT SHEAR PROPERTIES OF JOINTS IN MATERIAL C3

The performance of tension joints in material C3 will be described without reference to the in-situ field test results reported in the literature. A comparative discussion is given in the latter part of this section. The presentation of joint performance will be chiefly in visual form, by means of conventional shear force-displacement, dilation and strength envelope diagrams. Considerable importance will be attached to the variation of strength with displacement, since this has a fundamental bearing on slope behaviour. In most diagrams the model performance will be illustrated together with the scaled up prototype performance where appropriate.

The size of joint surfaces tested was as illustrated in Figure 1.3.3, namely 1 inch by 2.31 inches. At prototype scale this represents 96 feet by 42 feet, with the long axis along the direction of shearing. (The effect of scale and of roughness is discussed fully in Section 2.1 and will not be dealt with here.)

SECTION 1.3

A standard rate of shearing was used throughout, and eight different normal stresses were applied. Once again the lowest normal stress was generated by the weight of the model block lying above the joint. These details can be summarised as follows:

Model rate of shear		Prototype rate of shear
0.046 inch/min	x($\lambda^{\frac{1}{2}}$)	1.03 inch/min

	Model normal stress (lbf/in^2)	Prototype normal stress
1.	0.044	29.3
2.	0.168	112
3.	0.286	191
4.	0.477	318
5.	0.668	445
6.	0.954	635
7.	1.620	1080
8.	2.383	1589

The range of normal stresses encompassed the anticipated range for the large models reported in Part 3 of this thesis. These had vertical dimensions of 48 inches. The slopes which were excavated in these models generated normal stresses across steeply dipping joints no higher than the first four listed above. A minimum of two specimens were tested at each normal stress and only the mean of these results has been plotted where strength envelopes are presented. However the scatter of results was less than that obtained from the unconfined compression tests reported in Section 1.2, and considerably less than for the three flat joint types described earlier. The peak shear strength results showed a maximum scatter of approximately 10% for each normal stress. A surprising number of joints gave identical peak strength results when tested at the same normal stress.

Dilation measurements were taken throughout each test at one point only. This was the centre of the loading platten, and the point at which the normal stress was applied. Since the upper blocks were free to rotate with the loading system employed, the dilation measurement can be taken as the mean rise or fall of the whole block.

Figure 1.3.8 Shear force-displacement and dilation

(Note: Use of the word 'primary' in the above figure caption will become apparent shortly.)

It can be seen from the figure that the desired unstable joint behaviour was convincingly simulated by these tension joints. There was a greater relative fall from peak to ultimate strength the lower the normal stress level. The ultimate displacement of approximately 0.18 inch represented 7.7% of the total length of the shear surface. The word ultimate is used since it is unlikely that the residual strength was reached after the given displacement.

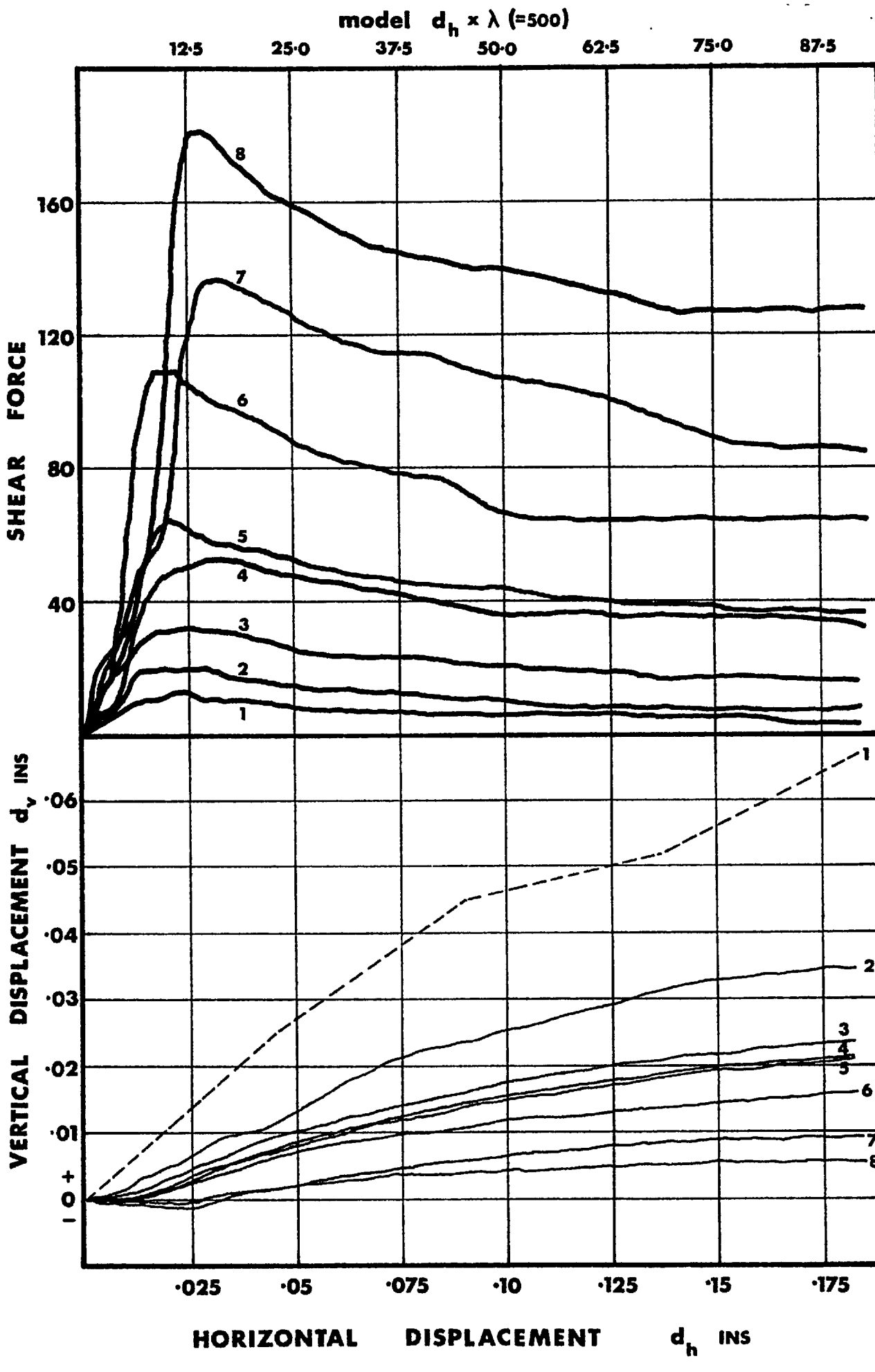

Figure 1.3.8 Shear force-displacement and dilation characteristics for primary tension joints in model material C3.

Reference to the dilation diagram shows that the specimen tested at the highest normal stress (No. 8) ceased dilating before the end of the test. However it is doubtful that this could be taken as positive evidence of residual conditions since the surface of the joint contained some large amplitude asperities right to the end of the test.

The enormous influence of normal stress on the dilatency of a rough joint is clearly demonstrated. The significance of a dilatant surface was discussed in Section 1.1 and has been the topic of several papers by Mencl[23]. He contrasted its effect on shear strength with that of a loose contractile type of surface. A second significant feature shown by this and all other dilation diagrams, for all the two hundred rough model joints tested, was that the maximum angle of dilation occurred at the same horizontal displacement as that of the relevant peak strength position. There was no dramatic change in dilation angle at the peak position, but unquestionably the maximum was approximately as indicated and generally just spanned the peak on either side. The horizontal displacements at which peak strength was mobilized lay between approximately 0.020 and 0.025 inch for the model. This becomes 10 to 12½ inches at prototype scale. It represents approximately 1% of the total length of joint surface.

Figure 1.3.9 Shear force-vertical displacement

This type of diagram demonstrates the relation between the vertical dilation across the joint surfaces, and the mobilized shear strength. It is significant that no total dilation was necessary for the peak strength to be mobilized at the two highest stresses. The dilatency effect was still in operation, but some contraction occurred after a small horizontal displacement. This can be interpreted as increased interlocking of the mating asperities. At prototype scale the peak strength was mobilized after a dilation of less than 2½ inches for all but the two lowest normal stresses.

Figure 1.3.10 Post-peak shear strength envelopes

The fall from peak strength to residual strength occurs during horizontal displacement across the loaded joints. The six strength envelopes presented give some idea of the nature of this drop in strength. It is significant that the complete loss of 'cohesion intercept' with displacement, that is generally and probably falsely assumed, was not demonstrated by these model joints.

It will be apparent from the ultimate envelope that this did not indeed represent residual conditions. A residual angle of friction of approximately 30° would be expected for material C3, based on the value of 28½° obtained from residual tests on flat surfaces of the material.

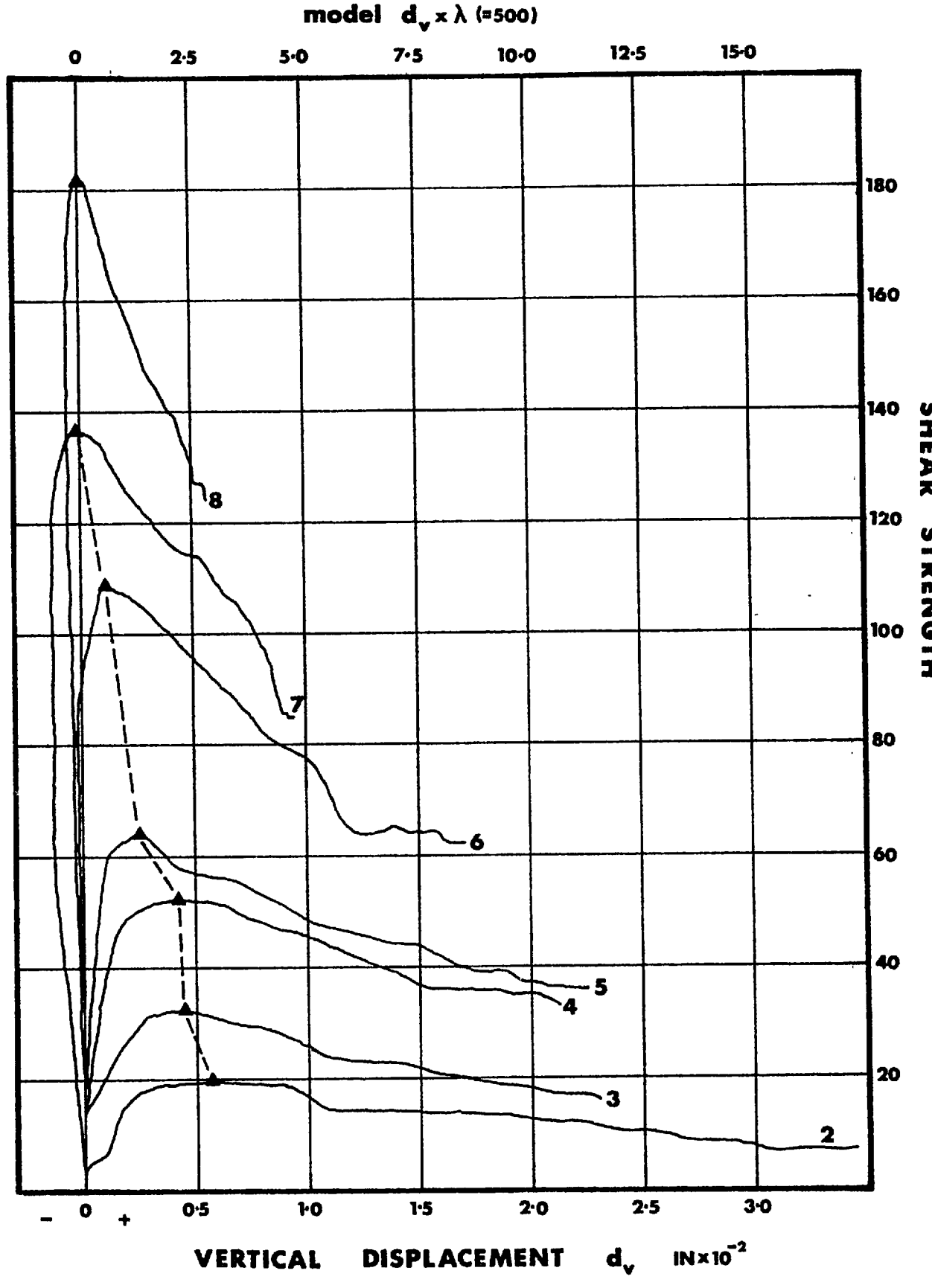

Figure 1.3.9 The relationship between shear strength and vertical displacement for primary tension joints in C3.

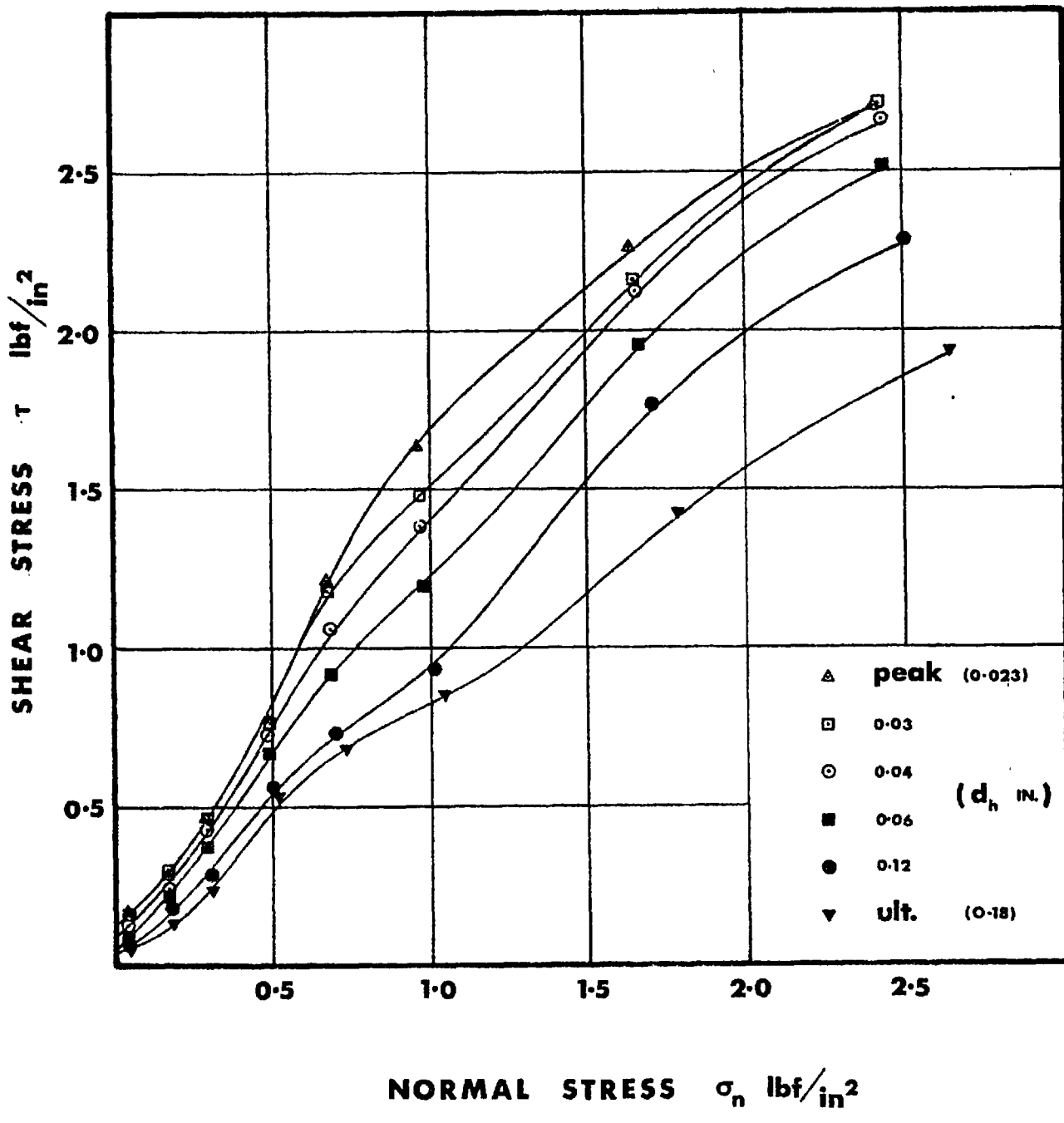

Figure 1.3.10 Variation of shear strength with shear displacement for primary tension joints in C3.

SECTION 1. 3

Figure 1.3.11 Post-peak Strength envelopes at low normal stresses.

Figure 1.3.12 Pre-peak

A magnified impression of the above post-peak behaviour is given by figure 1.3.11, in which the six envelopes are plotted at the four lowest normal stresses only. It is interesting to compare this with the pre-peak behaviour shown in Figure 1.3.12. This is rarely, if ever, considered in the literature, but has an important bearing on slope behaviour that will be appreciated in Section 2.3. Pre-failure displacements of rock slopes during excavation are predictable by the use of such diagrams. It is seldom appreciated that a joint which is undisplaced has more or less zero strength depending perhaps on the cohesion or 'interlock intercept' as it should be called. The concept of cohesion as applied to soils and clays seems hardly applicable to rock joints that are free of infilling material.

Primary and Secondary jointing

It was realized at an early stage that an important physical concept could be modelled using the guillotine devices for extension splitting of model bricks or slabs. This is the concept of primary and secondary jointing discussed by Price[24]. A primary joint set was described as the dominant set, while the secondary set in this connotation was the intermittent, non-continuous set of joints crossing the primary joints. The subject of jointing, particularly in igneous rocks, is of course extremely complicated but it may be justifiable to simplify it for this presentation.

The importance of primary and secondary joints sets in rock mechanics is that the former are continuous, except for intermittent en-echelon offsets. By comparison the latter are non-continuous and are effectively offset in crossing the primary joints. Therefore from the point of view of shear strength, secondary joints dipping into a rock slope would be favourable to stability compared to the more or less continuous primary joints. This difference highlights the problem of finding and testing those joints that are relevant to the failure mode anticipated, and not those irrelevant to it.

When a model block of one inch thickness was placed on the large guillotine slotted table (See Figure 1.3.6) and located between the blades, the first cut produced a 'primary' continuous tension joint. The properties of this type of joint were illustrated in Figures 1.3.8 to 1.3.12. If the split block was then carefully rotated, keeping the split halves together by some means, a second cut intersecting the first produced an offset at the intersection. In fact tensile forces were not transmitted uniformly across an existing crack, even if this was apparently 'closed'. A perpendicular

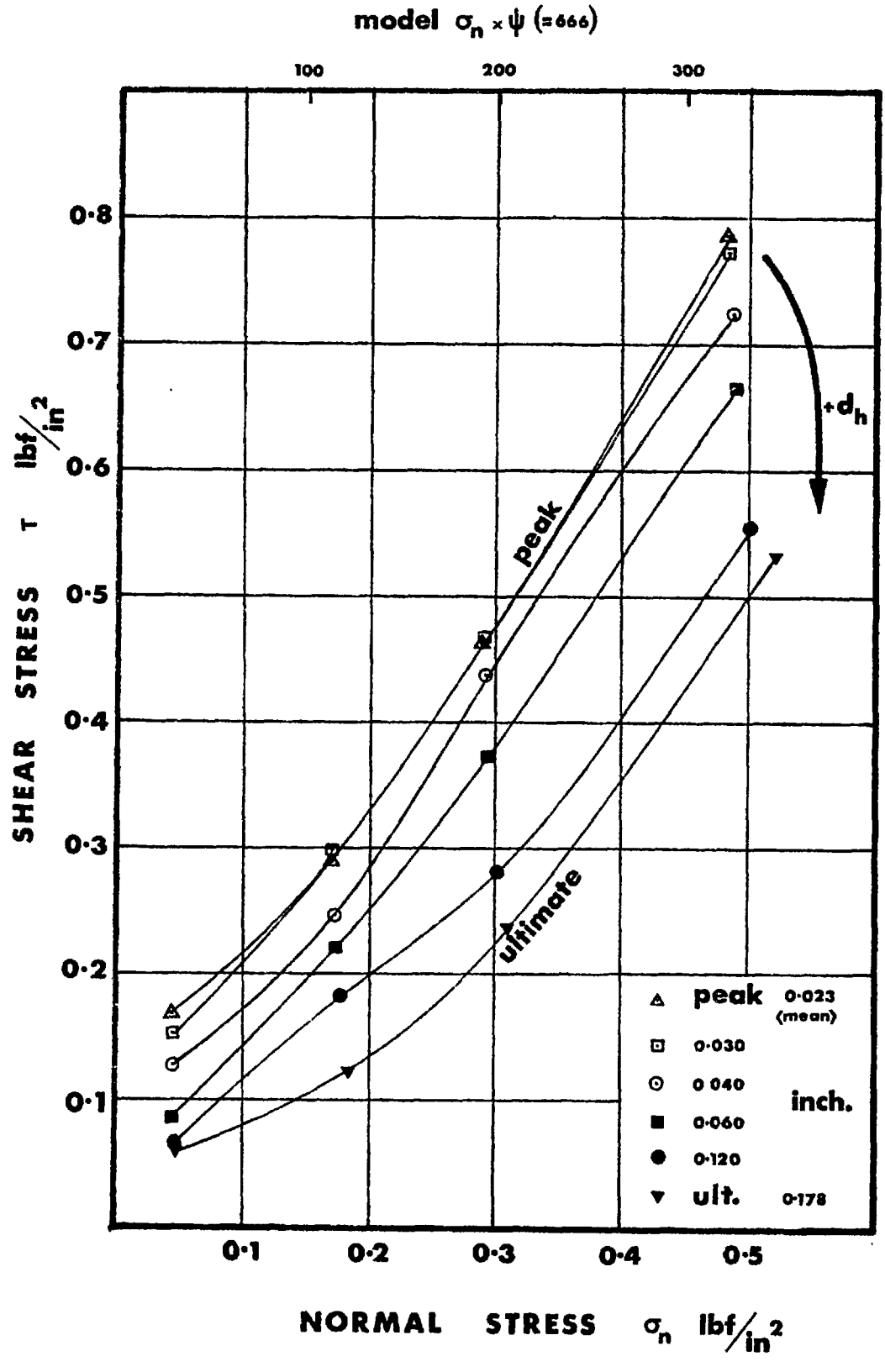

Figure 1.3.11 The post-peak shear strength behaviour of primary tension joints in C3, at low normal stresses

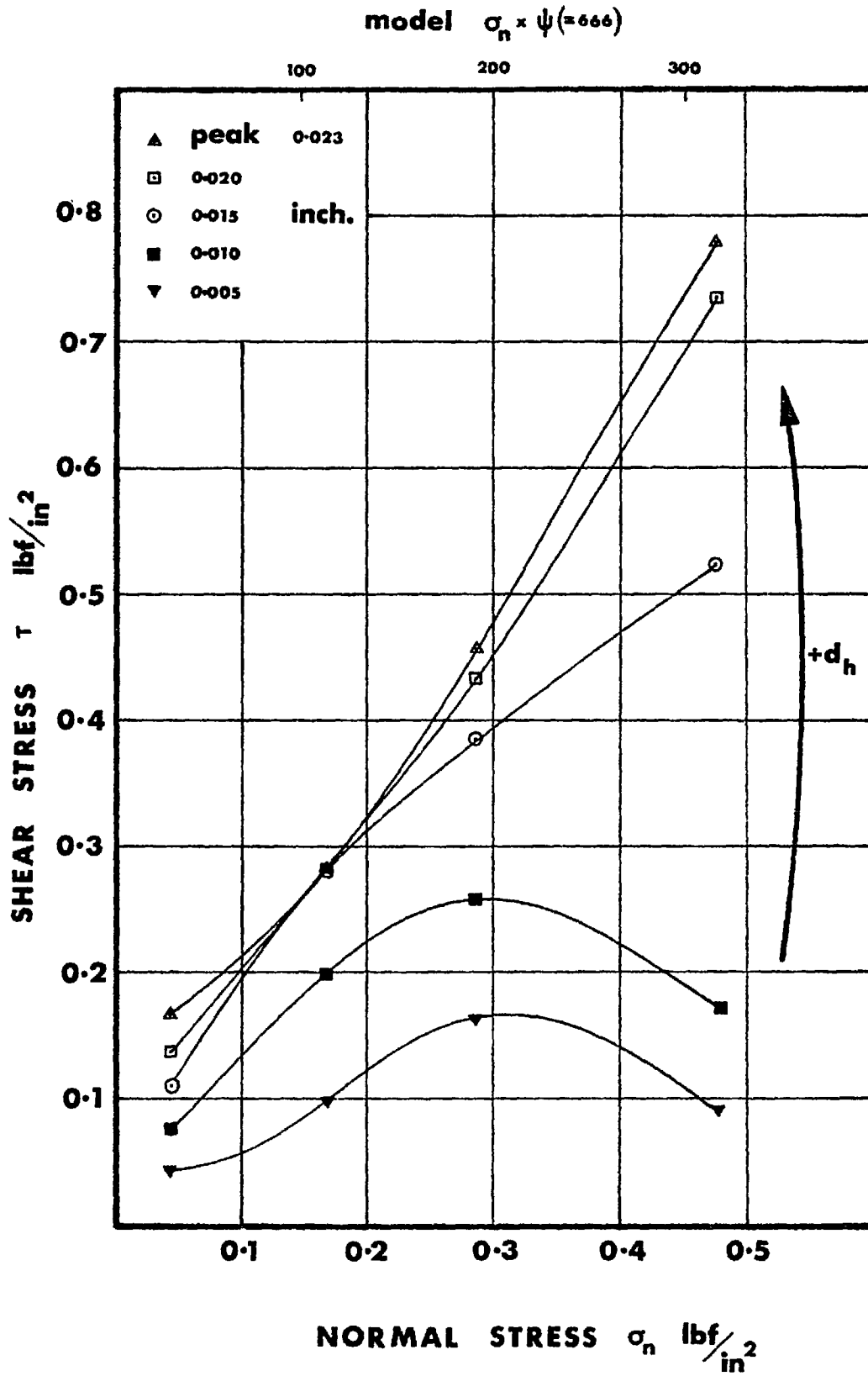

Figure 1.3.12 The pre-peak shear strength behaviour of primary tension joints in C3, at low normal stresses.

intersection between the two joints produced a 'secondary' joint surface which had a small vertical step across it. A large number of primary joints intersected by one perpendicular secondary joint resulted in an interlocking castellated type of secondary joint surface. Features such as these are illustrated in Section 3.1.

A third type of model joint generated in a similar manner was the primary joint intersected by a set of secondary joints. This produced no detectable offsets on the primary joint, but was a relevant joint to test since all the primary joints of the jointed slab models(reported in Part 3) were intersected by secondary joints. This type of joint has been termed 'primary cross jointed' (P.C.J.) The three joint types are illustrated in the inset to the next figure.

Figure 1.3.13 Strength envelopes of three model tension joints

The number of joints in each tested block was as shown in the inset. The large guillotine produced a joint spacing of $\frac{1}{2}$ inch. The comparison of strengths of the three joint types is quite illuminating. The secondary interlocked joints displayed the highest angle of friction and a cohesion or interlock intercept approximately two and a half times that of the primary or primary cross jointed surfaces. The difference was maintained up to high normal stresses when all three curves converged.

A significant separation in behaviour can be seen between the primary and primary cross jointed specimens. This was most marked in the transition stage, where the two peak strength envelopes became less steeply inclined, signifying a changing mode of failure of the type discussed by patton[20]. It appeared that the mode of failure involving shearing through of asperities was occurring at lower stress levels for the specimens (P.C.J.) than for the monolithic primary joints. There is a reasonable explanation for this. It will be realized that the large scale (first order) asperities were effectively reduced in length by the cross joints. Extending this concept, it will be acknowledged that a highly jointed rock mass dislays a markedly curved strength envelope, compared to the envelope obtained for a single joint. This has been reported by several authors including Rosengren and Jaeger[25], Jaeger[26], and Pentz[27]. Cross jointing has the effect of intersecting first order asperities and generally promoting a progressive mode of shear failure.

The model joints displayed ultimate envelopes that were more or less inseparable at low stress levels. However at high normal stress levels the specimens (P.C.J.) were strongest and the secondary joints weakest. The latter was probably due to the greater surface damage noticed for these joints after shearing, in which debris covered much of the lower surface, thereby controlling the strength to a marked degree.

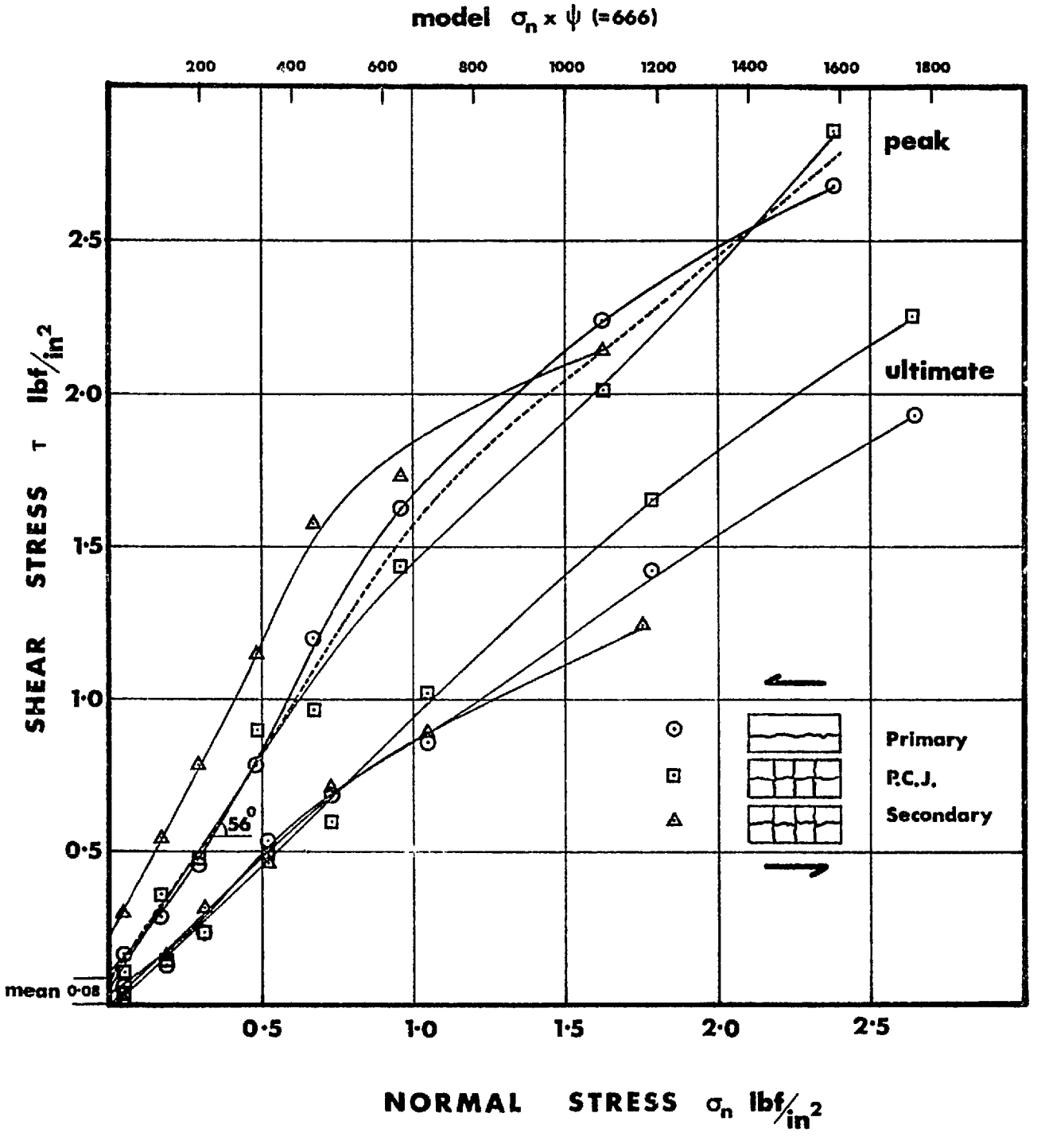

Figure 1.3.13 The shear strength envelopes of three tension joint characters in model material C3.

SECTION 1.3

Figure 1.3.14 Surface damage through shearing

The numbers 1 to 8 refer to the level of normal stress at which the particular specimen was tested. The direction of shearing was as shown by the offset of the upper and lower blocks. The lower blocks in the test were those with some debris still evident (C3(P) No. 7 for instance). In all cases the damage to the surfaces (smoothing of asperities) was most noticeable at normal stresses of No. 5 and above. This represented stresses above 0.67 lbf/in^2 on the model joints, and stresses above 445 lbf/in^2 on the prototype joints. It is significant that this corresponds to the onset of the transition stage, during which the changing mode of shear failure causes a flatter strength envelope to be approached.

Figure 1.3.15 Peak to ultimate strength ratio

The effect of normal stress on the relative drop from peak to ultimate strength is clearly demonstrated by this type of diagram. The interlock effect in the secondary joint surface is clearly shown by the large ratio (16.6 : 1) of peak to ultimate strength at the lowest normal stress. The curves appear to be assymptotic to a ratio of 1 : 1. This might be expected at extremely high stresses, when the presence of joints has no effect on the strength.

It is now necessary to try to relate some of the model joint behaviour just presented to the results reported in the literature for in situ tests on large areas of joint. This is the nearest comparison that can be drawn. Unfortunately it is a somewhat distant comparison due to the large difference in scale. It is inevitable and perhaps excusable, in view of the similarity with intact rock, that several model results will be taken to predict idealized large scale joint behaviour rather than to model it. Until large scale failures can be fully monitored and analysed this approach is inevitable. However it is wise to record the areas of doubt surrounding one or two aspects of the model simulation. These can be listed as follows:

1. The model joint roughness is considerable and should be scaled up and interpreted appropriately. Large scale exposures of joints having lower degrees of roughness will have reduced strength compared to the model prediction.

2. The model joints are completely free of soft infilling, unlike many joints encountered in the field. Likewise the joint walls are fresh fractures and are therefore unaltered by weathering.

3. The width of the model joints when unstressed is too large, probably due to a few loose particles becoming dislodged in the fracture process. For this reason the irrecoverable closure of the model joints when first stressed will exceed that of equivalent joints in the field. In other words a loading history is required to compact the joints

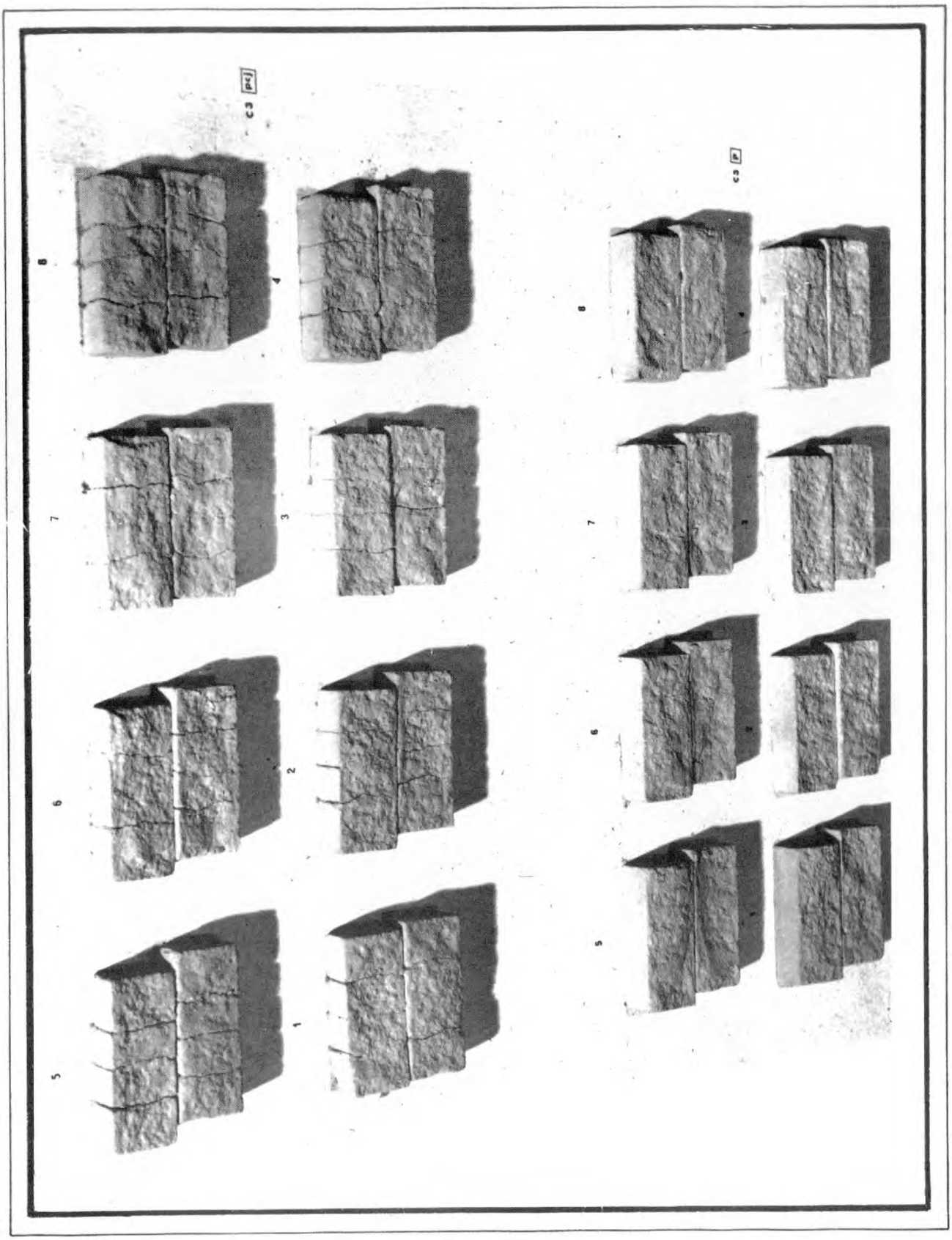

Figure 1.3.14 The surface damage to two tension joint characters after shearing at eight normal stress levels.

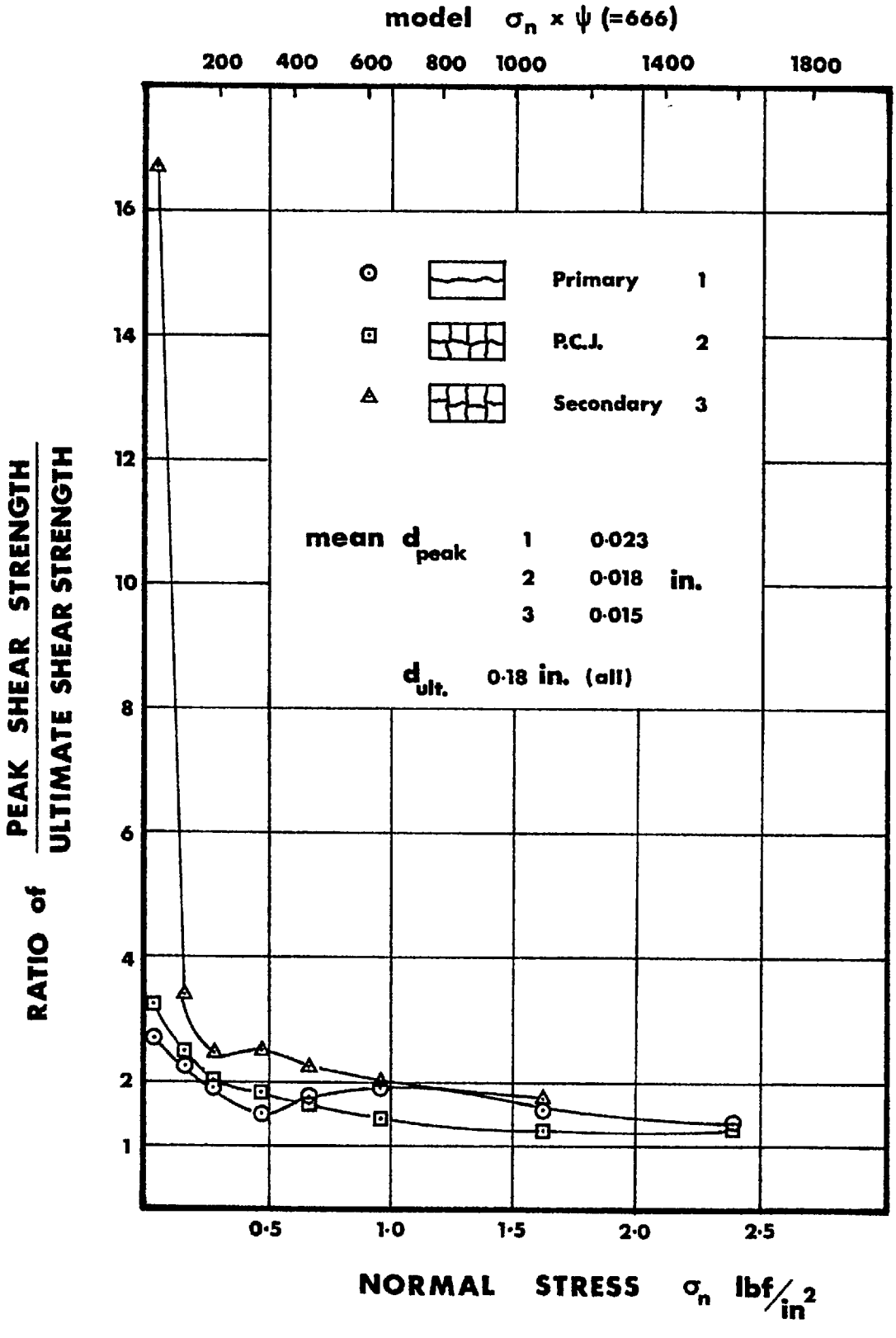

Figure 1.3.15 The ratio of peak to ultimate strength as a function of normal stress for three tension joints in C3

to the 'tightness' appropriate to the stress applied.

1.3.4 COMPARISON OF MODEL WITH LARGE SCALE TESTS ON ROCK

During the past five years several laboratories round the world have developed large shear machines capable of testing joint areas of approximately 1 to 2 ft^2. in the laboratory. The cost of field sampling and of mounting the blocks in these shear machines is of course quite high. However it may be assumed that the test conditions can be more reliably controlled than those operating in in-situ tests on larger joint surfaces in the field.

Large scale field tests are extremely expensive to set up. It is for this reason that the general approach has been to run one 'undistrubed'test for each test block prepared. This is usually taken only just past peak strength, following which a series of sliding tests are run at different normal loads. Thus a 'psuedo residual' envelope can be obtained from one test block. This has obvious financial implications.

The undisturbed point obtained from such tests generally lies above the psuedo residual envelope. (An exception to this is when the joints have some infilling material. Increased sliding can then result in increased rock to rock interference) The 'vertical' separation of the undisturbed point from the envelope has been interpreted as the 'cohesion' by Ruiz, Camargo, Midea and Nieble[29].

As a direct consequence of the expense and the above test proceedure, there is a limited amount of data from in-situ tests which can be compared with the model joint performance. In addition, many in-situ tests are performed where there is some doubt as to the contribution to strength of failure through intact material. It is not always possible to excavate a test block with a horizontal axis coincident with the strike direction of a joint.

A further problem encountered with large in-situ tests is the progressive failure which can be caused by applying the shear force at one end of a jointed block of rock. Krsmanovic and Popovic[30] describe in-situ shear tests on fissures in limestone of $5m^2(65ft^2)$ in area. The horizontal displacements of the blocks were measured at twenty locations across the surfaces. For all the blocks tested the profile of displacement was greatest at the rear end of the blocks where the shear force was applied, and least at the front. Differential displacements of between 25 and 40 mm. (1.0to 1.6 inches) were recorded. With such large differences between ends it is to be expected that the rear of the block would pass the peak strength and reduce towards the residual before the front of the block had even reached peak strength. Such progressive failure, while producing a conservative strength result, does not facilitate the interpretation of the strength data obtained.

SECTION 1.3

Comparison of Shear Strength

One of the largest in-situ tests ever performed was reported by Ruiz et al[29]. The base area of 34.9^2 (450 ft^2) was loaded normally by the weight of the block itself. This amounted to a stress of 1.71 Kg/cm^2 (24.3 lbf/in^2), which can be compared to the model tests at the lowest normal stress. The base of the block was arranged to be coincident with a basalt-breccia contact. The undisturbed and first sliding test gave peak values of arctan (τ/σ) of 69° and 68° respectively. A large proportion of this function was due to the contribution of the roughness of the brecciated surface. Peak dilation angles of 39° and 32° were measured for the above tests. The same authors described tests on 4 m^2 (52 ft^2) areas of sparsely jointed basalt. A question mark exists over the contribution of failure through intact material. However, the results are of interest since they demonstrate the different interpretations of peak strength envelopes that can be made. Two tests were performed at a normal stress of 2 Kg/cm^2 (28.4 lbf/in^2), and both gave peak values of arctan (τ/σ) of 73°. Two further tests were performed at a normal stress of 7 Kg/cm^2 (99.4 lbf/in^2), giving peak values of arctan (τ/σ) of 53° and 63°. Either these tests are interpreted as demonstrating an appreciable cohesion or interlock intercept, or they are taken as indications of a distinctly curved strength envelope inclined very steeply close to zero normal stress.

Assuming comparison with the model results is valid, the two normal stress levels corresponding to the tests above produced values of arctan (τ/σ) of 71° and 62° from the model joints.

Several series of shear tests on a large laboratory shear machine have been reported by Krsmanovic and co-workers. Figure 1.3.16 shows the strength curves for tests on 40 cm x 40 cm (15.75 inches square) surfaces of discontinuities in limestone. These were given in a paper by Krsmanovic, Tufo and Lango[10]. The discontinuities were described as 'stratification surfaces of different degrees of roughness'. This was in contrast to a series on 'fissures of great roughness'.

The unstable form of the shear force-displacement curves is quite similar to those obtained for the model (see Figure 1.3.8). However the peak strength envelope is uniformly curved compared to the envelopes obtained for model joints (Figure 1.3.13), which can be approximated to bi-linear relationships quite successfully. This may be indicative of a dominant wave form in the model roughness, which would promote a transition in the mode of failure within a distinct range of normal stress. By comparison a wide range of roughness wave forms would cause the uniformly curved envelope for the in-situ test.

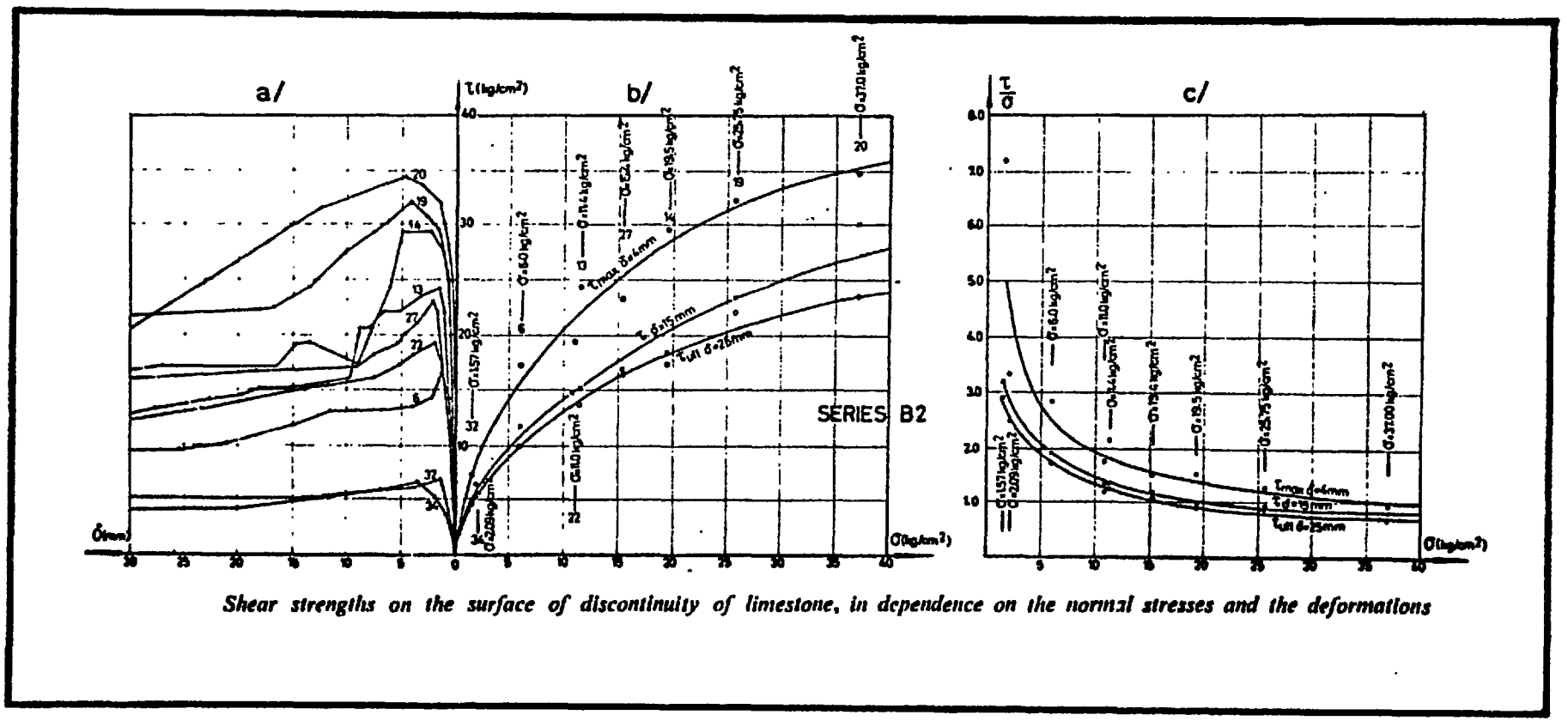

Shear strengths on the surface of discontinuity of limestone, in dependence on the normal stresses and the deformations

Figure 1.3.16 The results from tests on a large shear machine reported by Krsmanovic, Tufo and Langof[10].

The curvature of the ultimate envelope in Figure 1.3.16 reinforces the suspicion discussed earlier, that an apparent interlock intercept exists even after post-peak displacements have occurred. Some shear tests on sandstones reported by Krsmanovic[9], were taken to ultimate displacements of 4.5 cms (1.8 inches). The envelope obtained had an inclination of 33° and zero interlock intercept, thus corresponding more or less to residual conditions. However the strength envelope for a displacement of 0.5 cm (0.2 inch), though parallel to the ultimate envelope still displayed an appreciable interlock intercept.

Comparison of displacements at peak strength

From a comparison of model and in-situ results it would appear that the strength-size effect of joints is small compared to the displacement-size effect. The model joints provide controvertial evidence that large areas of joint require much larger displacements to reach peak strength than do small specimens of joint surfaces. It is clear that roughness plays a large role in this effect. However this will not be discussed further here since it forms the subject of much of Section 2.1.

The importance of the peak displacement is best illustrated by the results of Seraphim and Guerreiro[31]. A large number of in-situ tests were performed at three Spanish dam sites, both parallel and perpendicular to stratification planes. It was found that for equal normal stresses, the horizontal displacements at peak strength were 0.5 to 3.0 cms (0.2 to 1.2 inches) for the parallel tests, and 1.2 to 5.0 cms (0.6 to 2.0 inches) for the tests perpendicular to stratification planes. This result was also experienced in the model tests reported earlier. The tests through intact model material which presumably can be compared to the perpendicular tests above, showed peak strengths at a mean displacement of 0.055 inch. By comparison the numerous tests performed on model joints showed peak strengths at displacements averaging 0.020 inch. This is a suprising anomaly. It is presumably caused by the fundamental difference in the roughness and amplitude of roughness, between surfaces generated by shear stresses, and those generated by tensile stresses.

The same authors[31] give interesting results illustrating the effect of clay infilling of joints on the peak displacements. Two test types were distinguished.

1. Stratification plane partly covered with film of clay. Shearing occurring with considerable collaboration between the two blocks.

2. Stratification plane totally covered with film of clay. No collaboration whatsoever between upper and lower block.

The horizontal and vertical displacements at peak strength were approximately seven times smaller for the shear surface entirely within the clay film (type 2). Similar observations were apparently made at many other dam sites. It is an illustration of the unpredictability of rock masses in which clay infilling exists. Failure can be expected at much lower stresses on clay filled joints. In addition, displacement monitoring systems will be that much less effective in such environments. Unfortunately this important aspect of joint performance could not be modelled with the present method of joint simulation, so no comparisons are possible.

It appears from a literature review that the peak displacements obtained in large shear machines were of the order of 0.1 to 0.6 inch in general The large in-situ tests while showing somewhat larger peak displacements, were still mostly less than 1 inch. In his review of the deformability of joints Goodman[32] gives typical ranges of peak displacements for various types of joints. A mean value of 0.3 inch is quoted for undisturbed, clean rough fractures. In comparison, the range for filled joints, sheared zones, shale partings and smooth bedding was only 0.05 to 0.12 inch, which illustrates the effect of roughness on joint displacement.

Some tests on 12 inch by 9 inch areas of schist were performed by Kutter[33]. The specimens were tested parallel to bedding. Despite the fact that 'cohesive' bonds across the bedding had to be broken for shearing to occur, peak displacements were quite large and there appeared to be some relation between the magnitude of this displacement and the level of normal stress applied. Tests at normal stresses of 140, 400 and 800 lbf/in^2 gave peak displacements of approximately 1/10 1/5 and 3/5 inch respectively. An earlier series of tests on porphyry joints was performed on the same machine by Pentz[34]. This shear machine has been described by Hoek and Pentz[35]. The range of normal stresses was 500 to 1400 lbf/in^2, and the peak displacements were 1/5 to 3/5 inch. There was in this case no apparent relation of displacements with normal stress.

Several authors have recorded the variations of <u>vertical</u> displacement (dilation) with shear force. Ruiz et al[29] recorded contraction at the beginning of some shearing tests, and peak strength was often defined by the point at which this movement inverted to cause dilation. Nose[36] recorded initial contraction followed by up to 5 mm (0.2 inch) of dilation before peak strength was reached on large 10 m^2 (129 ft^2) in-situ blocks. Seraphim[37], and Jimenez Salas and Uriel[38] give shear force-vertical displacement diagrams describing the behaviour of model curves given in Figure 1.3.9, but unfortunately in-situ tests are seldom if ever taken past the peak without changing the normal stress to obtain a psuedo residual envelope. This practice which was discussed earlier, means that no continuous records of dilation from start to finish are available for model comparison.

SECTION 1.3

The controversial evidence of a displacement-size effect predicted by the model joints is provided by the table below. It will be remembered that the prototype joint surface simulated by the model had dimensions of 96 feet by 42 feet. This is five times as long as the largest in-situ test that has been reported to date.

Table 1. Prototype displacements extrapolated from the three joint types.

NORMAL STRESS	DISPLACEMENTS								
σ_n (lbf/in^2)	d_h peak (ins)			d_v peak (ins)			d_v ultimate (ins)		
(ALL)	C3(P)	C3(PCJ)	C3(S)	C3(P)	C3(PCJ)	C3(S)	C3(P)	C3(PCJ)	C3(S)
29.3	11.5	4.5	3.5	-	-	-	-	-	-
112	7.5	10.0	5.5	3.75	4.00	2.25	17.1	11.7	19.5
191	12.5	8.0	9.0	3.10	3.45	2.05	12.8	13.3	18.6
318	12.0	9.5	9.0	2.05	1.70	2.25	11.1	13.0	11.2
445	12.5	9.4	10.0	1.70	2.85	0.60	11.7	6.6	14.2
635	9.5	9.0	7.0	0.55	1.25	0.25	7.0	6.3	11.4
1080	11.0	10.5	9.5	0	0.80	0	5.4	4.6	2.1
1589	13.5	11.0	-	0.70	0.35	-	2.4	2.6	-

Where C3(P): represents single primary joints.
C3(PCJ): represents primary joints with perpendicular secondary cross joints.
C3(S) : represents secondary joints with perpendicular primary cross joints.

and d_h (peak) : is the horizontal displacement at peak shear strength.
d_v (peak) : is the vertical displacement at peak shear strength.
d_v (ultimate) : is the vertical displacement at the end of each shear test. The prototype scale d_h (ultimate) for all three series was 90 inches.

A full discussion of roughness and of the displacement-size effect is given in Section 2.1. However it is pertinent to point out here that a series of model shear tests has been performed on joints in different strengths of material. By inverting this dimensional problem the tests can be interpreted as representing a series of tests on different dimensions of joint, all performed on the same strength of material. A range of joint surfaces from $7\frac{1}{2}$ to 96 feet long was simulated by this means. It is significant that the peak horizontal displacements for the $7\frac{1}{2}$ feet prototype were from $\frac{1}{3}$ to 1 inch for the simulated range of normal stresses of $2\frac{1}{2}$ to 1640 lbf/in^2. This $7\frac{1}{2}$ feet dimension corresponds closely to the in-situ test dimensions often tested.

Conclusion

The tension joints generated in model material C3 are assumed to be realistic models of rough, undulating joint surfaces which might be encountered in the field. Critics of the excessive roughness of the joints may be misled by the ease with which planar joint exposures are seen in the field. In any open pit the planar joints exposed are immediately recognised due to their regular form and encreased reflection of light - particularly when wet. Rough joints are much less apparent from any cursory glance.

Large scale joint roughness is unfortunately outside the field of interest of structural geologists. Consequently the number of joint profiles available for comparison is extremely small. Patton[20] and more recently Rengers[39] are perhaps the only two authors to have systematically measured large scale roughness profiles. The Ph.D thesis (in preparation) by Rengers (Die Reibungseigensch aften von Gesteinstrenn flächen in Zusammenhang mit deren Oberflächen besch affenheit. University of Karlsruhe 1970) should provide some much needed information on joint roughness, and the effect of this on the shear strength.

It can be concluded that model joints have been produced which, whether too rough or too planar, display realistic characteristics when sheared. The magnitude of these characteristics is thought to be less important than the quality. Joints which are excessively rough will support steeper or higher rock slopes, but this should not effect the mode of failure induced.

SECTION 1.4

I.4. STIFFNESS OF JOINTS

SUMMARY

The results of normal loading tests on model joints are presented, and values of normal stiffness calculated. It is found that these values are stress dependent, and suprisingly reduce to a minimum with increasing stress before rising at higher stress levels when the joints become more tightly closed. This behaviour is also seen in some in-situ plate loading tests.

Some data on in-situ loading tests are analysed in which the joint spacing below the jacking plate was known. This produced a value of normal stiffness of 33,400 lbf/in^2 per inch which is in agreement with the projected model results at low stresses. The value of the modulus ratio (Emass / E intact) from this test and from some reported in the literature indicate that the jointed models have suitable values of this ratio, ranging from 1/2.4 to 1/5.0. It does not appear that normal stiffness is size dependent.

The shear stiffness of primary, primary cross jointed and secondary model joints are compared, and the corresponding prototype values presented. It appears from the model results that shear stiffness may be markedly size dependent as well as stress dependent. Values from 20 to 150 lbf/in^2 per inch were obtained for a simulated prototype normal stress range of 0 to 1600 lbf/in^2. The models represented a prototype length of joint of approximately 100 feet. In comparison, some large in-situ tests on lengths of joint of approximately 16 feet gave values of 130 and 160 lbf/in^2 per inch at low stresses, while values up to 3500 lbf/in^2 per inch were obtained from shear tests of joint lengths of only 1 foot, tested at high stress. An inverse proportionality between shear stiffness size was indicated.

1.4 STIFFNESS OF JOINTS.

INTRODUCTION

The behaviour of a joint when stressed is an important component of rock mass performance under load. At the stress levels encountered in near-surface excavations, it can be anticipated that joint behaviour will completely dominate the 'elastic' deformations of the intact rock. For this reason the shear and normal stiffness of joints have fundamental implications to the more sophisticated 'Finite Element' and 'Finite Difference' analyses of rock masses under load. (See Goodman, Taylor and Brekke [28]).

The normal stiffness of a joint is usually defined as the normal stress per unit closure, with units of lbf/in^2 per inch. Since this stiffness is generally lower than that for the intact rock separating the joints (depending on joint spacing), the mass E modulus may be as much as an order of magnitude less than the modulus measured from tests on unjointed laboratory specimens.

A second measure of stiffness of a rock mass is that concerning the shear displacement on a joint under a given shear stress. This shear stiffness is assumed to be uniform up to the peak shear strength, and is defined by the mean gradient of the shear stress - shear displacement diagram, taken as far as the peak strength. It has the same units as normal stiffness. Goodman et al[28] also define a residual shear stiffness in an attempt to model progressive failure numerically. However this will not be considered here since there is some doubt as to the shear displacement required to reach the true residual strength. (See Section 1.3)

SECTION 1.4

1.4.1 NORMAL STIFFNESS K_n

Normal loading and unloading tests were carried out in the small shear box (5.3 in^2) on various joints generated in the model materials. The joint dimensions were identical to those tested in shear, and represented prototype surfaces of 96 feet by 42 feet, when interpreted at the same scale as that reported in Section 1.3

It can be seen from Figure 1.4.1 that a datum normal stress of 0.30 lbf/in^2 was applied throughout. This was unavoidable since the vertical displacement and loading systems had to be applied via the light platten and loading yoke shown previously in Section 1.3 (Figure 1.3.3) These could not be removed between the normal load cycles without disturbing the specimens.

The results shown are the mean of three tests. Similar results were obtained for primary joints in material C2, and secondary joints in material C3. However it might be expected that the normal stiffness of interlocking secondary joints would be affected by an intermediate compressive stress acting in a direction such as to stress the interlocked teeth longitudinally. This loading refinement was not possible in the test arrangement used.

The first cycle of loading at each stress level produced a large and more or less irrecoverable closure of the joints. The load was applied for several minutes to 'pre-consolidate' the joints. It was then reduced to the datum and re-applied to produce an approximate stiffness line. The joint closures presented in Figure 1.4.1 have been corrected for the elastic displacements predicted for the solid material which was situated above the joint in the loading box. It should be noted that the maximum normal stress applied (5.07 lbf/in^2) was approximately one quarter of the unconfined compression strength of the intact material.

Table 1. summarises the model normal stiffness results and gives the prototype equivalents predicted from geometric and stress scales of 1 : 500 and 1 : 666 respectively. The conversion factor is the ratio of (ψ/λ) which is equal to 1 : 1.25.

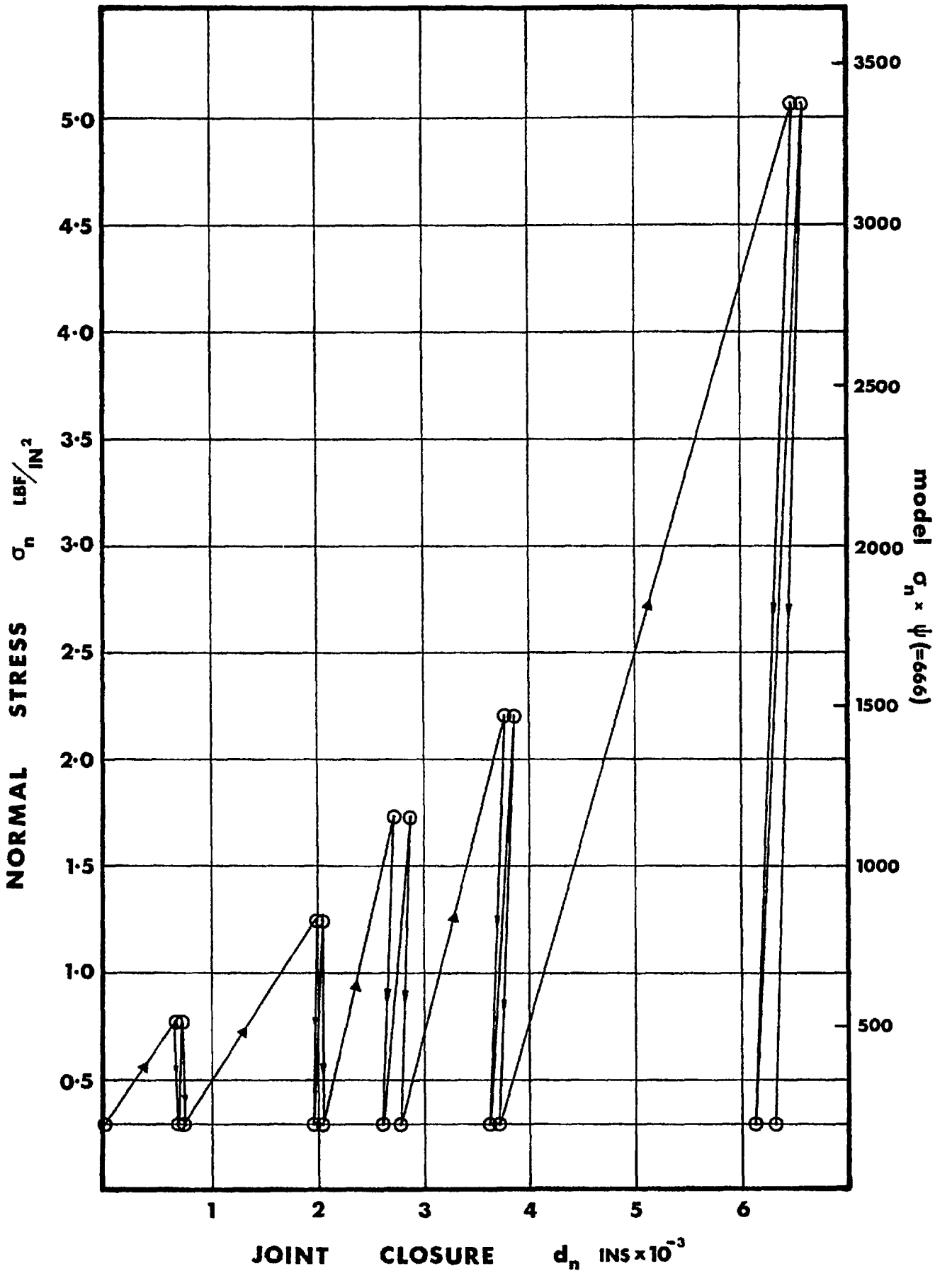

Figure 1.4.1 The effect of normal stress cycles on the closure of primary tension joints in model material C3.

SECTION 1.4

Table 1. Normal stiffness of primary joints from model material C3.

$\Delta\sigma$ (lbf/in^2) Model	d_n ($\times 10^4$) (lbf/in^2)	Total consolidation Stress (lbf/in^2)		Stiffness K_n (lbf/in^3)	
		Model	Prototype	Model	Prototype
0.477	0.31	0.774	516	1.54×10^4	2.04×10^4
0.952	0.88	1.249	832	1.09 "	1.45 "
1.429	2.70	1.726	1150	0.53 "	0.70 "
1.904	2.52	2.201	1468	0.76 "	1.01 "
4.770	5.17	5.067	3377	0.93 "	1.23 "

It can be seen that the stiffness under intermediate stresses was smaller than that at both lower and higher stress levels. This unexpected trend is shown in Figure 1.4. 2 (a). The lower bound value of 7000 lbf/in^3 at a prototype stress of 1150 lbf/in^2 presumably indicates some radical change in the mode of 'normal failure', with changing normal stress.

The first cycle of loading at each stress consolidated the joints, causing mostly irrecoverable closure appropriate to the stress level applied. This constituted a loading history, thereby colouring subsequent behaviour. The anomalous result for intermediate stress levels was probably due to the interaction of three modes. Namely, small elastic displacements (at low stress), loosening and rolling of particles on the asperity slopes (at intermediate stress), and large increases in true contact area (at high stress).

1.4.2 SHEAR STIFFNESS K_s

The shear stiffness of a joint was defined previously as the ratio of the peak shear stress to the shear displacement at this peak. It may have been noted from Section 1.3 that there was little variation in the peak displacements of the model joints for the range of normal stresses considered. For this reason one would anticipate considerable variation in shear stiffness for different normal stresses.

Table 2 shows the mean shear stiffnesses for the three types of tension joint generated in material C3 (see Section 1.3), for the eight normal stresses applied. Model stiffnesses are shown scaled up to the prototype stiffnesses ($\times \psi/\lambda$) in the right hand columns.

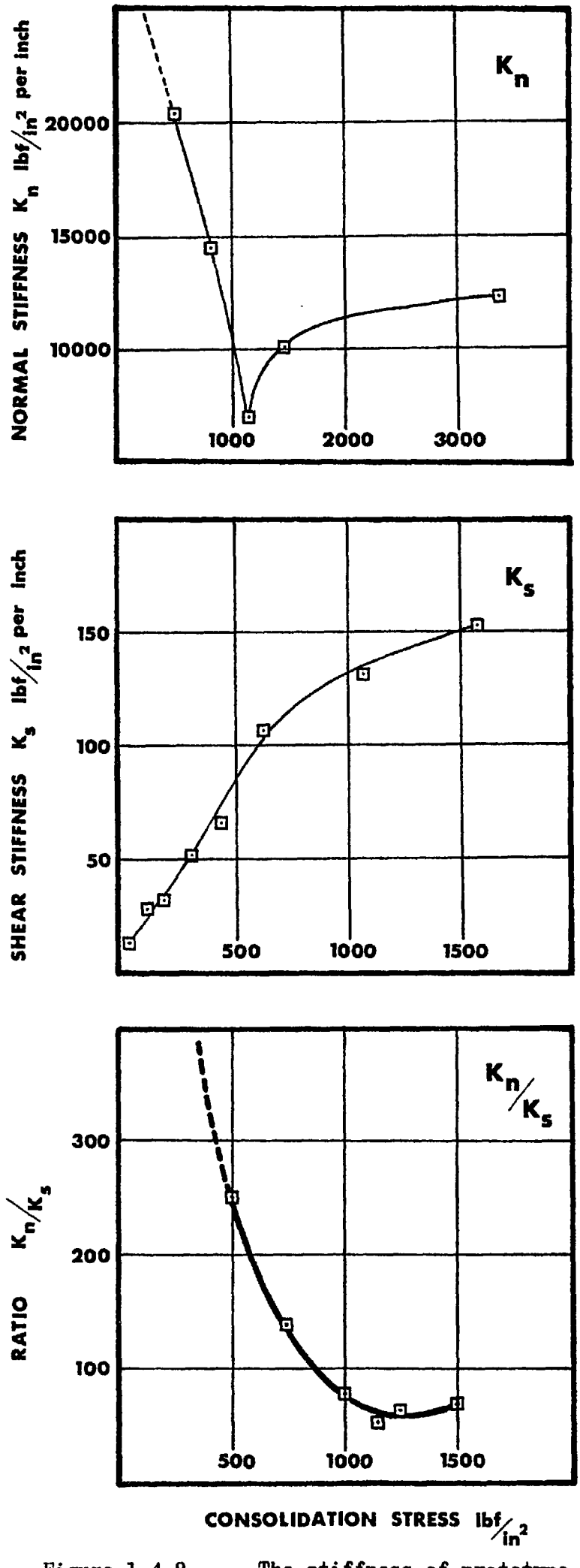

Figure 1.4.2 The stiffness of prototype joints.

SECTION 1.4

Table 2. Shear stiffness of model and prototype joints

MODEL				PROTOTYPE			
σ_n	K_s (lbf/in^3)			σ_n	K_s (lbf/in^3)		
lbf/in^2	C3 (P)	C3 (PCJ)	C3 (S)	lbf/in^2	C3 (P)	C3 (PCJ)	C3 (S)
0.044	7.4	12.0	43.0	29.3	9.8	15.9	57.1
0.168	24.2	17.8	49.0	112	32.2	23.7	65.4
0.286	18.2	30.0	43.3	191	24.2	40.0	57.8
0.477	31.0	46.5	63.7	318	41.3	62.1	84.7
0.668	49.3	51.0	78.8	445	65.8	68.0	105
0.954	84.0	77.5	123	635	112	103	164
1.620	102	96.2	112	1080	135	128	149
2.383	100	130	-	1589	133	172	-

Note: No specimens of secondary joints (C3.S) were available for tests at the highest normal stress, due to handling damage.

The mean trend shown by joints C3 (P) and C3 (PCJ) (primarary and primary cross jointed) are shown in Figure 1.4.2 (b). The shape of the curve is very similar to that of the peak shear strength envelopes given in Section 1.3 (see Figure 1.3.13) Diagram (c) of Figure 1.4.2 shows the ratio of normal and shear stiffness for primary joints in material C3. Due to the datum stress applied in the normal stiffness loading tests, it is not possible to compare the two stiffnesses below a prototype stress of 500 lbf/in^2. However it would appear from a tentative extrapolation that the ratio (Kn/Ks) might rise to between 500 and 1000 at very low stresses.

1.4.3 RELEVANCE TO ROCK MASS BEHAVIOUR.

Currently available literature on rock joint behaviour is limited almost entirely to shear testing (laboratory or in-situ) and plate bearing tests (in-situ). From the former it is possible to obtain shear stiffness data. However no normal stiffness data can be obtained from the latter unless the joint spacing is known. As far as the author is aware no data has been published of both shear and normal stiffness for the same joint surface. It is for this reason that normal stiffness measurements have been made on the model joints.

1. Comparison of shear stiffness

The model joint results reported in Section 1.3, and the large shear machine and in-situ tests reported in the literature indicate that there is no marked increase in peak shear displacements with increasing normal stress. Peak displacements appear to vary from approximately 0.1 to 0.6 inch for a wide range of normal stresses, and for a fair range of joint dimensions (say 1 to 10 feet in length). For this reason the values of peak shear stiffness are largely dependent on normal stress. Consequently the shear stiffness can be expected to vary from values of perhaps a hundred or two at low normal stresses up to several thousand at normal stresses above say 1000 lbf/in^2. Three examples can be cited:

a) The large in-situ test reported by Ruiz et al[29](Section 1.3) implies values of shear stiffness of 161 and 128 lbf/in^2 per inch for the undisturbed and first sliding tests. This was for a joint area of 450 ft^2, loaded normally by the self weight of the block to a stress of 24.3 lbf/in^2.

b) Goodman[32] gives a mean value of shear stiffness for undisturbed samples of clean, rough fractures of 3600 lbf/in^2 per inch, but without specifying the normal stress range which is applicable.

c) Tests on porphyry joints of approximately 1 ft^2 in area were reported by Pentz[34]. Normal stress levels of 500 to 1400 lbf/in^2 were applied in a large shear machine referred to in Section 1.3. Goodman, Taylor and Brekke [28] also refer to these tests and quote a shear stiffness of 3,780 lbf/in^2 per inch for one of the joints tested, presumably at a normal stress in excess of 1000 lbf/in^2 in view of the peak displacements.

It is clear therefore that joint shear stiffness is very much stress dependent. Model shear tests indicate that joint shear stiffness may also be markedly size dependent. Table 2. given earlier showed that for a range of modelled prototype normal stresses of 30 to 1600 lbf/in^2, and for simulated joint surfaces of 96 ft by 42 ft, the range of joint shear stiffnesses was approximately 10 to 170 lbf/in^2 per inch (see Figure 1.4.2 (b)).

SECTION 1.4

The effect of joint stiffness on the shear deformation of a rock mass can be readily evaluated. The shear nodulus (μ) is employed to predict the shear stiffness of the intact rock between the joints. The shear modulus is defined as:

$$\mu = \frac{Ei}{2(1+\nu)}$$

where ν = Poisson's ratio
Ei = Young's modulus of intact rock.

Ei model = 1.07×10^4_6 lbf/in^2.
Ei prototype = 7.13×10^6

If a Poisson's ratio of 0.2 is assumed for model and prototype, then the shear modulus for the prototype rock will be approximately 3×10^6 lbf/in^2.

The model joint spacing employed in all the models described in Part 3 was $\frac{1}{2}$ inch. At prototype scale this becomes one joint per 20.8 ft of intact rock. Thus the shear stiffness of the intact prototype rock will be approximately 12000 lbf/in^2 per inch. Therefore even with this extremely wide simulated joint spacing, the presence of joints completely dominate the deformation behaviour of the prototype mass that is being modelled. The joints appear to be between three and two orders of magnitude less stiff than the 21 ft of intact material separating them, depending on the normal stress level. The presence of three intersecting joint sets used in the models will probably accentuate the difference still more.

2. Comparison of normal stiffness

A large number of plate bearing tests are reported in the literature. These are generally performed at dam sites in an attempt to obtain a deformation modulus for the rock mass, for comparison with the E modulus of the concrete dam. Due to the complexity of jointing the deformation performance of each joint set is almost impossible to estimate. In fact even the joint spacing of horizontally bedded strata is seldom reported with any degree of certainty.

However, attention has recently been focussed on the possible influence of the state of stress on the joint water flow in rock masses. Several authors have considered this problem, and it is to be hoped that some much needed information on joint normal stiffness will ensue. Louis[40] and Louis[41] has given some data on plate bearing tests performed during a comprehensive series of in-situ tests to investigate the foundation and abutment performance at a French dam site. The dam was constructed on more or less horizontally bedded limestone with conveniently regular systems of discontinuities. It was noted that a lot of

the joints had some clay infilling material. A comparison of the deformation performance of the joints with laboratory tests on the intact limestone showed the following approximate results:

$$\text{Rock mass} \quad E_m = 710{,}000 \text{ lbf/in}^2$$

$$\text{Intact rock} \quad E_i = 7{,}100{,}000 \text{ lbf/in}^2$$

The loading tests were performed perpendicular to the bedding joints, which had a mean spacing of 60 cms (2 ft). Knowing the spacing it is possible to estimate the normal stiffness of individual bedding joints. For intact material which is assumed elastic:

$$\text{Normal stiffness} = \frac{\sigma}{d} = \frac{E_i}{L}$$

where (d) is the deformation of a dimension (L) of intact rock for a given stress (σ).

Therefore when considering intact rock divided by joints at a mean spacing (L), the components of deformation of the rock mass can be written as follows:

$$d_{mass} = d_{intact} + d_{joints} = \frac{\sigma L}{E_{mass}}$$

$$\text{where: } d_{intact} = \frac{\sigma L}{E_{intact}}$$

$$\text{and : } d_{joint} = \frac{\sigma}{K_n} \cdot \frac{L}{\ell}$$

Therefore one can write E_{mass} as follows:

$$E_m = \left[\frac{1}{\frac{1}{E_i} + \frac{1}{K_n \cdot \ell}} \right]$$

$$\frac{E_m}{E_i} = \left[\frac{K_n \cdot \ell}{K_n \cdot \ell + E_i} \right] \qquad \text{(1)}$$

The ratio of (E mass / E intact) given by Louis was ($1/10$). Therefore substituting in equation (1) one obtains an estimate of the normal stiffness of the joints that were tested.

$$K_n = 33{,}400 \text{ lbf/in}^2 \text{ per inch.}$$

The dimension of intact limestone with the same normal stiffness as one joint is therefore:

$$L = \frac{E_i}{K_n} = \frac{7.1 \times 10^6}{3.34 \times 10^4} = 212.5 \text{ inches} = 17.7 \text{ ft.}$$

It will now be of interest to compare this in-situ result with the prototype performacne predicted by the model joint results. The dimensions of model material having the same normal stiffness as one model joint can be calculated from the previous relationship. The model and prototype equivalent dimensions at five normal stresses are tabulated below.

Table 3. Dimensions of intact material with equal stiffness to one model joint.

MODEL		PROTOTYPE		
σ_n	L	σ_n	L	
(lbf/in^2)	(ins)	(lbf/in^2)	(ins)	(ft)
0.774	0.70	516	350	29
1.249	0.99	832	492	41
1.726	2.02	1150	1013	84
2.201	1.41	1468	706	59
5.067	1.15	3377	578	48

It should be noted that the stress distribution in the model tests was probably more uniform than that acting on the joints beneath the in-situ loading plates. The influence of boundary stresses in the latter would tend to 'stiffen' the result obtained. In comparison the model blocks were entirely separated from the influences of a boundary.

The ratio of (E mass/E intact) can also be calculated for the jointed model. Since it is a dimensionless number it should be identical for model and prototype if similitude is to be achieved. For simplicity only one set of parallel joints will be considered here. With a model joint spacing of $\frac{1}{2}$ inch (20.8 ft in prototype), and using the normal stiffness values given in Table 1, equation (1) gives the following ratios of (E mass / E intact):

$$1/2.4, \quad 1/3.0, \quad 1/5.0, \quad 1/3.8, \quad 1/3.3.$$

These values are for the five normal stress levels given in Table 3.

Coon and Merritt[42] give some interesting data of the ratio (E mass/E intact) collected from in-situ measurements at several dam sites in the U.S.A. The majority of results for gneisses, limestones and sandstones lie in the range 1/10 to 1/2.5. The model joint spacing is therefore seen to give quite representative values of the ratio.

The anomalous nature of the model result shown in Figure 1.4.2 (a) has already been referred to. For some reason the normal stiffness appeared to reduce to some minimum value with increasing normal stress, and consequently to rise as the joint became more closed. Coon and Merritt[42] show a load-deformation curve obtained from a plate jack test in which the apparent stiffness reduces with increasing normal stress over the range 500 to 1000 lbf/in^2. They conceed that the modulus can increase or reduce with increasing stress levels. It is therefore clear that considerable uncertainty surrounds the mechanism by which joints close under normal stress.

Conclusions

Observations of the model/prototype joints and comparison with some rock joint behaviour reported in the literature suggest that the following tentative conclusions can be drawn for clean rough joints:

1. Normal stiffness results are stress dependent and may range from over 30,000 lbf/in^2. per inch at very low normal stresses down to a minimum perhaps below 10,000 lbf/in^2 per inch at medium stress levels of say 1000 lbf/in^2. It must be anticipated that at high stress levels the stiffness will increase considerably. It seems unlikely that this type of inverted performance would be found in a clay filled joint. The minimum stiffness would surely occur at the lowest normal stress in this case. It does not appear that normal stiffness is size dependent.

2. Shear stiffness results are stress dependent and size dependent. Values predicted for a prototype joint 96 ft by 42 ft in area suggest that the range of values (10 - 150 lbf/in^2 per inch) for this size of joint are at least an order of magnitude less than those obtained from tests on rock joint areas an order of magnitude smaller. (100-4000 lbf/in^2 per inch say). An inverse proportionality between shear stiffness and size is indicated.

Conclusions apertaining to the future jointed models are as follows:

3. The normal stiffness of the simulated prototype rock mass is probably at least as high as that generally encountered in the field based on the values of the ratio (E mass/E intact). A closer or wider joint spacing than $\frac{1}{2}$ inch/20.8 ft would enable this aspect of performance to be modelled very closely.

4. The shear stiffnesses of the simulated prototype joints are probably at least on order of magnitude smaller than those predicted from conventional shear tests of limited dimension. (see 2 above) However, since the prototype joint spacing of 20.8 ft is an order of magnitude larger than that generally encountered, it may be assumed that the shear deformation of the prototype rock mass will be similar to that predicted from shear stiffness values obtained from rock joints of limited dimensions.

   If however shear stiffness does prove to be size dependent as suspected, then the model would be even more realistic if the joint spacing were closer.

In Part 3 of this thesis some of the above stiffness data is used in a comparative study of the 'Finite Element' prediction and the model performance of one of the large, excavated slope models containing three intersecting joint sets (St. John[43]). The predicted deformation behaviour is seen to be grossly dependent on the shear and normal stiffness values adopted. The jointed model rock slopes provide a unique opportunity for a comparison of this type since, unlike in the field situation, these joint properties are known with some degree of certainty.

PART 2

2.1 SHEAR PERFORMANCE AS A FUNCTION OF TEST DIMENSIONS AND JOINT ROUGHNESS

SUMMARY

Fractures generated in four different strengths of model material are taken to represent joint surfaces of four different dimensions. Direct shear tests performed on these surfaces indicate that, as far as peak shear strength is concerned, no appreciable strength-size effect is operating. By comparison, a marked displacement-size effect is indicated, with peak shear strength being developed at larger displacements for larger joint areas.

Fundamental concepts of shear resistance of rock joints are reviewed. A powerful phenomenological parameter of shear performance is introduced; the peak dilation angle, which is found to be a maximum at the instant of peak shear strength development.

In an effort to relate the stress dependent peak dilation angle to the roughness of the surfaces and to the shear strength developed, a set of photogrammetric roughness profiles for the model joints are reconstructed, in order to simulate the shearing process during a test. It is noted that only the steep tips of asperities are sheared through at low normal stress, compared to the larger asperities of lower inclination at high stress.

Analysis of the experimental results for all the model shear tests reveals that a linear relationship exists between the peak dilation angle and the peak stress ratio. It is also found that a simple relationship exists between the peak dilation angle and the ratio of the normal stress to the compressive strength. A criterion of peak shear strength for rough tension joints is formulated on the basis of these results.

A simple method is developed for statistically analysing the roughness profiles recorded for several different types of joint. This involves the computation of inclination angles for asperities of different base lengths. It is found that these quantities are analagous to the change of peak dilation angle for different normal stresses.

The practical application of this shearing analogy to slope stability is summarized and a typical example enumerated. Photogrammetric recording of the roughness of joints exposed on rock faces, and a statistical analysis of the data, enables an estimate to be made of the ratio of peak shear strength to normal stress, for any range of normal stress.

2.1 SHEAR PERFORMANCE AS A FUNCTION OF TEST DIMENSIONS AND JOINT ROUGHNESS

INTRODUCTION

A weak, realistic model material which could be split into tension fractures presented an ideal opportunity for studying both scale and roughness effects of joint surfaces. The problem of test dimensions and their effect on shear strength has long been of concern to slope stability engineers. Deere, Hendron, Patton and Cording[14] concluded that the strength of laboratory (6 inch), in situ (3 feet) and failure surface (10 to 100's of feet) 'specimens' would be mutually different for a wide range of surface profiles. It was thought that because the small specimens could only sample the second and third order scales of roughness, they could not be representative samples of the total failure surface problem. This scale effect was thought to be particularly true of rough undulating tension joint surfaces, and to a lesser degree of smoother surfaced undulating shear joints. By implication smooth, planar joint surfaces were not expected to exhibit any strength-size effect, which seems a reasonable conclusion.

The first part of this section is devoted to an investigation of the effect of test dimensions on the performance of rough undulating tension joints of the type produced in the model materials. Both strength-size and displacement-size effects are investigated.

It is common practice to design rock slopes on the basis of a residual shear strength for the joint sets concerned. There is no doubt that in many situations this conservative method is the only safe alternative. However there are converse situations in which, due to favourable drainage and an absence of joint infilling, a design based on something nearer peak strength is justified.

In the second part of this section a method is presented for predicting the peak strength envelopes (non linear) of clean unweathered joints from a statistical analysis of roughness profiles measured over representative exposures of the joints concerned.

2.1.1 THE EFFECT OF TEST DIMENSIONS ON SHEAR STRENGTH

Four model materials of the C series having widely different compressive strengths were used in the investigation. All these materials contained coarse filler which was a 50/50 mixture of sand/ballotini. The materials, nominally C2, C4, C9 and C25, were produced by extrapolating the quantities of plaster and water from those of the weaker materials shown on the design chart in Appendix 1.

The unconfined compression strength of the materials was as follows:

C2	10.2	C9	88.8	lbf/in^2
C4	56.2	C25	119.0	

It was intended to perform all direct shear tests on the same dimension of model tension joint, namely 2.31 inches by 1.00 inches. However, if all the four materials were taken to simulate the same strength of prototype rock, then by a simple dimensional relationship, the four model joint types would be simulating four different dimensions of rock joint surface.

The original geometric and stress scales of 1:500 and 1:666 were employed to convert C2 to a prototype compressive strength of 6800 lbf/in^2, and shear test dimensions of 96 feet by 42 feet. The three remaining materials were converted with respect to these scales. However, due to a reduction in density with increased strength (caused by an enormously increased plaster content) adjustments were required to the ratio of geometric to stress scales for C9 and C25. The scale factors and prototype dimensions are given below.

Table 1. Model - prototype scaling of four materials

Model Material	σ_c (lbf/in^2)	ρ (lbf/ft^3)	λ	ψ	Prototype (feet)	Prototype σ_c (lbf/in^2)
C2	10.2	120.7	500	666	96 x 42	
C4	56.2	120.8	91	121	17.5 x 7.5	
C9	88.8	117.4	56	77	10.7 x 4.7	6,800(all)
C25	119.0	108.7	38.6	57	7.4 x 3.2	

Each of the four model types were tested at different normal stress ranges such that, when these were converted to prototype stresses, the range for all four was the same and approximately 0 to 1600 lbf/in^2.

Model strength envelopes

The peak and ultimate shear strength envelopes for the four model joints are shown in Figure 2.1.1. Each plotted point is the mean of two tests at that normal stress. It should be noted that the peak envelopes for all four joints were more or less coincident over the lowest four of the eight normal stress levels applied in each case. In addition there was no apparent cohesion intercept. It is pertinent to state that in the event of genuine cohesion intercepts occurring, these would have to be in the same ratio as the compressive strengths of the four model materials. Otherwise the joint surfaces would not have been comparable scale models.

The appearance of the model joint surfaces after shearing is shown in Figure 2.1.2. Materials C2 and C4 showed negligible surface damage after shearing at the four lowest normal stress levels (specimens C2.1 to C2.8 and C4.1 to C4.8). By comparison, only the two highest stress levels applied to materials C9 and C25 caused any appreciable surface damage (specimens C9.11 to C9.14 and C25.11 to C25.14). It will be apparent from a careful examination of the photographs that C9 and C25, representing the smallest prototype dimensions, displayed somewhat smoother joint surfaces than the weaker materials C2 and C4.

Prototype joint roughness

The roughness of the four model joint types were recorded photogrammetrically before testing. The results of this investigation are reported in detail later in this section. For the present, four typical roughness profiles obtained from measurements off a stereo pair of photographs will be presented. The ground dimension of each one was 2.31 in length. Each was photographically reduced to the correct relative length. The comparative result is seen in Figure 2.1.3. A cursory glance would lead one to believe that the 96 feet long (C2) joint was considerably rougher than the 17.5 feet long (C4) joint. This in turn appeared rougher than the 10.7 or 7.4 feet long joints. However the relative amplitude of the first order roughness is a misleading yardstick for comparison.

Prototype strength envelopes

The model strength envelopes shown in Figure 2.1.3 were converted to the prototype values by applying the scale factors given in Table 1. The resulting values were all plotted on the same graph so that any differences in strength between the four test dimensions could be compared. Figure 2.1.4 shows the result. The closeness of the peak strength results leads one to the conclusion that there may not be a significant strength-size effect for rough joints of this type. The apparantly more linear profiles of the 7.4 and 10.7 feet simulated joints belie the fact that for many

Figure 2.1.1 The peak and ultimate shear strength envelopes of primary tension joints in model materials C2, C4, C9 and C25.

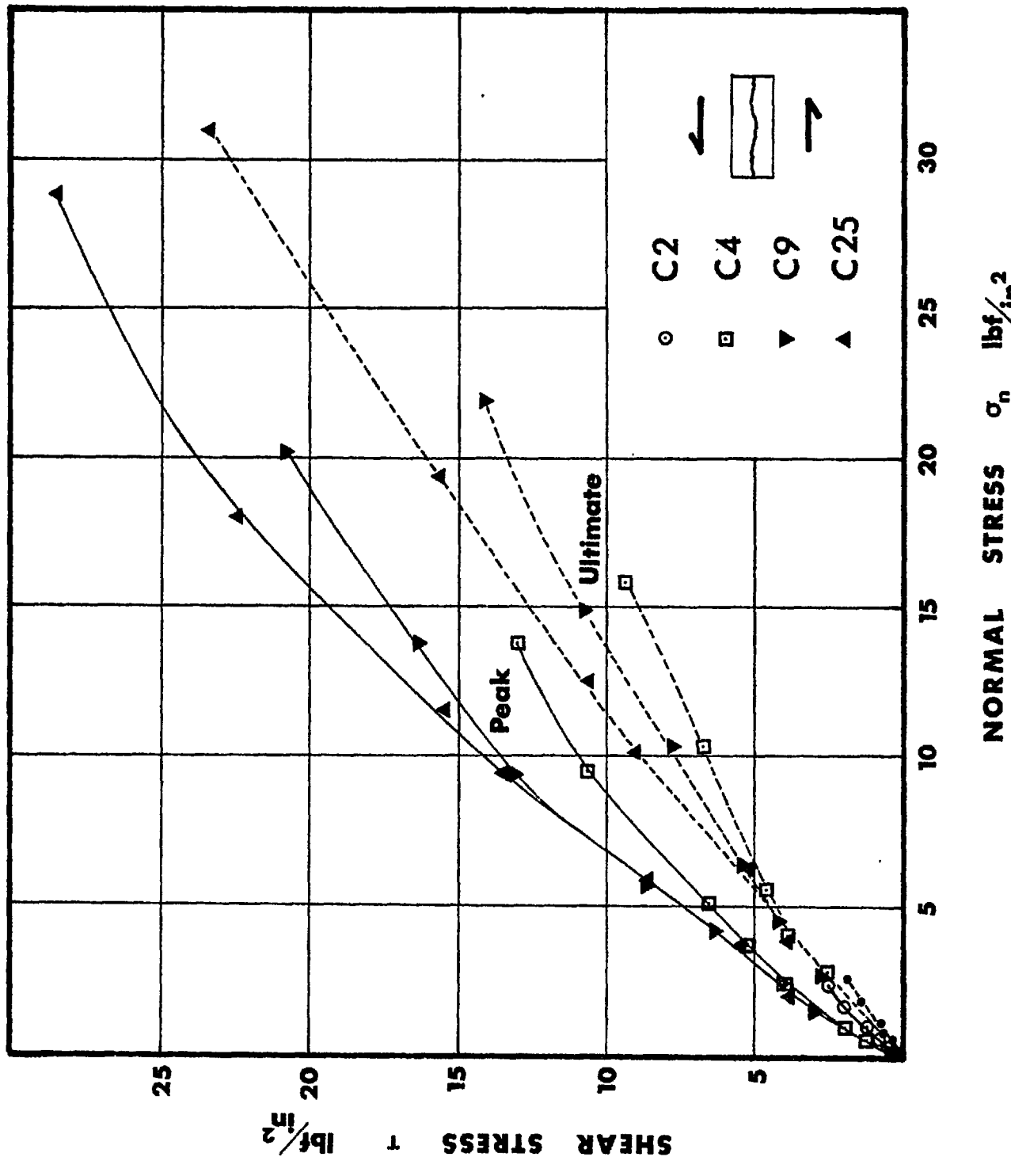

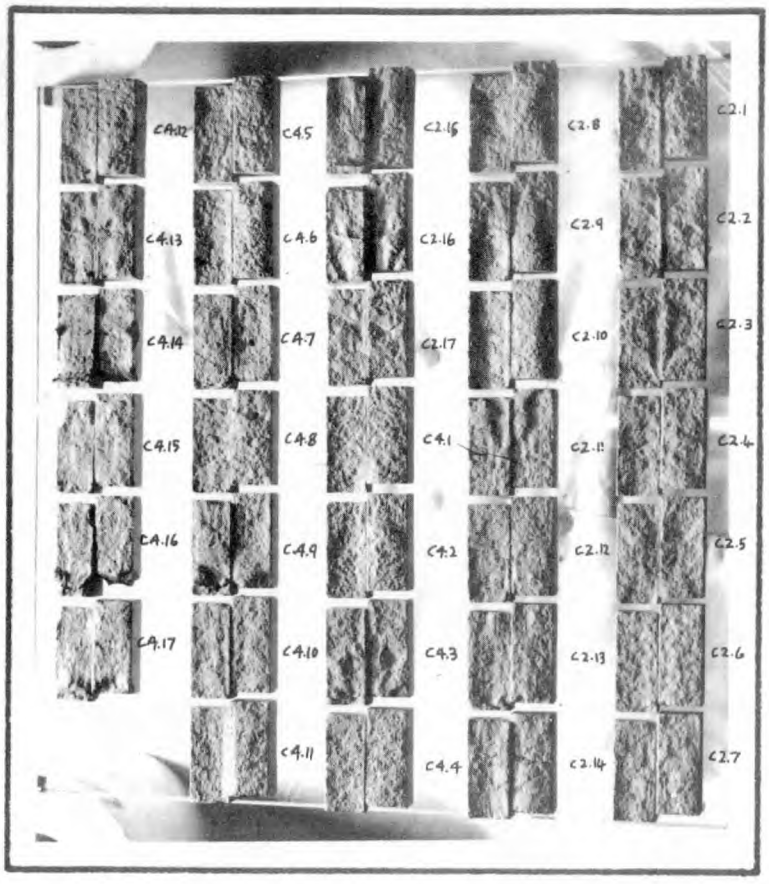

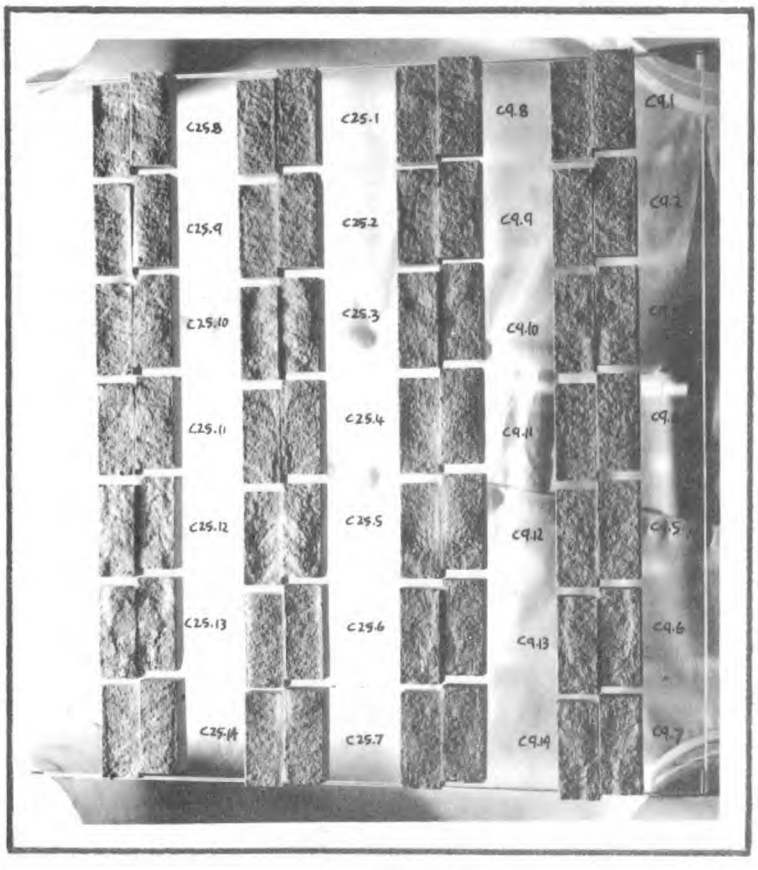

Figure 2.1.2 The appearance of the model joint surfaces after shearing at different normal stress levels.

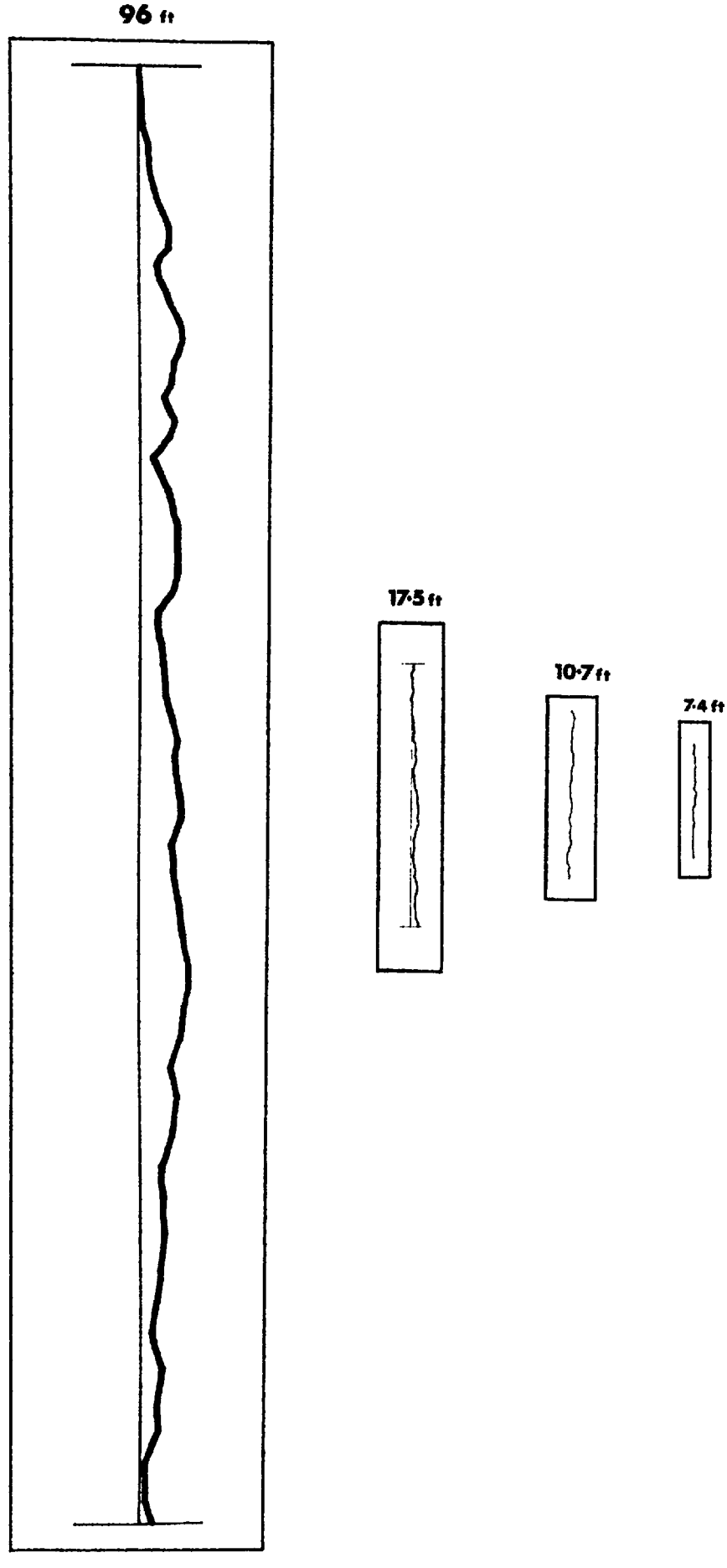

Figure 2.1.3 Four typical joint roughness profiles from four dimensions of modelled shear tests.

Figure 2.1.4 The shear strength envelopes at prototype scale predicted from four dimensions of shear test

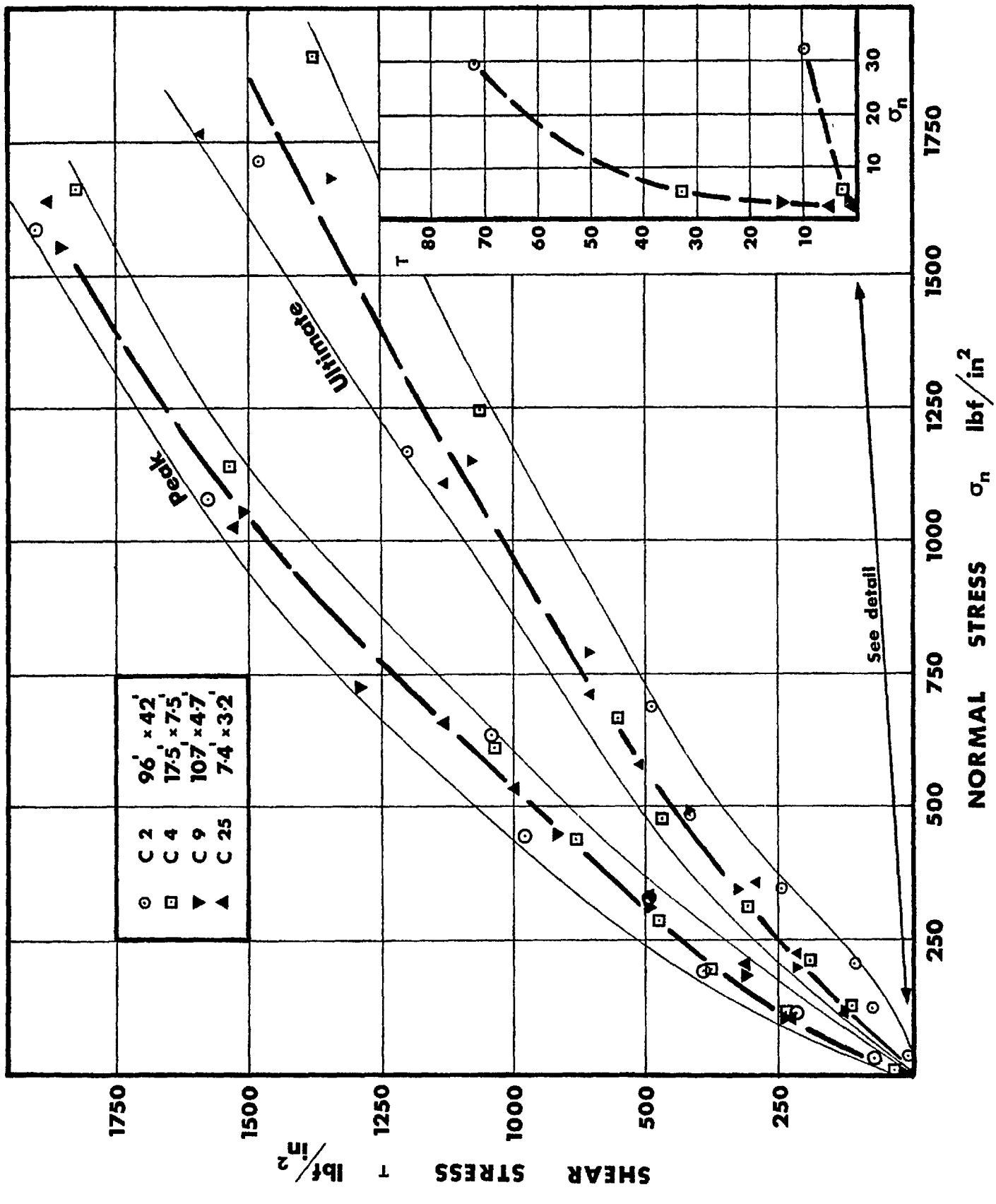

different joint dimensions there is probably a 'world within a world'. As will be seen later the small steep asperities seem to control the peak strength to a greater degree than the larger amplitude low inclination first order roughnesses. These only become dominant at normal stress levels considerably higher than encountered in slope stability problems. Consequently, for a given normal stress, shear failure on large or small joint surfaces may occur through failure of the same dimension of asperity.

Just how small or large a joint surface a particular strength can be extended to is hard to say. There is no doubt that greater confidence should be placed in shear tests or profile measurements of joint surfaces of tens of feet in length rather than of 'laboratory size' dimensions. However, if exposures of joints of only a few tens of square feet in area are accessible, the peak strength results measured or predicted may possibly be more representative than suspected.

Seraphim and Guerreiro[31] commented on this problem when reviewing a large body of experience of in-situ tests at dam sites in Spain. Test areas ranging from $10ft^2$ to $450ft^2$ apparently failed to indicate any marked effect of area on strength.

Cohesion apparent

As in previous model shear tests the lowest normal stress applied to each of the four joint types was generated by the weight of the upper block of model material only. When the dimensions of these blocks are converted to prototype, the $\frac{5}{8}$ inch model height becomes equivalent to rock overburdens of 26.0, 4.7, 2.9 and 2.0 feet for joint types C2, C4, C9 and C25 respectively. The corresponding normal stresses were therefore low enough to give an indication of the presence of any cohesion intercept of practical significance. The inset given in Figure 2.1.4 provides conclusive evidence that even for joints as rough as the model tension fractures no cohesion intercept actually exists. The peak envelopes merely become tangential to the shear strength axis.

2.1.2 THE EFFECT OF TEST DIMENSIONS ON DISPLACEMENTS

The shear displacement corresponding to the mobilization of peak shear strength is an important parameter in slope stability control. It has for instance, fundamental implications to rock bolting and to slope displacement monitoring. Particular attention has been focussed on the latter recently, due to the comprehensive programme undertaken at the Chuqicamata Mine, Chile. (Kennedy and Niermeyer[45]) The time of occurrence of an extremely large slide, estimated at several million tons, was accurately forecast by simple displacement-time graphs.

Laboratory size joint specimens (6 to 12 inches) generally reach peak strength after tangential displacements of small fractions of an inch. The largest in-situ tests performed likewise reach peak strength after only $\frac{1}{2}$ inch to 1 inch displacement at the very

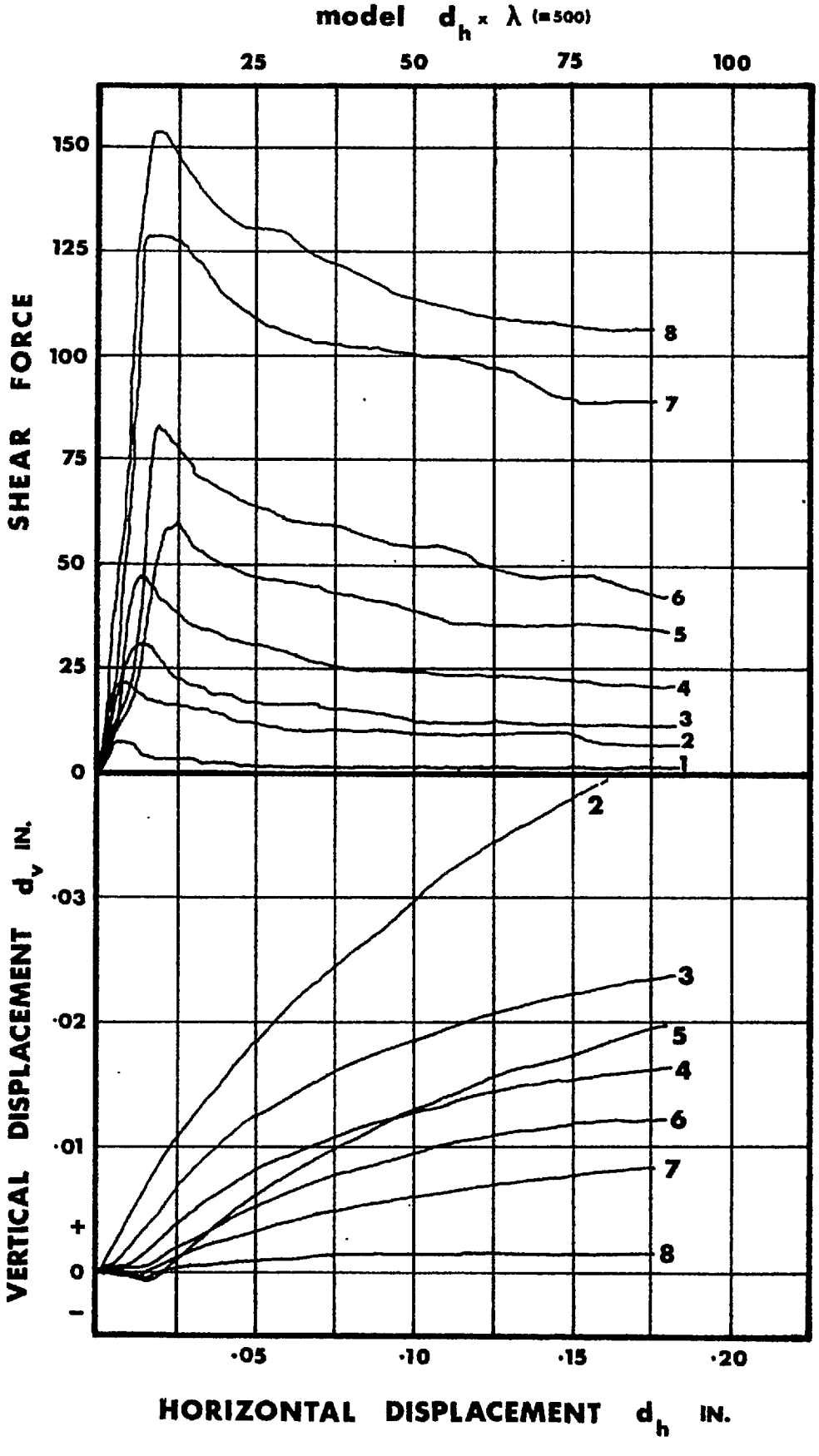

Figure 2.1.5 Shearforce-displacement and dilation characteristics for model joints simulating 96 feet length of prototype joint

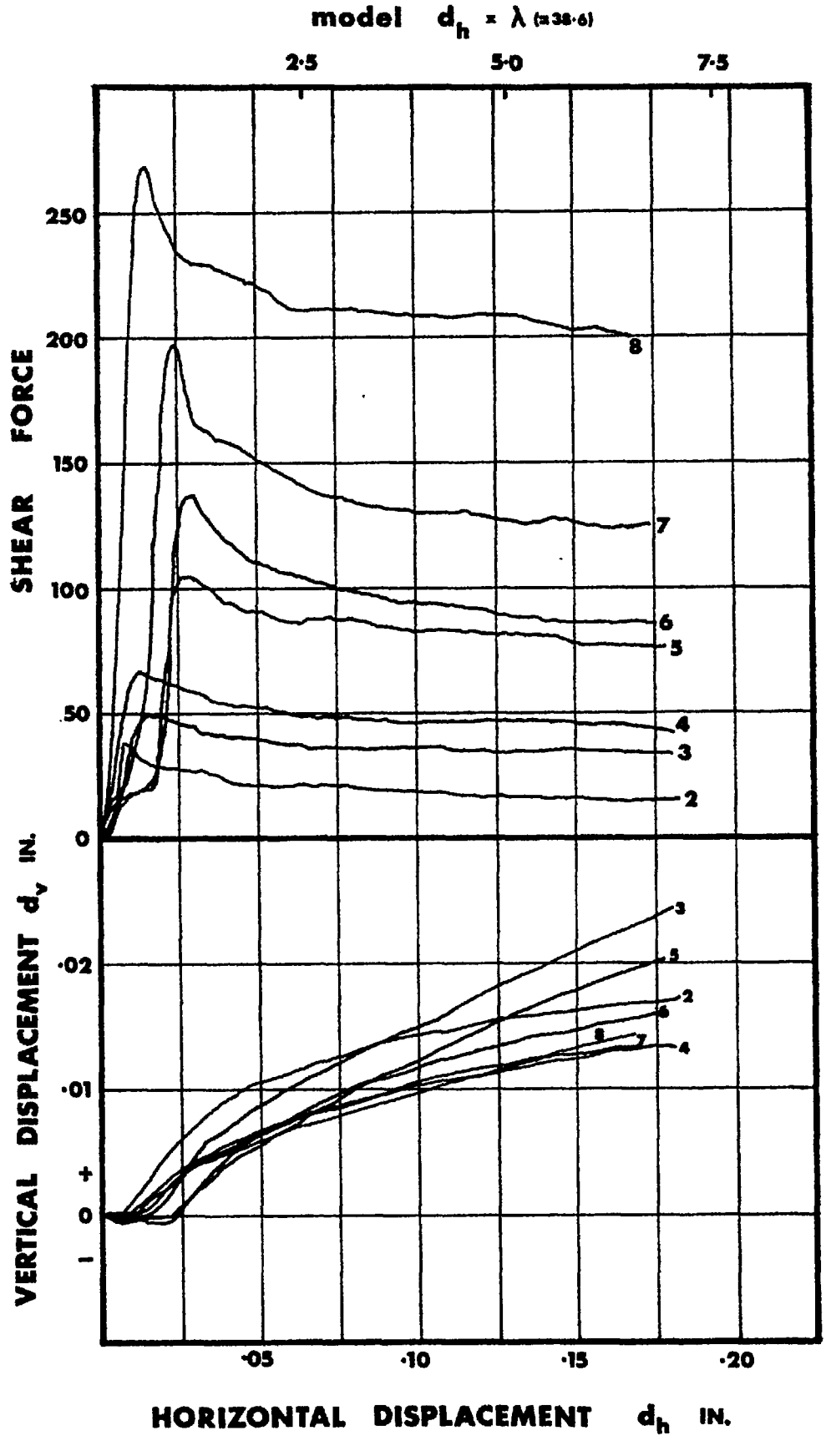

Figure 2.1.6 Shearforce-displacement and dilation characteristics for model joints simulating 7.4 feet length of prototype joint.

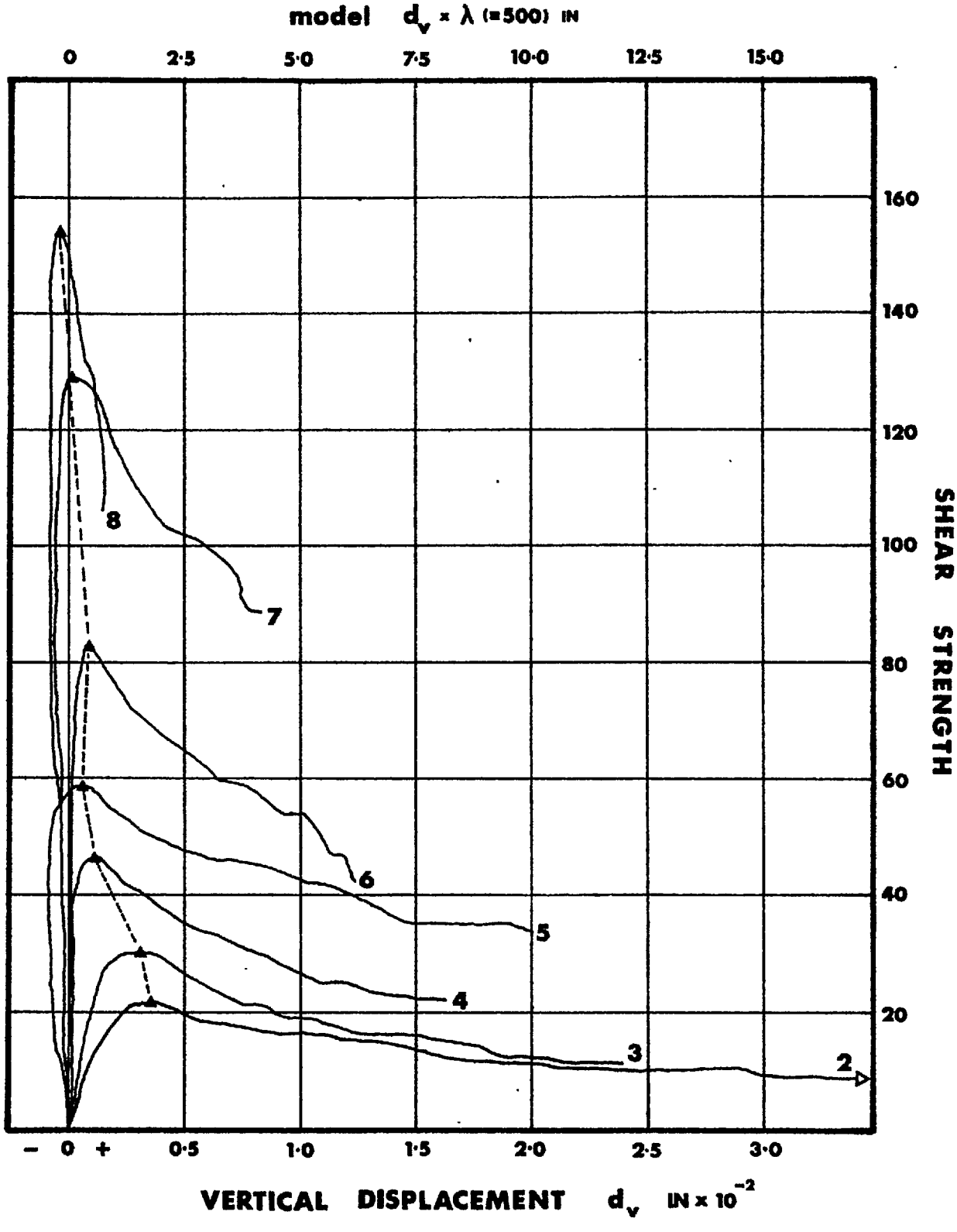

Figure 2.1.7 Shearforce-vertical displacement characteristics for model joints simulating 96 feet length of prototype joint.

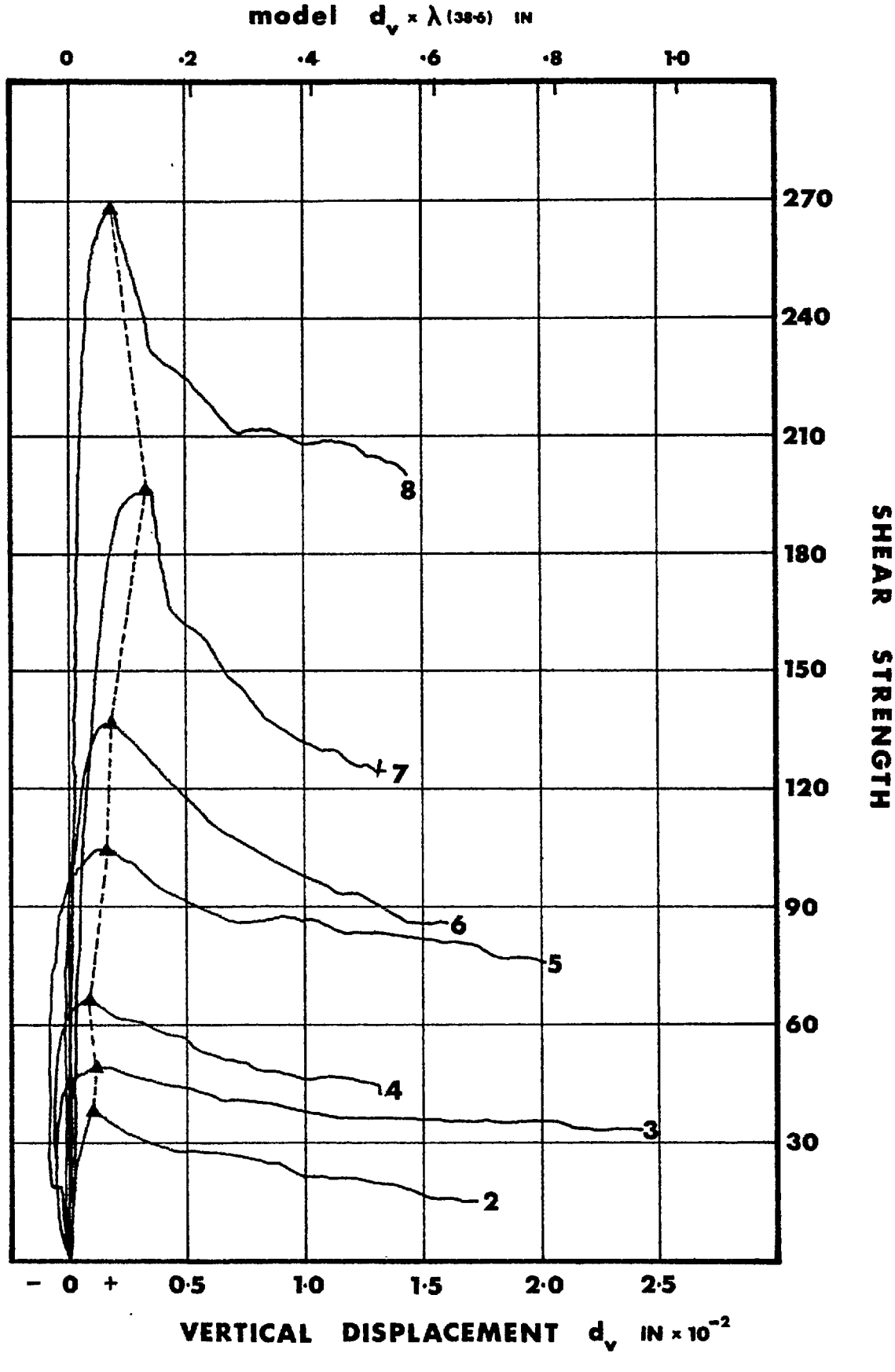

Figure 2.1.8 Shearforce-vertical displacement characteristics for model joints simulating 7.4 feet length of prototype joint

most. Consequently the large pre-failure slope displacements of the order of feet or even tens of feet exceptionally, are usually explained as surface manifestations of a progressive rearrangement of slope geometry leading up to final collapse.

The four model joints, representing prototype dimensions from approximately 7 to 96 feet in length, provided an opportunity for a comparative study of displacement - size effects. It seemed possible that a summation of the pre-peak shear displacements on all the critical joints lying above the toe of a slope could collectively explain the large pre-failure movements observed at the crest of unstable slopes. However, peak shear displacements on individual joints of greater than fractions of an inch were needed to explain these full scale phenomena.

Figures 2.1.5 and 2.1.6 demonstrate the shear force-displacement and dilation characteristics for two contrasted dimensions of test. Apart from rather sudden drops from peak strength, the shear force -displacement behaviour appeared rather similar between the model representing 96 feet, and that representing 7.4 feet of joint surface. However, when the model horizontal displacements were converted to prototype scale a wide separation in behaviour became evident. The prototype scales are illustrated on the top axis of the two figures.

The dilation diagrams illustrated in the lower half of each figure suggest that some fundamental difference of roughness did exist between the two dimensions of test. However it was the post-peak behaviour that was affected. Figure 2.1.4 confirms that the pre-peak behaviour , which leads up to the point of maximum dilation and maximum strength, was very similar for the four tests, despite the first order differences in roughness.

Figures 2.1.7 and 2.1.8 demonstrate further differences in behaviour between the two scales of test represented by C2 and C25. The simulated 96 feet test demonstrated a gradual reduction in the magnitude of the peak vertical displacement with increasing normal stress, to the extent that at the two highest normal stress levels no total dilation was required for peak strength to be mobilized. In direct contrast to this the simulated 7.4 feet test demonstrated a gradual rise in the peak vertical displacement with increasing normal stress. This important difference can be accounted for by consideration of the relative consolidation occurring across a rough joint and across a smoother joint when equal normal stresses are applied. Greater consolidation across the smoother joint (C25) would result in this tendency for increased vertical displacement occuring before the point of peak strength was reached.

All displacement-size effects are summarised in Table 2 overleaf.

Table 2. Prototype displacements extrapolated from four model materials

NORMAL STRESS σ_n (lbf/in^2)				DISPLACEMENT d_h peak (ins)				d_v peak (ins)				d_v ultimate (ins)			
C2	C4	C9	C25	C2	C4	C9	C25	C2	C4	C9	C25	C2	C4	C9	C25
29	5.3	3.4	2.5	3.35	0.54	0.35	0.34	N	O	R	E	S	U	L	T
112	115	110	109	5.12	1.40	0.71	0.55	2.30	0.15	0.11	0.06	18.70	2.06	1.58	0.93
190	196	184	207	5.32	1.04	0.66	0.70	1.65	0.13	0.06	0.06	11.10	1.86	0.80	0.84
318	288	316	327	8.46	1.40	0.71	0.46	0.75	0.09	0.06	0.03	11.10	1.10	1.21	0.51
445	439	449	535	9.45	1.36	0.71	0.93	0.25	0.17	0.04	0.07	10.20	1.17	1.03	0.76
635	611	726	658	11.61	1.36	0.75	1.05	0.45	0.13	0.09	0.08	5.95	0.97	0.57	0.61
1079	1140	1058	1026	9.65	2.37	0.91	0.79	-0.05	0.25	0.15	0.17	3.65	0.37	0.41	0.67
1588	1661	1551	1640	8.85	1.40	0.64	1.03	-0.10	0.16	0.07	0.05	0.75	-0.01	0.11	0.37

The symbols used in the tabulation represented the following:

d_h peak : is the horizontal displacement at peak shear strength
d_v peak : is the vertical displacement at peak shear strength
d_v ultimate : is the vertical displacement at the end of each shear test

Each model was sheared for a horizontal distance of 0.18 inches. (This was 7.7% of the length of each joint tested). Therefore when scaled up to the prototype dimensions d_h ultimate becomes:-

Material	λ	d_h ultimate (ins)	Test dimensions (feet)
C2	500	90.0	96 x 42
C4	91	16.4	17.5 x 7.5
C9	56	10.1	10.7 x 4.7
C25	38.6	7.0	7.4 x 3.2

From the results presented it would appear that there is a marked displacement - size effect for certain joint types. This would probably be most marked for rough undulating tension-type joints similar to those tested, and possibly negligible for planar, smooth surfaces such as unfolded bedding joints or planar shear joints. It is perhaps unwise to quantify these observations further, in view of the uncertain nature of the model roughnesses that were assumed to simulate the different dimensions of joint.

However, strictly as model observations the following are worth recording here:

1. The peak strengths were reached after tangential displacements approximately 1% of the lengths of the joints tested, whether these simulated 96 feet or only 7.4 feet at full scale. This figure is roughly the same as that obtained from large scale shear tests on rock (see Section 1.3).

2. The ultimate tangential displacements were the same for each model and represented 7.7% of the length of each simulated test dimension. From an examination of the drop from peak strength towards residual strength, it would appear that a displacement of approximately 10% would reduce the shear strength of similar rough joints to close to the residual strength.

2.1.3 FUNDAMENTAL SHEAR RESISTANCE OF ROCK JOINTS

INTRODUCTION

The cohesionless model

In the past, attempts have been made to relate the shear resistance of rock joints to the observed dilatant behaviour of granular materials such as sand. From considerations of statics, Newland and Allely[46] developed an equation of the following type:

$$\tau = \sigma \tan (\phi_b + i)$$

to denote the maximum shear strength of a granular mass. The angle (i) was the average angle of deviation of particle displacements from the direction of the applied shear stress, and (ϕ_b) was the angle of frictional sliding resistance between particles.

Rowe, Barden and Lee[47] developed the same relationship for cohesionless sands from energy considerations. For the direct shear test the total applied shear force was divided into three components. These took account of the external work done in dilating against the normal force, and the internal work done in overcoming dilational friction which was differentiated from the 'no volume change' frictional component. The sum of these three components produced the above relationship.

The bilinear model

Patton[20], and Goldstein etal[48] used the same realtionship to represent the shear strength of irregular rock surfaces and broken rock when tested at low normal stresses. At high normal stresses it was anticipated that most of the irregularities would be sheared off. Consequently the Coulomb equation was introduced. This can be written as:

$$\tau = c + \sigma' \tan \phi_b$$

where the constants (c) and (ϕ_b) denote the Coulomb shear parameters relating to the strength of the unjointed rock material. Thus Patton and Goldstein etal. proposed the familar bi-linear approximation to the anticipated curved strength envelope.

Patton's work is worth reviewing here since it provides a simple experimental basis for the development of more fundamental failure models. He performed a series of laboratory shear tests on idealised rock surfaces using plaster specimens having interlocking teeth. Specimens with teeth inclined at 45°, 35° and 25° (of the same height) produced peak strength envelopes which could be approximated to bilinear relationships. The initial linear portions (representing low normal stress) were inclined at 75°, 66° and 55°respectively. The second linear portions were all inclined at 30°, which was the same as the angle of residual friction. The bilinear transition points varied between the three types of specimen, with the 45° toothed surfaces reaching the transition at lower normal stress levels than the 35° or 25° models.

This was obviously a function of the relative base area of the teeth. It was therefore postulated that for a real joint surface the steepest teeth would be sheared off first.

Effective (i) Value

Patton had previously studied a large number of unstable rock slopes in the Rocky Mountains. Photographic observation and measurement of joint surface profiles, and a related series of residual shear tests on flat, sawn rock specimens led him to the conclusion that first order and second order irregularities had to be differentiated, if realistic parameters were to be obtained through back analysis. Figure 2.1.9 (taken from Patton[20]) demonstrates the significance of the two scales of roughness. In essence his conclusion was that an effective (i) value had to be used, rather than the absolute roughness of the small asperities lying on the slopes of the first order irregularities.

Figure 2.1.10 (a) demonstrates the static considerations of sliding up a smooth inclined rock surface which exhibits an angle of friction (ϕ_b) the same as the residual angle, and also obtainable from shear tests of flat sand blasted or sawn surfaces of the rock. Equating the resolved components of H and N for the condition of limiting equilibrium the following familiar relation is obtained :

$$H/N = \tan (\phi_b + i)$$

This is obtained more directly as follows. Sliding is just initiated when the resultant force is inclined at an angle ϕ_b from the normal to the inclined surface. Therefore the tangent of the 'total friction angle' is equal to the ratio of H and N.

Peak dilation angle

The real situation of shearing or sliding along a rough joint is illustrated in diagram (b) of Figure 2.1.10. A multitude of (i) values contribute to the shear strength, and the effective (i) value will be dependent on the normal stress acting across the joint. It is postulated that at the instant of failure (peak shear strength) the rock mass lying above the joint will move at an angle (i_p) to the mean plane. This is the effective (i) value, but it will now be termed the peak dilation angle. It is a very powerful phenomenological parameter of shear strength, since for a given normal stress it represents the minimum energy path between a 'sliding up' and a 'shearing through' mode of failure.

$$d_n = \text{maximum incremental } \frac{d_v}{d_h}$$

All the two hundred shear tests performed on rough model joints demonstrated a peak angle of dilation corresponding to the shear displacement at which peak strength was mobilised.

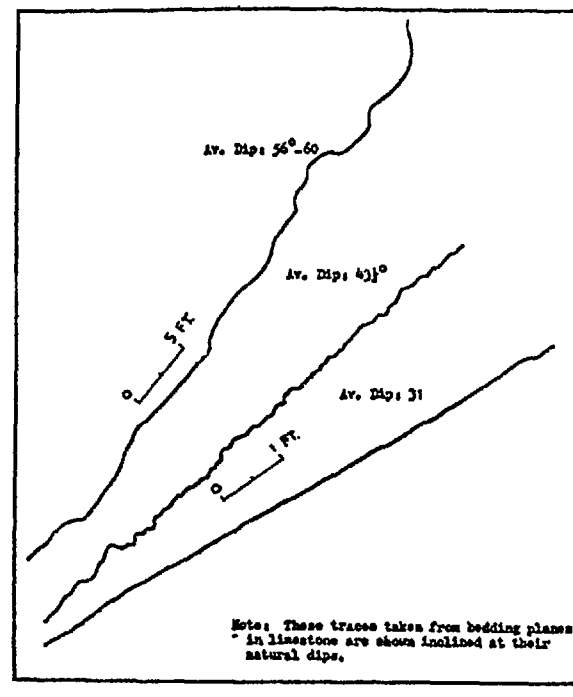

Examples of traces of rock discontinuities.

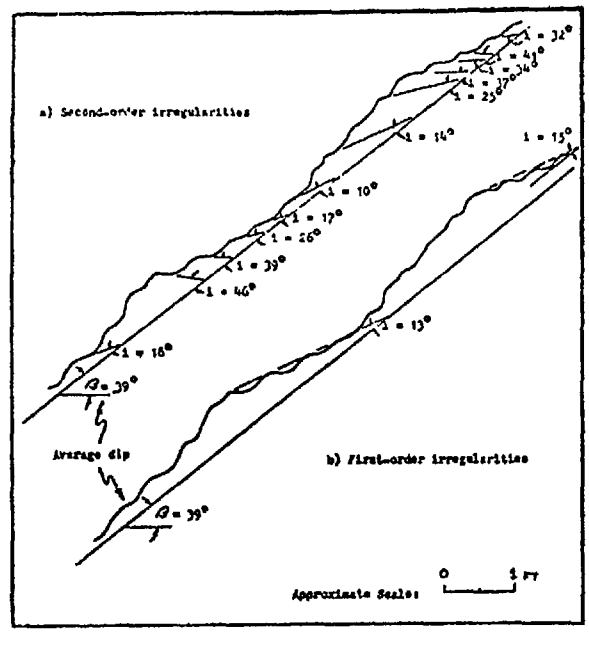

An example of a discontinuity illustrating first- and second-order irregularities.

Figure 2.1.9 First and second order irregularities of rock discontinuities (after Patton[20])

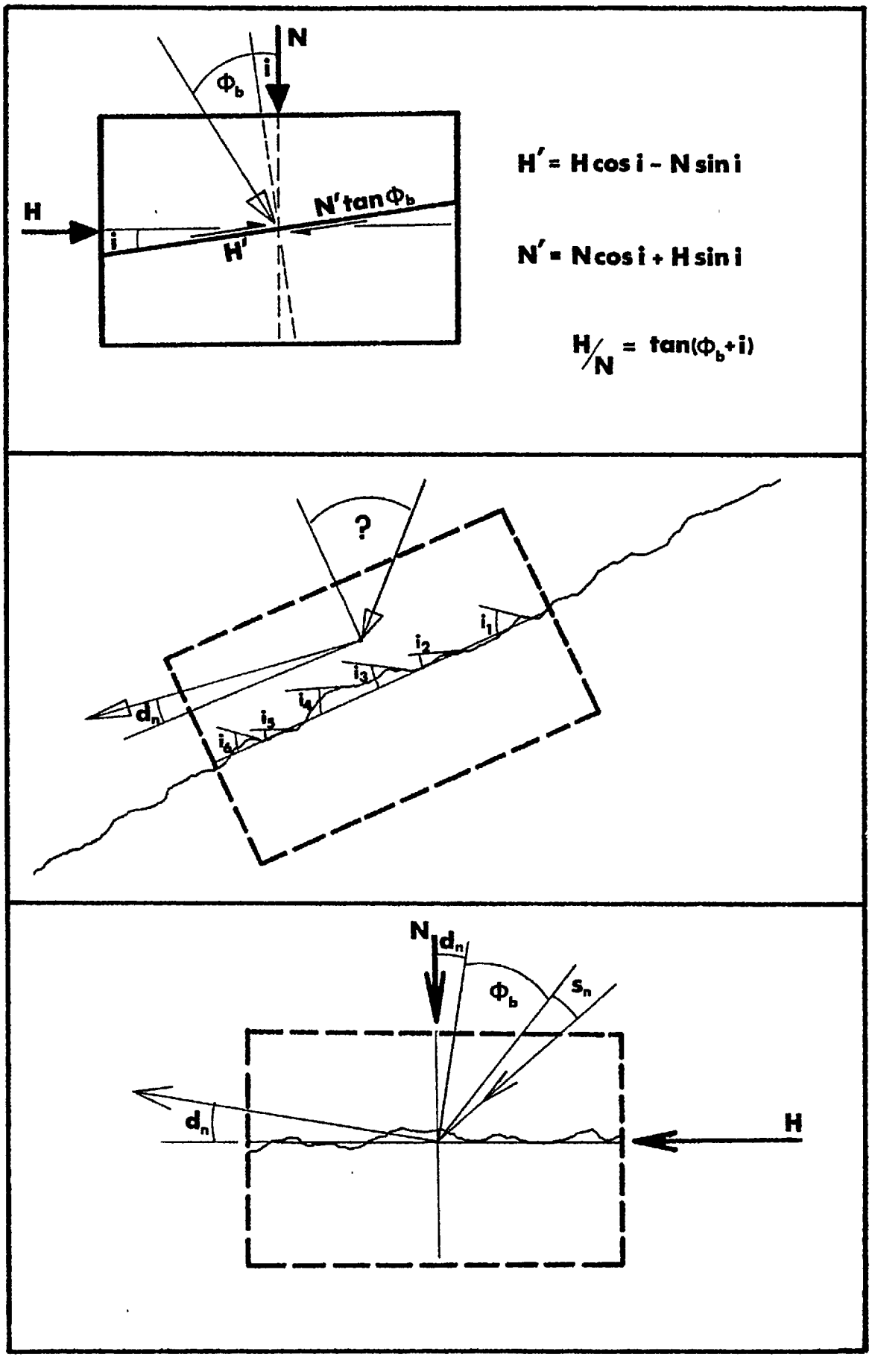

Figure 2.1.10 Three diagrams of joint shear behaviour.

Previous measurements of joint dilation

Unfortunately dilation measurements are seldom recorded in large scale shear tests of rock joints. This is the inevitable conclusion bearing in mind the almost complete lack of dilation measurements in the literature. However, it may be that the data is not published due to the wide scatter of results that one might expect when testing a limited number of joints. Only two references can be cited.

Ripley and Lee[47] reported an interesting series of direct shear tests on natural discontinuities in sandstone, siltstone and mudstone obtained from 6 inch diameter drill core. Dilation measurements were taken during each test. When expressed in terms of an apparant friction angle, the increase in sliding resistance due to 'riding up' on the rough joint projections was found to be from 10^o to 18^o for the peak values at low strain, and from 2^o to 13^o for higher strains. It is significant that their total angles of friction at higher strains 'corrected' to approximately the residual angle of friction, while the peak values when 'corrected' were somewhat higher than this.

For instance for the sandstone specimens:

Measured		Corrected	
Peak	ultimate	peak	ultimate
54^o	40^o	36^o	27^o

It was therefore apparent that the dilation 'correction' proposed by Skempton and Bishop[35] for direct shear tests on (cohesionless) sands could not be applied to the peak strength state of rock joints. Even at low normal stresses some failure of intact material was occurring at the tips of asperities in contact.

Ruiz, Camargo, Midea and Nieble[29] measured the peak dilation angles during a series of large in-situ tests on basalt. Their largest test, which was referred to in Section 1.3, was a shear test of approximately 450 ft^2 of basalt-breccia contact. Undisturbed, and first and second sliding tests produced the following results for a constant normal stress of 24.3 lbf/in^2.

$\tan^{-1}$ (τ/σ)	d_n
69^o	39^o
68^o	32^o
52^o	14^o

In addition to these measurements, dilation readings were recorded during concrete-basalt adhesion tests of approximately 40 ft^2 in area. Unfortunately the range of normal stresses

of 0 to 90 lbf/in^2 was low enough for the adhesive forces to be rather significant. A graph of arctan (τ/σ) versus peak dilation angle gives the following (approximate) linear relation:

$$\tau/\sigma = \tan (0.98\, d_n + 53^o)$$

which is probably a good deal higher than might be exhibited by a rock to rock joint interface.

Component of asperity strength

The theoretical maximum inclination of a smooth faced asperity which is to remain unsheared when tested at zero normal stress is as follows:

$$(i)_{max} = 90 - \phi_b$$

This is immediately apparant from inspection of the function $\tan (\phi_b + i)$, and was referred to by Ripley and Lee,[49] Withers[51] and Patton[20].

The large amount of experimental data reported in the literature suggests that more or less all rocks have basic angles of sliding friction (ϕ_b) the same as the residual angle and lying between approximately 25° and 35° (see for instance Ripley and Lee[49], Patton[20], Rosengren[22], Ross Brown and Barton[52]). For this reason smooth asperities inclined at between 55° and 65° may be sheared through even when the test is conducted at a theoretical zero normal stress.

Ladanyi and Archambault[18] proposed a failure model in which this small area of sheared material was given a strength component corresponding to the Coulomb relation for shear through unjointed material. They suggested that over the remaining area of the joint surface, only the frictional and dilational components were acting. This concept is no doubt a valid one, but unfortunately the number of unknown parameters in their relationship was impractically large.

Diagram (c) of Figure 2.1.10 illustrates the problem posed by this shear component. Peak strength is reached when the ratio of the shear and normal forces is equal to the tangent of the sum of ϕ_b, d_n, and s. The component (s) appears to be stress dependent in the same way that the peak dilation angle (d_n) is.

It will be apparant from this review of joint shear failure concepts that no practical method existed for predicting the peak shear strength envelopes of rock joints. A method which involved only the analysis of roughness profiles could therefore prove most valuable, despite the fact that only unweathered and unfilled joints could be considered. Obviously some relationship was required between the three parameters:

roughness of joint
peak dilation angle
normal stress

2.1.4 EXPERIMENTAL OBSERVATIONS OF MODEL JOINTS

Figure 2.1.11 is a photograph of twenty model joint surfaces representing seven types of joint. Each specimen is one of a mating pair, photographed before testing and later aligned in the shear box in a known direction.

The Photogrammetry Department of University College London, kindly performed photogrammetric analyses of the roughness of these model joint surfaces. The specimens were collectively set horizontally, and were photographed with a Galileo Santoni Stereometric camera on a 560 mm. base pointing vertically downwards. Observations of the stereo pair of photographs were carried out on a Thompson Watts Mark II plotting machine coupled to an automatic tape punch. Plotting intervals of approximately 1 mm. (0.040 inch) were considered adequate to cover the small scale asperity slopes. This interval resulted in approximately 70 spot height coordinates for each traverse. Two profiles were computer drawn for each specimen, taken longitudinally along the two third points of the 2.31 x 1.00 inch surfaces.

Figure 2.1.11 shows these roughness profiles (which are elevations) superimposed on the third points of the photographic plan views of the surfaces concerned. The following joint types correspond to the numbering shown in the figure.

A3	(P)	1,2,3	C 25	(P)	12,13, 14
C3	(P)	4,5	C4	(P)	15,16,17
C3	(S)	6,7,8	C9	(P)	18,19,20
C2	(P)	9,10,11			

The paler colour of the C25 (P) type joints is due to the larger amounts of plaster in this material, compared to the weaker orange material of the lower members C2, C3, C4 etc.

Reconstructed shear tests

As a preliminary to detailed analysis of the roughness profiles, it was decided to reconstruct some of the shear tests so that the effect of normal stress on asperity failure could be assessed.

A 16 x 20 inches sheet of Ilford film, 5/1000 inch thick, was partially exposed and developed to a uniform transparent grey. Computer drawn model roughness profiles were traced

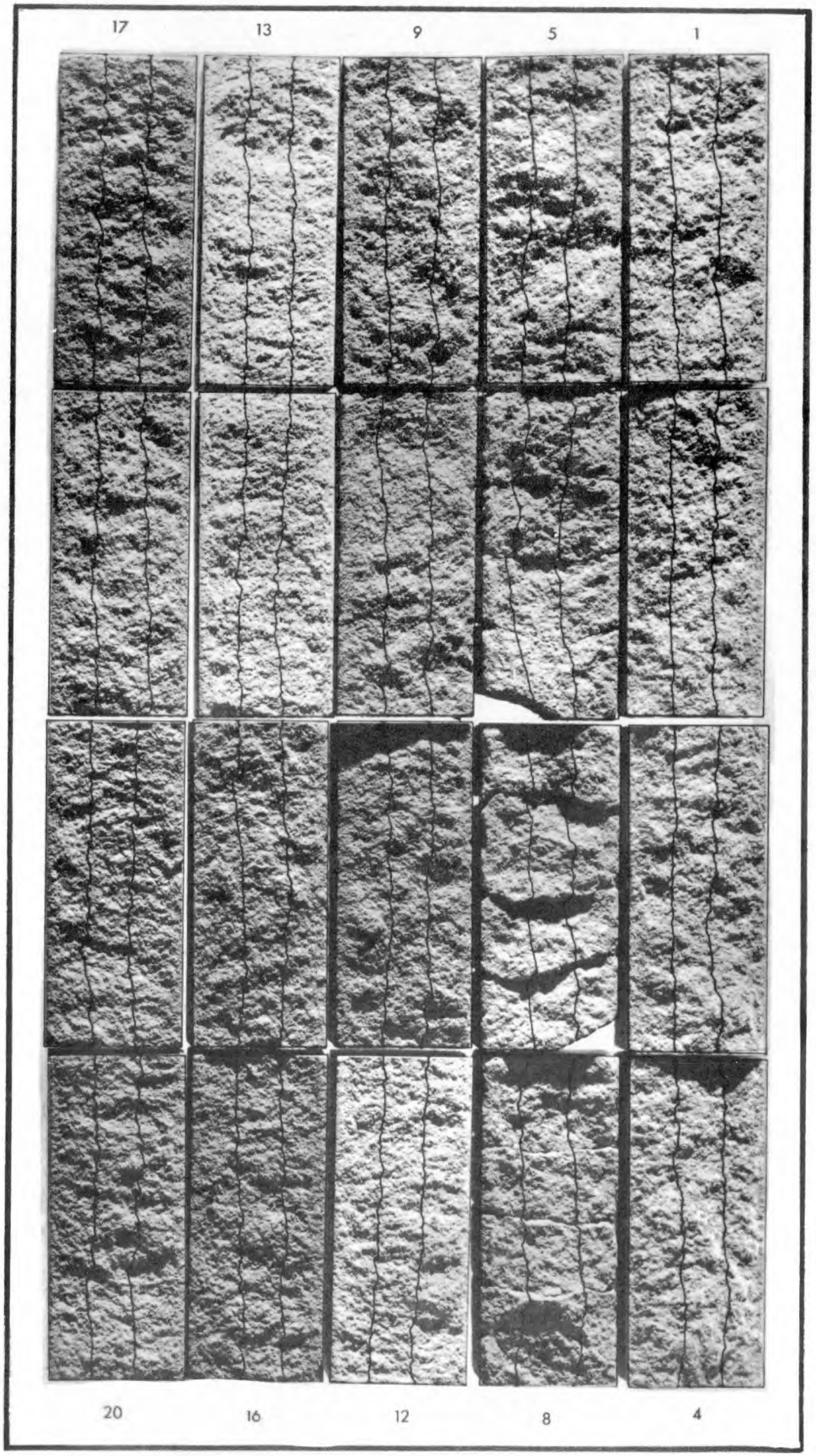

Figure 2.1.11 Photogrammetric roughness profiles superimposed on model tension joint surfaces

onto the transparent film at five times ground scale (approx. 1 ft. long), carefully cut out, and the two interlocking halves mated to represent one section through the model tension joint concerned. This proceedure was followed for both profiles of each specimen. The 'lower halves' of these reconstructed sections were glued to stiff, white card and the 'upper' matching halves were mated, representing the zero displacement position.

It will be recalled that vertical displacement measurements were taken during each shear test, from dial gauge readings at a single point vertically above the centre of the joint area. The recorded displacement was therefore the mean of possibly complex vertical movements of the upper half of the specimen. A pin was therefore pricked through the centre of the 'upper' mating reconstructed sections so that the white card was marked. These points were the origins for the dilation diagrams. Six coordinates of dilation were plotted on each card with pin pricks, after converting to the correct scale. These coordinates were the experimental results of shear tests performed on the model joints concerned. The following sketch shows the coordinate positions chosen.

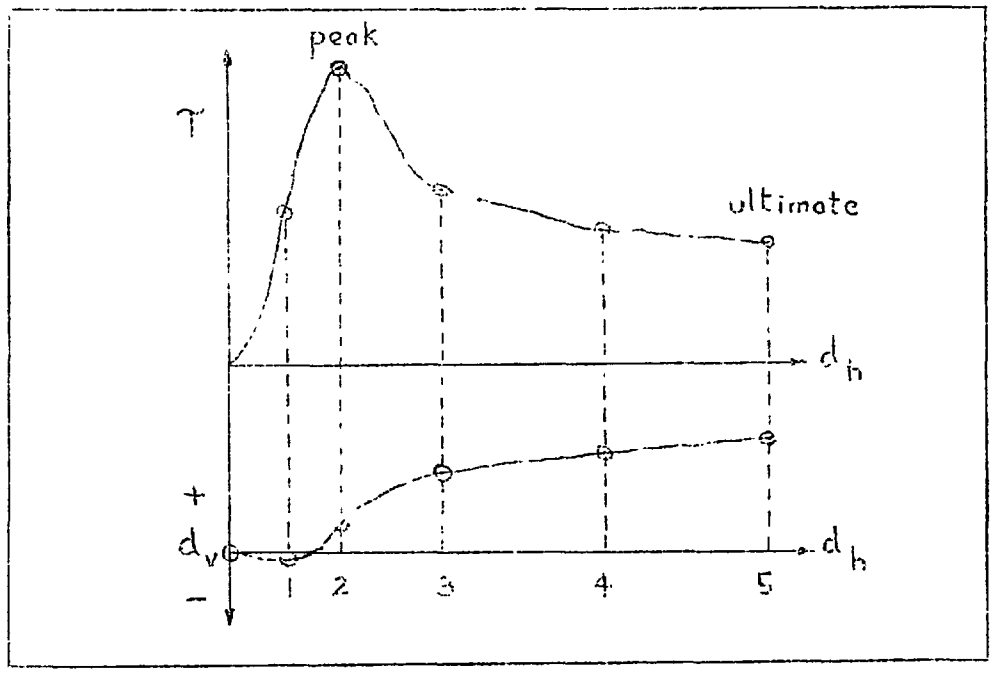

Position 1 represented the dilation at half the recorded d_h peak value.

Position 3 represented the dilation after the rapid drop from peak strength.

Position 4 was half way between 3 and 5.

Position 5 was the ultimate position, which approached that of residual strength.

When these six positions were reconstructed and photographed an interesting series of shearing events was observed. The sequence of shear positions are shown in Figures 2.1.12 and 2.1.13. for joint type C2(P), and in Figures 2.1.14 and 2.1.15 for joint type C25 (P). At prototype scale these models represent the following test parameters:

C2 (P) 96 feet long: $\sigma_{n}2$ = 112, $\sigma_{n}6$ = 635 lbf/in^2.

C25 (P) 7.4 feet long: $\sigma_{n}2$ = 109, $\sigma_{n}6$ = 658 lbf/in^2.

The prototype unconfined compression strength simulated by both model materials was 6,8000 lbf/in^2 as before.

It will be apparent from observation of the shear sequences that at the lowest simulated normal stress of approximately 100 lbf/in^2, the area of asperities in contact or sheared through was extremely small. Where the dilation diagram caused the reconstructed sections to overlap the double grey appeared as black, representing the shear of intact material. The balancing of areas of sheared material about the centre axis of the profiles was carried out by eye. It is hoped that this subjective operation approximately reconstructed the experimental shearing paths of the upper blocks in the shear box. The following observations are worth recording.

1. During the reconstruction of the shear tests a pin was used to locate the 'upper' sections in the particular dilation coordinates. It was noticed that very small rotations about this pin axis caused one end of the section to show sheared areas (black overlaps) of orders of magnitude greater than on the opposite side of the axis. This could not occur in reality without extreme variations of normal stress from one end of a shear plane to the other. It therefore seems likely that only very small rotational movements can occur during initial shear failure along rock joints, even if these are as rough as the model tension joints. This implies that limit equilibrium analyses of such failures may be more justified than expected.

2. It is clear from Figures 2.1.12 to 2.1.15 that dilation across the model joints caused enormous increases in the volume of the joint space. This phenomenon, although exaggerated for rough tension joints, has important implications to the flow of joint water along rock joints under high shear stress. It suggests a realistic mechanism by which a progressively failing rock slope could be temporarily arrested from catastrophic failure by enormously increased permeability along the shear plane. A period of water flow might be required for the permeability to deteriorate for the next cycle of dilation (or complete shear failure) to occur. An interesting series of perrmeability tests performed by Maini[53] on mating araldite impressions of rock joints shows that this drainage effect may be even more marked than expected.

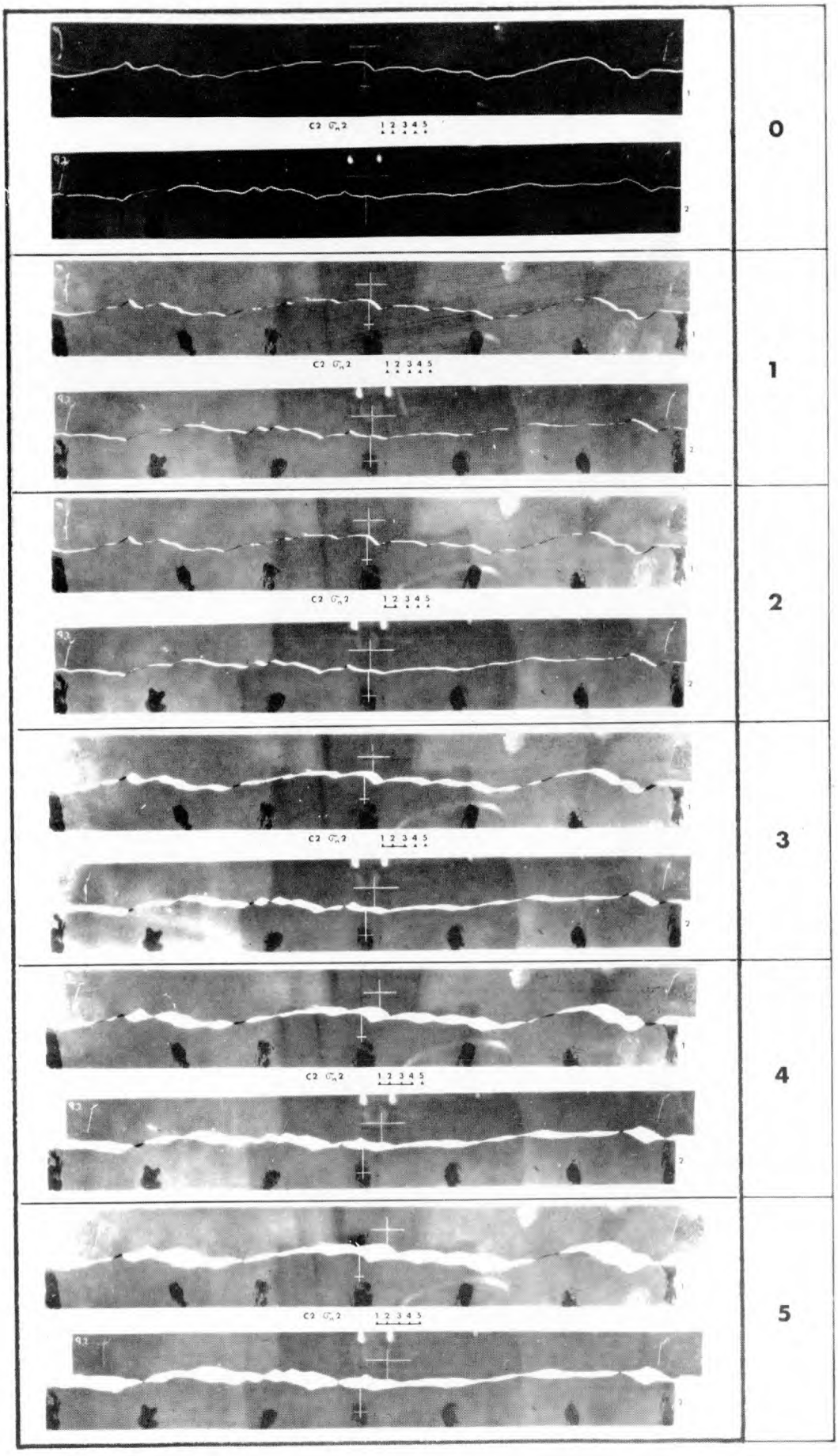

Figure 2.1.12 Reconstructed shear test sequence of type C2 (P) tested at a prototype normal stress of 112 lbf/in^2

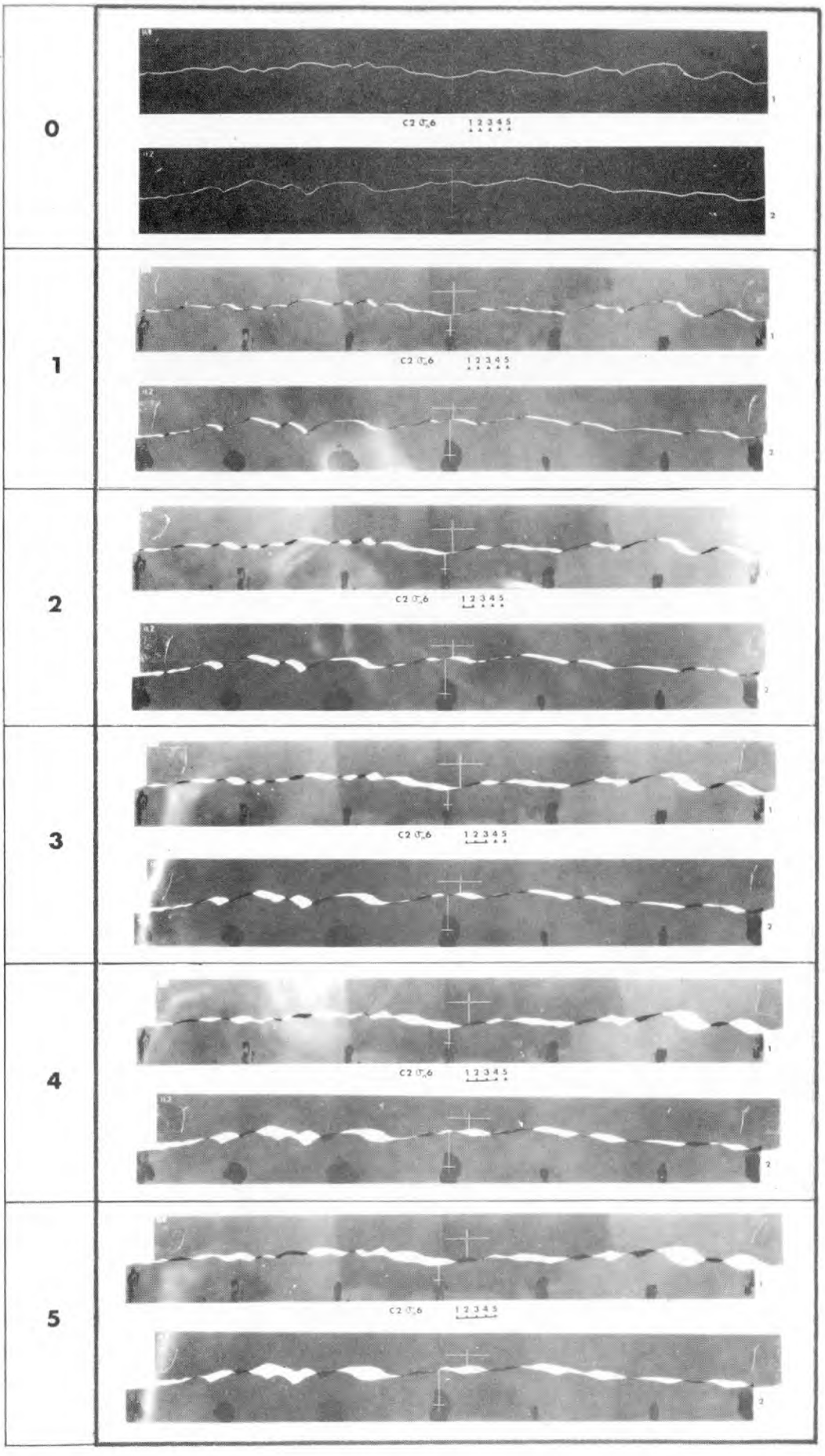

Figure 2.1.13 Reconstructed shear test sequence of type C2 (P) tested at a prototype normal stress of 635 lbf/in^2

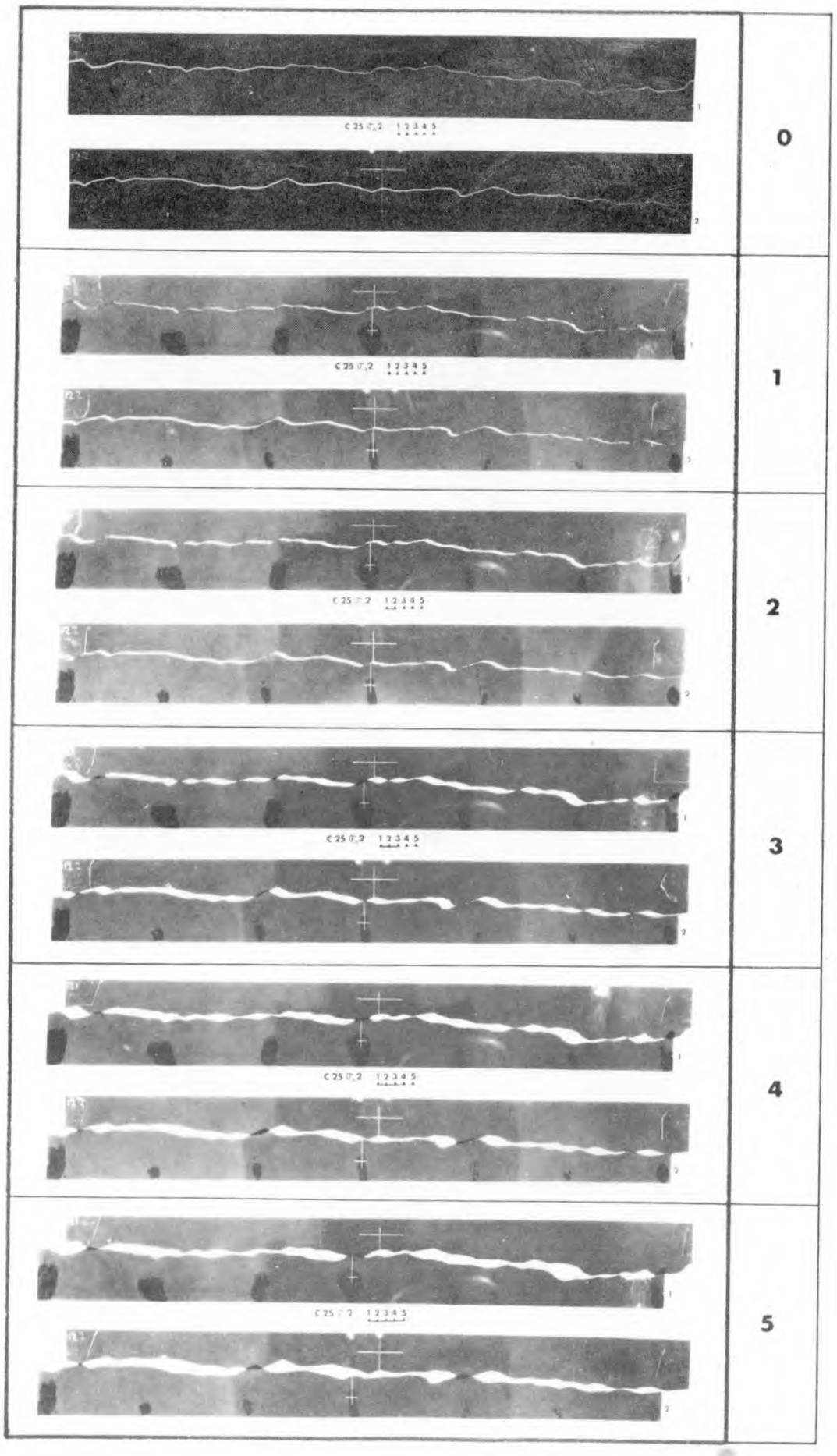

Figure 2.1.14 Reconstructed shear test sequence of type C 25 (P) tested at a prototype normal stress of 109 lbf/in^2

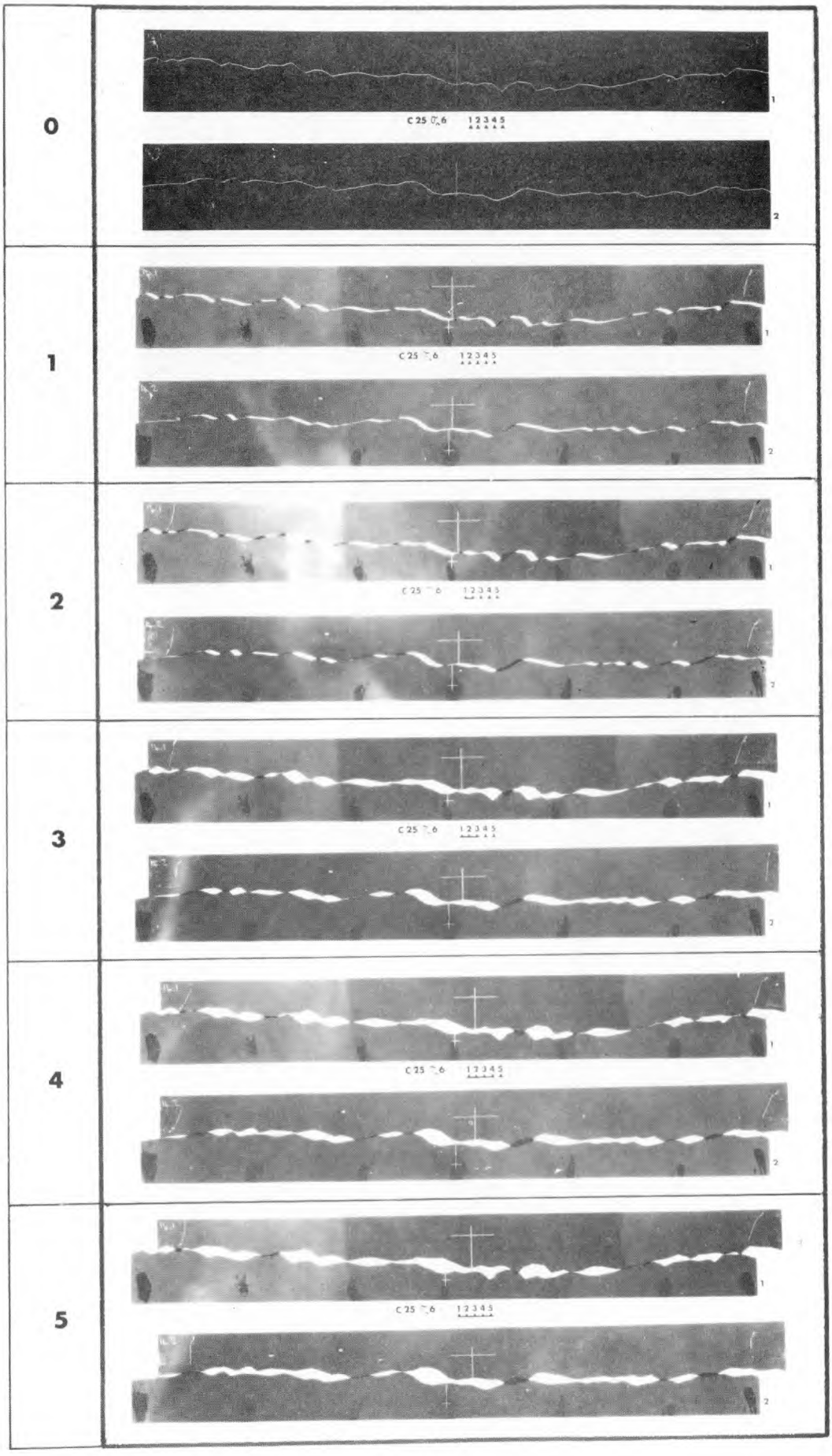

Figure 2.1.15 Reconstructed shear test sequence of type C25 (P) tested at a prototype normal stress of 658 lbf/in^2

Sharp [54] suggested that the failure of tips of joint asperities might cause a sudden reduction in the volume of the joint at some stage during the shearing process. It was envisaged that the resulting instantaneous water pressure increases would be a contributing factor to progressive failure. However, observations of the reconstructed shear tests suggest that joint volume continues to increase with increased shear displacement, at least up to displacements approaching the residual. Bearing in mind how many years rock slopes can take to progressively fail even after large displacements, a mechanism which explains the arrest of catastrophic failure is perhaps more appropriate than one which explains the acceleration of the same.

3. The steep tips of the model asperities appeared to be sheared off at an early stage in the shearing process. At low normal stresses (100 lbf/in^2 for prototype) only a few points were in contact, and the shearing damage was slight. However at the higher normal stress (650 lbf/in^2 for prototype) the area in contact and the 'area' sheared was greatly increased - perhaps as much as the square of the stress ratio. The sheared 'areas' had longer base lengths, and by implication a lower inclination of asperity was being sheared at the higher stress.

4. The overlapping black areas represented double density. This sheared area is in reality distributed over the surface as detritus, and since it is in granular form much of the joint 'spaces' generated by shearing will be partially filled. This will tend to increase the contact area, and reduce the permeability effect. However, these observations will only be relevant to shear under quite high normal stresses, unless the joint walls are sufficiently weathered for the effect to occur at lower stresses.

2.1.5 A PEAK STRENGTH CRITERION FOR ROCK JOINTS

It was established earlier that the angular summation of $(\phi_b + d_n)$ did not provide the correct experimental results of (ϕ peak) for rock joints. This was due to the component of strength resulting from shear through intact material. The peak dilation angles (d_n) measured during tests on model joints C3(P) and C3(PCJ) were substituted in the following relationship:

$$\tau/\sigma = \tan (\phi_b + d_n)$$

with assumed basic friction angle (ϕ_b) of 30°. It was found that at all normal stress levels there was a discrepancy between experimental and predicted peak arctan (τ/σ) of from 6 to 14°, with the predicted value always lower than the experimental result.

An accurate prediction of the experimental ratio (τ/σ) at very low normal stresses was given by the following:

$$\tau/\sigma = \tan (\phi_b + d_n) + c/\sigma$$

where (c) was the apparent cohesion intercept extrapolated from the lowest normal stress tested. However at higher levels of stress an error resulted, and this increased to values almost as high as the previous range 6 to 14°.

It was obvious that the shearing component had to be related to the shape of the peak curve defined by the ratios of τ/σ at different normal stresses. Consequently the following relation was tested:

$$\tau/\sigma = \tan (\phi_b + d_n) + K (\tau/\sigma)$$

$$\text{or} \quad \tau/\sigma = \frac{\tan (\phi_b + d_n)}{1-K}$$

Experimental data had only been evaluated for joint types C3(P) and C3 (PCJ) at this stage. It was found that the mean value of (1-K), obtained from experimental results at the seven different normal stresses, was 0.580. It happens that the tangent of 30° (the assumed value of ϕ_b) is equal to 0.577. This implied that a good experimental fit would be obtained using the relationship:

$$\tau/\sigma = \frac{\tan (\phi_b + d_n)}{\tan \phi_b} \qquad (1)$$

In fact this produced an extremely good fit over the lowest four or five normal stresses but seriously overpredicted the peak strength at the two highest normal stress levels.

It was noticed that the ratio of (τ/σ) given by equation 1, was insensitive to changes in the assumed value of (ϕ_b). Continued experimental fitting resulted in a second workable relationship, which produced a slightly improved fit at the higher normal stresses:

$$\tau/\sigma = \frac{\tan \left[\tan^{-1}\left(\frac{\sigma}{\tau}\right) + d_n\right]}{\tan \left[\tan^{-1}\left(\frac{\sigma}{\tau}\right)\right]}$$

This expression simplifies to:

$$\tan^{-1}\left[\frac{\sigma}{\tau}\right] = 45^\circ - d_n$$

$$\text{or} \quad \tau/\sigma = \tan(45^\circ + d_n) \qquad (2)$$

It seems probable that if a joint were sheared when under sufficiently high normal stress, it would not dilate even at the point of peak strength. Equations (1) and (2) imply that the ratio of peak (τ/σ) at this high normal stress would be equal to one. A value of arctan (τ/σ) of 45° seems unrealistically high for such high stress levels. At the lower end of the stress scale the maximum values of (d_n) implied by the two equations are ($90 - \phi_b$) and 45° respectively.

The relationship between peak stress ratio and peak dilation angle

Peak dilation angles and corresponding ratios of (τ/σ) were calculated for all the remaining model joints that were shear tested. In addition some experimental data for tension fractures in Blackstone granite were kindly supplied by de Freitas[55]. These were from tests on rough, artificial fractures of approximately 35 in^2 in area, which were produced in an effort to simulate the roughness of joints observed in the field. Unfortunately the experimental scatter for these five rock specimens was very large. However the results are presented for comparison with the model joints.

A total of approximately 150 experimental results were thus available for experimental trends to be established. These ranged from the rough interlocking secondary joints C3(s), down to the more regular primary joints of C25(P). A minimum of two model joints of one type were tested at each normal stress. The mean of these results are the values that were analysed. Unfortunately it was not possible to take dilation measurements at the lowest normal stress applied to each joint type, because these were loaded by self weight only. Any mechanical displacement measuring system would have increased this minimum normal stress (0.044 lbf/in^2) to unacceptable levels.

Initially the experimental data was plotted as the ratio of (τ/σ) versus the peak dilation angle (d_n). This resulted in a poorly distributed and slightly non linear configuration of points on the graph. Consequently the data was plotted in angular form; arctan (τ/σ)$^\circ$ versus (d_n)$^\circ$. The distribution of this data is shown in Figure 2.1.16.

A least squares analysis was carried out by Markland[56], and gradients and intercepts calculated for the best fit straight lines to each of the eight model joint types, and also for the total sample. The model results were doubly weighted compared to the

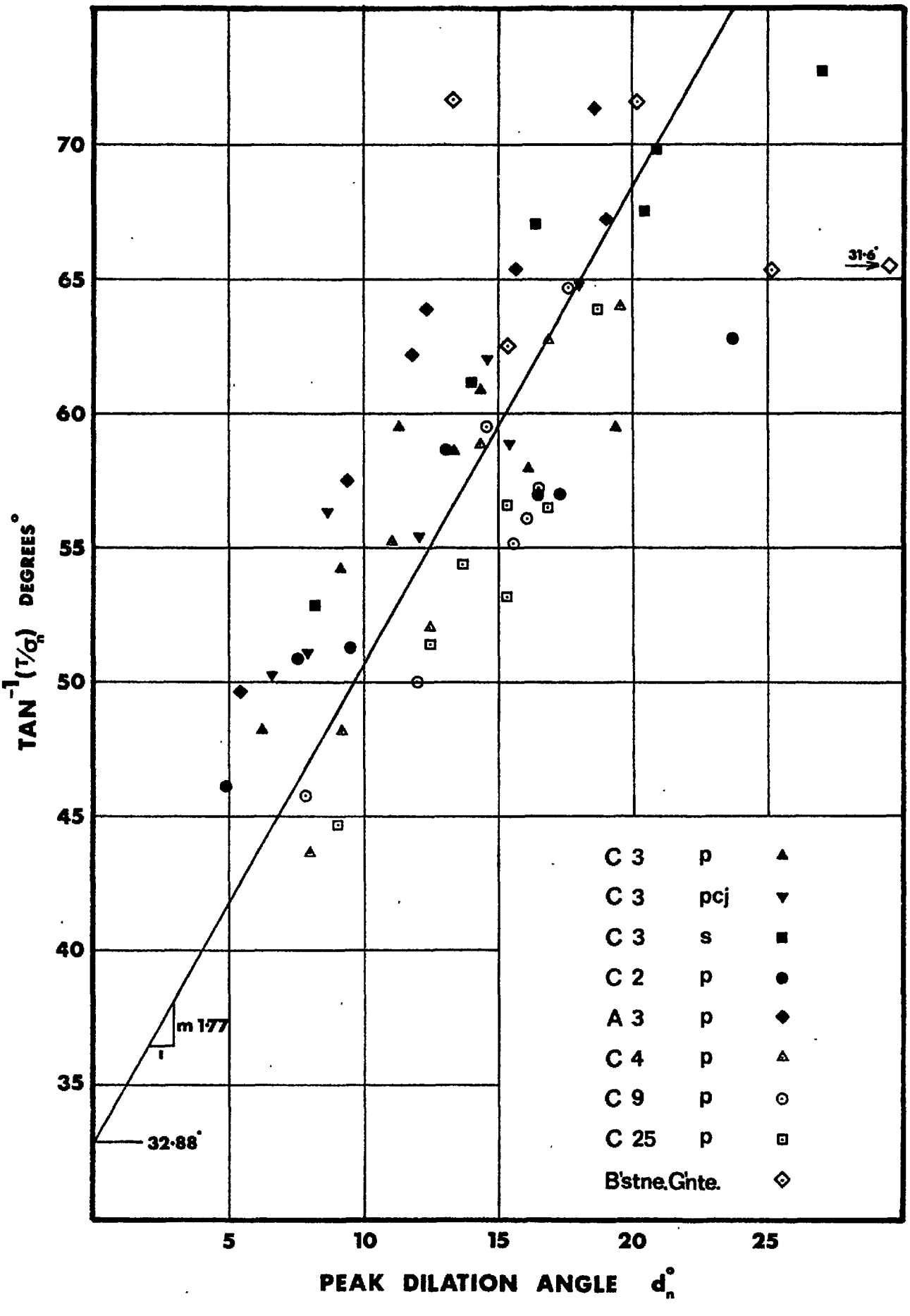

Figure 2.1.16 The angular relationship between peak stress ratio and peak dilation angle for all model joints.

single tests on granite, and the peak dilation angle (d_n) was taken as the dependent variable. The following table gives the results of this analysis:-

Joint type	Gradient (M)	Intercept (C)
C3 (S)	1.16	44.4°
A3 (P)	1.50	42.7°
C2 (P)	0.92	42.6°
C3 (P)	1.28	40.6°
C3 (PCJ)	1.34	41.0°
C4 (P)	1.91	30.0°
C9 (P)	2.04	26.2°
C25 (P)	1.94	26.2°

The following result was obtained for the total weighted sample:

$$\tau/\sigma = \tan (1.78\, d_n + 32.88^\circ)$$

Two important observations should be noted:

1. If d_n is put equal to the intercept (C) in the above equation the function (MC + C) is equal to 89.6°.

2. If this is done for all the model joint types presented in the table, a mean value of (MC + C) equal to 91.3° is obtained.

Bearing in mind the variety of joint surfaces, and the possible experimental scatter of results, it was felt that most reliance should be placed in the least squares fit to the whole test sample. The intercept of 32.88° was fortuitously close to the basic angle of friction of the model materials, and this suggested the following peak strength criterion:

$$\tau/\sigma_n = \tan\left[\left(\frac{90 - \phi_b}{\phi_b}\right) d_n + \phi_b\right] \qquad (3)$$

When ϕ_b is 30° this reduces to the simple form:

$$\tau/\sigma_n = \tan (2d_n + 30^\circ) \qquad (4)$$

It will be shown presently that this approximate equation has considerable potential as a means for predicting peak strength curves.

The relationship between normal stress and peak dilation angle.

The model joints were tested at a variety of normal stress levels, depending upon the relative compressive strengths of the materials concerned. Direct comparison was therefore only possible when the normal stresses were 'normalized' by dividing by the appropriate unconfined compression strengths. The dimensionless plot of (σ_n / σ_c) versus peak dilation angle (d_n) could then be compared with data for rock. Figure 2.1.17 shows the trends for this relationship. Once again each model result is the mean of two tests at the same normal stress.

A linear relationship is obtained if the data is replotted with the dimensionless ratio (σ_n / σ_c) on a logarithmic scale. Figure 2.1.18 indicates the experimental trend. A least squares fit to the total weighted sample gave the following equation:

$$\log 10 \left(\frac{\sigma_n}{\sigma_c} \right) = -0.1056\, d_n + 0.1184$$

It will be noticed that only a very small adjustment is required to produce the simple relationship:

$$\log 10 \left(\frac{\sigma_n}{\sigma_c} \right) = -0.100\, d_n$$

$$\text{or} \quad d_n = 10 \log 10 \left(\frac{\sigma_c}{\sigma_n} \right) \qquad \text{(5)}$$

The classic simplicity of this relationship suggests that the result may be most significant.

σ_c / σ_n	d_n
1.0	0°
10	10°
100	20°
1000	30°

When combined with equation (4) a very useful criterion of peak strength is produced:

$$\tau / \sigma_n = \tan \left[20 \log 10 \left(\frac{\sigma_c}{\sigma_n} \right) + 30^\circ \right] \qquad \text{(6)}$$

This would seem to have application in situations where the joint surface was statistically unknown, but sufficiently rough to bear comparison with the model tension joints. In addition a basic angle of friction (ϕ_b) of approximately 30° would be required. Some examples of possible applications will be cited, before going on to consider joint roughness and its effect on such a criterion.

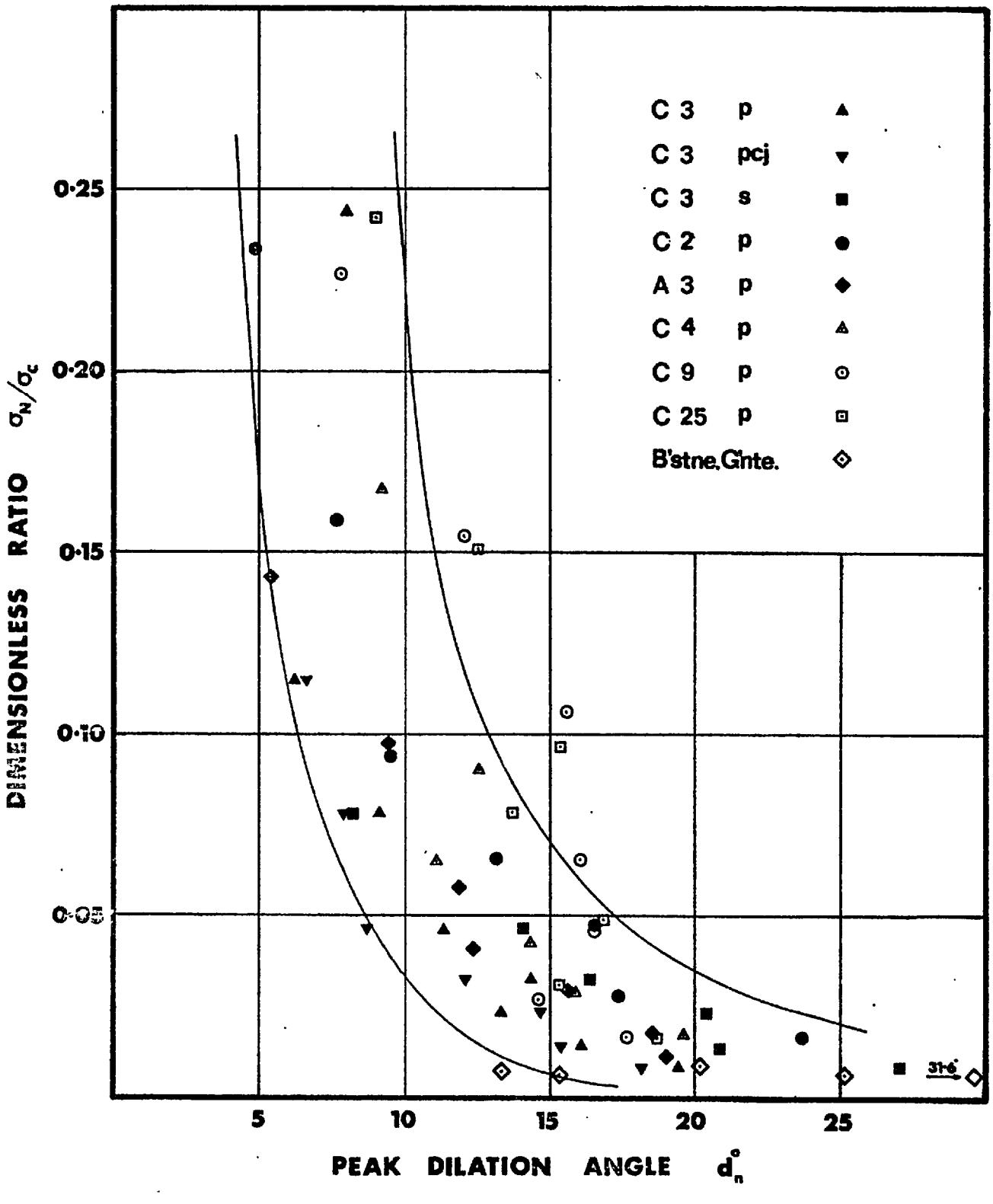

Figure 2.1.17 Peak dilation angle as a function of the normal stress compressive strength ratio.

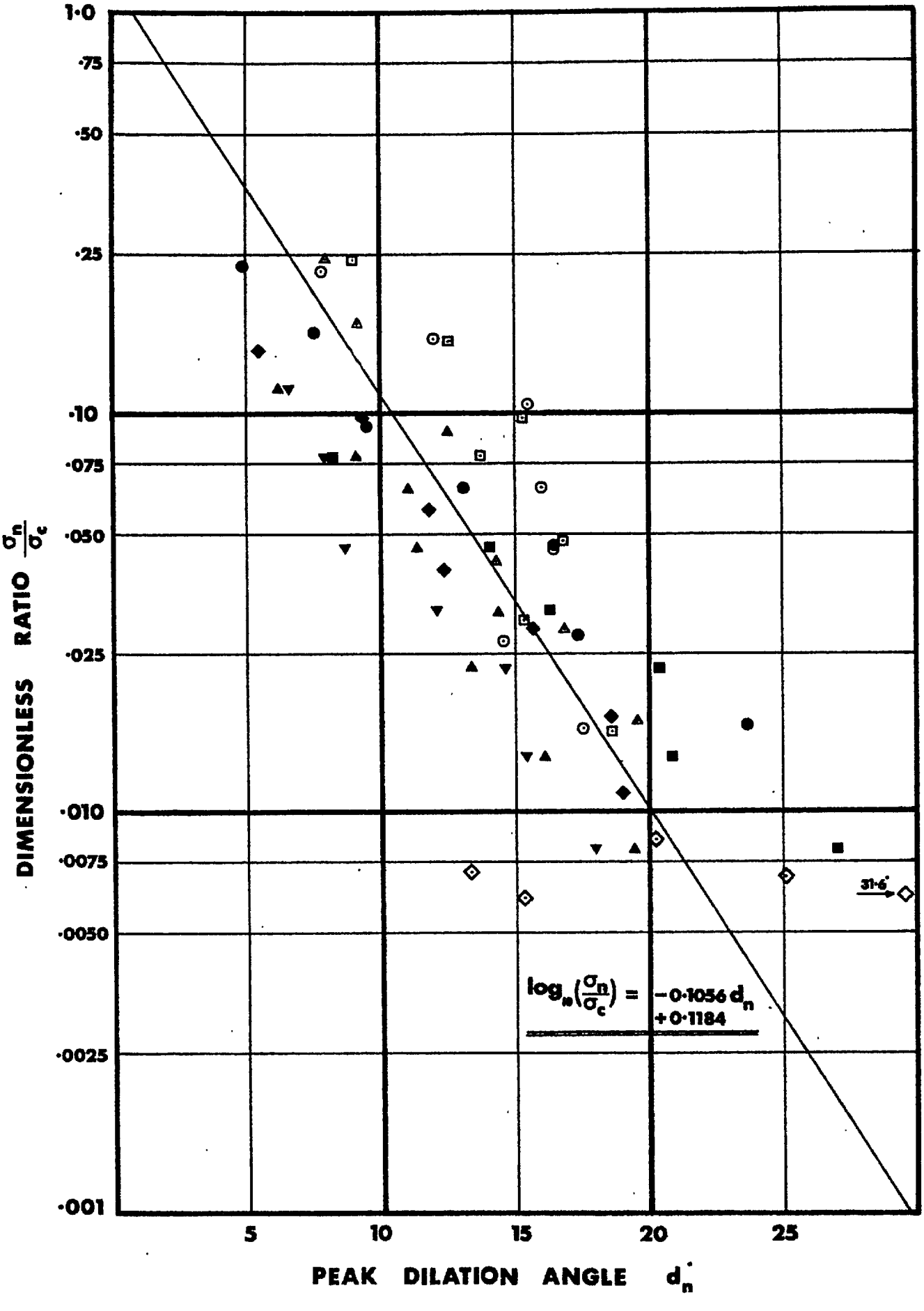

Figure 2.1.18 Peak dilation angle as a function of the logarithmic normal stress to compressive strength ratio.

The estimation of peak shear strength

Equation 6 is a non linear function relating the ratio of peak shear strength to normal stress, to the ratio of the unconfined compression strength to normal stress. It can be applied to practical situations in two ways:

1. The ratios of (τ / σ_n) for unweathered tension joints in rock can be estimated from a knowledge of the unconfined compression strength of the rock concerned.

   For example; the design chart shown by Figure 2.1.19 indicates that a rock of 10,000 lbf/in^2 in unconfined compression, when tested at a normal stress of 200 lbf/in^2 ($\sigma_c / \sigma_n = 50$) would give a ratio of (τ / σ_n) of approximately 2.06. Thus for a range of normal stresses the desired peak strength envelope could be estimated.

2. Weathered tension joints in rock present a more difficult problem since the unconfined compression strength of the sound rock cannot be easily related to the 'effective joint wall compressive strength' of the weathered material. Consequently the best approach here would be to perform a limited series of shear tests (in situ if possible) all at the same normal stress. The mean value of (τ / σ_n) obtained from these tests could then be used in the design chart.

   For example; suppose the mean value of (τ / σ_n) was 1.59 for a normal stress of 200 lbf/in^2. Figure 2.1.19 indicates that the ratio of (σ_c / σ_n) would be approximately 25. This implies an 'effective joint wall compressive strength' of 5000 lbf/in^2; half the previous value. This value could then be used to estimate the peak strength envelope for the normal stress range required.

(Note: Unconfined compression strength was the most convient 'normalising' parameter to convert the model results into dimensionless data. However, it is realised that 'shear' failure of asperities at peak strength is probably characterised by tensile failure in reality. Consequently an index test of the 'point load' variety might prove a useful method for assessing the effective joint wall strength).

The results of shear tests on rough joints in porphyry performed in the large shear machine at Imperial College (Pentz[34] and Kutter[33]) have been referred to in Part I. The joints had cross sectional areas of up to 1 ft^2, and were obtained from 9 inch diameter cores drilled along joints which were exposed in the bench faces of Corta Atalaya. This is a 900 feet deep open pit operated by Rio Tinto Espanola in southern Spain.

The results of the shear tests are shown in Figure 2.1.20. The residual values (obtained after approximately four inches of shearing) indicated a residual angle of friction of approximately 31°.

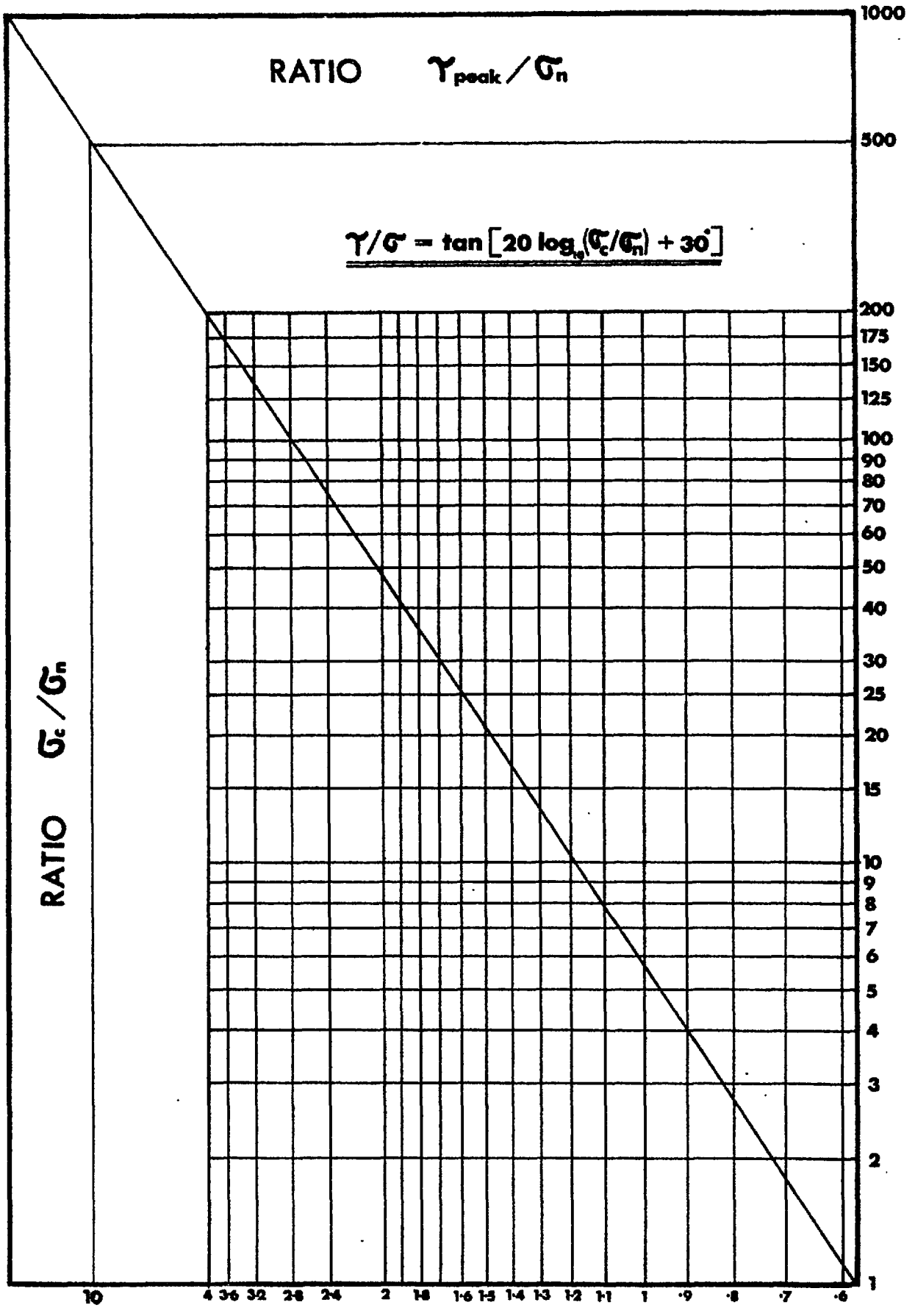

Figure 2.1.19 Design chart for general criterion of peak shear strength.

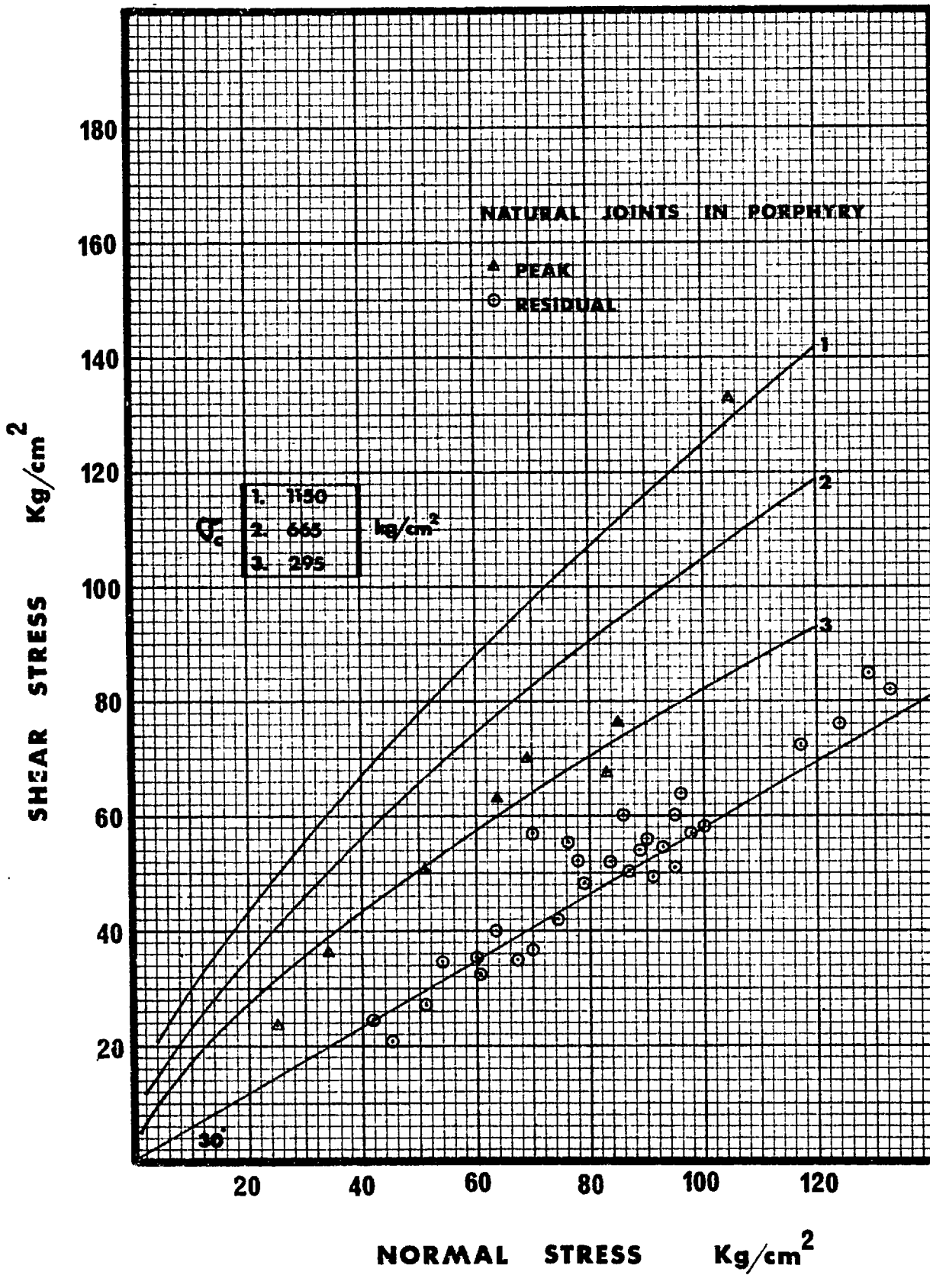

Figure 2.1.20 Comparison of general criterion of peak shear strength with shear test results, using three effective compressive strengths.

Ross Brown and Barton[52] measured a basic angle of friction (ϕ_b) for flat, sand blasted porphyry surfaces of $30\frac{1}{2}^{\circ}$. These specimens were obtained from the same location as the above.

In addition to shear tests, unconfined compression and triaxial compression tests were performed on the Rio Tinto porphyries (Ross Brown and Barton). Specimens of three varieties, taken from three open pits in close proximity produced the following mean values of unconfined compression strength:

1.	1150		(Corta Atalaya)
2.	665	Kg/cm^2	(Corta Filon Sur)
3.	295		(Corta Dehesa)

The Atalaya specimen was obtained from freshly fractured rock below a recent blast. That from Filon Sur also appeared freshly broken, since it was taken from the debris below a recent rock slide (see Section 2.2). However the cleaved variety taken from a bench of Corta Dehesa (which is now unworked) was badly weathered and fissured.

These three compressive strengths were taken as possible examples of 'effective joint wall compressive strength', and were used to estimate three peak shear strength curves. Figure 2.1.20 illustrates the possible application of such methods of intrapolation.

The highly weathered specimen appears to give a useful prediction of peak strength, which passes between the majority of the limited shear test data, and provides an estimate of peak strength at lower normal stresses. The single apparently inexplicably high test result may possibly be explained as being the result of a shear test performed on an unweathered, tight joint.

The three curves presented in Figure 2.1.20 are in reality all the same curve plotted at different scales according to the effective compressive strengths. Figure 2.1.21 shows the complete curve that is given by equation 6, taken as far as a normal stress equal to the effective compressive strength.

Modified Peak shear strength criterion

Equation 6 has been briefly demonstrated as a possible criterion of peak strength for rough rock joints which display comparable strength and frictional properties to the scaled up model joints. It will be noticed that changes in value of the basic friction angle (ϕ_b) result in changes of gradient and intercept in equation 3. A value of (ϕ_b) less than 30° results in a gradient greater than 2.0, and an intercept less than 30°. The validity of this concept seems to be in question since so far, changes in joint roughness have not been considered.

Figure 2.1.21 The dimensionless relationship of peak shear strength as a function of effective joint wall compressive strength

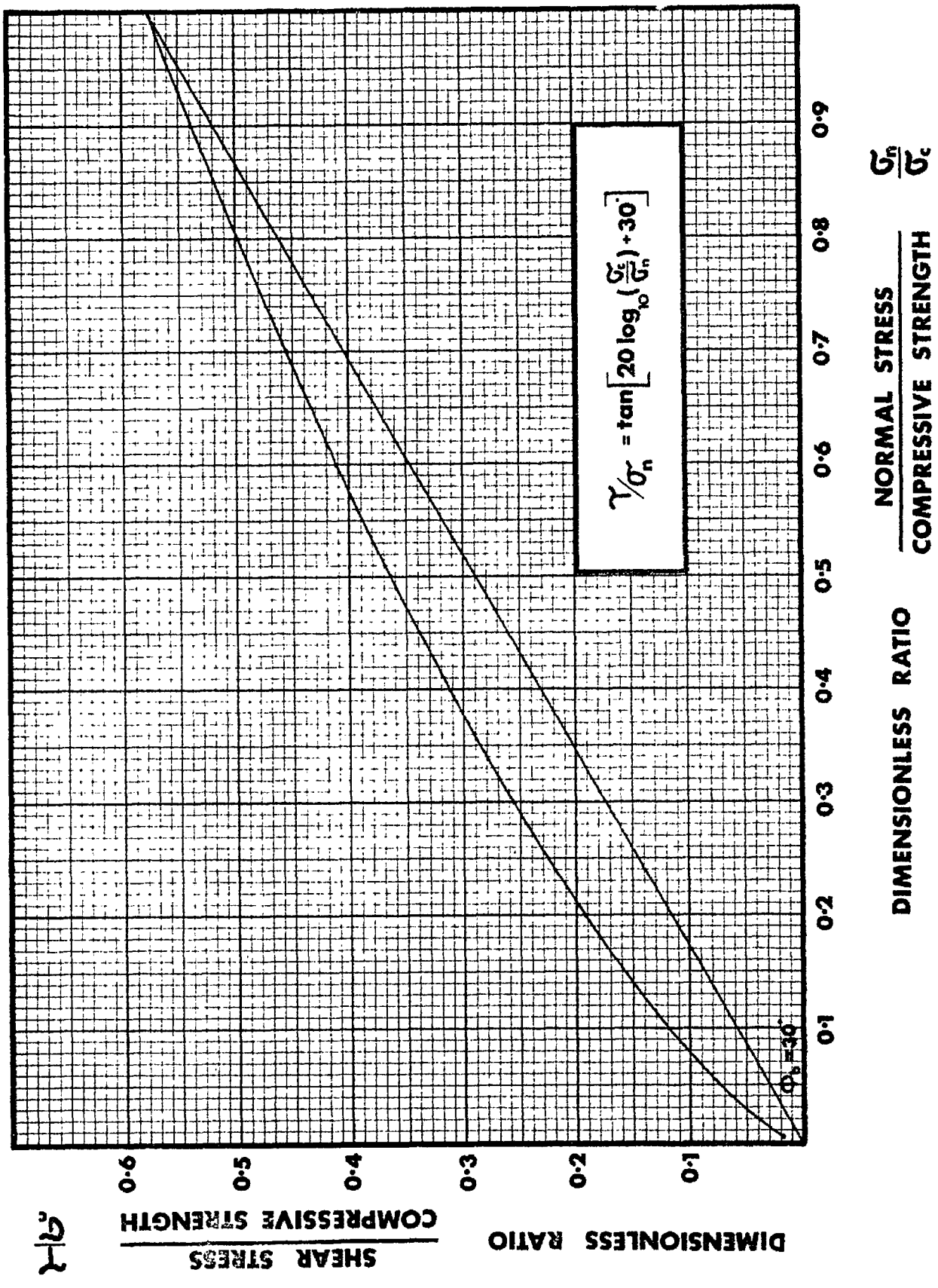

This dilemma can be resolved by closer attention to the details of behaviour of the individual model joints. The gradients and intercepts of the function:

$$\tan^{-1}(\tau/\sigma_n) = M\, d_n + C$$

were presented earlier for all eight different model joints. These values were obtained from least squares analyses, and were tabulated as far as possible in decending order of joint roughness. Thus the secondary offset joints C3(S) were obviously the roughest of all, and the primary joints C9 and C25 were smoothest. (The order of tabulation can be checked against the roughness profiles presented in Figure 2.1.11).

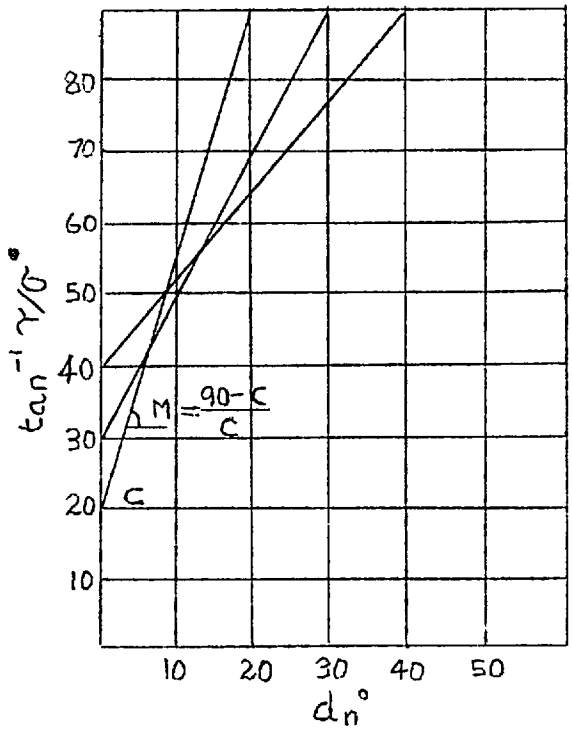

It will be recalled that the mean value of the relation MC + C for individual model joints was 91.3°, and for the least squares fit to all the data; 89.6°. This implies that the gradient M has the value given in the sketch on the left. Thus:

$$MC + C = \frac{(90-C)}{C}.C + C = 90^\circ$$

By implication, the dilation angle when $\tan^{-1}(\tau/\sigma)$ equals 90° is equal to the intercept C, when the dilation angle is zero.

Figure 2.1.18 indicated that average joint surfaces would cease to dilate only when the normal stress reached the same level as the effective compressive strength. ($\sigma_n/\sigma_c = 1.0$). Therefore the intercept C represents the value of $\tan^{-1}(\tau/\sigma_n)$ when the normal stress is equal to the compressive strength. Thus C, which is clearly dependent on joint roughness, appears to predict the shape of the strength curve. Rough joints having the highest C values, would also display the highest shear strength when the normal stress equalled the compressive strength. This seems a perfectly logical deduction.

One further detail is required before a modified criterion can be formulated. The sketch just presented implied that the dilation angle was equal to the C intercept, when the value of $\tan^{-1}(\tau/\sigma_n)$ was 90° . (i.e. at very low normal stress). The log. versus linear data shown in Figure 2.1.18 indicated an overall angle of dilation of

approximately 29.6° at the lowest 'intercept' of (σ_n / σ_c) of 0.001. For all practical purposes this ratio represents zero normal stress. However, when least squares analyses are performed for individual joint types, the 'intercepts' show close similarity to the C values given earlier. Taking the best five pairs the following is revealed:

Joint	C^o	$\hat{d}^o$
C3(S)	44.4	43.1
C2(P)	42.6	41.5
C4(P)	30.0	30.9
C9(P)	26.2	26.3
C25(P)	26.2	27.3

Again the data is tabulated in decending order of apparent roughness. The symbol $\hat{d}^o$ represents the 'maximum' angle of dilation for practically zero normal stress.

Thus for the range of normal stress:

$$\sigma_c > \sigma_n > \sigma_c/1000$$

and assuming the intercept C^o is very nearly identical to $\hat{d}^o$ for a given surface, the following modified criterion of peak shear strength is indicated:

$$\tau/\sigma_n = \tan\left[\frac{(90-\hat{d})}{\hat{d}} d_n + \hat{d}\right] \qquad \text{(7)}$$

It now remains to statistically analyse the roughness profiles of the model joints, and attempt to find a method for estimating the 'maximum' dilation angle $\hat{d}$ of a joint surface, and the stress dependent peak dilation angle d_n.

2.1.6 A MATHEMATICAL ANALOGY FOR SHEAR BEHAVIOUR

The reconstructed shear tests illustrated in Figures 2.1.12 to 2.1.15 indicated the following:

1. At low normal stress only the steep tips of asperities were sheared through. Thus only a small asperity base length (area) was involved.

2. At higher normal stress, less steep asperities with longer base lengths were sheared through.

3. The higher the normal stress the smaller the angle of peak dilation.

The forty roughness profiles illustrated in Figure 2.1.11 were available in the form of large scale computer plots (four are shown in Figure 2.1.22) and also as coordinates recorded on punched tape. It will be noticed that the measurements were made at points along the surfaces corresponding to the local high and low spots. This is clearly the most accurate way of representing a surface with a limited number of observations. However this means that coordinates were not recorded at regular intervals, though the mean distance between them was approximately 1 mm (0.040 inch) at ground scale.

It was appreciated that the positive and negative angles between consecutive coordinates represented extremely steep (i) values. However the positive or negative angles between every second or third coordinate, represented appreciably smaller values. Thus in a crude way the shear behaviour of joints was simulated by (i) values of different base lengths. The longer the base length the lower the (i) value, corresponding to shear through larger asperities at higher normal stresses.

A logical relationship was required between the two pairs of parameters:

1. normal stress
   dilation angle

2. asperity base length
   effective roughness (i) values.

Input data

The following computations were required (See Figure 2.1.22):

(a) Inclination between successive coordinates, (one step, positive or negative) shifting one step at a time. N coordinates (N-1) data points.

(b) Inclination between every second coordinate, (two steps, positive or negative) shifting one step at a time. N coordinates. (N-2) data points.

(c) Inclination between every nth coordinate, (n steps positive or negative) shifting one step at a time. N coordinates. (N-n) data points.

The majority of profiles were composed of approximately 65 coordinates. (N=65). Steps were taken at coordinate steps from 1 to 20. (n = 1 to 20). The ratio $^{n}/_{N}$ was defined as follows:

$$\frac{n}{N} \times 100\% = \text{asperity base \% (A.B. \%)}$$

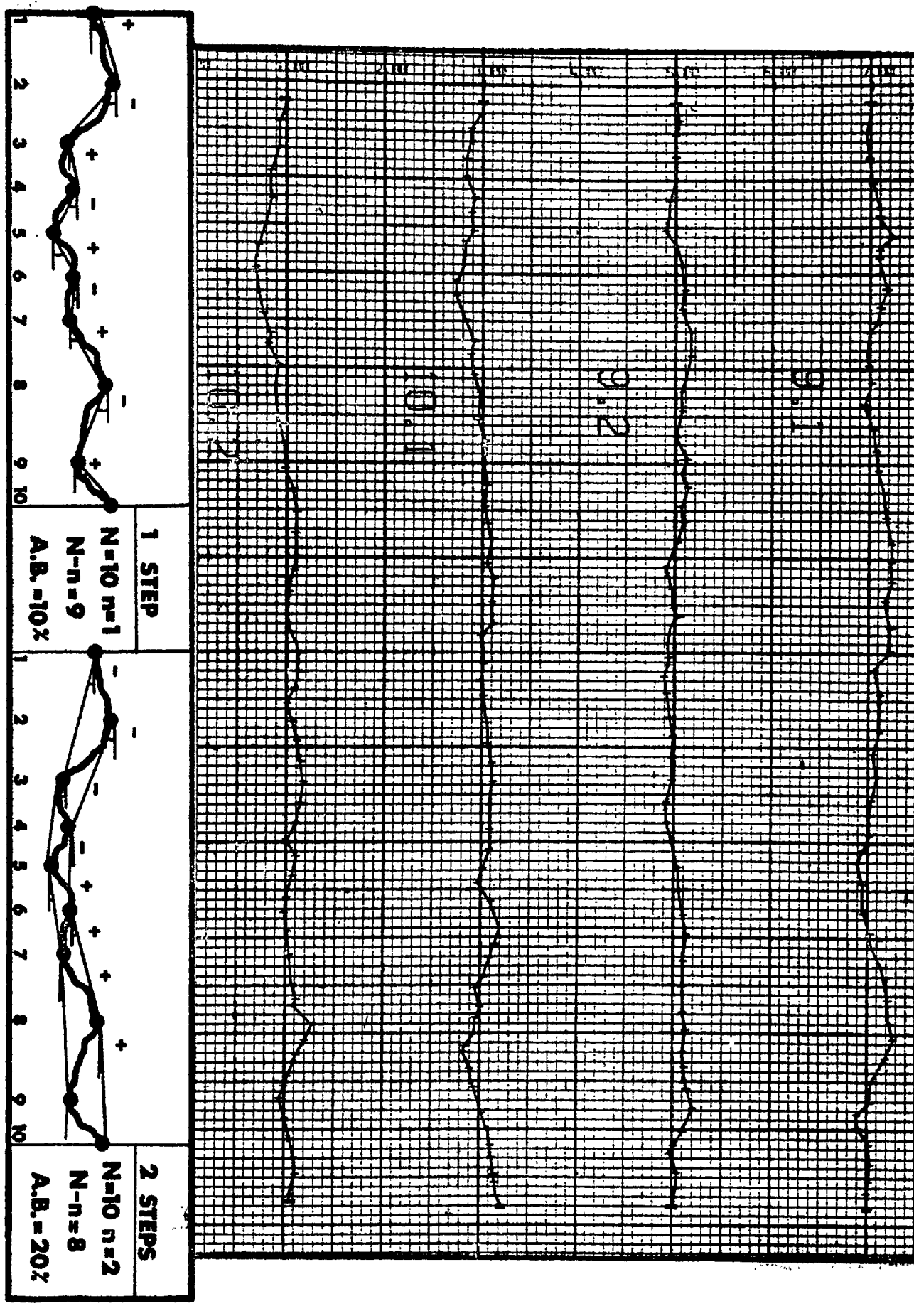

Figure 2.1.22 Typical computer drawn roughess profiles for two model joints.

The single coordinate steps which were spaced at approximately 0.040 inch, represented about 1.4 % of the total joint length.

Output data

The forty available profiles with approximately 65 coordinates each, represented a very large number of computations. Consequently a computer programme was developed (Cundall[57]) to produce the following output in the form of histograms:

1. No. of observations for a particular effective (i) value. (Positive and negative angles within the range 0^{o} to 55^{o} for intervals of 2.5^{o})

2. The same data for different asperity bases. (steps of 1 to 20)

A typical compound histogram is shown in Figure 2.1.23. For each histogram at each asperity base, the statistical mean, median and standard deviation were computed. This output was divided into positive, negative, and average angles.

It can be seen that as the asperity base (steps of 1,2,3 etc) increased the standard deviation of the effective (i) values reduced; rapidly at first and then very gradually. As it happened, the average standard deviations for all the profiles, for the smallest asperity base (1 step) ranged from about 14^{o} to 20^{o}. This was very similar to the largest values of peak dilation angle measured for each of the joints at low normal stress.

The twenty specimens shown in Figure 2.1.11 were sheared in a positive direction, with respect to the above output. However the average of the positive and negative standard deviations was considered more representative of a particular joint type. (It should be pointed out that one or two profiles demonstrated maximum positive and negative standard deviations as much as 8^{o} to 10^{o} different. The direction of shearing could therefore be most important).

Relationship between asperity base (A.B. %) and standard deviation of (i) values. (S.D. i^{o})

Figure 2.1.24 illustrates the distribution of S.D. (i) values for the lower range of asperity bases. The squares representing material C3(s) were widely separated from the main body of the results because of the offset, stepped nature of secondary joints compared to the continuous primary joints. With the exception of the secondary joints the data represented a well defined mean, and appeared to be approximately normally distributed.

PROFILE NO. 9.2 C2 (P)
NUMBER OF DATA POINTS = 60

STEPS OF =	1	2	3	4	5	6	7	8	9	10	11	12	13	14	15	16	17
TOTALS =	59	58	57	56	55	54	53	52	51	50	49	48	47	46	45	44	43
-55.0	0	0	0	0	0	0	0	0	0	0	0	0	0	0	0	0	0
-52.5	0	0	0	0	0	0	0	0	0	0	0	0	0	0	0	0	0
-50.0	0	0	0	0	0	0	0	0	0	0	0	0	0	0	0	0	0
-47.5	0	0	0	0	0	0	0	0	0	0	0	0	0	0	0	0	0
-45.0	0	0	0	0	0	0	0	0	0	0	0	0	0	0	0	0	0
-42.5	0	0	0	0	0	0	0	0	0	0	0	0	0	0	0	0	0
-40.0	1	0	0	0	0	0	0	0	0	0	0	0	0	0	0	0	0
-37.5	0	0	0	0	0	0	0	0	0	0	0	0	0	0	0	0	0
-35.0	0	0	0	0	0	0	0	0	0	0	0	0	0	0	0	0	0
-32.5	0	0	0	0	0	0	0	0	0	0	0	0	0	0	0	0	0
-30.0	1	0	0	0	0	0	0	0	0	0	0	0	0	0	0	0	0
-27.5	0	1	0	0	0	0	0	0	0	0	0	0	0	0	0	0	0
-25.0	2	1	1	0	0	0	0	0	0	0	0	0	0	0	0	0	0
-22.5	1	1	0	0	0	0	0	0	0	0	0	0	0	0	0	0	0
-20.0	4	1	1	0	0	0	0	0	0	0	0	0	0	0	0	0	0
-17.5	0	1	0	0	0	0	0	0	0	0	0	0	0	0	0	0	0
-15.0	4	0	0	0	0	0	0	0	0	0	0	0	0	0	0	0	0
-12.5	4	2	0	4	2	0	0	0	0	0	0	0	0	0	0	0	0
-10.0	0	0	5	2	1	1	1	0	0	0	0	0	0	0	0	0	0
-7.5	4	3	6	2	2	4	0	0	0	0	0	0	0	0	0	0	0
-5.0	2	7	4	5	8	5	6	2	5	3	5	5	2	1	1	0	0
-2.5	1	8	6	6	5	7	8	12	8	10	6	5	7	9	9	7	8
0.0	7	7	6	11	10	10	9	13	13	11	11	13	13	11	11	13	10
2.5	5	3	6	7	11	12	15	11	9	8	12	11	11	13	13	16	19
5.0	0	2	9	9	8	9	8	9	14	17	14	13	13	11	11	8	6
7.5	4	7	2	3	3	3	4	4	2	1	1	1	1	1	0	0	0
10.0	4	6	4	3	3	1	2	1	0	0	0	0	0	0	0	0	0
12.5	4	5	3	4	1	2	0	0	0	0	0	0	0	0	0	0	0
15.0	4	2	3	0	1	0	0	0	0	0	0	0	0	0	0	0	0
17.5	1	0	1	0	0	0	0	0	0	0	0	0	0	0	0	0	0
20.0	1	0	0	0	0	0	0	0	0	0	0	0	0	0	0	0	0
22.5	0	0	0	0	0	0	0	0	0	0	0	0	0	0	0	0	0
25.0	1	1	0	0	0	0	0	0	0	0	0	0	0	0	0	0	0
27.5	2	0	0	0	0	0	0	0	0	0	0	0	0	0	0	0	0
30.0	0	0	0	0	0	0	0	0	0	0	0	0	0	0	0	0	0
32.5	1	0	0	0	0	0	0	0	0	0	0	0	0	0	0	0	0
35.0	1	0	0	0	0	0	0	0	0	0	0	0	0	0	0	0	0
37.5	0	0	0	0	0	0	0	0	0	0	0	0	0	0	0	0	0
40.0	0	0	0	0	0	0	0	0	0	0	0	0	0	0	0	0	0
42.5	0	0	0	0	0	0	0	0	0	0	0	0	0	0	0	0	0
45.0	0	0	0	0	0	0	0	0	0	0	0	0	0	0	0	0	0
47.5	0	0	0	0	0	0	0	0	0	0	0	0	0	0	0	0	0
50.0	0	0	0	0	0	0	0	0	0	0	0	0	0	0	0	0	0
52.5	0	0	0	0	0	0	0	0	0	0	0	0	0	0	0	0	0
55.0	0	0	0	0	0	0	0	0	0	0	0	0	0	0	0	0	0
57.5	0	0	0	0	0	0	0	0	0	0	0	0	0	0	0	0	0
-MEAN.....	-13.3	-8.0	-7.3	-5.4	-4.9	-4.3	-3.8	-2.7	-3.0	-2.9	-3.1	-2.9	-2.5	-2.6	-2.6	-2.1	-2.4
+MEAN.....	12.2	8.3	6.4	5.1	4.2	3.7	3.1	3.3	3.0	3.1	2.7	2.8	2.8	2.5	2.4	2.1	1.8
AV. MEAN..	12.8	8.1	6.9	5.3	4.6	4.0	3.4	3.0	3.0	3.0	2.9	2.8	2.6	2.6	2.5	2.1	2.1
-MED.....	-13.4	-5.4	-6.6	-4.2	-4.5	-3.8	-3.4	-2.6	-2.5	-2.8	-2.5	-2.2	-2.1	-2.4	-2.4	-1.9	-2.3
+MED.....	10.6	7.9	4.7	4.2	3.3	2.9	2.4	2.9	3.1	3.2	2.8	2.8	2.8	2.4	2.3	1.9	1.6
AV. MED...	12.0	6.6	5.6	4.2	3.9	3.3	2.9	2.8	2.8	3.0	2.6	2.5	2.5	2.4	2.3	1.9	1.9
- S.D.....	16.7	11.0	9.3	7.0	6.1	5.2	4.5	3.1	3.6	3.4	3.7	3.5	3.0	3.0	3.0	2.4	2.7
+ S.D.....	15.1	9.5	7.9	6.2	5.4	4.7	3.9	3.9	3.4	3.3	3.1	3.1	3.1	2.9	2.7	2.4	2.1
AV. S.D...	15.9	10.3	8.6	6.6	5.8	5.0	4.2	3.5	3.5	3.4	3.4	3.3	3.0	2.9	2.8	2.4	2.4

Figure 2.1.23 An example of the computer output from the statistical analysis of model roughness profiles.

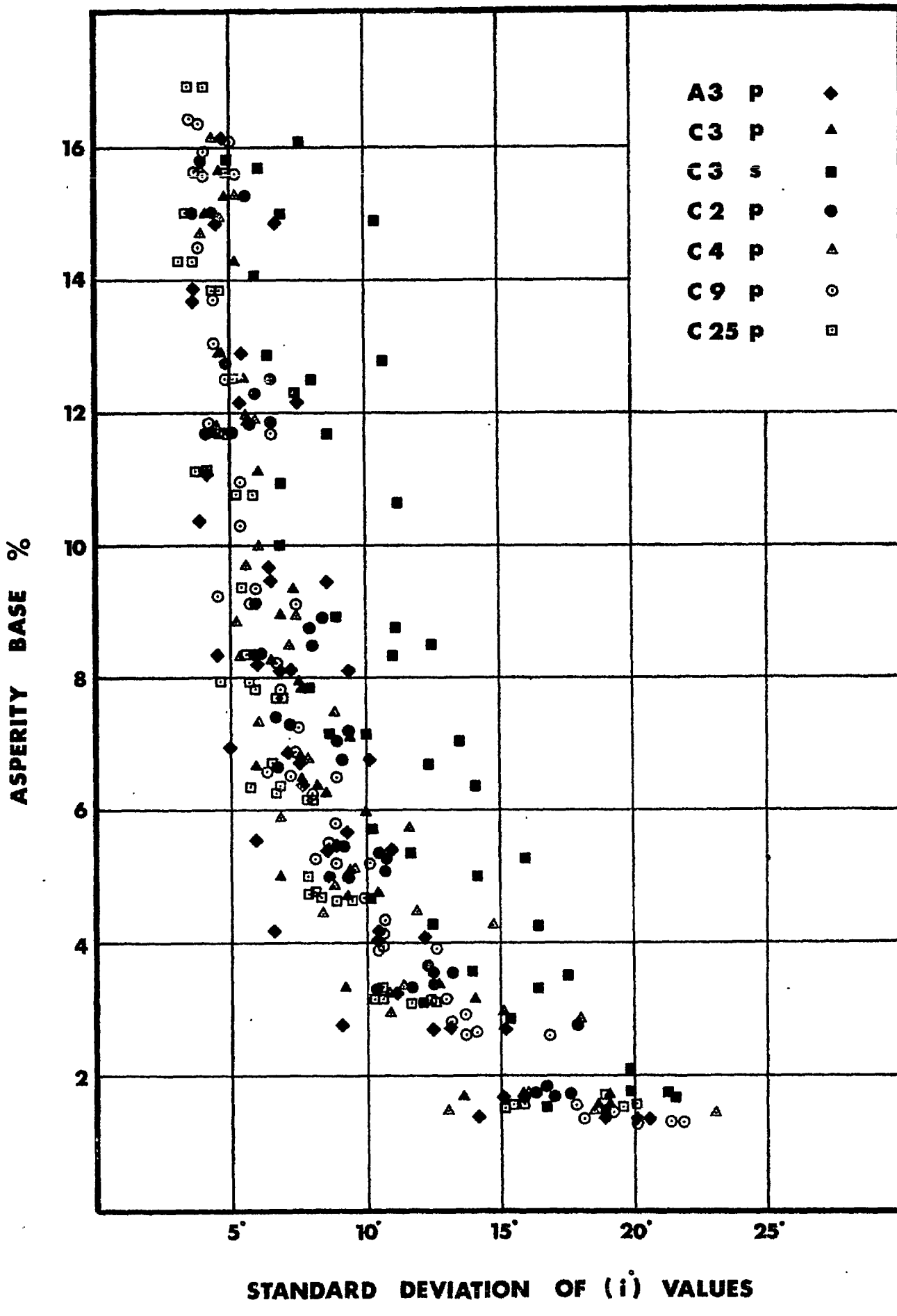

Figure 2.1.24 The results of a statistical analysis of seven different model joint types.

Sources of error

Computation of standard deviation involved root mean square calculations. As such, possible errors in the steepest (i) values would be distorted more than errors in the lower (i) values. It will be recalled that observations of the joint surfaces were made in a stereo comparator, where the floating point was focussed on high and low spots as they appeared, rather than to some fixed grid. Figure 2.1.22 shows that abrupt changes in topography were measured more closely than the undistinguished flat lying features. Consequently the steepest features (positive and negative) were exaggerated since their base length was smaller then the mean of approximately 1 mm (0.040 inch).

Thus the results for S.D. (i) of between 15^{o} and 20^{o} should be viewed with suspicion. The remainder of the data was probably only slightly distorted compared to a strictly rigorous solution. Unfortunately the latter would have required more time than was available.

Shearing analogy

The standard deviation of the (i) values is the position on a histogram for a particular asperity base, such that 67% of the observations lie below the S.D. (i) value, and 33% above it. Viewed as a shearing analogy, the 33% of observations of steeper (i) values are 'sheared' through, while the 67% of shallower angles remain unsheared.

The interesting feature of Figure 2.1.24 was its similarity with the plot of (σ_n / σ_c) versus peak dilation angles (d_n) (Figure 2.1.17). When these figures were overlapped for visual comparison a most encouraging feature was noticed. Figure 2.1.25 is a two colour figure, in which Figures 2.1.17 and 2.1.24 were overlapped and slightly off set so that the relative scales could be seen. It was noticed that the ordinate A.B. % was half the scale of the ratio (σ_n/σ_c), when the latter was converted into a percentage. The scales of peak dilation angle d_n, and standard deviation of (i) values were identical.

This unexpected result represented further evidence that a useful mathematical shearing analogy had been found. It will be recalled that each effective $(i)^{o}$ value was calculated with respect to a given base length (every nth coordinate). This angle, which could be positive or negative, apparently simulated the shearing path of an actual shear test, at an equivalent normal stress. As such, the angle and base length combined, represented the up slope or downslope of an imaginary controlling 'asperity', which just remained unsheared at the normal stress simulated. Therefore, by doubling this base length the whole controlling 'asperity' would be simulated. During a shear test it is of course the whole asperity base rather than half that is sheared.

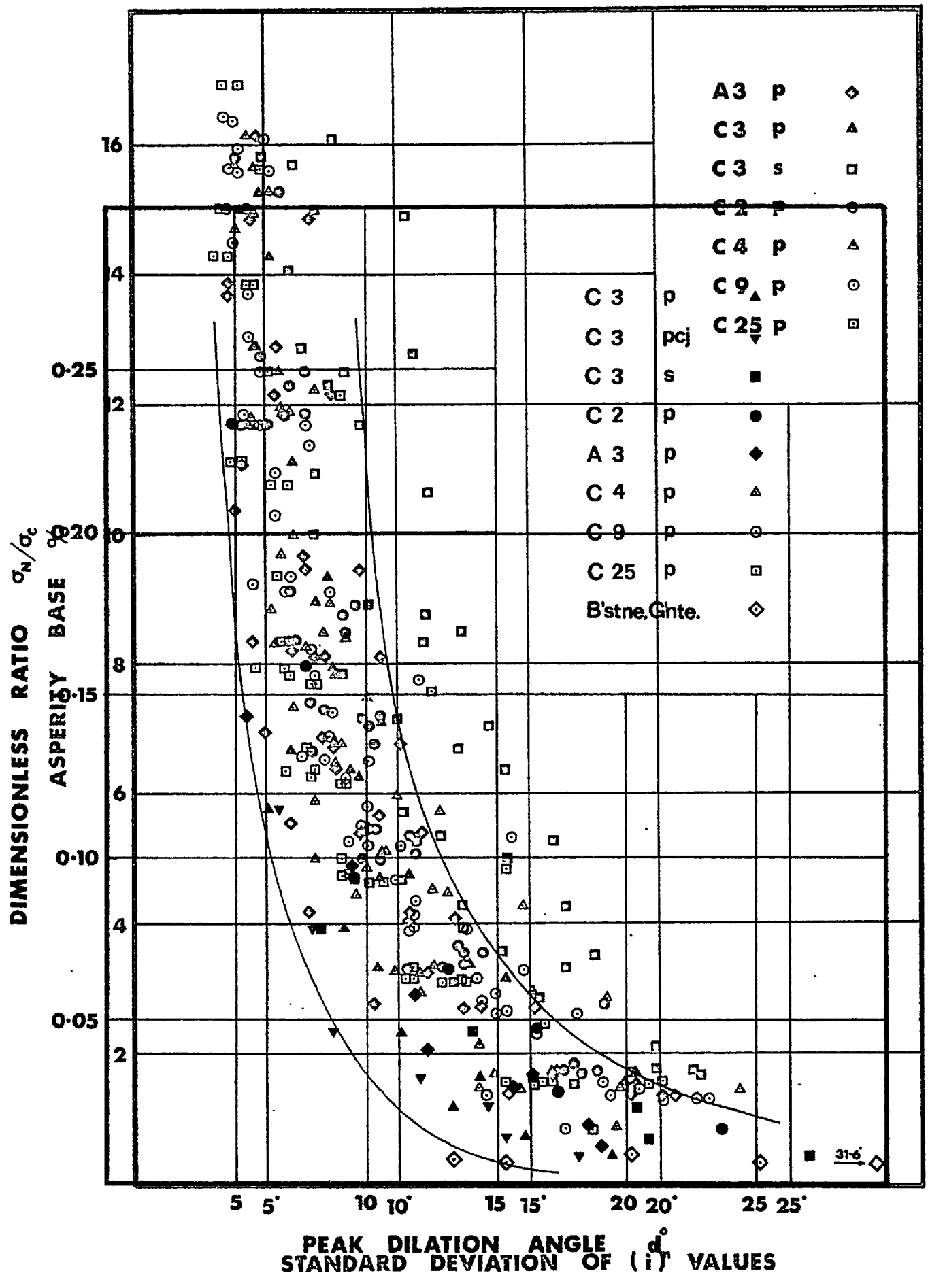

Figure 2.1.25 A statistical shearing analogy.

In other words asperity base (A.B. %) is really a misnomer since, as calculated, it is only half an 'asperity' base. It can be concluded from Figure 2.1.25 that the following are useful approximations:

1. $(\sigma_n / \sigma_c) \times 100 \ (\%) \approx 2 \times$ A.B. (%)

2. $d_n \approx$ S.D. (i)°

It only remained to check the 'intercepts' of a log. linear relationship between asperity base and standard deviation of (i) values, for a practical solution to joint roughness to be confirmed.

Log. linear relationship between A.B.% and S.D (i) values

Figure 2.1.26 shows two computer plots (kindly produced by Markland[56]) of the S.D (i) values obtained from the statistical analysis of model joints at the lower range of asperity bases. A group of results were also plotted for the highest values of A.B.% (n = 20 steps) which showed S.D. (i) values mostly between 2° and 4°. It appeared from the lower figure (linear - linear) that the S.D. (i) value was approaching zero degrees, as the asperity base was increased towards 100%. The serious scatter of results of high S.D. (i) values was due to the computational bious already discussed as a source of error.

The upper-most figure; a plot of S.D. (i) (linear) versus log. A.B.%, showed that in fact, the approximately linear scatter of intermediate values of S.D. (i) pointed to an intercept of log. A.B. equal to 1.7. An intercept of 2.0 (100%) was obviously not occurring here. However, the antilog of 1.7 is exactly 50 (A.B. = 50%).

It will be recalled that twice the asperity base was postulated as being equal to the ratio (σ_n / σ_c) expressed as a percentage. This was a highly satisfactory result since the intercept on the abcissa represented zero S.D. (i)°, or zero peak dilation angle (d_n) for a ratio of (σ_n / σ_c) equal to 100%. assuming the analogy was valid.

One further boundary value was required to verify the shearing analogy. This was the value of S.D. (i) for each joint type at a value of A.B.% equal to 0.05% (This corresponded to the lowest ratio of σ_n / σ_c equal to 0.001 or 0.1%)

Values of log. A.B.% of 2.0, 1.0, 0, - 1.0, - 2.0 represent linear values of 100, 10, 1, 0.1, 0.01 % respectively. With conventional terminology the log. of 0.05 is equal to $\bar{2}.70$. This can alternatively be expressed as above, as - 1.3.

The relevant point on the abcissa of the uppermost plot given in Figure 2.1.26 had to be located by extrapolating the log. axis over to the left hand side. The best fit straight line through all the data with the exception of high S.D.(i) values (>15°) and passing

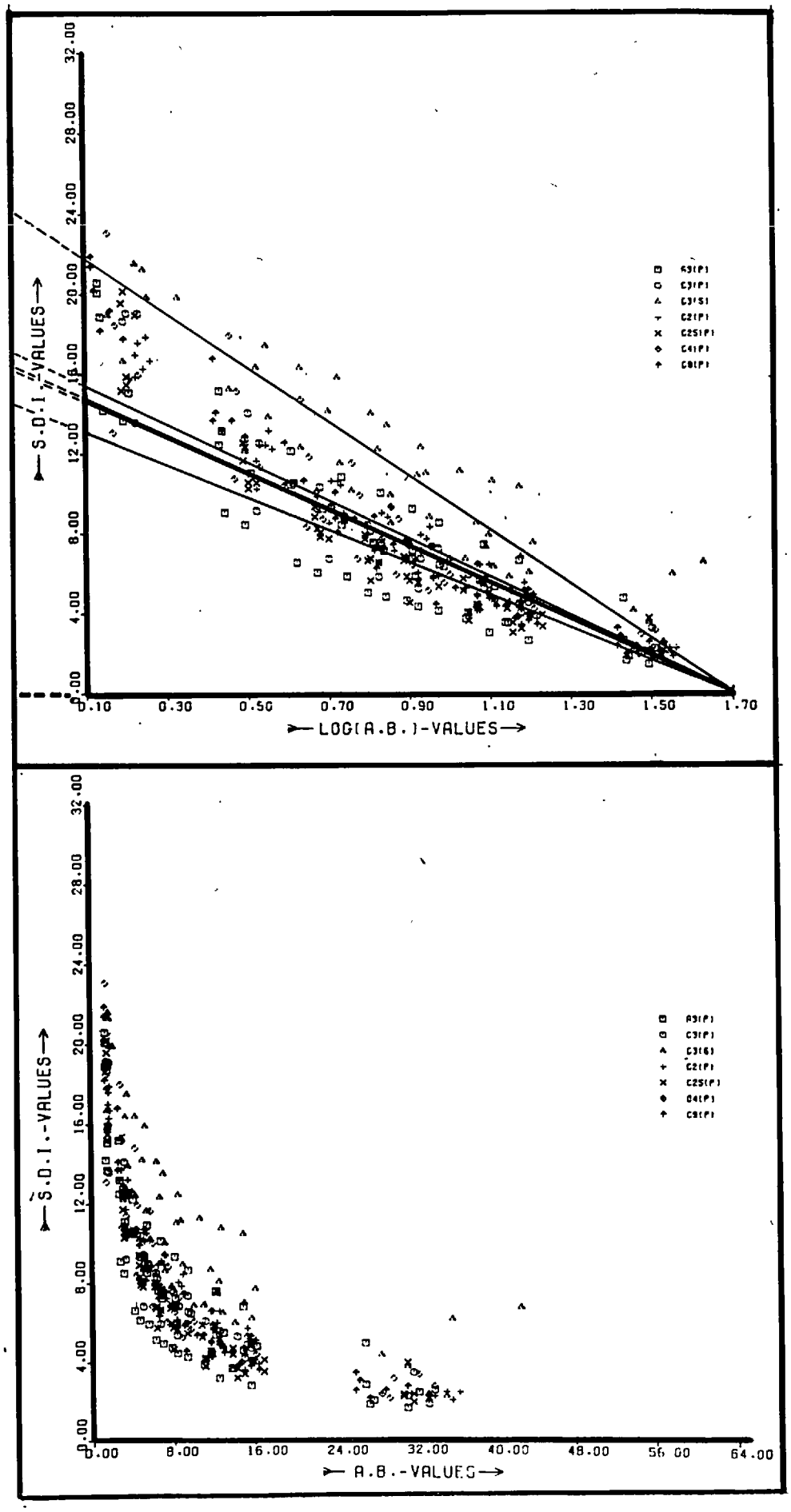

Figure 2.1.26 Two relationships between standard deviation of (i) values and asperity base percentages.

through the abscissa at log. A.B. equal to 1.7, gave an intercept of S.D.(i) of approximately 27.3°. This was very close to the maximum dilation angle of 29.6° ($\hat{d}$) given previously for a ratio of σ_n / σ_c of 0.001. (see Figure 2.1.18).

The final point to be verified was whether this statistical shearing analogy was sensitive to the different roughnesses of the joint surfaces.

The five straight lines reproduced in part in Figure 2.1.26, were best fit approximations to the data of five of the individual joints. Taken in descending order of steepness, these were for joint types C3(s), C4(p) C9(p) C3(p) and C25(p). The intercept values of S.D. (i) for an asperity base of 0.05% compared very favourably with the (d_n) values for a ratio of (σ_n / σ_c) of 0.1%. Once again, as a concession to the inevitable scatter of results, only the best five results out of seven will be compared:

Joint type	S.D. (i)° degrees (at A.B. = 0.05%)	d_n° (= $\hat{d}$) (at σ_n/σ_c = 0.1%)
C3(s)	40.8°	43.1°
C4(p)	28.7°	30.9°
C3(p)	27.6°	28.8°
C9(p)	26.0°	26.2°
C25(p)	24.4°	27.3°

It can be seen that the shearing analogy enables prediction of the 'maximum' angle of dilation to be made to within one or two degrees, at best. Real situations involving rock joints would obviously produce a wide scatter of results, and the only solution to this would be extremely large numbers of observations. A statistically viable sample could then be analysed on the basis of probabilities.

2.1.7 PRACTICAL APPLICATION TO SLOPE STABILITY

The possible variation of structural features with depth below surface, and the problem of joint weathering andinfilling material suggest that the method described above can only be used to advantage, in a limited number of situations.

The qualification of prime importance is that failure is anticipated by translational shear, rather than by rotational shear. This antomatically implies well developed and relatively widely

spaced joint sets, in basically competent rock. Given these conditions and sufficient economic impetus, the following steps are suggested:

1. Estimate the dimensions of the problem of concern (bench stability or complete slope stability), and the consequent range of normal stresses acting across the adversely orientated joints. (The normal stress range would normally be calculated from self weight stress assumptions.)

2. Estimate the down-dip length of the potential shear surface.

3. Estimate the effective joint wall compressive strength. This, combined with the normal stress range, puts the problem in correct perspective since the ratio of (σ_n/ σ_c) determines the range of asperity bases that should be measured. There are two test methods that could be used to obtain this mechanical property:

   (a) Unconfined compression tests on cylindrical specimens cored from the weathered rock adjacent to the joints. (Figure 2.1.20 illustrates that the effective joint wall compressive strength of the specimens cored from the bench faces of Corta Atalaya, was approximately one quarter of the compressive strength of the unweathered rock, assuming that equation 6 was applicable).

   (b) Perform a limited number of direct shear tests on representative joint specimens, loading all at the same normal stress. The mean value of (τ /σ_n) would then supply an approximate value of (σ_c/ σ_n) from Figure 2.1.19 (equation 6). This in turn, would give the value of σ_c.

Of the two methods (a) is preferred since (b) presupposes an approximate knowledge of the peak shear strength (equation 6).

Suppose the following values were obtained for the above estimates:

1. Normal stress range of relevance to the problem = 0 to 250 lbf/in^2.

2. Length of potential shear surface = 400 feet.

3. Effective joint wall compressive strength = 5000 lbf/in^2.

$\therefore$ σ_n/σ_c range = 0 to 5 %

Therefore the required range of asperity bases is 0 to 2.5 %, which represents 0 to 10 feet of the 400 feet potential shear surface.

Field measurement of (i) values

As already indicated, a large volume of data is required from a large number of joint exposures. A photogrammetric technique is the obvious solution from the point of view of economics, time and accessibility.

The larger the scale of the problem, the less sensitive is the range of asperity base. Consequently stereoscopic pairs of photographs could be exposed using a phototheodolite from as much as several hundred feet from the rock face, so that the stereoscopic overlap contained a large number of joint exposures. A smaller scale of problem would require a phototheodolite survey at much closer range, but since the asperity base would be reduced in proportion, the same amount of data could probably be obtained from one pair of photographs.

Ideally the photographs should be taken from as near perpendicular to the joint dip as possible. This facilitates the measurement of coordinates in the stereocomparator, but is not essential. Spot height coordinates measured along sections parallel to the dip direction could then be punched onto computer tape, and be statistically analysed in the specified manner.

In the numerical example above, the range of asperity bases was equivalent to 0 to 10 feet. Therefore spot height measurements could conveniently be made at 1 foot intervals, and taken up to say 20 feet, so that a value of A.B. of 2.5% involving ten steps would supply at least 10 (i) values for that base length, for each section measured: (N-n=20-10=10). Joint exposures having down dip dimensions of only 10 feet would therefore supply a limited number of data points for the high values of A.B.%.

Evaluation of peak shear strength

Equation 7, which is reproduced below:

$$\tau/\sigma_n = \tan\left[\left(\frac{90-\hat{d}}{\hat{d}}\right).d_n + \hat{d}\right]$$

contains one constant for a particular joint roughness, and three interdependent variables.

The maximum dilation angle $\hat{d}$ for a particular surface is estimated from the following relationship:

$$\hat{d}^\circ = S.D.(i)^\circ \text{ for A.B.\% = 0.05\%}$$

In the numerical example, 0.05% represents 0.2 feet. A statistical analysis of (i) values obtained for asperity base steps of only $2\frac{1}{2}$ inches is therefore required. This means that two scales of

phototheodolite photography are required, the second one for measurements of spot height coordinates for steps of only $2\frac{1}{2}$ inches.

The variable peak dilation angle (d_n), is dependent on normal stress and will be computed for different ratios of (σ_n / σ_c). The latter has been shown to be related to asperity base as follows:-

$$(\sigma_n / \sigma_c) \times 100\ (\%) = 2 \times \text{A.B.}\ (\%)$$

and $$d_n = \text{S.D.}\ (i)^{\circ}$$

Consequently the ratio of shear to normal stress (τ / σ_n) can be evaluated for a range of normal stresses.

CONCLUSIONS

The statistical shearing analogy represents a potentially economic method for estimating the peak shear strength of unfilled rock joints. It has been verified by comparison against model joint tests, which from the point of view of reproducibility represent nearly ideal conditions. Much field work is therefore required to establish its importance or otherwise to real rock problems. As a first stage in this investigation, it is to be hoped that joint roughness profiles will be measured with more frequency than has been the case in the past. A large amount of experience needs to be accumulated on the joint roughness of different joint sets, and in different rock types.

Secondly, systematic measurement and analysis of roughness profiles is required before performing direct shear tests on joints in the laboratory. (The thesis in preparation by Rengers on the effect of roughness on the shear strength of rock joints should provide some very useful results in this respect. Rengers[39] described a method of statistical analysis of roughness, in which curves of tan (i) (positive and negative) versus 'stepsize' were presented. The latter appears to correspond to the present asperity base. The maximum values of tan (i) were used to predict a dilation diagram for the joint, when the latter had 'free dilation possibilities' - i.e. zero normal stress. It is to be hoped that Renger's thesis will clarify these concepts. Comparison of results for rock joints with those for the model joints should prove most interesting.)

Thirdly, the measurement of effective joint wall compressive strength needs to be carefully evaluated. It seems possible that an instrument along the lines of the Schmidt hammer might be developed to estimate this in the field. This index would need to be carefully related to unconfined compression strength, over a wide variety of test conditions.

2.2. THE ESTIMATION OF IN-SITU SHEAR STRENGTH FROM BACK ANALYSIS OF FAILED SLOPES

SUMMARY

One month was spent on a field project in Rio Tinto, southern Spain. Particular attention was focussed on two failures in porphyry which had occurred in one of the older open pits. Field observations of geometry, geology, jointing and water are presented. A common cause of failure was thought to be the fracturing of surface drains by tension cracks. Both failures were reputed to have occurred after periods of prolonged rainfall.

The geometry of the slides was determined by Plane Table surveying. Three cross sections through each slide were measured and compared with the pre-failure slope profiles obtained from mine plans. The slide scars were characterised by steep rear faces some 30 metres high corresponding to the pre-existing tension cracks. These were relatively smooth faced shear-type joints. Lower down, the surfaces were extremely rough and littered with debris. The steps of vertical joints could be seen in various places.

Laboratory shear tests were performed on sawn planar specimens obtained from the debris. A residual friction angle of approximately 30° was indicated. Consequently a friction angle of 35° was estimated for the smooth rear faces of the slides. The sections that were fabricated through the slides were divided into slices corresponding to changes in surface roughness and inclination. By assuming an arbitrary angle of friction of 45° for the rough surfaces, the corresponding values of cohesion were obtained from back analyses of each section. The parameters c and ϕ were converted to shear and normal stress by calculating the mean normal stresses acting across the rough shear surfaces.

The steepness of the failure surfaces meant that the mean normal stresses were remarkably low even for the fully drained case (1 to 3 Kg/cm^2), despite the size of the failures; 60,000 and 100,000 tons. A method is presented for extrapolating the shear strength data to higher normal stress levels. Comparison with large shear box tests on porphyry joints suggest that the method may prove extremely useful.

2.2. THE ESTIMATION OF IN-SITU SHEAR STRENGTH FROM BACK ANALYSIS OF FAILED SLOPES

INTRODUCTION

The rational deepening of existing open-pit mines, and the design of slopes in virgin ground are two problems which frequently confront slope stability engineers. The problem of slope design in virgin ground is a very acute one since at best the structure, shear strength and joint water can only be assessed from recovered drill core and bore hole measurements. Occasionally some of this information might be found in local outcrops having similar structural features, but such distant extrapolation could be extremely hazardous.

However, the design of higher or steeper slopes in an existing open-pit excavation is somewhat easier since the designer is surrounded by in-situ evidence of what shear stresses can be tolerated by given joint sets. It is likely that localized slope failures will have occured during the life of the operation and every effort would normally be made to back analyse these. Slopes which are standing provide interesting height-inclination data, but it is only the slopes which have failed which provide the concrete evidence of a factor of safety reduced to below 1.0. It is then up to the designer to assess the possible role of water pressure in these failures, and estimate the shear strength accordingly. However as will be seen this is not the end of the problem. The mean normal stresses operating when the failures occurred is found to be extremely small even for failures as large as several hundred thousand tons. Once again an extrapolation of limited strength data is required, if the stability of whole slopes is to be assessed.

During the Spring of 1969 the author spent one month on a joint field project in Rio Tinto, Southern Spain by kind permission of Rio Tinto Española. (Ross Brown and Barton[52]). The stability of several rock slopes was studied, both in currently worked open-pits and in adjacent old workings. Particular attention was focussed on two failures in Corta Filon Sur. This open-pit has only been mined very locally since 1939, and it presented an ideal opportunity for back analyses to be performed. In view of the continental location of the field work, and the metric mine plans, all data is given in metric units in this Section.

2.2.1 FIELD ASSESSMENT OF TWO FAILURES IN CORTA FILON SUR

The two failures investigated occurred in 1935 and 1968 and involved approximately 60,000 and 100,000 tons of rock respectively. They were both located on the north wall of the pit where several benches had been removed during cutting back to the final slopes.

SECTION 2.2.

Pit geometry

The total surface dimension of the pit was 1200 metres by 600 metres, with the long axis approximately E - W. The slopes in porphyry on the north side rose to about 250 metres in height, while the slopes in slate on the south side were only some 120 metres high. Bench angles in the porphyry were generally in the range 60° to 70°, and overall slopes usually 45° to 50°. However these are somewhat misleading figures since the lower 150 metres (which incorporated the failures) were frequently much steeper (up to 65°), especially where some of the original benches had been removed in cutting back to the final slopes. Figure 2.2.1 gives an indication of these slope heights and inclinations and their relevance to failure of the slopes.

Geology

Most of the north side of Filon Sur was composed of strong chloritized porphyry, though towards the eastern end it appeared more sericitised and was white and crumbly. This was particularly marked due to the long period of weathering since the slopes were last excavated in that part of the pit. However it is thought that the two failures under investigation occurred entirely within the strong chloritized porphyry. Figure 2.2.2 shows sequence photos of these two slides S.1 and S.2. A third slide (S.3) immediately east of S.2 did appear to have occurred in weaker material, particularly at its upper limit.

Jointing

No systematic investigation of the jointing in the north face was undertaken due to the limitation on time. However it was apparent from the nature of the steep rear faces of slides S.1 and S.2 (See Figure 2.2.2) that there were two important steeply dipping joint sets defining the upper limits of the slides. These sets had dip directions approximately S.W and S.E. and dips ranging from 75° to 85°, and 85° to 95° respectively.

The slide scar of failure S.1 was accessible and there was evidence to suggest that the shearing failure involved the opening of a nearly vertically dipping set of joints in tension, giving the surface a rough stepped appearance. It was impossible to recognise a second joint set due to the large amounts of debris littering the surface. The slide scar of failure S.2 was unfortunately more or less inaccessible due to the danger from loose debris. However when standing immediately below, a brown stained set of nearly vertically dipping joints could be seen in various places. This made the surface appear extremely irregular and stepped. The general roughness of both these shear surfaces led one to suspect that some intact material had been sheared through. However,from astrength point of view this could only have been very localised.

Figure 2.2.1 Slope height - slope inclination data for failed and stable slopes in Filon Sur Porphyry

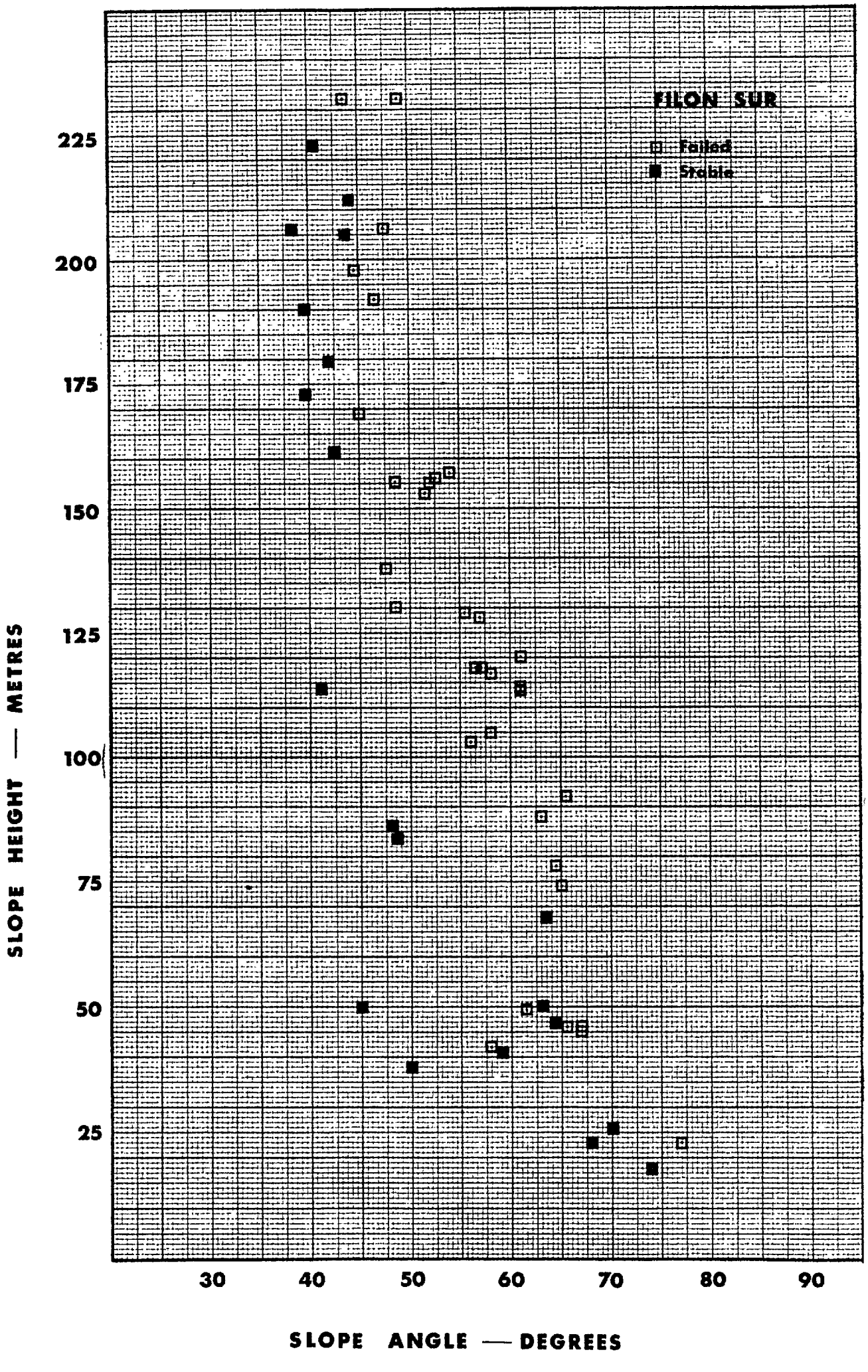

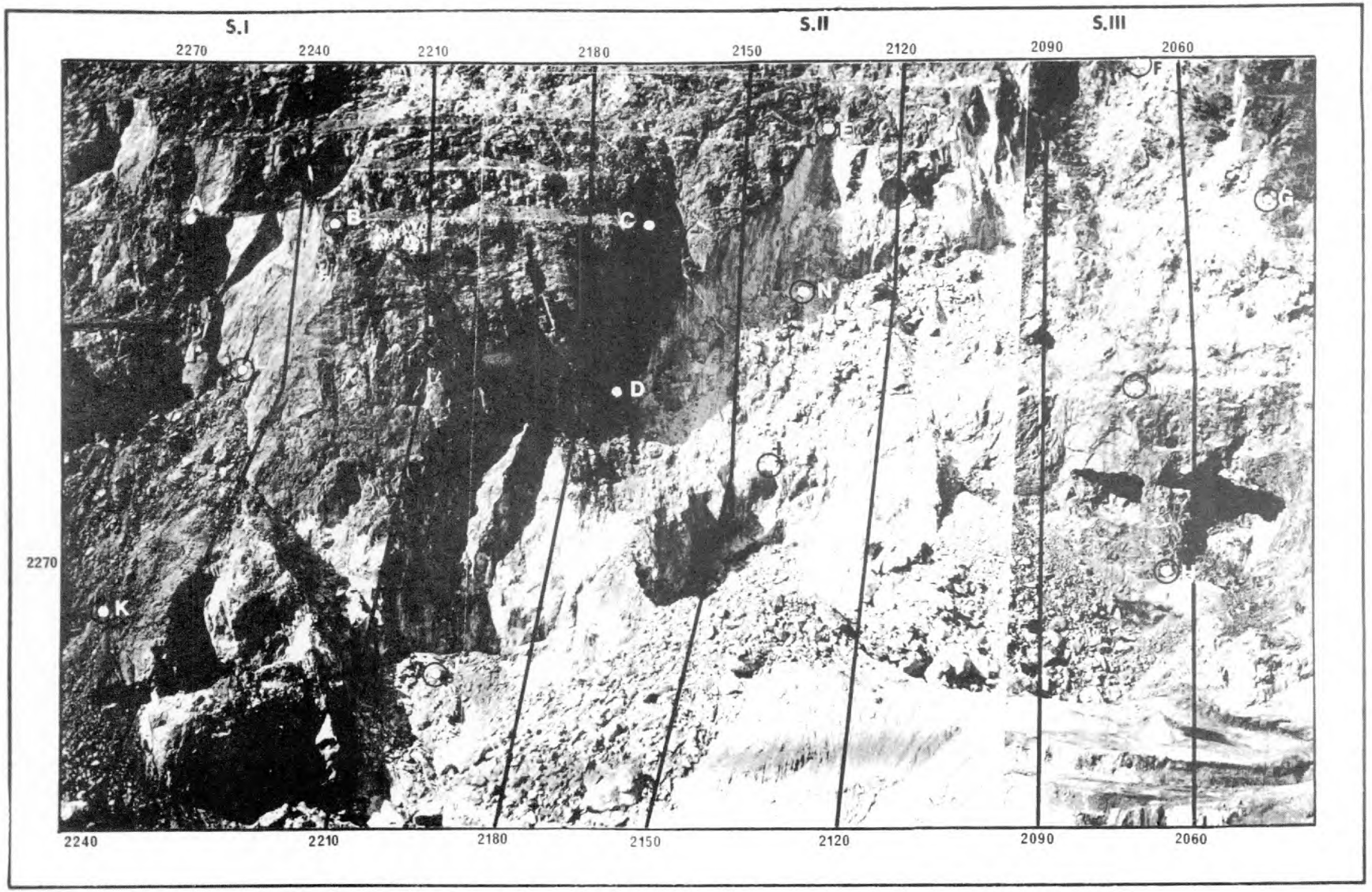

Figure 2.2.2. Sequence photographs of three slides in Filon Sur.

Influence of underground workings

In the interim period between 1935 (when slide S.1 occurred) and the present, four stoping areas were developed below what is now the failed area. Their location can be seen in Figure 2.2.2. Stope No. 1 with collapsed crown pillar is approximately below slide S.1, stope Nos. 2,3 and 4 are now visible below slides S.2 and S.3. since the entire roof area has collapsed. A lot of the slide debris from S.2 and S.3 was caught behind the lip of these stopes. However a large talus from S.2 is visible between sections 2180 and 2150. It will be seen later from sections through slide S.2 that this quantity of debris could not have passed over the lip of the stoping area unless the slide had occurred before the roof of the stope had collapsed. However, possible triggering of the slide by subsidence movements should be born in mind. No such problem existed with slide S.1 since it occurred before the stoping operation.

Influence of water

It is significant that slide S.1 (1935) is reputed to have occurred after a long period of rainfall. Likewise, slide S.2 occurred late in 1968 during an unusually wet winter, and during a night of very heavy rain. The date and conditions prevailing when S.3 occurred are not known precisely. However in a previous visit to Rio Tinto in April 1967 it was noticed that a 30 metres long section of a major concrete drainage channel had been removed by a slide. This was located just above point F (Figure 2.2.2) and defined the top vertical face of the slide. Smaller drainage routes were located at the back of several benches particularly below the crest of the north face of Filon Sur. It appears reasonable to assume that the joints defining the steep rear faces of the slides S.1 and S.2 were well supplied with water during the period immediately prior to failure, since these joints were probably open as tension cracks.

It is very doubtful whether rigid surface drains (in concrete or directly in the rock) achieve the desired result in situations as potentially unstable as open pit mine slopes, where tension cracks are accepted as partners to high ore/waste ratios.

Most surface drains encountered in Filon Sur and in other pits in the area were located near the crest of the slopes. This apparently ideal location is also where tension cracks are most numerous. Rigid drains will be cracked in the optimum positions for providing the tension cracks with surface run off, channeled from potentially large areas. Flexible plastic (P.V.C.) channels would seem a more economic alternative for unstable environments, despite the extra cost.

It is common practice for the National Coal Board to spread puddled clay round the crests of their opencast mines (Walton[58]). This would seem an ideal solution for certain environments, provided the moisture content remained high enough to prevent cracking.

SECTION 2.2.

Survey of slide dimensions

For the purpose of analysis it was necessary to survey the dimensions and locations of sections through the slides, and relate these to the correct transverse sections that were obtained from mine plans. The Plane Table method of surveying was employed using a Telescopic Alidade and setting up over two stations on the South side of the pit opposite the slides. These two stations defined a base line of approximately 120 metres in length, which was located on the plan of the open pit by resection from theodolite sightings to two shafts visible at the west end of the pit. Fourteen points were plotted by Plane Table Survey, all located on the failed north face, and chosen for maximum information, The location of these points is shown in Figure 2.2.2.

A plan view of the points is obtained directly by such a survey, while the elevation of the points is obtained by simple computation using the plan distances and telescope inclinations. The appropriate plan and elevation have been given by Ross Brown and Barton[52]. As an indication of the scale of the photograph, the points E and N defining the upper half of the slide S.2 were 35 metres apart vertically, and 7 metres apart in plan.

Due to the inaccessibility and loose nature of much of the slide area estimates of the variable inclination of the slide surfaces had to be made from below using clinometers. However it was possible to take a close look at slide S. 1. The zone between points K and L, and the rear faces of the slide were plotted with some certainty. Three vertical sections were measured for each slide scar at 10 to 15 metre intervals. The measurements were then related to the correct mine sections of the slopes as they existed before failure, using the Plane Table survey points. Figures 2.2.3 and 2.2.4 are scaled drawings of the three sections measured for each slide.

2.2.2. LABORATORY SHEAR TESTS

It is common practice to define the shear characteristics of rock joints in terms of the Coulomb constants namely, angle of friction (ϕ) and the cohesion intercept (c). These are convenient parameters since for a given normal stress they define a distinct coordinate of shear and normal stress (τ,σ). The fact that the peak strength envelope is curved in reality means that (c) and (ϕ) should be regarded not as constants but as piece-wise linear approximations to the shear strength for given normal stresses.

It was realised that the rock surfaces involved in the two failures ranged from smooth planar shear type joints in the upper half of each slide, down to very rough tension type joint surfaces and possibly even some failure through intact material in the lower half. Since this range of surfaces was encountered in each slide it was decided that the most rational method of back analysis would be one which was sensitive to these obvious changes in shear characteristics. Consequently the frictional resistance of the

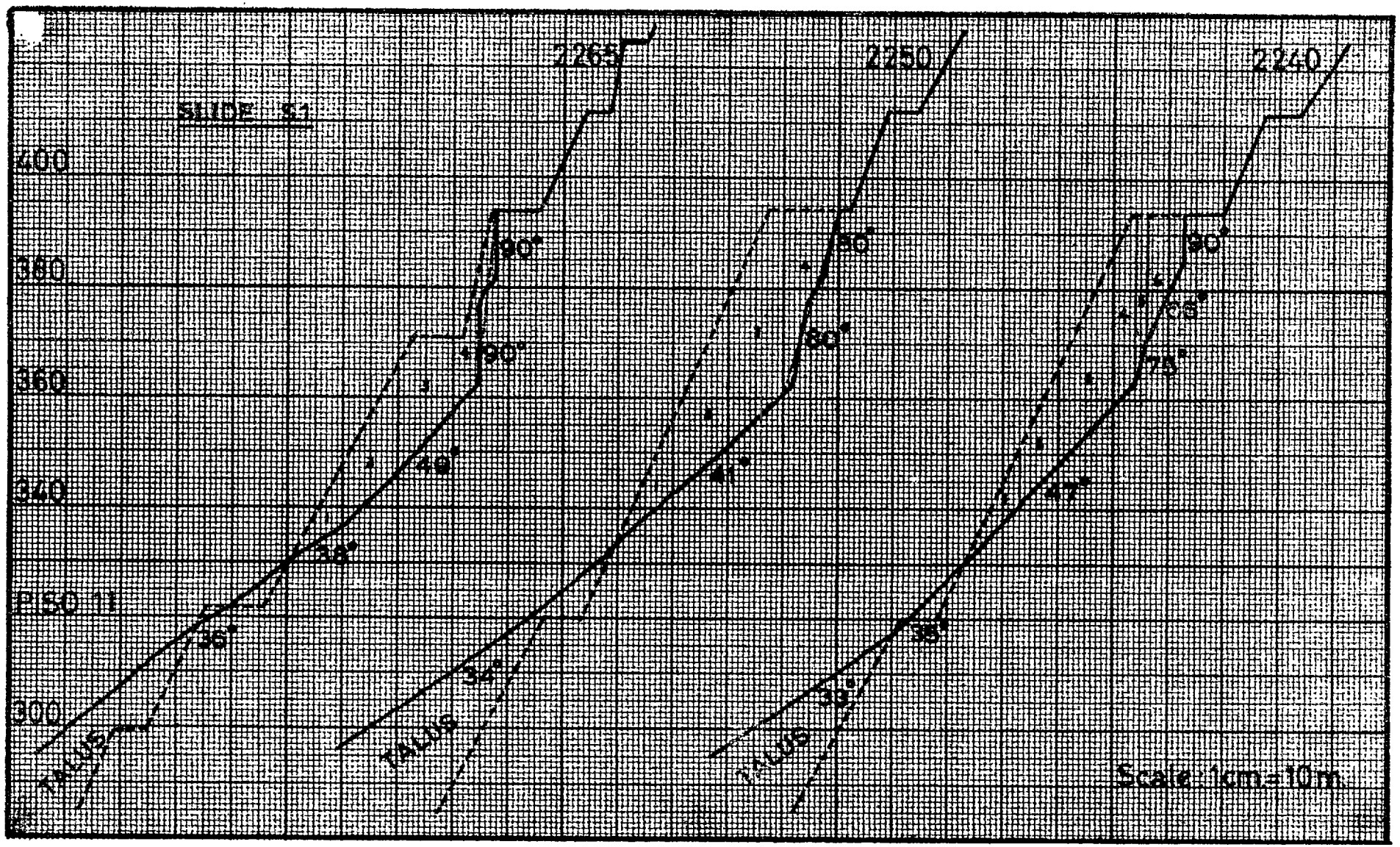

Figure 2.2.3 The geometry of three sections through slide S.1.

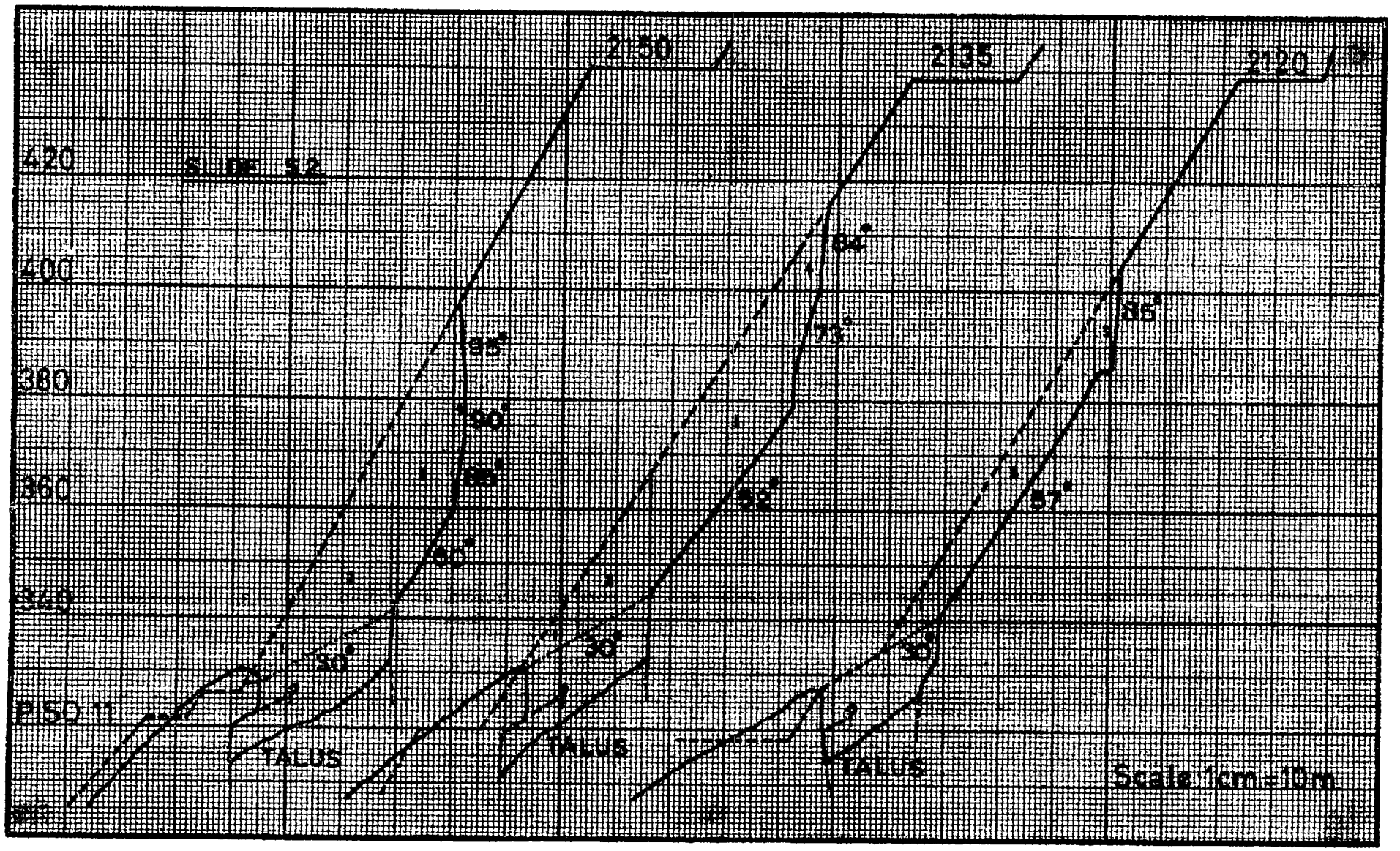

Figure 2.2.4 The geometry of three sections through slide S.2

smooth rear faces (when not vertical) would be based on an estimate a few degrees above the residual or basic friction angle for planar surfaces, and have an assumed zero cohesion. At the other end of the scale some coordinate (τ, σ) had to be obtained to describe the shear strength of the rough joints at the mean normal stresses operating.

An arbitary value of the angle of friction was therefore guessed, and the corresponding value of cohesion intercept calculated by back analysis. These two parameters and the mean normal stress then provided the required (τ, σ) coordinate.

Basic friction angle

The friction angle of the planar shear type joints was required with some degree of accuracy since this was one estimated parameter not obtained through back analysis.

Direct shear tests were performed on artificial planar surfaces sawn from 20 to 40 Kg. specimens which were transported back to the laboratory. The shear testing rig was capable of transmitting shear loads of the order of 200 Kg. to shear surfaces up to 35 cm^2 in area. The rate of shearing was approximately 1 mm. per minute and the range of normal stresses 0.5 to 11.0 Kg/cm^2.

The specimens were prepared using a large diameter diamond saw which produced surfaces that were somewhat smoother than anticipated. In addition, the number of specimens successfully prepared was limited to three or four shear pairs per rock type. The solution to both these problems was obtained by sand blasting the mating surfaces before testing. At the end of a test the high spots, which were in contact and consequently slickensided, were preferentially sand blasted. In this way the distribution of contact areas was changed between tests and the same specimen could be tested at several different normal stresses.

It appears from similar studies of artificial rock surfaces (Ripley and Lee,[49] Patton[20], Rosengren[22]) that the residual or basic friction angle of rock joints is most closely simulated by these artificial surfaces when shearforce-displacement characteristics show no appreciable peak, or fall to residual. In addition, the surfaces should not be so smooth that stick-slip oscillations occur, or so smooth that the frictional resistance rises due to roughening of the smooth surfaces with increased displacement. In other words the 'granular' texture of the rock should be exposed but not to the extent that macroscopic interlocking occurs. Sand blasting appears to satisfy all these requirements.

Shear force-displacement characteristics, and measurements of the slickensided areas as a function of normal stress have been given previously by Ross Brown and Barton[52]. For the present the results of prime interest are the values of basic friction angle obtained for the Filon Sur porphyry and for some other local rock types. Figure 2.2.5 demonstrates that the range was typical of other results reported in the literature.

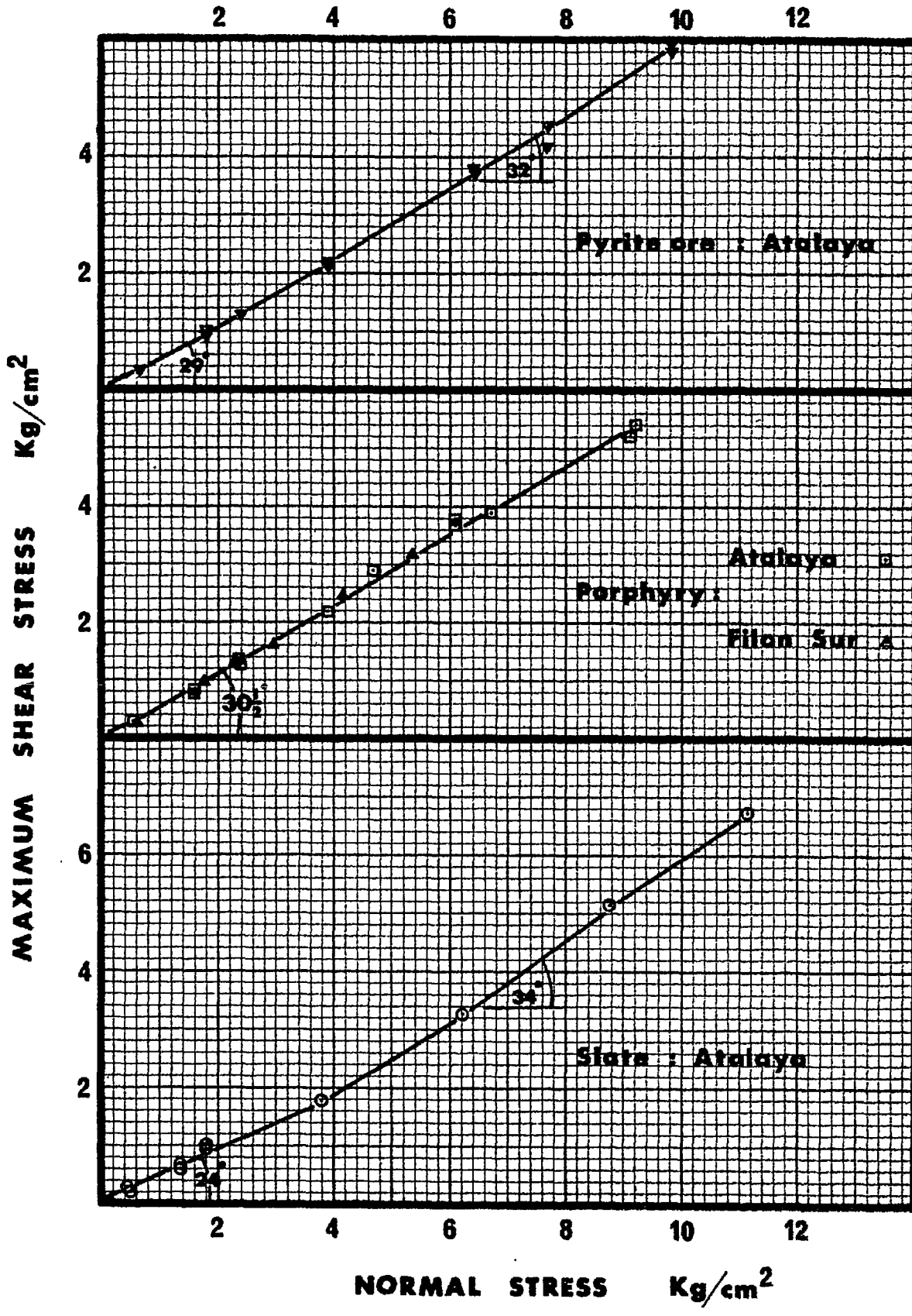

Figure 2.2.5 Shear strength results for planar, sand blasted rock surfaces.

Both porphyry specimens (from two adjacent open-pits) gave the same value of $\phi_b = 30\frac{1}{2}^{o}$.

2.2.3 MULTI-LINEAR METHOD OF SLICES

A simple method was developed in an attempt to account for changes in shear surface inclinations and changes in joint roughness. It can be seen from Figures 2.2.2, 2.2.3 and 2.2.4 that changes in joint roughness (implying changes in joint set) always coincided with changes in inclination. Therefore, bearing in mind, the near-vertical joint sets in the north face, the failed slopes were 'reconstructed' as discrete slices with vertical boundaries coinciding with the roughness and inclination changes.

The essential features of the multi linear method of slices are illustrated in Figure 2.2.6. The stability of each slice is dependent on the magnitude of the forces acting perpendicular and parallel to the failure surface beneath it and on the shear strength exhibited by the failure surface. The stability or instability of every slice is computed as a force acting along the failure surface, by simple limit equilibrium methods. If the sign of this force P is positive, this implies that a force of magnitude P acting <u>down</u> the slope is needed to bring that slice to limiting equilibrium. In other words the slice is stable, having a factor of safety greater than 1.0. If on the other hand, P is negative, this implies an unstable slice which requires a force of magnitude P acting <u>up</u> the slope to keep the slice from sliding.

The following equation describes the limiting equilibrium of forces beneath slice No. 1 (see Figure 2.2.6). It is assumed for the present that the slope is fully drained of water.

$$\tan \phi_1 = \frac{W_1 \sin\beta_1 - c_1 L_1 + P_1}{W_1 \cos\beta_1}$$

$$\text{or } P_1 = W_1 \cos\beta_1 (\tan \phi_1 - \tan\beta_1) + c_1 L_1 \quad \text{——— (1)}$$

where

		Suitable Units
P	is the downslope equilibrating force	(Kg)
W	is the weight of the slice	(Kg/unit thickness)
β	is the inclination of the failure surface below the slice	(degrees^{o})
ϕ	is the mean angle of friction of the failure surface below the slice	(degrees^{o})
c	is the mean cohesion intercept at the mean normal stress operating	(Kg/cm^2)
L	is the length of shear surface beneath each slice	(metres)

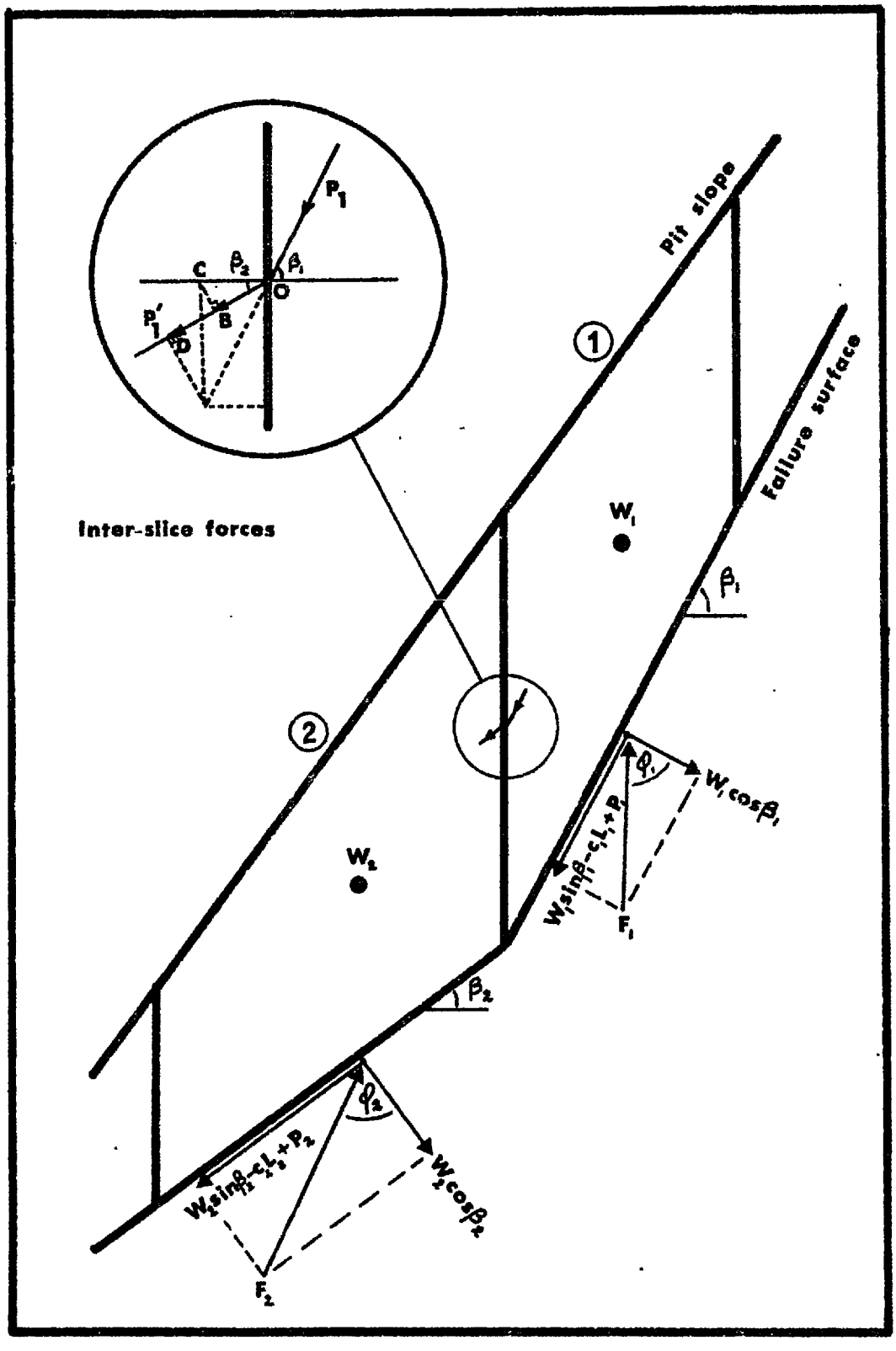

Figure 2.2.6 Limit equilibruim multi-linear method of slices.

All the slices chosen to simulate the mass of failed rock are analysed in this way. The parameters W, β and L will be known for each slice. However P, ϕ and c will be unknown, until the following substitutions are made:-

Planar surfaces	$\phi = \phi_b$	+ roughness estimate
	$c = 0$	
Rough surfaces	$\phi = 45^\circ$ (arbitrary)	
	c = back analysis result for particular mean normal stress.	

The equilibrating P forces act in directions which are parallel to the respective failure surface inclinations. It has been assumed in this method of analysis that both shear and normal forces are transmitted across slice boundaries. Supposing that slice No. 1 in Figure 2.2.6 is unstable (- P_1), then the component of instability or 'unstable excess' acting on slice No. 2 is assumed to be as follows:

$$P_1' = OD = P_1 \cos(\beta_1 - \beta_2) \qquad \text{——— (2)}$$

The local changes in normal stress on the failure surface that are implied by this assumption are ignored.

When considering the whole failure surface each slice is analysed in turn starting with the uppermost one. The P forces for each slice are resolved parallel to the assumed failure direction of the total sliding mass, which can generally be assessed from a glance at the sections (Figures 2.2.3 and 2.2.4) since the whole mass has failed anyway, the sum of the resolved P forces is zero.

$$\Sigma(P') = 0 \qquad \text{——— (3)}$$

Hence a simple solution is obtained for the unknown parameter cohesion.

It is realised that the application of limit equilibrium methods to a discontinuous body of rock sliding initially on different joint surfaces is open to criticism, since the interslice behaviour is really unknown. However, in the absence of other simple techniques it is felt that the method presented is at least an improvement on grossly approximating the failure surface to a single plane, when it is clearly apparent that this could not occur, due to the non verticality of the rear of the slice.

Undrained slopes

In the absence of water the normal stress acting across a failure surface is obtained by approximating it to the resolved component of the distributed self weight of rock lying above the surface. The normal component of this self weight stress is a function of $\cos^2 \beta$, where β is the inclination of the surface. It can be seen therefore that the normal stress on a steeply inclined surface may be a small fraction of the vertical overburden stress (γh), where (γ) is the density of the rock and (h) is the depth below surface:

$$\sigma_n = \gamma h \cos^2 B \qquad (4)$$

The effect of a water pressure distribution on this already small normal stress is to reduce the effective stress across the surface by an amount equal to the local water pressure:

$$\sigma'_n = \gamma h \cos^2 \beta - U_w \qquad (5)$$

This in itself leads to serious reduction in stability. However, tension cracks often delineate the rear face of potential rock slides, and these can be a great source of instability if they intersect surface drainage routes.

A deep tension crack which is well supplied with water can lead to an infinite variety of transient water pressure distributions in lower parts of the potential failure surface, depending upon the tightness of the joints and the drainage path involved. For the purposes of analysis, two quite pessimistic assumptions of transient water pressure distribution were analysed. These are illustrated in Figure 2.2.7. Distribution (A) which is the easiest to analyse in a slices method, represented one possible state where seepage was limited, but not to the extent of producing a static head distribution. Distribution (B) is an alternative and perhaps more realistic with-seepage distribution, and one which is frequently used (Sharp[59]). Both methods assume a zero exit pressure at the toe of the potential slide, and tension cracks which are full of water.

The water pressure distribution on each slice, whether it be triangular, rectangular or trapezoidal produces a reduction in the normal force beneath each slice equal to the product of the mean water pressure (U_w) and the base length (area) of the slice concerned. Therefore equation (1) can be modified as follows:

$$\tan \phi = \frac{W \sin \beta - cL + P}{W \cos \beta - U_w L}$$

$$\text{or } P = \tan \phi (W \cos \beta - U_w L) + cL - W \sin \beta \qquad (6)$$

In cases such as that illustrated by slice No. 1 (Figure 2.2.7), where the boundary of the slice is a water filled tension crack,

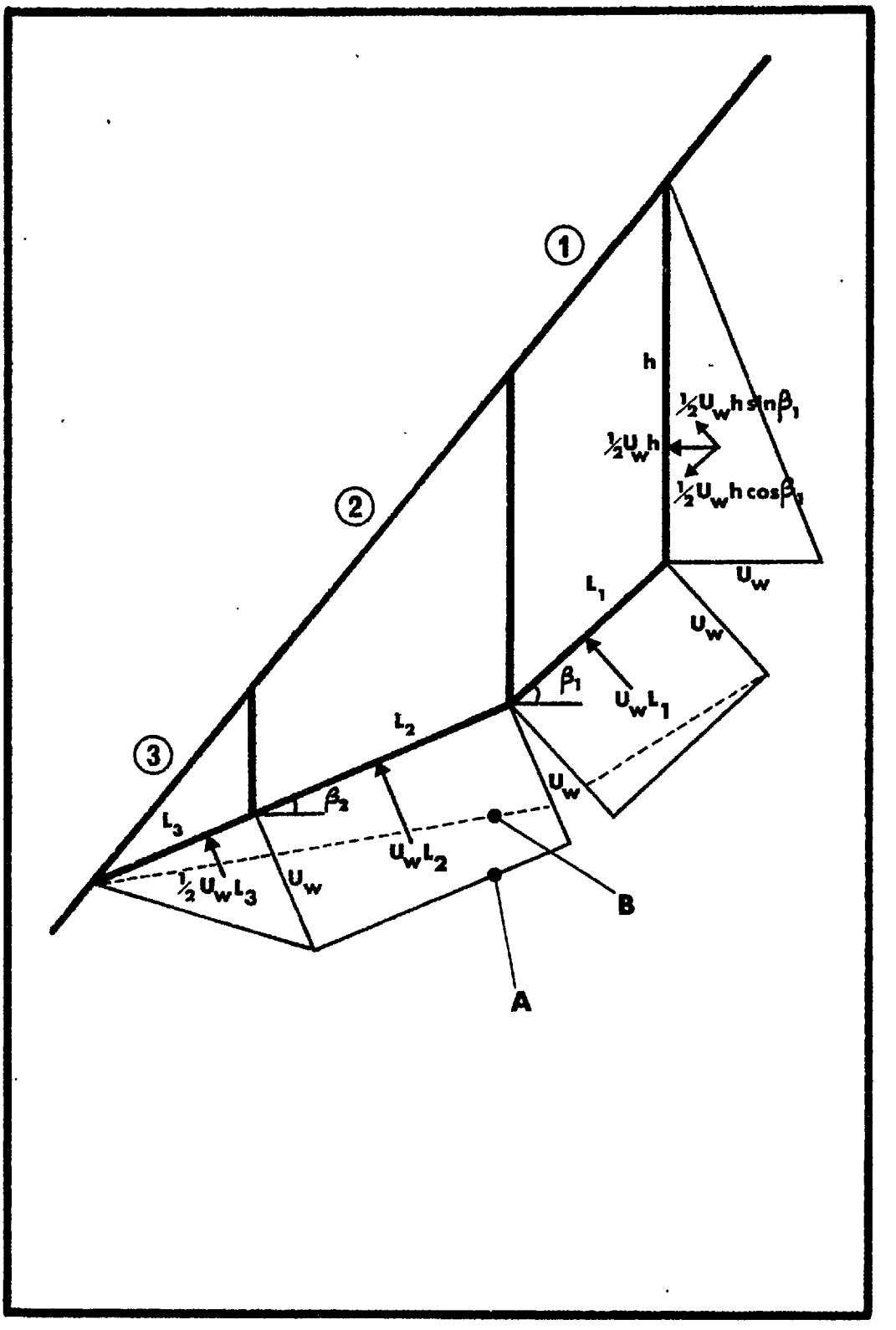

Figure 2.2.7 Two assumptions of water pressure distribution.

a slightly more complicated treatment is required. The horizontal force ($\frac{1}{2}$ $U_w h$) acting on the vertical rear face is resolved into its components perpendicular and parallel to the inclined surface beneath the slice. Hence equation (6) is modified to the following, for this special case:

$$\tan \phi_1 = \frac{W_1 \sin \beta_1 - c_1 L_1 + \frac{1}{2} U_w h \cos \beta_1 + P_1}{W_1 \cos \beta_1 - U_w L_1 - \frac{1}{2} U_w h \sin \beta_1}$$

or $$P_1 = \tan \phi_1 (W_1 \cos \beta_1 - U_w L_1 - \tfrac{1}{2} U_w h \sin \beta_1) + c_1 L_1 - W_1 \sin \beta_1 - \tfrac{1}{2} U_w h \cos \beta_1 \quad (7)$$

No attempt has been made to generalize on the orientation of the tension crack, which is assumed to delineate the top of the unstable mass of rock. It is a simple matter to modify the calculations for overhanging or sub-vertical joint faces.

Assumptions and results

The following parameter assumptions were made for both slides:

Planar joint surfaces $\phi = 35^\circ$ c = o
Rough sheared surfaces $\phi = 45^\circ$ c = unknown
Rock mass density 3.00 g/cc.

The assumed density was the measured mean of all the laboratory specimens of porphyry that were prepared before testing.

Three values of cohesion were calculated for each slice based on the three assumptions of water pressure distribution:

1. Drained
2. Distribution A
3. Distribution B

Table 1. Values of cohesion intercept from back analysis

SLIDE	SECTION	Cohesion c Kg/cm^2			Approx. mass of slide
		Drained	A	B	
S.1	2265 2250 2240	0.40 0.39 0.83	3.98 4.02 4.00	2.60 2.92 2.90	65000 (metric tons)
S.2	2150 2135 2120	(-)0.17 0.18 0.47	3.41 3.78 2.19	2.28 2.35 1.87	105,000 (metric tons)

SECTION 2.2.

The values of mean normal stress were calculated for each Section based on the assumption of self weight stresses (equation 4). However this was only done for the slices lying above 'rough sheared surfaces', since the above values of cohesion intercept were only relevant to these. The results tabulated below are again for the three cases; drained, and distributions A and B.

Table 2. Mean effective normal stresses on rough shear surfaces

SLIDE	SECTION	Mean effective normal stress Kg/cm^2		
		Drained	A	B
S.1	2265	2.31	(-) 0.57	0.72
	2250	3.41	(+) 0.67	1.76
	2240	2.23	(-) 0.33	0.74
S.2	2150	3.39	(-) 0.04	1.54
	2135	2.58	(-) 0.36	0.83
	2120	0.97	(-) 0.64	0.08

The mean effective normal stresses acting across the whole rough, shear surface of each slide were best approximated by 'weighting' the above results according to the relevant cross section areas. The following overall results were obtained for mean effective normal stress.

SLIDE	Drained	A	B	
S.1	2.74	(+) 0.015	1.15	Kg/cm^2
S.2	2.61	(-) 0.28	0.98	

It is clear that the limited seepage distribution A was an excessively severe assumption, since the above results implied negligible and even negative effective normal stresses. Consequently distribution B was adopted as giving a more realistic approximation to the water pressure distribution at failure.

SECTION 2.2.

2.2.4 THE PROBLEM OF STRENGTH EXTRAPOLATION

The weighted mean values of cohesion intercept obtained for slides S.1 and S.2 from Table 1 were as follows:

S.1 $c = 2.83$
S.2 $c = 2.23$ Kg/cm^2 (for distribution B)

Since these values were obtained for an assumed value of angle of friction of 45° the coordinates (τ, σ) are simply obtained from the following relation:

$$\tau = \sigma_n + c$$

S.1 $\tau = 3.98, \sigma = 1.15$ Kg/cm^2
S.2 $\tau = 3.21, \sigma = 0.98$ Kg/cm^2

The two slides that were back analysed were failures involving approximately 60,000 and 100,000 tons of rock. These are by no means enormous failures, but they are probably larger than those that generally occur in situations amenable to back analysis. Despite the fact that the failure surfaces were located at depths up to 35 metres below the pit face, the mean effective normal stresses acting over the failure surfaces were only 1.0 Kg/cm^2 or thereabouts, after the corrections for inclination ($\cos^2 \beta$) and mean water pressure (U_w). How then can a strength envelope be extrapolated realistically from results of (τ, σ) at such low normal stress levels?

There is a widespread and unfortunate tendency to shear test rock joints at normal stresses up to 100 or 200 Kg/cm^2 even though the projected slope heights rarely exceed 500 metres. Bearing in mind the effect of failure surface inclination and possible water pressures, a range of normal stresses of 0 to 40 Kg/cm^2 would seem more than adequate for any realistic shear testing programme for open pit design. However a back-analysis shear strength result at a normal stress of 1 Kg/cm^2 is still extremely low for extrapolation purposes, if shear tests cannot be performed.

The general equation of peak shear strength developed for model tension joints was tried in an attempt to provide a workable extrapolation of strength. It will be remembered from Section 2.1 that for a basic friction angle (ϕ_b) of 30° the following equation was indicated:

$$\tau/\sigma = \tan\left[20 \log_{10}\left(\frac{\sigma_c}{\sigma_n}\right) + 30^\circ\right] \qquad (8)$$

SECTION 2.2.

In view of the measured basic friction angle of $30\frac{1}{2}^{o}$ for planar porphyry specimens, the above relation will be accepted as a possible peak strength equation for the failures in porphyry.

Comparison with large shear tests on porphyry

The results of peak and residual shear strength for natural joints in porphyry obtained from Corta Atalaya (the adjacent open pit to Filon Sur) were presented in Section 2.1 (Figure 2.1.20 Pentz[34] and Kutter[33]). The large shear machine was capable of testing joint areas of approximately 0.1 m^2.

Unconfined compression tests were also performed on three porphyries from three pits in the Rio Tinto complex. (Ross Brown and Barton[52]). The most weathered specimen gave a mean strength value of 295 Kg/cm^2. It was found that, if this was taken as the hypothetical effective compressive strength for porphyry joints in situ, a strength curve could be predicted using equation 8 above, which was quite a good fit to the limited data.

This curve is reproduced again Figure 2.2.8 (uppermost curve), for a more realistic range of normal stresses. The two coordinates of (τ, σ) obtained from back analysis of failures S.1 and S.2 gave the following ratios of (τ/σ):

S.1 3.46

S.2 3.28

By using equation 8 or the design chart presented in Section 2.1 it is a simple matter to produce predicted values of the ratio of effective compressive strength to normal stress (σ_c/σ_n):

S.1 158

S.2 142

Therefore the two effective compressive strengths can be calculated since the two mean normal stresses (1.15 and 0.98 Kg/cm^2) are known:

S.1 $\sigma_c = 182$

S.2 $\sigma_c = 139$ Kg/cm^2

The predicted joint shear strength curve for the mean of these two effective strengths is shown in Figure 2.2.8. It passes between the two lowest shear test results, and if extrapolated would pass a little below the data obtained at normal stresses between 50 and 90 Kg/cm^2 (See Figure 2.1.20) It is significant that the curve lies between the peak and residual results.

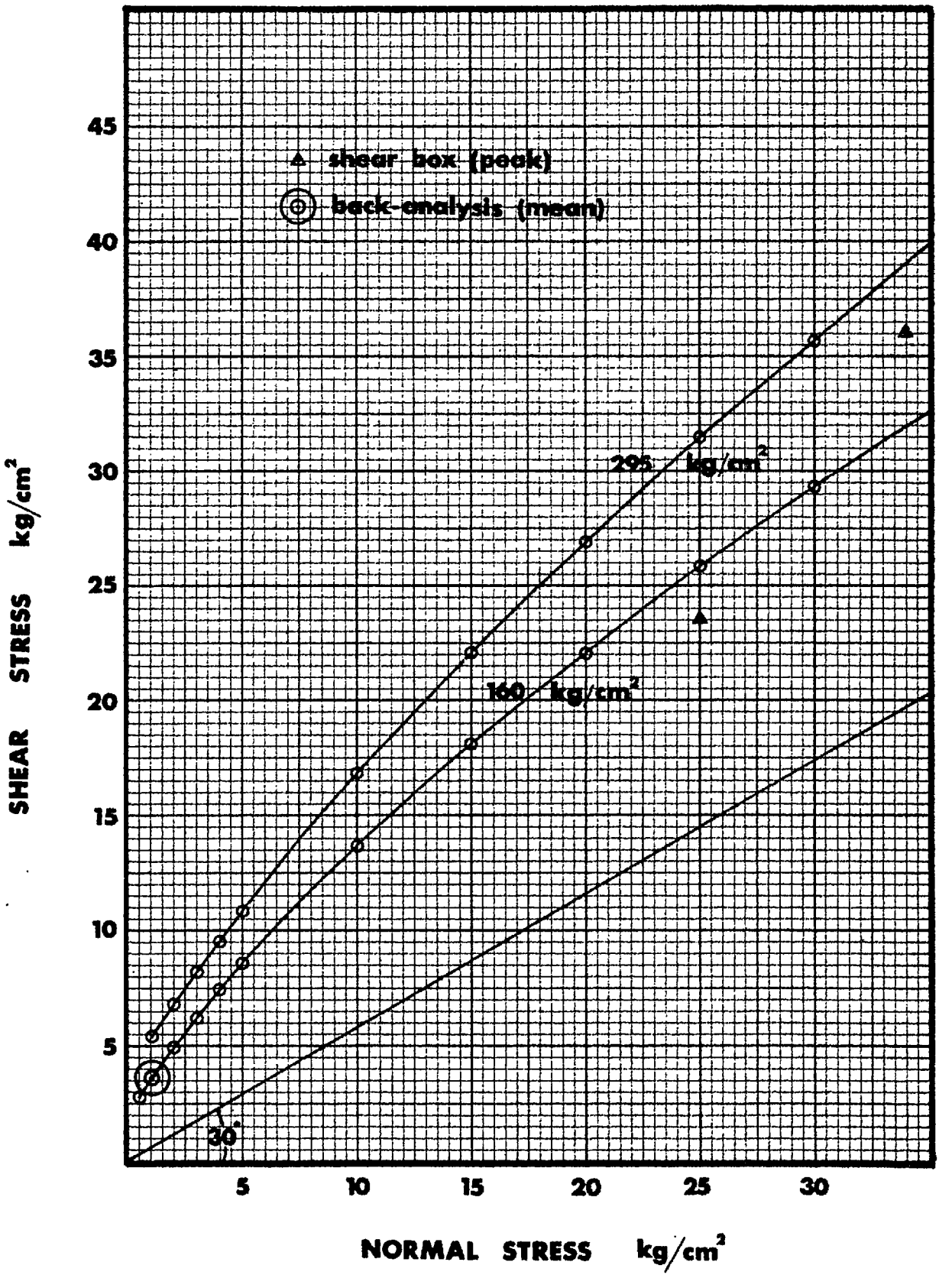

Figure 2.2.8 Predicted strength envelope from the back-analysis of two failures.

In view of the severe weathering that occurs in the acid environment of the Rio Tinto pyrite mines, it may not be coincidental that Slide S.1 which occurred in 1935 indicates an 'effective joint-wall compressive strength' at least 20% higher than slide S.2 which occurred in 1968.

However the uncertainties surrounding the water pressure distributions must always be appreciated. Despite this, the general equation of peak shear strength (equation 8) is seen to be a potentially very useful extrapolation method when one considers that strength envolopes may be required up to normal stresses perhaps one hundred times that operating during failure of the rock slides that can be back analysed.

SECTION 2.3.

2.3. A LIMIT EQUILIBRUIM APPROACH TO PROGRESSIVE FAILURE IN EXCAVATED ROCK SLOPES

SUMMARY

The stability of a rock slope is largely controlled by the presence of discontinuities in the rock. Their presence means that failure is generally of a translational type, and is therefore amenable to simple methods of analysis. The most unstable situation is chosen; one joint set dipping into the slope with a strike direction parallel to the slope face. This situation is amenable to a two dimensional approach.

A limit equilibrium method is used to analyse a simple plane failure. Three refinements are then incorporated; the division of the unstable rock mass into slices (representing vertically dipping joints), the assumption of zero tensile strength across the slices, and the effect of excavation on the assumed self weight stress distribution of the joints exposed by the excavation.

A method is developed whereby states of stability other than the limiting case can be analysed. The stability or instability of parts of the slope are characterised by forces acting parallel to the failure surface. The length of each joint that is overstressed is produced by this method. Consequently the depth of failure can be calculated without recourse to computing methods.

The concept of pre-failure shear displacements and increased weathering of overstressed joints is introduced. This progressive failure mechanism leads to a possible stepped portion of the failure surface. The predicted multi-linear slide scar is characterised by a vertical scarp passing through the crest of the slope, a stepped portion on which the vertical joints open, with sliding on the inclined joints, and shear failure on the inclined joint passing through the toe.

The stepped portion is caused by progressive failure, and residual shear strength parameters are suggested for design purposes. The method is illustrated by worked examples, in which the progressive failure mode is shown to reduce the failure depth considerably. A further reduction in stability is caused by transient water pressures. The pessimistic assumption of a full tension crack, and steady seepage reducing to zero exit pressure at the toe is used as an illustration.

SECTION 2.3

2.3 A LIMIT EQUILIBRIUM APPROACH TO PROGRESSIVE FAILURE IN EXCAVATED ROCK SLOPES

INTRODUCTION

The majority of rock slopes warranting stability investigations will be unstable due to one of two inherent structural features. This could be the chance interaction of the slope with unfavourably dipping fault surfaces or with clay filled joints or alternatively, the eventual overstressing of one or more sets of adversely orientated joints dipping into the slope. The overstressing mechanism may be one of joint water pressure increases caused by poor drainage, or simply due to excavation of the slope to steeper angles or increased cut heights. The failure mechanism may also be initiated by dynamic loading from earthquakes or very large blasts, but this type of loading will not be considered here.

The type of failure to be investigated will be limited to that occurring on adversely dipping joints, associated with at least one further joint set. A two dimensional approach, and consideration of progressive failure lead to the development of a multi-linear failure surface. However this belies the fact that the mode of failure is purely translational. (Skempton and Hutchinson[61]) There is no rotational component.

The stability of rock slopes has been the subject of several recent papers, in which the three dimensional graphical method of analysis has been utilized (Wittke,[62] Londe, Vigier and Vormeringer,[63, 64] and John[65].) There is no doubt that in any open pit excavation there are more potentially adverse rock tetrahedra defined by the intersection of two joint sets, than there are unstable wedges defined by single joint sets. However, the frequency of occurrence is somewhat overshadowed by the fact that potential failures delineated by two shear planes are inherently more stable than those delineated by one shear plane. At present the graphical methods do not incorporate any stress or limit analysis for determining the position of tension cracks in the unstable tetrahedra. Consequently the results obtained are dangerously under-conservative.

The two dimensional approach which will be adopted here, incorporates sliding on combinations of a single joint set and opening of tension cracks in a secondary joint set. This is the most pessimistic failure mode and consequently the one demanding most attention.

Stresses induced by self weight

It is assumed in the present analysis that all stresses are initiated through self weight loading of a rigid body. This assumption is made in spite of the current fashion for computer produced elastic stress distributions. Mueller and John[66] once suggested that the concept of overburden depth and self weight stresses used in shallow soil slopes was not applicable to steep unsupported rock slopes, due to the severe stress concentrations around the toe of these steep slopes.

These stress concentrations have been indicated in numerous photoelastic and finite element studies of elastic materials. They have also been demonstrated by rock bursts at the base of steep fjord slopes in Norway. However, fjords generally lie at the foot of mountain ridges which are frequently in excess of 5000 feet high. It is well known that such areas are tectonically active. In addition and more importantly, most steep fjord slopes have extremely sparse jointing limited almost entirely to relief or 'sheet' type jointing (Bjerrum and Jorstad[67]).

Recent studies have indicated that elastic stress distributions can be very misleading when applied to normally jointed rock, as encountered in most open pit locations. St. John[68] has suggested that a redistribution of stress can occur in these highly stressed zones due to the discontinuous nature of the jointed rock. This redistribution of stress has been clearly demonstrated by Cundall[69], from finite difference studies of discontinuous block models.

The physical models of jointed, excavated rock slopes (reported in Part 3) which were loaded horizontally and by gravity, indicated that the assumption of a self weight distribution of stress may be the most valid one, even for steep slopes.

2.3.1 SIMPLE FAILURE ON A SINGLE PLANE.

A trivial approach will be followed initially as this helps to clarify the essential elements of the problem. Failure is assumed to occur on the failure surface AB illustrated in Figure 2.3.1., with the whole mass sliding coherently on this plane. The only stresses acting on this failure plane are assumed to be self weight stresses caused by gravity. No joint water pressures are considered for the present.

The shear strength characteristics of the failure plane are assumed to be adequately described by the parameters (c) cohesion intercept, and (ϕ) angle of friction. For the present a linear shear strength envelope will be assumed, taken as the best piecewise linear approximation to the actual curved envelope.

From the geometry of Figure 2.3.1 the weight of material W above the assumed failure plane AB can be calculated as follows:-

$$CB = H(\cot\beta - \cot\alpha)$$

$$W = \frac{\gamma H^2}{2}(\cot\beta - \cot\alpha) \qquad \text{(1)}$$

where: H = the height of the slope

γ = the average density of the rock mass

β° = the inclination of the assumed failure plane

α° = the inclination of the overall slope

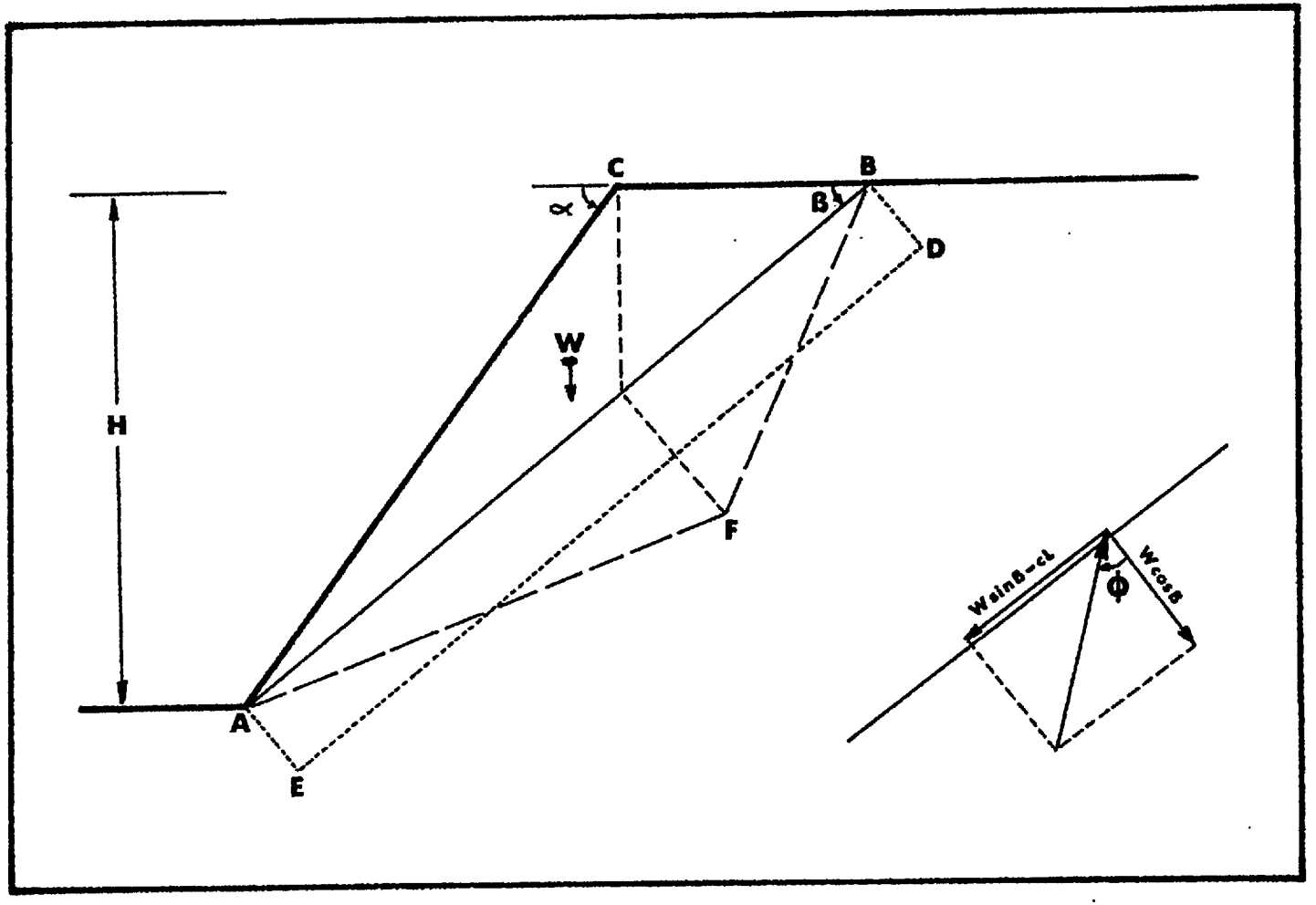

Figure 2.3.1 The equilibrium of forces on a planar joint induced by a self - weight stress distribution.

Based on the assumption of self weight stresses, the maximum stress occurs on the failure plane vertically below the crest C. The component of stress perpendicular to AB can be represented by the dashed lines AFB. It is assumed for the present that this can be approximated to a 'rectangular' distribution of normal stress such as AEDB, where AE is equal to half the height of AFB.

The limiting equilibrium equation describing the normal and shear forces acting on the failure plane is as follows:-

$$\tan \phi = \frac{W \sin \beta - cL}{W \cos \beta} \qquad (2)$$

where L = the length of failure plane AB = $H/\sin\beta$

(The third dimension is unity in this two dimensional approach)

Substituting for W and L in equation 2 gives the following relationship:-

$$\tan\phi = \tan\beta \left[1 - \frac{2c}{\gamma H} \left(\frac{1}{(\cot\beta - \cot\alpha)\sin^2\beta} \right) \right] \qquad (3)$$

Simple Method of slices

Following this trivial approach the wedge of material above the plane AB is now split into parallel-sided slices. Figure 2.3.2 illustrates four slices which are chosen such that the dimensions DE and EC are equal, and similarly CF and FB.

Since GF is parallel to AB, triangle CFG is geometrically similar to triangle CBA. Therefore the weights of the four slices are related as follows:-

$$W_2 = 3W_1 \qquad W_3 = 3W_4$$

It is assumed that the stress distribution beneath each slice can be approximated to a rectangular distribution. The validity of this assumption clearly is increased for larger numbers of slices. The limiting equilibrium equations for the four slices can be obtained by substitution in equation 2. The equations for slices 1 and 2 are as follows:-

$$\tan\phi = \tan\beta \left[1 - \frac{4c}{\gamma H} \left(\frac{1}{(\cot\beta - \cot\alpha)\sin^2\beta} \right) \right] \qquad (4)$$

$$\tan\phi = \tan\beta \left[1 - \frac{4c}{3\gamma H} \left(\frac{1}{(\cot\beta - \cot\alpha)\sin^2\beta} \right) \right] \qquad (5)$$

Hence if treated as separate blocks lying on the failure plane, slices 1 and 2 must have different values of cohesion intercept (c) or angles of friction (ϕ), acting across the failure plane for them to both be at limiting equilibrium. Alternatively it can be

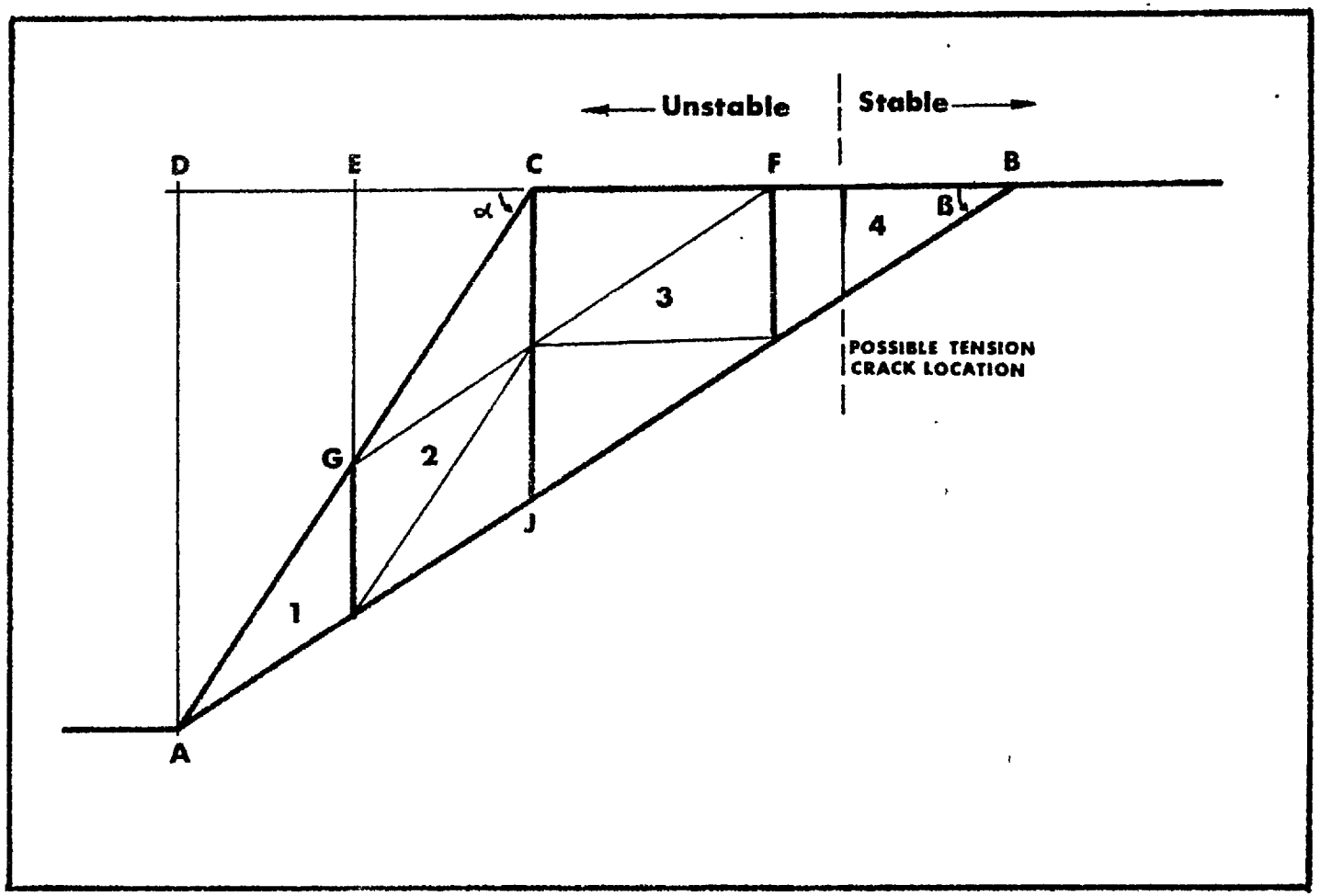

Figure 2.3.2 The geometry of four slices dividing an unstable 'wedge'.

said that slice 1 is inherently more stable than slice 2 given the same shear strength parameters. The same can be said of slice 4 and slice 3.

No-tension concept

This simple idea can be extended by dividing the two triangles ACJ and CBJ into a larger number of slices. It is obvious that given certain conditions, several of the lighter weighted slices could be stable if they could be considered as independent blocks lying on the failure plane. It will be assumed from now on that the tensile strength of the rock mass in a direction perpendicular to the slice boundaries is zero. This assumption is readily justified if one considers the slice boundaries to represent a parallel set of more or less vertically dipping joints intersecting the rock mass with a strike direction perpendicular to the plane of the figure. The adoption of this "no-tension" concept leads to partial separation of the 'unstable' mass into a possible stable portion lying at the top of the failure plane, and a less stable remainder. The separation between the two parts will be referred to as a tension crack. It is assumed that the tensile nature of the movements across these cracks reduces their shear strength to negligible proportions. Figure 2.3.2 illustrates the concept. No tension crack occurs near the bottom of the failure plane since the slice boundaries in this zone are obviously under compression.

It is important to realise that a stability analysis based on the assumption of a coherent wedge sliding on a plane failure surface will generally produce a stability estimate that is under-conservative. That is, the stability of the slope will be overestimated. A simple 'no-tension' assumption is a first step towards improving this estimate, provided that the orientation of one of the joint sets makes the assumption reasonable.

Excavation to increased slope heights

The division of the unstable zone into slices will now be extended to include different depths of excavation. Figure 2.3.3 illustrates the critical failure planes for four depths of excavation, each with the same slope angle. The steeply dipping planes can be regarded as a persistent set of parallel joints. At each stage of excavation a different joint will be most critically stressed.

It is assumed that the presence of joints does not affect the stress distribution compared to an unjointed model. This would probably be valid if no shear displacements occurred on any of the joints. The degree to which the initial stress distribution collapses during progressive failure is of course a subject in itself, and cannot be accounted for in any simple presentation of this type. However, in a global sense the total stress across such failure surfaces remains the same during progressive failure. The discontinuous nature of a rock slope should not be forgotten, when stress concentrations are imagined.

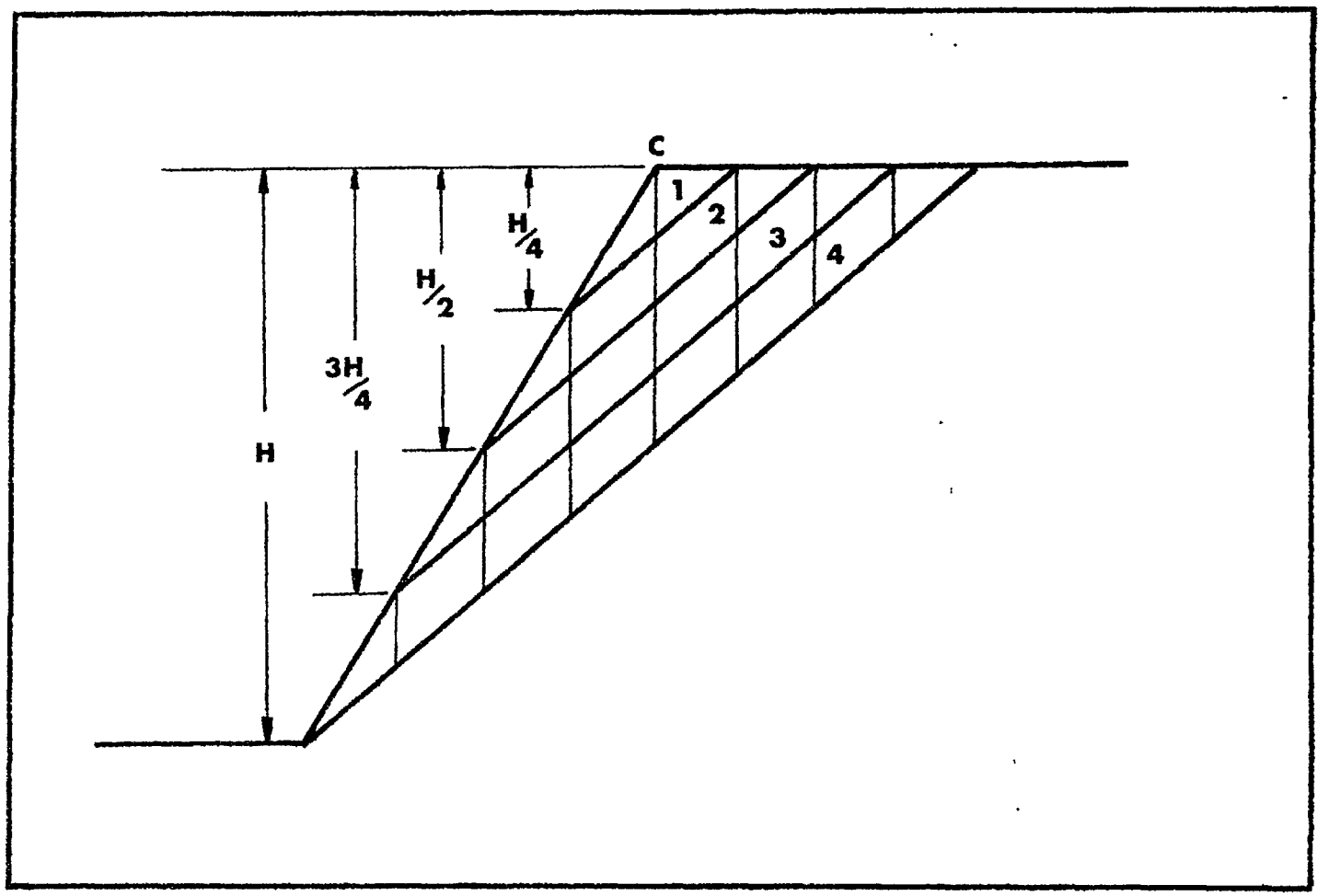

Figure 2.3.3. The critical joint planes at four depths of excavation.

The four critical failure planes illustrated in Figure 2.3.3 delineate four geometrically similar triangles, each having as their third apex the crest position (C). It is a simple matter to modify equation 3 to account for the different limit equilibrium equations describing the slope instability at each depth of excavation. Supposing an unchanged angle of friction was assumed for each failure plane, then for limiting conditions at each depth of excavation the ratios of cohesion values would need to be as follows.

$$c_4 = {}^4/_3 \cdot c_3 = 2c_2 = 4c_1$$

This is clearly a hypothetical way of viewing the relative stability at each excavation depth, but it illustrates the obvious point that stability is successively reduced as excavation proceeds. It is pertinent to point out here that if the failure planes (joints) exhibited zero cohesion intercept, then the problem would be dimensionless, and the stability identical for all depths of excavation.

However, since peak shear strength envelopes are curved in reality the problem is far from dimensionless, whether the cohesion intercept (for zero normal stress) is zero or not.

2.3.2. THE CONCEPT OF AN UNSTABLE EXCESS

It has been established that individual slices will tend to be operating at different 'factors of safety' for equal shear strength parameters. It would therefore be useful if a simple method were developed, whereby the stability or instability of each slice could be computed separately. Integration of all the slices below the tension-crack would then give a more realistic interpretation to the problem.

An unstable excess is proposed, whereby the limit equilibrium equation (equation 2) is generalised to include states of stability other than the limiting case. This method was used in Section 2.2 for estimating the stability of slices during back analyses of failed slopes.

The stability of any slice is dependent on the magnitude of the forces acting perpendicular and parallel to the failure plane beneath the slice, and on the shear strength exhibited by the failure plane. If the sign of this force P is positive, this implies that a force of magnitude P, acting down the plane, is needed to bring that slice to limiting equilibrium. In other words the slice is stable. If on the other hand, P is negative, this implies an unstable slice which requires a force of magnitude P acting up the plane to keep the slice from sliding down. The slice has an 'unstable excess' of magnitude P. It is assumed that any unstable excess will be transmitted to the slice immediately below, but this aspect will be dealt with shortly.

Figure 2.3.4 illustrates the equilibrium of forces beneath an individual slice (number n) of weight W_n. The limiting equation is as follows:

$$\tan\phi = \frac{W_n \sin\beta - cL_n + P_n}{W_n \cos\beta}$$

or

$$P_n = W_n \cos\beta\,(\tan\phi - \tan\beta) + cL_n \qquad (6)$$

where L_n = the length of sloping base beneath the slice.

Returning to the geometry of Figure 2.3.1 the new limiting equilibrium equation for the whole slope, from equation 6, will be as follows:

$$P = \frac{\gamma H^2}{2}(\cot\beta - \cot\alpha)\cdot\cos\beta\,[\tan\phi - \tan\beta] + \frac{c.H}{\sin\beta} \qquad (7)$$

It has already been proposed that when splitting a part of the slope into slices, the width of the slices should be made equal to one another. Thus in the upper triangle CBJ (see Figure 2.3.5) all the slices are of equal width. Likewise, in the lower triangle ACJ, the widths of the slices are also equal, though not necessarily equal to those of the upper triangle.

It is most convenient to treat the upper and lower triangles separetely. It only remains to formulate the two limit equilibrium equations for these two triangles, for the 'unstable excess' values to be obtained for all the individual slices dividing each triangle.

From the geometry of Figure 2.3.5 the following limiting equilibrium equations can be obtained:

UPPER Δ :
$$P = \frac{\gamma H^2}{2}(1-\cot\alpha\tan\beta).(\cot\beta - \cot\alpha)\cos\beta\,[\tan\phi - \tan\beta] + \frac{cH\,(1-\cot\alpha\tan\beta)}{\sin\beta} \qquad (8)$$

LOWER Δ :
$$P = \frac{\gamma H^2}{2}(1-\cot\alpha\tan\beta)\cot\alpha.\cos\beta\,[\tan\phi - \tan\beta] + \frac{cH\cot\alpha\tan\beta}{\sin\beta} \qquad (9)$$

If both the upper and lower triangles are divided into N slices each, then the individual lengths of the sloping bases beneath each slice are as follows:

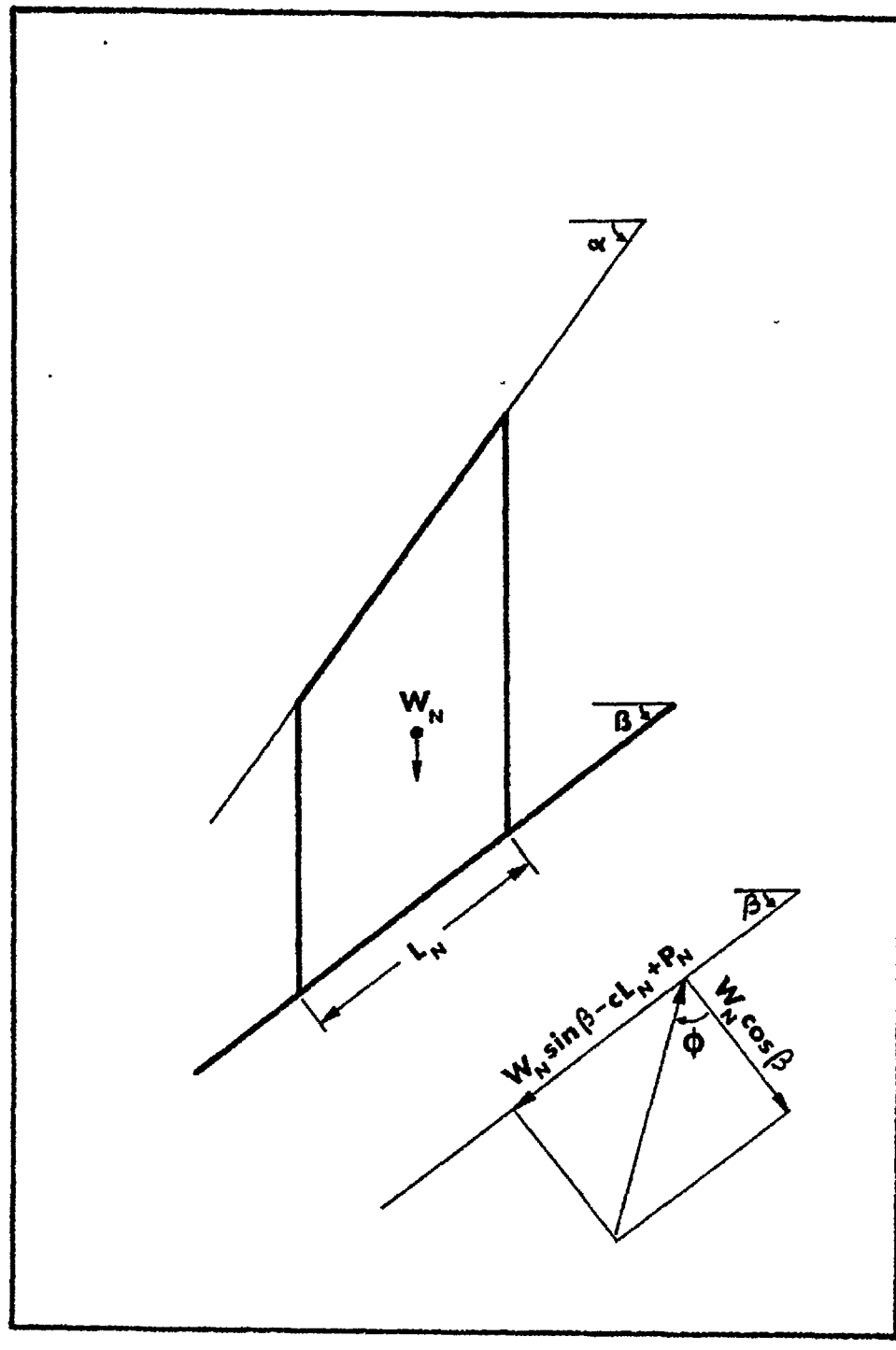

Figure 2.3.4 The limiting equilibrium of forces beneath one slice.

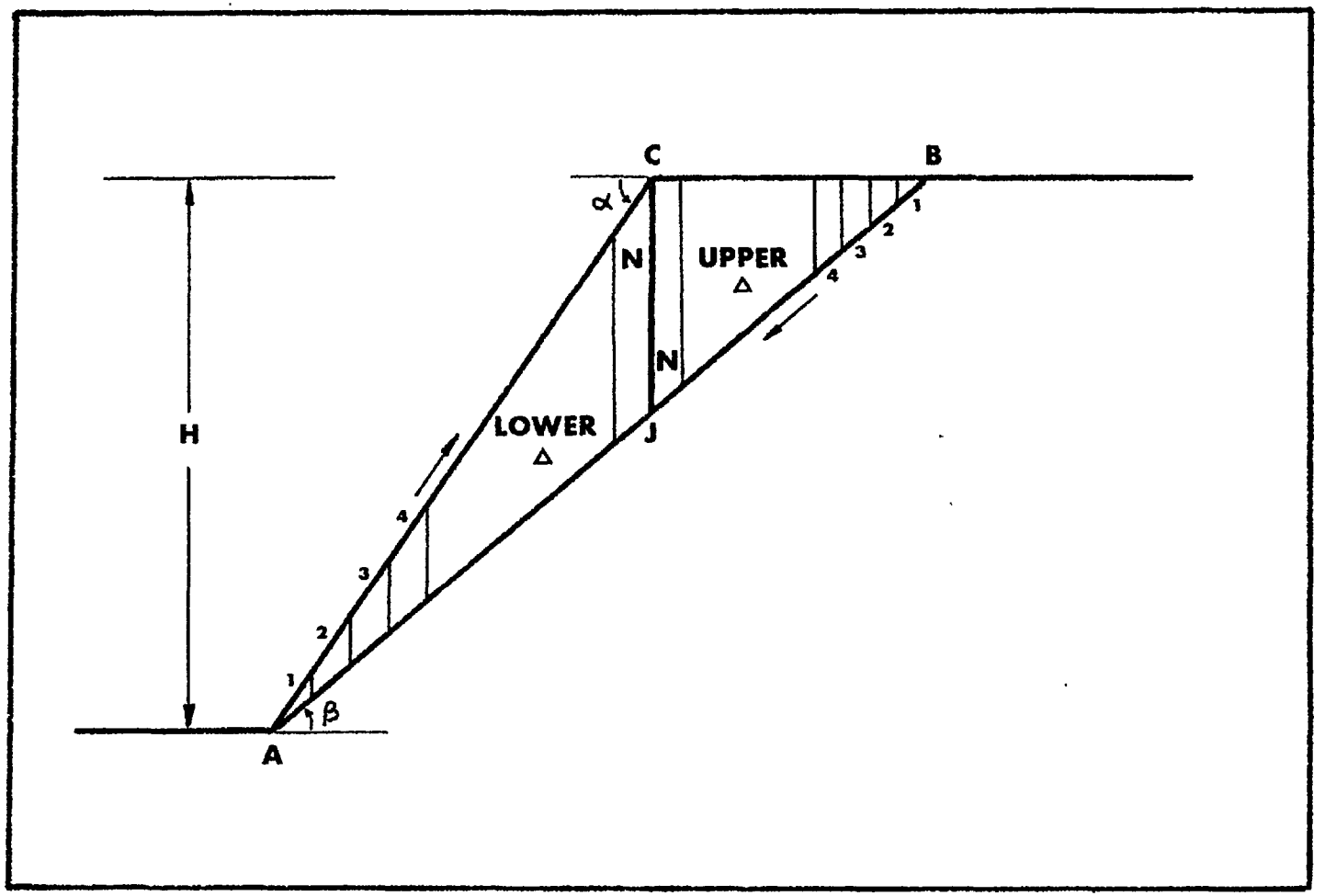

Figure 2.3.5 The nomenclature of the slices dividing the upper and lower triangles.

UPPER Δ : $1/N\ H\ \frac{(1-\cot\alpha\tan\beta)}{\sin\beta}$ LOWER Δ: $1/N\ H\frac{(\cot\alpha.\tan\beta)}{\sin\beta}$

The other variables which are dependent on the slice widths are the weights of individual slices. From the geometrical similarity of Figure 2.3.2 it can be easily verified that the weights of the slices as proportions of the respective upper or lower triangles are simply:-

$$1/N^2,\ 3/N^2,\ 5/N^2,\ \ldots\ldots\ldots\ldots\ldots\ \frac{2N-1}{N^2}$$

where the slices are taken in order (1 to N) as in Figure 2.3.5

Thus, with the nomenclature of Figure 2.3.5 the limiting equilibrium equations giving the values of 'unstable excess' for each slice are:-

UPPER Δ :

$$P_{1-N} = \left[\frac{1,3,5\ldots2N-1}{N^2}\right]\frac{H^2\gamma(1-\cot\alpha\tan\beta).(\cot\beta-\cot\alpha)\cos\beta[\tan\phi-\tan\beta]}{2} + \frac{1}{N}.\frac{cH\ (1-\cot\alpha\tan\beta)}{\sin\beta} \quad \text{(10)}$$

LOWER Δ :

$$P_{1-N} = \left[\frac{1,3,5\ldots2N-1}{N^2}\right]\frac{H^2\gamma\ (1-\cot\alpha\tan\beta)\cot\alpha.\cos\beta[\tan\phi-\tan\beta]}{2} + \frac{1}{N}\ \frac{cH\ (\cot\alpha\tan\beta)}{\sin\beta} \quad \text{(11)}$$

where:
- H = the height of the slope
- γ = the average density of the rock mass
- β^o = the inclination of the assumed failure plane
- α^o = the inclination of the overall slope
- c = the cohesion intercept exhibited by the failure plane
- ϕ = the angle of friction exhibited by the failure plane
- N = the number of slices dividing each triangle.

Solution for P is simply a matter of substitution. Slices with P values (units of force) that are positive are stable individually, and those with negative P values are unstable. The choice of N is arbitrary, since once equations 10 and 11 have been reduced to simple expressions by substitution, it takes only a few minutes longer to compute the P values for twenty slices (total of forty) than for ten slices (total of twenty.)

The theoretical existence of a tension crack will be clearly revealed by the P values obtained for the upper triangle. Taking the slices in order (from 1 to N), if a tension crack exists the P values will reduce successively from positive values, through zero to

increasingly negative values - the greatest of these lying beneath the crest of the slope (the most overstressed position). The position of the tension crack is obviously where the P value becomes zero. The rock mass above this position will theoretically be stable independently, and failure of the remainder of the slope will be characterised by a slide scar having a vertical rear face (depending on the second joint set) and a planar slide surface.

Markland[60] has shown that by minimising the length of failure surface lying beneath the corresponding weight of slope, the position of the tension crack can be found directly. The distance of the tension crack behind the crest of the slope (t) is found to be purely dependent on geometry, and independent of the shear strength parameters:

$$t = H \left[\sqrt{\cot \beta \cdot \cot \alpha} - \cot \alpha \right] \qquad (12)$$

The angles (α) and (β) refer to the inclinations of the pit slope and failure surface as before.

However, when going on to consider progressive failure, the unstable excess of all the slices is required for a full understanding to be gained. A failure mode not involving simple separation at one tension crack will be investigated.

The method will be illustrated by some worked examples before moving on to considerations of progressive failure, which may be induced by excavation.

Worked example No. 1.

Firstly, an example will be chosen which illustrates the different results that are obtained when using a slices method, and when analysing the slope as a coherent 'wedge'. Figure 2.3.6 illustrates the problem to be considered. Substituting the data in equation 3 (the limiting equilibrium equation for a single coherent 'wedge' lying on a plane failure surface), it is found that failure will occur on one of the steeply dipping joints when the depth of excavation (H) exceeds 1000 feet.

However, a method of slices analysis using equations 10 and 11 (assuming that the rock mass exhibits zero tensile strength in a direction perpendicular to the slice boundaries) predicts failure at a depth of excavation appreciably less than 1000 feet, as will be shown.

Substituting the data in equations 10 and 11 the following relations are obtained:

$$\text{UPPER } \Delta P_{1 \to N} = \frac{1,3,5 \ldots 2N-1}{N^2} \; (-8.05 \times 10^5) + \frac{1}{N} \; (8.05 \times 10^5) \; \frac{\text{lbf}}{\text{ft}}$$

$$\text{LOWER } \Delta P_{1 \to N} = \frac{1,3,5 \ldots 2N-1}{N^2} \; (-17.75 \times 10^5) + \frac{1}{N} \; (17.75 \times 10^5) \; \frac{\text{lbf}}{\text{ft}}$$

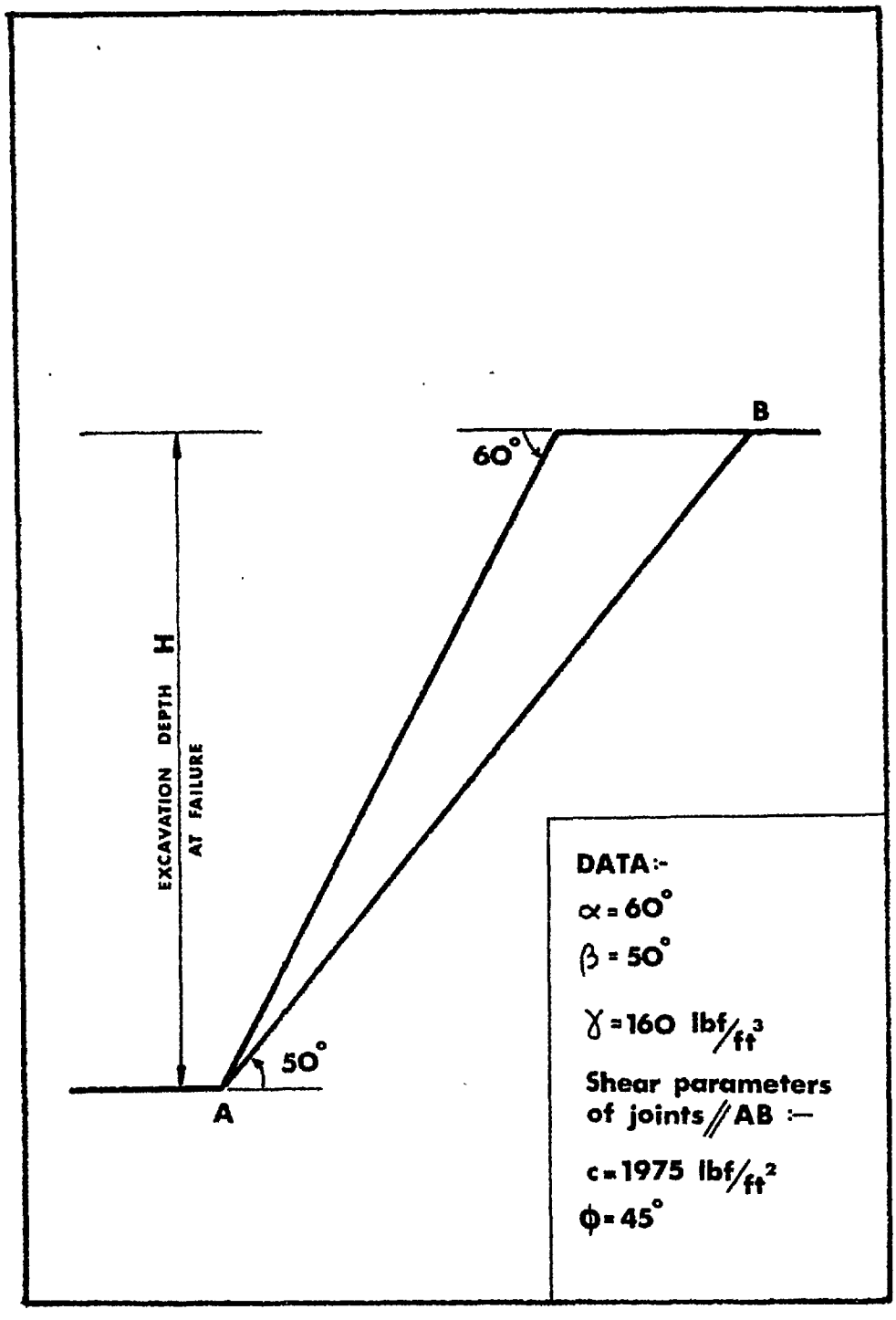

Figure 2.3.6 Worked example No. 1

Choosing an N = 10 analysis (total of 20 slices), the P values of all the slices can be rapidly obtained and are as follows:-

(Note: slice nomenclature as in Figure 2.3.5).

P VALUE (Units) lbf/ft x 10^5	UPPER △	LOWER △
P1	[+0.724	+1.598
P2	+0.564	+1.242
P3	+0.402	+0.887
P4	+0.242	+0.532
P5	+0.080]	+0.177
P6	-0.080	-0.177
P7	-0.242	-0.532
P8	-0.402	-0.887
P9	-0.564	-1.242
P10	-0.724	-1.598

It is important to realise that the striking symmetry of results is strictly a function of the data chosen for this example. The P values are for slices dividing a 1000 feet slope which is at limiting equilibrium, and their summation (P) is equal to zero as would be anticipated.

Since the failure surface is planar the total unstable excess is correctly interpreted as the summation of the individual P values of each slice. However, as pointed out before, the first few slices of the upper triangle may be stable (positive P values). These results have been bracketed in the table above. Thus in a 'no tension' analysis the overall unstable excess is the summation of all P values with the exception of the five values in brackets.

Hence for H = 1000 ft $P = -2.013 \times 10^5$ lbf. per foot*

i.e. the slope has theoretically failed.

(* per foot refers to the third dimension)

Calculation of failure depth by intrapolation

A total of 20 slices (N = 10) have been chosen to divide the 1000 ft. slope. From previous arguments it will be apparent that, due to the uniform spacing of the slices, eighteen (N = 9) slices of unchanged width will cover 900 feet, sixteen (N = 8) slices will cover 800 feet, and so on. Thus within the results for twenty

slices there exists all the information required for calculating the actual depth at which failure occurs. Hence the following table:

No. of slices included	1	2	3	4	5	6	7	8	9	N = 10
Equivalent depth (feet)	100	200	300	400	500	600	700	800	900	1000
ΣP lbf/foot x 10^5	-	-	-	-	-	-	-	+2.11	+.309	-2.013

The three results tabulated in the bottom row are sufficient for plotting a graph of depth of excavation versus unstable excess (Σ P). Where the curve crosses the $\Sigma P = 0$ line, the equivalent depth of excavation will be that at which limit equilibrium is reached. (See Figure 2.3.7) The shear stress along the failure plane will just have reached the available shear strength.

Results:

1) The intrapolated failure depth is 915 ft

2) The tension crack is approximately 110 feet back from the crest of the slope. (Equation 12)

Worked example No. 2. (using metric units)

Question: At what depth will a pit fail, if excavated at 60° in jointed rock, where one of the joint sets dips into the pit, at an average of $52\frac{1}{2}°$? The shear strength parameters of the joint set are:- c = 2.5 tons/m^2, $\phi = 45°$. Density of the rock mass is equal to 2.5 tons/m^3.

As previously shown, the final result depends upon intrapolation of the results from a particular depth of excavation. The first step is therefore to make an informed guess of the depth at which failure will occur using equation 7. It is important that this value of H (or a guessed one) is greater than the actual depth of failure, since the result cannot be extrapolated, only intrapolated from the P values.

Try H = 100 metres. For an N = 10 analysis, substitution in equations 10 and 11 gives:

$$\text{UPPER}\Delta P_{1-10} = \frac{(1,3,5,\ldots 19)}{100}(-109.0) + 7.8 \text{ Tons/metre}$$

$$\text{LOWER}\Delta P_{1-10} = \frac{(1,3,5,\ldots 19)}{100}(-329.0) + 23.8 \text{ Tons/metre}$$

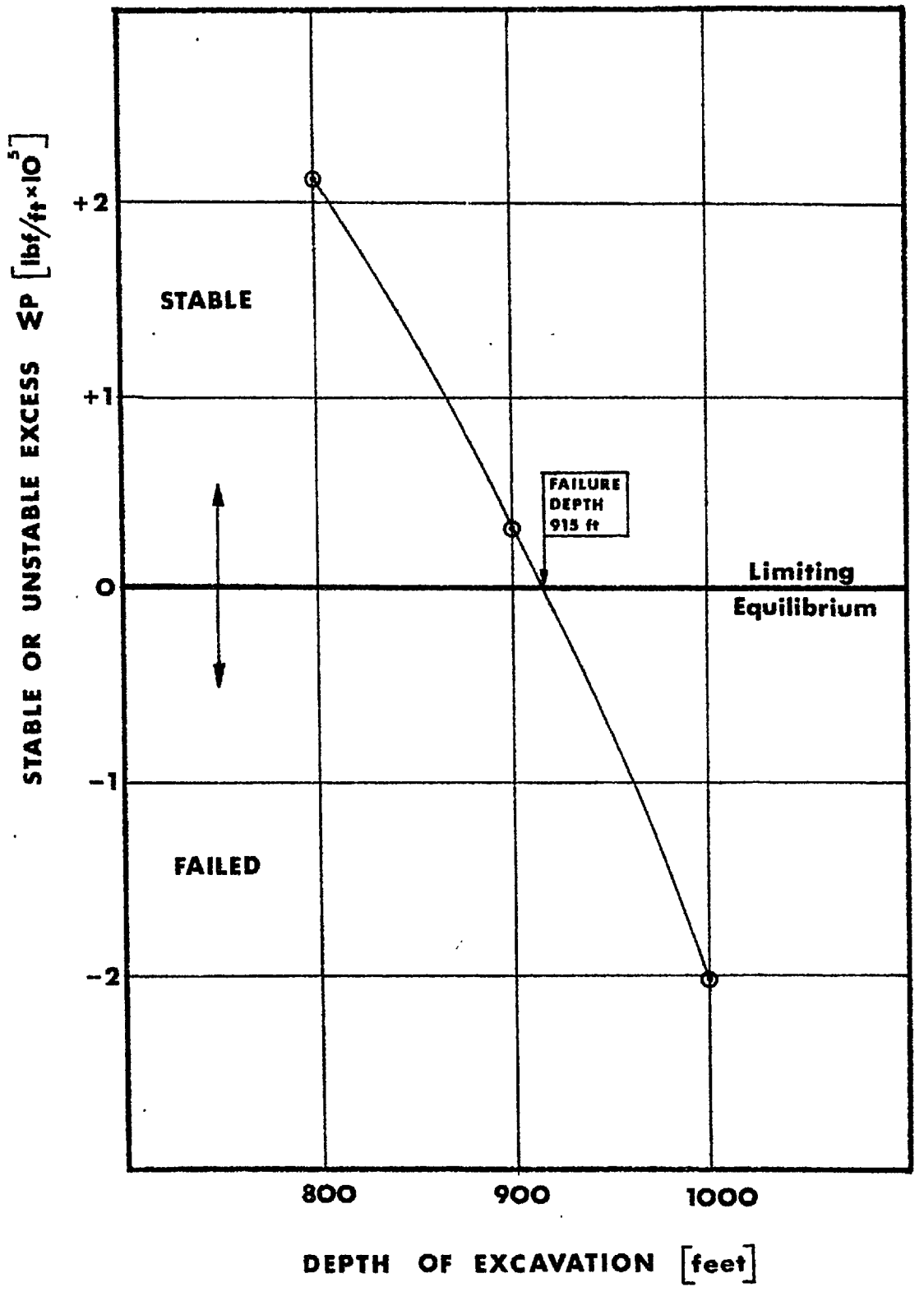

Figure 2.3.7. Graph of depth of excavation versus unstable excess.

The P values are therefore as follows:-

P value Tons/metre	UPPER △	LOWER △
P1	+6.7	+20.5
P2	+4.5	+13.9
P3	+2.3	+ 7.3
P4	+0.2	+ 0.8
P5	-2.0	- 5.8
P6	-4.2	-12.4
P7	-6.4	-19.0
P8	-8.6	-25.5
P9	-10.7	-32.2
P10	-12.9	-38.7

Slices 1,2,3, and 4 of the upper triangle are assumed to be independently stable as before. By selective summation of the P values for different depths of excavation, the second table of results are obtained, from which the failure depth can be intrapolated.

No. of slices included	1	2	3	4	5	6	7	8	9
Equivalent depth (metres)	10	20	30	40	50	60	70	80	90
P tons/metre	-	-	-	-	+34.7	+18.1	-7.3	-41.4	-

A plot of the four P values against equivalent depths of excavation indicates that a zero value of P (limiting conditions) is obtained when the depth of excavation is 67.5 metres. Figure 2.3.8 illustrates the shape of the slide scar ABCD predicted by this method. AB is the crack which opens up at the surface, BC is the zone which is overstressed (negative P values), and CD is the remaining portion of the failure surface which fails due to the unstable excess of all the slices lying above it, between C and B.

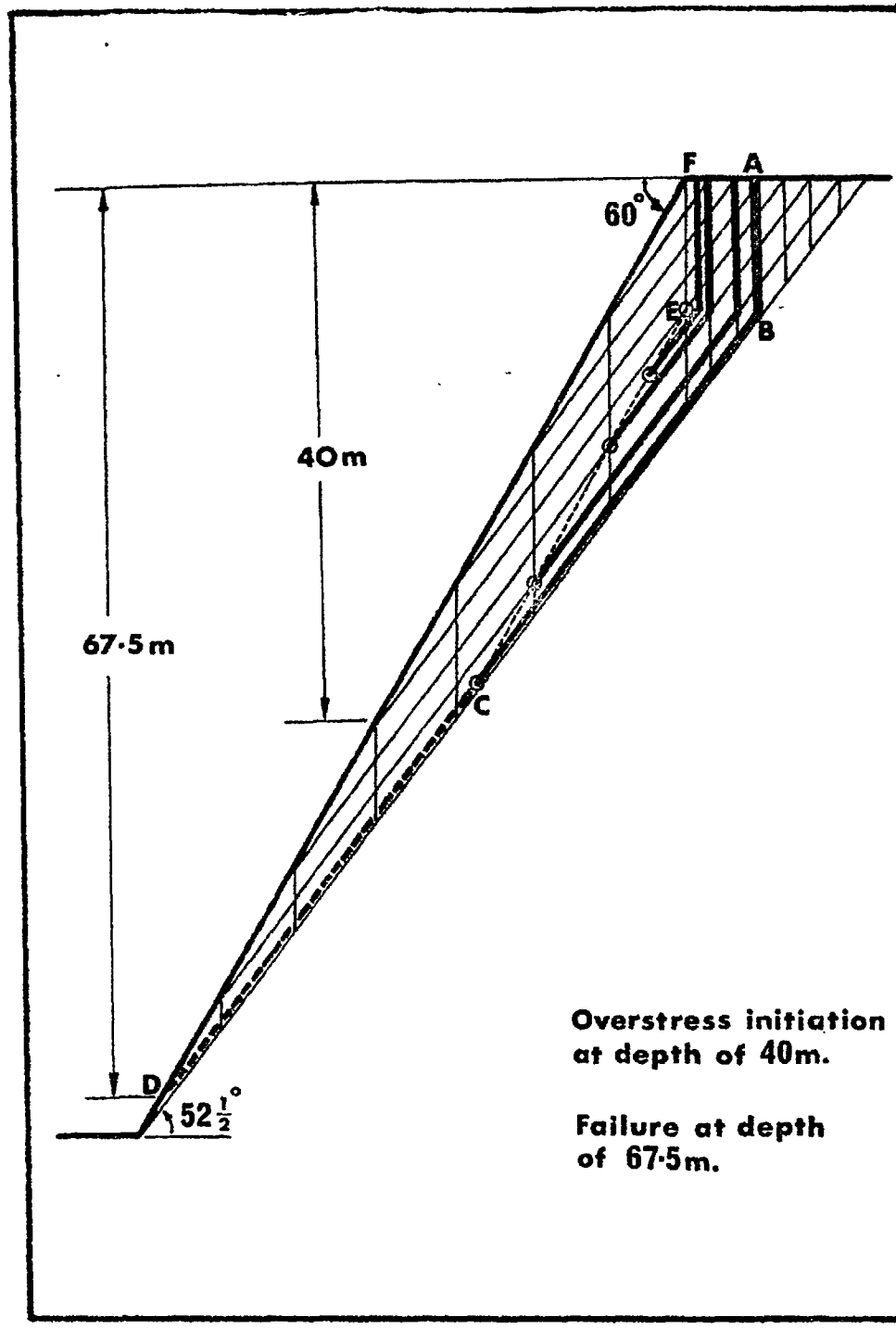

Figure 2.3.8 A diagrammatic representation of the overstressed joints predicted by worked example No. 2.

It will be apparent from the negative P values (see above table), that parts of several of the unfavourably dipping joints located above the latter are also overstressed. The thick parallel lines shown in Figure 2.3.8 represent the lengths of some typical joints which are overstressed. Each of these will have a consequent tension crack opening to the surface. (This theoretical prediction is frequently confirmed in practice.)

The overstressing mechanism is seen to initiate at a depth of 40 metres plus, and progresses with excavation until, at a depth of 67.5 metres, the total unstable excess becomes greater than the available stable excess. With the given assumptions, failure will be expected on the first joint to intersect the slope at a depth of 67.5 metres or more.

2.3.3 TWO CONCEPTS OF PROGRESSIVE FAILURE

Attention will first of all be focussed on the progression of the overstressed zone as excavation proceeds. A second, and most important factor to be considered, is the progressive failure brought about by the unstable shear strength characteristics of most joint surfaces.

1. Progression of overstressed zone.

In figure 2.3.8, the lower end of each of the idealized overstressed joints is circled. It is suggested that at these points there exists the maximum unstable excess for the particular joint in question. One of these joints is illustrated in Figure 2.3.9.

The overstressed portion CD, of joint AB has negative P values. The area of the shear stress distribution triangle AGB which is in excess of the maximum shear strength level (CE = DF) is represented by the shaded area EFG. Each of the slices between C and D is overstressing the joint surface beneath it, and if shear displacements can occur with these localized 'failures' then the unstable excess will progressively increase between D and C by simple summation. The slices between C and A will be supporting the full unstable excess of part CD, which is at a maximum at the slice interface above C. If this concept is accepted, then the slice above C can be expected to be the one most highly overstressed with respect to direct shear. For the present, the reduction in shear strength (and consequent rise in unstable excess) implied by these displacements will be ignored.

It is proposed that failure of the rock slope illustrated in Figure 2.3.8 could possibly occur on a failure surface defined by points FECD, rather than the originally proposed ABCD.

The portion EC is the locus of maximally overstressed points on each critical joint that dips unfavourably into the slope. It is suggested that the rock mass might slide on a stepped surface between E and C, where each step is the secondary joint set (having zero tensile strength). In this way sliding would occur on

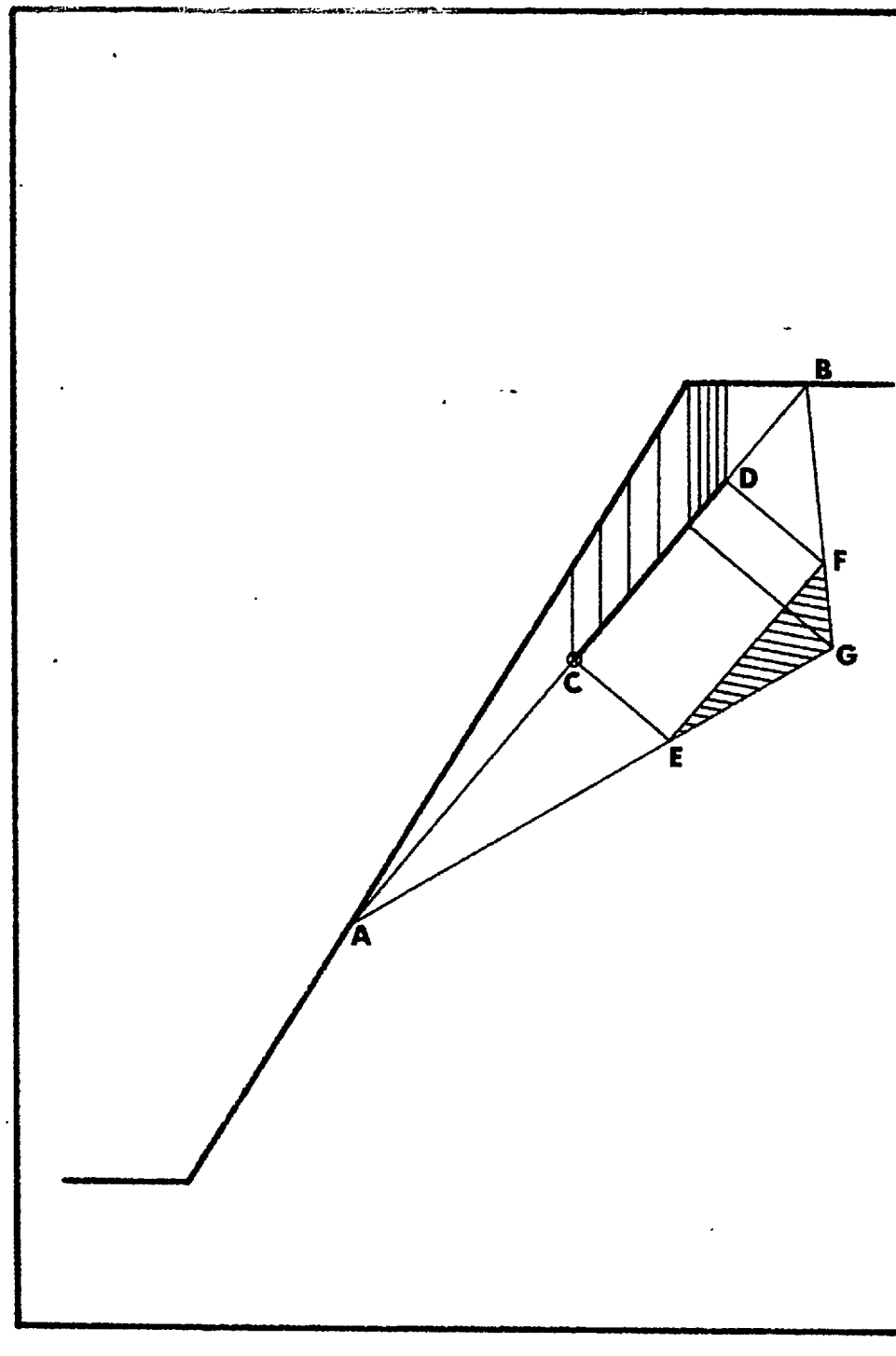

Figure 2.3.9 The distribution of shear stress assumed to act on an over-stressed joint, before displacements occur.

portions of all the overstressed joints, stepping down progressively from one joint to the next immediately beneath. This concept is illustrated diagramatically in figure 2.3.10.

It should be pointed out that the secondary joint set need not be vertical for this type of failure to be analysed by the proposed methods. The vertical slice boundaries and the vertical steps illustrated so far should just be taken as the most simple method of illustrating secondary joint opening. In reality these artificial planar boundaries between slices could be saw-toothed. (Eg. two orthogonal joint sets dipping at 45° each). However it is unlikely that such a system would have zero tensile strength in a horizontal direction, and in any case in practice at least one near-vertical joint set can be expected, more commonly two.

The stability of the stepped and direct failure modes illustrated in Figure 2.3.10 were checked, and compared with the original failure surface ABCD. The parameters of worked example No. 2 were used, with unchanged shear strength values:-

(a) Stepped shear surface. P = +42.9 tons/metre (stable)

Note: CE is parallel to the 60° slope DF. However the actual sliding surface is parallel to the joint dip of $52\frac{1}{2}^{\circ}$. The consequent reduced length of shear surface is accounted for in the above.

(b) Direct shear surface. P = +4.6 tons/metre (just stable)

Note: It was assumed that both shear and normal components of stress would be transmitted across the vertical slice boundary above point C. The unstable excess for the upper surface (60° dip) was resolved into the dip direction of the lower surface ($52\frac{1}{2}^{\circ}$), by the correcting factor: $\cos (60^{\circ} - 52\frac{1}{2}^{\circ})$. This method was adopted in Section 2.2 for integrating the unstable excess of slices lying on differently inclined failure surfaces.

The latter mode of failure, although apparently predicting greater instability, is questionable because it will not be feasable unless the rock is very highly jointed. The location of the failure surface might then be independent of the structual discontinuities.

However it is generally agreed that a 'circular stability analysis' can be usefully applied to rock slopes when the dimensions of the slope are very large compared to the joint spacing. The problem then approaches the soil mechanics end of the spectrum, and a rotational failure mode which is not structurally controlled can be anticipated, rather than failure mode No. 3 in Figure 2.3.10.

However, the more usual rock mechanics problem is one of relatively wide joint spacing. The potential failure surface is then almost totally controlled by structural discontinuities. Translational shearing then becomes the dominant mode of failure.

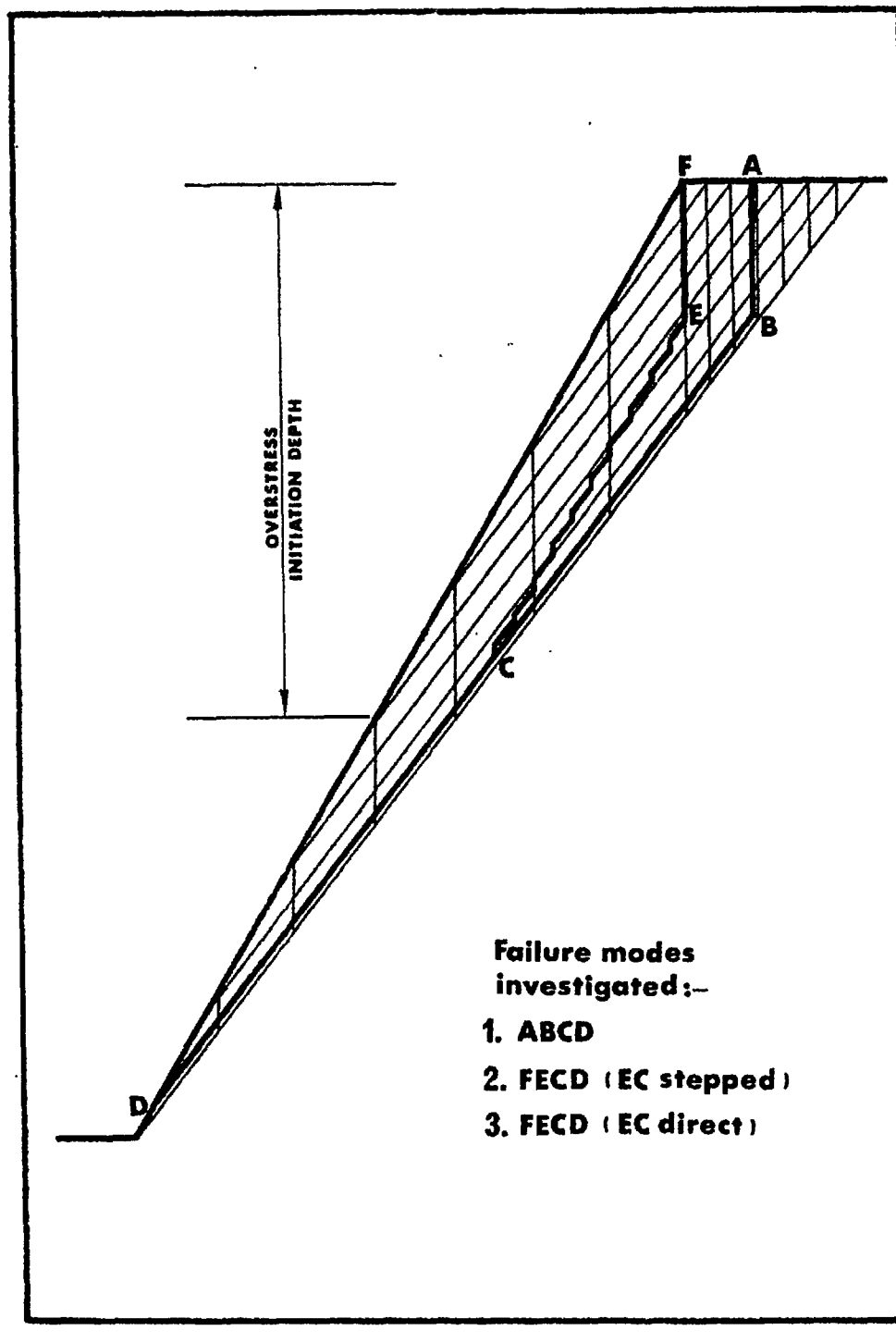

Figure 2.3.10 The multi-linear failure surfaces investigated.

Jennings and Robertson[70], and Jennings[71], developed an involved 'mathematical' treatment to account for the discontinuous nature of joints. They considered a stepped failure surface involving sliding down one joint set, opening on a second joint set and shear and tensile failure of the intact rock between the two. Some of the parameters involved are almost impossible to estimate in the field.

For this reason the approach adopted by Terzaghi[72] is considered more useful. He suggested that the rock bridges between joints would in all probability be eliminated by splitting, when the shearing stresses rose significantly due to erosion or excavation of the slope concerned. It is anyway safer to design slopes on (c) and (ϕ) parameters no larger than those obtained from shear tests on continuous joints. The contribution of any failure through intact material is best ignored for design purposes.

The progression of the overstressed zone as excavation (or erosion) proceeds has been illustrated as a possible mechanism for inducing a stepped multi-linear failure surface. (Mode No. 2 Figure 2.3.10). However this mode of failure has been shown to be the most stable when using unchanged peak shear strength parameters.

Consequently a second mechanism of progressive failure has to be invoked to justify consideration of the stepped failure mode. This concerns the effects of displacement and weathering on the shear strength of joints in-situ.

2. Unstable joint characteristics.

The shear strength parameters of rock joints have been idealized to those shown in Figure 2.3.11. The curved peak strength envelope is approximated to a straight line displaying(c)and(ϕ)parameters appropriate to a particular range of normal stress. Since this range is limited at low stress it may be necessary to interpret the curve in a piece-wise linear fashion.

It will be noted that peak shear strength is reached after relatively small shear displacements. In addition the strength can drop significantly for displacements only a little greater than the peak displacements.

However, before peak or residual strength characteristics can be meaningfully applied to parts of an unstable slope, certain questions need to be considered.

1. Can relative shear displacements occur within the overstressed zone of the rock slope before final failure is approached?

2. If so, will the 'slices' at the lower (down dip) ends of the overstressed joints be those most highly overstressing the joints concerned?

Figure 2.3.11. The simplified direct shear characteristics of an interlocking joint surface.

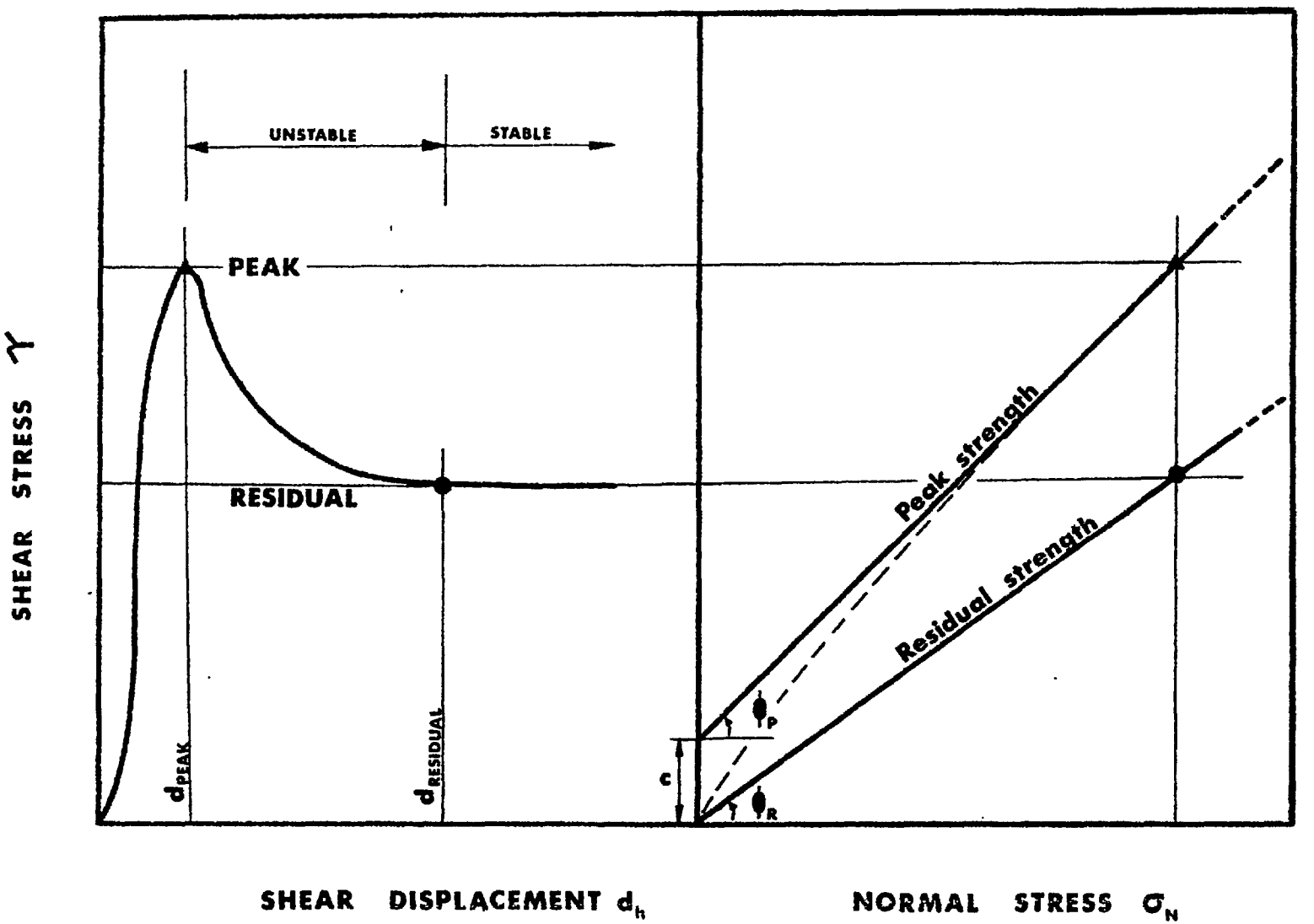

3. Will the fact that parts of the joints became overstressed at a relatively early stage of excavation, mean that their shear strength will have reduced by the time the failure depth is approached?

4. If displacements can occur within the rock slope, will these be large enough for a significant reduction from peak shear strength towards residual strength?

It is believed that the answer to all four questions is yes. However it is realised that positive answers depend upon No. 1 being true. Certain observations can be cited in support.

(a) Mueller[73] has referred to slope bulging in the lower half of rock slopes of from 7 to 8% of the slope height. This exceptional figure was presumably for a slope in an advanced state of collapse.

(b) Tension cracks are regularly found at and behind the crest of slopes. Exceptionally these can be ten or more feet wide. A graben is often in evidence; the unstable portion below the crack having fallen vertically several feet. Ross Brown and Barton[52] recorded vertical and horizontal displacements of 5 and 2 metres respectively, at the crest of a 100 metre high slope that was in the process of failing. Kennedy and Niermeyer[45] recorded vertical and horizontal displacements of up to 2.5 and 5 metres respectively. This was measured on a bench roughly in the middle of the enormous Chuquicamata Slide, approximately two weeks before catastropic failure occurred.

(c) The excavated models reported in Part 3 indicate significant down dip displacements on unfavourably dipping joints. These tended to be greatest where the overburden depth was greatest.

Down dip shearing displacements imply closure of joints in a direction at right angles to the joints, if one assumes zero shear stresses at the free face of the excavation. Figure 2.3.9 illustrates the distribution of shear stress on a typical joint that is obtained when analysing the situation with self weight stress assumptions. The shear stress on AB builds up from zero at the free face (A) to a maximum beneath the crest of the slope. If there are joint sets intersecting AB, then closure across these can be expected, due to the incremental increase in shear stress when proceeding from A towards C. (The effect of shear stress on the pre-peak displacements of model tension joints was given in Section 1.3., Figure 1.3.12. The closure of joints under normal stresses has been discussed in Section 1.4).

In section 2.1 it was shown that small shear displacements across an interlocking joint surface could cause considerable increases in joint volume. (Figures 2.1.12 to 2.1.15). In an area of significant rainfall, this increase in effective permeability would surely accelerate the process of joint weathering. Over a period of time the shear strength of joint walls might be considerably reduced. In view of the fact that open pit mining operations

are frequently in excess of 30 years duration, it is possible that rock slopes could be excavated in which overstressing of the peak strength of the joints initiated ten or more years before the final depth of the pit was reached.

It appears a practical possibility that residual strength could be approached on the critical stepped failure surfaces introduced earlier. From a design point of view such an assumption would surely be a more realistic 'worst case' than assigning a universal residual strength to the whole slope. Even in extreme cases slope failure is hardly a dimensionless problem.

2.3.4 ANALYSIS OF MULTI-LINEAR FAILURE SURFACE

Figure 2.3.12 represents a section through an idealized jointed rock slope. It is assumed that the strike of the joints in relation to the slope face, allows the problem to be analysed in two dimensions. As already indicated this is the worst case from the point of view of stability.

In the absence of computing methods, or simple design charts such as those developed by Hoek[74], the failure depth (H) for a fully drained block TCGD will be found by utilizing equations 10 and 11.

The position of the corresponding tension crack TC can be most easily found by using equation 12 (Markland[60]).

$$\text{Thus: } AT = H\left[\sqrt{\cot\alpha \cdot \cot\beta} - \cot\alpha\right] \qquad (12)$$

The proposed failure surface AEGD conveniently divides the unstable part of the slope into two portions:

1. The block AEGF, lying on the stepped surface EG. The mean dip of EG is parallel to the slope face AF. Since residual strength is envisaged for the stepped surface (for design purposes), it will be termed the 'residual block'.

2. The 'toe triangle' FGD. Peak strength parameters are suggested for the planar surface GD.

Estimation of failure depth for a DRAINED slope

(a) The dimensions of the residual block AEGF are obtained from the geometry of Figure 2.3.12.

$$AB = H(\cot\beta - \cot\alpha)$$

$$TC = TB \cdot \frac{AJ}{AB}$$

$$AE = TC = \frac{H(1-\cot\alpha \cdot \tan\beta)(\cot\beta - \sqrt{\cot\alpha \cdot \cot\beta})}{(\cot\beta - \cot\alpha)} \qquad (13)$$

Figure 2.3.12 The geometry of the multi-linear failure surface.

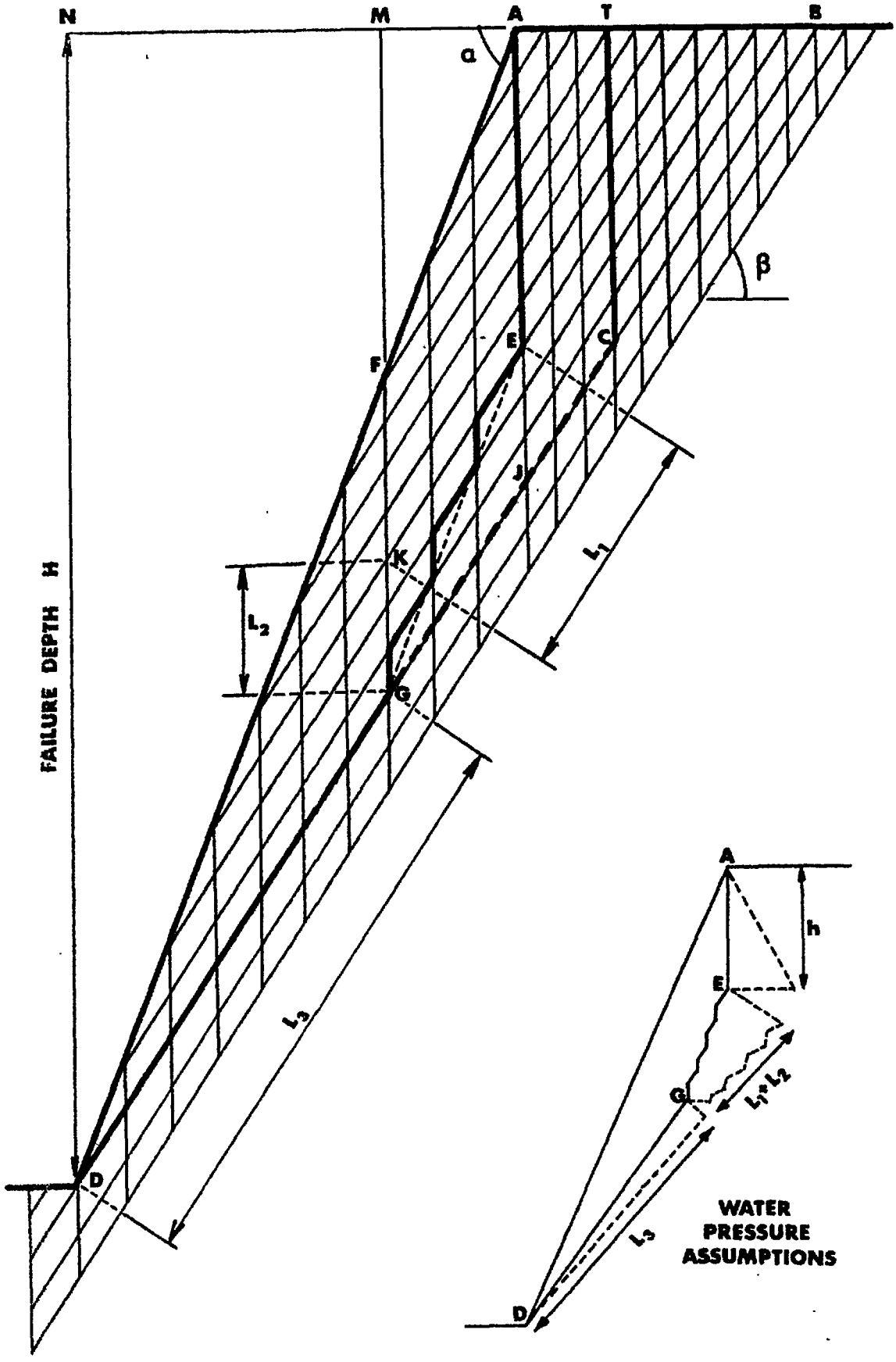

$$NA = H \cot\alpha$$

$$MA = NA. \frac{EJ}{AJ} = NA. \frac{AT}{AB}$$

$$MA = \frac{H \cot\alpha \left(\sqrt{\cot\alpha . \cot\beta} - \cot\alpha\right)}{(\cot\beta - \cot\alpha)} \qquad (14)$$

Since AE = FG

1. the area of the 'residual block' AEGF = AE.MA
2. the length of shear surface beneath it = L_1
   where $L_1 = MA. \sec\beta$

The unstable excess (P_1) of this block is given by equation 6, thus:

$$P_1 = W_1 \cos\beta \left[\tan\phi_r - \tan\beta\right] \qquad (15)$$

(Note residual parameters: $\phi = \phi_r$, $c = 0$.)

(b) The dimensions of the toe triangle FGD are obtained in a similar manner:

FG = AE = TC (equation 13)

$$NM = NA. \frac{TB}{AB} = \frac{H \cot\alpha (\cot\beta - \sqrt{\cot\alpha . \cot\beta})}{(\cot\beta - \cot\alpha)} \qquad (16)$$

1. the area of the 'toe triangle' FGD = $\frac{1}{2}$. FG. NM
2. the length of shear surface beneath it = L_3
   where $L_3 = NM. \sec\beta$

If peak strength parameters are assumed for the surface DG, then the stable excess (P_3) is given by:-

$$P_3 = W_3 \cos\beta \left[\tan\phi_p - \tan\beta\right] + cL_3 \qquad (17)$$

For complete failure on the multi linear surface AEGD, the unstable excess of the residual block must just exceed the stable excess for the toe triangle. At limiting conditions:

$$P_1 + P_3 = 0$$

The failure depth is most simply obtained when equations 13 to 17 are evaluated in general terms, with H the unknown. Several values of H can then be tried (all less than for block TCGD).

A graph of stable or unstable excess plotted against depth H will give an intercept P = 0 at the required failure depth. (see Figure 2.3.7 for example).

Estimation of failure depth for a TRANSIENT WATER PRESSURE assumption

It is believed that the above assumption of residual shear strength for the stepped portion of the failure surface represents a realistic 'worst case' for design purposes. However there are many situations which also require pessimistic assumptions for possible water pressure distributions. Of the five slope failures investigated in the Rio Tinto area of southern Spain (Ross Brown and Barton[52]), three were almost certainly caused by the surface run off entering tension cracks through fractured drainage routes. (See Section 2.2.). The possibility of tension cracks becoming filled with water must therefore be considered in areas where flash floods and consequent transient water pressures can be anticipated.

The water pressure distribution assumed as one possible 'worst case' is shown in the inset to Figure 2.3.12. The full tension crack generates a hydrostatic pressure at its base of:

$$U_w = h\gamma_w$$

where h the depth of crack is given by equation 13, and γ_w is the density of water. It is assumed that this pressure reduces linearly in proportion to the length of drainage path, such that at D the exit seepage pressure is zero. It may be optimistic to expect constant permeability down the length of EGD. However there are in reality an infinite variety of possible assumptions. A tension crack only partially filled with water, and a reduced permeability along EGD is an alternative which could generate equal instability to the one assumed.

Some attention may need to be paid to the equilibrium of the slide mass, since a severe assumption of water pressure can lead to zero effective pressures across the potential shear surfaces. Whether this could be expected at failure is not known.

From the geometry of Figure 2.3.12:-

1) Depth of tension crack h = AE=TC (equation 13)

2) Length of inclined surface L_1 = MA. $\sec\beta$ (equation 14)

3) Total length of vertical steps between E and G = L_2

where L_2 = EJ = AJ. $\frac{AT}{AB}$

$$\therefore L_2 = \frac{H(1-\cot\alpha.\tan\beta)\left(\sqrt{\cot\alpha.\cot\beta}-\cot\alpha\right)}{(\cot\beta-\cot\alpha)} \qquad (18)$$

4) Length of inclined surface between G and D = L_3

where L_3 = NM. sec β (equation 16)

The mean water pressures assumed to act on the four surfaces above are as follows:

1) AE (length h) $U_w = \frac{1}{2}h\gamma_w$ _____ (19)

This has force components perpendicular and parallel to the dip direction (3) of:

(a) $\frac{1}{2}h^2\gamma_w \sin\beta$

(b) $\frac{1}{2}h^2\gamma_w \cos\beta$

2) EG (length $L_1 + L_2$)
Since the pressure at G is $\left[\frac{L_3}{L_1 + L_2 + L_3}\right] h\gamma_w$

the mean water pressure between E and G is:

$$\left[\frac{L_1 + L_2 + 2L_3}{L_1 + L_2 + L_3}\right] \frac{h\gamma_w}{2} \quad \text{_____ (20)}$$

(a) This is distributed on the vertical steps of length L_2 with components sin β and cos β as before (1).
(b) It is also distributed on the inclined surfaces of length L_1. (Perpendicular component only).

3) GD (length L_3)
The mean water pressure is $\left[\frac{L_3}{L_1 + L_2 + L_3}\right] \frac{h\gamma_w}{2}$ _____ (21)

The failure depth for these transient water pressure assumptions is obtained by calculating the unstable excess (P_1) of the residual block AEGF, and the stable excess (P_3) of the toe triangle FGD. Once again, at failure:

$$P_1 + P_3 = 0$$

The limiting equilibrium equation for the residual block can be derived from equation 6. The tangent of the friction angle is equated to the ratio of forces acting parallel to the dip (β), and those acting perpendicular to it, thus:

$$\tan\phi = \frac{W_1 \sin\beta + \frac{1}{2}h^2\gamma_w \cos\beta + \left[\frac{L_1 + L_2 + 2L_3}{L_1 + L_2 + L_3}\right] \frac{h\gamma_w}{2} L_2 \cos\beta - cL_1 + P_1}{W_1 \cos\beta - \frac{1}{2}h^2\gamma_w \sin\beta - \left[\frac{L_1 + L_2 + 2L_3}{L_1 + L_2 + L_3}\right] \frac{h\gamma_w}{2} L_2 \sin\beta - \left[\frac{L_1 + L_2 + 2L_3}{L_1 + L_2 + L_3}\right] \frac{h\gamma_w L_1}{2}} \quad \text{_____ (22)}$$

Hence P_1. Note: For residual parameters, $\phi = \phi_r$, c = o.
The limiting equilibrium equation for the toe triangle is:

$$\tan\phi_p = \frac{W_3 \sin\beta - cL_3 + P_3}{W_3 \cos\beta - \left[\frac{L_3}{L_1 + L_2 + L_3}\right]\frac{\gamma_w . h L_3}{2}} \qquad (23)$$

Worked example

The parameters of worked example No. 1 will be used to illustrate the effects of the given failure mode on stability. (See Figure 2.3.6)

$\alpha = 60^o$ $\quad \phi_p = 45^o \quad p = 160$ lbf/ft^2 per ft.
$\beta = 50^o$ $\quad c = 1975$ lbf/ft. per ft.

The residual shear strength parameters will be assumed as follows:

$$\phi = 30^o, \; c = 0$$

Substitution of the peak shear strength parameters resulted in the following estimates of failure depth. (See Figure 2.3.12 for lettering).

1. Coherent wedge ABD sliding on plane DB with no tension crack. H = 1000 feet. Fully drained. Equation 7.

2. Block ATCD. Method of slices and tension crack separation. H = 915 feet. Fully drained. Equations 10 and 11

Equations 13 to 17 were used to calculate the failure depth for the assumption of a multi-linear failure surface, with residual strength on the stepped surface between E and G. With the given geometry, and fully drained conditions:

3.
AE = 0.171 H feet
MA = 0.264 H feet
$P_1 = (-)2.84\ H^2$ lbf/foot. (unstable)

NM = 0.314 H feet
L_3 = 0.489 H feet
$P_3 = 965\ H - 0.524\ H^2$ lbf/foot.

$\Sigma P = P_1 + P_3 = 965\ H - 3.364\ H^2$ lbf/foot.

A graph of ΣP versus H gives the failure depth as 290 feet.

Equations 18 to 23 were used to calculate the failure depth for the transient water pressure assumptions. Once again residual parameters were taken to describe the remaining shear strength on the stepped part of the failure surface.

L_1 = 0.264 H feet
L_2 = 0.143 H feet

$$P_1 = (-)\ 6.92H^2 \text{ lbf/foot}$$
$$P_3 = 965\ H - 1.747\ H^2 \text{ lbf/foot}$$
$$\Sigma P = P_1 + P_3 = 965\ H - 8.587\ H^2 \text{ lbf/foot}$$

A graph of ΣP versus H gives the failure depth as 115 feet.

It should be noted that the above assumption of a full tension crack (for a given geometry and density) generated such high water pressures that the effective normal stress on the inclined shear surfaces below the residual block just became negative. In other words the shear strength assumptions for this surface became meaningless. However the effective normal stresses beneath the toe triangle remained positive with the given seepage assumption.

It may be argued that this state of affairs is preferable to one in which poor drainage causes the two triangle to 'float'. However this only serves to highlight the uncertainties of what form stress distributions can take at failure. An effective normal stress reducing to zero is certainly an ideal failure mechanism. Is it right to reject it purely from a subjective assessment of what seems possible?

In conclusion the following observations should be made as qualifications to the multi-linear failure mode:

1. The ratio of the depth of tension crack (TC) to the depth of the shear surface beneath the crest (AJ) was found by a limit analysis. This was performed with the assumption of drained conditions, and for a particular geometry.

   The ratio determined what proportion of the total shear surface ($L_1 + L_3$) was stepped (L_1). This proportion was assumed constant for a given geometry for all states of stress. In other words, for all conditions which produced failure, a geometrically similar shear surface was assumed.

2. The concept of a multi-linear failure mode was based on the effect of excavation on the overstressing of joints. The weakening mechanisms of time and displacement were introduced to predict a failure surface with a stepped portion of reduced strength.

   The adoption of residual strength for this part of the failure surface led to considerably reduced failure depths. (i.e. 915 feet down to 290 feet). Paradoxically, if the slope was designed to the reduced height in the first instance, then in all probability the stepped/residual mode would not initiate. Consequently the proposed methods are conservative, and serve to emphasize the severity of a residual strength assumption.

PART 3

3.1 OBSERVATIONAL BEHAVIOUR OF MODEL SLOPES ROTATED TO INDUCE FAILURE

SUMMARY

Small jointed slope models were constructed from fractured, 1 inch thick slabs of model material. These were inserted into two dimensional frames for tilting experiments. The models were rotated in a vertical plane from a stable position, until the ratio of shear and normal stresses reached a critical value on steeply dipping joints. The failure mechanism was studied on enlargements of successive frames of a cine film, run at between 18 and 30 frames per second.

The following effects were studied:

1. Different angles of intersection between primary and secondary joints.

2. Different orientations of joints with respect to the slope.

3. Models with and without vertically dipping joints at failure.

The only irrecoverable effect of a rotating stress distribution appeared to be the opening of tension cracks in positions which were no longer optimal when failure occurred. Back analyses of simple planar shear failures were performed and compared with the direct shear tests on single joints in the same material.

Three principle failure modes were recognised; translational shear, translational shear with tensile opening, and toppling shear. The first two were caused by the absence or presence respectively, of joints within a few degrees of vertical when failure occurred. Only then could tension cracks open up prior to failure, thus separating the sliding mass from the stable remainder. One joint set dipping steeply into the slope and a second set near vertical represented the least stable configuration possible.

Toppling failure is discussed with respect to recent analytical and numerical studies of idealized block models. It is concluded that, other than for planar weathered joints, or for loosened blast shattered rock, toppling shear is a self inhibiting mechanism, in view of the dilatency of joints in shear.

3.1 OBSERVATIONAL BEHAVIOUR OF MODEL SLOPES ROTATED TO INDUCE FAILURE

INTRODUCTION

Part 3 of this thesis is devoted to observations of jointed model slopes which were induced to fail by two methods of gravity loading:

1. Rotating two dimensional jointed models about a perpendicular axis so that the shear stresses on unfavourably dipping joints reached their limiting value. These models were cut to the required slope and joint angles before being inserted into 'tilt frames', for controlled rotation.

2. Physically excavating slopes in pre-loaded jointed models, until the slope height or angle became critical and caused failure. These models were very large and only a limited number could be tested.

The philosophy, test proceedures, and observations of failure of the large excavated models are presented in Sections 3.2 and 3.3. The present section will be devoted to observations of a few simple modes of failure which were induced by different joint orientations and slope angles. Experience gained from these small scale slope failures helped to define the best approach for design of the joint patterns in the large excavated models.

Appendix 3 contains a summary of the sequence of operations that were required for production of jointed slabs of model material on the large guillotine.

The construction of jointed models for tilting experiments provided valuable experience in this respect. Due to the delicate nature of the material it was several months before joint production became a routine operation. One of the tilt models will be presented as an example of the problems that can occur.

The failures were recorded on cine film, and most of the figures to be presented are prints of consecutive frames. The first series of models were recorded on 8 mm. film, which was unfortunate in view of the limited clarity of the resulting enlargements. Consequently 16 mm. film was used and in general this produced satisfactory results. The record of one or two failures were almost lost due to incorrect exposure when changing from colour to black and white film. The bright orange colour of the models needs to be test photographed before embarking on a series of experimental recordings.

The presentation will be chiefly in visual form, with brief comments on each mode of failure. Dominant modes will be summarized at the end of the section.

3.1.1 A SELF WEIGHT SHEAR MODEL.

Figure 3.1.1 illustrates stages in the construction of a diamond shaped jointed shear model. Orthogonal jointing was tested initially, and the character of the two joint sets is shown in the first two diagrams. The primary joints (1) which were generated first are seen to be continuous, while the secondary joints (2) are effectively offset when crossing the existing joints, and result in an interlocked higher strength surface.

Diagram C shows a model cut to shape before inversion into the perspex and aluminium tilting frame. The unusual design was for the following reasons:

1. To support the model in a stable un-titled position with zero shear stress on the primary joints.

2. To develop uniform shear and normal stresses on the primary joints when tilted 45° to the approximate anticipated failure angle.

3. To rigidly support the toe of the slope and be adjustable so that different overburdens could be shear tested.

The frame was tilted in a vertical plane by rotating a screw thread. The angle of tilt was measured with a plumb bob and angular scale, and could be seen in the cine films as a check on the reading taken at failure.

The frame was designed concurrently with a test programme of direct shear tests on individual joints. It was intended as a check on the shear strength of a jointed mass compared to individual joints, since the effect of progressive failure was unknown at this stage. As it turned out, the shear strength of the joints was too high for shear failure to occur with the designed maximum 'overburden' of sixteen blocks. The jointed structures were still unsheared when the frame was tilted to a 45° dip on the primary joints, and most failures were recorded when the dip was approximately 60°. Consequently the shear and normal stresses were not as uniform as had been hoped, since shear failure occurred when the front of the model was overhanging by approximately 15°, with a converse effect at the rear. However, as will be seen later, the results were comparable with conventional direct shear tests, and it is arguable that the stresses were as good as those operating in the conventional test with its known limitations.

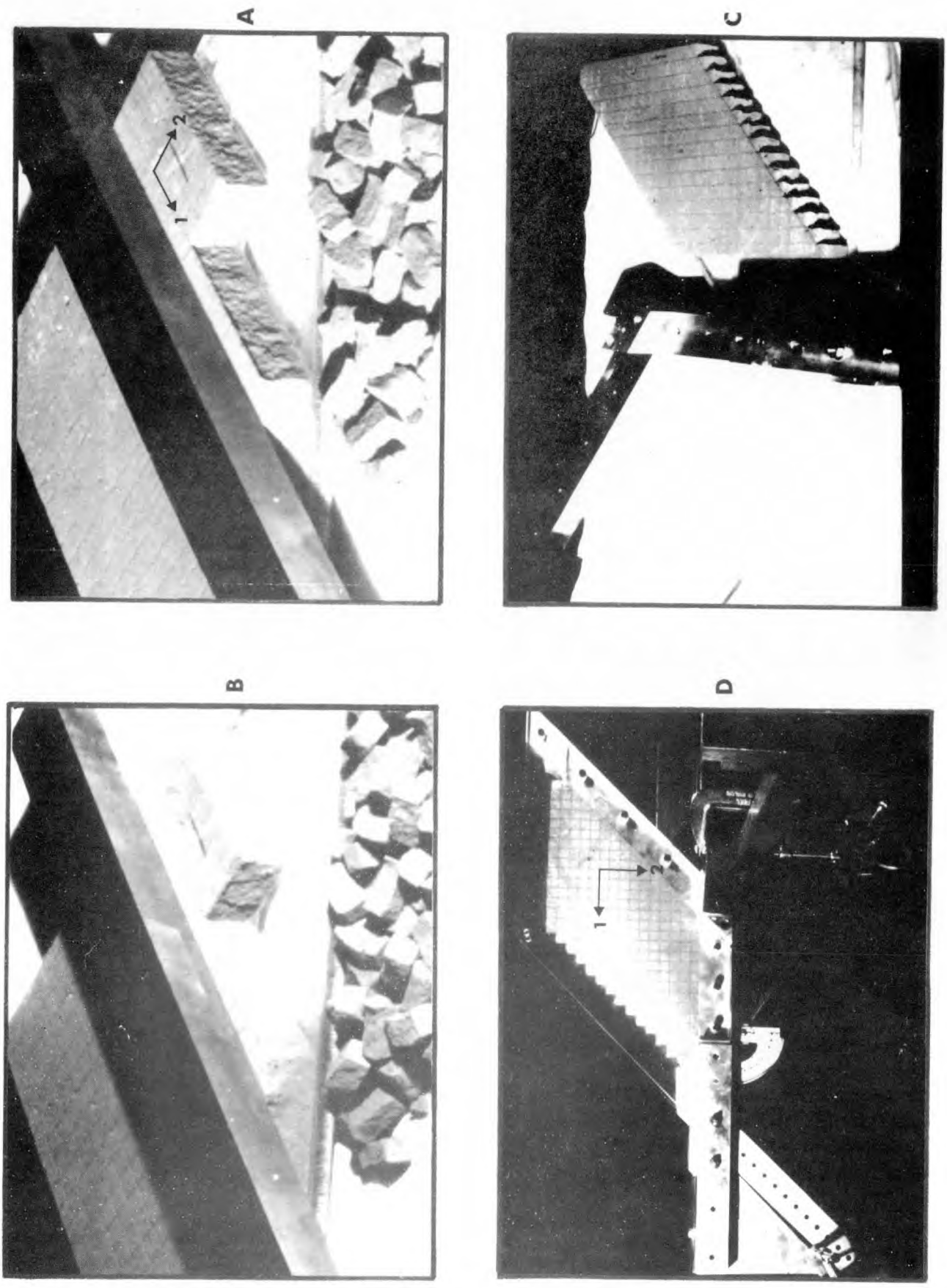

Figure 3.1.1 Construction of a jointed tilt model

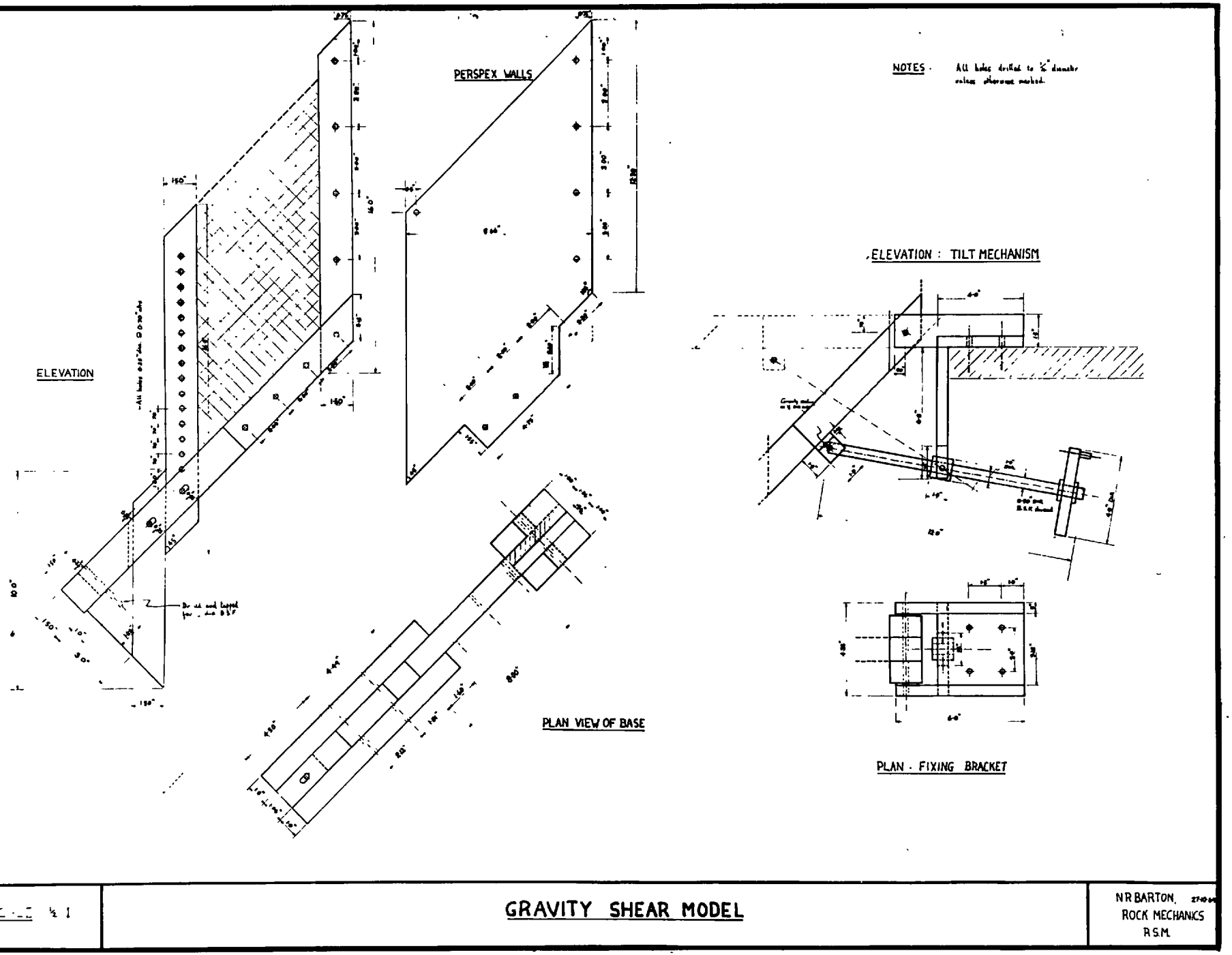

Figure 3.1.1 (E) Design drawings of gravity shear model.

Figure 3.1.2 Tilt model M.17 (30 frames per sec.)

The nomenclature of this and later figures is as follows:

1. The numbers land 2 with dense arrows refer to the primary and secondary joint directions respectively.

2. The unshaded arrow refers to the direction of gravity.

3. The angle of dip of the critically dipping joints is given in degrees. Where a sequence photograph is unmarked, an unchanged angle of dip is implied.

All models had a joint spacing of $\frac{1}{2}$ inch.

Mode: Planar shear failure on the primary joint that was most highly stressed. The two joints below this were rigidly fixed at the toe. No joints were near vertical when failure occurred, and consequently no 'tension cracks' opened.

Total Time (secs.)	Total displacement (ins.)
0	0
1/30	0.059
1/15	0.312
1/10	0.742
2/15	1.500

Figure 3.1.3 Tilt model M.3 (18 frames per sec.)

The secondary offset joints were the critical ones for this model. The overburden was approximately 15% increased compared to the previous figure, and shear failure occurred for more or less the same angle of dip.

Mode: The interesting feature was the stepped mode of failure which initiated beneath the point of maximum overburden depth. Tensile opening on the primary joints occurred more easily in this case, than tensile opening on the interlocked secondary joints of the previous failure. Hence the whole mass was able to separate so that shearing occurred along the stepped surface which was most highly stressed. Note the shear displacements of diagram A causing separation at the back of the model. It is probable that small shear displacements were occurring on all the dipping joints since the ratio of shear stress to normal stress was more or less the same for each (= tan $60\frac{1}{2}^{\circ}$).

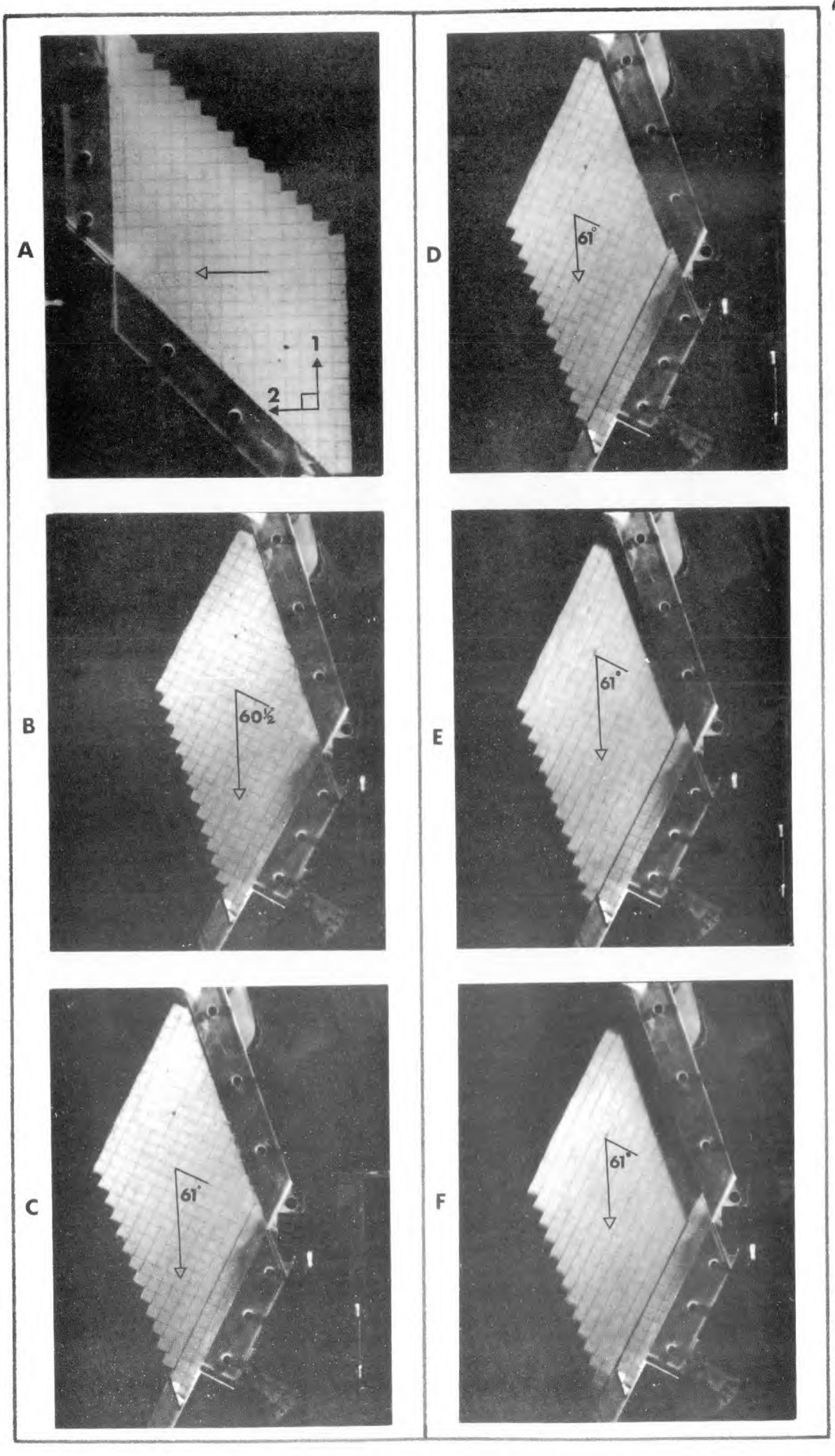

Figure 3.1.2 Tilt model M.17. Linear failure on primary joint

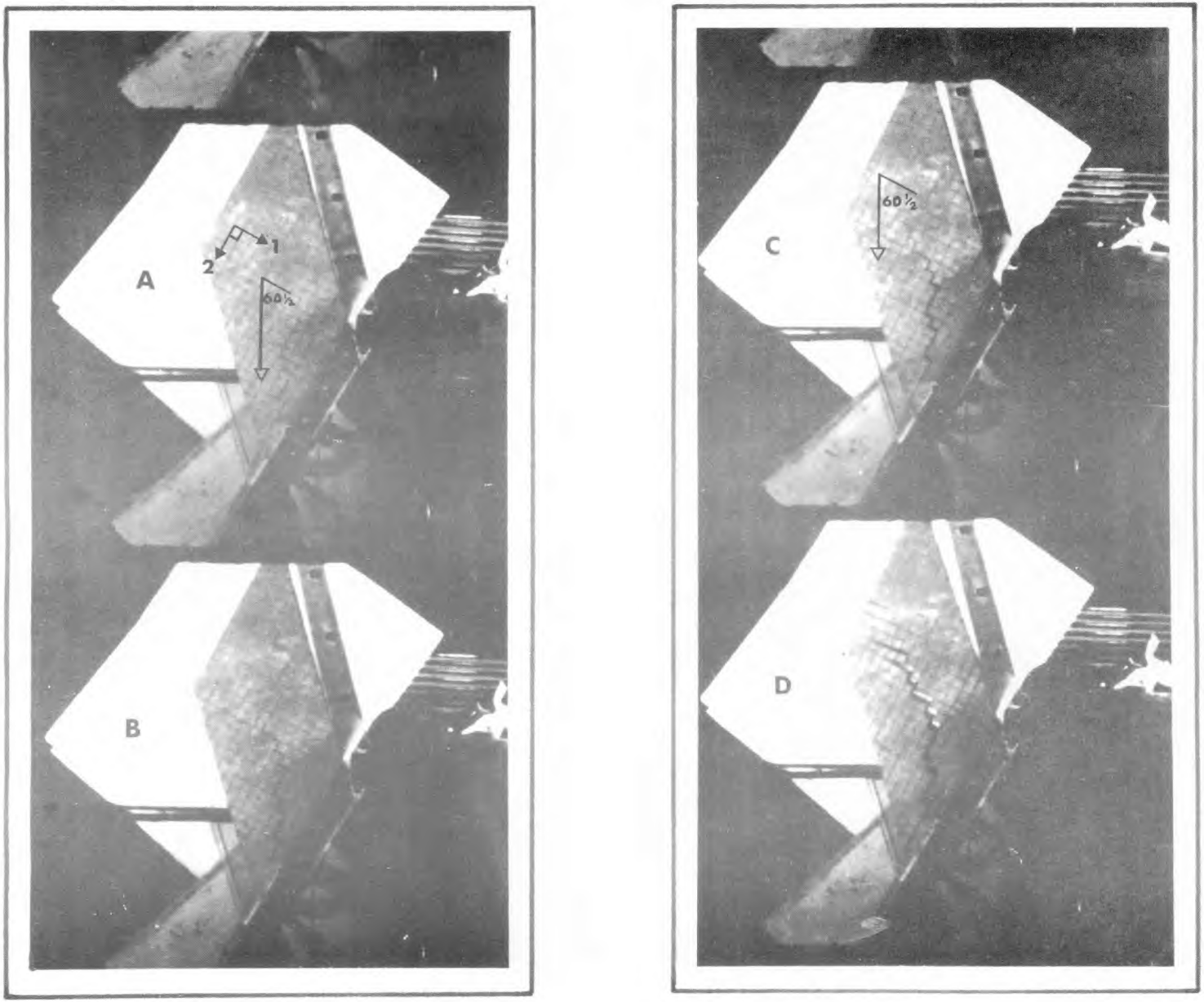

Figure 3.1.3 Tilt model M.3. Multi-linear failure on secondary joints

---

Figure 3.1.4 Tilt model M.5 (24 frames per sec)

The secondary joint set was less than 10° from vertical when failure occurred, and consequently tensile opening was possible on these joints despite possible interlocking.

Mode: The tension crack six blocks from the front of the model opened when the dip of the primary joints was 43°. It remained open right up to the point of shear failure on the primary joints, after a further 9° of rotation. When the dip was increased a further $3\frac{1}{2}$°, failure initiated once again by shearing, before any toppling mode. A toppling mode of failure relies on relative slip across the secondary joints. Since the shear strength of this set is greater than that of the primary, toppling failure cannot occur unless the secondary joints become loosened or open.

Figure 3.1.5 Tilt model M.6 (24 frames per sec)

Identical jointing to the previous model. Tension crack formation a few degrees before the joint reached vertical.

Mode: Once again frontal shear failure occurred. It is probable that this only occurs in the front half of the model, since greater loosening of the secondary joints can occur there. This loosening progressed in the upper half of the model and resulted in a pure toppling mode seen in progress in diagram D.

Note the manner in which the toe of the shearing mass kicks out relative to its centre of gravity. This is undoubtedly caused by the unstable joint strength. The drop from peak to residual shear resistance results in an acceleration of the toe since the shearing force remains more or less constant.

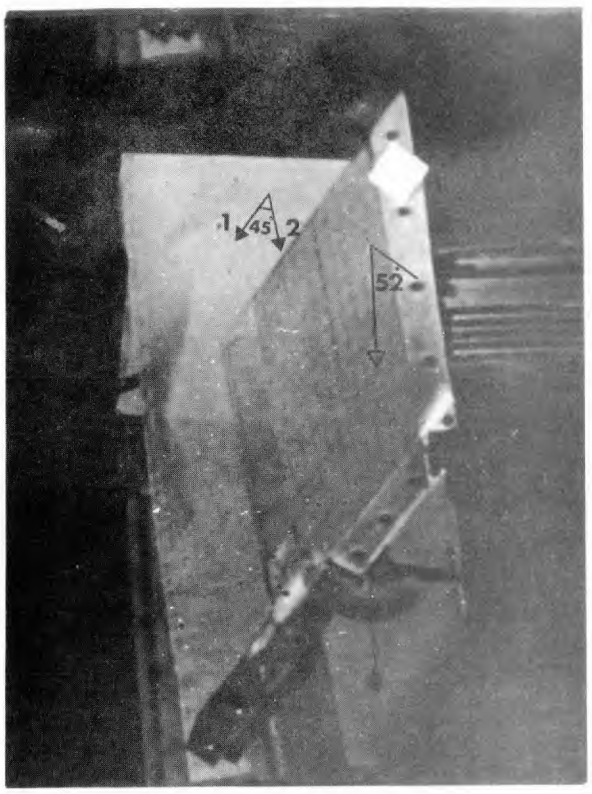

A

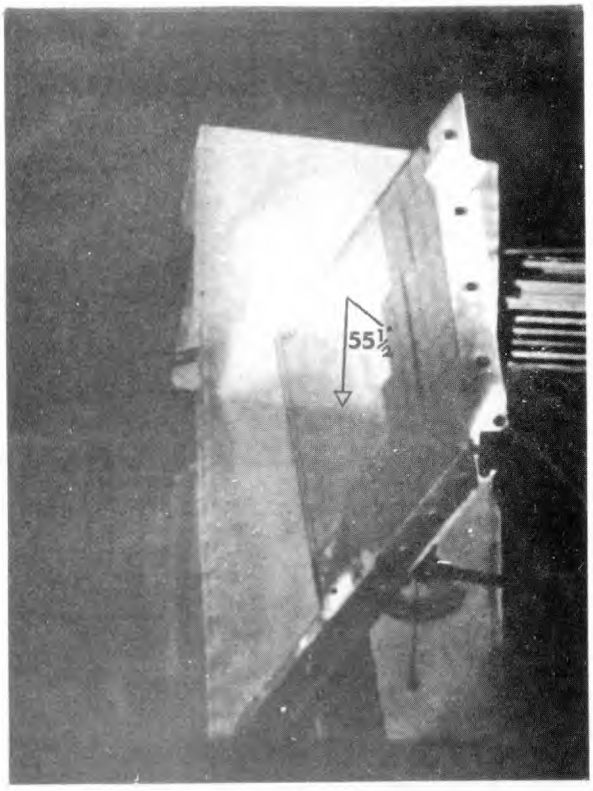

C

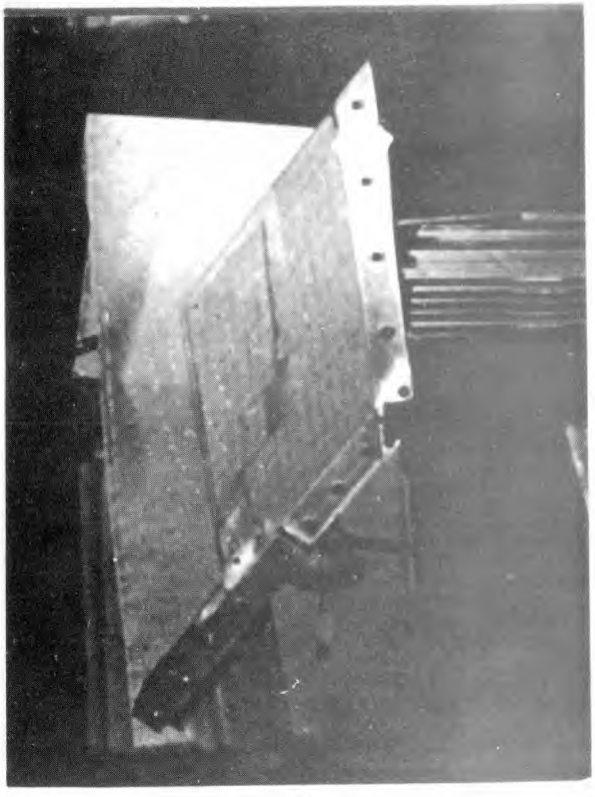

B

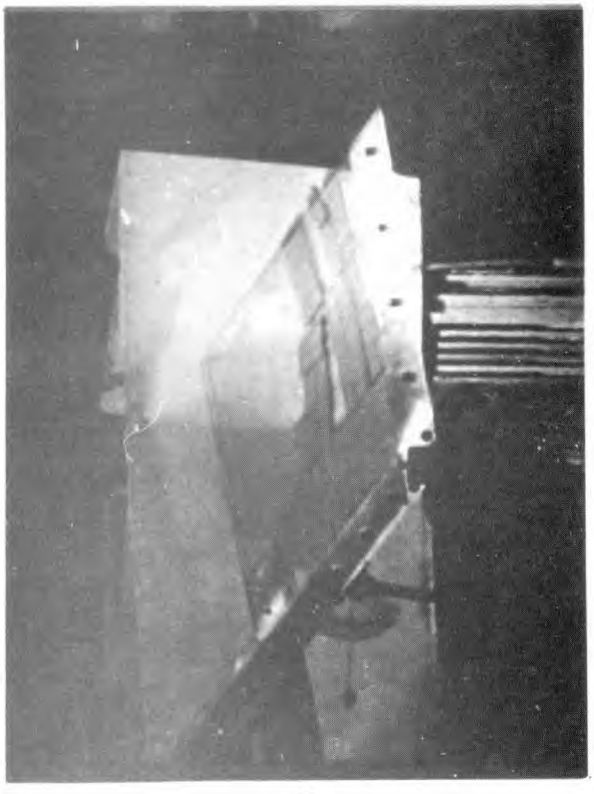

D

Figure 3.1.4 Tilt model 3.5. Shear failure on primary joints. Tensile opening of secondary joints

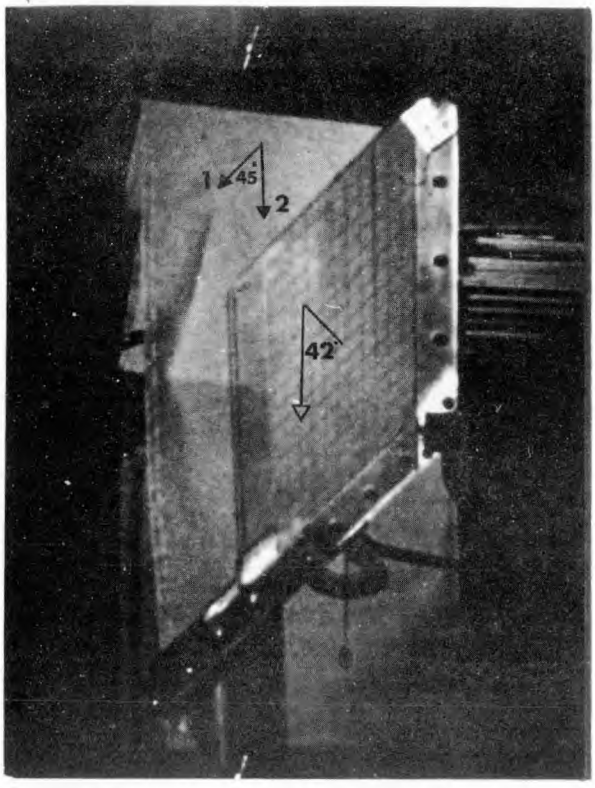

A

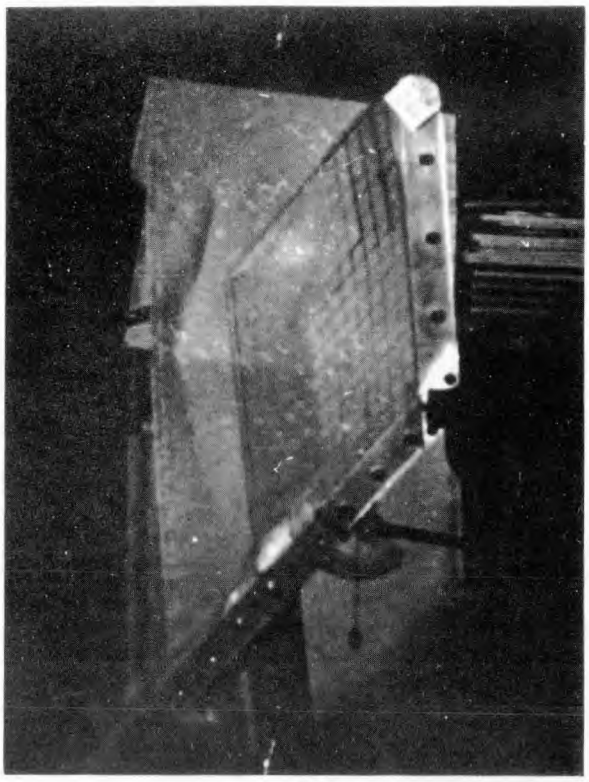

C

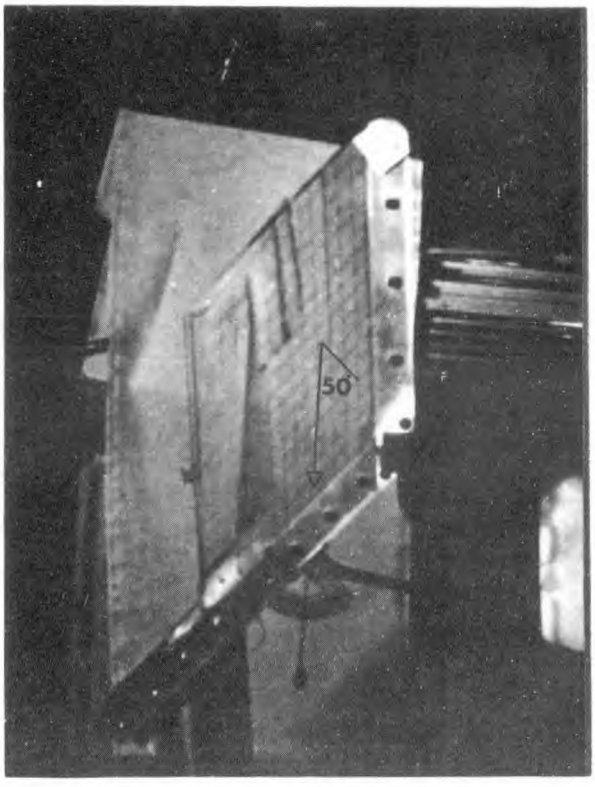

B

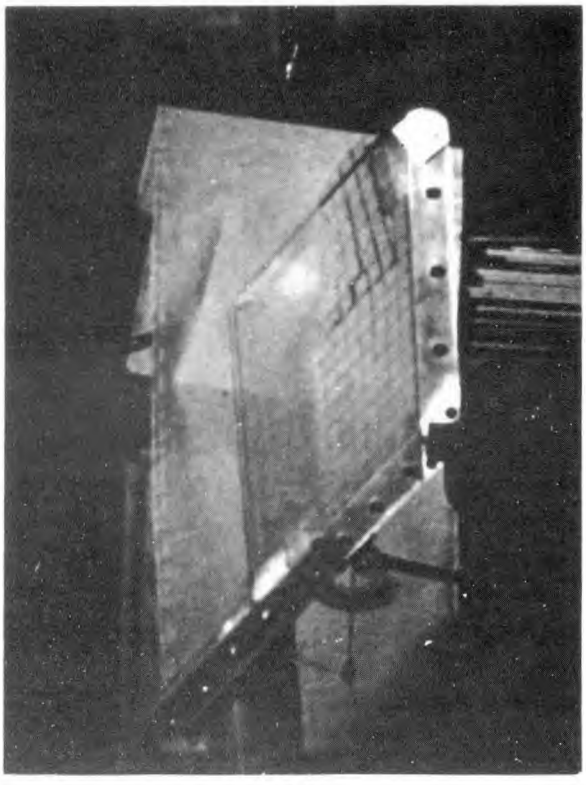

D

Figure 3.1.5 Tilt model M.6. Shear failure on primary joints. Tensile opening of secondary joints.

Figure 3.1.6 Tilt model M.7 (24 frames per sec.)

In contrast to the two previous models the lower strength primary joints were the near vertical set. Consequently relative shearing and opening could occur on these joints more easily than shear failure on the secondary joints, even though these dipped at 52° when failure occurred.

Mode: Classical toppling failure beginning at the front of the model and progressing backwards and upwards. There appears to be some limit on the height of column that can topple in a 'uniform' manner before a hinge develops. This is probably related to the limited loosening that can occur at depth.

Figure 3.1.7 Tilt model M.8 (24 frames per sec)

Joint orientations were chosen such that shear failure on a single joint set was impossible. This model was only comparable with the previous in that both had near vertical primary joint sets. The secondary set dipped away from the slope in this case.

Mode: A preliminary frontal toppling occured at about the same angle as in the previous model. However the different orientation of the secondary set appeared to inhibit a further toppling failure. It was noticeable that the vertical joints were tending to open in tension when the model was a few degrees on either side of a 45° dip (vertical primary joints). Further tilting caused these slightly open joints to close, and the steady increase in normal stress across them inhibited opening until final collapse when the angle of dip was up to 63°. A limited toppling mode occurred, with relative shear on a small number of steeply dipping joints. A jagged hinge is just appearing in diagram C.

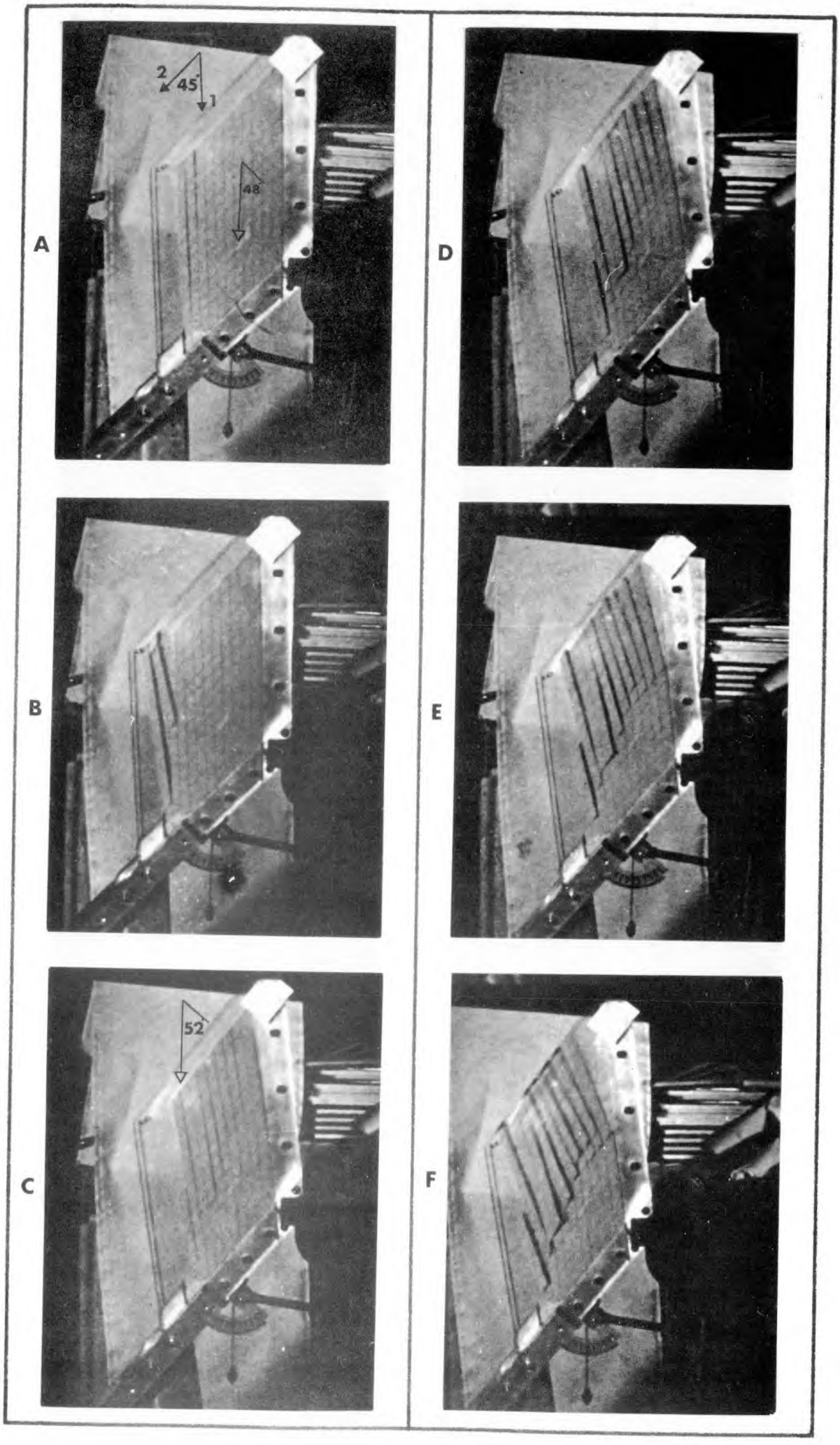

Figure 3.1.6 Tilt model M.7. Opening of primary joints causing a multiple toppling failure

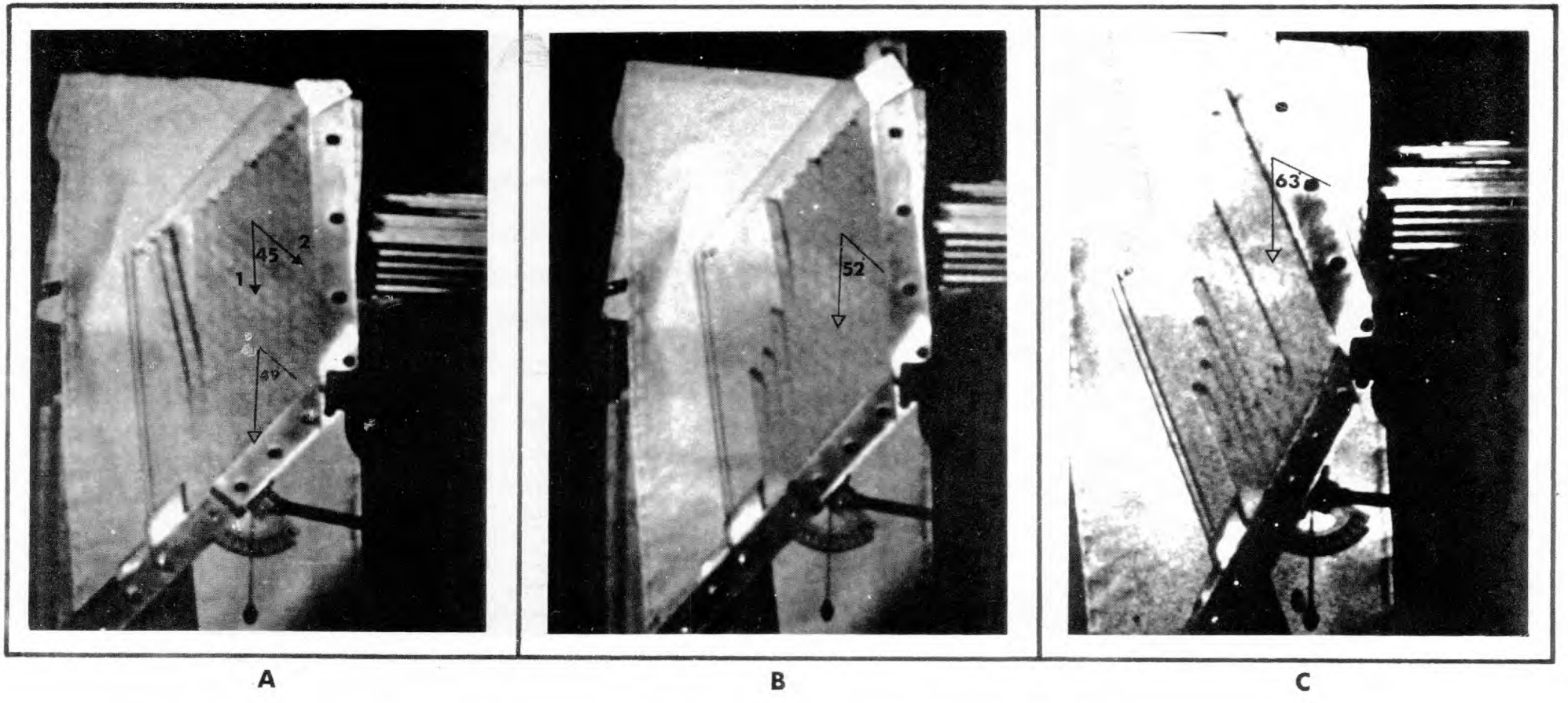

Figure 3.1.7 Tilt model M.8. Eventual toppling failure of stable configuration of joints

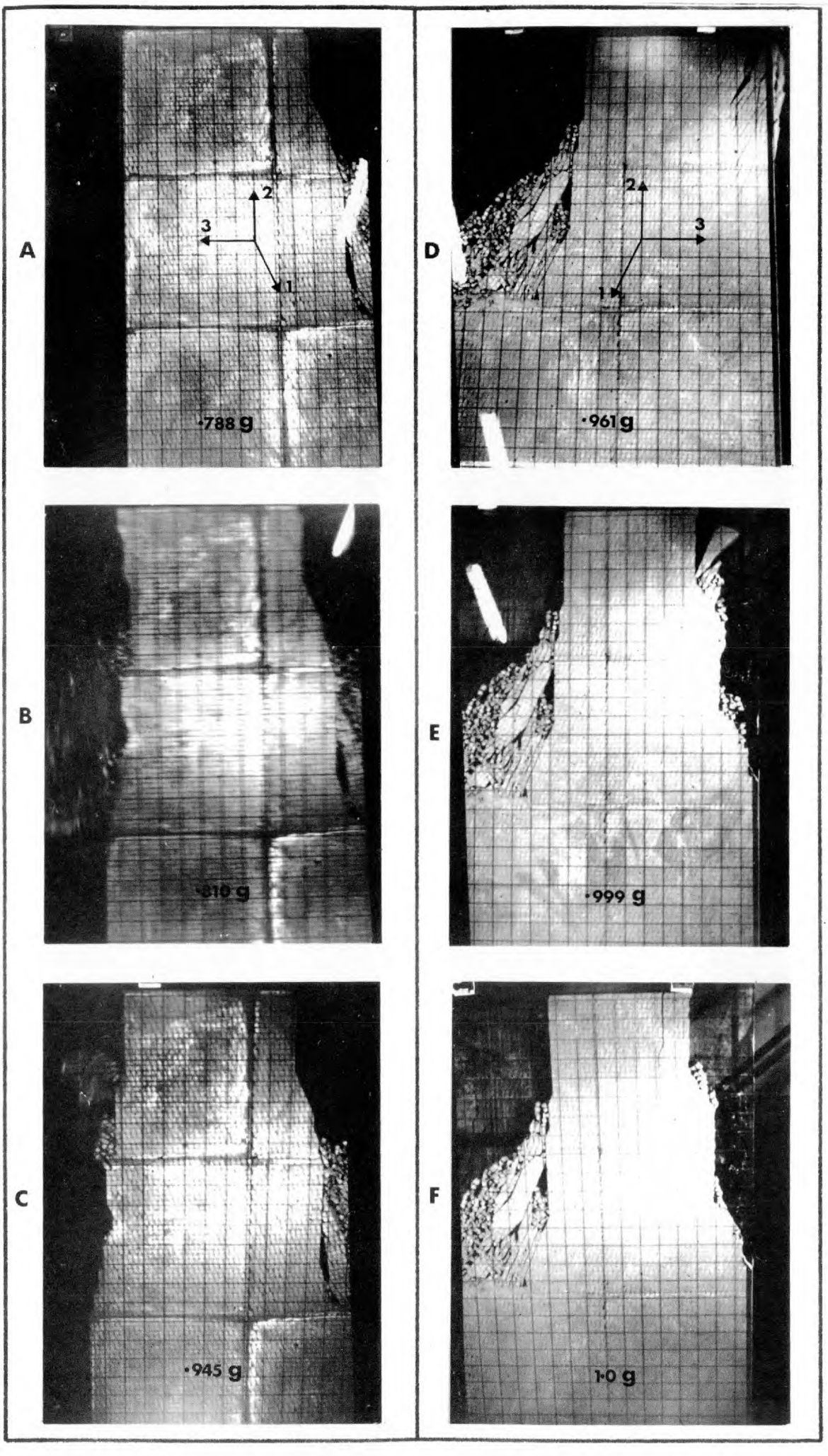

Figure 3.1.8 Failures induced in an unsupported edge when rotating the large model frame into a vertical plane.

Figure 3.1.8 Demolition failures of one large excavated model

The two sets of photographs A,B,C and D,E,F represent the left and right hand edges of one of the large models to be reported in Section 3.3. Failures induced by excavation when in a vertical plane can be seen on the inside. The object of the present excercise was to rotate the whole model into a horizontal plane, remove the edge supports, and then rotate the model slowly back into the vertical. In this way an increasing gravity field was simulated, which was proportional to the sine of the angle of tilt, if friction between the model and the glass walls (12°) was ignored.

For convenience each side of the model was studied separately, hence the different proportions of gravity.

Mode: Conventional shear failure was impossible with the given joint orientations. The mode of failure was primarily one of relative shear along the primary joint directions, thus causing dilation and consequent toppling failure. Both slides eventually reached a stable slope through a series of limited toppling failures. The height of the model was 4 feet.

3.1.2 SMALL TILT MODELS OF STEEP SLOPES

A series of tests were performed on jointed models that were pre-cut to resemble steep slopes. Different joint orientations were tested ranging from about 75° down to 20° of angle of intersection. The models were cut from one 16 inch by 16 inch by 1 inch slab. Unfortunately this limitation on size meant that, with the given slope angle relative to the primary joint dip, shear failure did not occur until the slopes were tilted almost vertically.

Figure 3.1.9 Tilt model M.9 (24 frames per sec)

Diagram A shows the model with the primary joints horizontal and therefore unstressed in shear. The lowermost joint is rigidly held at the toe. This can be likened to the base of a slope where the unexcavated rock acts as a buttress to all dipping joints that have not been exposed by excavation. An attempt was made to improve these artificial boundary conditions by placing the model on $\frac{1}{8}$ inch strips of sponge rubber which were cemented to the perspex base. This was highly frictional and hopefully it helped to distribute the shear and normal stresses in a reasonably uniform manner.

Mode: Unfortunately the cine film was not running when failure initiated. Diagram B shows that some failure had occured at the toe where the overburden depth was greatest. The formation of a bilinear tension crack involved opening of the secondary joint set, and shearing at low normal stress on the uppermost primary surface. In other words the given joint system could be expected to exhibit a tensile strength greater than zero across any vertical plane. From what can be seen of the sliding mass in diagram C, failure appears to have occurred by shearing along the primary joint. No toppling failure is in evidence. The small amount of slope left standing after collapse suggests that the mass did indeed have some tensile strength since the shear strength of the joints would normally support a higher rear face to the slide.

Figure 3.1.10 Tilt model M.10 (24 frames per sec.)

Mode: The tensile strength of potential vertical tension cracks is again illustrated. The secondary joints dip away from the slope at such a shallow angle that any opening is followed by overturning and complete failure occurs with no rear face left standing.

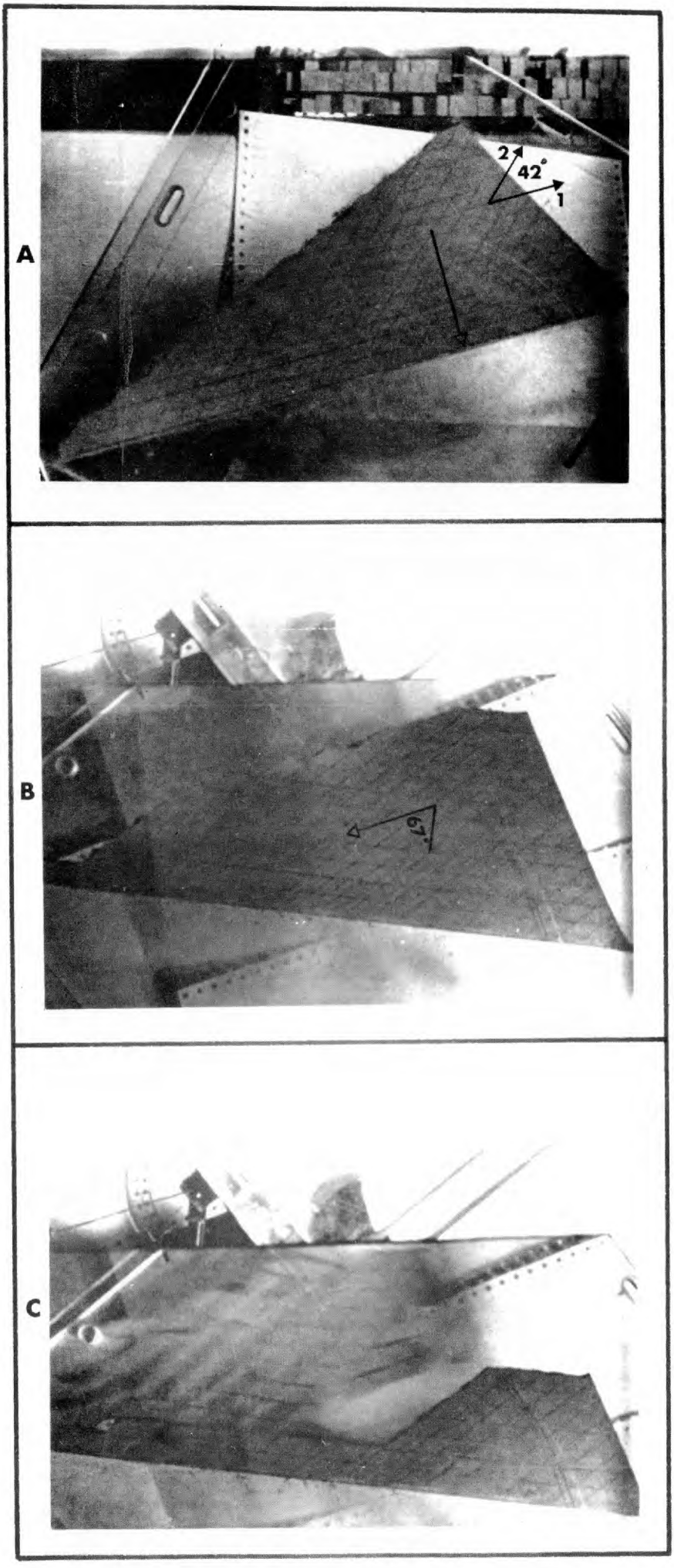

Figure 3.1.9 Tilt model M.9. Shear failure on primary joints with opening on a bilinear tension crack.

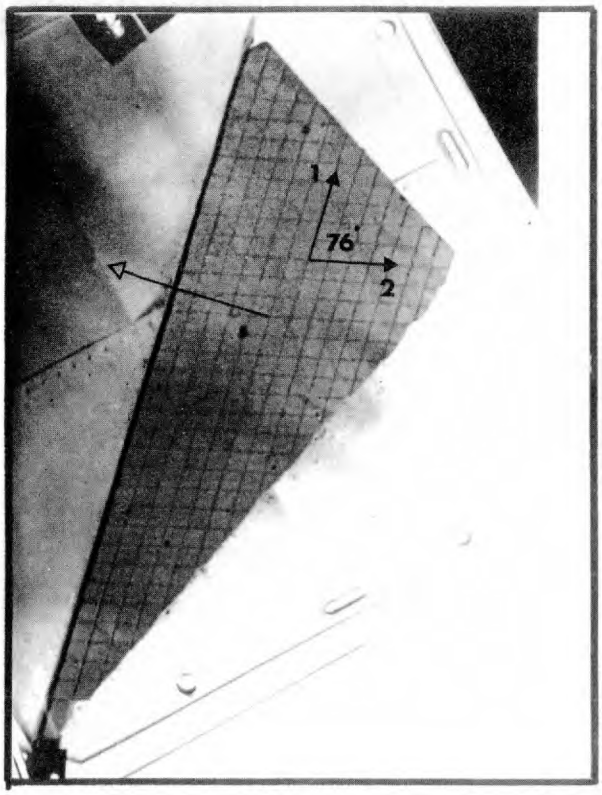

A

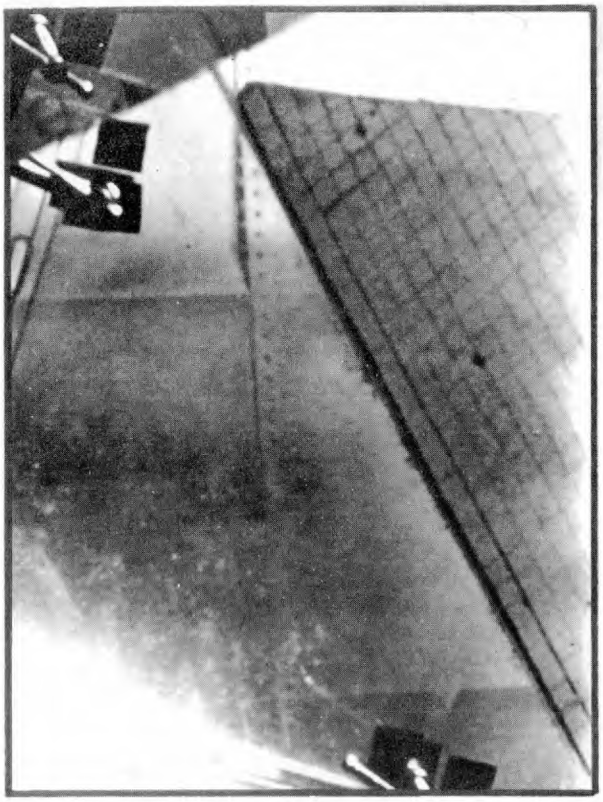

C

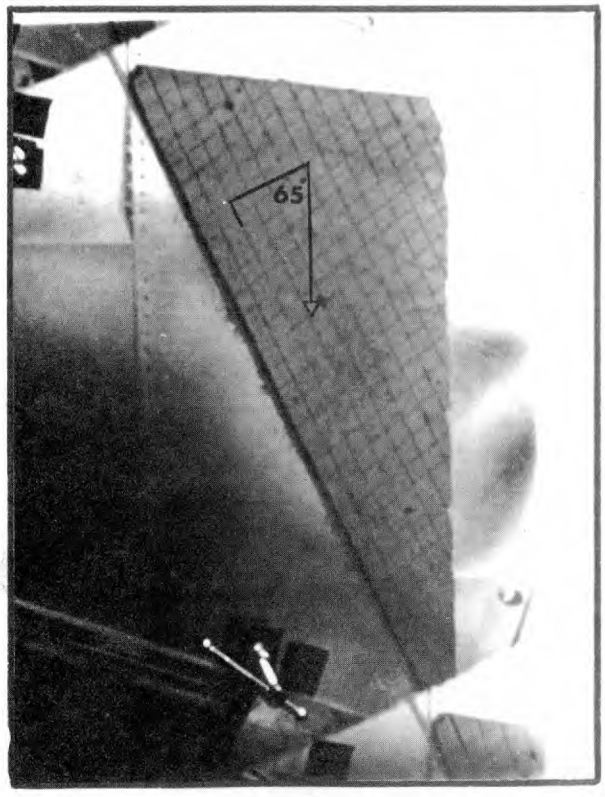

B

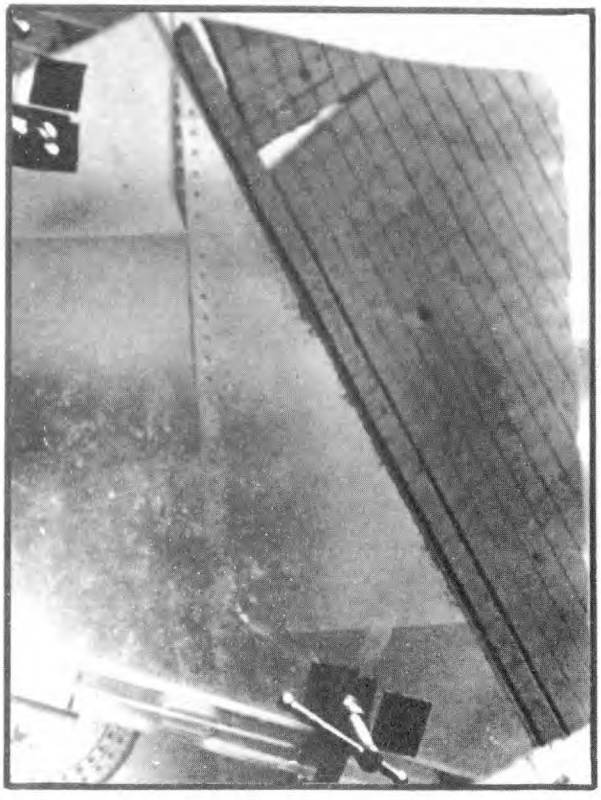

D

Figure 3.1.10 Tilt model M.10. Shear failure on primary joints with partial toppling at rear

Figure 3.1.11 Tilt model M.11 (24 frames per sec.)

Mode: Diagram B illustrates the shear strength of secondary joint surfaces. Despite undercutting and almost zero normal stress, the interlocking nature of secondary joints provides sufficient strength to support a column of blocks. Further tilting causes internal strains associated with the formation of a tension crack, and progressive failure ensues.

Careful study of consecutive frames indicated that the tension crack propagated in depth simultaneously with the progressive toe ravelling. The two processes coincided at the position of shear failure, half way up the vertical slope.

The secondary failure induced by tilting a further 6°, again indicated some relationship between tension crack depth (i.e. loosening) and the position in which shear failure initiates despite higher shear stresses on lower joints.

Figure 3.1.12 Tilt model M. 12 (24 frames per sec.)

Mode: A progressive mode similar to that in the previous model was indicated. However here the ravelling which progressed upwards from shear failure at the toe, passed beyond the deepening tension crack. Shear failure occurred on a stepped surface nearer the toe of the slope.

A pertinent question is raised by this failure: what inaccuracy is introduced by back analysing for instantaneous shear failure along all the stepped surface shown in diagram F, when in reality failure occured at the toe about 0.1 second before general failure?

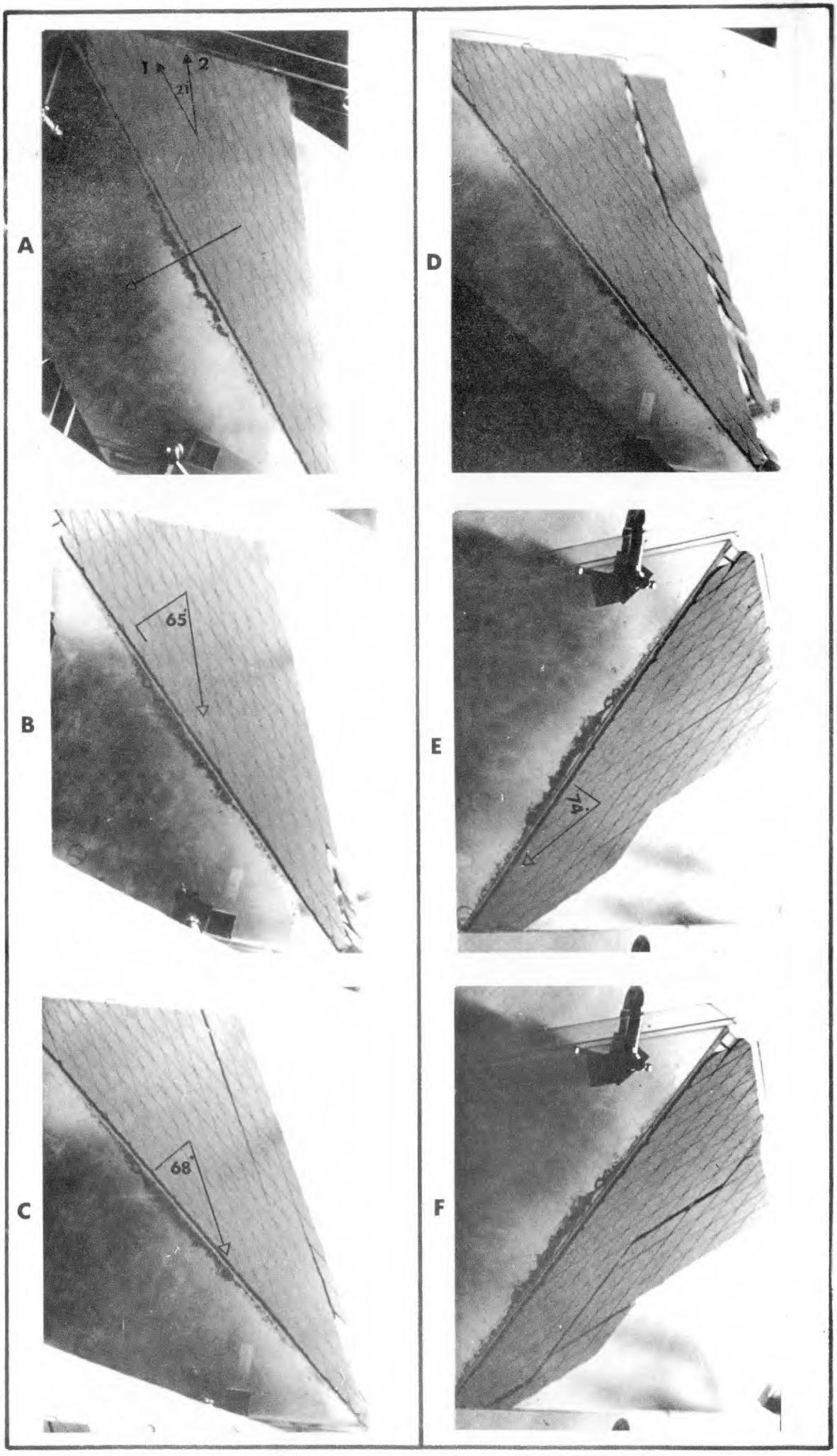

Figure 3.1.11 Tilt mode M.11 illustrating progressive failure.

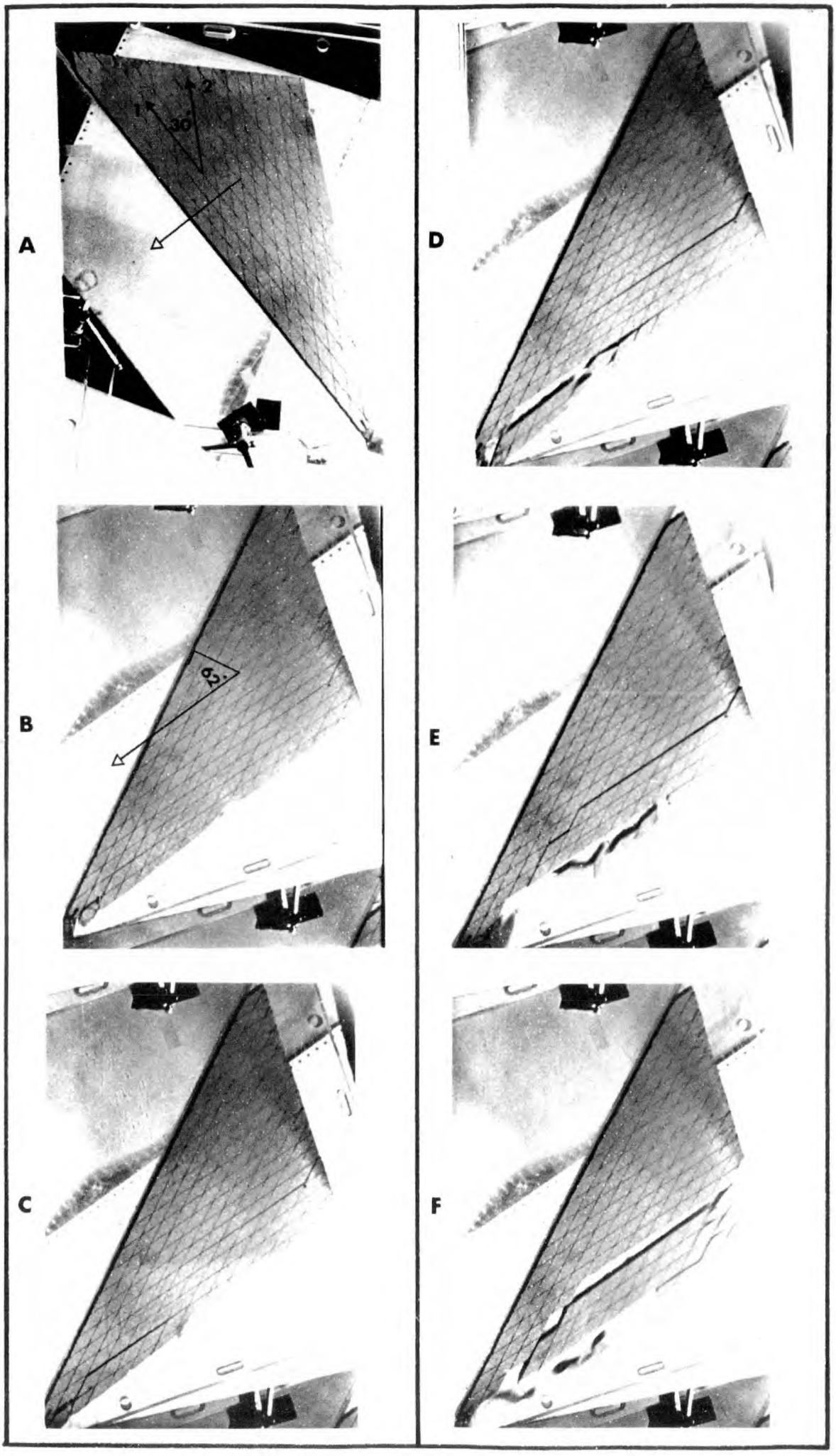

Figure 3.1.12 Tilt model M.12 illustrating progressive failure

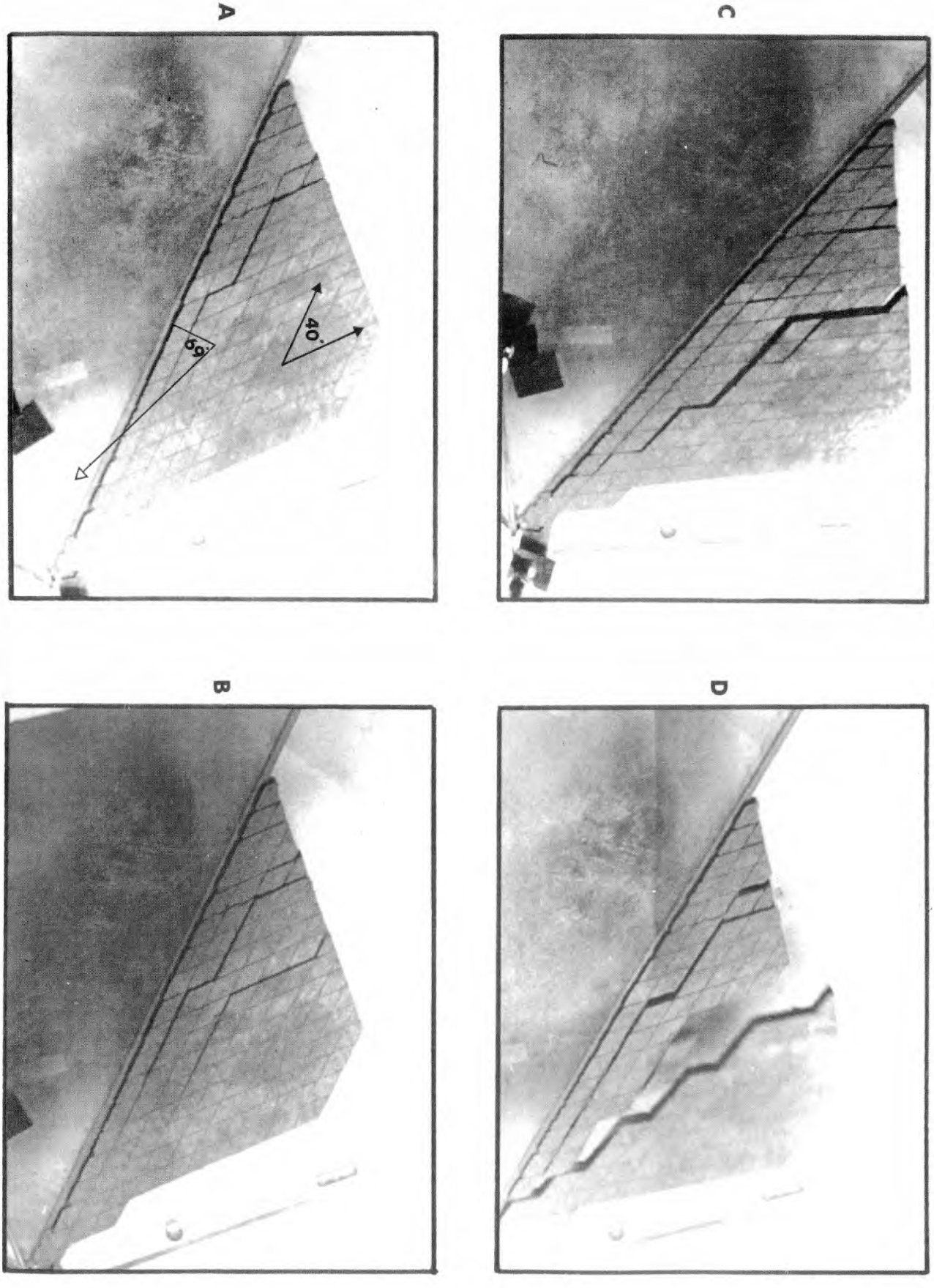

Figure 3.1.13 Tilt model M.13 illustrating overturning failure

Figure 3.1.13 Tilt model M.13 (24 frames per sec)

This model was damaged during construction, hence the reduced size and unconventional shape. It is of limited interest since an overturning failure caused by an overhang must be of rare occurrence, certainly in open pit operations.

Mode: Tensile opening, with no apparent shear component, initiated on a stepped primary surface. The resulting movement presumably translated the centre of gravity of a smaller, loosened block, to beyond the toe. Shear failure occurred as a secondary mode, possibly as a result of a momentarily reduced normal stress.

3.1.3 LARGE TILT MODELS WITH THREE JOINT SETS.

The remaining tilt models to be presented, were performed concurrently with the excavation experiments in the large loading rig. These large models were constructed of eighteen 16 inch by 16 inch by 1 inch jointed slabs, making a total dimension of 8 feet long by 4 feet high, with a 1 inch wall thickness. Slopes were failed by excavating down to a depth of 32 inches, between the glass supporting walls on each side of the model.

Large tilt models were consequently tested, to compare the modes of failure between the two cases. Identical jointing and slope heights were used.

Figure 3.1.14 shows one of the large tilt models being 'cut' to shape, by removing blocks from one side of a straight edge. The models consisted of two jointed slabs placed one against the other. These were carefully fractured in the guillotine, so that the jointing matched between slabs. The character of the three different joint types is clearly ullustrated. The numbers 1,2 and 3 refer to the primary, secondary and tertiary joint directions. The models were cut so that the lowest strength primary joints dipped steeply into the slopes, both for the tilt models and the excavated models to be reported in Section 3.3.

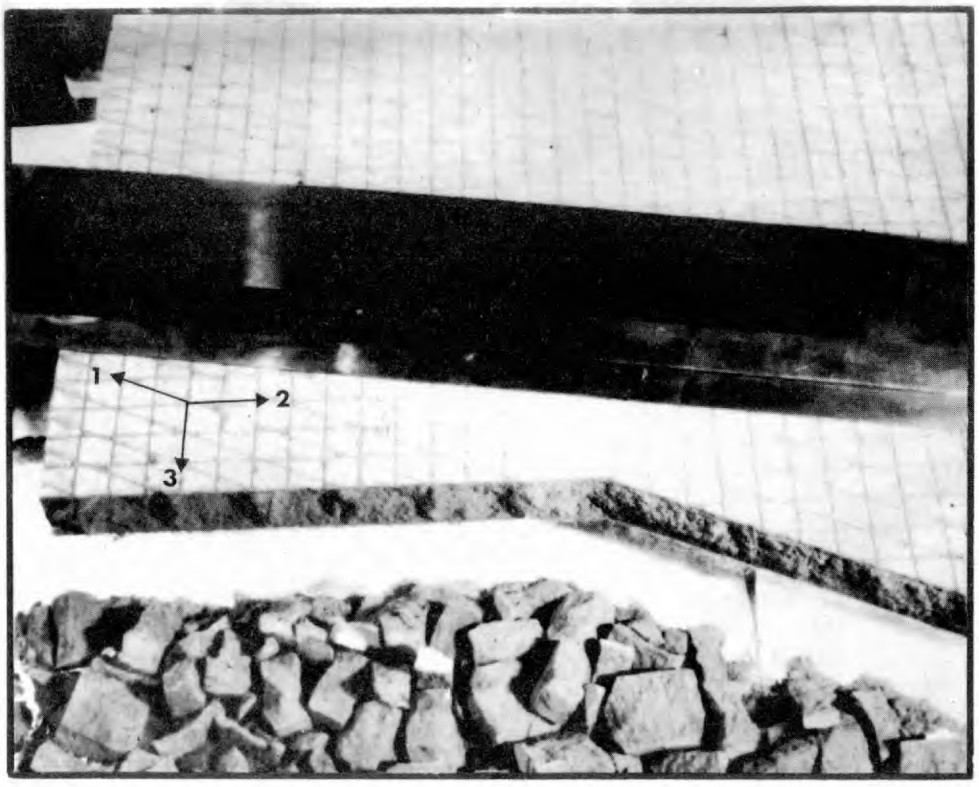

A

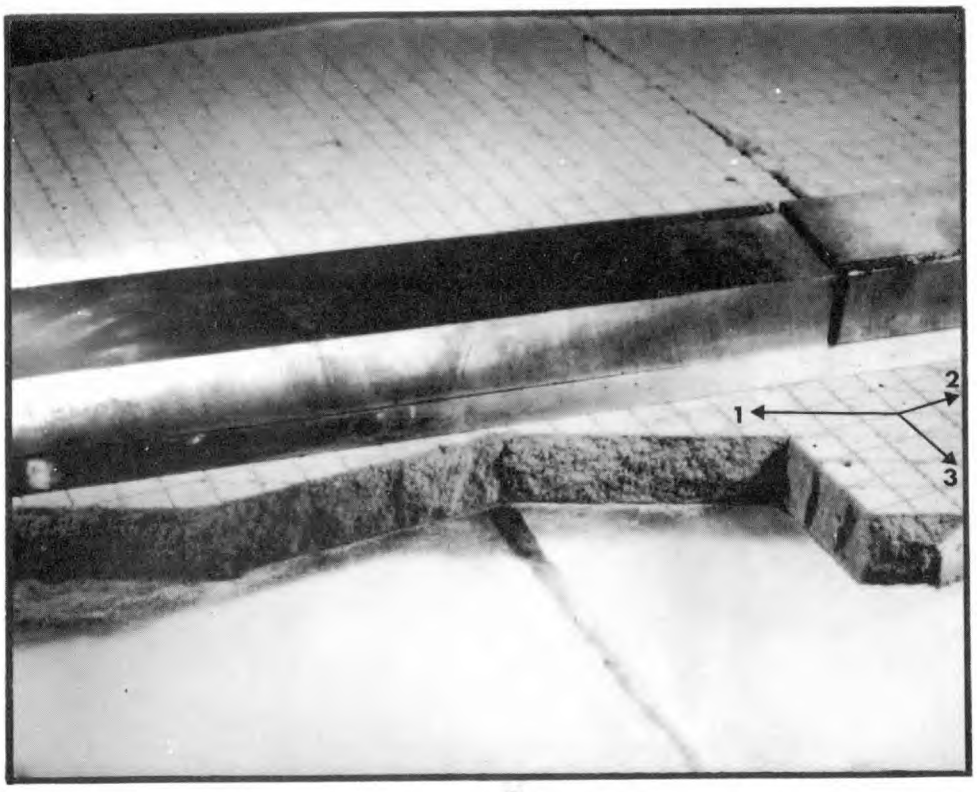

B

Figure 3.1.14 The joint surfaces produced by three intersecting joint sets.

Figure 3.1.15 Large Tilt model M.14 (18 frames per sec.)

The six sequence photographs were consecutive frames of an incorrectly exposed 16 mm. cine film. The tension crack seen in diagram A opened when the angle of tilt was approximately 63°, in other words 3° before the secondary joints became vertical.

It should be noted that, because of an intersection angle between primary and secondary joints of only 24°, the previous interlocking character of secondary joints was not exhibited in these models.

Mode: Diagram B shows shear failure initiating in the zone vertically below the crest of the slope. The zero tensile strength between the two slabs allowed failure to propagate in the lower half fractionally before shear failure followed on a stepped surface through the upper half. The horizontal tertiary joints exhibited interlock of similar character to the original orthogonally intersecting secondary joints (compare Figures 3.1.14 and 3.1.1). Two features of particular interest should be noted:
1. The vertical crack in the lower slab shown in diagram B did not partake in the eventual stepped shear surface shown developing in diagram C.
2. The tension crack opening to the surface in diagram A was not involved in the major shear failure shown in diagram C. This is significant since a limit analysis (Equation 12, Section 2.3) predicts that the first tension crack was inside the zone which was potentially stable, when substituting the slope and joint inclinations existing at failure. The tension crack position giving minimum factor of safety was theoretically 3.2 inches back from the crest. The crack actually involved in failure was 3.5 inches from the crest. Presumably shear failure of the column between these two cracks occurred due to the loosening and vibrations induced by the main failure. This double tension crack may have been a function of the rotating stress distribution during tilting. This could be one irrecoverable effect compared to the static distribution. It appears from later comparison with the more realistic excavated models that this is the only way in which the two results differ. The major failure mode is the same in both cases.

Figure 3.1.16 Large tilt model M.19 (30 frames per sec.)

Mode: Diagram B,C and D show the development of several tension cracks as the slope is rotated through the position of vertical secondary joints. The resulting strain in the body of the slope resulted in several block falls from the middle and lower parts of the slope.

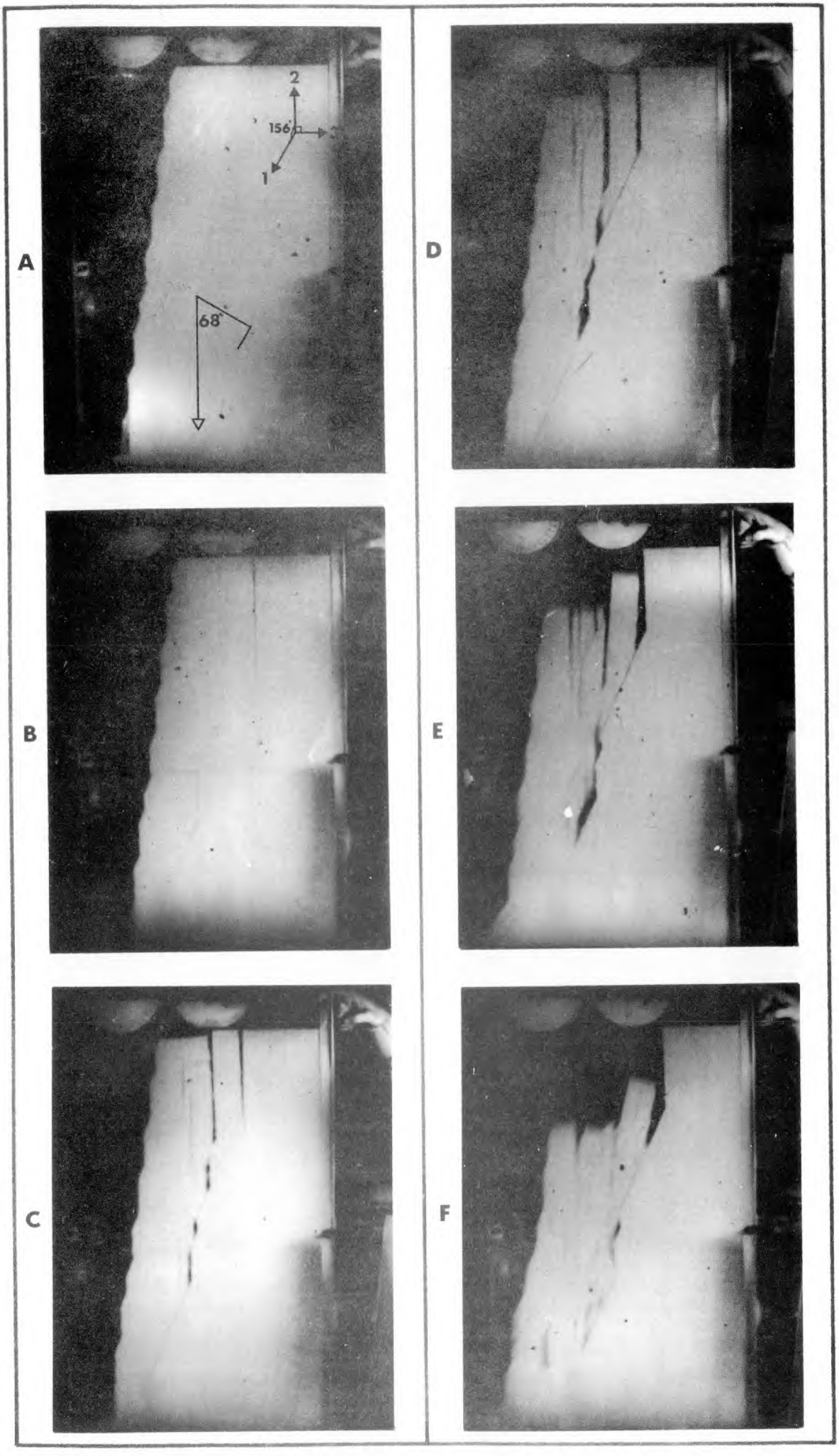

Figure 3.1.15 Failure of large tilt model M.14
on multi-linear failure surface

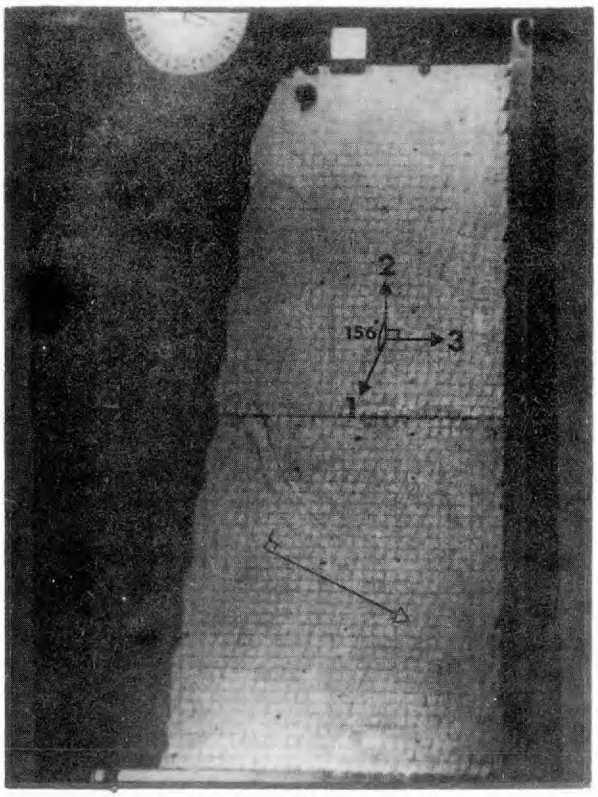

A

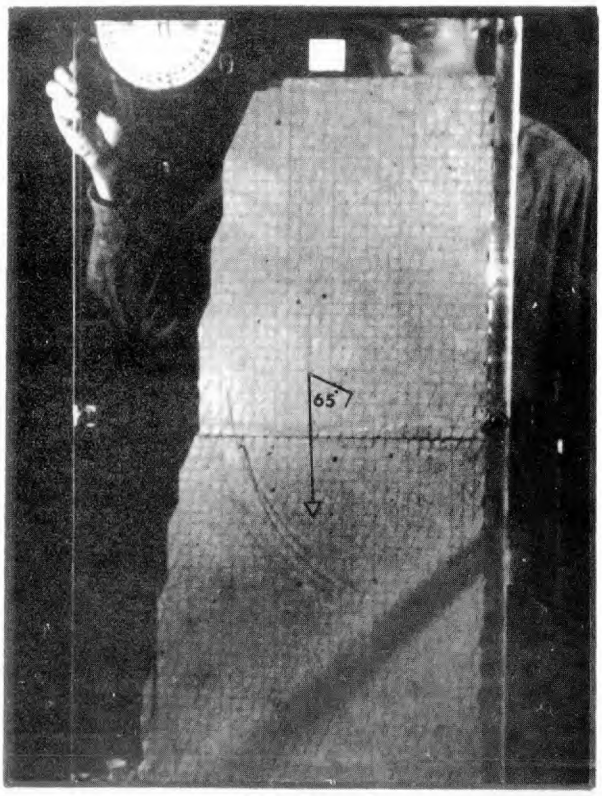

C

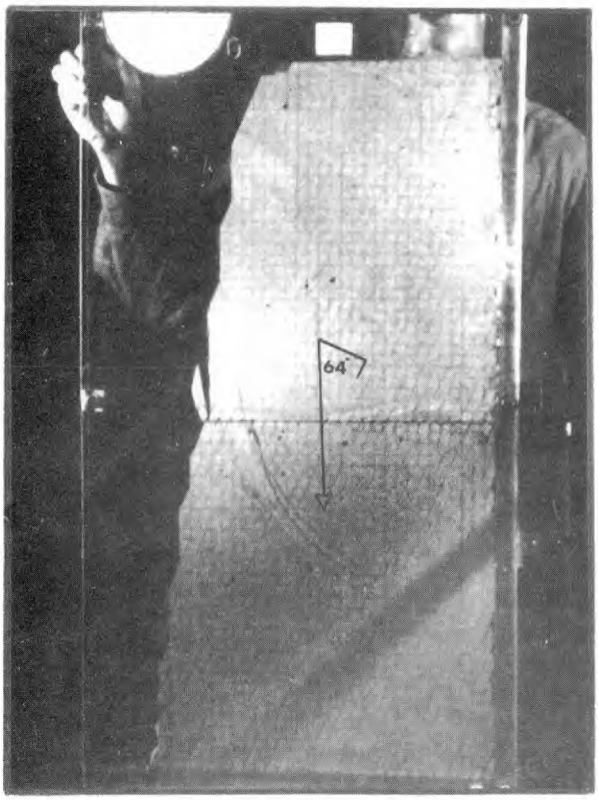

B

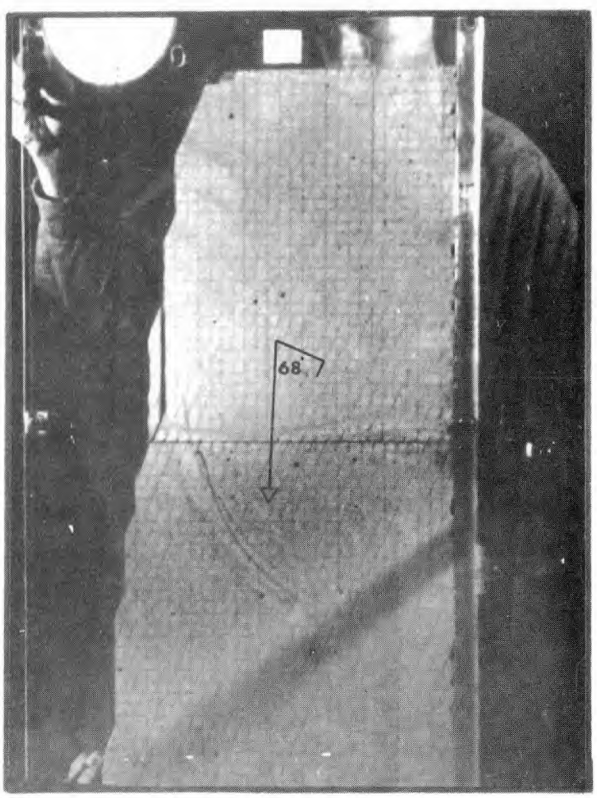

D

Figure 3.1.16 Large tilt model M.19, showing the development of tension cracks and block falls that preceed failure

Figure 3.1.17 Large tilt model M.19 (continued)

The remaining four diagrams illustrate a further block fall, increased opening of tension cracks and eventual shear failure of a somewhat superficial nature, when the angle of tilt was several degrees more than that predicted for failure. This sequence has been presented by way of introduction to pitfalls encountered when splitting slabs on the large guillotine:

1. The model slabs were cast in a large steel mould which had been machined and ground to close tolerences with respect to slab thickness. The first large excavated model, which was of an experimental nature, involved the casting of a large number of slabs before sufficient uncracked ones had been recovered from the moulds (see Appendix 3). The mould was always hammered to agitate and remove air bubbles while pouring the mixes. It was eventually noticed that over a period, the residual stresses in the steel had caused the hammered side of the mould to bow slightly. This resulted in slabs which were up to 0.015 inch too thick in the centre.

2. When splitting these slabs on the guillotine, the uppermost blade penetrated the slabs 0.015 inch deeper than usual, in the humped region. This resulted in an abnormally large increase in dimensions in the slab, due to the combined width of all the joints. (Conventionally there is about 1% increase in dimensions).

It happens that model M.17 consisted of two unmatched slabs. The uppermost slab was produced on the guillotine after the mould had been remachined when the hump was discovered. (Both slabs of model M.20, Figure 3.1.18 were also split after the fault was put right). However the lower slab was an extra one which had not been used when the first large excavated model was constructed. Due to its slightly larger dimensions it was, in ignorance, carefully consolidated by pressing straight edges along its boundaries. In this way its dimensions were matched with the upper slab.

The consequence of this mistake is evident from Figure 3.1.17. The artificial consolidation had stiffened and strengthened the lower slab, and it resisted shear failure at the predicted angle of tilt, and up to four degrees past this point.

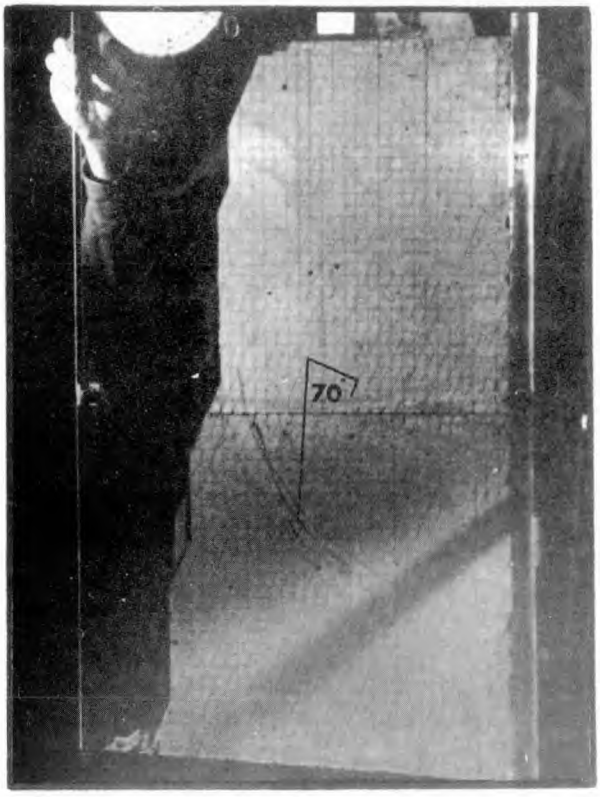

E

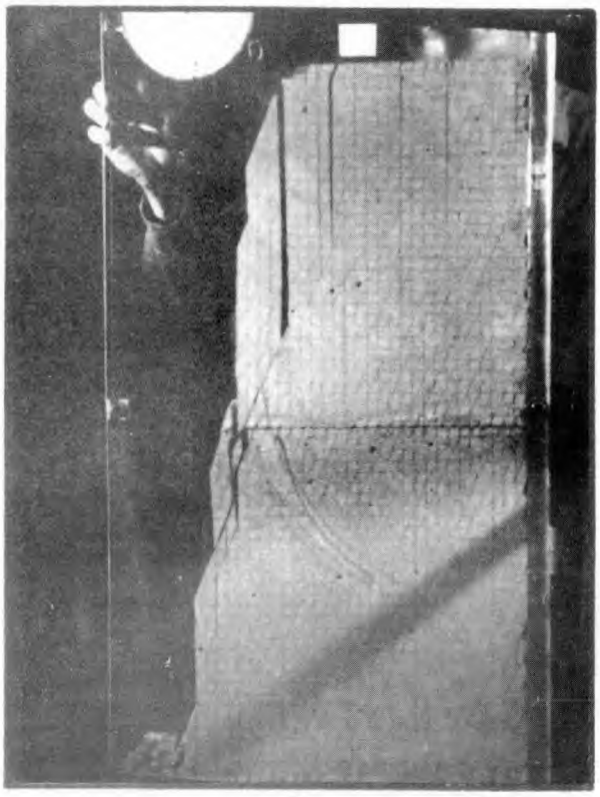

G

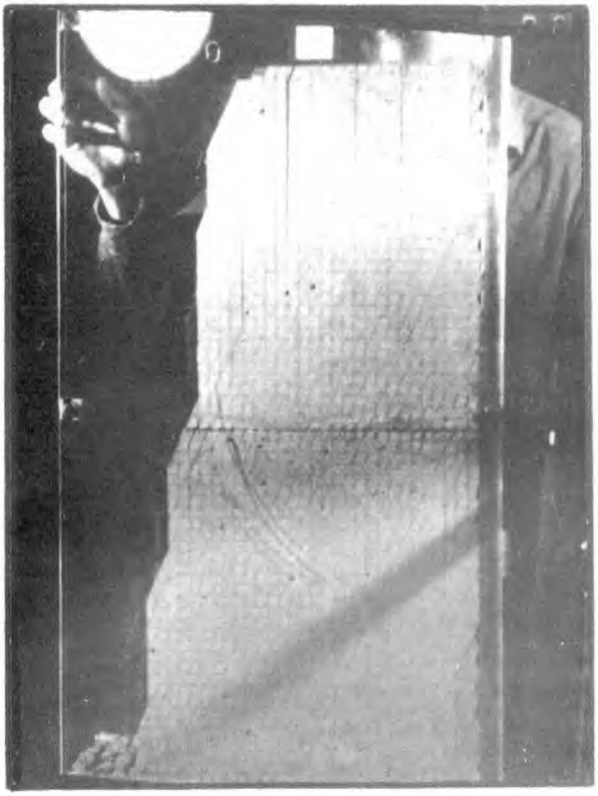

F

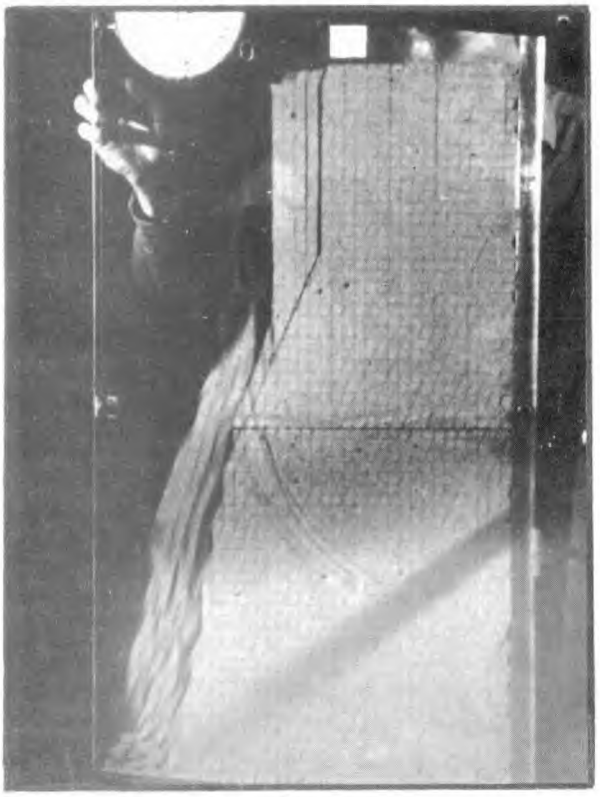

H

Figure 3.1.17 Final collapse of large tilt model M.19 which illustrates the effect of differential consolidation

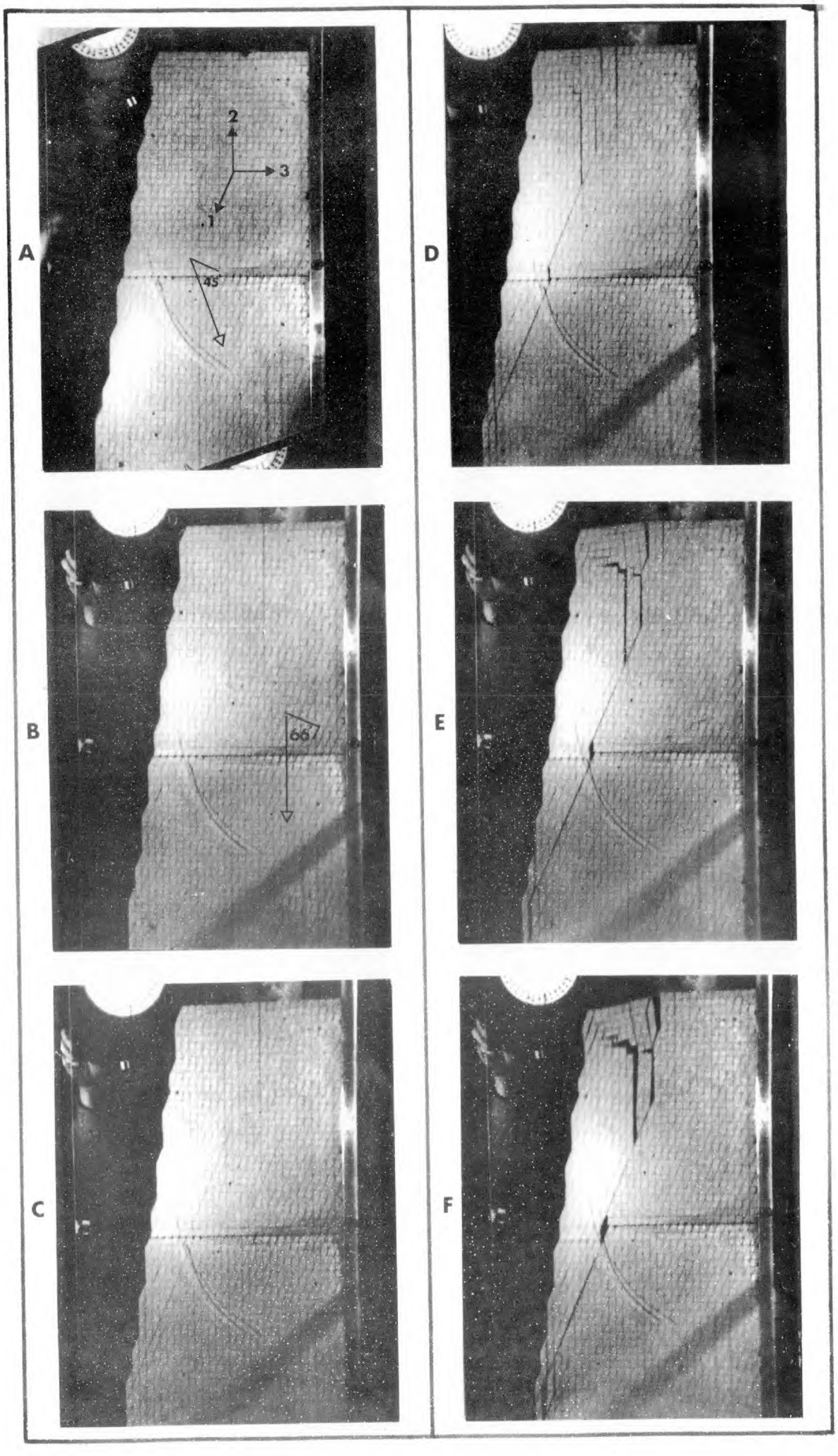

Figure 3.1.18 Large tilt model M.20 illustrating failure at the predicted slope angle for a uniformly consolidated model

Figure 3.1.18 Large tilt model M.20 (30 frames per sec.)

Mode: The tension crack shown in diagrams B and C initiated when the model was in a position 3° before the secondary joints became vertical. Once again it developed in the zone which, at failure, was theoretically stable. The theoretical position for a tension crack giving the minimum factor of safety was 3.46 inches back from the crest.

It can be seen that the double tension crack which opened during shear failure was 3.0 and 4.0 inches from the crest. Failure occurred at the predicted slope angle and dip angle (81° and 66° respectively) but the height of the failed slope was one joint spacing less than the predicted height. The shear strength parameters used in these predictions will be introduced next.

3.1.4 BACK ANALYSIS OF SIMPLE SHEAR FAILURES

Several of the tilt models presented earlier failed in a manner which was amenable to back analysis. In particular, some of the self weight shear models (sub section 3.1.1) with orthogonal jointing provided useful information on the shear strength of jointed masses, where failure occurred along one joint which was intersected, but not offset, by several others. These were termed primary cross-jointed surfaces (PCJ) in Part I.

The following table gives the results of the simple back analyses. No attempt was made to split the unstable masses into slices, since the stresses were considered to be uniform enough for approximation to mean values. The ratio of (τ/σ) is equal to the tangent of the angle of dip of the shearing joints.

Model	τ (lbf/in^2)	σ (lbf/in^2)
M.1	0.53	0.25
M.1	0.42	0.18
M.1	0.48	0.21
M.5	0.61	0.42
M.9	0.60	0.25
M.10	0.54	0.25
M.12	0.64	0.34
M.17	0.76	0.42

SECTION 3.1

Model M.1 was not illustrated previously since it did not represent modes of failure any different to M.17 (Figure 3.1.2) Both M.1 and M.17 had orthogonal jointing. However in the former, the adjustable toe support of the self weight shear apparatus (Figure 3.1.1 D) was set to different heights. The smaller the overburden depth the greater the angle of tilt required for shear failure:

Model No.	No. of blocks of overburden	Angle of joint dip at failure
M.1	5	67°
M.1	6	66°
M.1	7	65°
M.17	13	61°

In Figure 3.1.19, the eight coordinates of shear strength are compared with the shear box results reported in Section 1.3. In both cases the model material was C3. This has been described in detail in Part I.

The failures chosen for back analysis did not exhibit progressive failure, at least not in a visual sense. This is also clear from the comparison of shear strength, since the jointed mass appeared stronger than individual joints. The unexpected result can be explained (with the benefit of hind sight) as follows:

1. The primary joints involved in failure were horizontal before tilting commenced.

2. When at the point of failure the dip of these joints was approximately 60°. As a result the normal stress was reduced by a factor approximating $\cos^2 60^\circ$ (= 0.25). Consequently there was a reduction of normal stress during the test of about 4 to 1, with a corresponding rise in shear stress proportional to the sine of the angle of tilt. This is not a conventional loading path for a direct shear test.

   However it represents a most important practical consequence of excavation, which was the second method of inducing failure by gravity loading. The unexpected results of 'preconsolidated' shear tests will be reported in a later section.

   In the absence of later test results the data presented in figure 3.1.19 was used as a rough guide to mass shear strength. The (c) and (ϕ) parameters approximating the nearly linear part of the envelope of peak strength were changed from the original 0.08 lbf/in^2 and 56° for single joints, to 0.10 lbf/in^2 and 58° respectively. These values were used in the design of the jointing, slope angle and slope height of the large excavated models. The method of slices developed in Section 2.3 was employed. These design calculations are summarized in Section 3.1

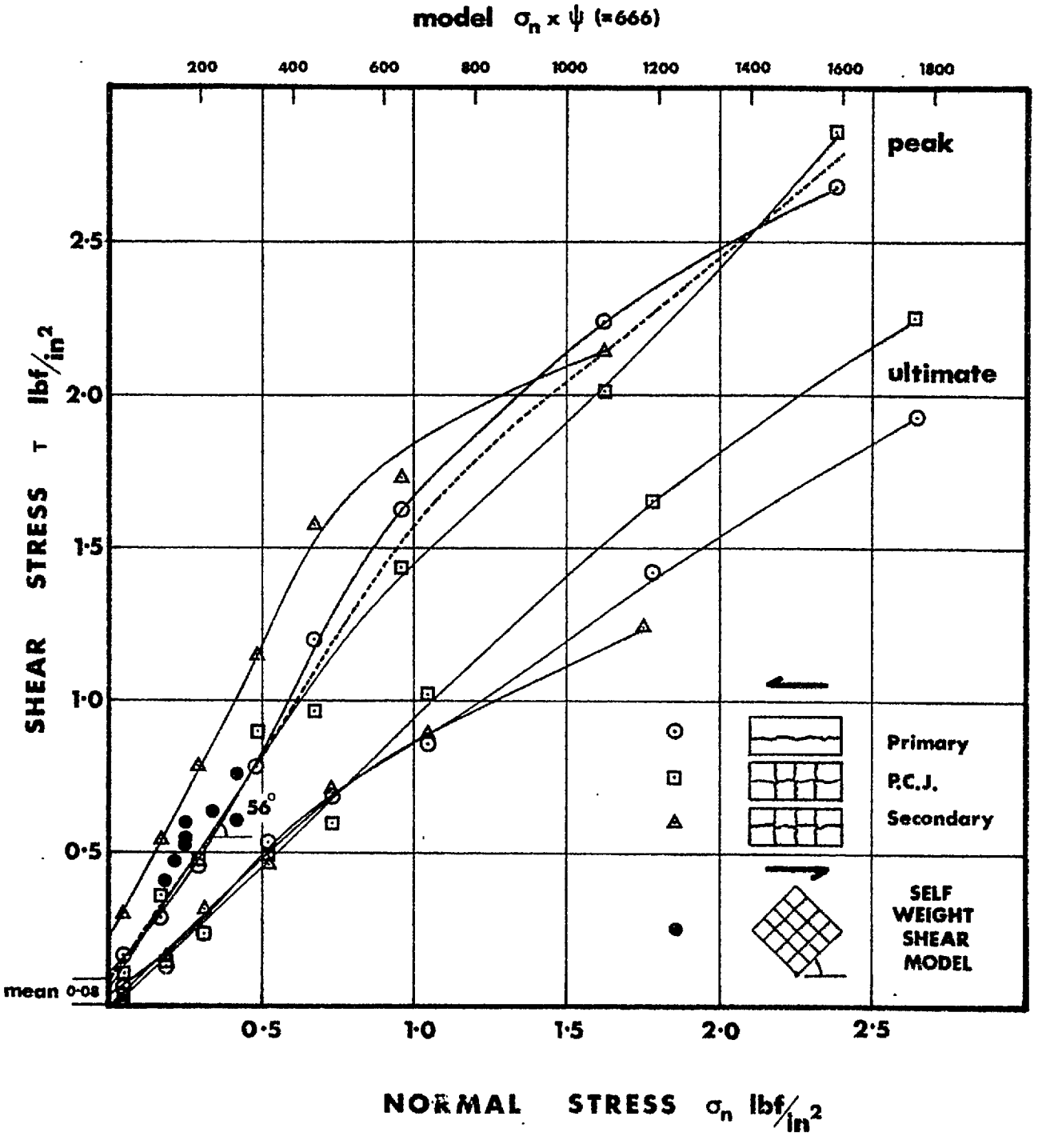

Figure 3.1.19 Comparison of shear strength of jointed mass with direct shear tests on individual joints

3.1.5 SUMMARY OF PRINCIPLE FAILURE MODES.

It is clear from an examination of all the failures shown in the preceeding figures that the following two parameters fundamentally affect the mode of failure:

1. The relative orientation of the primary and secondary joints with respect to the slope, and with respect to the gravity field.

2. The orientation of the joint set not involved in translational shear failure. Depending upon this orientation, tensile opening within the slope may or may not be possible.

These two parameters dictate whether the mode of failure is one of purely translational shear, translational shear with tensile opening, or toppling shear. These three modes are illustrated by Figures 3.1.2, 3.1.18 and 3.1.6 respectively.

A. Translational shear

This will only occur if none of the joint sets dip to within 10° or 15° of vertical. Admittedly, non vertical cracks can open up during the final failure process, but since an overhanging rear face is inherently unstable, the mass lying above the crack invariably fails with, or fractionally after, the main translational failure. The volume finally involved in collapse is more or less identical in each case.

B. Translational shear with tensile opening

This mode of failure is perfectly illustrated by situations in which a primary (lower strength) joint set dips steeply into the slope, while other joints are within a few degrees of vertical. When the strike direction of these two joint sets coincides with the slope direction, (as in the two dimensional models) this configuration can represent the minimum possible factor of safety.

The joint set that dips to within a few degrees of vertical allows tension cracks to open up prior to failure, thus separating the sliding mass from the stable portion above it. Similar situations having non-vertical joints would be inherently more stable since tension crack separation would be inhibited by the effective tensile strength of the intersecting joints.* The more stable zone lying above the potential tension cracks, would then contribute to the overall strength of the slope. This cannot occur when tension cracks open prior to failure.

* The terms; tension crack and tensile strength are used in a loose, observational sense. The phenomenon of joint opening is caused primarily by the collective effect of small pre-peak shear displacements lower down the slope. As such the tension crack zone behind a jointed rock slope will not necessarily correspond to the tensile zones predicted by elastic stress distributions.

It was suggested in Section 2.3 that in real environments, weathering of overstressed joints prior to failure might cause translational failure to occur on a partially stepped surface below the tension crack. Even without the benefit of weathering, one or two models illustrated this type of failure mode. (Figure 3.1.15 C in this Section, and one or two excavated slopes reported in Section 3.3)

C. Toppling shear failure

For this mode of failure to occur one of two features has to exist:

(a) higher frictional resistance on the joint set dipping into the slope than on the near vertical (overhanging) set potentially involved in toppling shear, or

(b) an angle of dip for the joint set dipping into the slope, low enough to preclude shear failure on this set.

The frictional resistance of the joint set potentially involved in toppling presumably controls the post-vertical angle required for relative shear to initiate.

Bray[75] and Cundall[69] have conducted some interesting theoretical and numerical analyses of toppling failures. Using a finite difference approach Cundall produced computer drawn diagrams of the progressive toppling mechanism in idealized block models.

Toppling failure is seen to initiate through a process of relative shear across the 'overhanging' joint set. This mechanism allows the 'columns' of blocks to bend by the development of hinges on the second joint set which intersects the leaning columns. Eventually, further opening between the columns is inhibited at depth, and a line of major hinges develops, thus separating the toppling mass from the part no longer involved in failure.

The effect of joint dilation

This toppling mode of failure represents an interesting digression from the conventional rotational, or translational shear mode. However one important property of rock joints has been overlooked. That is the property of dilation during shear. It is appreciated that the numerical methods of toppling analysis are complex enough without introducing this component of volume change. However, in this instance dilation is unquestionably more important than shear strength itself.

The range of normal stresses acting across the potential toppling joints will be extremely low, in view of their near vertical orientation. Consequently during relative shear across these joints, large dilation angles can be expected. Depending upon the joint roughness, it would appear from Section 2.1 that the peak angles of dilation could be anything from 15° to 40° at such low stresses. Obvious exceptions to this would be:

(a) smooth, loosened cleavage surfaces (particularly in slates).
(b) severely weathered, planar, shear type joints.
(c) any joints near the surface opened by blast damage.

For these reasons toppling would appear a valid mechanism for predicting limited surface failures such as those involving steep benches in opencast mines.

However, unless the above exceptions are relevant, a toppling mechanism which involves shear displacements on a large number of joints is impossible, due to the dilational characteristics of the joints.

A fundamental concept of soil mechanics can be cited in support of this generalization. Cassagrande, the originator of the critical density concept, found that sands dilated in shear in relation to the density of packing existing before shearing commenced. This concept was developed further by Roscoe[76], who coined the phrase 'critical state'. Put simply, granular materials such as sands were found to dilate in shear, if the density of packing was greater than critical. Conversely they contracted in shear if less dense than critical. The latter represents an extremely loose state which, in rock mechanics, might be approached by blast shattered rock, and presumably by rock fill.

The important consequence of this dilation or contraction in shear is that shear failure is forced to occur on a minimum number of shear surfaces (usually one) when the medium is denser than critical. This is obvious from simple energy considerations.

Jointed rock masses are clearly much denser than critical, even when simple shear failure on individual joint surfaces is envisaged without block rotations. Consequently, shear failure on a single surface is a prerequisite of near-surface shear failure within a rock mass. Undoubtedly, limited shear displacements occur on many joints surrounding the critical one, but it should be remembered that only smooth joints can be expected to stop dilating after passing their peak strength. Rough, large scale joints may dilate several inches more than their peak strength dilation, particularly at low normal stresses.

Consequently toppling, which has to initiate by relative shearing between many joints, would seem to be a totally self inhibiting mechanism for dilatent joints. The failure illustrated in Figure 3.1.6 could only occur because of progressive loosening of the steeply dipping joints when the slope was past vertical. Conventional open pit slopes of 30° to 60° do not present the opportunity for deep seated loosening of the jointed rock mass. Consequently toppling failures would probably be limited to steep benches where blast damage could render suitable joint configurations prone to toppling failure. Frost wedging and similar weathering mechanisms might have a similar effect near the surface of steep slopes.

SECTION 3.2

3.2 A MODEL LOADING RIG: PHILOSOPHY AND TEST PROCEEDURES

SUMMARY

Near-surface stress measurements reported in the literature suggest that a model loading rig should be designed to apply horizontal stresses which increase linearly with the depth of the model. This triangular distribution is in marked contrast to the rectangular distributions required of biaxial loading frames for testing underground mining situations.

The advantages of two-dimensional simulation of near-surface rock masses are argued. Problems which arise from two dimensional simulation of underground (high stress) situations are thought not to be relevant to near-surface situations, since failure here occurs primarily on joints perpendicular to the plane of the model, in contrast to failure through intact material at high stress levels.

The concept of a soft loading system capable of storing a fixed amount of strain energy, equivalent to a stressed slice of rock surrounding the model is presented. The horizontal loading beams eventually designed consisted of a rigid beam loaded by a hydraulic piston at its lower third point. This triangular distribution transmitted to opposite edges of the model via proving rings and independent plattens, twenty four per beam.

The proceedures involved in loading the model horizontally and by gravity are discussed. Cyclic loading is employed to imprint a consolidation pattern on the model, consistent with the desired stress distribution.

During stage by stage excavation of the model, pre-failure displacements are recorded by a photogrammetric method. Comparison of successive photographic plates in a stereocomparator allows vertical and horizontal displacements to be calculated. The actual failures induced by excavation are recorded on 16 mm. cine film and video tape.

The limit equilibrium method of slices developed previously, is used to design slopes which will fail when the desired slope height and angle is reached. The predicted zone of overstressed joints and the tension crack position are presented.

SECTION 3.2

3.2. A MODEL LOADING RIG: PHILOSOPHY AND TEST PROCEEDURES

INTRODUCTION.

The components of rock mass behaviour have so far been simulated in stages, before attempting to combine them in a realistic model of a loaded rock mass. The previous section on tilt models represented only a first stage, in which jointed models were loaded by a rotating gravity field, until the ratios of shear to normal stress became limiting. The problem remaining, and the one of most relevance, was to load a model both horizontally and by gravity, making the boundary conditions as realistic as possible. Excavation of model slopes in this stressed environment would then indicate the relevance of stress history, and stress concentrations, to the eventual failure of the slopes.

Photoelastic and finite element studies indicated that in elastic materials (with isotropic or anisotropic properties), stress concentrations at the toe of slopes were very real, particularly when 'excavating' in a high horizontal stress field. (see for instance Blake [77, 78].)

However the effect of discontinuities and non linear deformation properties on these theoretical stress distributions was not known. It was hoped that by performing more realistic physical model tests, the failures induced by excavation would give some clue as to the relevance or otherwise, of conventional numerical methods for predicting slope failures and deformations within and around the slopes.

There was obviously no reason to beleive that the jointed model material created complications with respect to a real rock mass. On the contrary it was more likely that, due to the absence of weathering, variable structure and joint water, the models presented an extremely simple version of idealised rock mass behaviour. Yet despite this, the complexity of the components of model joint behaviour (in particular dilation) even now defies numerical simulation in anything but crude terms (see for instance Mahtab and Goodman[79], Zienkiewicz, Best, Dullage and Stagg[80], St. John[43] and Cundall[69]) In addition, existing computer storage limits numerical simulation to a relatively small number of discrete blocks, where discontinuous rock masses are concerned.

It will therefore be seen that the large models to be described in Section 3.3 were designed not only to clarify rock mass behaviour where possible, but also to determine whether or not it was justifiable to view existing numerical analyses with some scepticism.

The fundamental differences between modelling underground and open cast excavations have been discussed previously in Section 1.1 These related chiefly to differences in scale and stress distribution, and in particular to the negligible importance of self weight stresses in underground situations. These differences will be expanded upon before going on to consider practical details.

3.2.1 NEAR-SURFACE STRESS DISTRIBUTIONS TO BE MODELLED

It is clearly apparent from the large number of rock stress measurement studies (for instance Hast[81], Wisecarver, Merrill, Ransch and Hubbard[82], Li[83] and Pallister, Gay and Cook[84],) that although a hydrostatic distribution may be a universal mean, wide variations can occur. Horizontal stresses ranging from one third to three times the vertical stress are encountered, and even the vertical stress is not necessarily related to the depth of overburden and rock density.

The well known measurements by Hast[81], which were made in mines in three Scandinavian countries, indicated that an almost linear relationship existed between the sum of the two horizontal stresses ($\sigma_1 + \sigma_2$) and the depth of overburden. When intrapolated to the surface these measurements indicated that a stress sum in excess of 2000 lbf/in^2 might exist at or just below the surface. Although these measurements have been received somewhat sceptically they do at least focus attention on a subject which is full of anomalies.

However the linear increase of horizontal stress with depth has been confirmed by several other measurements. Most of these have indicated a less marked increase in stress with depth than found by Hast, and also a negligible stress ellipsoid at the surface.

In view of these measurements the model loading rig was designed to apply a triangular stress distribution to the vertical sides of the model, which could be changed in gradient as desired. The density of the model material used in all the jointed models (material C3, see Sections 1.2 and 1.3) was 121 lbf/ft^3. This meant that for every 1 foot of model overburden the vertical stress increased by 0.84 lbf/in^2. When converted to prototype scale these values represented a 550 lbf/in^2 stress increase for every 500 feet of prototype overburden. (Geometric scale λ = 1:500, stress scale ψ = 1:666) The model loading frame was designed to apply a horizontal stress of the following range of intensities:

$$\sigma_h = (\tfrac{1}{3} \text{ to } 3)\sigma_v$$

where σ_h = horizontal stress

σ_v = vertical stress (0.84 lbf/in^2 per foot)

3.2.2. MODEL BOUNDARIES FOR SIMULATION OF NEAR-SURFACE ENVIRONMENTS

1. Two-dimensional simulation

It was decided at an early stage that the models should be two dimensional. Any three dimensional loading system complicates the measurement of model displacements and recording of slope

failures to an impractical degree. In fact the advantages of cross-sectional observation are entirely lost with three dimensional models, unless one is thinking of crude photoelastic type 'rock mechanics' in which the 'stress freezing' method is utilized.

For this reason it was only necessary to apply horizontal stresses down the opposite vertical edges of the jointed models, which would be supported between glass walls, to give lateral support against possible buckling.

Experience with high stress biaxial loading frames for simulating underground mining situations, has indicated that certain problems are created by two dimensional models which can only be overcome when loading and modelling in three dimensions, thereby substituting a different set of problems.

These relate to the fracture of intact material between the joints, which will occur around underground excavations, if the horizontal to vertical stress ratios are sufficient to cause shearing and tensile failure. Ergun[5] reported these problems in his study of the stability of underground openings, when modelling jointed rock in a large two dimensional biaxial loading frame designed to test 40 inches by 40 inches models.

The stresses applied to the edges of these 1 inch thick models were so high (design range 0 to 10,000 lbf/in^2) that thick perspex and glass support walls were designed to prevent buckling. When the models were dismantled brick by brick after testing, it was found that the limited zones of shear failure around the excavations actually extended through larger areas of the model without previously having been detected. Tensile fractures were occurring parallel to the plane of the model, inside the plaster model bricks, and therefore invisible from the surface.

However this invisible fracturing, which in itself would have been a valid mode of failure in certain three dimensional stress situations, was sufficient to cause wedging between the glass walls after a certain amount of movement had occurred. This was an unfortunate situation, since Ergun[5] demonstrated that only a very small lateral pressure was required to prevent buckling, if the bricks were closely supported on each side. This lateral pressure increased enormously if appreciable buckling could occur. This anomaly meant that a wider spacing of the support walls was not a very satisfactory solution to the problem.

Fortunately, near-surface modelling did not appear to present these problems since, unless the rock to be modelled was excessively weak and the slopes extremely high (an unlikely combination), failure would probably only occur along pre-existing joint surfaces. At the relatively low stresses operating in opencast mining situations, the shear strength of the joints is low compared to the shear strength of the intact material, and consequently intact strength is seldom mobilized. The pre-existing joint surfaces in the models were all designed to have strike directions perpendicular to the plane of the

model. Consequently wedging was not likely to occur during failure.

All that was required for support of the model in the third dimension was two rigid glass walls, with a small clearance between the model and the glass, sufficient to allow unhindered movement, but small enough to inhibit any tendency for buckling. Due to the lower relative stress range operating in a near surface environment, buckling was less likely anyway. (It was found later that the angle of friction between the model material and the glass walls was approximately 11° to 12°. The verticality of the model and the lack of buckling meant that interaction between the glass walls and the model could be ignored.)

The two model boundaries in the third dimension left the base of the model and the two horizontally loaded edges as the remaining artificial influences on the planned model. In an effort to reduce their influence, these three edges were separated from the model by a mi 'mum of two, face to face strips of P.T.F.E. (Teflon) low friction tape. A coefficient of friction of 0.05 meant that shear stresses on the boundaries were minimal.

2. Horizontal stress simulation

The conventional methods for loading the boundaries of biaxial models consist of constant load devices usually hydraulic pistons, which transmit boundary stresses via distribution plattens. Three methods can be cited:

1. A loading system incorporating an equal number of pistons as plattens, on four edges of the model (for instance Hobbs[4])

2. A loading system incorporating only one piston on each of the four edges of the model. The load from each piston is distributed in turn to two, four, eight and sixteen semi circular plates of reducing diameter, supported in line contact from leaf springs. This method was developed by Hoek[85], and results in a more uniform distribution of stress on the boundaries than the above.

3. A loading system incorporating a large number of P.T.F.E. lubricated steel shims, all of which are loaded by end contact with hydraulically pressurized adiprene rubber bags. This method, which was developed and successfully used by Ergun[5] is an extremely good one, and results in a very uniform distribution of stress even when differential displacements occur at the boundaries.

All the above systems were designed to apply constant loads which were independent of displacements at the boundaries. They were also designed to apply rectangular distributions of stress, rather than triangular, since self weight stress gradients can be

ignored in most underground mine operations. (The vertical extent of the workings is generally small compared to the depth below surface).

The larger scale of opencast excavations, and the necessity to model as much of the surrounding rock mass as possible, presented considerable problems. These were to some extent resolved by the development of the very weak model material. Nevertheless the dimensions of the model compared to the dimensions of the slopes to be excavated in it presented a difficult decision.

The only data available concerning the influence of an excavation on the stresses and displacements surrounding it were from finite element solutions for idealized elastic materials. The effect of joints and non linear deformation properties on these solutions was unknown.

It was therefore decided that the model should be made as large as was practical for the available laboratory space, so that vertical boundary effects would be reduced to a minimum. If, during excavation of a model pit, it was found that the limited dimensions were effecting the problem, then the depth and width of the pit would obviously need to be reduced.

It was originally intended that enough of the surrounding rock mass should be modelled to allow horizontal loading via two rigid beams. Piston loading at the lower third points of these beams could then produce the desired stress gradient, and solve the problem of a triangular distribution in a very simple manner.

However it was suggested by Bray[86], that, since the loads were being applied just outside the middle third of the beam, small displacements in the upper part of the model would result in separation of the model from the beam in the upper levels of the model. A novel solution to the problem was suhgested by Hoek[87]. Third point loading of the beams would be combined with individual loading of plattens via proving rings, which would distribute the triangular stress to the model, and greatly reduce the non uniformity of stress when relative displacements occurred at the boundaries.

The implications of this method became apparent when a design was attempted. There were two possibilities.

1. Loading of the beams with a constant piston force, while the models were excavated, so that the total distribution of stress was constant. Local variations in stress could be detected by dial gauges mounted across the proving rings.

2. Loading the beams with the required force before locking them in position when excavation was to begin. The strain energy initially stored in this system would be that of the triangularly stressed model, and the triangular

distribution of load in the proving rings.

Displacements occurring at the boundaries for case No.2 would result in a fall off in the stored strain energy (therefore load) of individual proving rings, which could be monitored by dial gauges, and would occur in a linear manner depending on the stiffness of the rings.

After a lot of thought it was decided that such a system was a much closer approximation of near-surface rock mass loading, than the conventional constant force devices. It was conceeded that these were probably justified for underground situations where displacements were small, and the stresses so high that the surrounding rock mass effectively applied a constant stress field, independent of displacement. However, for open cast operations, where the unloading by excavation was enormous, it seemed likely that the surrounding rock mass was far removed from any constant stressing device. The duration of opencast operations was insignificant on any geological time scale, and the rheological properties operating during tectonic movements were surely irrelevant here.

It was therefore concluded that near-surface rock masses (excluding tectonically active mountain chains) had a limited potential for storing strain energy, due in particular to the low stress levels and also the presence of joints with irrecoverable deformation properties. It was thought that stored strain energy that existed would be dissipated irrecoverably by unloading displacements caused by excavation.

However, accepting the limited strain energy of the system, what dimension of rock could be said to be 'active', in terms of responding to displacements?

In the complete absence of relevant information, an arbitary decision was made. The proving rings (24 each side), were designed with a stiffness equivalent to that of half the model dimension of unjointed model material. This meant that the design was based on the value of Young's modulus (E) for the intact model material. The sketch overleaf illustrates the 'equivalent slice' concept of the 'soft' loading system.

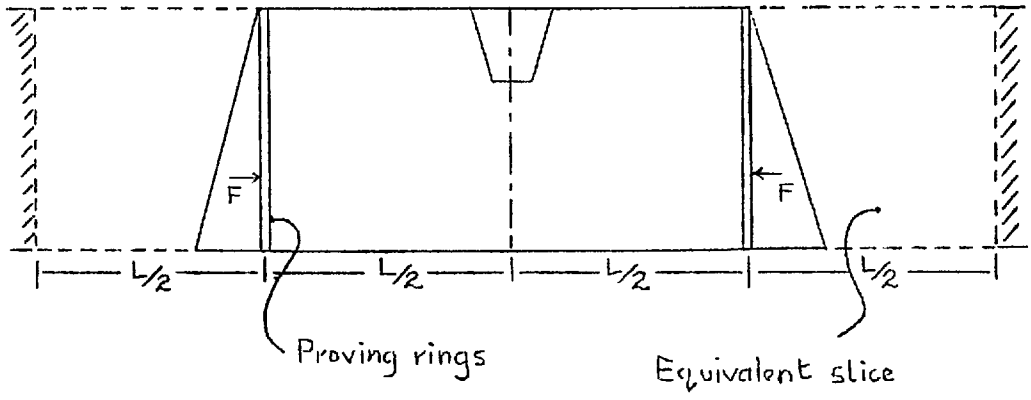

Figure 3.2.1 illustrates the completed loading frame and included model (measuring 8 feet by 4 feet by 1 inch) held in a vertical plane prior to excavation between the glass walls. Some design features of the loading frame, and in particular the loading beams and proving rings are given in Appendix 4.

The model dimensions, when converted to prototype scale (geometric scale λ = 1:500) represented a jointed slice of rock, 4000 feet long and 2000 feet high. The model joint spacing of $\frac{1}{2}$ inch meant that a model with two joint sets was split into approximately 40,000 blocks. This meant that the models were acceptably 'discontinuous', with probably more elements than previously attempted in rock mechanics terms, both physically and numerically.

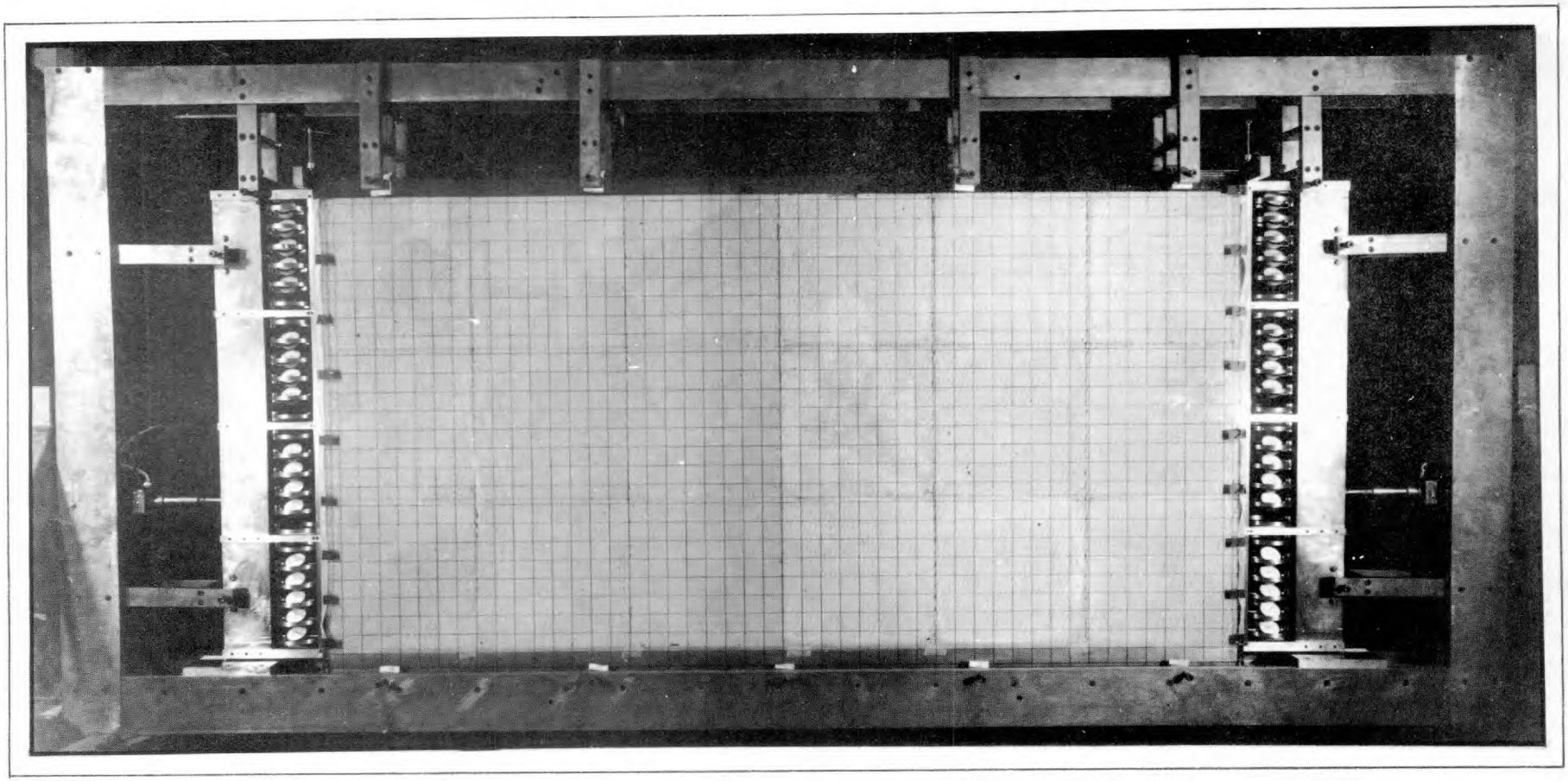

Figure 3.2.1: A large loading frame for near-surface stress simulation in two-dimensional models

3.2.3 TEST PROCEEDURES

1. Cyclic loading of the model

The models were constructed from eighteen jointed slabs of model material, each measureing 16 inches by 16 inches. The construction proceedures are discussed and illustrated in Appendix 5. (The sequence of operations involved in production of jointed slabs are given in Appendix 3)

After construction of the models, the front wall of glass was replaced while in a horizontal plane, and the all round model-glass clearance adjusted to approximately 0.040 inch. The loading beams could then be positioned in place of the steel straight edges supporting opposite edges of the model.

In a horizontal plane (see Figure 3.2.2) and with no force applied to the two loading beams, the model was in an unstressed state. ($\sigma_v = \sigma_h = 0$.) The loading proceedure was as follows. The dead weight compensated loading tank (Appendix 4) was filled at a uniform rate from a constant head water supply thereby pressurizing the two, third point loading pistons. Simultaneously, the model was rotated towards a vertical plane by screwing the large worm reduction gear seen in Figure 3.2.2. The model was rotated at a rate approximating a linear increase in the sine of the angle of inclination from horizontal. The rate was chosen so that both horizontal and vertical (gravity) stresses should reach their maximum at the same time. Thus as far as was possible the model was loaded under a constant ratio of horizontal to vertical stress, whatever horizontal stress level was chosen ($\sigma_h = \frac{1}{3}$ to $3\,\sigma_v$). This meant that the loading history, at least from the end of construction, was known with some certainty.

The non uniform loading history induced by unavoidable construction loadings, and the desire to consolidate the joints appropriate to the design stresses, suggested that the models should be loaded cyclically (Morgenstern[88]). This would help to dissipate the irrecoverable displacements, in much the same way that the 'hysteresis' is reduced or even removed by repeated loading and unloading in plate bearing tests. Only then would the strain energy in the system be known, at least with some degree of confidence.

The models were therefore loaded and unloaded (see Figure 3.2.3) with the same attention to the stress ratio. After each loading the displacements that had occurred at the top and vertical edges of the model were recorded, and the proceedure repeated. It was found that about three cycles was sufficient to consolidate the models, such that no further displacements could be detected. Each model was cycled five times in all, before leaving it in a vertical plane, and locking the loading beams in position. The frame was actually rotated about 2° past vertical so that the model just rested on the front glass wall. This removed the shadow of the 2 inch square grid, which was etched on the inside of the front glass wall, adjacent to the model.

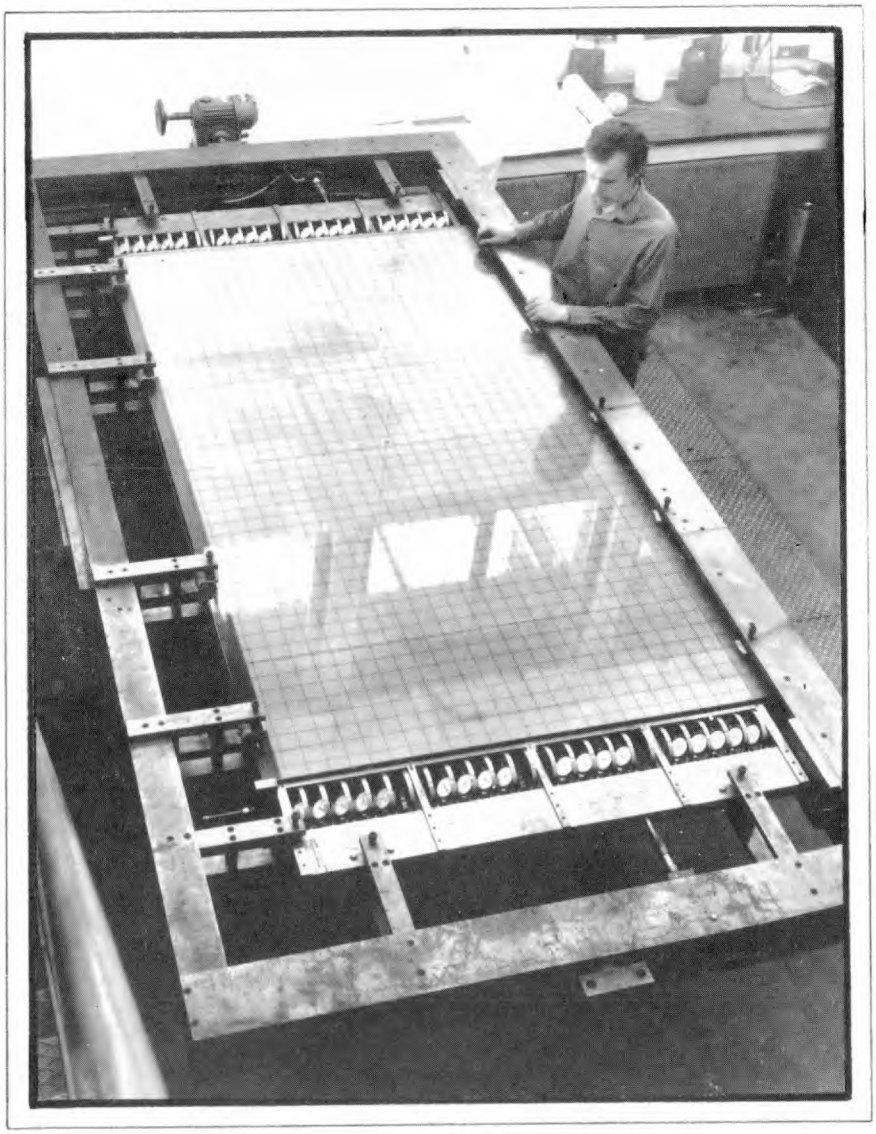

Figure 3.2.2: A jointed model lying in a horizontal plane before loading

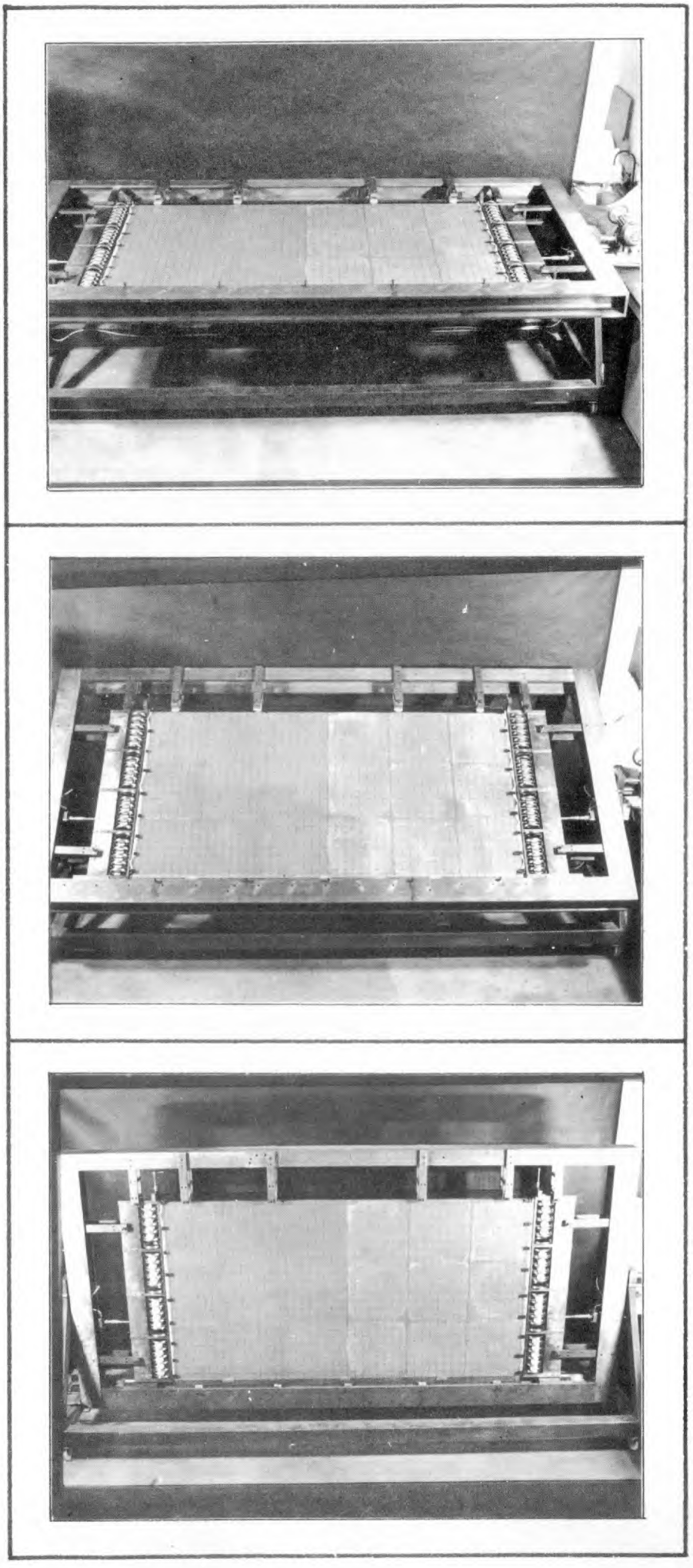

Figure 3.2.3: Rotation of a model to induce gravity loading while applying an increasing horizontal stress.

2. Excavation of the model

This operation, which initially appeared likely to cause considerable problems, in fact proved quite simple. A large industrial vacuum cleaner with tubular extension, was connected to one exit at the top of a sealed oil drum. The drum was half filled with water, and a second exit tube positioned so that the bottom of the tube was a few inches below the water surface. The top of this tube was connected via flexible hose, to variable lengths (9 inches to 3 feet) of thin walled plastic tube which was steamed into an oval shape so that it would fit between the glass walls which were spaced at just over 1 inch apart. According to the current depth of the excavation, one or other of the oval sections was used to touch the bottom and sides of the excavation, thereby removing whole model blocks and smaller debris by suction forces. This debris was sucked through the water in the oil drum, thereby removing the dust problem. Every so often, the sludge in the bottom of the drum was washed out and the tubes cleaned internally or replaced to reduce internal caking, and improve suction.

It was found that a sharp steel pin, when fixed to the end of $\frac{1}{4}$ inch diameter steel rods, was a useful tool for loosening between blocks. Joints were scratched in a direction perpendicular to the plane of the model so that no adverse forces were applied to the excavated slopes. Extension pieces for the steel rods allowed excavation down to the maximum depth, of 32 inches. It was particularly noticeable that as the depth increased the tightness of the joints also increased, making excavation more difficult.

It will be seen from photographs of the excavations reproduced in Section 3.3, that 'tight' excavations were initially at down to full depth, and the slopes steepened until failure occurred. The failed debris was then sucked out and new slopes excavated on each side, again until failures occurred. In this way four failures were obtained from each model, with the exception of the first trial model.

3.2.4 DISPLACEMENT AND BOUNDARY STRESS MEASUREMENT.

The kind and most helpful cooperation of the Photogrammetry Department, University College, London, resulted in all pre-failure displacement measurement being made using photogrammetric techniques. The failures themselves were recorded on 16 mm. cine film, running at 30 frames per second, with a stand by video tape recording system in case the cine film was not running when failure occurred.

Figure 3.2.4 shows the recording systems in operation behind a black sheet of paper, designed to reduce reflections in the front glass wall.

1. Displacement measurement using photogrammetry

One of a pair of Gallileo-Santoni cameras was used, set up on a 560 mm. bar and positioned to give coverage of the whole 8 feet by 4 feet model. Stereoscopic overlap of two cameras was not required

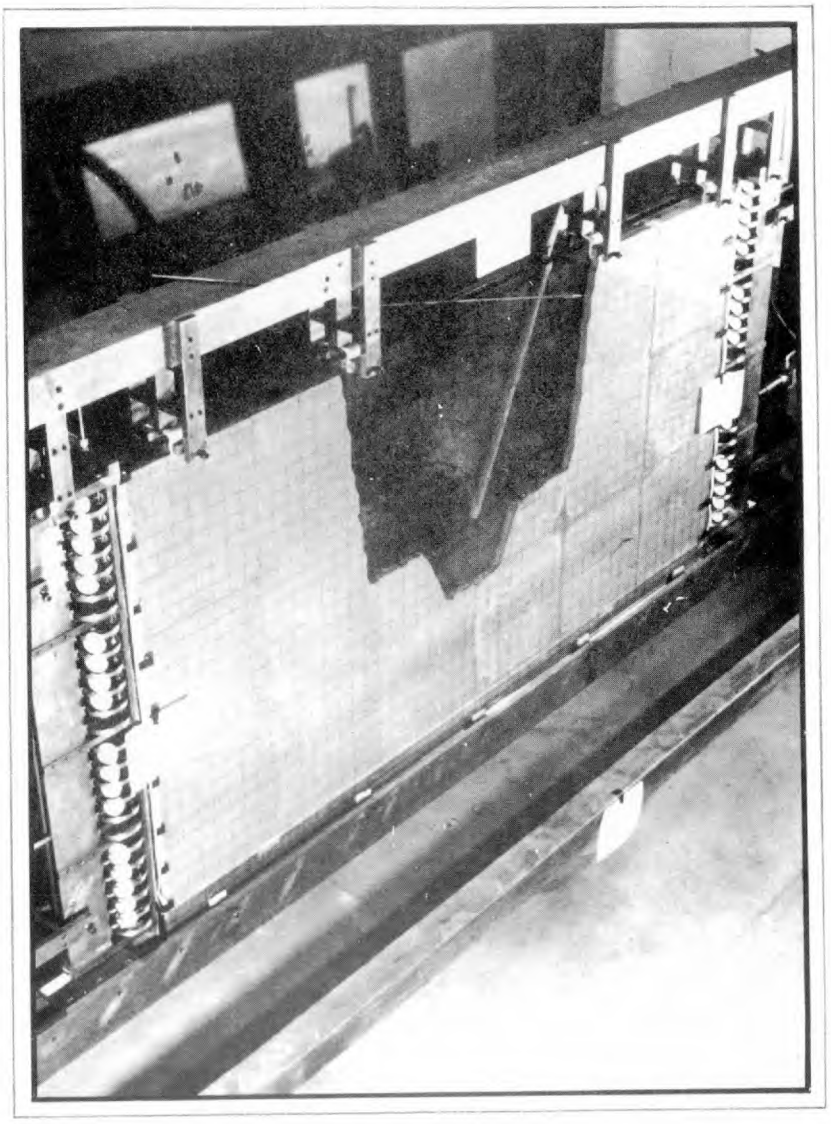

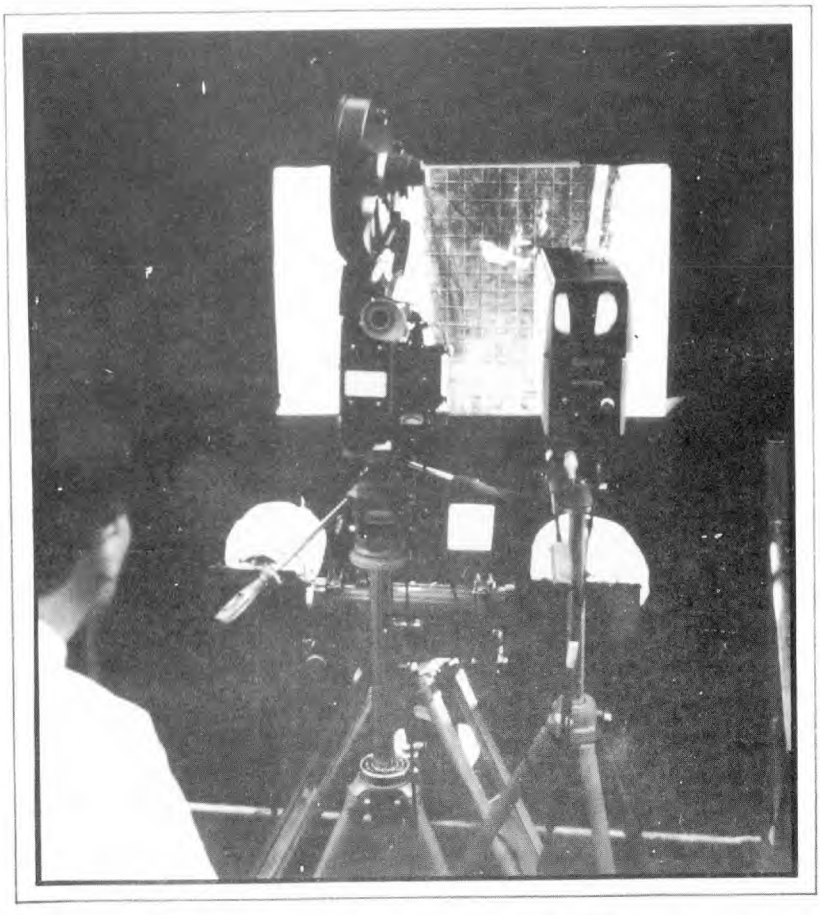

Figure 3.2.4: Three recording techniques for displacement and failure observations used during excavation of model slopes.

since the method involved comparison of the unexcavated model with successive stages of excavation. The method has been described in detail by Wickens and Barton[89]. For the present, the following steps will be taken to summarize the procedures:

1. The camera was set up on a rigid tripod whose legs were placed in holes drilled in the concrete floor of the laboratory. It was essential that no movement of the camera occurred during the two to three days taken to excavate the model, stage by stage.

2. A photograph of the model was taken when it was fully loaded, but before excavation took place. This was the control model, which was taken to represent the zero displacement condition.

3. Photographs were taken when the pit was 8,16, 24, and 32 inches deep and for several steepening stages, until failure occurred. A second set of photographs were taken when the slopes were excavated behind the inner failures.

4. The control photograph, and each of the others in turn were viewed in a stereocomparator. Horizontal displacements occurring as a result of excavation caused the displaced parts of the model to 'bend' away from the 2 inch grid on one side of the model, and 'bend' forward on the opposite side. This three dimensional parallax effect enabled the x (horizontal) displacements to be computed for any points on the model. For convenience this was always done at grid intersections.

5. Rotation of the same photographic plates through 90° enabled the y (vertical) displacements to be measured in the same way.

The sensitivity of measurement was $\pm$ 0.15 mm. (0.006 inch) at best, and individual displacements of nearly 3 mm. (0.120 inch) were recorded near the crest of several slopes. When converted to prototype scale, these represented 3 inches and 60 inches respectively. This was for prototype pit depths of 330, 670, 1000 and 1330 feet deep. The displacement vectors for all the excavation stages of all three large models tested, are presented in Section 3.3

2. Measurement of boundary stresses and displacements

When the models had been finally loaded before excavating commenced, the readings of all the dial gauges on each loading beam were recorded. These displacements represented the approximately triangular distribution of load in each bank of proving rings. They also represented the zero displacement condition.

At each stage of excavation corresponding to each photograph taken, all the dial gauges were gently tapped and read. It was therefore possible to compute the reduction of applied stress at the boundaries and the displacements causing this reduction.

Boundary displacements could be read to approximately one fifth of an 0.0C0linch division. At prototype scale this represented ± 0.01 inch which was extremely sensitive. Similarly, boundary stress changes could be read to approximately ± 2.5 lbf/in^2 at prototype scale (see Appendix 4) All these results are recorded in Section 3.3

3.2.5 DESIGN OF EXCAVATIONS FOR FAILURE

Unlike most mining situations, the model slopes to be excavated needed to be designed to fail when it was considered that sufficient displacement measurements had been obtained. They were in fact designed to fail just after the slopes had been cut to 32 inches height, during the steepening operations.

The information available on the shear strength of the model joints was that obtained from direct shear tests (Section 1.3) and from tilting slope experiments (see Figure 3.1.19, Section 3.1)

The Coulomb parameters appropriate to the normal stress range estimated from self weight stress assumptions were as follows:

cohesion c = 0.10 lbf/in^2

angle of friction ϕ = 58°

(These parameters refer to the primary, continuous joints.) The limitations on the values of possible joint dip angles have been discussed in Appendix 5. In view of these considerations the slopes were designed to be cut in slabs having primary joints dipping at 66°. (Preliminary calculations with dips of 58° and 62° showed that shear failure could not be induced without using steeper angles.) Secondary (and tertiary) joints were taken into account purely as no-tension surfaces, and it was assumed that vertical tension cracks could open unhindered, behind the crest of the slopes.

The limit equilibrium method of slices developed in Section 2.3 was used to calculate the depth of failure for slope angles of 81.7°. This extremely steep slope angle was chosen by trial and error as a convenient slope grade having regard for the dimensions of bricks making up the slopes. The steepness reflects the high shear strength of the rough model joint surfaces, and the absence of water pressure as a failure inducing agent.

For the following input information:

c = 0.10 lbf/in^2

ϕ = 58°

γ = 0.07 lbf/in^3

α = 81.7°

β = 66°

trial value of depth (H) = 36 inches

equations 10 and 11 (Section 2.3) yield the following simplified expressions:

Upper △ :

$$P_{1\rightarrow 10} = \left[\frac{1,3,5 \ldots 19}{100}\right](-2.408) + 0.265 \quad \text{lbf/inch}$$

Lower △ :

$$P_{1\rightarrow 10} = \left[\frac{1,3,5 \ldots 19}{100}\right](-1.170) + 0.129 \quad \text{lbf/inch}$$

The following tabulation of stable and unstable excess forces acting on each of the twenty slices, delineates the stable portion (bracketed).

P values	Upper △	Lower △
P_1	[+ 0.241	+ 0.117
P_2	+ 0.192	+ 0.094
P_3	+ 0.144	+ 0.071
P_4	+ 0.096	+ 0.047
P_5	+ 0.048]	+ 0.024
P_6	- 0.001	+ 0.001
P_7	- 0.049	- 0.023
P_8	- 0.097	- 0.047
P_9	- 0.145	- 0.070
P_{10}	- 0.193	- 0.093

A tension crack is predicted between slices in the upper triangle, denoted by P_5 and P_6. The forces bracketed, represent the portion of the slope that is independently stable, assuming a tension crack can open.

The following pairs of values were plotted to determine the failure depth (at $\Sigma P = 0$):

H (inches)	P (lbf)
36.0	-0.363
32.4	-0.077
28.8	+0.138

The intercept with the $\Sigma P = 0$ (limiting) axis, predicted failure for slopes higher than 31.2 inches.

The above tabulation was for a slope height of 36 inches. Consequently a reiteration with H=31.2 inches was needed to produce an

accurate tabulation of the P values for slices dividing a slope of 31.2 inches in height. Alternatively equation 12 (Section 2.3) could be used to find the position of the tension crack behind the crest, using the minimising relation suggested by Markland[60]. However this would not delineate the zones where joints were theoretically overstressed, which was of interest in terms of pre-failure displacement measurements.

The reiterated calculations and tabulations are given below.

Upper $\triangle$: $P_{1\rightarrow 10} = \frac{(1,3,5,\ldots.19)}{100}\ (-1.809) + 0.229$ lbf./inch

Lower $\triangle$: $P_{1\rightarrow 10} = \frac{(1,3,5,\ldots.19)}{100}\ (-0.879) + 0.112$ lbf/inch

P values	Upper	Lower
P_1	[+0.211	+0.103
P_2	+0.175	+0.086
P_3	+0.139	+0.068
P_4	+0.103	+0.051
P_5	+0.067	+0.033
P_6	+0.031]	+0.015
P_7	-0.006	-0.002
P_8	-0.042	-0.020
P_9	-0.077	-0.037
P_{10}	-0.114	-0.055

The value of P for all values with the exception of those bracketed was + 0.002 lbf/inch which confirmed the accuracy of the iteration.

The approximate length of joints overstressed, and some stages of excavation are shown in the scale drawing reproduced in Figure 3.2.5. The heavy vertical and horizontal lines represent the 2 inch square grid etched on the glass in front of the model, and also coincide with vertical and horizontal, secondary and tertiary joints. The steeply dipping primary joints ($\beta = 66^\circ$) are marked with dashed lines where the shear stresses calculated from self weight stress assumptions, exceed the shear strength defined by c = 0.10 lbf/in^2, $\phi = 58^\circ$. The failures of tilt models shown in Section 3.1 (Figures 3.1.15 and 3.1.18) should be compared with these theoretical limit equilibrium predictions. The agreement is remarkably close.

It is shown in Section 3.3 that slopes excavated in high horizontal stress fields ($\sigma_h = 2\sigma_v$) produce most unexpected slope failure angles, which contradict current opinion on the effect of stress concentrations at the toe of steep slopes.

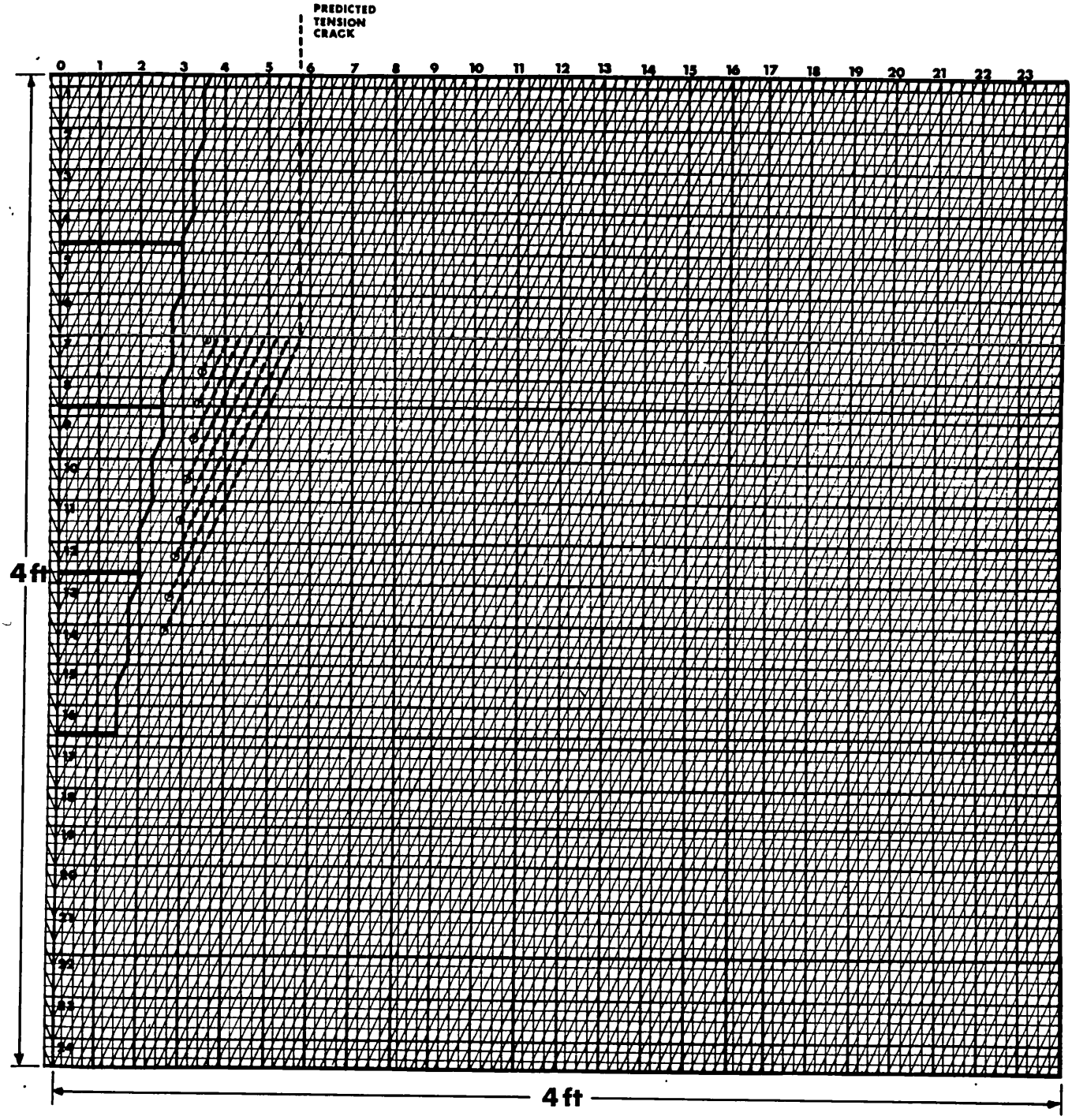

Figure 3.2.5 A scale drawing illustrating half a jointed model and the zone of overstressed joints beneath a 32 inch slope.

3.3 PRE-FAILURE AND POST-FAILURE OBSERVATIONS OF THREE MODEL OPEN CUTS.

SUMMARY

The displacements occurring behind model slopes as a result of excavation are plotted as scaled vectors on photographs of the excavations. These vectors, which were obtained from photogrammetric measurements, indicate the far reaching effect of even small open cuts on displacements in the surrounding rock. The displacement vectors are given for several stages of excavation for three large models. The first two were tested with a high horizontal (tectonic) stress but had different jointing. The last model was tested with a low horizontal stress.

The displacements and stress changes occurring out at the vertical boundaries of the model as a result of excavation, were monitored at corresponding stages of excavation. These show the relevance of a fixed strain energy loading system.

An unexpected joint closure phenomenon is reported. It was found that the normal and shear stresses acting on a given joint set before excavation, reversed in magnitude when slopes were excavated above the joints. This meant that a joint involved in shear failure as a result of excavation had previously been consolidated at a much higher normal stress. A series of pre-consolidated direct shear tests were performed and demonstrated the important effect of mass closure on shear strength.

The post-failure characteristics of steep model slopes are shown by means of sequence photographs, taken from cine films of the failures. The steepness of the slopes at failure was seen as a direct result of the mass closure effect. The failures were back analysed by simple limit equilibrium methods.

3.3 PRE-FAILURE AND POST-FAILURE OBSERVATIONS OF THREE MODEL OPEN CUTS.

INTRODUCTION

This final section on model behaviour presents all the results of the large model tests, in which highly discontinuous models were loaded both by gravity and horizontally. Open cuts were excavated from the surface of these models, and the eventual slope failures recorded on 16 mm. cine film. The displacements occurring within the slopes as a result of stage by stage excavation were recorded and measured by means of simple photogrammetric techniques. Displacements and stress changes at the boundaries of the model caused by the excavations were also monitored.

A total of three large models were constructed and excavated to failure. The first one, which was of an experimental nature, was jointed in two directions neither of which coincided with the vertical and horizontal slab boundaries (see Appendix 5). In the light of experience gained with this first model, the two subsequent ones were jointed in three directions, two of which coincided with the slab boundary directions.

The last two models were structurally identical, but were loaded horizontally to two different levels of stress. Firstly, a triangular distribution approximately twice the vertical gravity stress was applied. It was anticipated that this would induce failure at slope heights and inclinations of lower values than for the second model, which was loaded to a stress level equal to only half the vertical gravity stress. As will be shown, this proved to be a false assumption.

The observations and measurements of pre-failure displacements, both in the slopes and at the model boundaries, will be presented for each of the three models in turn. Following this the post-failure deformations will be shown in the form of sequence photographs taken from the cine films of the failures. The unexpected effect of different horizontal stresses on stability is convincingly explained by a series of specially designed shear tests.

3.3.1 PRE-FAILURE OBSERVATIONS OF MODEL L.M. 1

The first model test differed from the following ones in two ways:

1. The jointing was symmetrical about a vertical plane, such that the two joint sets dipped at 66° and 114° (66°) It was arranged so that a symmetrically excavated cut would be intersected on both sides by primary joints dipping at 66°. The centre of the model was therefore an axis of symmetry.

2. Overlapping pairs of photographs were taken to give stereo coverage of the central two thirds of the model. This technique proved to be unnecessary, and the following models were photographed with only one camera, placed centrally to give complete coverage of the model. Displacements were measured by comparing the undisplaced photograph taken before excavation, with succeeding photographs of different stages of excavation.

Figure 3.3.1 illustrates this jointing and also the non-symmetry of the camera position. The white sheets of paper fixed to the model frame were placed so that the collimation marks of the camera would be visible in the exposed plates.

Model L.M.1 was loaded horizontally to a stress level approximately equal to twice the gravity induced self-weight stress. ($\sigma_h = 2\sigma_v$). However a stress intercept of 1.4 lbf/in^2 was found to exist at the surface, based on the dial gauge readings. Tests conducted on the loading beams prior to model construction indicated that when loading against a flat, rigid steel beam in place of the model, relatively linear triangular distributions of load were recorded in the proving rings showing zero stress at the surface (see Appendix 4.) For design distributions of $\sigma_h = \frac{1}{2}$ and $3\sigma_v$, overall errors of 11.4 and 11.7% were recorded in these trial loadings, which were presumably caused by frictional losses in the pistons.

However, the surface stress intercept obtained when loading the discontinuous models indicated that the model resistance was trapezoidally distributed. This was perhaps a function of the active and passive resistances of the models. An unloaded vertical model slope 4 feet high tends to topple outwards in the upper third (see Figure 3.1.8) which constitutes an active pressure on the loading beam compared to the passive resistance lower down.

1. Slope deformations

Figures 3.3.1, 3.3.2 and 3.3.3 illustrate stages A,B and C of excavation in model L.M.1. A limited number of displacements were measured, mainly to delineate the optimum positions for measuring displacements in the later models.

The mean displacement vectors for both sides of the excavations shown in these figures, and in all the others to follow, are drawn to a scale of 5:1 (0.2 inches representing 1 mm. of model displacement). They are drawn in the overall direction of maximum displacement for each excavation stage. Any points on the model which indicated an undetectable amount of displacement are indicated by blank circles. The sensitivity of measurement was no better than $\pm$ 0.15 mm ($\pm$ 0.006 inch), therefore elastic displacements resulting from unloading were undetectable.

The magnitude of the displacements at the measurement points closest to the slope crests for each of the stages A,B,and C are given overleaf.

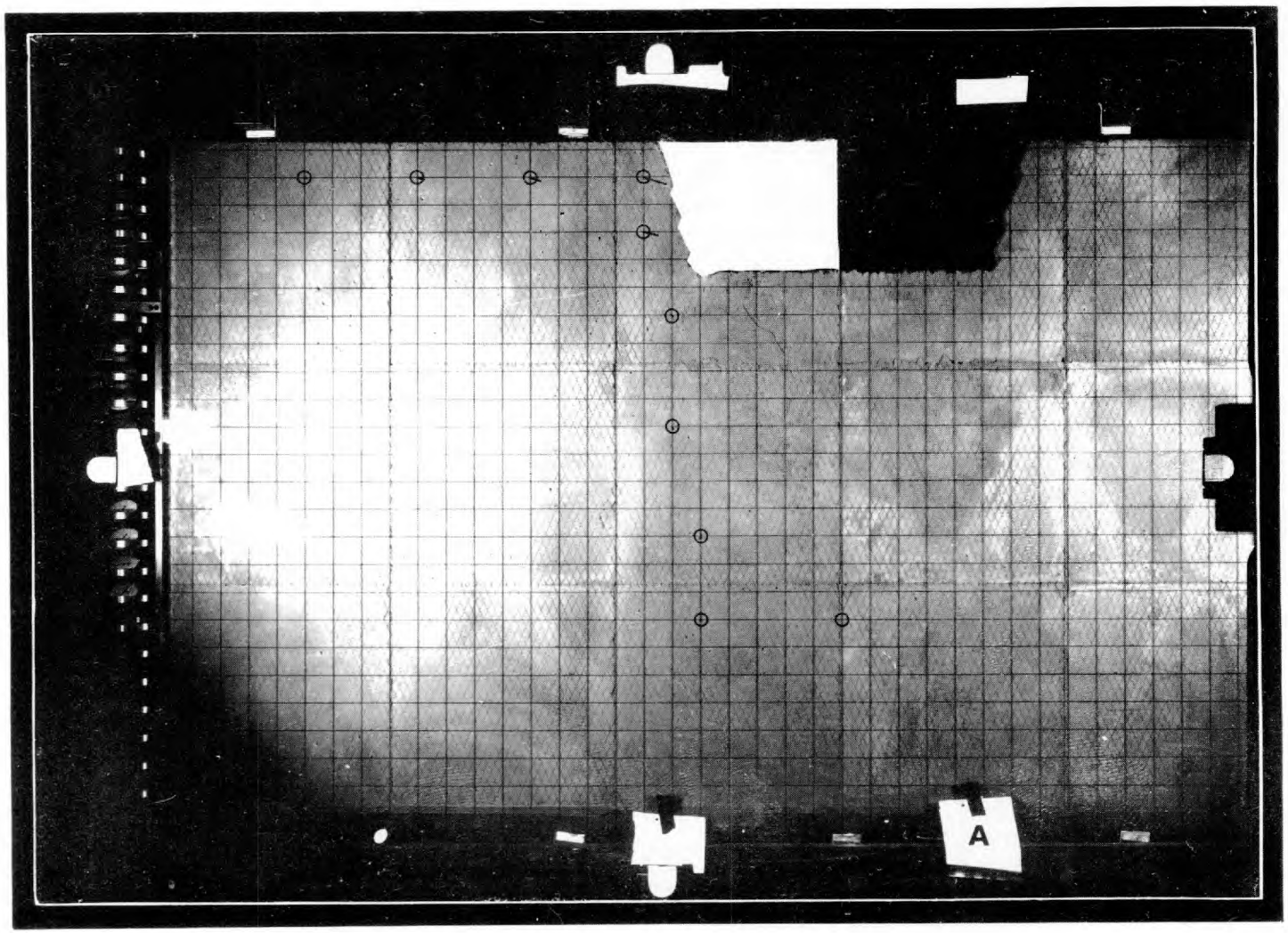

Figure 3.3.1 Mean displacements, Stage A of model L.M.1.

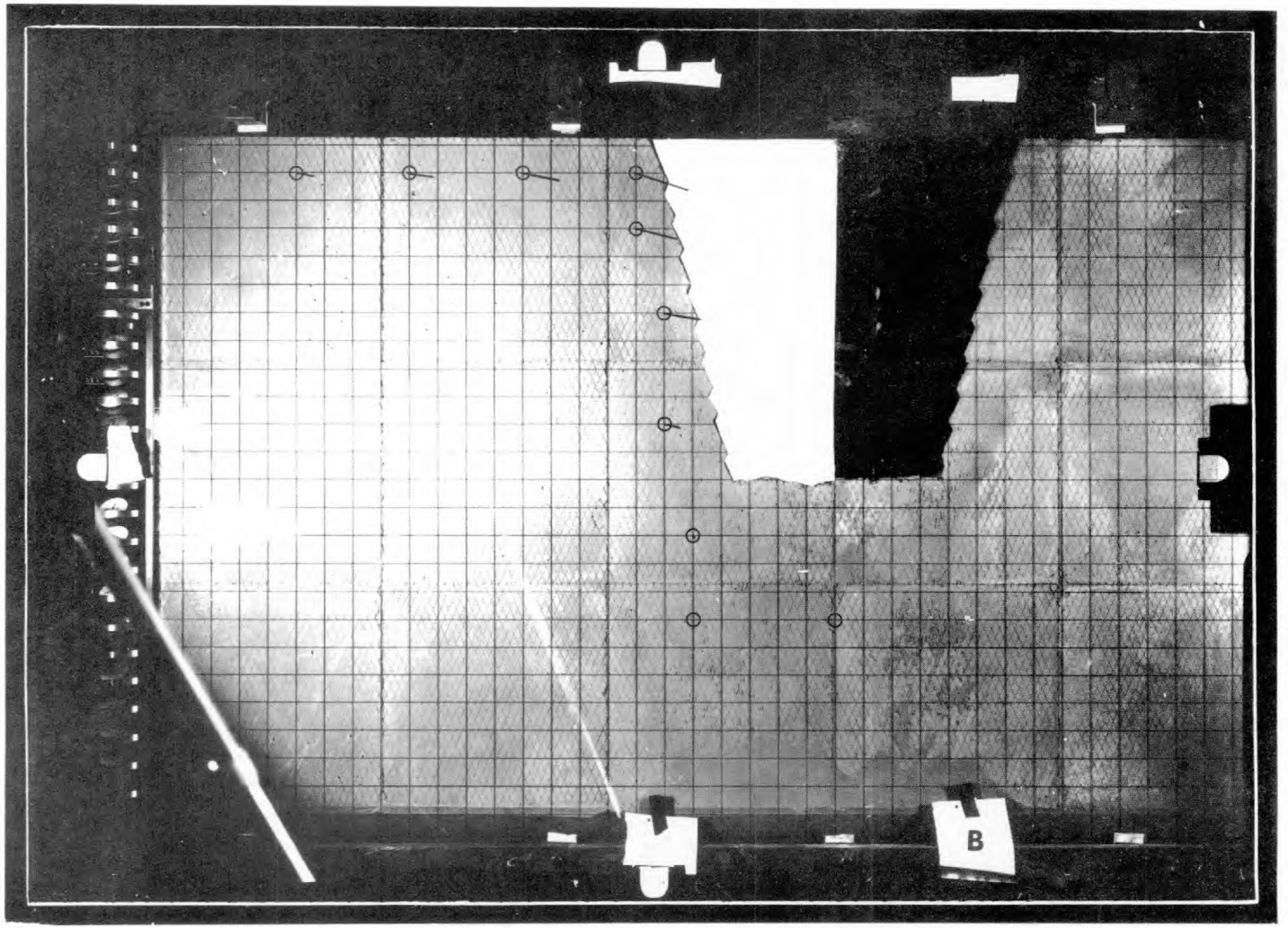

Figure 3.3.2 Mean displacements, Stage B of Model L.M.1

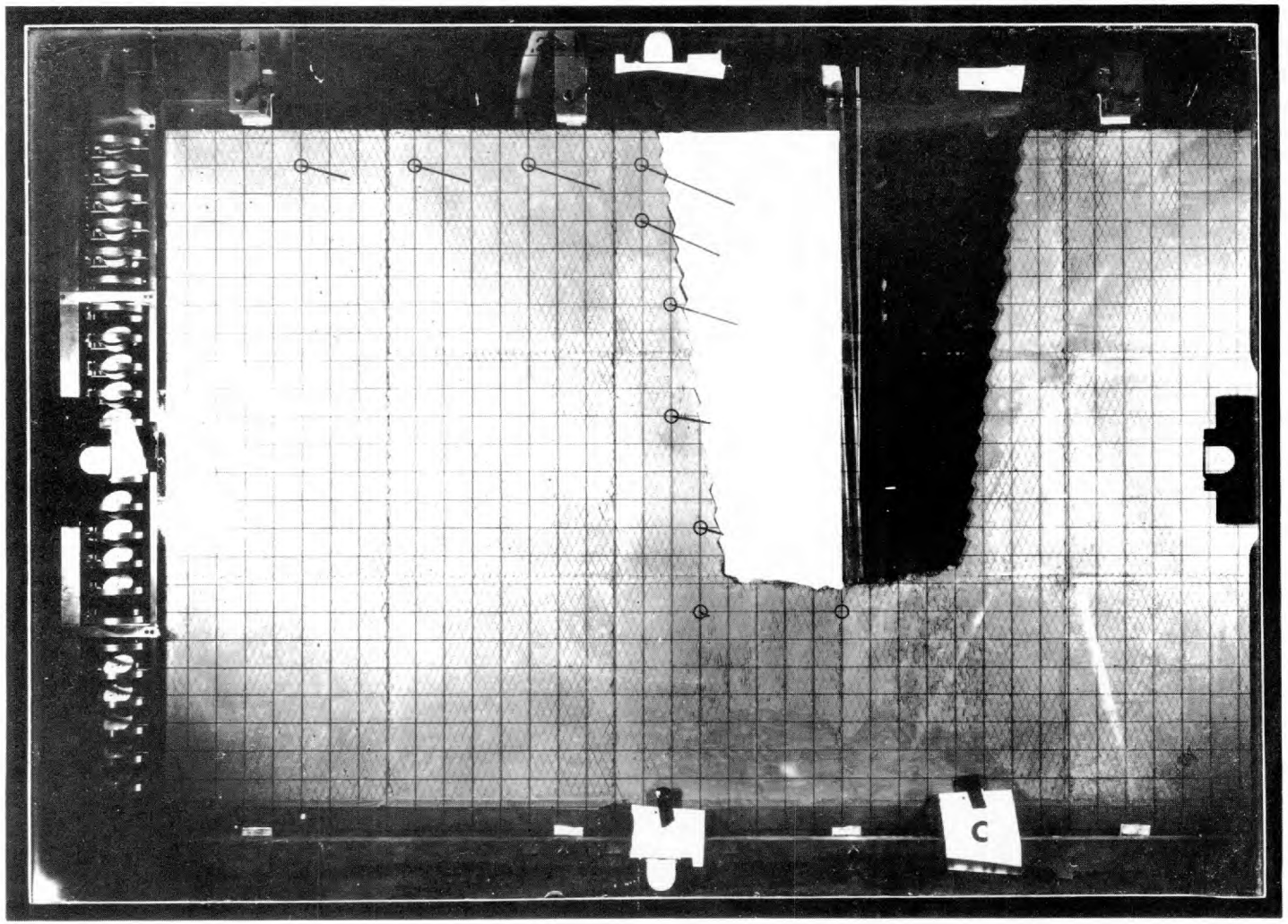

Figure 3.3.3 Mean displacements, Stage C of model L.M.1

Stage	Displacement	Inclination
A	0.028 inch	17°
B	0.063 inch	18°
C	0.116 inch	23°

When converted to prototype dimensions (λ = 1:500), the slope heights, inclinations and crest displacements have the following values:

Stage	Slope		Displacement at
	Height	Inclination	Crest (inches)
A	375	77°	14.0
B	1020	77°	31.5
C	1330	81°	58.0

The displacement vectors illustrated in the three figures suggested the following conclusions:

1. At no point in the models were uplift displacements detectable as a result of unloading.

2. The maximum displacements occurred at the crest of the slopes and reduced with increasing depth below the crest. This was presumably a function of the small pre-peak displacements occurring on all the joints which dipped steeply into the excavation. The joints nearest the crest would obviously be less highly stressed in shear than those lower down. However, since the normal stress acting across these joints was also reduced (τ / σ = tan 66°), the small pre-peak displacements occurring on all the exposed joints were contributing to the total displacement.

   The fact that the displacements were not a maximum in the 66° dip direction was probably due to two phenomena in particular:
   a) The low normal stress range acting across the steeply dipping joints meant that pre-peak shear displacements were probably following steeply dilatant paths due to the joint roughness (Section 2.1).
   b) Small approximately vertical tension cracks were noticed behind the crest of most of the slopes once the slope height was approaching that of stage B.

3. In the early stages of excavation, photogrammetric measurement points located behind the crest in a horizontal line showed

undetectable displacements close to the model boundaries. However, as the excavations became deeper (and steeper) the displacements increased enormously. It will be seen presently that the models eventually came out of contact with the loading plattens. The displacements occurring as a result of the excavations were so large that the strain energy in the system was dissipated in the upper third of the models and proving rings.

It is clear that the usual constant stress loading devices would have been artificial in the extreme, for such model situations. The fixed strain energy 'soft' loading system was clearly more relevant, though the most realistic 'equivalent slice' to be designed remained an unknown.

2. Boundary displacements

Figure 3.3.4 shows the displacements occurring over the full height of the model, as recorded on the proving ring dial gauges. Six of the proving rings could not be fitted with gauges and the displacements occurring here are shown dashed.

It will be recalled from Appendix 4 that boundary displacements as small as 0.00002 inch could be recorded on these sensitive dial gauges. (This was 300 x the sensitivity of the photogrammetric method.) At prototype scale this represented 0.01 inch which was still extremely sensitive. The plot of displacements was not drawn to this accuracy, but despite this the sensitivity of the boundaries to excavations can be clearly seen. Stage A excavation which was only 9 inches deep effected the boundaries 36 inches away horizontally, and down to a depth of 48 inches. At prototype scale these represented 1500 feet and 2000 feet respectively, for a pit depth of only 375 feet.

The photogrammetric displacements of the points closest to the boundaries are given by points a, b and c. These correspond to the excavation stages A,B and C respectively. They indicate that the small amount of strain energy stored in the upper-most proving rings was dissipated early on in the excavation sequence, since an obvious discrepancy exists between the two displacement records. It can be concluded that approximately one-third of the model was no longer stressed or even in contact with the loading beams, by the time stage C was reached.

3. Stress changes at boundary

Figure 3.3.5 shows the irregular nature of the initial stress distribution (O) recorded from dial gauge readings before excavation commenced. It was suggested in Appendix 4 that the real distribution of stress at the face of the models was more uniform than that

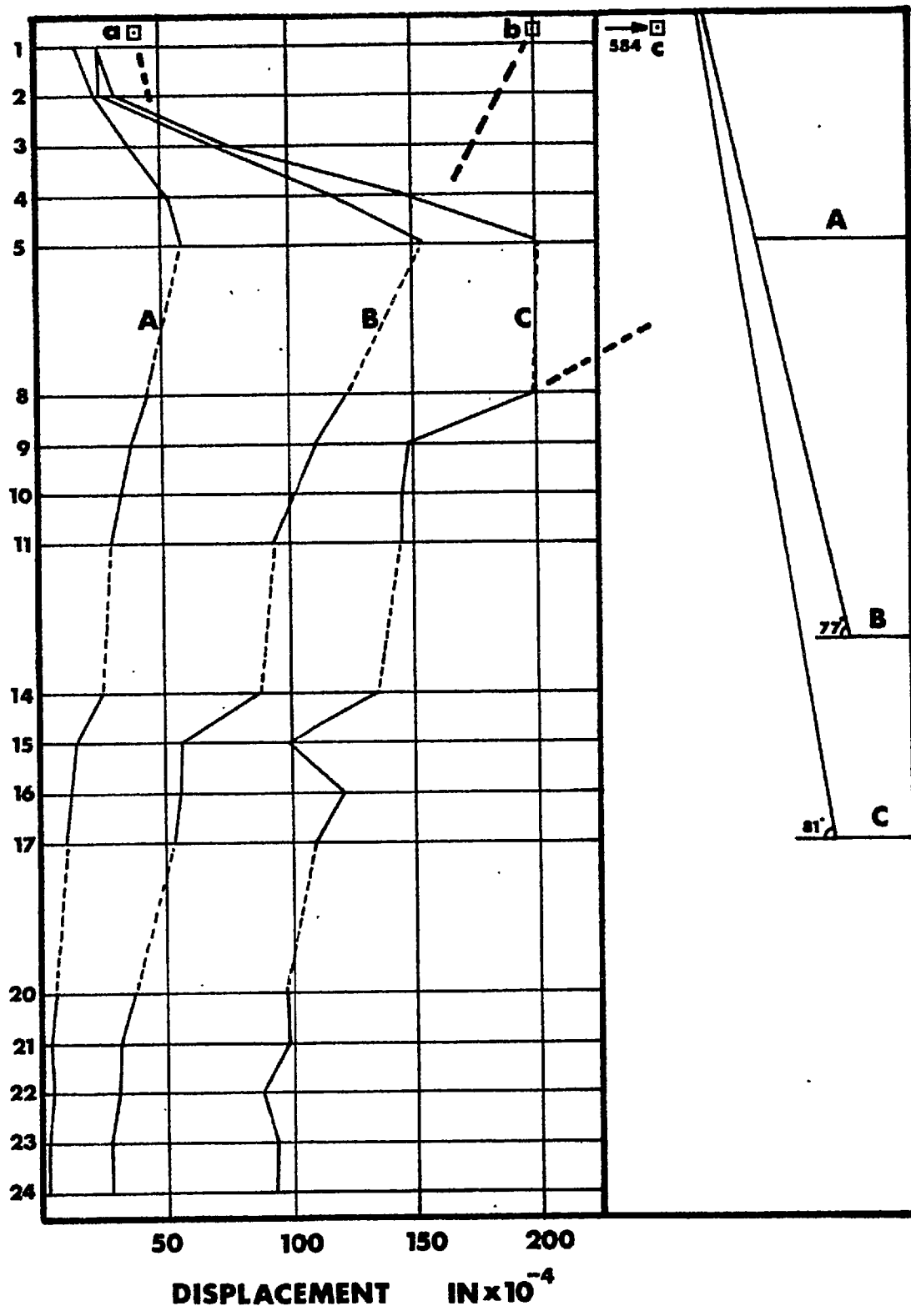

Figure 3.3.4 Mean displacements at boundaries of model L.M.1

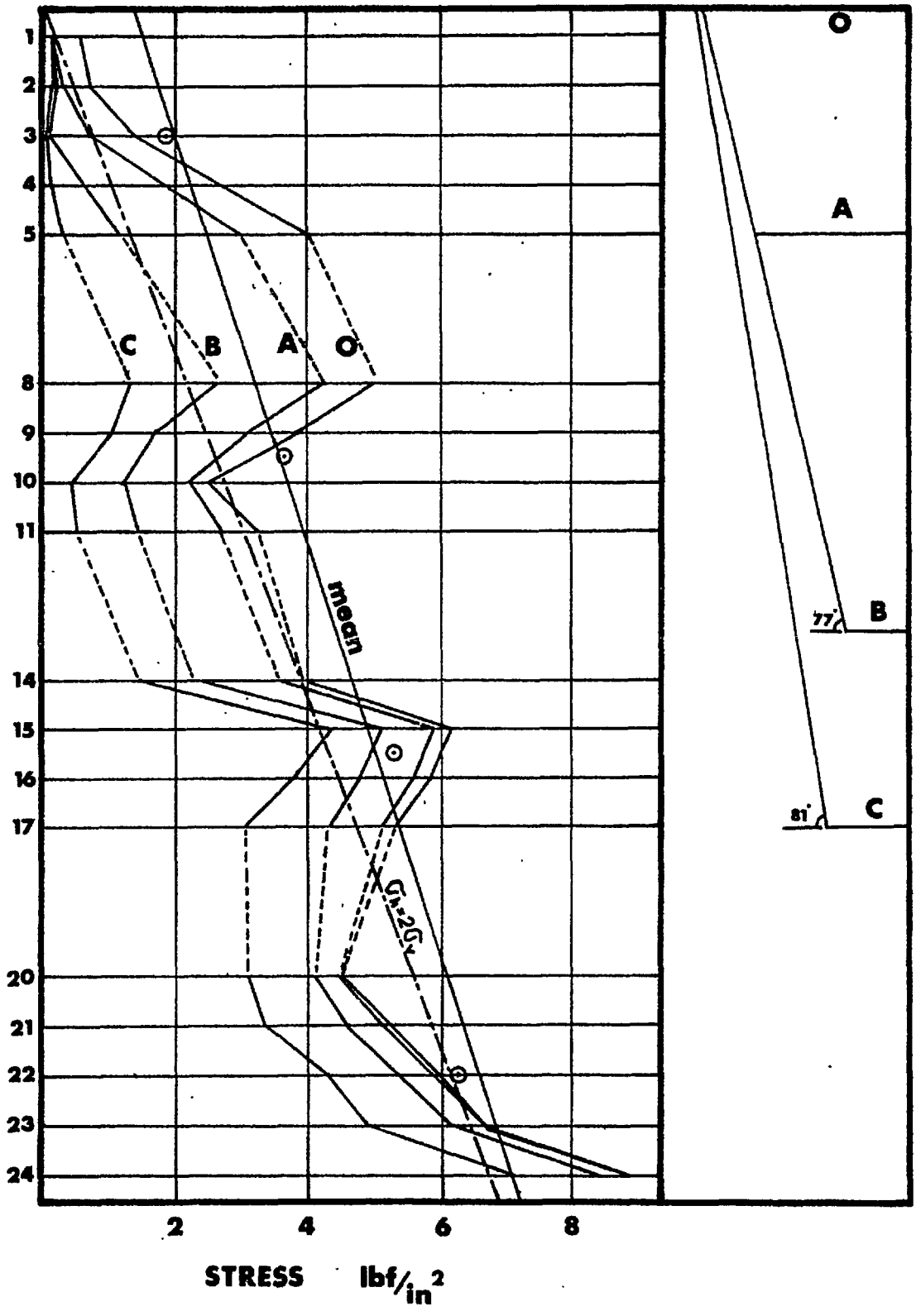

Figure 3.3.5 Mean horizontal stresses at boundaries of model L.M.1

recorded across the proving rings, due to the precautions taken to distribute the platten loads via P.T.F.E. lubricated laminations of rubber. It is not however possible to verify this one way or the other.

The changes of applied stress with excavation were a function of the displacements occurring across the proving rings due to model relaxation. These changes were proportional to the boundary displacements presented in Figure 3.3.4.

The mean linear distribution of stress is seen to be somewhat higher than the triangular distribution ($\sigma_h = 2\sigma_v$). The following equations describe the mean values for the model:

$$\sigma_h = 1.40 + 0.121h$$
$$\sigma_v = 0.07h$$

lbf/in^2 (h in inches)

Conversion to the prototype values depends on the ratio of the stress to geometric scales (ψ/λ), since the equations relate stress to depth. Thus for the prototype with (ψ/λ) = $^{666}/_{500}$:

$$\sigma_h = 933 + 1.94\,h$$
$$\sigma_v = 1.12\,h$$

lbf/in^2 (h in feet)

The surface intercept of 933 lbf/in^2 is of a similar magnitude to half the horizontal stress sum ($\sigma_1 + \sigma_2$) deduced from stress measurements by Hast [81] (see Section 3.2). Therefore although not zero as designed, it is at least no more severe than has been measured in certain situations. It can perhaps be taken to represent possible stress levels in a tectonically active area.

3.3.2 PRE-FAILURE OBSERVATIONS OF MODEL L.M.2

Figure 3.3.6 illustrates the jointing employed in this and model L.M.2. Once again it was designed so that primary joints dipped steeply into the slopes at 66° on both sides of the excavations. The vertical centre line of the model was therefore an axis of symmetry, and the displacement vectors shown are the mean of both sides of the excavation. Exceptions to this will be indicated in the text. The horizontal stress distribution was similar to that applied to model L.M.1

1. Slope deformations

The unexcavated stage A of Figure 3.3.6 shows the total number of points which were measured for displacement monitoring, during the various stages of excavation. The crest positions for stages B and C of Figure 3.3.6, and for D,E and F of Figure 3.3.7 indicated the following magnitudes and directions of displacement:

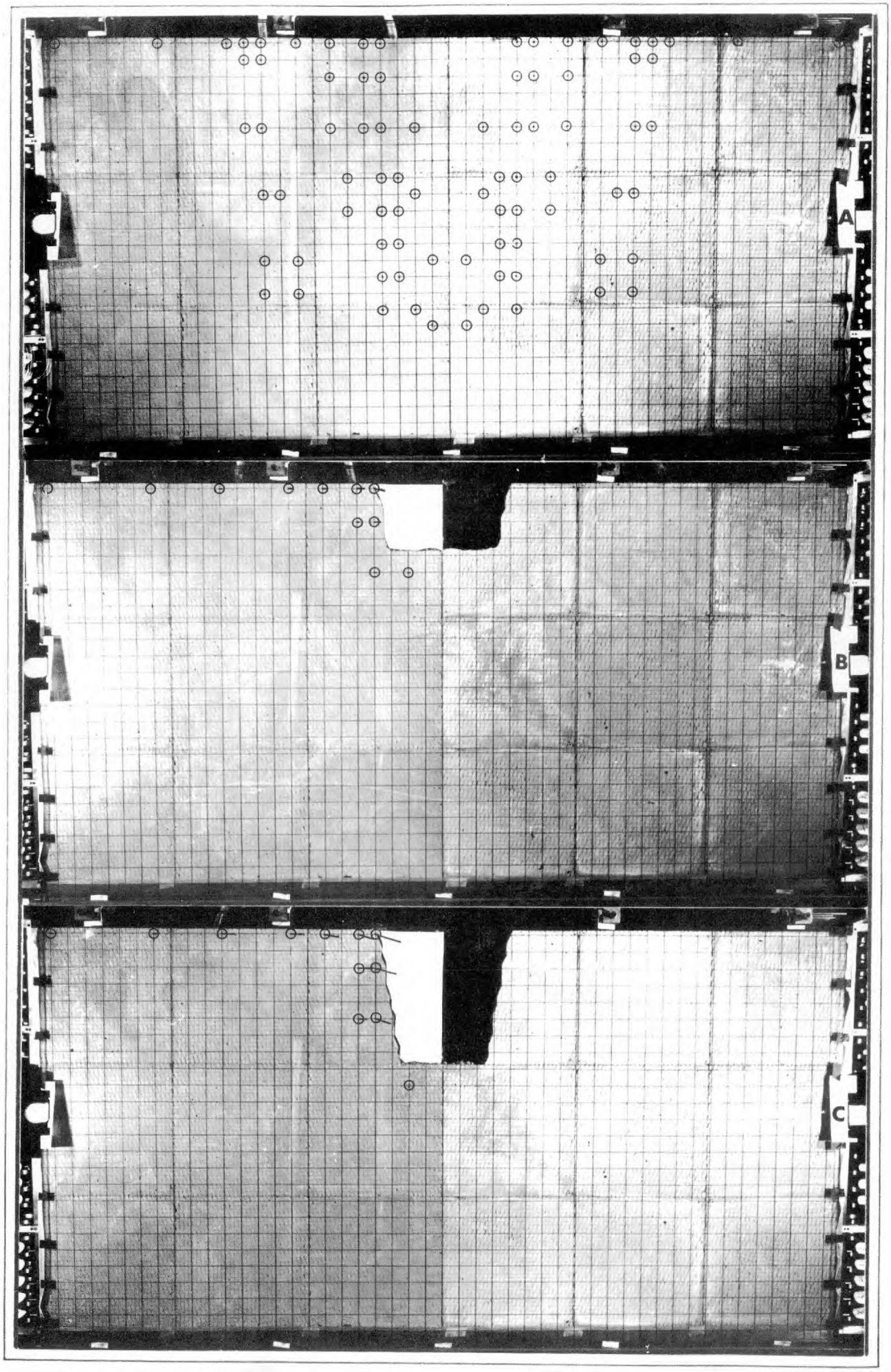

Figure 3.3.6 Mean displacements, stages A, B and C of model L.M.2

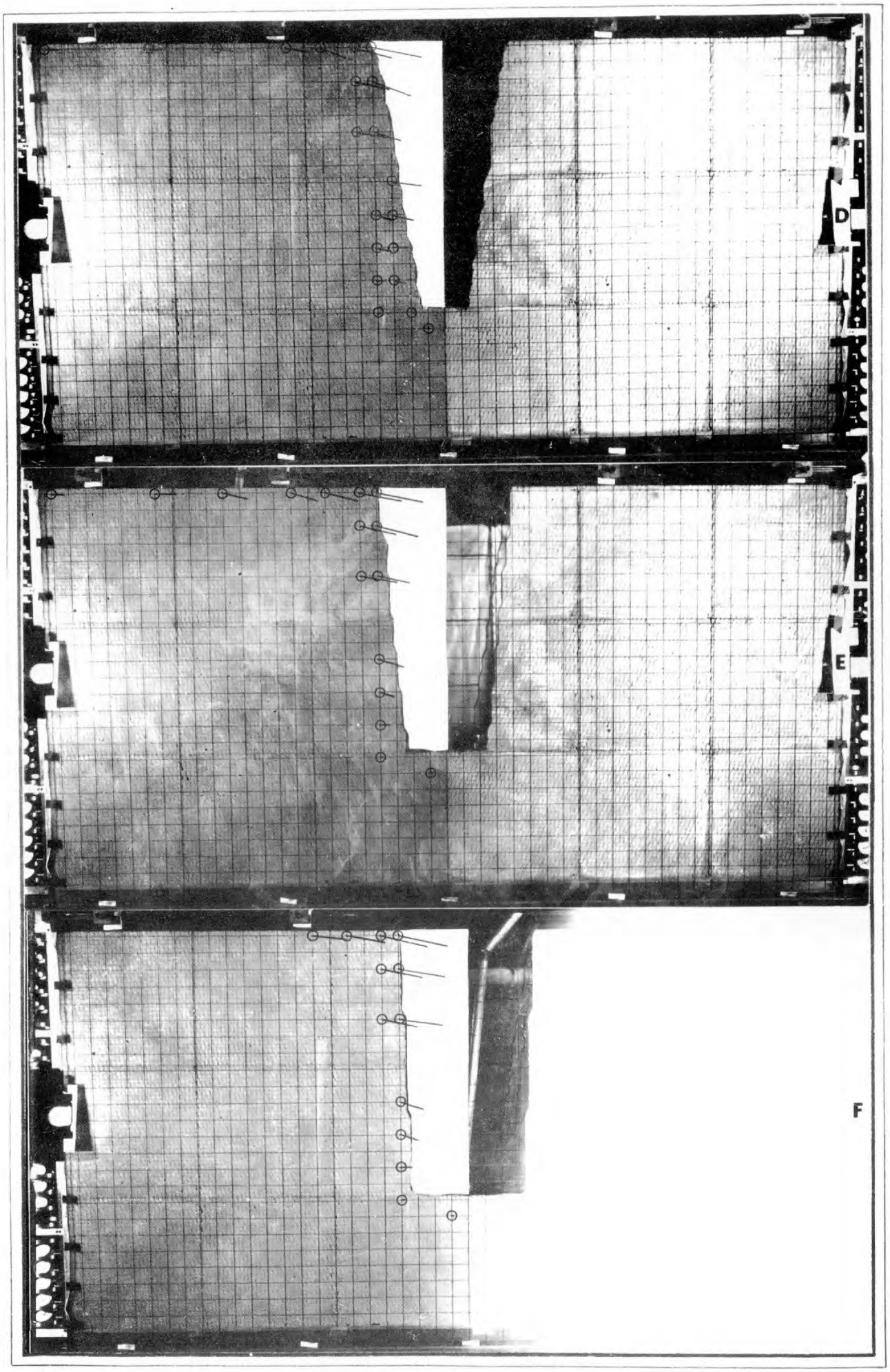

Figure 3.3.7 Mean displacements, stages D.E and F of model L.M.2

Stage	Displacement (inch)	Inclination
B	0.018	13°
C	0.042	17°
D	0.078	12°
E	0.076	12°
F	0.082	12°

When converted to prototype dimensions, the slope heights, inclinations and crest displacements have the following values:

Stage	Slope		Displacement at crest (inches)
	Height (ft).	Inclination	
B	333	81°	9.0
C	667	81°	21.0
D	1330	81°	39.0
E	1330	84°	38.0
F	1330	87°	41.0

Due to a faulty exposure, the displacements measured for stage F were only those of the left hand side of the excavation.

It can be seen from the tabulation of pit slope inclinations, that the model slopes were standing at considerably steeper angles than the predicted maximum of 31 inches/81° derived in Section 3.2. When failure did eventually occur the debris was cleared and two new slopes were excavated closer to the boundaries, in essentially unstressed 'ground'. Figure 3.3.8 shows that failure had not occurred even when the slopes were vertical, for this highly stressed model. There is a fundamental reason for this which will be introduced after the sequence photographs of failures have been shown.

The crest displacements for the new stages G and H were .072 and 0.093 inch, and were inclined at 8° and 16° respectively. The increased inclination of the displacement vectors caused by steeping the slopes from 81° to 90° are clearly shown in Figure 3.3.8.

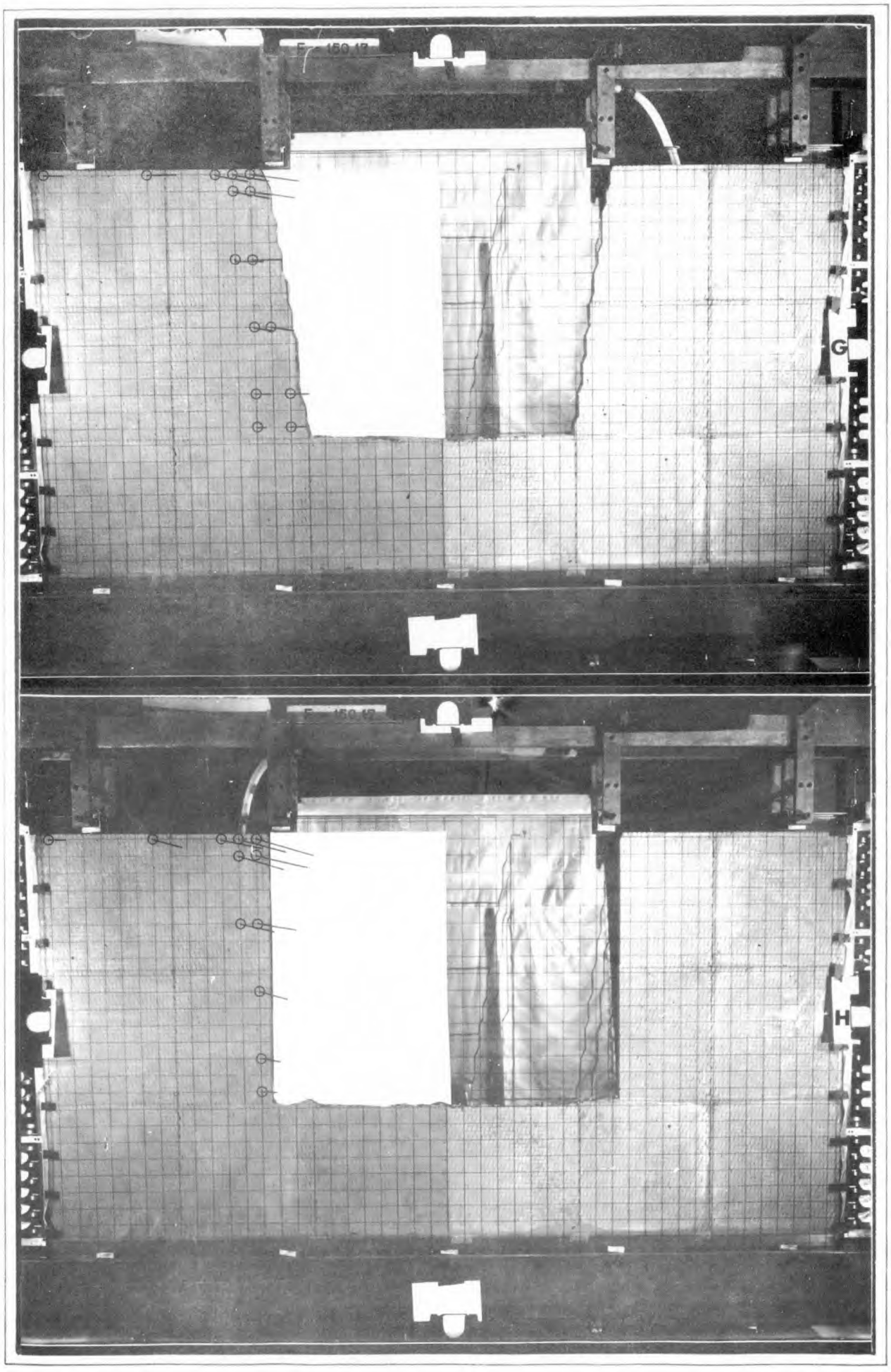

Figure 3.3.8 Mean displacements, stages G and H of model L.M.2

A particularly noticeable feature of the displacement vectors was the horizontal nature of the surface displacements behind the crest of the slopes. However, nearer the crest a marked declination of the vectors occurred. This appeared to initiate at the surface intercept of the most highly stressed joints which were exposed right at the toe of the excavations. It can therefore be seen as a direct result of pre-peak shear displacements occurring on the steeply dipping joints.

The displacement vectors of points behind the toe of the slopes are seen to flatten out with increasing depth below the crest. Most of the vectors are horizontal in the bottom 4 inches of the slopes, and reduced to undetectable magnitudes at and below the toe of the slopes.

Comparison of the magnitudes of displacement between models L.M.1 and L.M.2 reveal that the displacements in the latter were as little as 65% of those of the first model. In view of the fact that the stress distributions were fairly similar this must be a reflection of the differences of joint directions. Normally one would expect a 33% increase in the number of joint sets to cause larger displacements. However model L.M.2 was jointed horizontally and vertically, with only one joint set inclined to the principle stress directions operating before excavation. In comparison, both joint directions were inclined in model L.M.2, which meant that shear stresses were developed on twice the number of joints.

It should be remembered that the displacements occurring in these models were several orders of magnitude larger than the elastic displacements which would be predicted from analyses of unjointed models. The enormous influence of jointing was dominated by the low shear stiffness effect. Therefore two sets of joints subjected to shear stresses during unloading would be expected to have far greater influence than only one set.

2. Boundary displacements

Figure 3.3.9 shows the incremental displacements for eight stages of excavation in model L.M.2. Unfortunately the photogrammetric record of the unlettered stage between B and C was spoiled. However the boundary displacements are recorded for completeness

It is interesting to compare Figures 3.3.9 with the equivalent Figure 3.3.4 for model L.M.1. Comparison of an equivalent stage of excavation (D and C respectively) reveal that the difference in the joint orientations also affected the boundary displacements at the base of the model. This difference was maintained to a great extent, for most of the height of the model. Note in particular the photogrammetric displacements plotted at the top of the figures (points d and c).

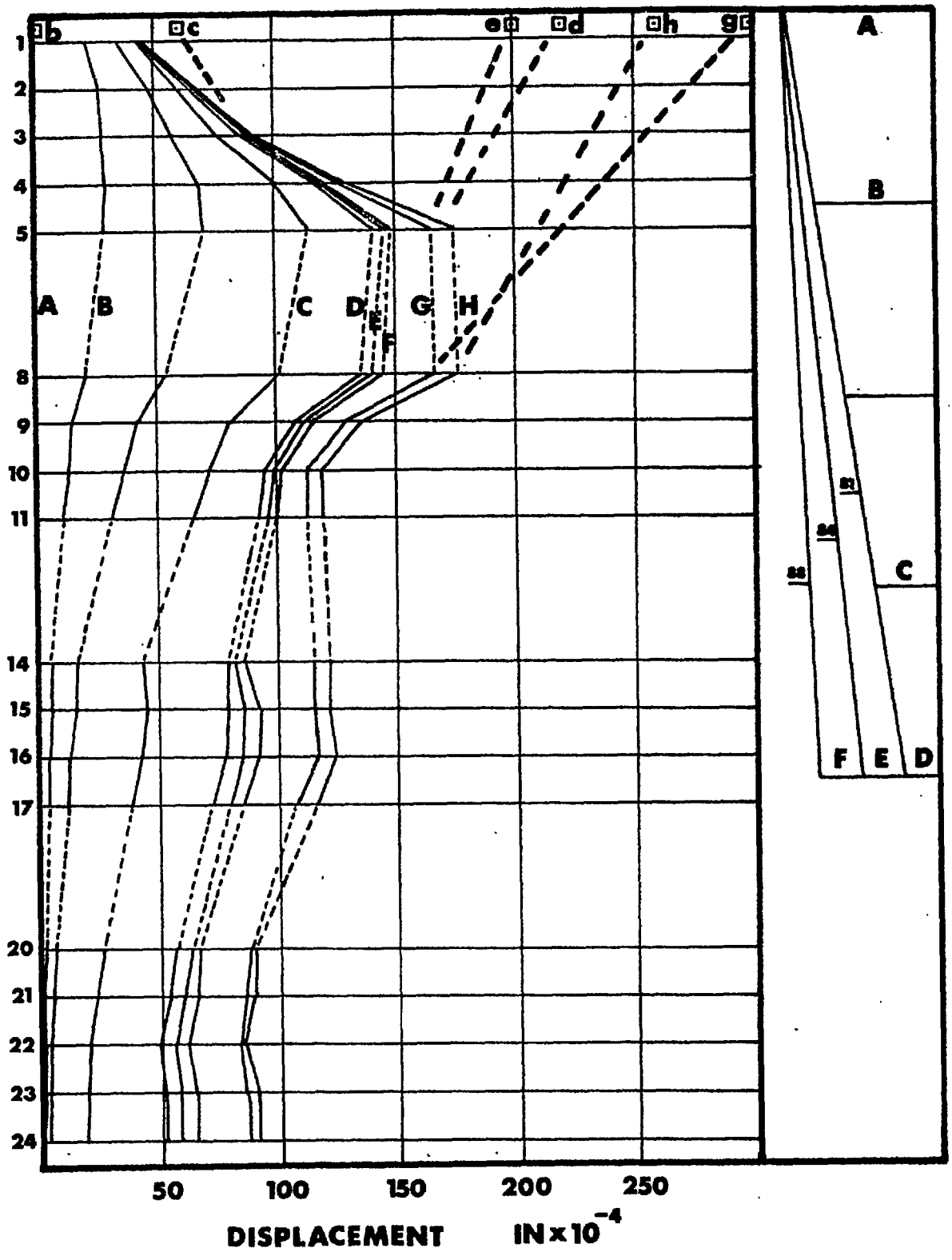

Figure 3.3.9 Mean displacements at boundaries of model L.M.2

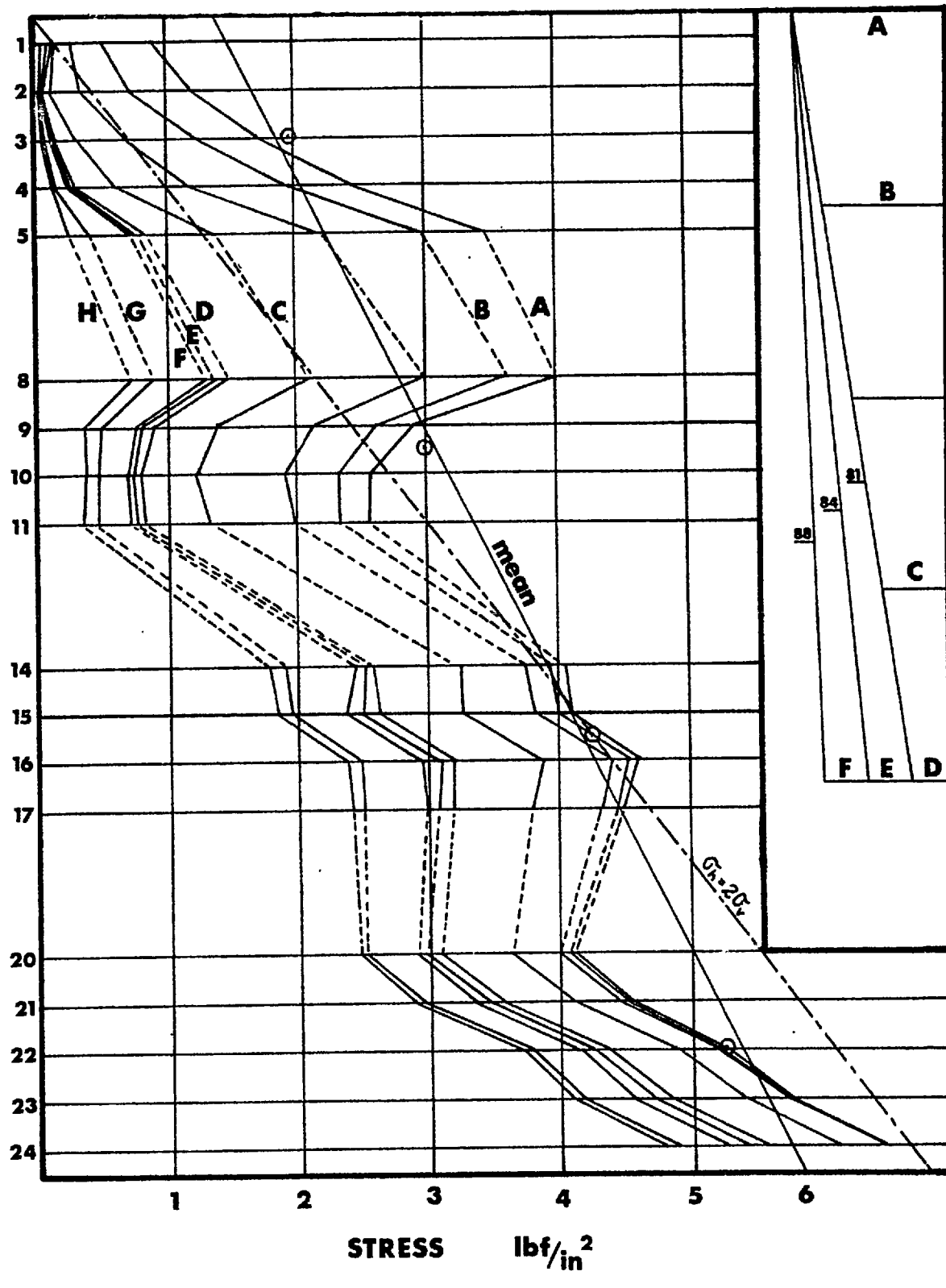

Figure 3.3.10 Mean horizontal stresses at boundaries of model L.M.2

3. Stress changes at boundary

Figure 3.3.10 reveals another non-uniform distribution of stress with a particularly marked bulge in the upper third of the model. Once again it must be assumed that this is a result of the active and passive regions of model resistance.

The equations describing the mean model and prototype principle stress distributions are given below:

Model: $\sigma_h = 1.39 + 0.093\,h$

$\sigma_v = 0.07\,h$

lbf/in^2 (h in inches)

Prototype: $\sigma_h = 926 + 1.48\,h$

$\sigma_v = 1.12\,h$

lbf/in^2 (h in feet)

The surface intercepts of stress for this model, and for model L.M.1 are seen to be almost identical. However for some reason the gradients differed by about 25%. Again this may be a function of the different jointing causing differences in the active and passive resistance. The same piston load was actually applied in each case.

3.3.3 PRE-FAILURE OBSERVATIONS OF MODEL L.M.3

Figure 3.3.11 illustrates the jointing used in model L.M.3 which was identical to that of model L.M.2. The only difference between the two models was the lower horizontal stress. A distribution approximately equal to $\frac{1}{2}\sigma_v$ was applied in this case. Therefore the vertical self weight stress was now the principle stress direction.

It was noticeable when excavating this model that the whole structure was looser. Blocks could be sucked out of place with much greater ease and more care had to be taken when excavating. For this same reason tension cracks developed somewhat earlier, and sometimes one 'major' opening was accompanied by small loosening movements of 'columns' adjacent to the slope face.

1. Slope deformations

As a result of the lower magnitude of stored strain energy in the proving rings, the displacements occurring near the boundaries of this low stressed model were less than both the previous cases. However, stages B,C, D and E (right had side only) indicated that the slope displacements were similar. The following magnitudes of crest displacement were recorded:

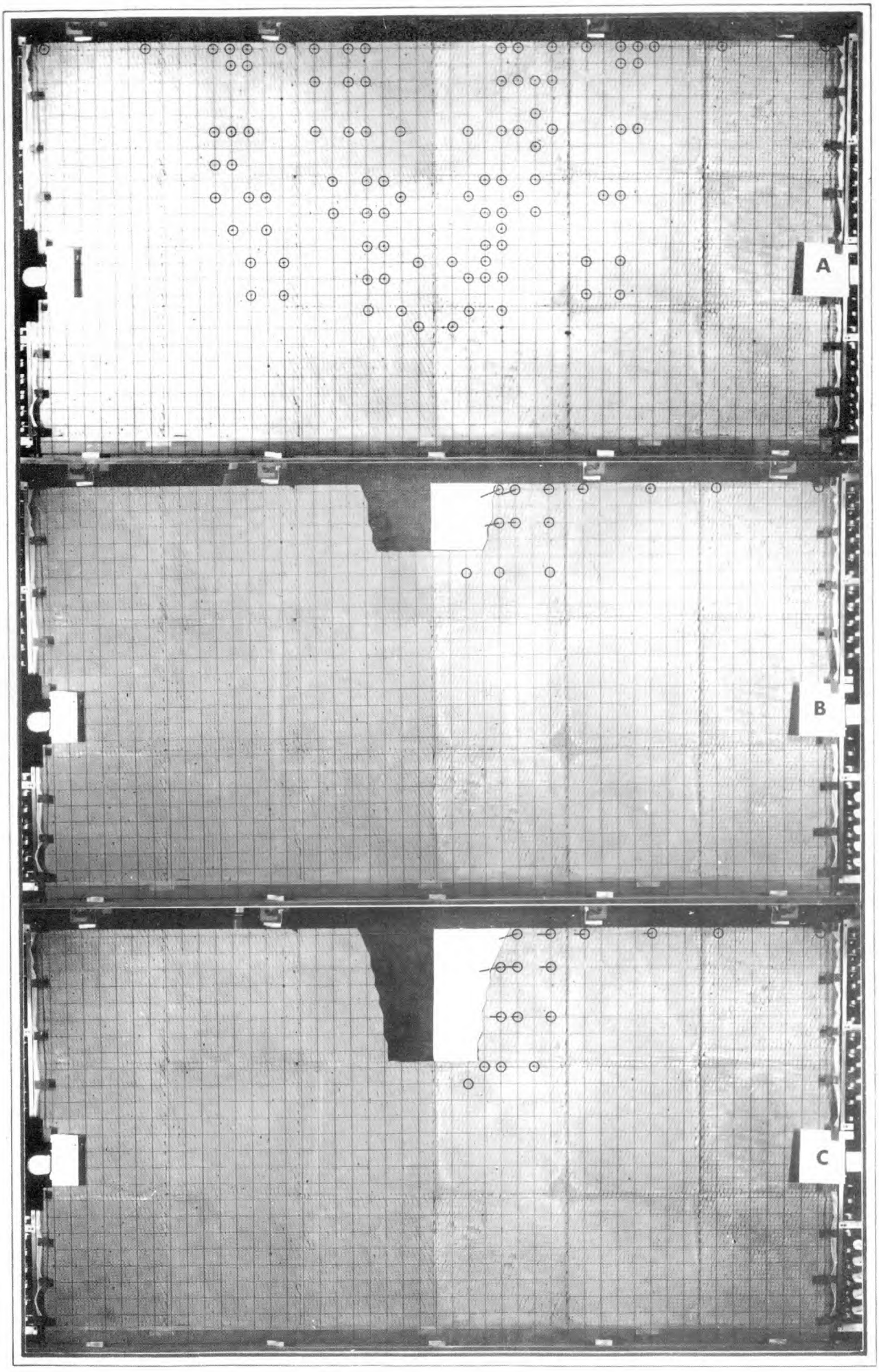

Figure 3.3.11 Mean displacements, stages A,B and C of model L.M.3

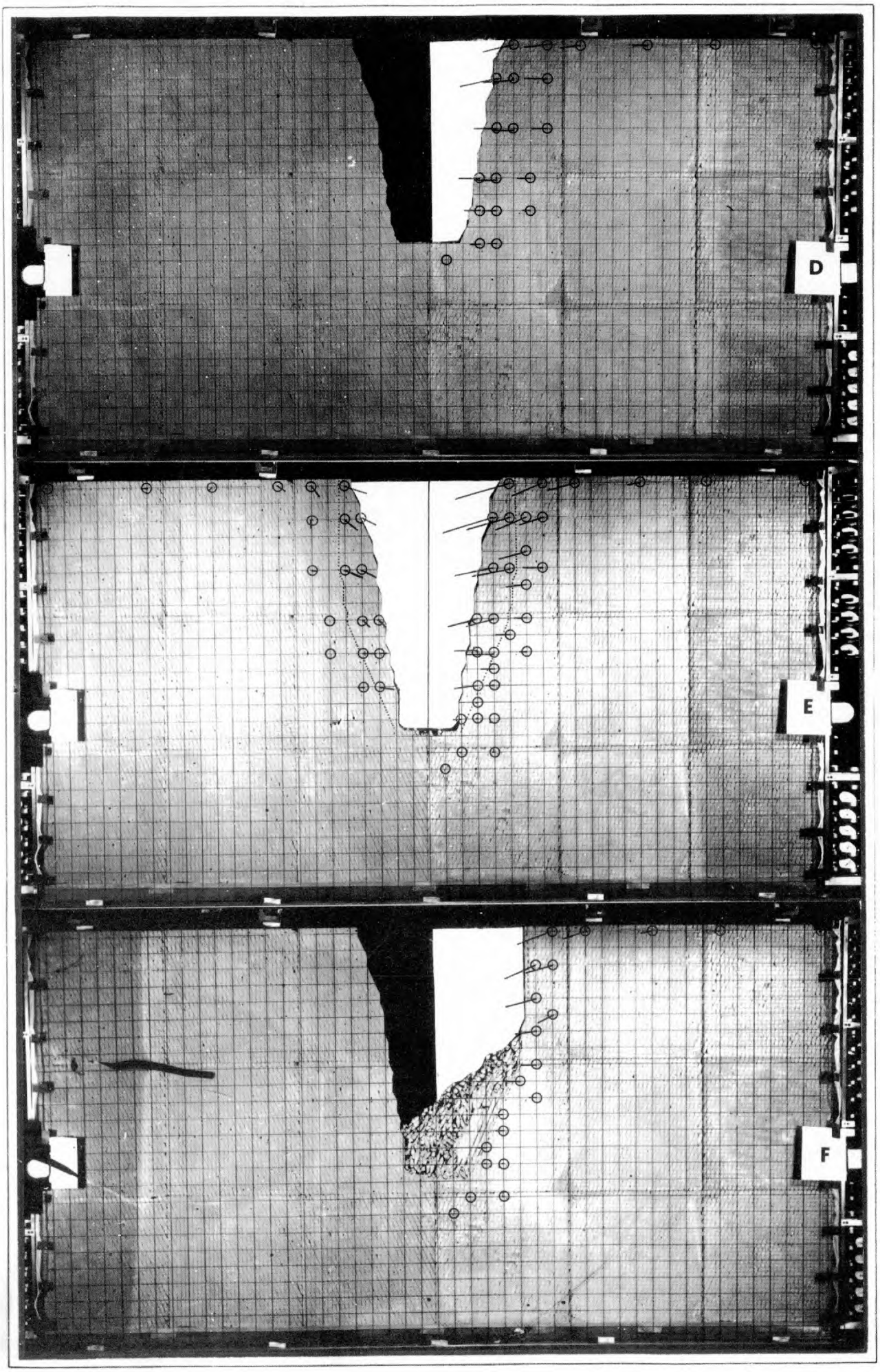

Figure 3.3.12 Mean displacements, stages D, E and F of model L.M.3

Stage	Displacement (inch)	Inclination
B	0.034	21°
C	0.031	15°
D	0.049	14°
E	0.086	16°

The corresponding pairs of Figures: 3.3.6 and 3.3.11, and 3.3.7 and 3.3.12 should be carefully compared to verify these differences. The result of the unusually small boundary displacements was that the excavation was partially isolated from the boundaries, at least to a greater extent than in the previous two models. This was probably due to the greater possibility of loosening of the jointed mass close to the excavations, with the formation of many fine tension cracks coinciding with the vertical secondary joints. These were not identified visually or by photogrammetry, but it was clearly apparent that the joints were less tight.

Figure 3.3.12, stage E shows the total displacement vectors for the right hand slope. The fine dotted line illustrates the eventual failure surfaces. These consisted of a deep vertical tension crack, a stepped shear surface, and a long planar shear surface extending down to the toe. This right hand slope was particularly interesting since during the excavation from stage D to E, the tension crack and planar shear surface suddenly developed, but without causing failure. The reason for this was that the long planar shear surface was not quite intersected by the toe of the slope.

Figure 3.3.13 illustrates the shear surface in detail. Even by eye, the shear and dilational components of displacement can be detected by comparing the vertical and horizontal joints with the fixed 2 inch square grid. It was noticed that the maximum shear and dilation occurred some 4 to 6 inches from the toe, up the critical joint. Displacements could not be detected by eye either adjacent to the toe, or at the upper end shown in diagram D of Figure 3.3.13. Therefore the only significant shear displacements were occurring from a position roughly below the crest of the slope down to three or four inches from the toe. The relative change of displacement along the length of the joint was particularly significant, since it indicated that closure of intersecting joints was occurring. (See Section 2.3)

The displacement vectors drawn on the left hand side of Figure 3.3.12 are those of the relative slope deformations that occurred in the right hand slope, when the excavation was deepened from stage D to stage E. It was hoped that this increment would delineate the areas of maximum displacement prior to failure.

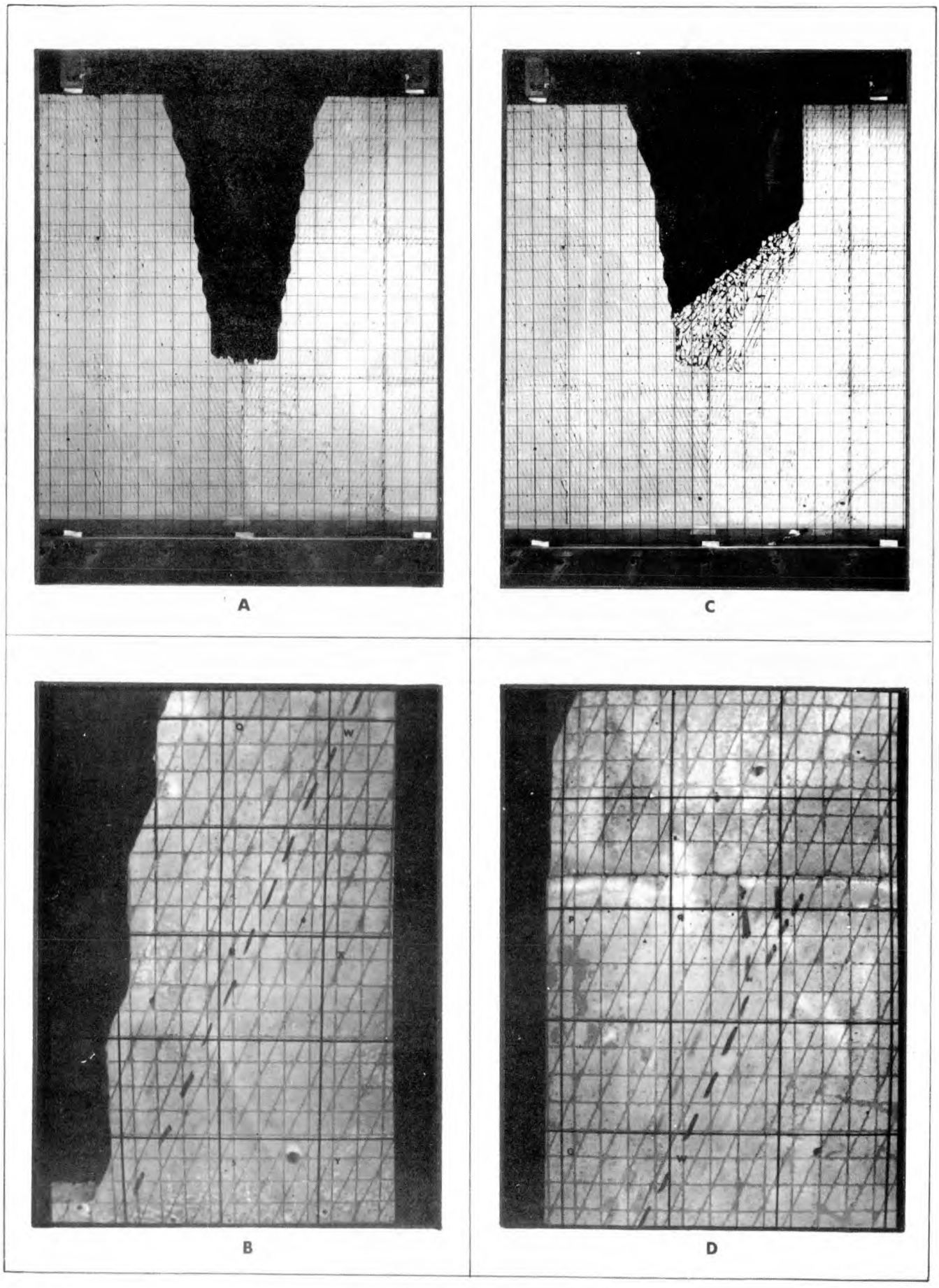

Figure 3.3.13 Close-up of pre-failure shear surface developed at stage E of model L.M.3

The vectors drawn in the upper half of the slope demonstrate the effect of the tension crack very clearly. Even more convincing are the three pairs of vectors nearest to the toe. These delineate the down dip shear displacements occurring on the upper part of the eventual failure surface, and show the effect of dilation superimposed on this. It results in an almost horizontal translation towards the face in the lowest part of the slope.

Some interesting backward displacements are in evidence along the surface of the model, away from the slope. These were presumably the result of relaxation of the jointed mass behind the slope, after the transfer of stress resulting from the shear displacements. The slope failed when the excavation was deepened another $\frac{1}{2}$ inch (24 feet at prototype scale). This was sufficient to expose the overstressed joint, from which shear stress had been transferred to the narrow 'column' at the toe.

Figure 3.3.14 shows the final stages of excavation in which 'outer' slopes were excavated after removal of the 'inner' failures. Diagram G shows the vectors for the right hand side only. An interesting relaxation can be seen in the berm at the toe of the uncompleted slope. This is the only significant relaxation measurement that was recorded for any of the models. Why it should be so marked in this instance is uncertain. The slope excavated above it represented no larger an unloading than previous excavations.

It might be partially explained by considering the direction of the 'lines of force' that elastic analyses indicate, below the base of excavations or notches in idealized, stressed materials. The applied horizontal stress at the boundaries of the model must be in equilibrium with the resistance generated by the stressed model. Excavations disturb this equilibrium with the result that the 'lines of force' are channelled and concentrated below the base of the excavation. On either side of the axis of symmetry these lines of force will be inclined appreciably. Therefore measurement points located within these zones would tend to exhibit inclined displacements which would dominate any possible upward displacements due to relaxation. The two points located in the berm in Figure 3.3.14 G are somewhat 'protected' from this force field, which is probably insignificant anyway in view of the graded nature of the excavation, and the low horizontal stresses.

Diagram H of Figure 3.3.14 illustrates the incremental movement in the left hand slope, when the latter was steepened from approximately 83° (H) to 84° (J). It is significant that the only movements that could be detected, occurred at the lower ends of some of the most critically stressed joints, and in a vertical plane just down dip from that passing through the crest. This incremental displacement, and the one discussed above (Figure 3.3.12 E) should be compared with the concepts put forward in Section 2.3, and also with the diagram showing the zone of overstressed joints (Figure 3.2.5).

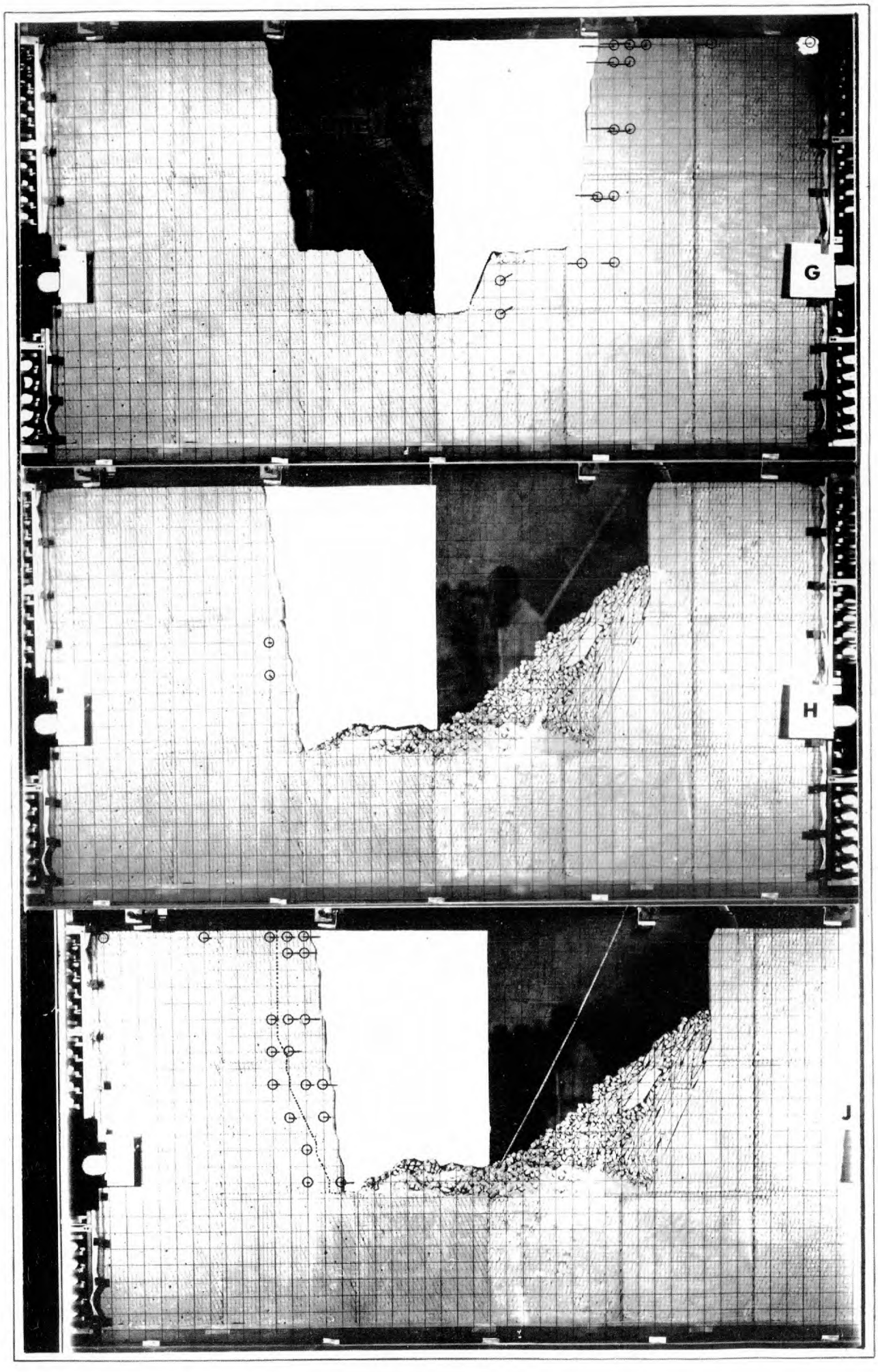

Figure 3.3.14 Mean displacements, stages G,H and J of model L.M.3

Diagram J of Figure 3.3.14 shows the total displacement vectors for the final stage of excavation. The predominantly horizontal direction of total displacement for this stage and stage G is presumably a reflection of the loosened nature of the slopes, each of which contained more than one vertical tension crack. However it is suprising that tension crack formation should dominate any pre-failure down dip displacements to such an extent. It might be significant that only the lower part of the model was stressed horizontally at this stage. Almost half the proving rings appeared to be unloaded. It is possible that this could induce a backward rotation.

2. Boundary displacements

Comparison of Figure 3.3.15 with Figure 3.3.9 reveals that the displacements occurring at the boundaries of model L.M.3 were approximately one fifth of those occuring in the highly stressed model. This is undoubtedly a function of the greater amount of strain energy stored in the proving rings in the latter. However it is believed that the looser nature of the jointed mass was also significant. The formation of tension cracks, some of which could be traced to a depth of 8 or 10 inches (330-400 feet in the prototype) tended to isolate the unloading effects from all but the immediate vicinity.

3. Stress changes at boundary

Figure 3.3.16 shows that the mean horizontal stress applied to model L.M.3 was triangular, and just slightly higher than the design value of ($\sigma_h = \frac{1}{2}\sigma_v$).

The model and prototype mean principle stress equations are given below:

Model $\sigma_h = 0.0385\,h$

$\sigma_v = 0.07\,h$ lbf/in^2 (h in inches)

Prototype: $\sigma_h = 0.62\,h$

$\sigma_v = 1.12\,h$ lbf/in^2 (h in feet)

The reason for the distribution being triangular and not trapezoidal as in the previous two cases is frankly not understood. Roscoe[76] indicated in his Rankine Lecture that retaining wall problems were not amenable to conventional analysis, and several model results were presented to confirm this. The present case is different from these in that:

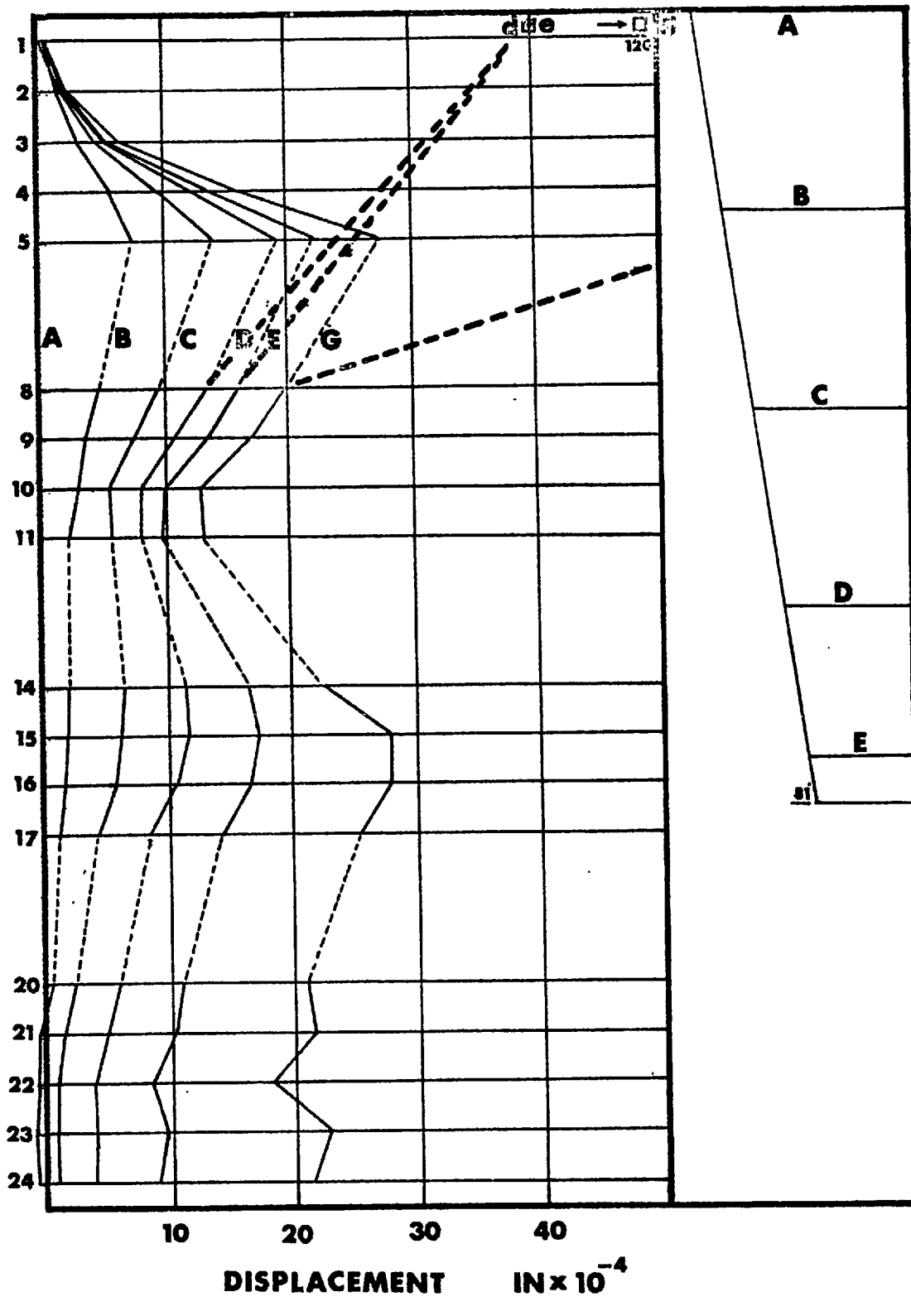

Figure 3.3.15 Mean displacements at boundaries of model L.M.3

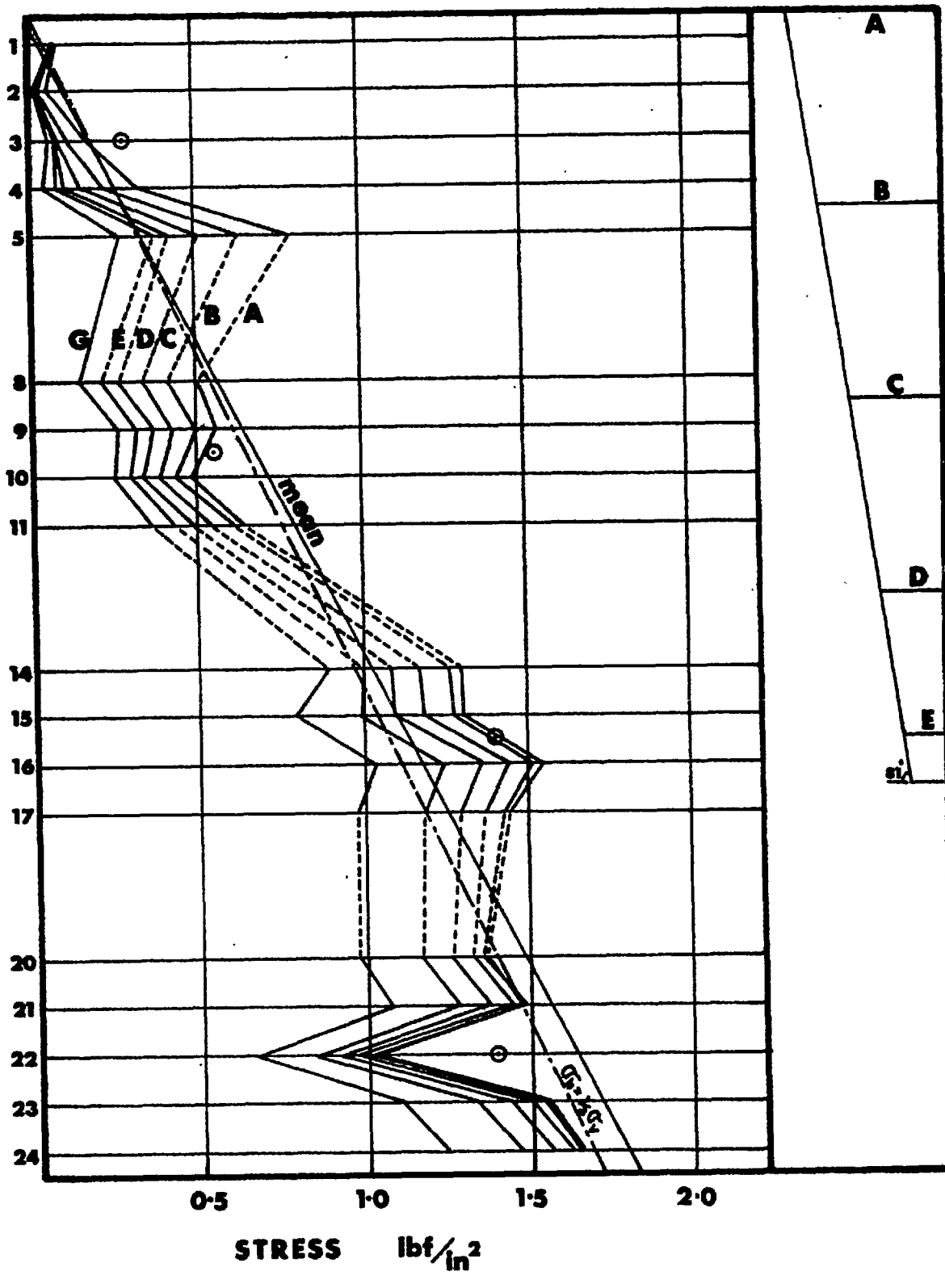

Figure 3.3.16 Mean horizontal stresses at boundaries of model L.M.3

a) the material is not homogeneous but jointed

b) the loading beam is both translated and rotated about the top (slightly) when loading the model

c) the beam is moved at the same time as the model is 'activated', by rotation into the vertical plane

d) the loading beams are 'soft'.

These complications put the problem in a higher plane of complexity than need be considered in this thesis.

3.3.4 SHEAR STRENGTH AS A FUNCTION OF MASS CLOSURE

Before presenting sequence photographs of the slope failures induced in the three models, a most important phenomenon needs to be introduced.

Excavation of the first model L.M.1 proved to be somewhat disconcerting, when it was found that:

a) slopes did not fail at slope angles less, or even equal, to the predicted values, even though the horizontal stress was high

b) slopes did not even fail when vertical

c) failure could only be induced by undercutting at the toe of vertical slopes

(significantly, the failures that occurred were planar failures, involving simple shear along a steeply dipping joint and tension crack opening. Despite the verticality and undercutting, no rotational or toppling mode was induced).

This unexpected result caused a lot of concern. It was thought that two explanations were possible:

a) incomplete fracturing of the slabs on the guillotine
b) the absence of any vertical joints for tension crack formation

Consequently the two models L.M.2 and L.M.3 were designed with three sets of joints, one of which was vertical. Great care was also taken to check that the guillotine was fracturing the slabs correctly. It was at this stage that the large tilt models presented in Section 3.1 were tested.

Model L.M.2, which was loaded to the same high stress as the first large model was anticipated with great interest. However once again undercutting of vertical slopes was required to induce failure. In comparison, model L.M.3 which was stressed to only one half of the vertical stress, could be excavated to failure at angles equal to or at least only a few degrees steeper than the design value.

It will be recalled that the design shear strength parameters: $c = 0.10$ lbf/in^2, $\phi = 58^\circ$, were deduced from the combined results of direct shear tests of single joints, and back analysis of the simple tilt models (see Figure 3.1.19). The conventional loading path used in a direct shear test consists simply of the application of the desired normal stress (applied instantaneously or gradually) followed by a gradually increasing shear stress, which rises until peak shear strength is mobilised.

Virgin stress levels

Failures occurred in all the models by shear failure along the steeply dipping joints ($\beta = 66^\circ$), combined with tension crack formation. They could therefore be regarded as shear tests where the ratio of shear stress to normal stress was more or less constant along the steeply dipping joints, assuming that self weight stresses were applicable.

i.e. $\tau / \sigma = \tan 66^\circ$

Failure occurred as a result of increased loading (through excavation), such that the stress ratio line inclined at 66° and passing through the origin, eventually crossed the shear strength envelope, as illustrated below. However, the point which had been overlooked was that the normal stress acting across the steeply dipping joints at failure, was lower than that which originally applied at the same location, in the virgin or unexcavated state.

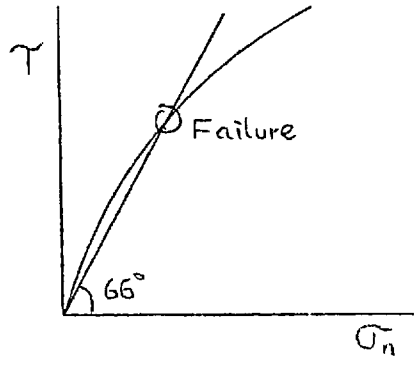

The original horizontal and vertical stresses could be regarded as the principle stresses applied to the boundaries of the jointed, unexcavated models. Depending on whether the horizontal stress was higher or lower than the self-weight stress, it was either the major or minor principle stress. Only the one joint direction was of interest ($\beta = 66^\circ$) in these symmetrically jointed

slopes. The sketches below illustrate the idealized case of a singly jointed model (see for instance Bray[90]).

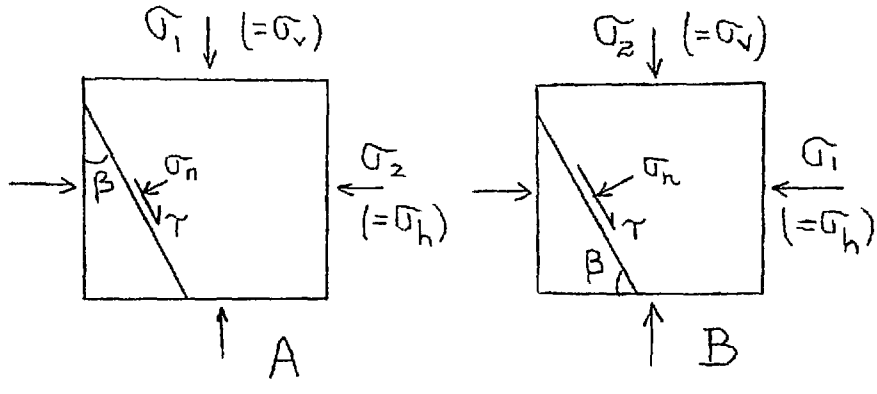

The normal and shear stresses acting on the joint can be written as follows:

$$\sigma_n = \tfrac{1}{2}(\sigma_1 + \sigma_2) - \tfrac{1}{2}(\sigma_1 - \sigma_2)\cos 2\beta$$

$$\tau = \tfrac{1}{2}(\sigma_1 - \sigma_2)\sin 2\beta$$

Diagram A refers to the model with low horizontal stress, for which $\beta = 24^\circ$. Diagram B refers to the models with high horizontal stress, for which $\beta = 66^\circ$.

The mean equations for σ_h and σ_v were presented previously for each of the models. These were evaluated, and the depth-dependent values of σ_1 and σ_2 inserted in the above equations. Figure 3.3.17 shows the resulting linear relationships, which will be assumed to represent the virgin stress state. (The possible influence of stress history cannot be evaluated and will therefore be ignored).

It is significant that, due to the steep dip of the relevant joint set, even the model loaded with the low horizontal stress displayed a ratio of virgin normal to shear stress of approximately 4 to 1, at intermediate depths. However, excavation of slopes above these joints caused the stress ratio to reverse, and at failure the ratio of normal to shear stress was approximately 0.44 to 1.

Approximate back analyses of the slope failures induced in the high and low stress models, revealed that the normal stress across a given joint dropped by as much as 8:1, between the stage when the model was unexcavated and just before failure. In all cases the factor was at least 4 to 1.

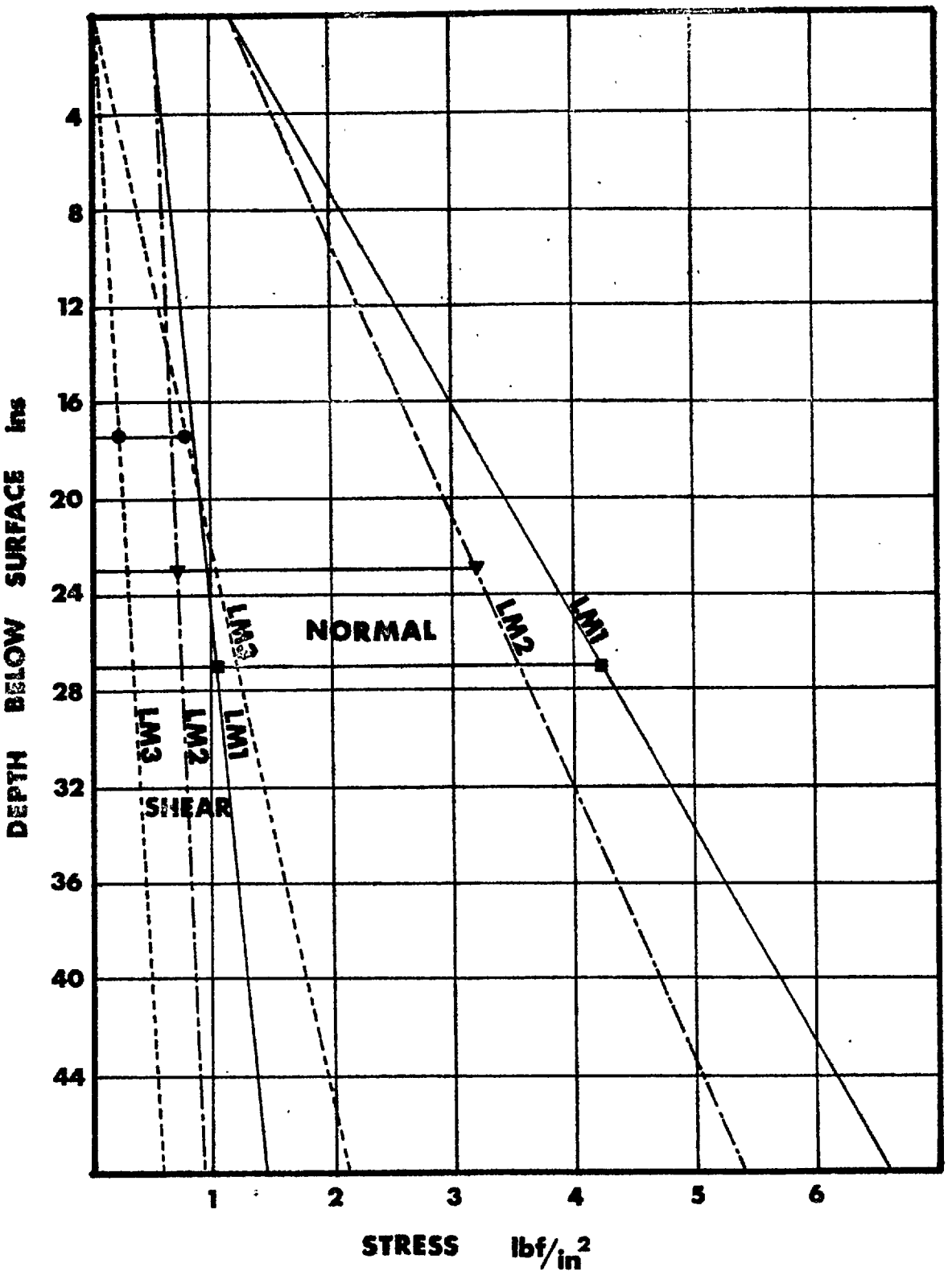

Figure 3.3.17 Assumed distribution of shear and normal stresses on the steeply dipping joints, prior to excavation of the models.

Pre-consolidated shear tests

This important fact suggested a series of direct shear tests in which joints would be pre-consolidated with a high normal stress, before shearing them at a lower level of normal stress.

(Skempton[91] has referred to the terms 'consolidation'and 'gravitational compaction' to describe the well known soil mechanics phenomena which result in soft muds consolidating through clays, to mudstones and shales. The process invelves primarily the squeezing out of pore pressure under increasing weight of overburden. The present use of the term 'pre-consolidated' is not intended to imply any pore or joint water changes, although undoubtedly these might well be involved in an in-situ test on a rock mass. A better term for the present rock behaviour might be 'joint closure' or 'mass closure', since, as will be shown, the process is one of joints closing tightly under high normal stress levels).

Joints were generated in prismatic specimens of model material C3, which was used in all the jointed models. Two series of shear tests were performed:

1. σ_n (initial) / σ_n (test) = 8/1
2. σ_n (initial) / σ_n (test) = 4/1

The comparative effect on the shear strength, particularly when compared with the conventional (1/1) test, was quite dramatic. Figure 3.3.18 shows the three peak strength envelopes and two of the ultimate curves. (The coordinates obtained from back analysis will be discussed later.)

The initial normal loads were applied for two or three minutes before reducing carefully to the test loads. Reference to Section 1.4, Figure 1.4.1 indicates the amount of irrecoverable closure that takes place when these model joints are loaded initially. This effect is particularly noticeable for the model joints since they are generated in tension and are placed together manually before loading.

The real geological situation is different in that the degree of closure of joints insitu cannot be easily observed, at least not at depth. It is probably true to say that all the present methods of obtaining or exposing rock joints for shear testing involve such a degree of disturbance that any mass closure effect is lost. Therefore it is postulated that shear testing may be a very conservative method of estimating strength, if the joints are:

1. relatively unweathered, clean and rough
2. steeply dipping

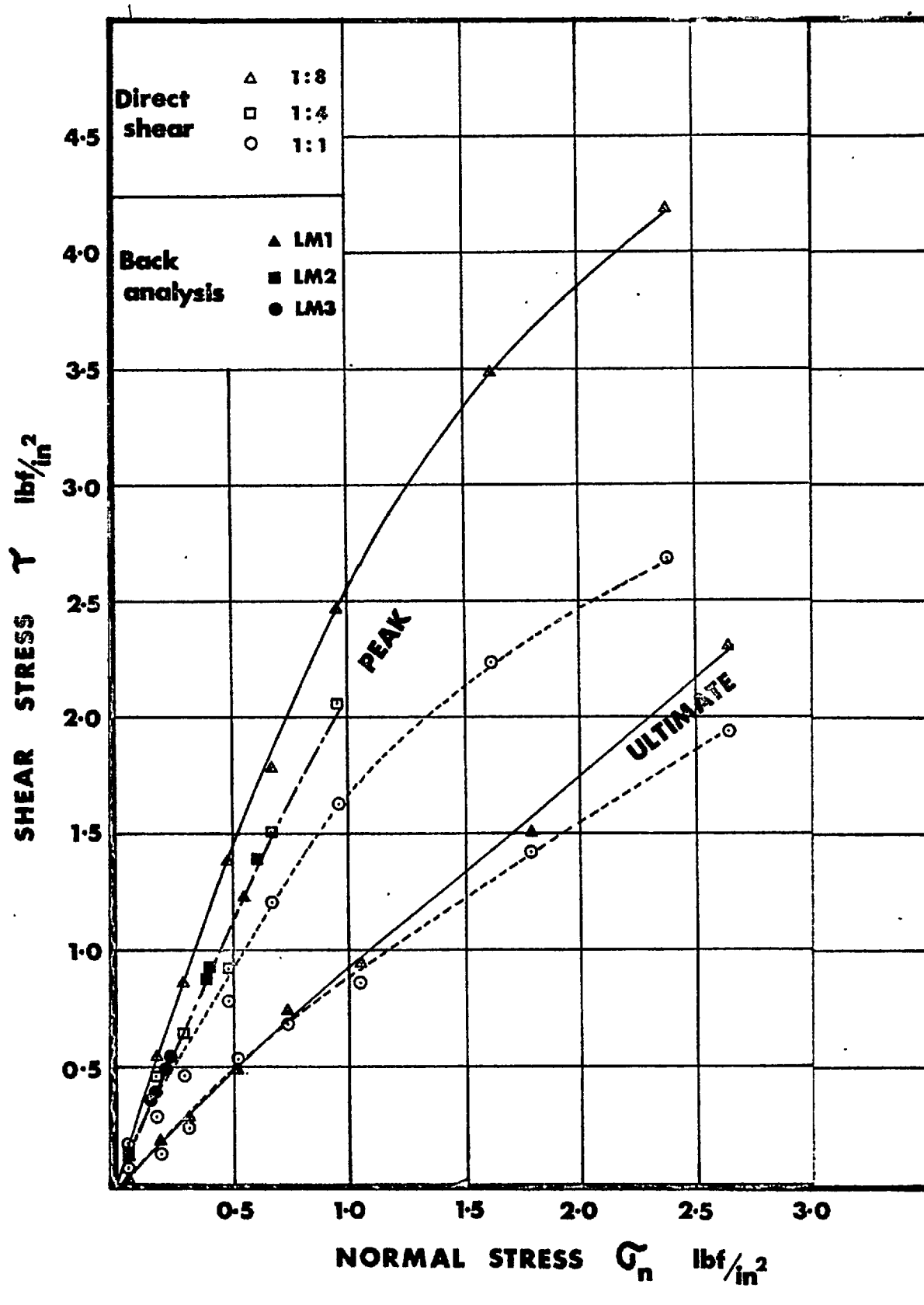

Figure 3.3.18 Comparison of pre-consolidated model shear tests with conventional loading tests, and with back analyses of model failures.

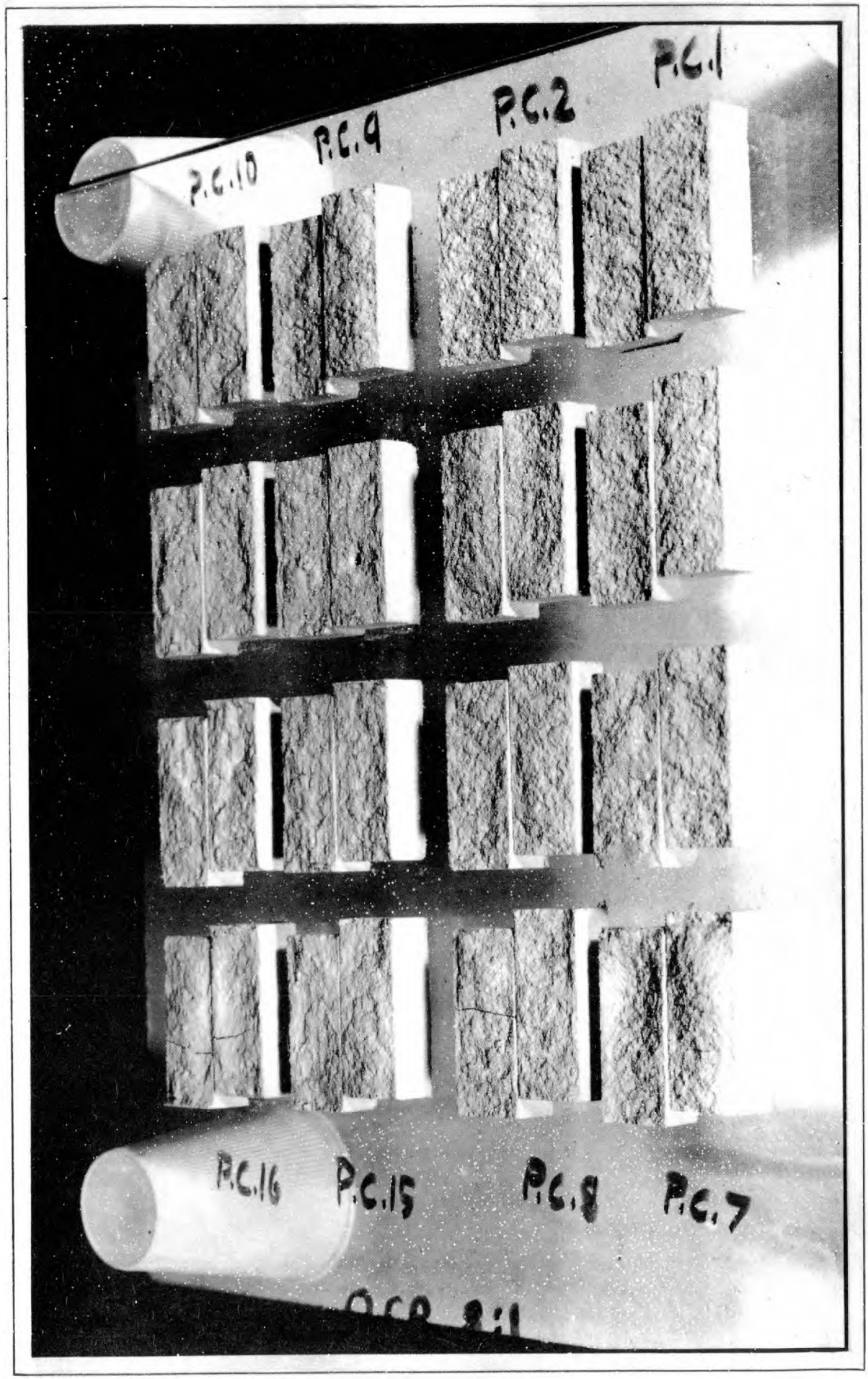

Figure 3.3.19 The surface damage caused by shearing of preconsolidated model joints

Figure 3.3.19 shows the surface roughness of the joints after testing at a ratio of 8/1. Specimens P.C.1 to P.C.6 show negligible surface damage compared to the specimens tested at the highest normal stress P.C. 15 and 16.

It is inevitable that the above concepts will be viewed with suspicion, since the model joints are totally unweathered, and display roughness characteristics which are certainly very high, when converted to prototype. However two practical observations can be cited in support.

Seraphim[37] reported a comprehensive series of deformability plate-bearing tests in jointed granites at several dam sites. He noted that "once the joints are closed, the adhesion forces between the faces of the fissures or between the adsorbed layers prevent their opening until a certain unloading is reached."

De Freitas[55] has performed a series of shear tests on rough tension fractures in granite in a large laboratory shear machine. (These were referred to in Section 2.1) Apparently, in the early stages of this work the normal load was once accidentally increased to the maximum capacity of the machine (10 tons). However this mistake was not noticed until large strains were observed in the shear loading ring. The specimen could not in fact be sheared. What was suprising was that, when the jointed specimen was removed from the machine it could not be prised open without mechanically wedging it apart.

The model joints were obviously behaving in the same way. However, the reason for the large increase in shear strength was probably not only due to the adhesive forces generated by interlocking asperities. The increased closure of the joints meant that for peak strength to be mobilized, slightly more dilation was required. Since peak strength is reached after approximately 0.020 inch, the closure of several thousandths of an inch that is indicated from Figure 1.4.1, represents a possible increase of dilation angle of several degrees. This alone might be enough to explain the model results shown in Figure 3.3.18.

3.3.5 POST-FAILURE OBSERVATIONS

The failures induced in the three large models will be communicated primarily by the following ten pages of sequence photographs. A minimum of commentry is required but the following observations will be recorded.

Figure 3.3.20 This was the only slope which proved to have an additional unwanted joint in it. This can be seen in the lower half of the slope, diagram B. A model slab that has an unnoticed hair line

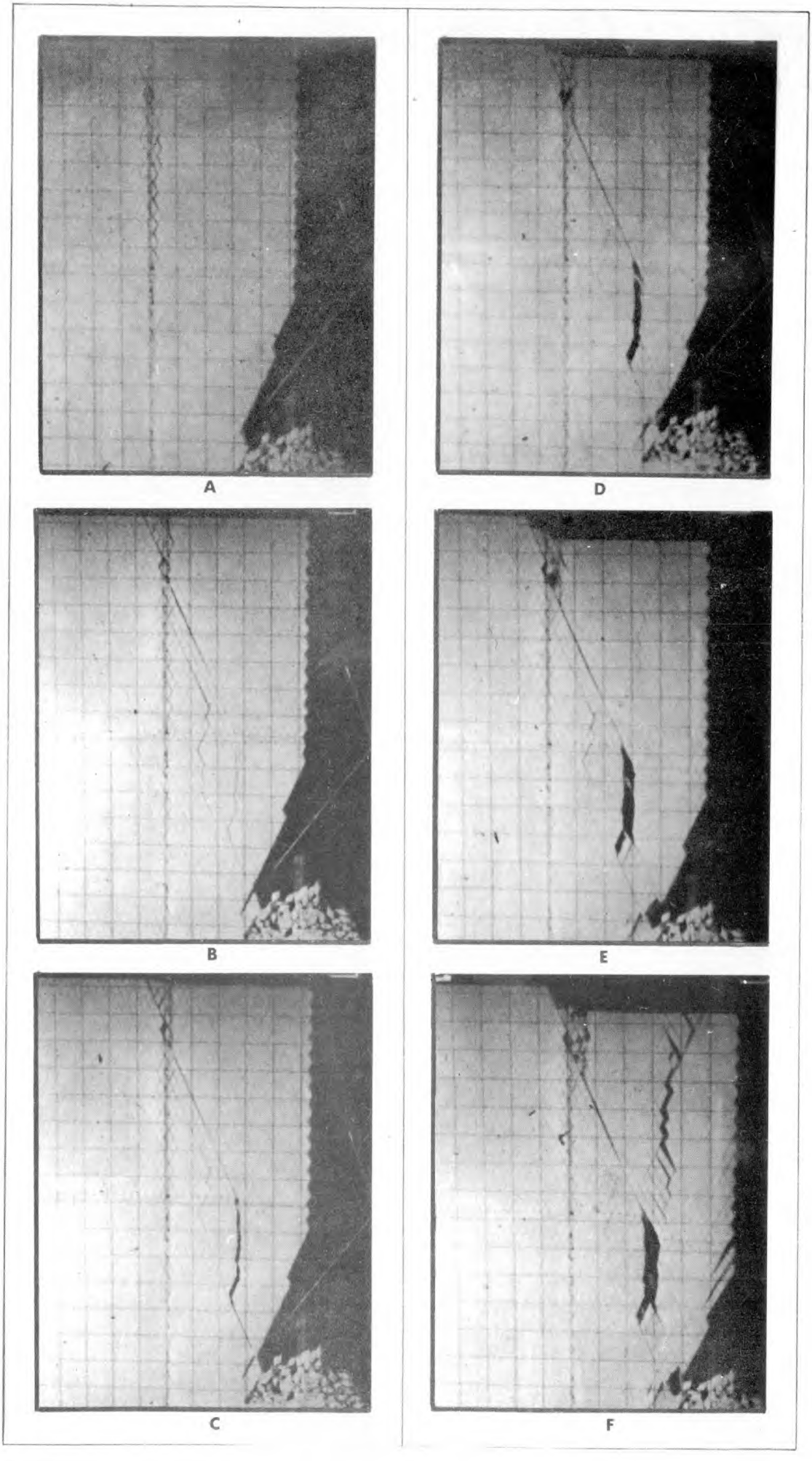

Figure 3.3.20 Failure sequences of model L.M.1 (L.H.S. outer)

crack in it cannot be 'reclaimed' by developing fractures across it. The crack will always be primary and therefore continuous. For this reason this failure was not back analysed.

The failures shown in Figures 3.3.20 and 3.3.21 could only be induced by undercutting to a more serious degree than was required for any of the failures in model L.M.2 (Figure 3.3.22 to 3.3.25). This was due to two factors:
a) a higher pre-consolidation ratio
b) the absence of vertical tension cracks.
Opening of a saw-tooth crack will inevitably involve a certain amount of shearing, and consequently it will have a small effective tensile strength.

Figure 3.3.26 — The position in which shear failure initiated has been referred to previously for this slope. Excavation through the 'column' of blocks at the toe of the slope resulted in immediate collapse.

Figure 3.3.27 — The cine film was not running when failure occurred and the four sequences were photographed from a screen linked to a video tape recorder. Unfortunately it is not possible to obtain a very clear 'still' frame, and photography of an animated sequence is unsatisfactory since shutter speeds faster than about $^{1}/_{20}$ sec. result in an incomplete picture. However, both the slope profile immediately prior to collapse, and the shear surface, are recorded clearly in diagrams A and F. The failure was therefore amenable to accurate back analysis.

Figure 3.3.28
Figure 3.3.29 — These two series of sequence photographs add further weight to the opinion that slope failure actually initiates through shearing on a deep seated surface, rather than by being triggered by tension crack opening. It appears that the point of initiation lies somewhere between the toe, and a position vertically below the crest of the slope. Close-up high speed photography would delineate this position accurately.

Figure 3.3.30 — This shows the debris from four failures. The upper pair were denoted as 'inner' failures in the preceeding figure captions, and the lower pair; 'outer' failures. Both illustrate remarkably similar failure scars.

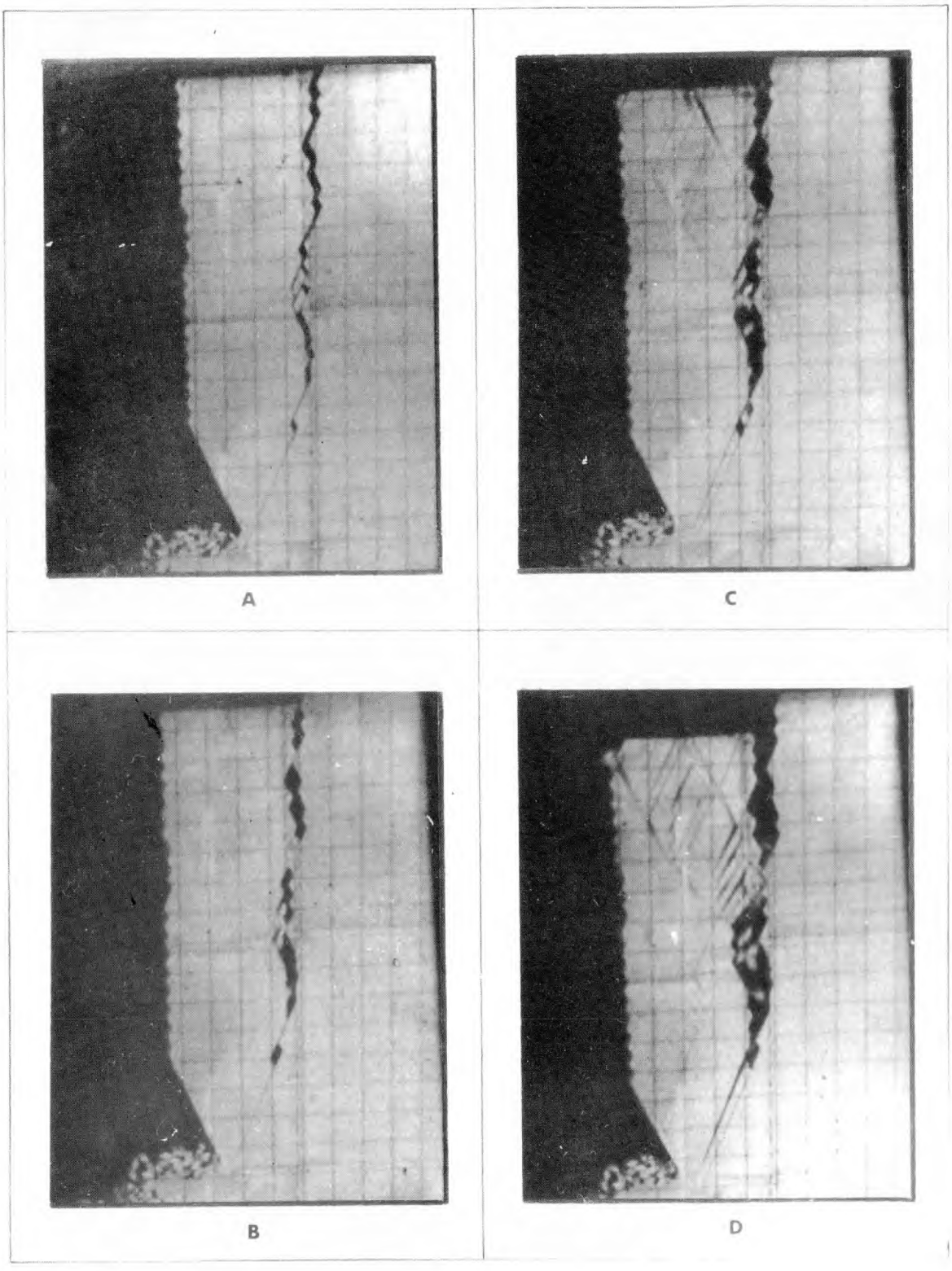

Figure 3.3.21 Failure sequences of model I.M.1 (R.H.S. outer)

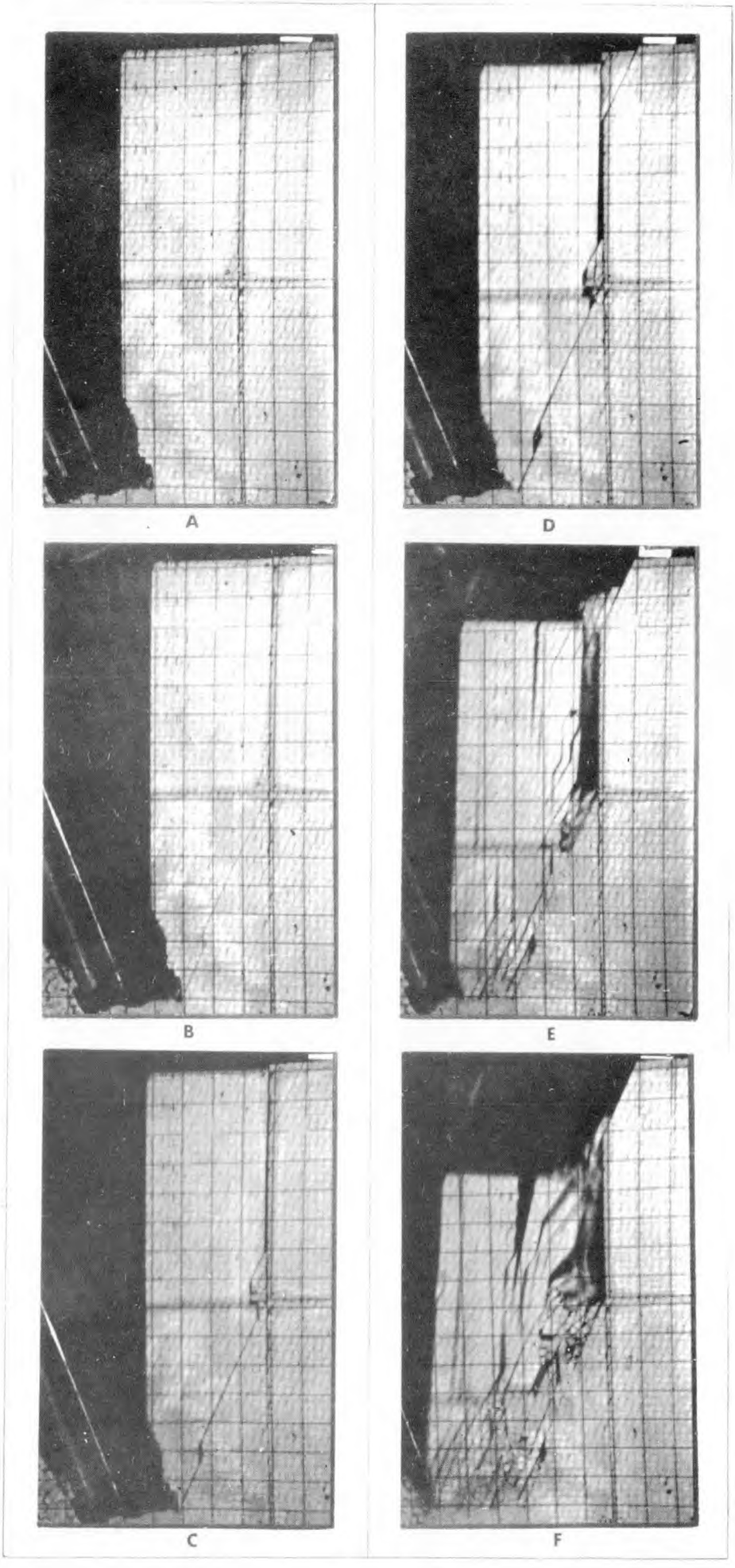

Figure 3.3.22 Failure sequences of model L.M.2 (R.H.S. inner)

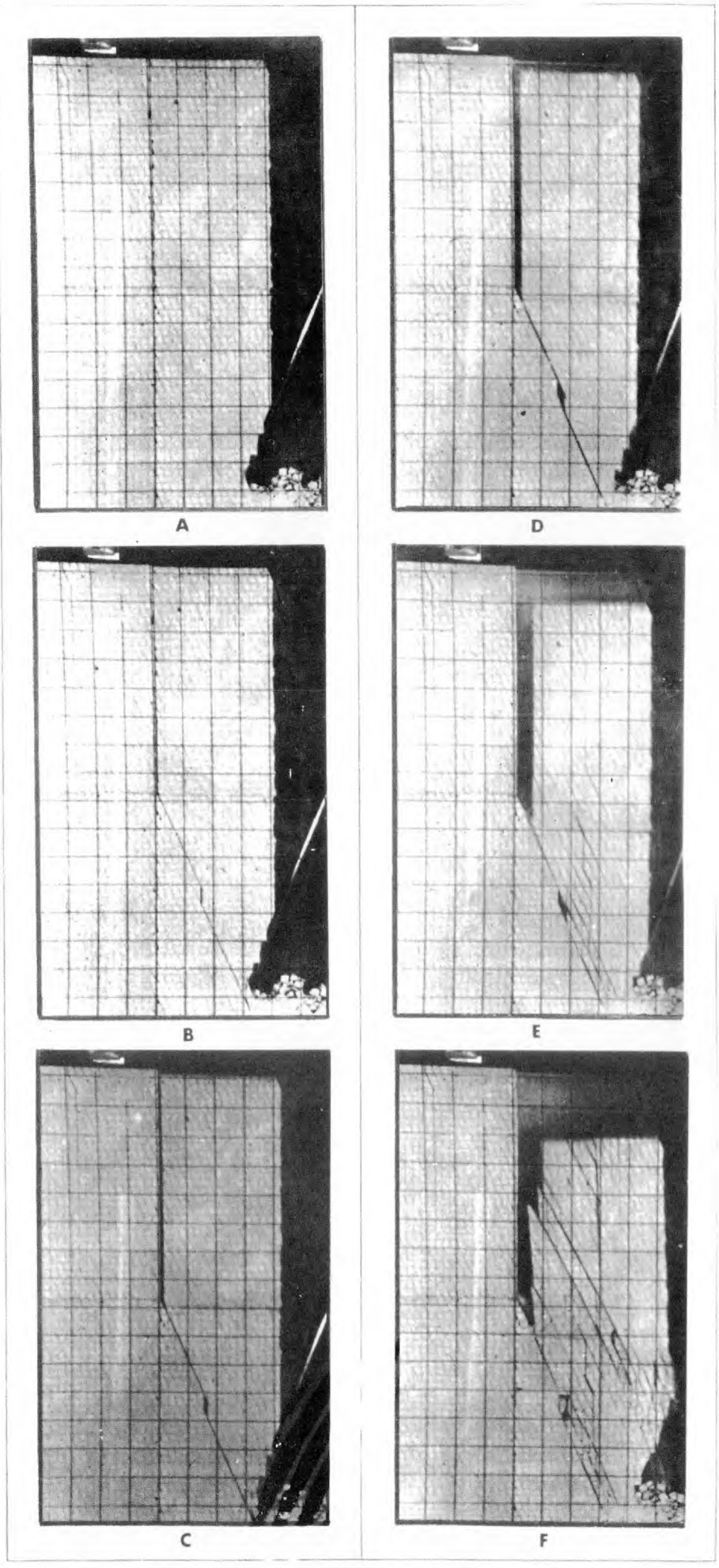

Figure 3.3.23 Failure sequences of model L.M.2 (L.H.S. inner)

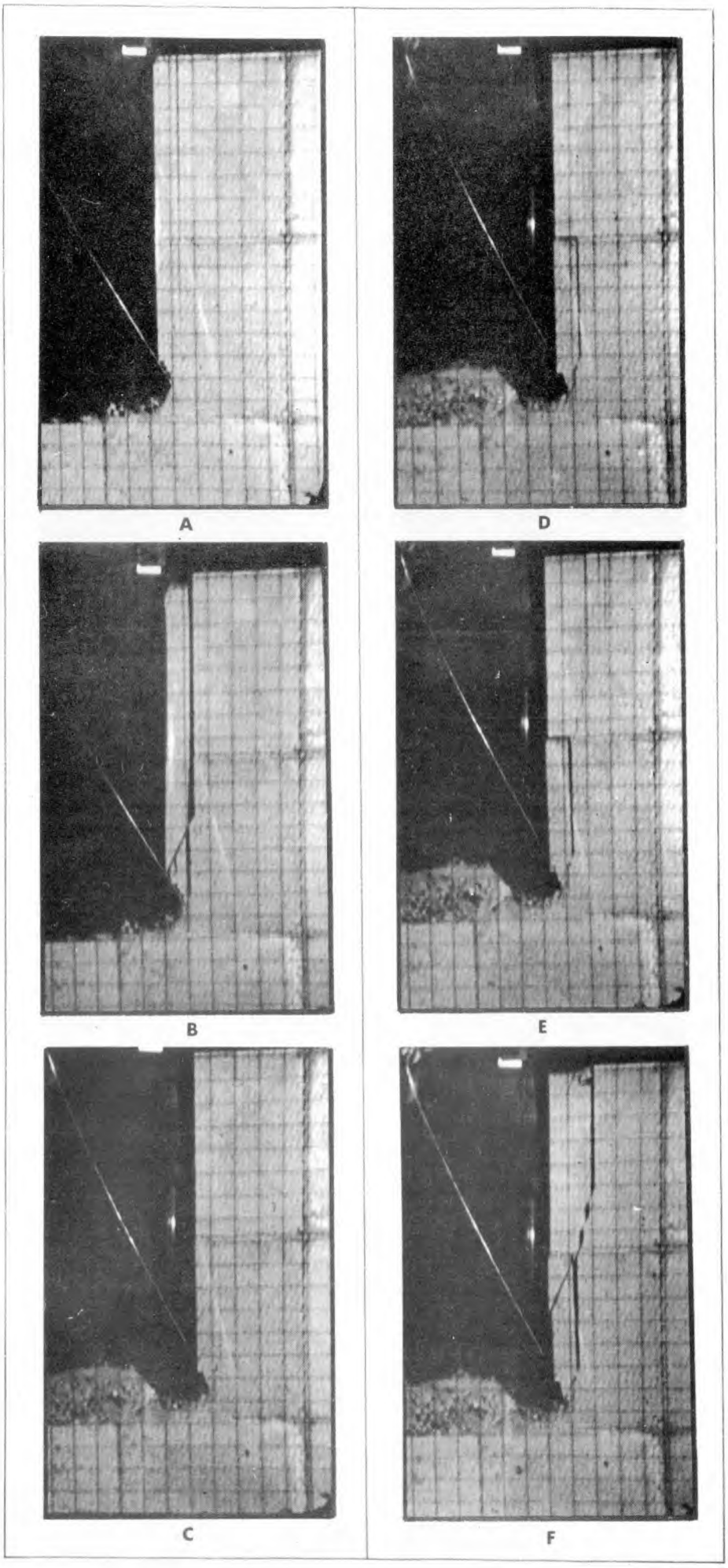

Figure 3.3.24 Failure sequences of model L.M.2 (L.H.S. outer)

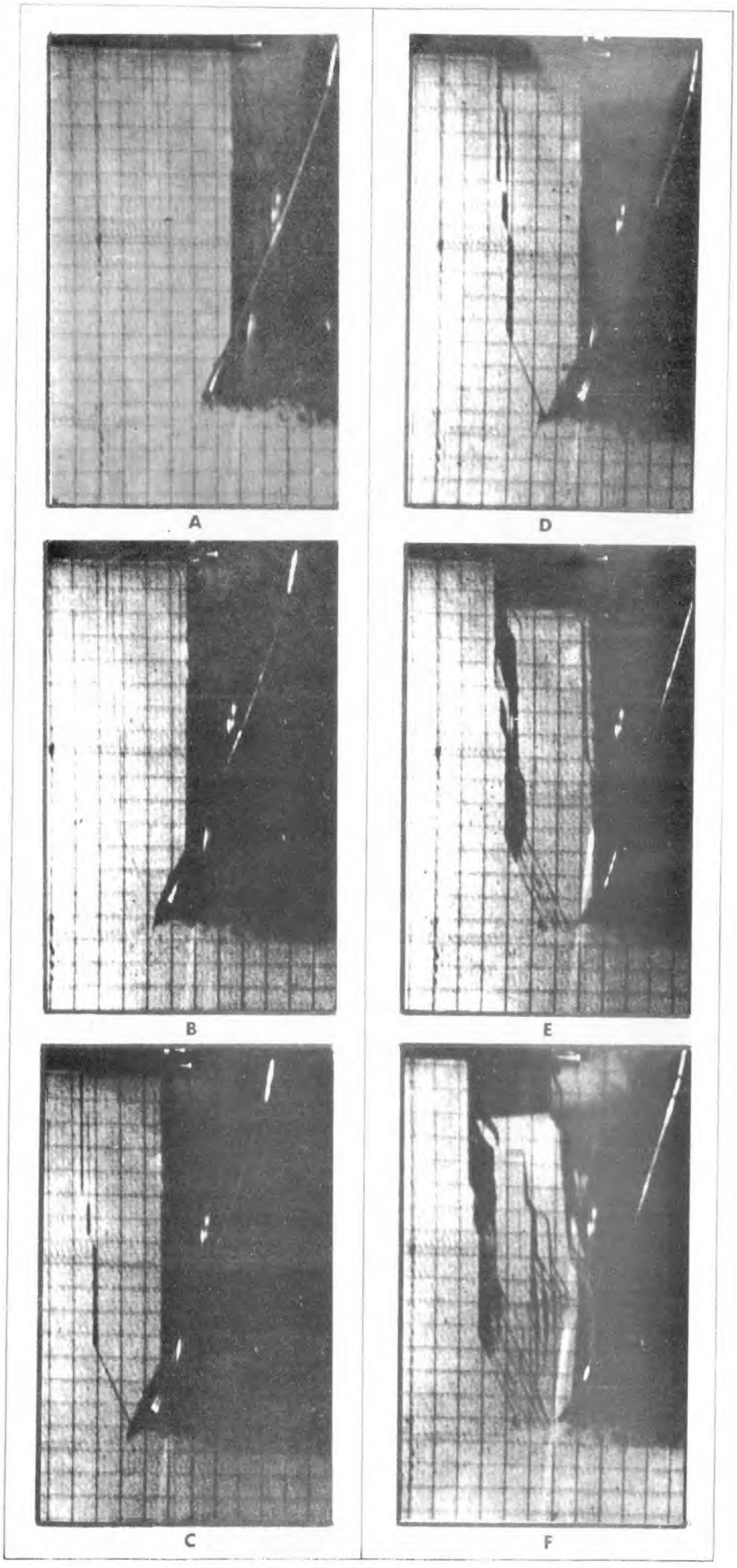

Figure 3.3.25 Failure sequences of model L.M.2 (R.H.S. ou

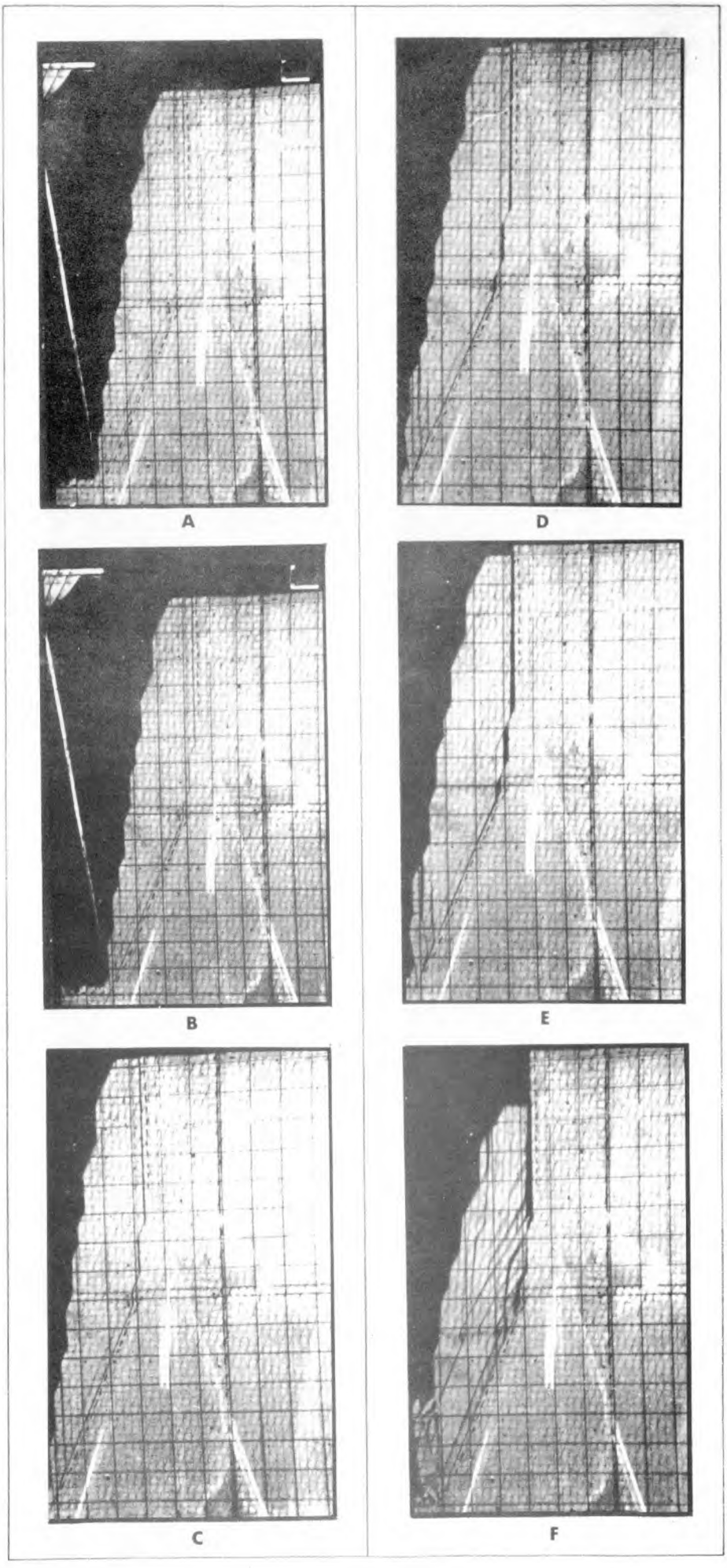

Figure 3.3.26 Failure sequences of model L.M.3 (R.H.S. inner)

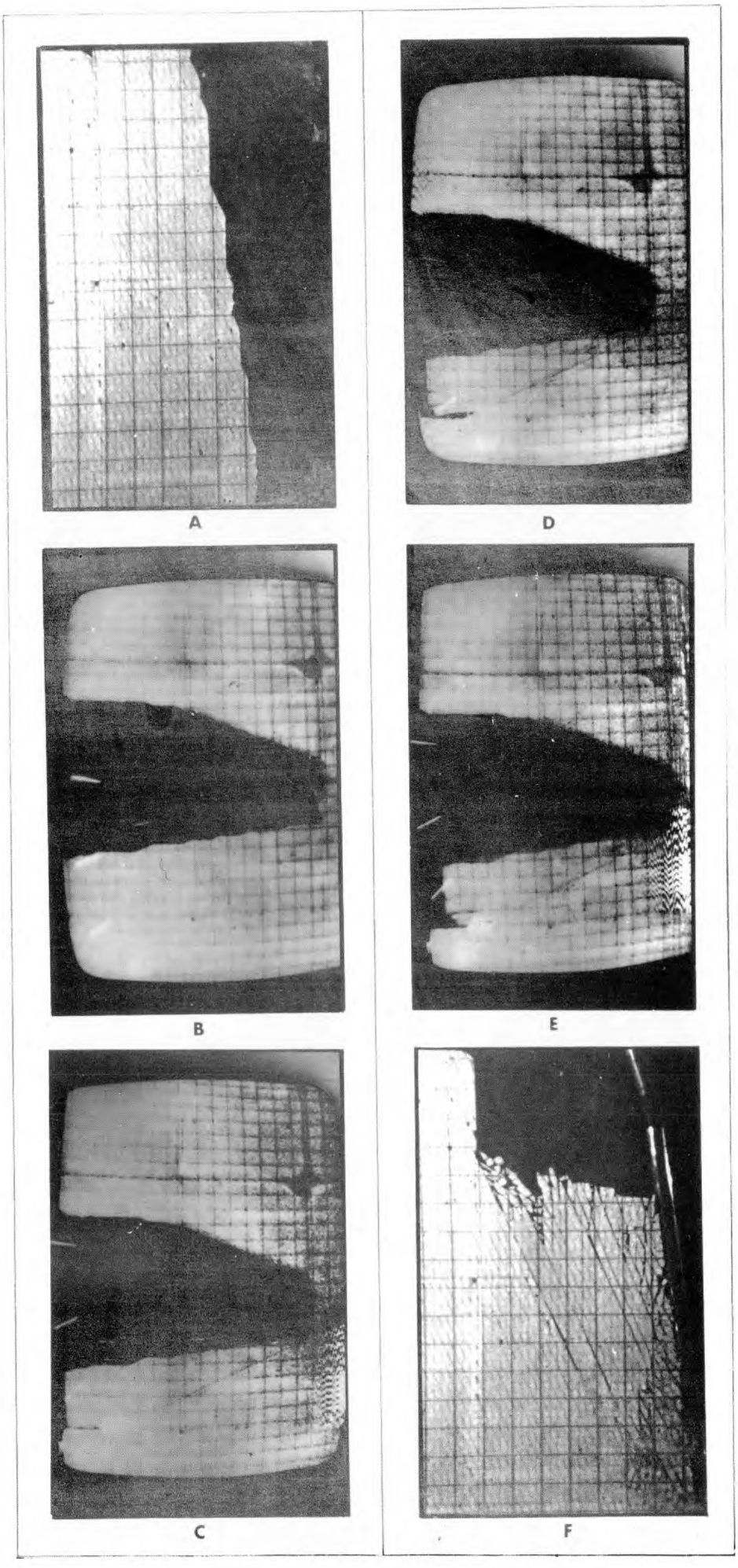

Figure 3.3.27 Failure sequences of model L.M.3 (R.H.S. inner)

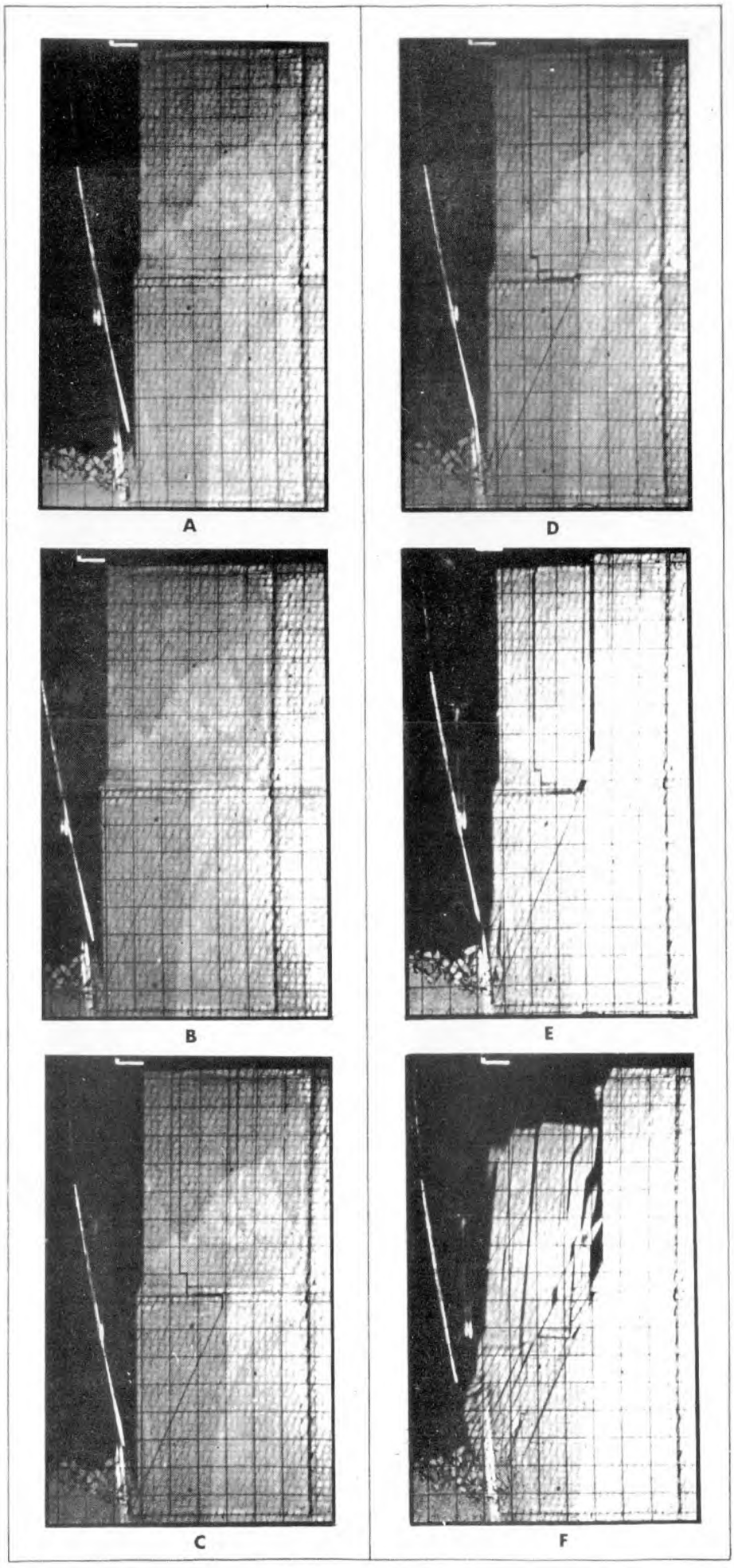

Figure 3.3.28 Failure sequences of model L.M.3 (R.H.S. outer)

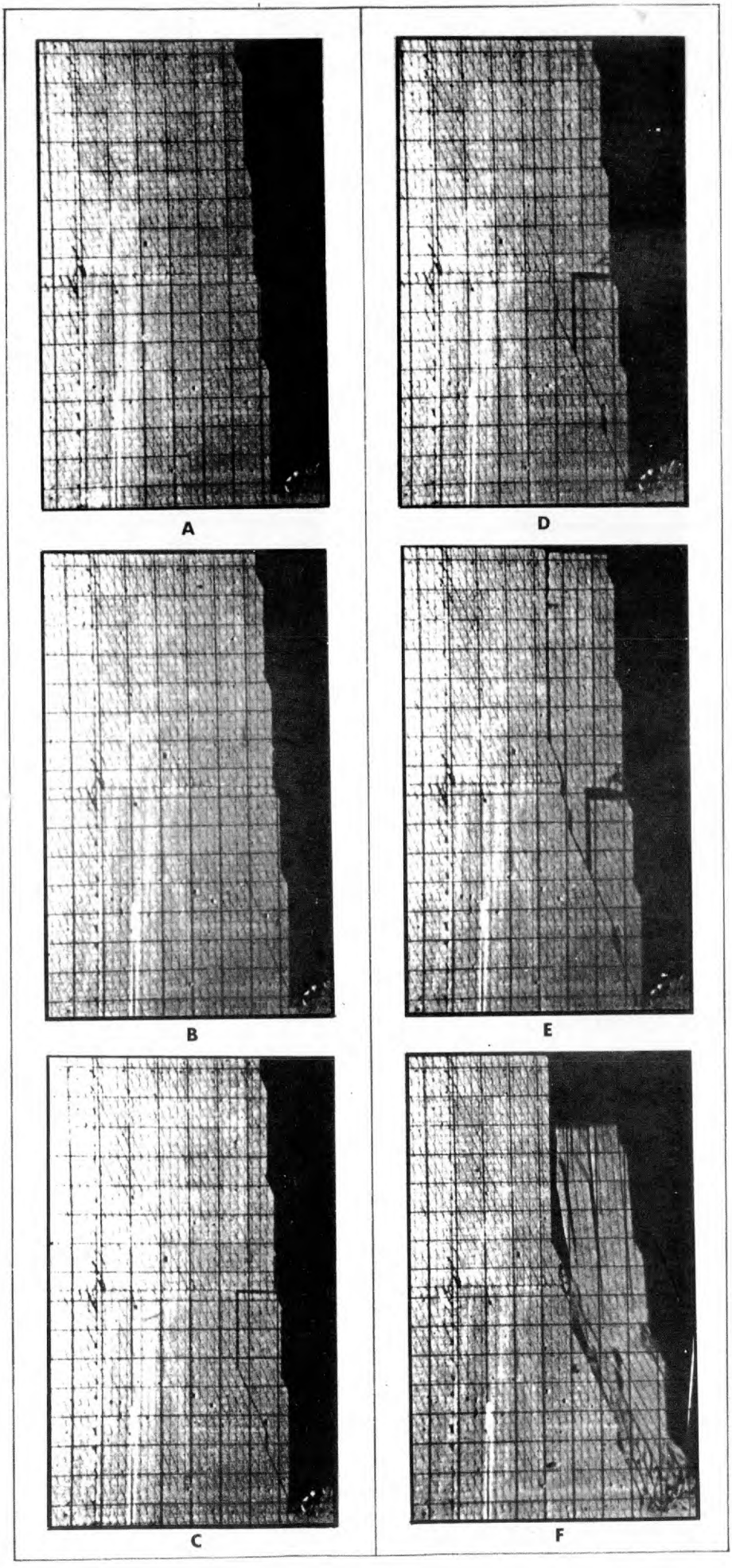

Figure 3.3.29 Failure sequences of model L.M.3 (L.H.S. outer)

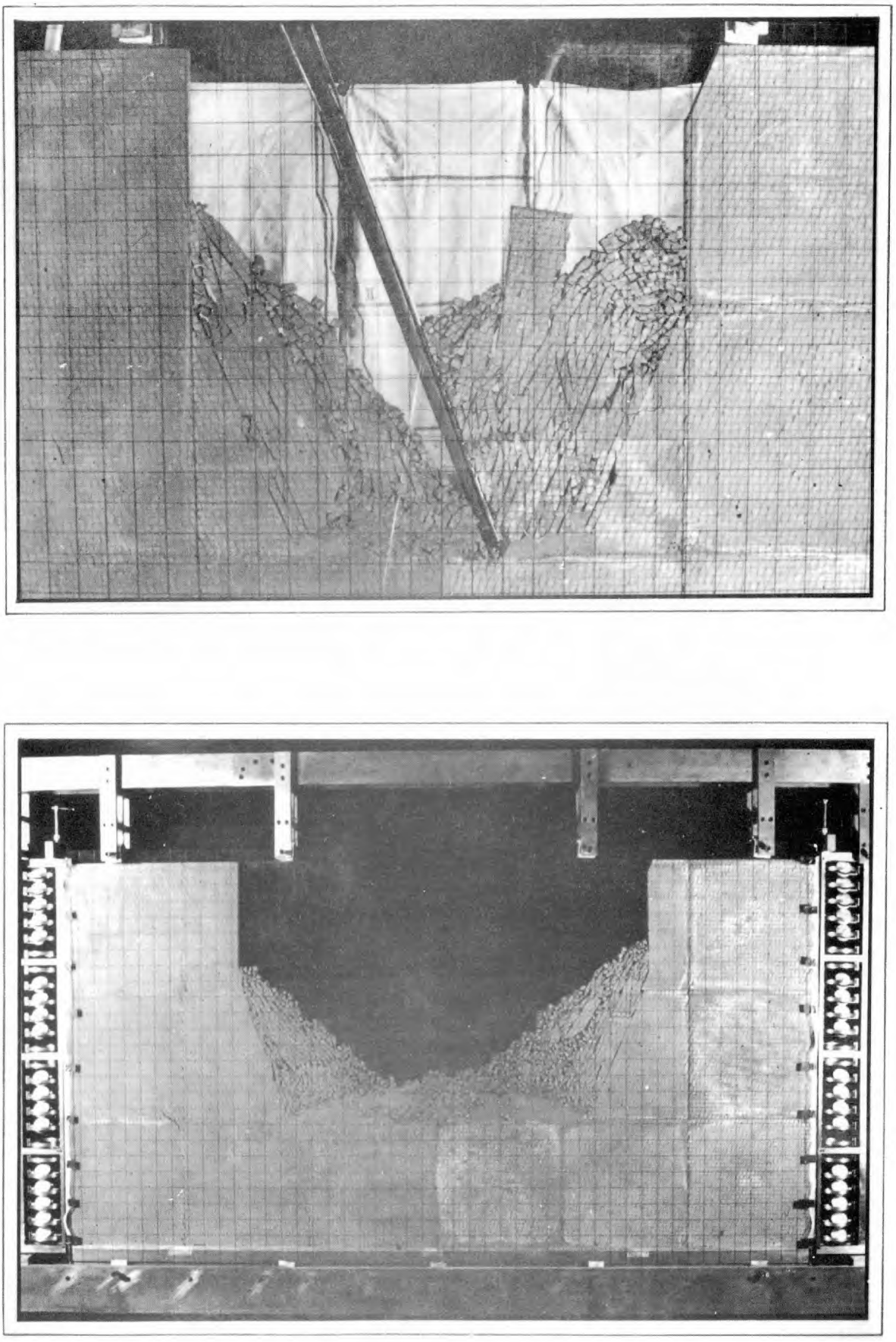

Figure 3.3.30 Two pairs of model slope failures illustrating symmetrical modes of failure.

It is interesting to note the large intact blocks lying amongst the smaller debris. There is no reason for a moving mass of interlocked rock blocks to separate, unless relative shear stresses are applied at the boundaries. The presence of the vaccuum tube or the needle excavation rod, invariably reduced the magnitude of these stresses. Consequently the final stages of collapse were somewhat artificial in most cases, since the sliding mass did not hit the floor of the excavation under natural conditions.

3.3.6 BACK ANALYSIS OF FAILURES

The failures illustrated in the preceeding figures were for the most part quite trivial to analyse by limit equilibrium methods. No attempt was made to divide the failing mass into slices and the assumed shear and normal stresses acting across the failure planes were treated as mean values.

The following assumptions were made:

1. The stresses acting on a given failure surface were due solely to the weight of unstable material lying above the surface.

2. The total weight / unit thickness of slide mass (which could be very accurately measured) was converted to mean shear and normal stress components, by dividing by the total area of shear surface.

3. The ratio of mean shear stress to mean normal stress was equal to the tangent of the angle of dip of the failure surface (tan $66^{\circ} = 2.25$)

4. Failure was assumed to occur simultaneously along the whole length of the shear surface.

The mean depths of the shear surfaces were carefully measured and the corresponding mean virgin stress levels read from Figure 3.3.17. The following tabulation gives the results of the back analyses, and the approximate pre-consolidation ratios for each slide. The stress units are lbf/in^2.

Photograph of failure	Virgin stresses		Failure stresses		Pre-consolidation ratio
	τ	σ	τ	σ	
3.3.21 A	1.00	4.10	1.23	0.55	7.5
3.3.22 B	0.71	3.19	0.88	0.39	8.1
3.3.23 B	0.71	3.20	0.92	0.41	7.8
3.3.25 C	0.75	3.54	1.39	0.61	5.8
3.3.26 C	0.26	0.99	0.36	0.16	6.2
3.3.27 C	0.23	0.88	0.39	0.17	5.2
3.3.28 D	0.25	0.97	0.53	0.24	4.1
3.3.29 D	0.26	0.99	0.49	0.22	4.5

Figure 3.3.18 shows these eight pairs of failure stresses plotted for comparison with the pre-consolidated shear tests. It will be realized that all these points lie on a line inclined at 66° and passing through the origin. By a strainge twist of fate this line happened to be almost coincident with the strength envelope obtained from the test conducted at a pre-consolidation ratio (P.C.R.) of 4 to 1. Therefore the angles of intersection between the line $\tau = \sigma . \tan 66^{\circ}$ and the relevant peak strength envelopes, were vanishingly small. Consequently failure was possible for a range of normal stress levels.

This meant that failure was to some extent independent of the slope angle. This unexpected result explains why a variety of slope angles induced failure, in the range 80° to 90°.

One further unexpected result should be recorded. Figures 3.3.28 and 3.3.29 illustrate two failures which were obviously progressive. It is these types of failures which would traditionally be rejected for limit equilibrium analyses, since shear failure clearly was not occurring simultaneously along the whole length of the surfaces.

However, the pre-consolidation ratios for these failures were 4.1 and 4.5 respectively. This means that the shear parameters estimated from back analysis were almost exactly the same as the peak values measured in the shear box. Why these two failures should apparently occur when peak strength was mobilized, and the remainder when the mean shear stress was below peak strength, is frankly uncertain.

Mass closure effect in tilt models

The jointed slopes that were rotated to failure (Section 3.1) indicated back analysis (c) and (ϕ) parameters that were slightly higher than the results obtained from direct shear tests. The mass closure effect discussed above was clearly responsible for this.

It will be recalled that before tilting the models, the primary joints were horizontal and therefore were unstressed in shear. However these same joints were consolidated by the self weight of the reclining slope. Large tilt models such as that illustrated in Figure 3.1 18 were subjected to a triangular distribution of normal stress acting across the horizontal primary joints. This 'virgin' stress was a maximum beneath the crest of the slope. The mean normal stress acting across the full length of the critical joint (that exposed at the toe of the slope) was approximately 0.31 lbf/in^2. At failure, when this same joint was dipping at approximately 66^o, the mean normal stress acting across the shear surface was approximately 0.2 lbf/in^2. Even this small pre-consolidation ratio of 1.5 to 1 was sufficient to increase the shear strength to a noticeable degree.

CONCLUSIONS

The large models described in this section represented an unusual departure from conventional modelling techniques for two reasons:

1. The models were exceptionally discontinuous. (Models L.M.2 and L.M.3 were jointed into at least 40,000 discrete blocks.)

2. The models were not constructed of smooth faced regular bricks.

The latter was responsible for the fundamental differences in behaviour between the present models, and the usual brick models. These differences can be summed up in one word: dilation.

A model rock mass consisting of smooth joints will deform in the initial stages, purely as a result of the frictional characteristics of the joints. Consequently the initial shear surfaces will develop in direct response to increased shear stresses, which may result in slip on several surfaces at any one time. This is a conventionally held belief and one that must be questioned.

Joints which exhibit dilational characteristics, whether these be as high as those of the present model joints, or as low as might occur on smooth shear joints in rock, will tend to inhibit shear failure of slopes to a minimum number of surfaces, usually one.

The only exceptions to this fundamental energy concept can be joints which, for various reasons, do not dilate in shear. Therefore slopes which are badly weathered, or internally strained as a result of deeper seated shear movements will probably perform in a similar manner to the conventional brick models, at least near the surface. (Hofmann[92] and Müller and Hofmann[93])

If weathering could have been simulated at the surface of the present models, the result would have been extremely realistic. For this reason all types of discontinuous models should be carefully evaluated since, in all probability one or other of the many phenomena exhibited in progressive failure will be illustrated.

CONCLUSIONS

1. COMPARISON OF MODEL WITH NUMERICAL METHODS OF SLOPE ANALYSIS

The normal and shear stiffness data presented in Section 1.4 represented valuable input information for a numerical analysis of the model slopes described in Section 3.3. A comparison was made between the deformation behaviour measured in model L.M.3 (Figure 3.3.12 E), and that predicted from a simple finite element analysis. This study, which was kindly performed by St. John[94], represents the initial results of a more extensive study to be reported at a later date (St. John[43]).

The finite element program was used to simulate the excavation of a slope geometrically similar to the physical model, and subject to similar boundary conditions. The only difference was the total vertical extent. For the real model the total depth (4 feet) was approximately $1\frac{1}{2}$ times the slope height, while the finite element model was three times the slope height in depth. The deformed slope profiles are shown with and without correction for this difference in Figure 3.4.1.

Two analyses were conducted. First the model was considered as unjointed and possessing the elastic properties of the intact model material. The displacements for this isotropic model show the elastic recovery of the model due to the removal of material from the excavation. The corrected displacements (solid lines) indicate approximately 0.001 inch upward heave in the base of the pit. This is approximately six times smaller than that detectable by the photogrammetric method employed to measure displacements.

The stresses obtained from this isotropic analysis were used to perform a 'ubiquitous joint analysis'(Duncan and Goodman[95]). No slip was indicated on the primary joint set (dipping at 66°), assuming the joint strength parameters determined by testing. It will be recalled that these same joint parameters ($c = 0.10$ lbf/in^2 and $\phi = 58^{\circ}$) caused failure for the same pit depth of 31.2 inches, when used in a limit equilibrium method of slices (see Section 3.2).

In the second numerical model, an attempt was made to take into account the deformability of the joints by linear superposition of the elastic properties of the modelling material, and the stiffnesses of the three joint sets. The latter were obtained from the relevant values tabulated in Section 1.4. Figure 3.4.1 shows that the resulting displacements were nearly three orders of magnitude greater than for the isotropic case. The influence of the primary joints, 'soft' in shear, that dip steeply into the excavation was clearly demonstrated.

The corrected displacements shown in the upper part of the slope appear to be similar to those found in the model (Figure 3.3.12 E, right side) although a little larger. However, due to the theoretical elastic recovery, slope bulge and floor heave are

Figure 3.4.1 Slope displacements predicted by two finite element analyses of the modelled rock slopes.

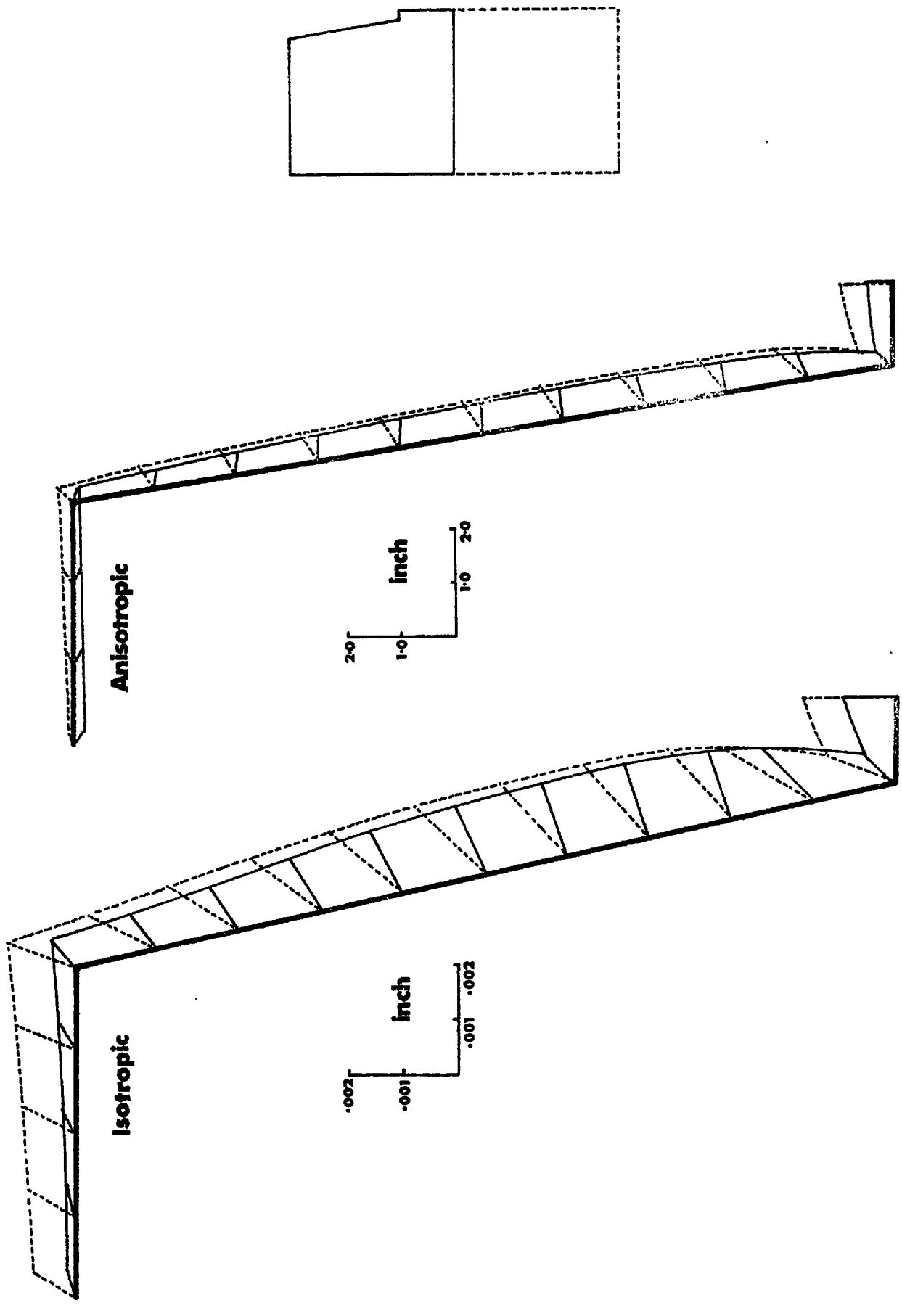

enormous with the anisotropic deformation properties. A floor heave of approximately $\frac{1}{2}$ inch is predicted, which at full scale represents more than 20 feet.

The stress distribution obtained for the anisotropic case was markedly different to the isotropic elastic model. A second 'ubiquitous joint analysis' indicated a potential slip on primary joints over approximately 80% of the slope height and a maximum of 30% of the slope height inwards. However no conclusion as to the stability of the slope can be drawn from these observations as slip on joints may only cause a redistribution of stress (St. John[68]).

It can therefore be seen that the shear and normal stiffness of joints should not be treated as elastic properties since clearly they are not recoverable to any marked degree. It is possible that under normal loading and when pre-consolidated, joints may almost behave elastically. However it seems probable that shear deformation is largely irrecoverable, even just up to the development of peak shear strength. The extreme 'softness' of joints in shear, means that even slight inelasticity here will make the overall behaviour grossly inelastic.

Joint analyses have been developed in an attempt to overcome these difficulties. The sophisticated numerical methods being developed, (for instance Mahtab and Goodman[79], Zienkiewicz, Best, Dullage and Stagg[80], Cundall[69] and St. John[43]) while representing significant advances are, in real terms still extremely crude simulations of real processes.

One of the fundamental limitations of conventional finite element methods appears to be the conservation of energy that is demanded in the course of computation. It is for this reason that anisotropic deformation properties cause such an impossibly large 'elastic' recovery, when slopes are excavated in a loaded model.

The 'finite difference' approach adopted by Cundall[69] appears to be one method of overcoming this problem. Multiple block models are loaded in any desired manner, and the deformations and failure movements resulting from removal of blocks are plotted by computer in consecutive stages. Energy is lost during these relative movements, and there are few limitations on the strength and deformation properties that can be simulated.

The modes of failure illustrated by the Cundall method (which includes simple shear, toppling and rotation) closely resemble the failures induced by excavation of slopes in conventional brick models. A very interesting comparison can be made between this numerical method and the slope model study reported by Hofmann[92], and Muller and Hofmann[93].

2. COMPARISON OF MODEL WITH HOFMANN'S BRICK MODEL

As far as the author is aware the only other model study of jointed rock slopes was that performed by Hofmann at the University of Karlsruhe. This study was more or less contemporary with the present one. The two models differed in two important aspects:

1. The present model was loaded horizontally in an effort to simulate the linear increase of stress with depth. As far as can be ascertained Hofmann's model was loaded only by gravity.

2. The present model was more highly jointed, and joint surfaces were rough and interlocked compared to the smooth sided orthogonal bricks used by Hofmann.

The first of the above differences was shown to be very important due to the mass closure effect exhibited by rough interlocking model joints (Section 3.3). However it would probably have had much less effect on a smooth-jointed model.

The second of the above differences was of overriding importance for several reasons:

1. The present model had to be excavated to extremely steep slopes to induce failure, due to the high shear strength of the rough joints. By comparison the brick model began to exhibit signs of incipient failure early in the excavation process, due to the greater possibility of toppling and multiple slip.

2. The present model evantually failed in a translational manner, on a single compound shear surface. The brick model (which was jointed in such a manner as to exclude simple translational shear) failed by multiple toppling and gross loosening of the jointed mass. Such failure modes were seen to be self inhibiting for rough joints (See Section 3.1).

The extent of loosening and brick rotation illustrated in the paper by Muller and Hofmann[93] was particularly significant since the resulting concentration of forces at the tips of bricks caused fracture of the intact material in these enormously dilated zones. No fracture of intact material was detected in the present model, until catastrophic failure occurred. However, differences in prototype dimensions and strengths were not responsible for this, as can be seen from the following comparison.

	Present model	Hofmann's brick model
Maximum excavation depth:	1330 ft.	135 ft. (40 metres)
Compressive strength:	13,800 lbf/in^2	2270 lbf/in^2(160 Kg/cm^2)
Geometric scale	1:500	1:50

It is apparent from comparison of the two models that widely different characteristics are simulated. For this same reason enormously different modes of failure are exhibited. Since only two model slope stability studies have been reported to date, this is perhaps advantageous. There can be no clear demarkation of 'correct' joint behaviour since, depending on the conditions, a whole range of properties will need to be simulated.

It may be valid to conclude that the present model represented a realistic simulation of high rock slopes in which the unconfined compression strength of 13,800 indicated the unweathered nature of the prototype rock. By comparison the brick model, simulating a slope height one tenth as high, had a compressive strength low enough to suggest weathered conditions. Highly weathered loosened joints (i.e. near surface) can perhaps be realistically simulated by smooth non-dilatant model joints. Deeper seated, unweathered joints can only be simulated realistically by the model tension joints that have formed the foundation of this study.

APPENDICES

APPENDIX 1.

4.1 PREPARATION OF THE MODEL MATERIAL

The multi-component mix consisting of red lead-sand/ballotini -plaster-water was finalised after a long period of development. In this appendix details of the component materials are given, together with notes on the design of the mixes, and the method of production. Following this a more detailed description is given of the physical and chemical changes that occur during mixing and curing. Some problems of repeatability are discussed, and simple methods of solution given.

The constituent elements used in the preparation of the material can best be termed as follows:

(i) dense filler (red lead powder)
(ii) coarse filler (sand-ballotini)
(iii) cementing agent (plaster and water)

The ratio of (i) to (ii) was finally fixed at 1:2 by weight. A range of strengths were produced simply by varying the content of cementing agent. A range of inherent shear characteristics were produced by varying the proportions of sand and ballotini in the coarse filler.

a) Coarse filler

Three different sands were tried before a satisfactory grading was found. A sand between the extremes of fine and coarse must be used, with the latter limit depending upon the desired frictional properties of the fractured material. The practice of removing certain fractions of the sand was avoided, since the overall aim was to develop a material which could be reproduced with readily available products. The grading distribution for the selected sand is given in Figure 4.1.1 It can be seen that 60% is retained on a B.S. sieve No. 150. The average chemical analysis is as follows:-

SiO_2	Al_2O_3	Fe_2O_3	CaO	Na_2O	K_2O	
98.4	0.82	0.15	0.03	0.04	0.33%	Loss on Ign: 0.25%

The loss on ignition represents the organic matter in the sand. The significance of this impurity is described in a later section of this appendix.

Coarse filler, consisting of a combination of sand and ballotini, was used in an attempt to vary the internal frictional properties of the material. Ballotini consists of small spherical beads of glass and, despite the fact that it consists entirely of SiO_2, the internal friction of a mass of the material is much lower than for sand, since the spherical surfaces are so smooth by comparison. The grading distribution of the ballotini used throughout in the present work is given in Figure 4.1.2

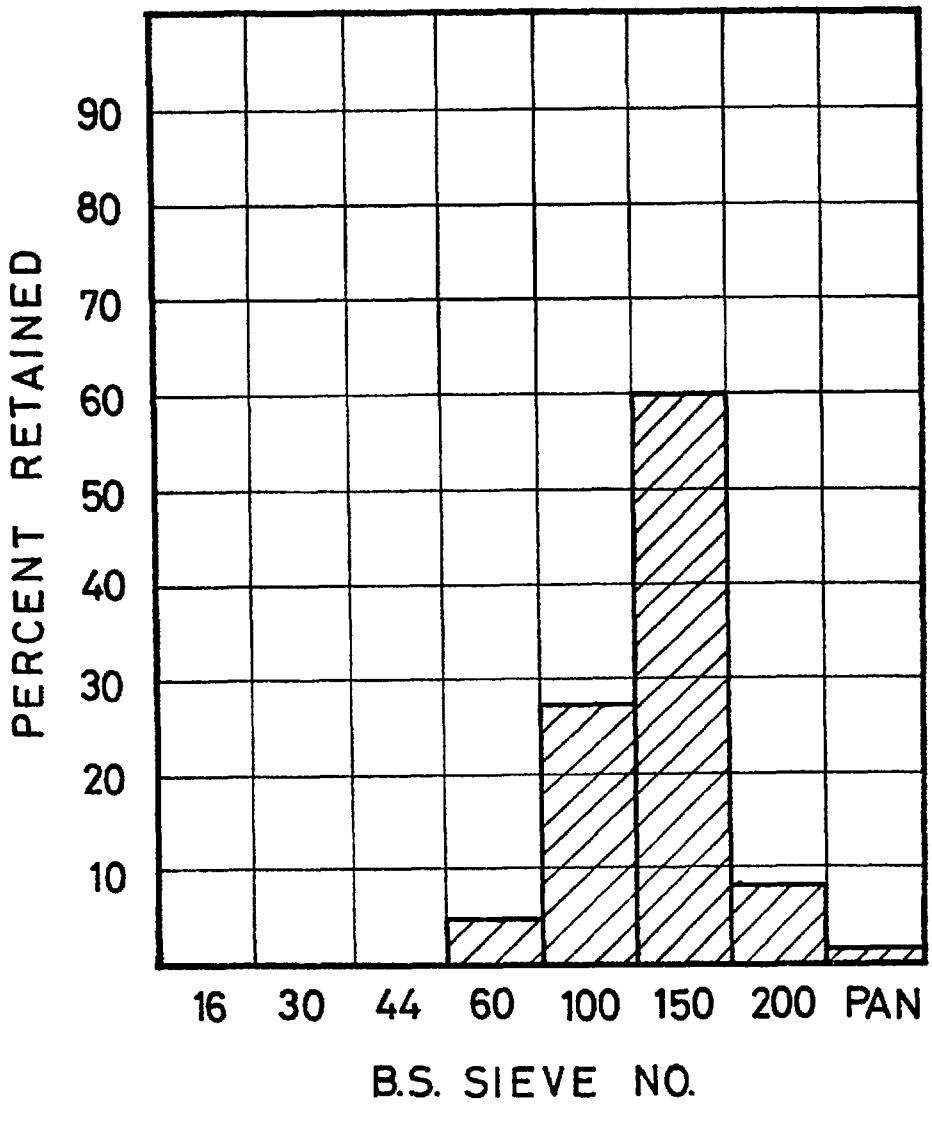

Figure 4.1.1 Average physical analysis of Kingslynn(ss) sand used in the model materials

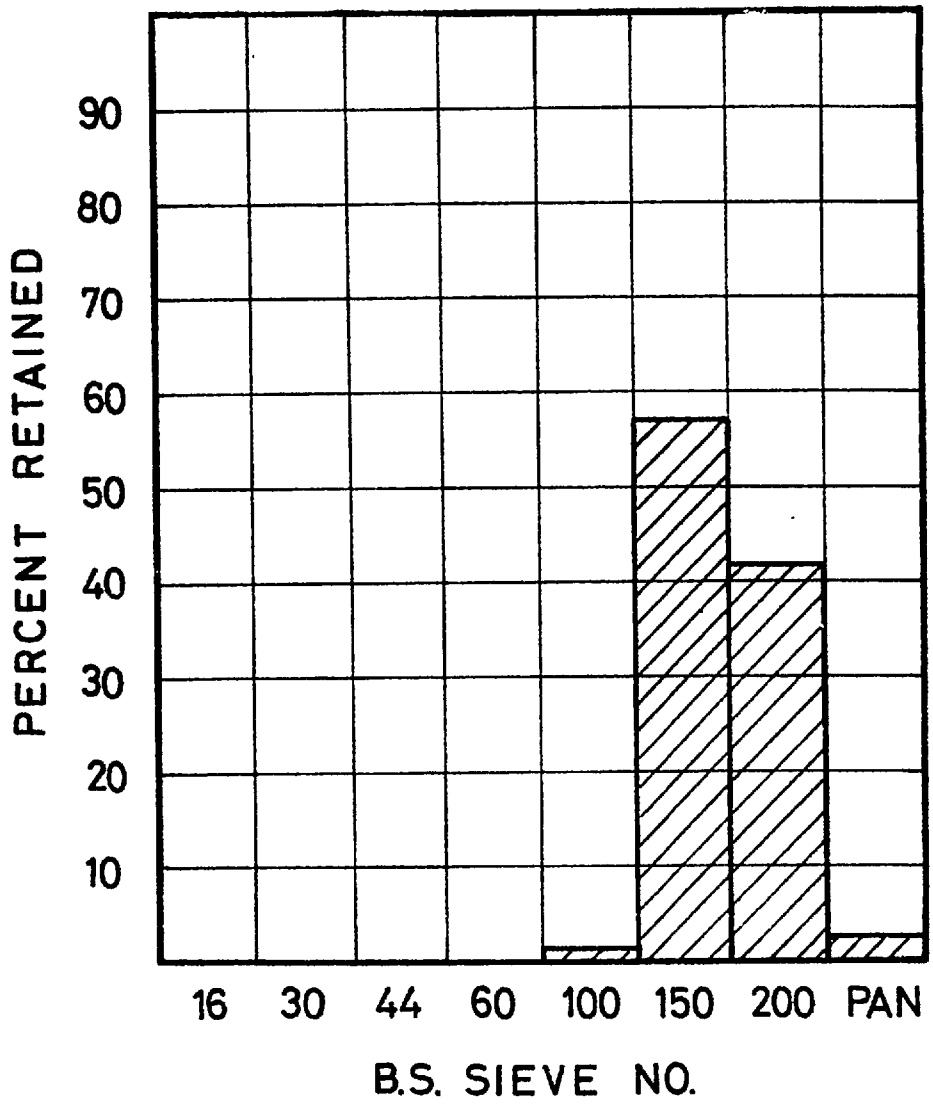

Figure 4.1.2 Average physical analysis of Grade (AF) Ballotini used in the model materials

APPENDIX 1

b) Dense filler

Red Lead (Pb_3O_4) is obtainable from any large chemicals firm. Since it is a fine powder, it was preferable to store it in moisture proof containers, to reduce the possible uptake of water.

c) Cementing material

A widely used fine casting plaster was preferred to some of the faster setting varieties, since the set strength of quick setting plasters is generally much higher. Again, dry storage was a necessity.

d) Suppliers of materials in Britain

The material trade names and distributors are given below:-

Sand: Kingslynn (SS)British Industrial Sands Ltd., Surrey
Ballotini: Ballotini (AF) Ballotini Manufact'ng Co. Ltd., Yorkshire
Red lead: Pb_3O_4 (5112) Hopkin and Williams Ltd., Essex
Plaster: Fine white casting plaster: British Gypsum, Ltd

MIX DESIGN

The range of mixes appropriate to rock modelling when employing the stress scale (ψ) of 1:666 are summarised by Figure 4.1.3 A standard mix consisted of a fixed ratio of 1:2 by weight of dense to coarse filler. The proportions of sand-ballotini which make up the coarse filler were chosen according to the frictional properties desired. Type A is seen to consist of 100% sand (1200 weight units), type C of 50/50 (600/600 weight units) and type B of 100% ballotini (1200 weight units). Since the water demands of mixes containing either 100% sand or 100% ballotini were different, the five design lines have a finite gradient.

Mix numbers 1,2,3,4 and 5 represent the quantity of plaster in the mix; 50,75,100,125 and 150 units of weight respectively. This is in a standard mix of 600:1200 weight units of dense to coarse filler. The choice of mix number was of course based on the desired strength of the mix. The amount of water required for the selected mix was read off from the abscissa. These quantities were obtained after careful experimentation, so that the whole range of mixes, while easily poured, did not 'bleed' excessively while setting.

Example Type C, mix No.4 (C4)
is 600-600/600-125-431 by weight
of Pb_3O_4 - sand/ballotini-plaster-water

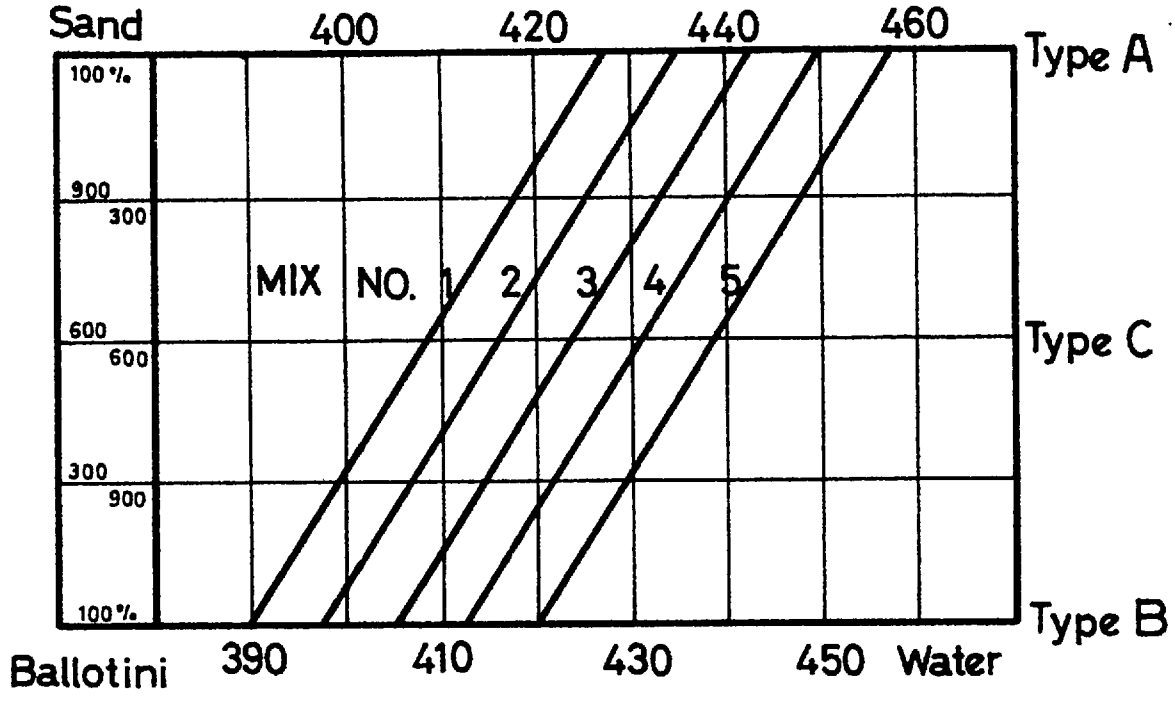

Figure 4.1.3 Design chart for modelling materials

APPENDIX 1

(weighing quantities in grammes (i.e. 600 gms. of Pb_3O_4 etc.) gave a batch of suitable volume for casting a dozen compression specimens of dimensions 1" x 1" x 2").

a) Notes on mixing

The optimum order for combining the materials in the mixing bowl was: water, coarse filler, dense filler and plaster. A Kenwood Major electric mixer was used (double orbital type) and run at its slowest speed setting to combine the materials with the minimum of air entrainment. A stop clock was set to time the mixing from the instant when the plaster was added. Obviously the optimum mix times and consequent set times depend on the materials used and the desired pourability. Mix times in this study ranged between 6 and 14 minutes, and the set times (total from start from 9 to 24 minutes.

All materials were stored in the same room, which was kept at 24°C±1°. The water was adjusted to this temperature as necessary. Care was needed to ensure that the mixing bowl (stainless steel) was also at room temperature. Small mix volumes began to set several minutes early if the mixing bowl was still hot after a hot water rinse, with consequent alteration in the physical properties of the mix when cured.

b) Notes on vibration

A useful technique for improving the uniformity of results was obtained by vibrating the moulds for 15-20 seconds while pouring the mix. This was adopted as standard practice for all the mixes tested and reported in this paper. Any air entrained during mixing was almost entirely removed. The set specimens were removed from the moulds about 1 hour after pouring and were placed on trays ready for oven curing.

c) Notes on curing

An oven curing temperature of 105-110°C was employed, together with forced ventilation across the shelves. All batches of the material were cured for a minimum of five days under these conditions, and no mechanical testing was begun until at least 3 hours after removal from the oven. In this way the material had time to cool and stabilise its surface moisture distribution. A photograph of the oven containing all the 18 slabs for one of the large models is shown in Figure 4.1.4.

Dehydration of the gypsum cementing material begins at temperatures above 70°C, and the hemihydrate thus obtained is stable up to about 150°C, above which further dissociation occurs. The rate of dehydration is increased if the vapour pressure is kept low (Holdridge and Walker)[1] which suggests that higher curing temperatures might be needed in an oven having no forced ventilation.

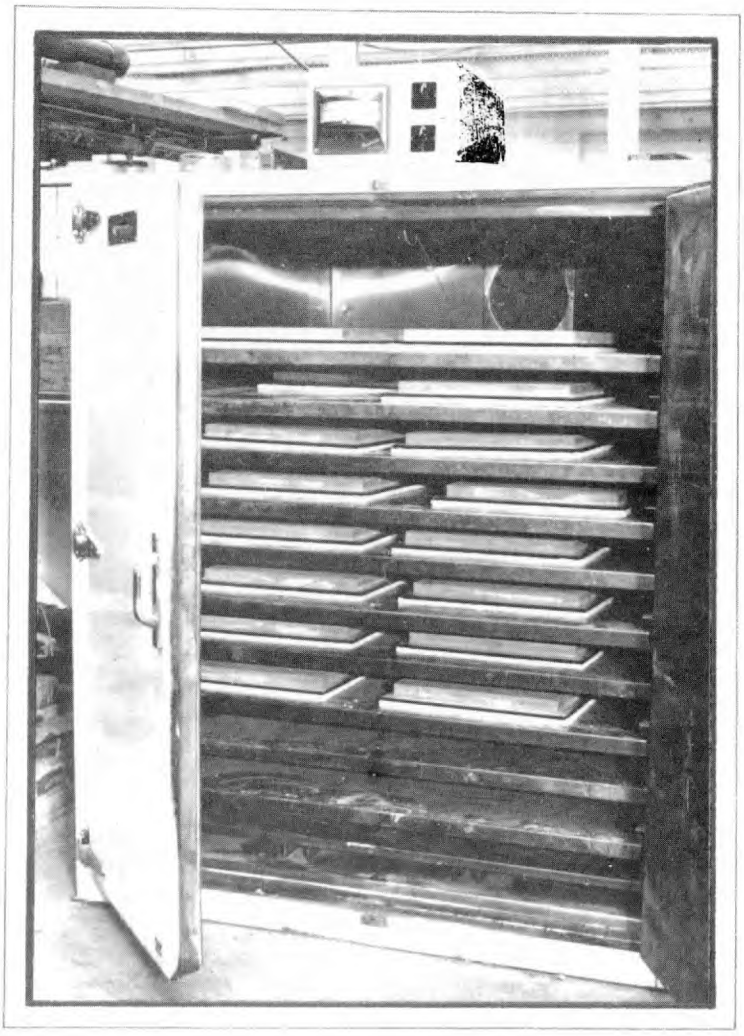

Figure 4.1.4 The large oven used for curing the model material

APPENDIX 1

The importance of adhering closely to a standard preparation procedure should finally be emphasised. The mechanical properties were noticeably affected if the above procedures were not followed in every case when preparing a set of supposedly identical mixes.

As a guide to potential users of the material; some comments on the physical and chemical processes involved when mixing and curing are given in the next section. Problems which can arise and cause variations in the setting times are also summarised.

PHYSICAL AND CHEMICAL CHANGES DURING MIXING AND CURING

The constituent elements used in the preparation of the material have been termed as follows:-

(i) dense filler (red lead powder)
(ii) coarse filler (sand-ballotini)
(iii) cementing agent (plaster and water)

It will be obvious that for a larger proportion of plaster to filler, a larger quantity of water is required. The demand for water is threefold:-

(i) chemical hydration of the plaster
(ii) saturation of the dense and coarse filler
(iii) rheological requirements of the mix

The quantity of water required to obtain a pourable mix is considerably in excess of that needed for hydration, even for plaster-water systems alone (Schiller,[2]). The addition of a fine powder such as red lead increased this demand greatly, and the further addition of a frictional material like sand increased it yet again. It will be clear therefore that the set material was quite porous, since so much excess water was evaporated during oven curing.

a) Porosity of the cured material

Hemihydrate plaster sets in accordance with the equation:-

$$CaSO_4.\ \tfrac{1}{2}H_2O + \tfrac{3}{2}\ H_2O = CaSO_4.\ 2H_2O$$

or 145.15 g. hemihydrate + 27.03g water gives 172.18 g. gypsum. If the gypsum is cured above its dissociation temperature of 70°C (Holdridge & Walker), the hemihydrate is re-obtained but in crystalline form.

If it is assumed that at the curing temperature used (105-110°C) there was 100% dissociation to the hemihydrate, and further, that the free moisture content was reduced to zero, then a simple estimate of the porosity of a given mix can be made. Selecting a typical one; 600-1200-100-442.5 by weight of red lead-sand-plaster-water (A3), it is assumed that all 442.5 portions of water were evaporated during curing. Using gramme units of weight, if there was no volume change there would be 442.5 ccs.

of pore volume in a cured material which weighed 1900 gms. Experimentally, the bulk density of the cured material (A3) was 122.2 lbf/ft^3 or 1.96 gms/cc.

$$\text{bulk volume} = \frac{1900}{1.96} \text{ ccs.}$$

Hence, porosity p (volume of voids/bulk volume) = $442.5 \frac{1.96}{1900} = 45.7\%$

For the range of mixes considered, the porosities should lie between approximately 40 and 47%, if the above assumptions are valid. This range is high but not excessively so compared with plaster-water systems in general use (30 to 80% or more). (The range may be a little lower than 40 to 47%, since the small volume of water lost by surface evaporation. and by bleeding has been ignored, both of which occur during the setting period).

b) Lubrication phenomenon

The characteristics exhibited by the material when mixing the constituents together have considerable influence on the properties of the material when cured. The four components were added to the mixing bowl in the following order; water, sand, red lead and plaster. A few seconds' mechanical mixing of the water-sand phase removed all the air from the sand and it settled to the bottom of the bowl with perhaps $\frac{1}{2}$ inch of water above it. The addition of the red lead caused the 'free' water to be absorbed and the whole mass became stiff as negative pore pressures were developed, due to the capillary action of the pores. It gave every appearance of being too dry to mix any further, and certainly too dry to accept the plaster which had still to be added. However, after a few seconds of churning what from all appearances was a solid, a remarkable change occurred and the mass became a creamy orange fluid, and readily absorbed the additional plaster. It appeared that, in some way, the saturated red lead was acting as a lubricant and reduced the frictional resistance of the sand, thereby making the mixture readily mixable and pourable. It was clear that this phenomenon reduced the water demand appreciably and thus ensured that the porosity was not excessively high when cured. A most important consequence is that the amount of 'bleeding' which occurred in a setting mix was much less for this material than it would be for a multi-component mix which relies solely on the addition of water for its rheological properties.

c) Variations in the setting times

Three problems which occurred and can cause considerable difficulties are summarised below:

1) Small concentrations of salt (NaCl) in the sand may have a catalytic effect on the setting of the mixes. Increased compressive strengths and increased modulus ratios were the unfortunate side effects. The simple solution was to obtain

dried batches of washed sand from a reliable source.

2) Small amounts of organic matter in the sand (represented by % loss on ignition analysis) had a retarding effect on the setting of mixes. Most sands have insufficient quantities to cause any worries, the problem arises from (3) below.

3) Initially, careless storage and handling of sand batches caused fines to predominate in the lower half of the storage bins, coarse particles to predominate in the upper half, and organic matter to steadily work its way to the surface. If sand batches were withdrawn from the top of the bins, the effect during bin use was the following:

a) the setting of mixes became successively less retarded
b) the water demand successively increased due to the increasing fines content

The combined effect was a considerable reduction in the setting times during the 'life' of any sand bin. To prevent this occurring, the purchased bags of sand were eventually carefully mixed and placed in the storage bins manually, so that all batches withdrawn were very close to the average physical and chemical analysis. It is pertinent to state here that successive mixes had closer mechanical properties, the larger the batches mixed at any one time.

APPENDIX 2

4.2 STRENGTH TEST EQUIPMENT

The development of materials as weak as 5 lbf/in^2 in unconfined compression made it necessary to use apparatus of the soil mechanics testing range, for sufficient sensitivity of load measurement to be obtained.

a) Unconfined compression test

Unconfined compression and tensile testing (Brazilian disc method) was performed on a standard direct shear apparatus (Clockhouse Engineering Ltd.), but with the following fundamental modifications which can be seen in Figure 4.2.1 (a). The shear box and runners were removed, and the apparatus was set in a vertical plane, with the constant rate of advance jack moving vertically downwards. A spring-retained ball seated platten was bolted to the jack to act as the upper platten. The lower platten which was similarly mounted, was bolted to the proving ring fixture. Both plattens had ground faces in an attempt to improve the stress distribution on the specimens. The proving ring dial gauge (sensitivity 0.0001"/division) could be used for both load measurement and axial deformation readings, since the jack advance rate was accurately known. This method removed the need for a separate axial deformation dial gauge, or strain gauge methods which would have been impractical for such a weak material.

b) Triaxial compression test

Triaxial testing was also performed with soil mechanics apparatus. Cylindrical specimens of 1½ ins. diameter were cast and were placed in standard thin-walled rubber membrane sleeves. The only modification to the apparatus that was required was a more sensitive method of cell pressure measurement. A mercury U tube manometer was used, with the conventional constant pressure mercury pot devices. The essential features of the apparatus can be seen in Figure 4.2.1 (b). The low range of confining pressures (0-3.4 lbf/in^2) made it imperative to correct for several factors which would normally have been ignored both in soil and rock mechanics practice. The following is a summary of the factors allowed for when computing the magnitudes of σ_1 (axial pressure) and σ_3 (confining pressure) acting at the mid-height of the 3-inch high cylindrical specimens.

Confining Pressure σ_3

(i) The pressure gradient due to the head of water between the mercury manometer and the cell

(ii) The pressure gradient due to the head of water in the cell itself (0.108 lbf/in^2 across the 3-inch cylinders)

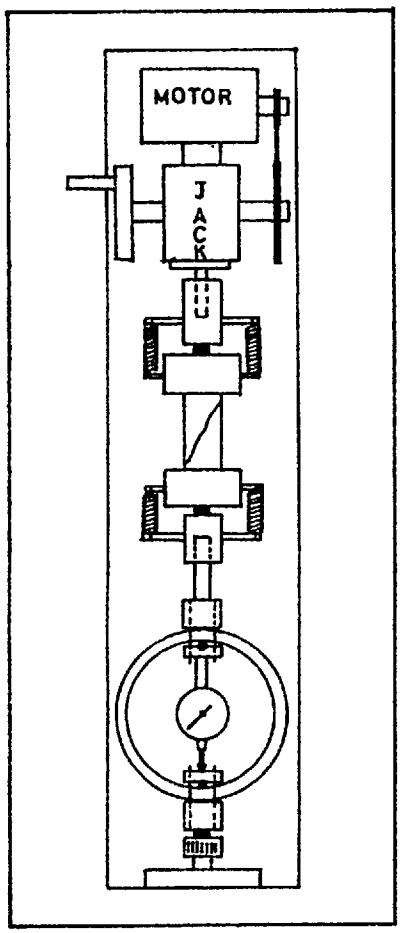

UNCONFINED
COMPRESSION
APPARATUS

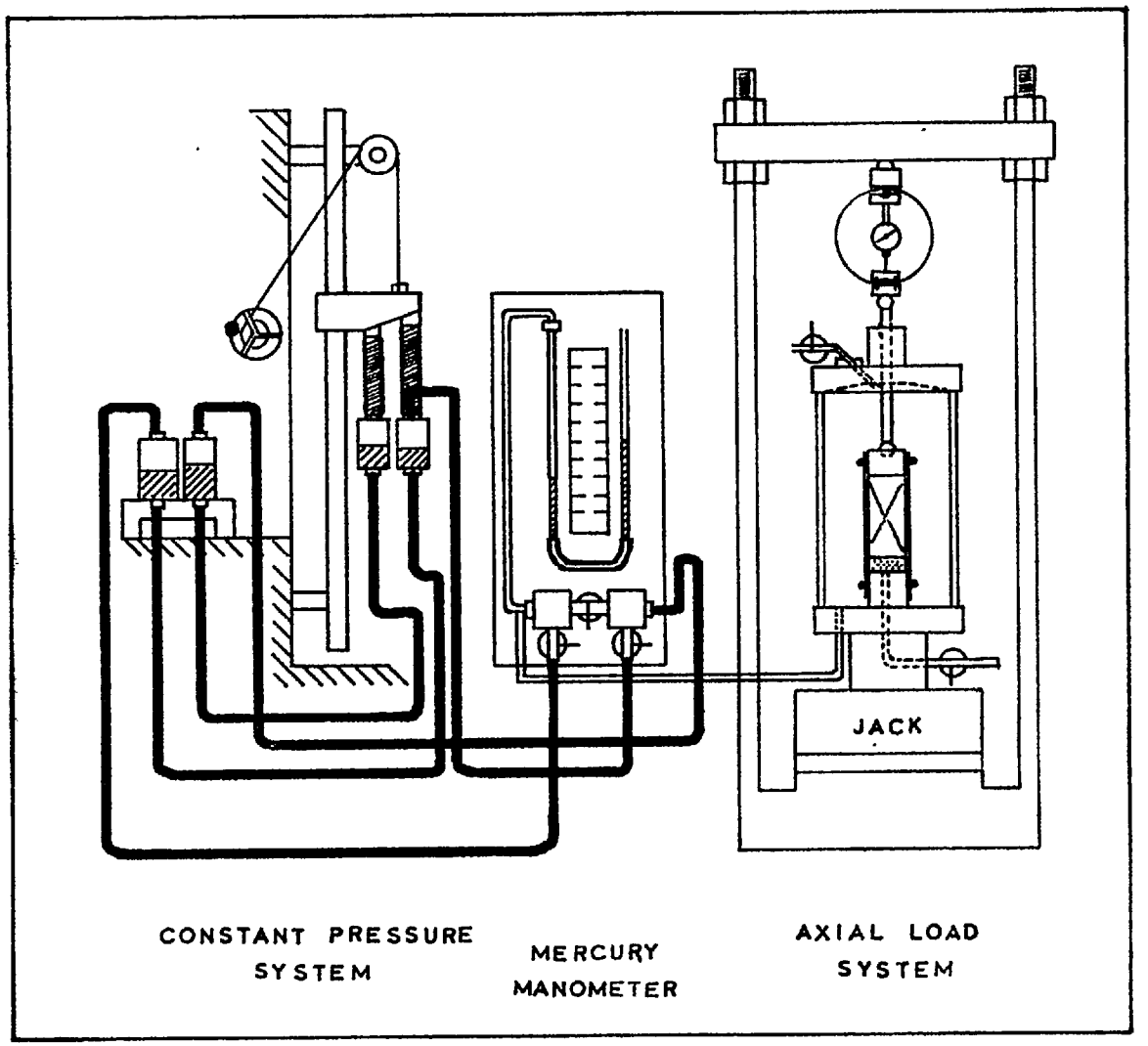

TRIAXIAL COMPRESSION
APPARATUS

Figure 4.2.1 Compression test equipment used on the model material

APPENDIX 2

Axial Pressure σ_1	(i)	The self weight stresses in the model material
	(ii)	The weight of the capping platten and ball bearing
	(iii)	The cell pressure acting at the level of this platten
	(iv)	The effective weight of the piston and upper ball bearing
	(v)	The reduction in the latter due to the cell pressure acting at the level of the lower end of the piston.

Factors which were ignored were the following:

(i) The confining effect of the rubber membrane when slight 'barrelling' occurred in the tests at the highest σ_3 values.

(ii) The change in elevation of the cell during any one test. (The jack drives the cell vertically upwards against the loading yoke).

The six confining pressures employed in the tests ranged from zero to 3.42 lbf/in^2. The tests under zero confining pressure were performed with the specimen in the rubber membrane for consistency, but with the cell empty of water and open to the atmosphere. The next cell pressure of 0.25 lbf/in^2 (acting at mid-height on the specimen) was obtained by simply filling the cell with water, but applying no additional pressure. In the other four cases, the uppermost valve on the cell was closed, and the desired pressures were generated by small increments in the elevation of the dual mercury pot system. The mercury manometer was calibrated so that head differences between the two arms could be related directly to the confining pressure acting at the mid-height of the specimens.

c) Stiffness of machines and loading rates

The following proving ring stiffnesses were used for the three standard testing procedures. They represent the 'machine stiffness' and are compared with the range of material moduli.

Unconfined compression:	400 lb. proving ring	2.97×10^{-4}	ins/lb.
Brazilian disc test:	50 lb. proving ring	2.26×10^{-3}	ins/lb.
Triaxial test:	400 lb. proving ring	2.97×10^{-4}	ins/lb.

For specimen under test : Deformation/unit load = L/AE

where L = length of specimen
A = cross-sectional area
E = Young's modulus.

APPENDIX 2

For the case of unconfined compression, when testing 1" x 1" x 2" prisms of the material, the following simple result is obtained:

Deformation of specimen/unit load = 2/E ins/lb.

which will be termed the stiffness

Range of Young's moduli tested :

A2	0.358	$\times 10^4$ lbf/in^2
B4	2.56	$\times 10^4$ lbf/in^2

Thus, the stiffness range for the material is 5.59×10^{-4} to 0.78×10^{-4} ins/lb. It can therefore be seen that the proving ring used for unconfined compression loading had a stiffness of the same order of magnitude as the prismatic specimens tested. Clearly, the machine must be considered 'soft'. The important difference to rock testing was that the amount of strain energy stored in the machine was extremely small; thus, at the point of peak material strength the strain energy was released much less explosively, so that in most cases a fair amount of the descending portion of the load-deformation curve could be followed quite easily.

With the system of loading through proving rings, actual loading rates depended on the relative stiffness of the specimen under test, and the proving ring applying the lead. A specimen of equal stiffness to the proving ring would be loaded at half the jack advance rates given below:-

Unconfined compression) Brazilian disc)	0.0064 ins/min
Triaxial test	0.0051 ins/min.

APPENDIX 3

4.3 THE SYSTEMATIC PRODUCTION OF MODEL JOINT SETS

Certain design features of the large guillotine will be summarized before going on to consider the sequence of operations required to produce jointed slabs of the model materials.

4.3.1 DESIGN FEATURES OF THE LARGE GUILLOTINE

The requirements of a system for generating uniform sets of tension fractures in model slabs of dimensions 16" x 16" x 1" can be summarized as follows:

1. Two long blades are required which strike the upper and lower surfaces of the slabs simultaneously. This ensures the most uniform distribution of tensile stresses, and consequently the most uniform and reproducible fractures.

2. The blades must travel in the same plane so that fractures are produced which are perpendicular to the slab faces. In addition the blades must move parallel to one another, so that the slabs are penetrated to a uniform depth everywhere.

3. The depth of penetration must be controlled so that the excess momentum of the blades does not force the fracture open, after generating the crack.

4. The slab of model material must be capable of perpendicular movement relative to the blades, so that a set of parallel tension fractures can be generated from one edge or corner of the slab to the other.

Figure 4.3.1 shows end and side views of the guillotine that was finally developed. Letters (aa) and (bb) represent the upper and lower blades. These travel towards each other down the same machined slot, on ball race roller bearings: (cc) and (dd). The depth of penetration is controlled by two adiprene rubber pads (ee) fixed to the ends of the upper blade. These make contact with corresponding steel pegs at each end of the lower blade, just at the point of crack propagation. Penetration of the blades is thereby limited to approximately .020 inch, by which time the excess momentum of both blades has been adsorbed.

The electric motor, which drives the blades through a worn reduction gear (j) and a series of pulleys, causes the blades to move at approximately 5 inches/sec. Each blade weighs approximately 25 lbf. and the combined momentum is more than sufficient to generate corner to corner fractures (23 inches) in the slabs of model material.

The operation was made semi-automatic by a relay switching system (k) linked to two limit micro-switches (m). The sequence of events was as follows:

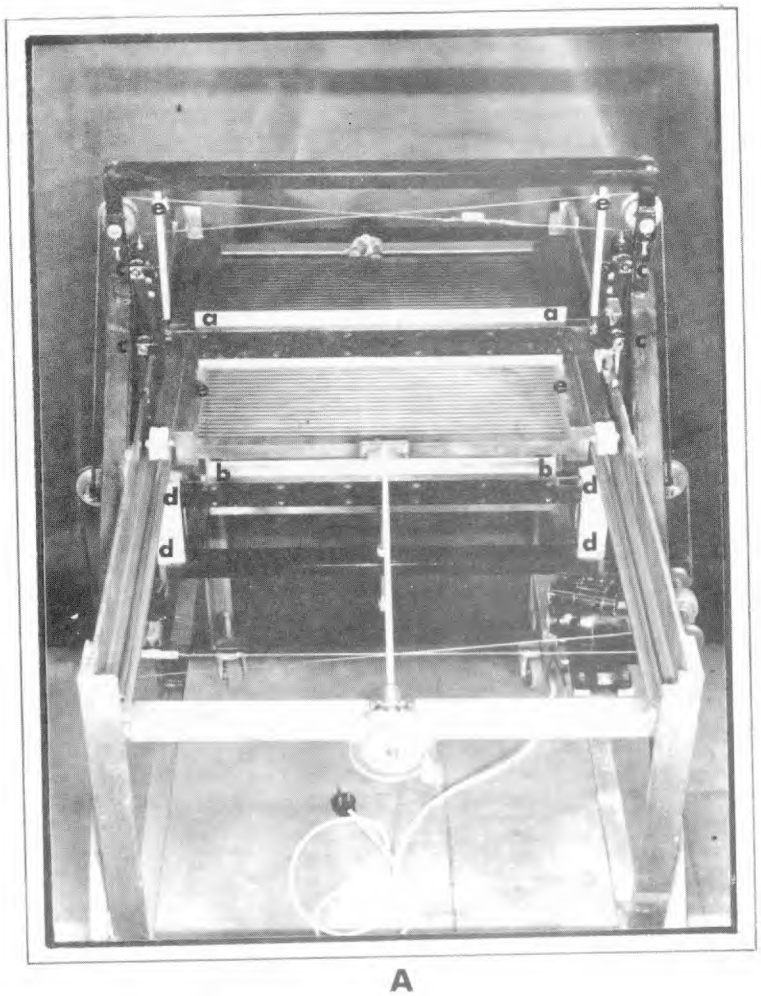

A

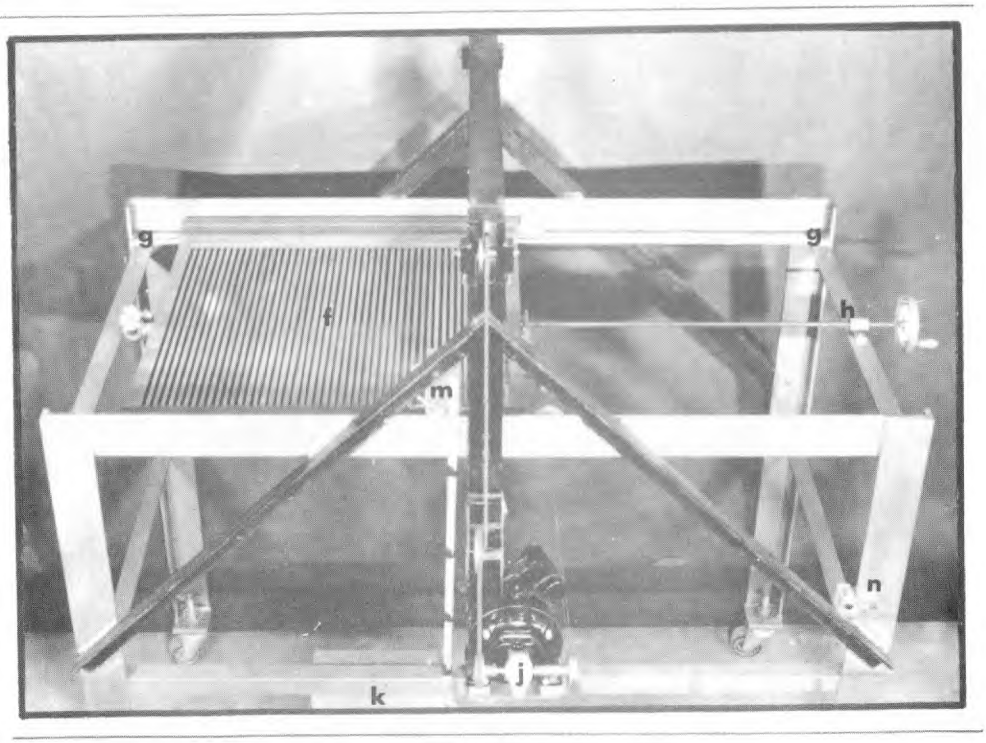

B

Figure 4.3.1 Design features of the large guillotine

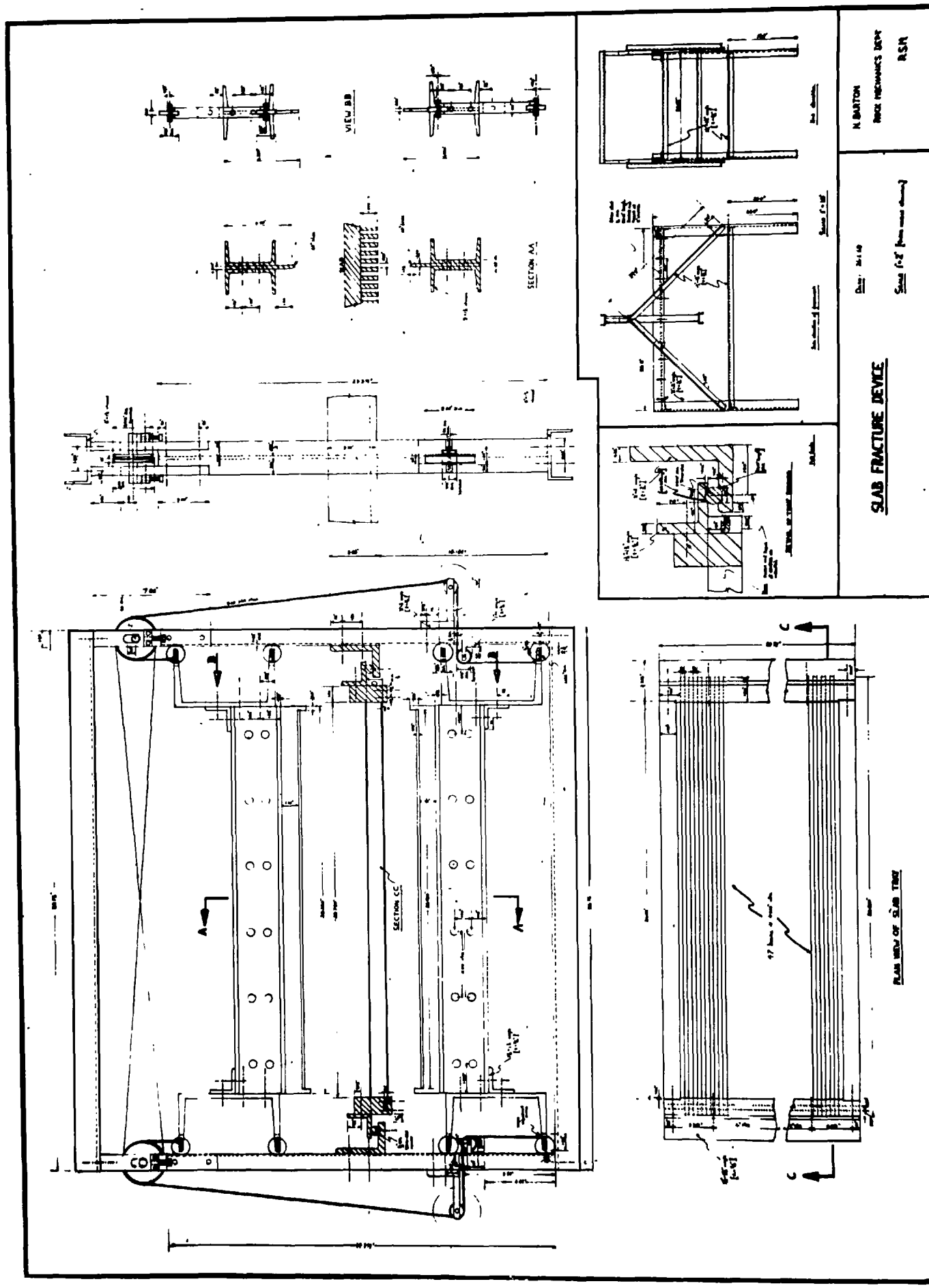

Figure 4.3.1 (C) Design drawings of Large guillotine.

1. Press button (n). Electric motor switched on.
2. Blades driven towards each other, causing contact break with uppermost micro-switch.
3. Blades strike slab simultaneously, and switch lower micro switch to the off position. Electric motor switched off, and momentum of blades destroyed by adiprene pads.
4. Time delay relay reverses motor, blades are driven back to start position where upper micro-switch completes the cycle of events. The momentum of the blades at the end of the cycle is again adsorbed by rubber pads.

The slab of model material which is placed on the slotted tray (f) can be moved perpendicularly to the blades by a screw feed (h). Ten turns moves the slotted tray exactly $\frac{1}{2}$ inch along the runners (g g), so that the lower blade travels up the centre of the adjacent slot, when the next fracture is generated.

A feature of the design which caused the manufacturers considerable problems was the runners (gg). These had to be parallel on each side of the frame, absolutely flat, and perpendicular to the plane of movement of the blades. Variations in blade penetration of little more than ± .005 inch could be tolerated, when generating fractures along the length of any slab. This point also emphasises the need for accurate moulds. A uniform slab thickness of 1.000 ± 0.005 inch was required as a minimum.

4.3.2 SLAB CASTING

One of the most difficult operations of the entire production sequence was the casting of slabs. The preliminary operations of material mixing, pouring and vibrating to remove bubbles presented no problem. However, stripping the mould and removing the model slab without fracturing it was extremely difficult, and unlike most operations it never became entirely routine. Many slabs were rejected for this reason. The problem can best be explained by quoting the tensile strength of the model material which was used for all the jointed models: (C3) σ_t = 2.44 lbf/in^2.

The following list summarizes the operations which were required to optimize the chances of recovering an unfractured slab from the mould:

1. The constituent materials had to be accurately weighed before mixing, so that the volume of water was never large enough to cause 'bleeding' and never small enough to cause premature setting during pouring. Approximately 2% change in the water content, or a few degrees change in ambient temperature was sufficient to cause these problems.

2. A minimum of approximately 30 minutes setting time was required before attempting to strip the mould.

3. The cohesive bond between the top face of the mould and the top face of the slab had to be broken by rotating the mould face across the slab.

4. The same operation was required to break the cohesive bond across the lower face of the slab.

5. If the water content and temperature were correct these cohesive (suction) bonds were minimal, and the slab could then be slid off the mould onto a flat perspex tray with edge supports.

It was possible to produce approximately one slab every hour when all conditions were optimal. The slabs were cured in the large oven (See Figure 4.1.4) for approximately three days.

4.3.3. SYSTEMATIC PRODUCTION OF JOINTED SLABS

All the components required for the production of jointed slabs are shown in Figure 4.3.2. The slabs were removed from the oven after curing and left to cool on sheets of plate glass insulated with $\frac{1}{2}$ inch asbestos board. When cold, a 1 inch strip of P.V.C. tape was gently fixed round the edge of each slab. This reduced the amount of damage that could occur to the edges when a slab was highly jointed. The slab was then inverted onto the perspex tray shown in diagram (F). This was an indispensable piece of equipment since the slabs could not be directly handled either when jointed or completely unjointed. All handling was performed by a process of invertion, taking care that the two edges of the perspex tray were supportive, rather than redundant. Six sequences can be summarized as follows:

1. Diagram A. The unjointed slab is carefully clamped between the perspex tray and the slotted tray of the guillotine, while in a vertical position. The supporting crutch shown in the diagram holds the slab in the correct position for generating a set of parallel joints inclined at 66° / 24° to the slab edges.

   The assembly is then hoisted into a horizontal position on the runners of the guillotine, and the perspex tray is removed by unscrewing the2 BA nuts and bolts which pass through the slots of the guillotine tray. The position of the slab is checked, and then one complete set of parallel fractures is generated with $\frac{1}{2}$ inch spacing.

2. The perspex tray is replaced, and the singly jointed slab is reclamped to the slotted tray. This assembly is hoisted off the runners and lowered to the floor in a vertical position. The slab and perspex tray are unclamped and removed to a horizontal surface. Diagram (B) shows an aluminium bar supporting the left hand edge of the slab. Thus three edges of the slab are supported in preparation for reclamping to the slotted tray for a set of 0° / 90° fractures.

   The sequence; hoisting, unclamping, fracturing, clamping, hoisting is repeated.

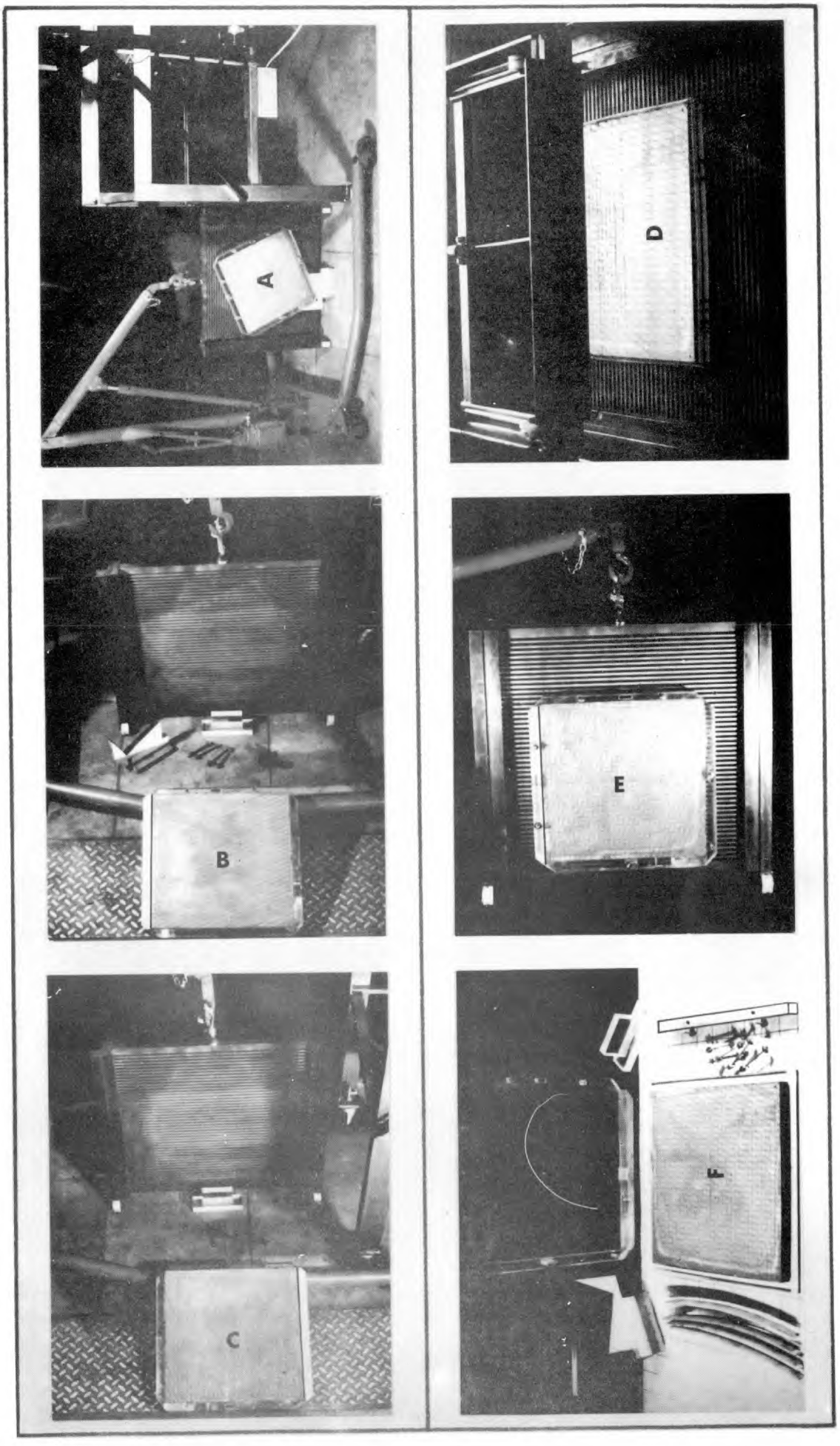

Figure 4.3.2 Six sequences in the production of a jointed model material

APPENDIX 3

3. Diagram (C) shows two joint sets generated. The aluminium bar is now fixed to the right hand edge of the slab, so that the correct three edges are supported before clamping in position for a second set of 0° / 90°

4. Diagram (D) shows the tertiary set of joints being developed on the guillotine. When completed, the perspex tray and aluminium bar are reclamped.

5. Diagram (E) shows the fully jointed assembly hanging from the hydraulic hoist.

6. Diagram (F) shows all the components used in the slab support proceedures. One set of components has so far been omitted. These are the curved perspex slats on the left hand side of the jointed slab. The convex side of these slats is covered with $\frac{1}{8}$" foam rubber strips. When a slab has been hoisted into position on the guillotine tray, the perspex tray is unclamped and removed. However before commencing the fracture routine, the four curved slats are interlocked round the edge of the slab, thus providing a reasonably uniform and gentle pressure round all four edges of the slab. After fracturing the slab they are removed temporarily, before being replaced for the next set of fractures.

This proceedure, combined with the P.V.C. tape proved to be a most useful method for reducing damage to the edges of the jointed slabs. The fracture process vibrates the slabs sufficiently to dislodge bricks round the edges, unless these supporting devices are employed.

One or two problems have been passed over in this brief summary of joint production. Attention can usefully be drawn to one of these. It was found that orthogonal joint sets developed parallel and perpendicular to the slab edges caused an increase in the dimensions of the slab of approximately 1%. In other words a slab of dimensions 16"x 16" x 1" when cast, became 16.15" x 16.15" x 1" when jointed symmetrically in two directions. The fracture spacing of $\frac{1}{2}$ inch. implies that 31 joints had a total width of 0.15 inch. In other words each fracture was approximately 0.005 inch wide when in this (almost) unstressed state. When designing jointed slabs to fit into fixed dimensions, this expansion must be allowed for, and the mould designed approximately 1% under-size.

In conclusion, it can be seen that the method of fracturing slabs provides a realistic simulation of ideally jointed rock masses. The primary set of joints are continuous with no offsets, and thus represent the dominant joint set that is frequently encountered in practice. The secondary and tertiary sets are not continuous, and are effectively offset where they cross the primary set, and each other. Consequently they are of minor importance where shear failure is concerned. Figures 3.1.1. and 3.1.14 in Section 3.1 illustrate the surface appearance of these three types of joint.

APPENDIX 3

A slab of model material measuring 16" x 16" x 1" can be split into three sets of joints in approximately one hour. In other words approximately 2000 discrete blocks can be generated in this time. Even allowing for the casting time, this is considerably faster then individual smooth bricks can be produced. More important, the 2000 blocks are already assembled, and no problem exists in obtaining identical sizes of bricks, so that they can be built to form continuous 'joints'.

APPENDIX 4

4.4. DESIGN FEATURES OF THE LARGE MODEL LOADING FRAME.

Design features of the loading frame and loading beam assembly will be described with reference to two reduced scale engineering drawings, which are reproduced in Figures 4.4.1 and 4.4.2. In addition, three photographs reproduced in Figure 4.4.3 will be used to illustrate the details of the loading beams, and the whole assembly.

4.4.1 RECTANGULAR LOADING FRAME (Figure 4.4.1)

The large rectangular frame, which was supported on bearings at each end (See Figure 4.4.3 D), was designed to support two plate glass walls of dimensions 8 feet by 4 feet by 1 inch, the jointed model also of dimensions 8 feet by 4 feet by 1 inch, and apply a reaction force for the loading beams at each end.

Section AA through one of the glass wall supports, illustrates the rubber strip which was used to regulate the clearance between the model and the glass walls. When unstressed the rubber spaced the glass at $1\frac{1}{8}$ inch. However when $\frac{1}{2}$" B.S.F. screws were tightened on all the glass supports, the space between the walls could be reduced to 1 inch, representing zero clearance with the sandwiched model. The all round clearance aimed for was approximately 0.040 inch. Apart from the function of regulating the glass clearance, the rubber pads were essential for preventing fracture of the front glass wall when this 450 lbf. sheet was lifted into position after construction of each model.

The rubber beds at the base of the glass walls are shown in Section BB. Unfortunately the clarity of this detailed section has been lost by the reduced size of the figure. However, the member marked X was a hardened (E.N.8) steel beam with a machined tongue. On each side of this tongue were V notches. The tongue slid inside a groove and was located centrally by $\frac{1}{8}$ inch diameter ball bearings. The model was supported on this hardened steel beem, and could in fact be translated to the left or right so that, after construction, it could be moved symmetrically to the glass walls. It also effected a regulation of the stress distribution along the vertical edges of the model, since any serious mismatching of the applied forces would result in the model moving to one end or the other, thereby tending to equalize the applied stresses. In direct line with this tongue and groove arrangement were 1 inch wide rectangular slots for the location of the loading beam rollers.

4.4.2 LOADING BEAM DESIGN (Figure 4.4.2)

The requirement of a triangular stress distribution, to simulate the increase in horizontal stress with depth below surface, meant that the loading beam design was unconventional to say the least. However, in addition to applying a triangular distribution of stress, it was decided that the loading system should be capable of storing strain energy (see Section 3.2) to represent the stiffness of an

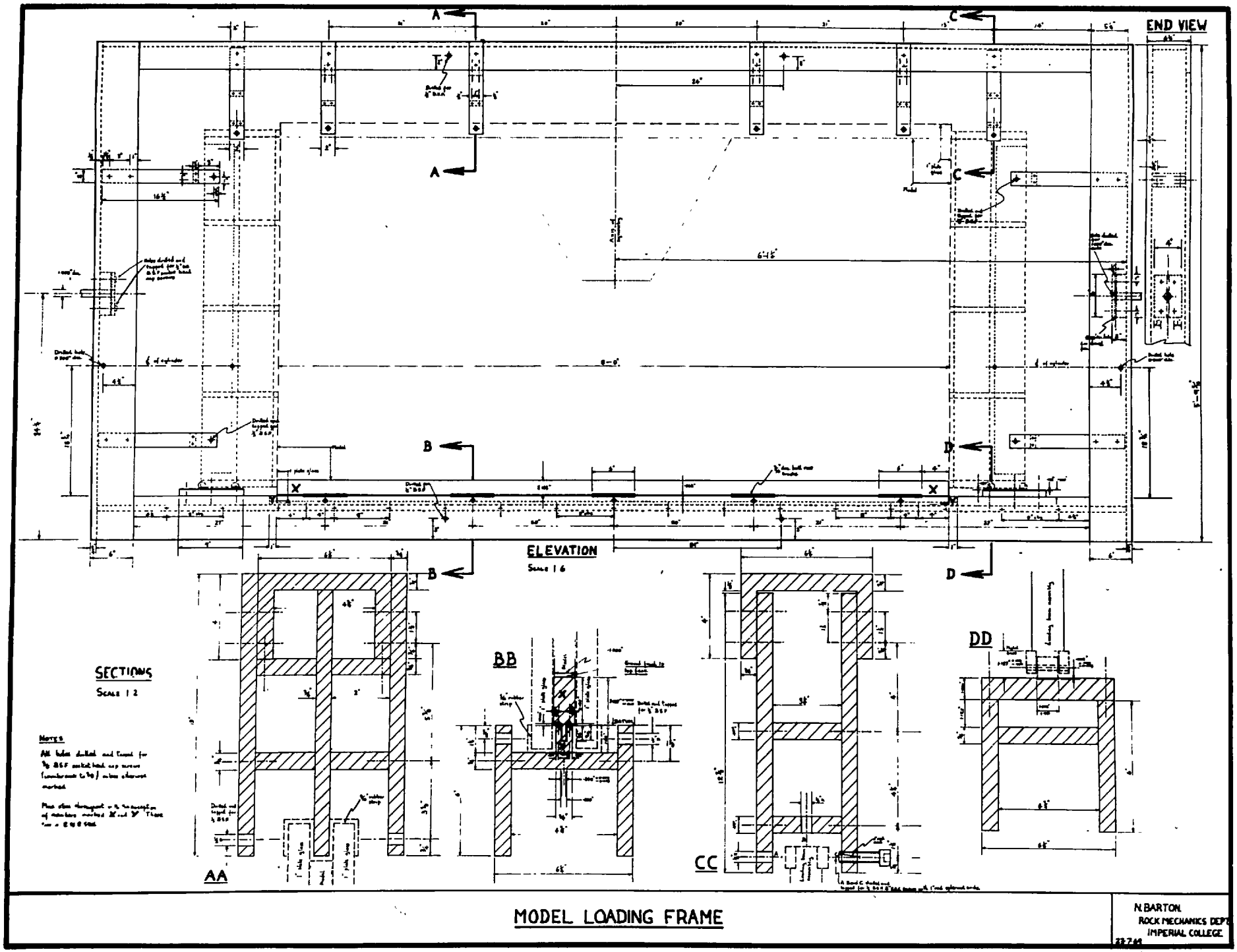

Figure 4.4.1 Design drawings of model loading frame.

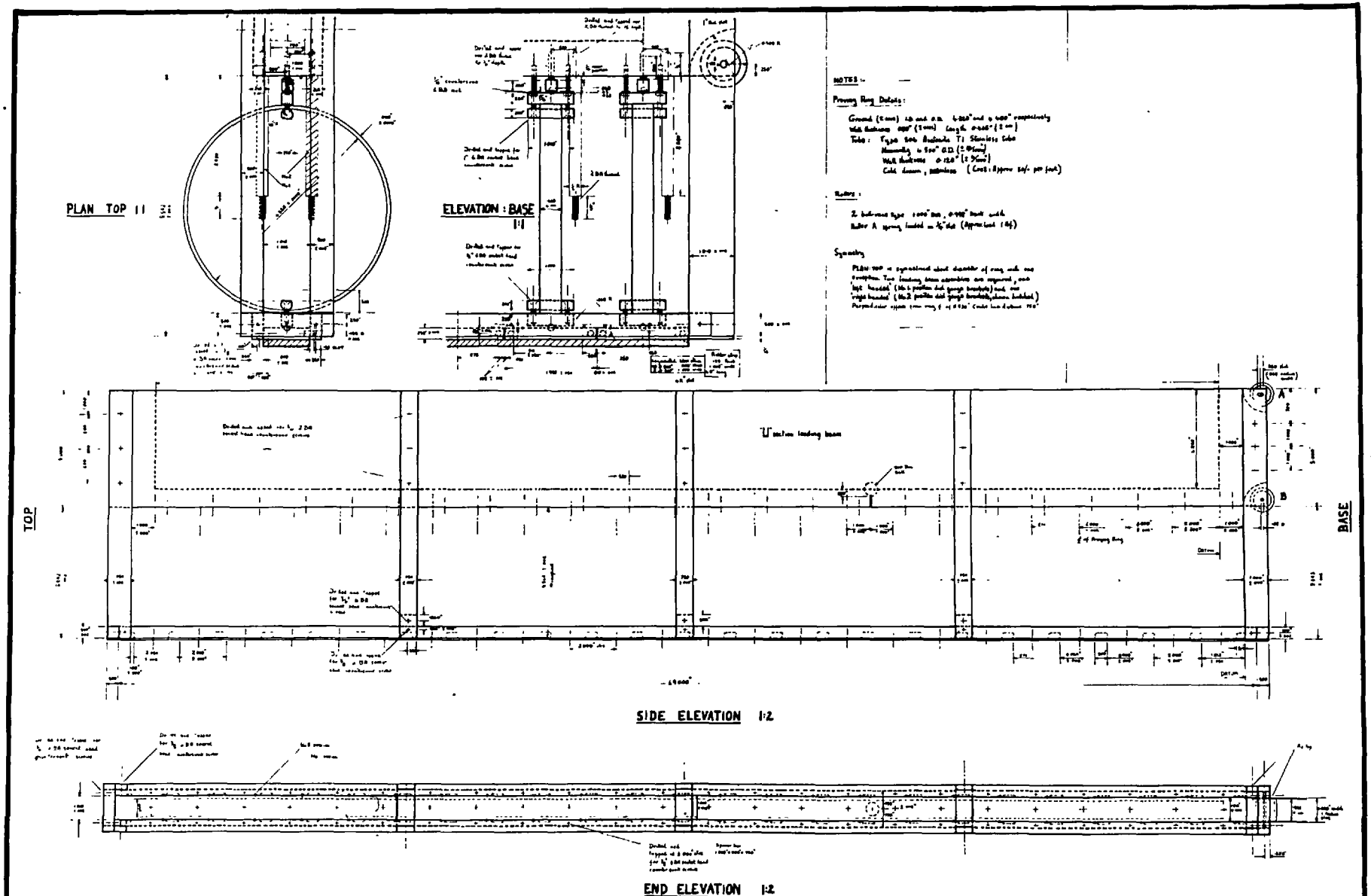

Figure 4.4.2 Design drawings of loading beam assembly.

additional slice of model jointed rock. These requirements will be dealt with separately:

1. Triangular distribution of stress

The side elevation shown in Figure 4.4.2., shows one of the deep 'U' section beams, which were designed for minimum weight and maximum stiffness. Each beam was loaded internally at the third point of its length, via a ball seating and hydraulic piston rod.

Each beam was located in a vertical position above a milled slot, by two roller bearings at its base. The central bearing marked B had a fixed axis of rotation, while the one marked A at the bottom edge of the beam was spring loaded. The dimensions of the beam were so designed that the whole beam pivotted about the bearing B (only one or two lbf. of counter-balance weight was required to achieve this). Thus the rear, spring loaded roller merely acted as a locating device ensuring that the beam moved in the plane of the model. (see Figure 4.4.3 A). The pivotting facility was required since when appling the triangular stress distribution:

a) the model was consolidated more at the base than at the top, which involved a small rotation of the loading beam.

b) the proving rings at the base were also deflected more than those at the top, again causing a small rotation of the beam.

Each beam was loaded at its third point internally in an effort to apply the load vertically above the pivot point, and as close to the edge of the model as possible. In this way, the rotation of the beams during loading caused the minimum misalignment of the applied forces with respect to the third points of the edges of the model.

As already stated, at the lower end of the loading beams alignment with the model was achieved by the two roller bearings, rolling(and sliding) in the machined slot. The performance of the beams was improved by inserting P.T.F.E. (Teflon) strips in an enlarged machined slot (see figure 4.4.3.C) The upper ends of the beams were positioned in the same vertical plane as the model by screwing or unscrewing P.T.F.E. faced $\frac{1}{2}$ inch diameter bolts which located onto each side of the beams.

During the loading and unloading cycles, when the whole frame was rotated between horizontal and vertical, these locating bolts were loosened slightly so that the beams could move unhindered. However, when the model was finally loaded the bolts (six to each loading beam, Figure 4.4.3 C) were screwed tightly against opposite sides of the beams to lock the stress distribution both in the bank of proving rings and in the model itself. Excavation of the model could then take place in a stressed environment of more or less known initial values.

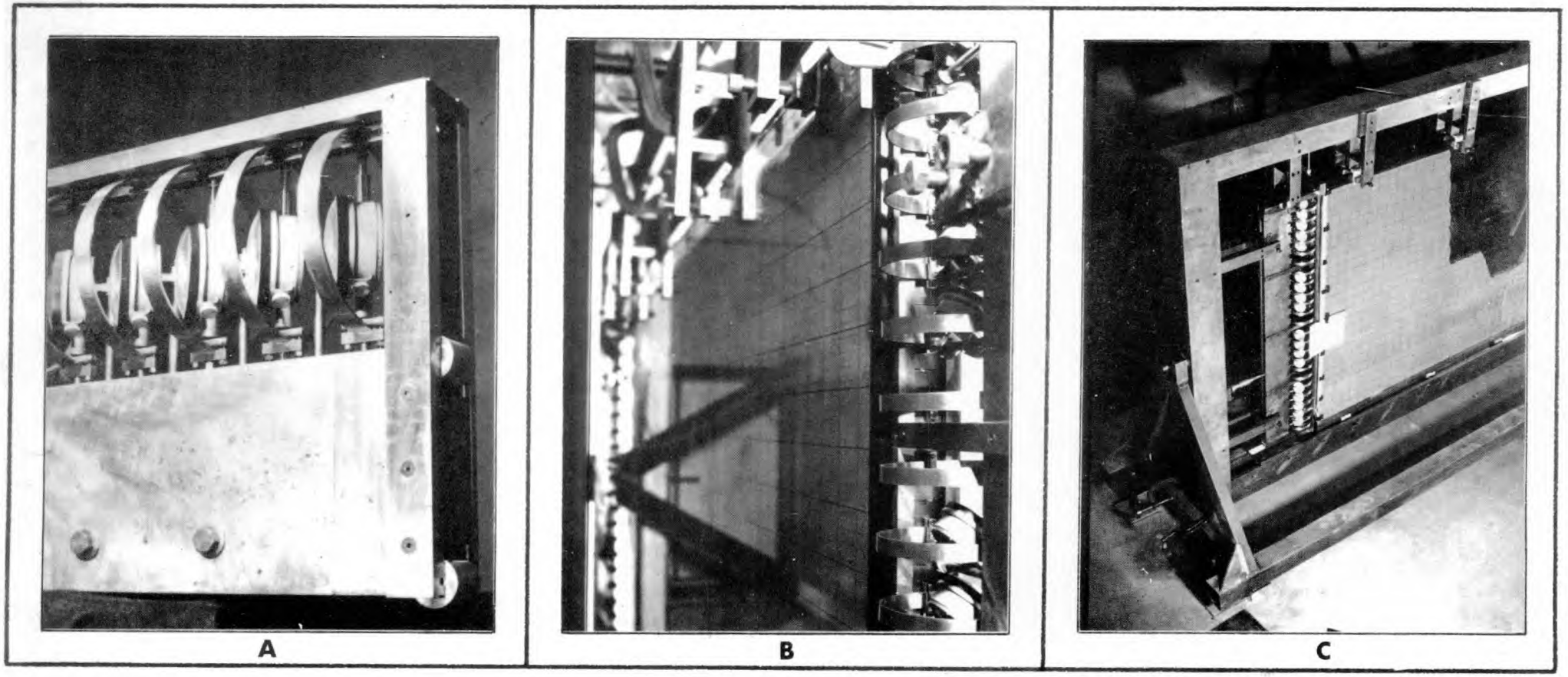

Figure 4.4.3: Detailed design features of the loading beams
and their assembly in the loading frame

2. Local distribution of stress

The two uppermost drawings of Figure 4.4.2, and Figure 4.4.3.A show the method of locating proving rings between the 'U' section beam and the individual 2 inch by 1 inch plattens. Dial gauges were fixed across the supports of each proving ring so that displacements of the rings occurred during loading, when the model was sufficiently consolidated to resist further displacements from the applied triangular stress distribution.

The individual plattens, which were designed to hang loosely from steel pegs located in machined slots on either side, transmitted resistance via centrally located ball bearings, to the diametral axis of each proving ring. Thus although the mean stress distribution was approximately triangular down the edges of the model, it could perhaps be more correctly described as step-triangular, since each platten (24 per beam) transmitted a theoretically rectangular distribution of stress.

It was realized that serious discontinuities of stress were likely to be caused unless steps were taken to distribute the load from the plattens themselves. This was done as follows. Strips of rubber 48 inches long, 1 inch wide (same as plattens) and $\frac{1}{8}$ inch thick were prepared with 0.005 inch thick pressure sensitive P.T.F.E. tape stuck to back and front. Each model was loaded through a minimum of three thicknesses of these laminated rubber strips, depending on the completed dimensions of the model. The rubber was a relatively hard one, but the P.T.F.E. lubricated laminations made the assembly extremely flexible.

As precaution against possible tensile stresses due to deformation of the rubber adjacent to the model, this outer face was covered with segments of accurately cut steel shim 1 inch wide, $\frac{1}{2}$ inch high and 0.005 inch thick. This layer was itself covered with a final 0.005 inch thickness of P.T.F.E. pressure sensitive tape, followed by a loose layer. There was therefore the minimum possible friction between the loading system and the edge of the model. The above precautions meant that the apparent stress distribution, as recorded from dial gauge readings of proving ring deformations, was probably considerably improved at the model face itself.

3. Loading beam simulation of stiffness

The theoretical reasons for favouring a loading system which has a capacity for storing strain energy, and releasing it according to a simple linear stress-displacement relation, have been presented in Section 3.2 The proving rings were designed to have a stiffness equivalent to a slice of model of dimensions 48 inches by 48 inches. This represented half the dimensions of the model. Thus, in a very crude manner the proving rings at each end of the model effectively doubled the amount of strain energy that could be stored. However since the mass E modulus was lower than the intact E modulus which was used in the design, the simulated slices were somewhat

less than half the model dimensions.

A) Force-displacement relation.

The stiffness of the proving rings was designed by assuming elastic isotropic properties for the model:

$$\text{thus} \quad \varepsilon = \frac{F/A}{E} , \quad d = \frac{FL}{2AE}$$

where ε = strain
F = force applied
A = area of application of force
E = Young's modulus
d = displacement at each end of model
L = length of model

Considering each individual platten of area $A = 2$ in^2, and the length of model $L = 96$ inches:

$$\text{then} \quad d = 24\ F/E \text{ inches} \qquad (1)$$

where F is the force on one platten applied by the strained proving ring, and resisted by the model material.

The rings were designed according to the E moduli of model materials C3 and A3.

$$\text{Average } E_{\text{intact}} = 0.9 \times 10^4 \text{ lbf/in}^2$$

Since the stiffness of the proving rings was chosen to equal the stiffness of an unjointed 48 inch by 48 inch slice of model material, the force-displacement characteristic required from the proving rings was as follows:

$$d/F = \frac{24}{0.9} \times 10^{-4} = 26.65 \times 10^{-4} \text{ ins/lbf} \qquad (2)$$

B) Range of loads

The required range of horizontal stresses capable of simulation in the model were calculated with respect to the density of the model material. It was decided that a range of horizontal stresses of from one third to three times the vertical weight stresses was sufficient:

$$\sigma_H = (\tfrac{1}{3} \longrightarrow 3)\,\sigma_v$$

ρ model = 121 lbf/ft^3
At 48 inch depth: $\sigma_v = \frac{121 \times 48}{144 \times 12} = 3.36$ lbf/in^2

Therefore the required range of horizontal stresses calculated for a 48 inches depth (zero at surface) were as follows:

Minimum σ_H = 1.120 lbf/in^2

Minimum σ_H = 10.08

This meant that the range of loads to be applied by the lowest proving rings (located at 47 inches depth) was approximately 2.24 to 20.16 lbf respectively. Therefore with the stiffness given by equation 2, the minimum and maximum displacements required of the lowest proving rings were 0.006 and 0.054 inch respectively.

C) Stress drop sensitivity.

During excavation of the models while under load, displacements occur at the boundaries, which result in a reduction in the applied stress. It was of interest to known what sensitivity could be achieved in monitoring these changes of stress during excavation.

The stiffness of the proving rings given by equation 2 was:

$$d/F = 0.002665 \text{ ins/lbf}$$

Using dial gauges of 0.0001 inch / division, each division was equivalent to 0.0375 lbf. Therefore for a platten of area 2 in^2., the stress change represented by 1 division was 0.0187 lbf/in^2. This model sensitivity could be converted to prototype sensitivity by multiplying by the stress scale (ψ) of 666. Thus a stress change of 12.5 lbf/in^2 in a prototype could be simulated by the model.

In fact the stress changes during excavation of the model were monitored to an estimated accuracy of better than $1/5$ th of a division. Thus it was possible to detect stress changes at the boundary of the model equivalent to about 2.5 lbf/in^2 in a prototype situation.

D) Design of proving ring dimensions.

The standard equations for design of proving rings, which have been experimentally verified by Hock[3] are as follows:

$$\Delta = 0.149 \frac{P r^3}{E.I.} \qquad (3)$$

$$(f)_{max.} = 0.318 \frac{P.r.y}{I} \qquad (4)$$

where E = Young's modulus for the ring material
Δ = radial deflection
P = load
r = radius of ring
I = moment of inertia for section (rectangular)
$(f)_{max.}$ = fibre stress
y = distance from neutral axis at which $(f)_{max.}$ occurs (= d/2)

Note: r = mean radius = $\frac{D - d}{2}$

$$I = {}^{1}/_{12} \cdot b d^3$$

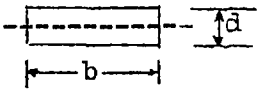

in this case:

$$\frac{r^3}{bd^3} = \frac{26.65 \times 10^{-4} \times 30 \times 10^6}{0.149 \times 12} = 4.475 \times 10^{-4} \ (\text{in}^{-1}) \qquad (5)$$

The dimensions (r) and (d) of the ring were chosen so that the rings would conveniently fit in the loading beam frames and produce a ring width (b) which was small enough to allow the dial gauges to be read with ease (Note that the dial gauges were all turned at 45° to facilitate this; see Figure 4.4.3 A)

The following dimensions were chosen:

O.D 4.480 inches
I.D. 4.320 inches [mean radius] = 2.200 inches
wall thickness (d) = 0.080 inch

These dimensions represented a minimum of machining, when the following stainless steel tube was used:

Type 304 Austenitic T.I. (Tube Investments) stainless Standard tube. (.old drawn, seamless)
Nominally: 4.500 inches O.D (± 0.010 inch)
Wall thickness 0.120 (± 0.004 inch)

When the above dimensions were inserted into equation 5, the ring width (b) obtained was:

$$b = 0.465 \text{ inch}$$

Fibre stresses: $$(f)_{max} = \frac{0.318 \times 20.4 \times 2.2 \times 0.04 \times 12}{0.465 \times 0.08 \times 0.08 \times 0.08}$$

$$= \underline{28{,}800 \text{ lbf/in}^2}$$

(Yield point for steel = 47,100 lbf/in^2)
(Tensile strength = 96,300 lbf/in^2)

When the proving rings had been machined and ground, and assembled in the loading beam, a series of load-deformation checks were made. The mean values of eight random tests produced extremely consistent results which indicated that the stiffness achieved was:

$$d/F = 27.50 \times 10^{-4} \text{ inches/lbf.}$$

This was within 3.1% of the design value of 26.65×10^{-4} ins/lbf.

4.4.3 DEAD WEIGHT COMPENSATED LOADING SYSTEM

The two hydraulic cylinders used to apply the third point loads to the loading beams had 1 inch diameter, 1 inch stoke pistons. (Martonair Ltd). They were originally designed for accurate position control mechanisms. These had the lowest piston friction that could be obtained, consistent with sealing effeciently up to the maximum expected load of approximately 240 lbf/in^2. A very low vicosity hydraulic fluid (Shell Tellus 13) was used to improve this quality.

As already explained in Section 3.2 the loading of the model had to be carried out at a uniform rate, so that while the loading beams were applying a linearly increasing (or decreasing) load, the whole frame was being rotated at a rate approximating a linear increase (or decrease) of sine (α), where α was the angle of tilt of the model. In this way the principle stresses σ_H (horizontal) and σ_V (gravity) were increased to their final values in a fixed ratio.

The maximum load to be applied to the loading beams was approximately 250 lbf ($\sigma_H = 3\sigma_V$) and the minimum load only 28 lbf ($\sigma_H = \frac{1}{3}\sigma_V$). Therefore to achieve a uniform increase of load from zero to less than 30 lbf, required an extremely finely controlled 'Amsler Valve' or similar device.

It was decided that the simplest system would be a dead weight loading device in which a graduated tank was filled with water at a constant rate from a constant head supply. The increasing weight of this tank acted as the pressurizing force acting on a third piston held in a vertical plane. This single piston supplied the hydraulic pressure to both the loading beam pistons, which were connected to the latter via equal lengths of nylon tube, so that the response of both sides would be the same.

One problem had to be overcome. The perspex tank used to hold up to 250 lbf. of water had a dead weight of approximately 30 lbf. Pressures increasing from zero could only be applied if the self weight of the tank was supported by a spring. However, during loading of the model, each beam moved towards the model due to consolidation and proving ring deformation. This effective increase in hydraulic volume resulted in the longer stroke vertically mounted piston moving downwards under the weight of the filling tank. Paradoxically, the spring supporting the self weight of the tank was now stretched further and applied an upward force greater than the self weight of the tank.

APPENDIX 4

This problem was overcome by a marker device fixed across the length of the spring. The marker was set when the spring was supporting the empty weight of the tank. During filling of the tank the spring was kept at a constant length, by screwing a stretcher device. The rate of increase of hydraulic pressure was then purely a function of the rate of water flow from the constant head supply. The maximum load($\sigma_H = 3\sigma_v$) was applied in about 5 minutes, with the given water supply. During this period the whole frame was rotated at an approximately linear rate of increase of Sin α, the angle of tilt.

APPENDIX 5

4.5 THE CONSTRUCTION OF LARGE JOINTED MODELS.

Appendix 3 contained a summary of the sequence of operations required to produce jointed slabs of model material. One problem which was referred to then, and concerns the present model construction, was the expansion of slab dimensions due to the finite width of the fractures generated through them. It was found that by suitably reducing the mould size, jointed slabs could be produced to the required final dimensions.

4.5.1 JOINT CONTINUITY BETWEEN SLABS

The large models were constructed from three rows of six slabs. Each of the slabs was approximately 16 inches by 16 inches by 1 inch, making a total size of 8 feet by 4 feet. Obviously uniformly sized slabs were required. However in addition to this, each set of fractures had to be continuous across slab boundaries, so that one fracture at one corner of the model could be traced across several slab interfaces in a continuous line. Only then would the vertical and horizontal boundaries of slabs effect the total shear performance to a minimum degree. There was no practical solution to the effective offsetting of apparently continuous joint lines, when crossing the (primary) slab boundaries.

The two diagrams below, illustrate the two joint systems that were used in the large models. The one on the left illustrates two requirements:

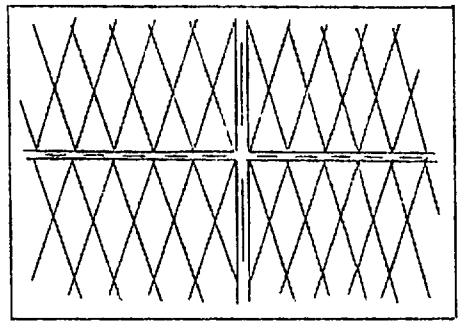

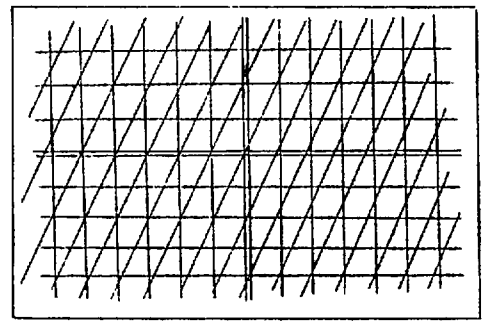

1. Continuity of all joints across slab boundaries.

2. Intersection of both joint sets at the slab boundaries so that half bricks were created along the slab edges, which mated exactly with opposite halves on the edges of adjacent slabs.

The half bricks illustrated in the left hand diagram were cemented together to remove the structural defect of smooth horizontal and vertical slab edges. Clear 'Bostic' adhesive was painted between joint intersections, so that no joints would be affected.

The diagram on the right illustrates only the one problem of continuity. The horizontal and vertical fractures were convenient

in that the slab boundaries then merely represented additional joints in a given set, though with reduced frictional properties.

The fixed dimensions of the 1 inch thick glass supporting walls, and the given loading system, required a completed model dimension of 8 feet by 4 feet with tolerances of approximately $\pm \frac{1}{2}$ and $\pm \frac{1}{4}$ inch respectively. Therefore if the model was to be constructed from 16 inch by 16 inch slabs, the tolerances on these dimensions needed to be better then $\pm$ 0.1 inch. In other words the slab dimensions were more or less fixed.

It will be appreciated that the two diagrams of jointing implied a whole number of half bricks or cross joints per slab edge of 16 $\pm$ 0.1 inches. In addition, the guillotine produced a fixed joint spacing of $\frac{1}{2}$ inch. (This could of course be increased to multiples of $\frac{1}{2}$ inch if desired). These two 'constants' meant that the possible angles of intersections of the joints with each other, or with the edges of the slabs was limited to those producing whole numbers of intersections. The figure below illustrates the general case, which is then modified to the case with $\frac{1}{2}$ inch spacing for each set.

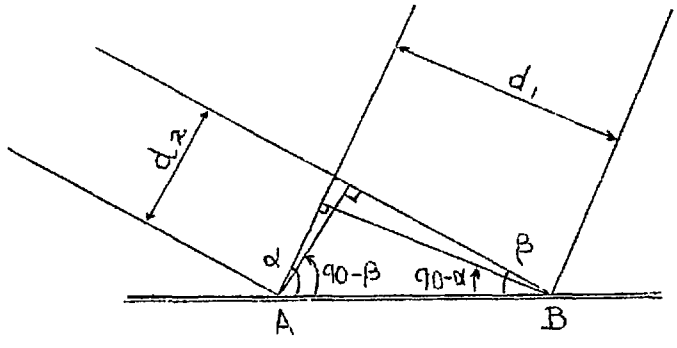

$$\text{Slab edge intercept AB} = \frac{d_1}{\cos(90-\alpha)} = \frac{d_2}{\cos(90-\beta)}$$

where d_1 and d_2 are the two joint spacings.
In the present case:

$$d_1 = d_2 = \tfrac{1}{2} \text{ inch}$$
$$\therefore \alpha = \beta = \theta \text{ (say)}$$

$$\text{i.e. } AB = \frac{1}{2\cos(90-\theta)}$$

The angles θ and $(90-\theta)$ had to be chosen to satisfy the following:

n. AB = 16 $\pm$ 0.1 inch.
where n = whole number.

This condition limited possible angles of intersection (with respect to slab edges) to approximately:

58° / 32° , 62°/ 28°, 66°/ 24°, 70°/ 20°,

in the range of dips consistent with possible shear failure of a slope intersected by joints with these inclinations. (See Section 3.2)

4.5.2 CONSTRUCTION SEQUENCES FOR MULTI-SLAB MODELS

The sequence of operations is most easily communicated by reference to a series of photographs taken during construction of the final large model to be tested. Figures 4.5.1 (A to F) and 4.5.2 (G to J) show the stages involved:

A. The large loading frame is tilted to within about 10° of vertical so that slabs will lie on the rear plate glass wall without toppling forward. A line of mating slabs is already in position, with the left hand vertical edge supported rigidily by a straight edge clamped over the full height of the completed model. The next slab is inverted from its $\frac{1}{2}$ inch plate glass tray, into the perspex support tray. (This was described in Appendix 3). An aluminium bar is screwed into position on one side of the tray so that three edges and one face of the slab is supported. The slab and tray are then lifted in a sub-vertical position onto the loading frame, and firmly rotated through vertical so that the unsupported rear face of the slab comes into contact with the glass wall which supports the back of the model.

The large frame is then rotated into a horizontal plane, by which time the perspex support tray and the perpendicular straight edge can be safely removed.

B. The P.V.C. tape surrounding the edges of the slab is carefully cut, and even more carefully removed. It should be noted that this tape is two thicknesses, with the adhesive inside. One thickness of tape with the adhesive outside will tend to stick to the perspex walls of the tray. One thickness with the adhesive inside will remove the entire outside edge of the slab brick by brick, when the tape is removed.

C. It is at this stage that adhesives should be applied with a set square, after brushing away the small pieces of material that are inevitably dislodged when the tape is removed.

D. Note the axis of symmetry at the centre of the model. The jointing was designed so that the steeply dipping set of joints (primary) dipped into any symmetrical excavation on both sides. This involved turning half the eighteen slabs back to front, if the same guillotine proceedures were used throughout.

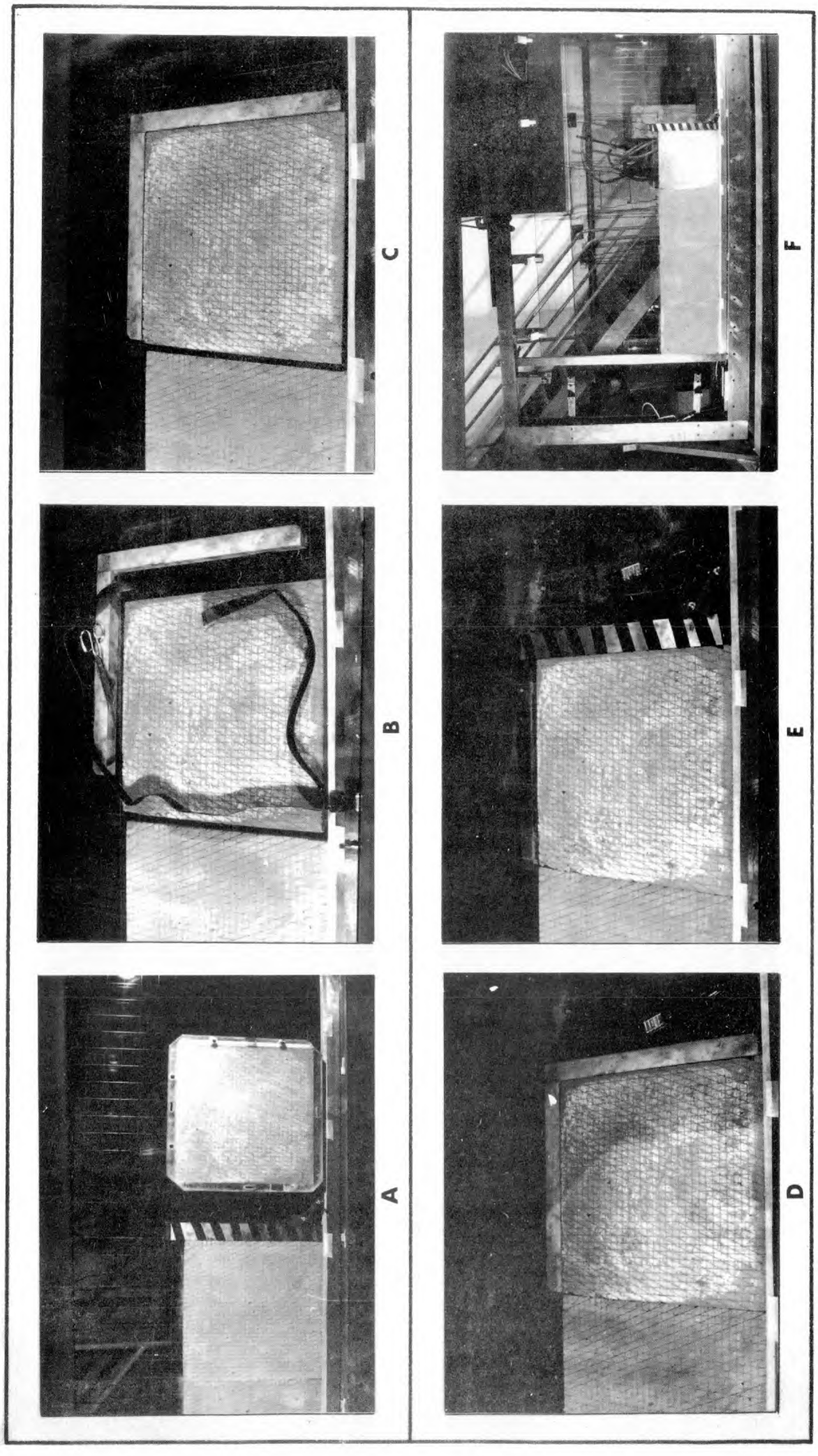

Figure 4.5.1: Six sequence photographs of the construction procedures for building the large model

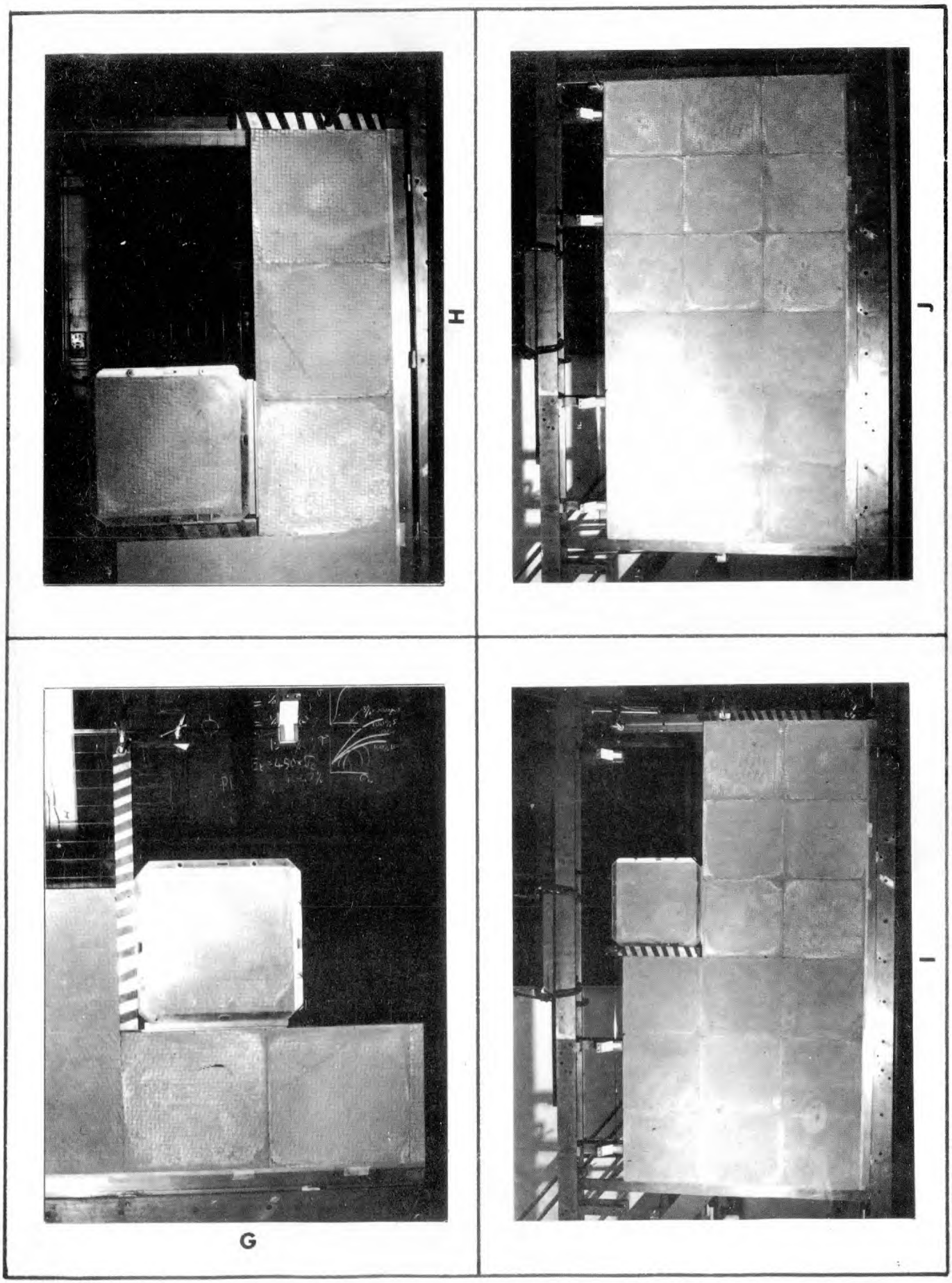

Figure 4.5.2: The final stages of model construction

E. A 16 inch straight edge is clamped against the edge of the slab while the frame is still horizontal.

F. The frame can then be rotated back to within about 10° of vertical. Note the steel beam at the left hand edge of the slabs. This is clamped in position throughout the construction, so that slabs line up correctly and are supported when the frame is rotated. The right hand edge has to be supported in stages as will be seen.

Figure 4.5.2 shows the remaining sequences of clamping operations that have to be employed to ensure the stability of all unsupported slab edges.

G. This shows an L shaped clamp fixed to the top of the glass wall, to support the edge of one of the second row slabs.

H. The end slab of the bottom row also has to be supported while the second row is being built up. Note that this end clamp is fixed to a wooden recessed beam, The front face of this is flush with the glass and acts as an extension to the glass wall for the placing of the extreme right hand edge slabs.

I. The 32 inch and 16 inch straight edges are reversed in position when the second row is completed.

J. The completed model is supported at both ends by rigid, steel straight edges. The model is rotated from horizontal to a few degrees from vertical and allowed to consolidate under its own row uniformly distributed weight.

It should be noted that the above proceedures represented a collection of extremely non uniform 'loading histories'. For this reason loading and unloading cycles were religiously performed before finally stressing a model for testing. (See Section 3.2). It was hoped that this would help to 'imprint' a joint consolidation pattern (stress history) of a uniform nature.

The last two stages of model construction consisted of lifting the 450 lbf, 1 inch thick glass wall into position on rubber pads in front of the model, while the model was horizontal. The glass could be uniformly translated towards or away from the model until an all round clearance of approximately 0.040 inch had been achieved. Finally the two loading beams were substituted in place of the straight edges. The loading frame had then to be kept horizontal, until the beams were loaded at the third points to apply a triangular stress distribution simultaneously with the model rotation.

REFERENCES

REFERENCES

1. Langhaar, H.L. DIMENSIONAL ANALYSIS AND THEORY OF MODELS. J. Wiley and Sons., New York 1951.

2. Hoek, E. THE DESIGN OF A CENTRIFUGE FOR THE SIMULATION OF GRAVITATIONAL FORCE FIELDS IN MINE MODELS. Journal South African Inst. Min. and Met. April 1965 pp. 455-487.

3. Fumagalli, E. MODEL SIMULATION OF ROCK MECHANICS PROBLEMS. Rock Mechanics in Engineering Practice. Eds. Stagg and Zienkiewicz. J. Wiley and Sons. Ch. 11, 1968.

4. Hobbs, D.W. SCALE MODEL STUDIES OF STRATA MOVEMENT AROUND MINE ROADWAYS. Apparatus, technique and some preliminary results. Int. J. Rock Mech. Min. Sci. Vol.3 pp. 101-127 1966.

5. Ergun, I. STABILITY OF UNDERGROUND OPENINGS IN JOINTED ROCK. Ph.D. Thesis. 1970 Royal School of Mines, Imperial College London.

6. Evans, I. and Pomeroy, C.D. THE STRENGTH OF CUBES OF COAL IN UNIAXIAL COMPRESSION. The mechanical properties of non-metallic brittle materials. Butterworths, London (1958) pp. 5-25.

7. Bieniawski, Z.T. THE EFFECT OF SPECIMEN SIZE ON COMPRESSIVE STRENGTH OF COAL. Int. J. Rock Mech. Min. Sci. 5 pp. 325-335 (1968).

8. Deere, D.U. GEOLOGIC CONSIDERATIONS. Rock Mechanics in Engineering Practice. Eds. Stagg and Ziewkiewicz. J. Wiley and Sons. Ch.1. 1968.

9. Krsmanovic, D. INITIAL AND RESIDUAL SHEAR STRENGTH OF HARD ROCKS. Geotechnique XVII No.2 June 1967. pp. 145-160.

10. Krsmanovic, D. Tufo, M. Langof, Z. SHEAR STRENGTH OF ROCK MASSES AND POSSIBILITIES OF ITS REPRODUCTION ON MODELS. Int. Rock Mech. Conf. Lisbon 1966 Paper 3.52. pp. 537-542.

11. Stimpson, B. MODELLING MATERIALS FOR ENGINEERING ROCK MECHANICS. Int. Rock Mech. Min. Sci. Vol.7 pp. 77-121. 1970.

12. Hobbs, D.W. THE BEHAVIOUR AND SIMULATION OF SEDIMENTARY ROCKS. National Coal Board Pub. Mining Research Establishment, Middlesex. 1966.

13. Raphael, J.M. PROPERTIES OF PLASTER-CELITE MIXTURES FOR MODELS. Symp. on concrete dam models. Lisbon, Paper 15 1963.

14. Jaeger, J.C. BRITTLE FRACTURE OF ROCKS. Failure and breakage of rocks. Ed. Fairhurst. Proc. 8th Symp. on Rock Mech. Ch. 1, 1967.

15. Hoek, E. BRITTLE FAILURE OF ROCK. Rock Mechanics in Engineering Practice. Eds. Stagg and Zienkiewicz. J. Wiley and Sons. Ch. 4, 1968.

REFERENCES

16. Franklin, J.A. A STRENGTH CRITERION FOR ROCK. Imperial College. Rock.Mech. Res. Report. No.6 1968.

17. Morgenstern, N.R. and Tamuly Phukan, A.L. NON-LINEAR DEFORMATION OF A SANDSTONE. Proc. of Ist. Cong. Int. Soc. Rock Mech. Lisbon, Vol. I, pp. 543-548, 1966.

18. Ladanyi, B. and Archambault, G. SIMULATION OF SHEAR BEHAVIOUR OF A JOINTED ROCK MASS. Pre-print. 11th Symp. on Rock Mech. Berkeley pp. 1-31 1969.

19. Krsmanovic, D. and Tufo, M. and Langof, Z. SHEAR STRENGTH OF ROCK MASSES AND POSSIBILITIES OF ITS REPRODUCTION ON MODELS. Proc. Ist. long. Int. Soc. for Rock Mech. Lisbon 3.52 pp 537-542. 1966.

20. Patton, F.D. MULTIPLE MODES OF SHEAR FAILURE IN ROCK AND RELATED MATERIALS. Univ. of Illinois. Ph.D. Thesis 1966.

21. Jaeger, J.C. THE FRICTIONAL PROPERTIES OF JOINTS IN ROCK. Geofisica Pura e Applicata. Milano Vol.43 pp. 148-158 1959.

22. Rosengren, K.J. ROCK MECHANICS OF THE BLACK STAR OPEN CUT, MOUNT ISA. Ph.D Thesis. Aust. Nat. Univ. 1968.

23. Menel, V. DILATENCY OF ROCKS. Felsmechanik (Rock Mechanics) Vol. III/2 pp. 58-61 1965.

24. Price, N.J. FAULT AND JOINT DEVELOPMENT IN BRITTLE AND SEMI-BRITTLE ROCK. Pergamon Press. 1966.

25. Rosengren, K.J. and Jaeger, J.C. THE MECHANICAL PROPERTIES OF AN INTERLOCKED LOW POROSITY AGGREGATE. Geotechnique XVIII No.3 pp 317-326. 1968.

26. Jaeger, J.C. THE BEHAVIOUR OF CLOSELY JOINTED ROCK. 11th. Rock Mech. Symp. Berkeley. 1969.

27. Pentz, D.L. PRIVATE COMMUNICATION. Rock Mechanics Dept. Imperial College 1969.

28. Goodman, R.E. Taylor, R.L. and Brekke, T.L. A MODEL FOR THE MECHANICS OF JOINTED ROCK. Proc. ASCE Vol. 94. S.M. 3 pp 637-659 1968.

29. Ruiz, M.D. Camargo, F.P. Midea, N.F. and Nieble, C.M. SOME CONSIDERATIONS REGARDING THE SHEAR STRENGTH OF ROCK MASSES. Int. Symp. Rock Mech. II.5 pp 159-169 Madrid. Oct. 1968.

30. Krsmanovic, D. and Popovic, M. LARGE SCALE FIELD TESTS OF THE SHEAR STRENGTH OF LIMESTONE. Int. Rock. Mech. Cong. Paper 3.90 Lisbon 1966.

31. Seraphim, J.L. and Guerreiro, M. SHEAR STRENGTH OF ROCK MASSES AT THREE SPANISH DAM SITES. Int. Symp. Rock Mech. II.4 pp. 147-157 Mardrid Oct. 1968.

32. Goodman, R.E. THE DEFORMABILITY OF JOINTS. Determination of the in-situ modulus of deformation of rock. A.S.T.M. S.T.P. 477 1970 pp 174-196.

REFERENCES

33. Kutter, H. PRIVATE COMMUNICATION. Rock Mechanics Dept. Imperial College.

34. Pentz, D.L. PRIVATE COMMUNICATION. Rock Mechanics. Imperial College 1967.

35. Hoek, E. and Pentz, D.L. THE STABILITY OF OPEN PIT MINES. Imperial College Rock Mechanics Res. Rept. No.5 Feb. 1968.

36. Nose, M. ROCK TEST IN-SITU, CONVENTIONAL TESTS ON ROCK PROPERTIES AND DESIGN OF KUROBEGAWA No. 4. DAM BASED THEREON. 8th I.C.O.L.D. Edinburgh Vol. I pp. 219-250 1964.

37. Seraphim, J.L. ROCK MECHANICS CONSIDERATIONS IN THE DESIGN OF CONCRETE DAMS. State of stress in the earth's crust. Santa Monica Conf. 1963.

38. Jimenez Salas, J.A. and Uriel, S. SOME ROCK MECHANICS TESTING IN SPAIN. 8th I.C.O.L.D. Edinburgh. Vol.I pp. 995-1021. 1964.

39. Rengers, N. INFLUENCE OF SURFACE ROUGHNESS ON THE FRICTION PROPERTIES OF ROCK PLANES. 2nd Int.Cong. Rock Mech. Belgrade. Paper 1.31 1970.

40. Louis, C. PRIVATE COMMUNICATION. Rock Mechanics Dept. Imperial College 1970.

41. Louis, C. A STUDY OF GROUNDWATER FLOW IN JOINTED ROCK AND ITS INFLUENCE ON THE STABILITY OR ROCK MASSES. Translation of Ph.D Thesis Karlsruhe 1967 (Imperial Coll. Rock Mech. Res. Rept. No.10 Sept. 1969).

42. Coon, R.F., and Merritt, A.H.. PREDICTING IN-SITU MODULUS OF DEFORMATION USING ROCK QUALITY INDEXES. DETERMINATION OF THE IN-SITU MODULUS OF DEFORMATION OF ROCK. ASTM. STP 477 1970 pp 154-173.

43. St. John, C.M. Ph.D. Thesis (in preparation) Rock Mech. Dept. Imperial Coll. London 1970.

44. Deere, D.U. Hendon, A.J. Jr., Patton, F.D. Cording, E.J. DESIGN OF SURFACE AND NEAR-SURFACE CONSTRUCTION IN ROCK. Failure and Breakage of Rock. Ed. Fairhurst. Eighth Symposium on rock mechanics. Ch. 11 pp. 237-302 1966.

45. Kennedy, B.A. Niermeyer, K.E. SLOPE MONITORING SYSTEMS USED IN THE PREDICTION OF A MAJOR SLOPE FAILURE AT THE CHUQUICAMATA MINE, CHILE. The theoretical Background and planning of Open Pit Mines with special reference to slope stability. Symp. S. Afr. Inst. Min. Metall. Johannesburg, Sept. 1970.

46. Newland, P.L. Alley, B.H. VOLUME CHANGES IN DRAINED TRIAXIAL TESTS ON GRANULAR MATERIALS. Geotechnique, 1957 Vol. No. 1 pp 17-34.

47. Rowe, P.W. Barden, L. Lee, I.K. ENERGY COMPONENTS DURING THE TRIAXIAL CELL AND DIRECT SHEAR TESTS. Geotechnique, 1964 Vol.14 No.3 pp.247-261

REFERENCES

48. Goldstein, M. Goosev, B. Pyrogovsky,N. Tulinov,R. Turovskaya, A. INVESTIGATION OF MECHANICAL PROPERTIES OF CRACKED ROCK. Proc. Ist. Cong. Int. Soc. Rock Mech. Lisbon 1966. Vol. 1. 521-529.

49. Ripley, C.F. Lee, K.L. SLIDING FRICTION TESTS ON SEDIMENTARY ROCK SPECIMENS. Int. Cong. Large Dams. 7th Rome. 1961 IV pp. 657-671.

50. Skempton, A.W. Bishop, A.W. MEASUREMENT OF SHEAR STRENGTH OF SOILS. Discussion by A.W. Bishop. Geotechnique 1950 Vol. 2. No. 2. p 113.

51. Withers, J.H. SLIDING RESISTANCE ALONG DISCONTINUITIES IN ROCK MASSES. Ph.D. Thesis University of Illinois 1964.

52. Ross Brown, D.M. Barton, N.R. ROCK MECHANICS CONSIDERATIONS AND THE STABILITY OF THE OPENCAST MINES AT RIO TINTO, SPAIN. Imperial Coll. Rock. Mech. Res. Rept. No.D7. Sept. 1969 pp. 1-81.

53. Maini, T. Ph.D Thesis (in preparation) Rock Mech. Dept. Imperial Coll. London, 1970.

54. Sharp, J.C. FLUID FLOW THROUGH FISSURED MEDIA. Ph.D. Thesis. University of London 1970.

55. De Freitas, M. PERSONAL COMMUNICATION. Eng. Geol. Dept. Imperial Coll. London. 1970.

56. Markland, J. PERSONAL COMMUNICATION. Rock. Mech. Dept. Imperial Coll. London 1970.

57. Cundall, P.A. PERSONAL COMMUNICATION Rock Mech. Dept. Imperial Coll. London 1970.

58. Walton, G. PERSONAL COMMUNICATION Rock Mech. Dept. Imperial Coll. London 1970.

59. Sharp, J.C. PERSONAL COMMUNICATION Rock Mech. Dept. Imperial Coll. London 1969.

60 Markland, J. PERSONAL COMMUNICATION Rock Mech. Dept. Imperial Coll. London 1970.

61. Skempton, A.W. and Hutchinson, J.N. STABILITY OF NATURAL SLOPES AND EMBANKMENT FOUNDATIONS. State of-the-art report. VII Int. Conf. Soil Mech. Found. Eng. Mexico 1969 pp. 291-340.

62. Wittke, W. A NUMERICAL METHOD OF CALCULATING THE STABILITY OF SLOPES IN ROCKS WITH SYSTEMS OF PLANE JOINTS. English translation Imperial College Rock Mech. Res. Rept. No.4 Sept. 1970. from original in German. (Rock Mech. and Eng. Geol. Suppl. I. 1964).

REFERENCES

63. Londe, P. Vigier, G. and Vormeringer, R. STABILITY OF ROCK SLOPES, A THREE DIMENSIONAL STUDY. J. Soil Mech. Found. Div. Proc. A.S.C.E. S.M.I. pp. 235-262. Jan. 1969.

64. Londe, P. Vigier, G. and Vormeringer, R. STABILITY OF ROCK SLOPES - GRAPHICAL METHODS. J.Soil. Mech. Found. Div. Proc. A.S.C.E. S.M. 4 pp. 1411-1434. July 1970.

65. John, K.W. GRAPHICAL STABILITY ANALYSES OF SLOPES IN JOINTED ROCK. J. Soil. Mech. Found. Div. Proc. A.S.C.E. S.M.2 pp. 497-526 March 1968.

66. Mueller, L. and John, K.W. RECENT DEVELOPMENT OF STABILITY STUDIES OF STEEP ROCK SLOPES IN EUROPE.Trans.Soc.Min.E. 1963.

67. Bjerrum, L. and Jorstad, F.A. STABILITY OF ROCK SLOPES IN NORWAY. Norwegian Geotechnical Institute Pub. No. 79 Oslo 1968.

68. St. John, C.M. A NOTE ON THE USE OF STRESS DISTRIBUTIONS IN SLOPE STABILITY CALCULATIONS. Contribution to discussion. Symp. on open pit planning. Johannesburg. 1970.

69. Cundall, P.A. Ph.D. Thesis (in preparation) University of London 1971.

70. Jennings, J.E. and Robertson, A. Mac G. THE STABILITY OF SLOPES CUT INTO NATURAL ROCK. VIIth Int. Conf. Soil Mech. Found. Eng. Mexico 1969 pp. 585-590.

71. Jennings, J.E. A MATHEMATICAL THEORY FOR THE CALCULATION OF THE STABILITY OF SLOPES IN OPEN CAST MINES. Symp. on open pit mine planning. Johannesburg. 1970.

72. Terzaghi, K. STABILITY OF STEEP SLOPES ON HARD UNWEATHERED ROCK. Geotechnique Vol. XII No. 4. 1962 pp. 251-270.

73. Mueller, L. THE STABILITY OF ROCK BANK SLOPES AND THE EFFECT OF ROCK WATER ON SAME. Int. J. Rock Mech. Min. Sci. Vol. I pp. 475-504. 1964.

74. Hoek, E. ESTIMATING THE STABILITY OF EXCAVATED SLOPES IN OPENCAST MINES. Inst. Min. and Metall. Trans. Vol. 79. Oct. 1970 pp 109A-132A.

75. Bray, J. SEMINAR ON TOPPLING FAILURE. Rock Mech. Dept. Imperial Coll. London 1969.

76. Roscoe, K.H. ' THE INFLUENCE OF STRAINS IN SOIL MECHANICS. Tenth Rankine Lecture. Geotechnique 20. No. 2 pp 129-170. 1970.

REFERENCES

77. Blake, W. STRESSES AND DISPLACEMENTS SURROUNDING AN OPEN PIT IN A GRAVITY-LOADED ROCK. U.S.B.M. Rept. of Investigations R.1 7002 pp. 1-20 August 1967.

78. Blake, W. FINITE ELEMENT MODEL STUDY OF SLOPE MODIFICATION AT THE KIMBLEY PIT. Trans. Soc. of Min. Engrs. A.I.M.E. Vol. 241 December 1968.

79. Mahtab, M.A. and Goodman, R.E. THREE DIMENSIONAL FINITE ELEMENT ANALYSIS OF JOINTED ROCK SLOPES. Paper 7.12 Vol. 3 Proc. of 2nd Cong. of Int. Soc. for Rock Mech. Belgrade 1970.

80. Zienkiewicz, O.C Best, B. Dullage, C. Stagg, K.G. ANALYSIS OF NON LINEAR PROBLEMS IN ROCK MECHANICS WITH PARTICULAR REFERENCE TO JOINTED ROCK SYSTEMS. Paper 8.14. Vol. 3. Proc. of 2nd Cong. of Int. Soc. for Rock Mech. Belgrade 1970.

81. Hast, N. THE STATE OF STRESS IN THE UPPER PART OF THE EARTH'S CRUST. Eng. Geol. 2(1) pp. 5-17. 1967.

82. Wisecarver, D.W. Merrill, Rausch, D.O. Hubbard, S.J. INVESTIGATION OF INSITU ROCK STRESSES, RUTH MINING DISTRICT, NEVADA, WITH EMPHASIS ON SLOPE DESIGN PROBLEMS IN OPEN-PIT MINES. U.S.B.M. Rept. of Investigations. R.1 6541 March 1964.

83. Li, B. NATURAL STRESS-VALUES OBTAINED IN DIFFERENT PARTS OF THE FENNOSCANDIAN ROCK MASSES. Paper 1.28 Vol. 1. Proc. of 2nd. Cong. of Int. Soc. Rock Mech. Belgrade 1970.

84. Pallister, G.F. Gay, N.C. and Cook, N.G.W. MEASUREMENT OF THE VIRGIN STATE OF STRESS IN ROCK AT DEPTH. Paper 1.5 Vol. 1 Proc. of 2nd. Cong. of Int. Soc. Rock Mech. Belgrade 1970.

85. Hoek, E. Private communication. Rock Mech. Dept. Imperial College. London 1968.

86. Bray, J. Private communication. Rock Mech. Dept. Imperial College. London 1968.

87. Hoek, E. Private communication. Rock Mech. Dept. Imperial College. London 1968.

88. Morgenstern, N. Private communication. Civil Eng. Dept. Imperial College. London 1968.

89. Wickens, E.H. and Barton, N.R. APPLICATION OF PHOTOGRAMMETRY TO THE STABILITY OF EXCAVATED ROCK SLOPES. Photogrammetric Record (Photogrammetry Society, London) No. 37 Vol. 6 April 1971

90. Bray, J.W. A STUDY OF JOINTED AND FRACTURED ROCK. Part I. Felsmechanik Vol. V 2-3 pp 117-136 1967.

REFERENCES

91. Skempton, A.W. THE CONSOLIDATION OF CLAYS BY GRAVITATIONAL COMPACTION. Q. J l. Geol. Soc. London Vol. 125 pp. 373-411. 1970.

92. Hofmann, H. THE DEFORMATION PROCESS OF A REGULARLY JOINTED DISCONTINUUM DURING THE EXCAVATION OF A CUT. Paper 7.1 Vol. 3. Proc. of 2nd. Cong. of Int. Soc. Rock Mech. Belgrade 1970.

93. Muller, L. and Hofmann, H. SELECTION, COMPILATION AND ASSESSMENT OF GEOLOGICAL DATA FOR THE SLOPE PROBLEM. Symp. on Open pit mine planning. Johannesburg 1970.

94. St. John, C.M. Private communication. Rock Mech. Dept. Imperial College, London 1970.

95. Duncan, J.M. and Goodman, R.E. FINITE ELEMENT ANALYSIS OF SLOPES IN JOINTED ROCK.Contract report S-68-3. Univ. of California, Berkeley. 1968.

REFERENCES IN APPENDICES

1. Holdridge, D.A. and Walker, E.G. THE DEHYDRATION OF GYPSUM AND THE REHYDRATION OF PLASTER. Trans. Brit. Cer. Soc. Vol. 66 pp 485-509 1967.

2. Schiller, K.K. POROSITY AND STRENGTH OF BRITTLE SOLIDS (with particular reference to gypsum). MECHANICAL PROPERTIES OF NON-METALLIC BRITTLE MATERIALS. Ed. Walton. Butterworths, Ch. 3, 1958.

3. Hoek, E. Private communication. Rock Mech. Dept. Imperial College London. 1968.